ÉCOLE POLYTECHNIQUE DE BRUXELLES
UNIVERSITÉ LIBRE DE BRUXELLES

Analysis of the Stability of a Flat-Plate High-Speed Boundary Layer with Discrete Roughness

Thesis presented by Iván PADILLA MONTERO
with a view to obtaining the PhD Degree in Engineering Sciences and Technology ("Docteur en Sciences de l'Ingénieur et Technologie")
Academic year 2020-2021

Supervisor: Prof. Axel COUSSEMENT
Co-supervisor: Prof. Gérard DEGREZ
Co-supervisor: Dr. Fabio PINNA

Thesis jury:

Alessandro PARENTE (Université Libre de Bruxelles, President)
Gérard DEGREZ (Université Libre de Bruxelles, Secretary)
Axel COUSSEMENT (Université Libre de Bruxelles)
Stefan HEIN (Deutsches Zentrum für Luft- und Raumfahrt)
Vassilis THEOFILIS (University of Liverpool)
Fabio PINNA (von Karman Institute for Fluid Dynamics)

European Commission

von KARMAN INSTITUTE FOR FLUID DYNAMICS

Université Libre de Bruxelles
École Polytechnique de Bruxelles
Departement d'Aéro-thermo-mécanique

von Karman Institute for Fluid Dynamics
Aeronautics and Aerospace Department

Analysis of the Stability of a Flat-Plate High-Speed Boundary Layer with Discrete Roughness

Iván Padilla Montero

Thesis presented in order to obtain the degree of
Doctor of Philosophy in Engineering Sciences
Université Libre de Bruxelles
May 2021

Université Libre de Bruxelles
École Polytechnique de Bruxelles
Departement d'Aéro-thermo-mécanique

von Karman Institute for Fluid Dynamics
Aeronautics and Aerospace Department

Supervisors:
Dr. Fabio Pinna (von Karman Institute for Fluid Dynamics, Belgium)
Prof. Axel Coussement (Université Libre de Bruxelles, Belgium)
Prof. Gérard Degrez (Université Libre de Bruxelles, Belgium)

Doctoral Committee:
Prof. Gérard Degrez (Secretary, Université Libre de Bruxelles, Belgium)
Prof. Alessandro Parente (President, Université Libre de Bruxelles, Belgium)
Prof. Axel Coussement (Université Libre de Bruxelles, Belgium)
Dr. Stefan Hein (Deutsches Zentrum für Luft- und Raumfahrt, Germany)
Prof. Vassilis Theofilis (University of Liverpool, United Kingdom)
Dr. Fabio Pinna (von Karman Institute for Fluid Dynamics, Belgium)

von Karman Institute for Fluid Dynamics
Aeronautics and Aerospace Department

Waterloosesteenweg 72, 1640 Sint-Genesius-Rode
Phone: +32 359 96 11, https://www.vki.ac.be

D/xxxx/xxxx/xxx, T. Magin, Editor-in-Chief
Published by the von Karman Institute for Fluid Dynamics with permission.

ISBN xxx-x-xxxxx-xxx-x

A mis padres, Maribel y Alfonso.

Acknowledgments

This doctoral work would not have been possible without the guidance, inspiration and support of many different people during the last four and a half years. For this reason, I would like to dedicate the following lines to express my gratitude for their role and contributions.

First of all, I feel deeply thankful to my supervisor Fabio Pinna, whose door was always (and I really mean always) open for discussion and whose continuous guidance and motivation allowed me to stay on track and keep climbing the mountain. Fabio, you trusted me since the beginning and enabled me to be part of a great European network, which put my life in a suitcase during the first half of this PhD and opened the door to many international experiences. For me, that I had never left my nest before, this journey brought along an immense personal growth. At the same time, you directly made me part of the phenomenal team that you assembled during the past few years at the von Karman Institute, your beloved "transition group". It is also to the other members of this team, Fernando Miró, Ludovico Zanus, Simon Demange and Florian Danvin, that I would like to express my most sincere gratitude for the time we spent together and for all the lessons I could learn from them. Our strong synergies allowed us to see further and grow our ambitions. In particular, Fernando, your love and dedication for this subject encouraged and accelerated our progress, and pushed us forward to reach goals that we could not possibly have foreseen in the beginning. Even today, after these years, I am still appreciating the magnitude of your work. Ludovico, our daily discussions in the office and your accurate physical insight served as a great source of inspiration to spark new ideas and solve problems.

I would like to acknowledge that this work was not built from scratch. Rather, it was developed on a solid base crafted with the effort of the several previous contributors that brought the VESTA toolkit to an integral and functional piece of software. In this regard, besides the original outstanding effort of Fabio Pinna, I also feel grateful to Koen Groot for his extraordinary prior work on the BiGlobal stability solver in VESTA, which, together with his detailed master thesis dissertation, helped me to understand many of the devilish details behind the theory and the numerical implementation of the tool. Thanks Koen for your detailed explanations and your advice during the few times that we met. A big thank you goes also to Miguel Hermanns from Universidad Politécnica de Madrid for happily shar-

ing his library of computational routines that implement the FD-q discretization, which greatly enhanced the performance of our solver.

Being part of the SSeMID European network allowed me to take part in numerous workshops and conferences around Europe and USA. Now, after the project has finished, I also feel a strong sense of gratitude to those colleagues from the network with whom I shared multiple trips and uncountable good moments. Thanks to this network, I could also learn a lot from my visiting appointments at DLR in Göttingen and at the PETAL facility in Purdue University. Thank you Stefan Hein for your warm welcome in Göttingen and for showing me the history and beauty of the DLR site, as well as for making me feel a member of your team. I must thank Alex Theiss, Francesco Tocci and Juan Alberto Franco for making my time in Göttingen a great experience and for showing me how father's day should be properly celebrated in Germany. Alex, I want to acknowledge that the best student paper award in the flight physics category of the EUCASS 2017 conference is yours. The way in which it was assigned to me in second place is not fair and will never be. Despite this particular circumstance in which we got to know each other, today I am very happy to tell that our overlapping research topics made us build a very good friendship during my time at DLR and I could learn a lot from you.

Thank you Guillermo Paniagua for the opportunity to work in your team and your lab during my period in West Lafayette. It was during those three intense months of freezing north American winter that I could learn all that I now know about experimental fluid mechanics. I want to thank all the members that were part of the PETAL team back then, specially Jorge Saavedra, David González, James Braun and Francisco Lozano for making me feel part of it since the very first day. Lastly, I would also like to thank Antonio García-Uceda for my brief visits at Numeca International.

I feel also very grateful to the VKI and the working environment it provided during this period. Its multi-cultural familiar atmosphere (very often Italian-biased during these years) is something that I will surely miss in the future. Sharing lunch with so many colleagues every day brings a rewarding experience and the opportunity to continuously meet many different people. A big thank you goes to my closest VKI friends with whom I also spent most of my time in Belgium. Special thanks go to Charline Fouchier for the time we shared together in the office and for the numerous squash matches that we played; to Ludovico Zanus for the running sessions and the races we did together; and to Andrea Attavino for all the lunches, dinners and parties in the flat which made me discover the awesomeness and pride behind Italian food. Thank you also to Simon Demange, Florian Danvin, Fran Torres, Riccardo Zamponi, Vincent F. Giangaspero, Adriana Enache and many others for the time spent together.

A thankful thought goes also to those teachers who, with their passion and dedication, inspired and encouraged me to pursue the goals that I targeted. I feel specially thankful to Roberto Flores from Universitat Politècnica de Catalunya for supporting my PhD application.

I would also like to express my gratitude to the jury members of this doctoral

thesis, for their effort in evaluating the work and for providing a very valuable feedback.

Thinking outside of the Brussels life, I want to thank as well my lifelong friends back home, in Ripollet, for supporting me with my decision to embark on a PhD endeavour abroad but also for making me feel that, when we are together, our essence remains intact despite the distance during the last years. This includes also you, Enric, for your untouchable memory helped me through the most difficult moments during this period, and surely it will continue to do it in the future. The other members of the "aero" team from our beloved EETAC also deserve a mention here, as the numerous games we played made it easier to relieve my mind from the daily research challenge, specially during the last year when we had to stay at home for long periods of time. I am forever grateful for your jokes, shouts and songs.

Finally, I must wholeheartedly thank my family for their invaluable support throughout these years. In particular to my parents, for their continuous love and understanding during this long stage far from home. Our (almost) daily calls helped to keep my mind in peace and to stay focused on the most important things.

Thank you all!

Iván Padilla Montero
Brussels, May 2021

This doctoral work is part of a project that has received funding from the European Union's Horizon 2020 research and innovation programme under the Marie Skłodowska-Curie grant agreement No 675008. This work would not have been possible without the mobility and research independence that this funding provided during the first three years of this PhD.

Email address for correspondence: ivan.padilla6@gmail.com

Abstract

Boundary-layer transition from a laminar to a turbulent regime is a critical driver in the design of high-speed vehicles. The aerothermodynamic loads associated with transitional or fully turbulent hypersonic boundary layers are several times higher than those associated with laminar flow. The presence of isolated roughness elements on the surface of a body can accelerate the growth of incoming disturbances and introduce additional instability mechanisms in the flow field, eventually leading to a premature occurrence of transition.

This dissertation studies the instabilities induced by three-dimensional discrete roughness elements located inside a high-speed boundary layer developing on a flat plate. Two-dimensional local linear stability theory (2D-LST) is employed to identify the instabilities evolving in the three-dimensional flow field that characterizes the wake induced by the roughness elements and to investigate their evolution downstream. A formulation of the disturbance energy evolution equation available for base flows depending on a single spatial direction is generalized for the first time to base flows featuring two inhomogeneous directions and perturbations depending on three spatial directions. This generalization allows to obtain a decomposition of the temporal growth rate of 2D-LST instabilities into the different contributions that lead to the production and dissipation of the total disturbance energy. This novel extension of the formulation provides an additional layer of information for understanding the energy exchange mechanisms between a three-dimensional base flow and the perturbations resulting from 2D-LST.

Stability computations for a calorically perfect gas illustrate that the wake induced by the roughness elements supports the growth of different sinuous and varicose instabilities which coexist together with the Mack-mode perturbations that evolve in the flat-plate boundary layer, and which become modulated by the roughness-element wake. A single pair of sinuous and varicose disturbances is found to dominate the wake instability in the vicinity of the obstacles. The application of the newly developed decomposition of the temporal growth rate reveals that the roughness-induced wake modes extract most of their potential energy from the transport of entropy fluctuations across the base-flow temperature gradients and most of their kinetic energy from the work of the disturbance Reynolds stresses against the base-flow velocity gradients. Further downstream, the growth rate of the wake instabilities is found to be influenced by the presence of Mack-mode disturbances developing on the flat plate. Strong evidence is observed of a continuous synchronization mechanism between the wake instabilities and the Mack-mode perturbations. This phenomenon leads to an enhancement of the amplification rate

of the wake modes far downstream of the roughness element, ultimately increasing the associated integrated amplification factors for some of the investigated conditions.

The effects of vibrational molecular excitation and chemical non-equilibrium on the instabilities induced by a roughness element are studied for the case of a high-temperature boundary layer developing on a sharp wedge configuration. For this purpose, a 2D-LST solver for chemical non-equilibrium flows is developed for the first time, featuring a fully consistent implementation of the thermal and transport models employed for the base flow and the perturbation fields. This is achieved thanks to the automatic derivation and implementation tool (ADIT) available within the von Karman Institute extensible stability and transition analysis (VESTA) toolkit, which enables an automatic derivation and implementation of the 2D-LST governing equations for different thermodynamic flow assumptions and models. The stability computations for this configuration show that sinuous and varicose disturbances also dominate the wake instability in the presence of vibrational molecular energy mode excitation and chemical reactions. The resulting base-flow cooling associated with the modeling of such high-temperature phenomena is found to have opposite stabilizing and destabilizing effects on the streamwise evolution of the sinuous and varicose instabilities. The modeling of vibrational excitation and chemical non-equilibrium acting exclusively on the perturbations is found to have a stabilizing influence in all cases.

Table of Contents

Nomenclature

Acronyms

2D-LST	Two-dimensional local linear stability theory
3D-NPSE	Three-dimensional non-linear parabolized stability equations
3D-PSE	Three-dimensional parabolized stability equations
ADIT	Automatic derivation and implementation tool
AHLNS	Adaptive harmonic linearized Navier-Stokes
BC	Boundary condition
BL	Boundary layer
BLTFE	Boundary-layer transition flight experiment
CAS	Computer algebra system
CFD	Computational fluid dynamics
CGL	Chebyshev-Gauss-Lobatto
CNE	Chemical non-equilibrium
CPG	Calorically perfect gas
DEKAF	Digits by Ethan, Koen, Alex and Fernando
DMD	Dynamic mode decomposition
DNS	Direct numerical simulation
DSMC	Direct simulation Monte Carlo
EI	Entry interface
FFT	Fast Fourier transform
GEVP	Generalized eigenvalue problem
GW	Gupta-Wilke transport model

HLLC	Harten-Lax-van Leer contact approximate Riemann solver
HYTHIRM	Hypersonic thermodynamic infrared measurements
IRAM	Implicitly restarted Arnoldi method
ISS	International space station
IVP	Initial value problem
LAPACK	Linear algebra package
LDNS	Linearized direct numerical simulation
LNSE	Linearized Navier-Stokes equations
LST	Local linear stability theory (one-dimensional)
LTE	Local thermodynamic equilibrium
M2D	Two-dimensional (spanwise constant) Mack mode obtained using 2D-LST
MO#	Oblique Mack mode number # obtained using 2D-LST
NPSE	Non-linear parabolized stability equations
NS	Navier-Stokes
ODE	Ordinary differential equation
PIV	Particle image velocimetry
PNS	Parabolized Navier-Stokes
POD	Proper orthogonal decomposition
PSE	Parabolized stability equations
RCC	Reinforced carbon-carbon
RHS	Right-hand side
RQI	Rayleigh quotient iteration
RRHO	Rigid rotor and harmonic oscillator thermal model
SI	Système international (international system of units)
SIN1	Most unstable sinuous instability
STS	Space transportation system
SVD	Singular value decomposition

TCNE	Thermo-chemical non-equilibrium
TPG	Thermally perfect gas
TPS	Thermal protection system
TS	Tollmien-Schlichting wave
TTP	Thermodynamic and transport properties
TVD	Total variation diminishing
VCOS1	Most unstable varicose instability
VESTA	VKI extensible stability and transition analysis
VKI	von Karman Institute
WKB	Wentzel-Kramers-Brillouin approximation

Greek Symbols

α	Perturbation complex streamwise wavenumber [1/m]
β	Perturbation complex spanwise wavenumber [1/m]
δ	Dirac delta function [-]
δ_{99}	Boundary-layer thickness [m]
η	Transformed variable along the second dimension of the collocation grid [-]
η	Wall-normal coordinate in the transformed boundary-layer equations [-]
Γ	Integration boundary [m^2]
γ	Ratio of specific heats [-]
$\hat{\delta}$	Modified Dirac delta function [-]
λ	Bulk viscosity coefficient (mixture bulk viscosity coefficient) [kg/(m s)]
λ_x	Perturbation streamwise wavelength [m]
λ_z	Perturbation spanwise wavelength [m]
μ	Dynamic viscosity (mixture dynamic viscosity) [kg/(m s)]
μ_s	Dynamic viscosity of species s [kg/(m s)]
ν	Kinematic viscosity (mixture kinematic viscosity) [kg/(m s)]

$\nu''_{s,r}$	Stoichiometric mole number of the product species s in reaction r [-]
$\nu'_{s,r}$	Stoichiometric mole number of the reactant species s in reaction r [-]
Ω	Integration domain in three-dimensions [m^3]
ω	Perturbation complex angular frequency [rad/s]
ϕ_s^μ	Mixing coefficient of species s in Wilke's mixing rule [-]
ρ	Density (mixture density) [kg/m^3]
ρ_s	Density of species s [kg/m^3]
σ	Shift-invert parameter [various]
τ_{xx}, τ_{yy}, τ_{zz}	Viscous normal stresses [Pa]
τ_{xy}, τ_{xz}, τ_{yz}	Viscous shear stresses (identical to τ_{yx}, τ_{zx} and τ_{zy}, respectively) [Pa]
Θ	Perturbation phase function [-]
θ	Wedge angle (also for ramp roughness shape) [deg]
ξ	Streamwise (marching) variable in the transformed boundary-layer equations [kg^2/(m^2 s^2)]
ξ	Transformed variable along the first dimension of the collocation grid [-]
ξ_x	Streamwise vorticity [1/s]

Roman Symbols

$(\Delta h_f)_s^{T_{\text{ref}}}$	Enthalpy of formation of species s at a reference temperature T_{ref} [J/kg]
Δu_{st}	Streak amplitude [m/s]
Δx	Streamwise step size [m]
$\dot{w}_s$	Mass production rate of species s [kg/(m^3 s)]
$\hat{E}_K$	Amplitude function of the disturbance kinetic energy [J]
$\mathbf{A}_\alpha$, $\mathbf{B}_\alpha$, $\mathbf{C}_\alpha$	Matrices of the spatial LST/2D-LST differential generalized eigenvalue problem [various]
$\mathbf{A}_\omega$, $\mathbf{B}_\omega$	Matrices of the temporal LST/2D-LST differential generalized eigenvalue problem [various]

$\mathbf{D}_\xi, \mathbf{D}_\eta$	First derivative differentiation matrix along the ξ or η directions [-]
$\mathbf{D}_{\xi\eta}$	Cross derivative differentiation matrix [-]
$\mathbf{D}_{\xi\xi}, \mathbf{D}_{\eta\eta}$	Second derivative differentiation matrix along the ξ or η directions [-]
$\mathbf{e}_x$	Unit vector along x [-]
$\mathbf{e}_y$	Unit vector along y [-]
$\mathbf{e}_z$	Unit vector along z [-]
$\mathbf{f}$	Forcing vector in the system of non-linear parabolized stability equations [various]
$\mathbf{I}$	Identity matrix [-]
$\mathbf{J}$	Energy diffusion flux [J/(m^2 s)]
$\mathbf{j}_s$	Mass diffusion-flux vector of species s [kg/(m^2 s)]
$\mathbf{L}$, $\mathbf{M}$, $\mathbf{N}$	Matrix operators containing the coefficients of the PSE system of governing equations [various]
$\mathbf{M}$	Diagonal matrix with the coefficients multiplying each disturbance variable in Chu's energy norm [various]
$\mathbf{q}$	Vector of state variables [various]
$\mathcal{D}_{eff,s}$	Effective diffusion coefficient of species s [m^2/s]
$\mathcal{D}_{sm}$	Multicomponent diffusion coefficient for the diffusion of species s into the mixture [m^2/s]
$\mathcal{R}$	Set of all the reactions in a mixture [-]
$\mathcal{S}$	Set of all the species in a mixture [-]
Pr	Prandtl number [-]
$\mathscr{D}$	Perturbation dispersion relation [rad/s]
$\mathscr{M}$	Molar mass (mixture molar mass) [kg/mol]
$\mathscr{M}_s$	Molar mass of species s [kg/mol]
$\mathscr{R}$	Universal gas constant (8.3144 J/(mol K))
$\tilde{E}$	Non-dimensional total disturbance energy according to the definition of Chu [-]

$\tilde{Q}$	Non-dimensional specific disturbance heat source [-]
$\mathbf{V}$	Velocity vector [m/s]
A	Perturbation amplitude [-]
a	Speed of sound [m/s]
$A^0_{m,n}$	Initial amplitude of mode defined by the mth and nth harmonics of the fundamental spanwise wavenumber and frequency [-]
A^f_r	Arrhenius pre-exponential factor for reaction r [(m^3/mol)$^{\sum_s \nu'_{s,r}-1}$ s^{-1} K$^{-n^f_r}$]
A^μ_s, B^μ_s, C^μ_s	Polynomial coefficients for the curve fits of the Gupta-Wilke viscosity model [various]
A^k_s, ..., E^k_s	Polynomial coefficients for the curve fits of the Gupta-Wilke thermal conductivity model [various]
$a_{1,s}, ..., a_{5,s}$	Coefficients of the polynomial curve fits employed to model the variation of the specific heat at constant pressure of species s as a function of temperature (see equation (2.45)) [various]
$b_{1,s}, b_{2,s}$	Additional curve-fit coefficients employed to model the variation of the static enthalpy and Gibbs free energy of species s as a function of temperature (see equation (2.45)) [various]
C	Chapman-Rubesin parameter [-]
c_f	Skin friction coefficient [-]
c_g	Group velocity [m/s]
c_p	Specific heat at constant pressure (mixture specific heat at constant pressure) [J/(kg K)]
c_s	Mass fraction of species s [-]
c_v	Specific heat at constant volume (mixture specific heat at constant volume) [J/(kg K)]
$c_{p,s}$	Specific heat at constant pressure of species s [J/(kg K)]
c_{ph}	Phase velocity [m/s]
$d\mathcal{V}$	Infinitesimal volume element [m^3]
dS	Infinitesimal surface element [m^2]
e	Specific internal energy (mixture specific internal energy) [J/kg]

f	Perturbation frequency [Hz]
f	Stream function in the transformed boundary-layer equations [-]
G	Optimal transient growth [-]
g	Ratio of static enthalpy to static enthalpy at the boundary-layer edge [-]
g_s^{atm}	Specific Gibbs free energy of species s at atmospheric pressure [J/kg]
h	Roughness height [m]
h	Specific static enthalpy (mixture specific static enthalpy) [J/kg]
h_0	Specific total enthalpy (mixture specific total enthalpy) [J/kg]
h_s	Specific static enthalpy of species s [J/kg]
i	Imaginary unit [-]
k	Thermal conductivity (mixture thermal conductivity) [W/(m K)]
k_s	Thermal conductivity of species s [W/(m K)]
$k_{b,r}$	Backward reaction-rate constant of reaction r [(m^3/mol)$^{\sum_s \nu''_{s,r}-1}$ s^{-1}]
$K_{c,r}^{eq}$	Equilibrium constant of reaction r based on concentrations [(m^3/mol)$^{\sum_s \nu'_{s,r}-\nu''_{s,r}}$]
$k_{f,r}$	Forward reaction-rate constant of reaction r [(m^3/mol)$^{\sum_s \nu'_{s,r}-1}$ s^{-1}]
$K_{p,r}^{eq}$	Equilibrium constant of reaction r based on pressure [(Pa)$^{\sum_s \nu''_{s,r}-\nu'_{s,r}}$]
Kn	Knudsen number [-]
l	Boundary-layer length scale (reference length used for non-dimensionalization) [m]
M	Freestream Mach number [-]
m	Spanwise wavenumber harmonic number [-]
N	Integrated logarithmic amplification factor [-]
n	Coordinate normal to the wall [m]

n	Frequency harmonic number [-]
N_η	Number of collocation points along the η direction [-]
N_ξ	Number of collocation points along the ξ direction [-]
N_m	Total number of spanwise wavenumber harmonics [-]
N_n	Total number of frequency harmonics [-]
n_r^f	Arrhenius temperature exponent for reaction r [-]
N_s	Total number of species in a mixture [-]
n_x, n_y, n_z	Components of the outward unit vector normal to Γ [-]
N_x, N_y, N_z	Number of grid points along x, y or z [-]
p	Pressure (mixture pressure) [Pa]
p_{atm}	Atmospheric pressure (101325 Pa)
p_s	Pressure of species s (partial pressure) [Pa]
Pr	Freestream Prandtl number [-]
Q	Generic dependent flow quantity [various]
q	Generic independent flow quantity [various]
q_p	Degree of the interpolating polynomials in the FD-q discretization method [-]
q_x, q_y, q_z	Components of the conductive heat-flux vector [W/m^2]
R	Specific gas constant (mixture gas constant) [J/(kg K)]
r	Generic reaction [-]
R_s	Specific gas constant of species s [J/(kg K)]
Re	Freestream Reynolds number based on the boundary-layer length scale l [-]
Re_h	Roughness Reynolds number [-]
$Re_{h,w}$	Modified roughness Reynolds number (viscosity evaluated at the wall) [-]
s	Generic species [-]
s	Specific entropy (mixture specific entropy) [J/(kg K)]
S_μ	Sutherland temperature for μ [K]

S_k	Sutherland temperature for k [K]
Sc	Schmidt number [-]
St	Stanton number [-]
T	Temperature [K]
t	Time [s]
T_r^f	Arrhenius activation temperature for reaction r [K]
T_{ad}	Adiabatic wall temperature [K]
u	Velocity component along x [m/s]
u_s	Streamwise shear magnitude [1/s]
v	Velocity component along y [m/s]
w	Velocity component along z [m/s]
x	Streamwise coordinate in the Cartesian reference frame [m]
X_s	Mole fraction of species s [-]
y	Wall-normal coordinate in the Cartesian reference frame [m]
y^+, y^-	Generic upper and lower limits of integration along the y direction [m]
z	Spanwise coordinate in the Cartesian reference frame [m]
z^+, z^-	Generic upper and lower limits of integration along the z direction [m]

Subscripts and Superscripts

$\bar{q}$	Base-flow quantity
$\check{q}$	Time-dependent amplitude function of a perturbation quantity $\tilde{q}$
$\hat{q}$	Amplitude function of a perturbation quantity $\tilde{q}$
$\mathbf{q}^{\mathrm{T}}$	Transpose of vector or matrix quantity $\mathbf{q}$
$\mathbf{q}^H$	Hermitian transpose of vector or matrix quantity $\mathbf{q}$
$\tilde{q}$	Perturbation quantity
q'	Non-dimensional quantity
q^*	Complex conjugate of quantity q

q_0	Stagnation (total) quantity
q_∞	Value of quantity q in the freestream (equivalent to the far-field boundaries of the computational domain)
q_e	Value of quantity q at the boundary-layer edge
q_i or $\Im\{q\}$	Imaginary part of complex quantity q
q_r	Reaction-specific quantity
q_r or $\Re\{q\}$	Real part of complex quantity q
q_s	Species-specific quantity
q_w	Value of quantity q at the wall
q_{ref}	Value of quantity q at a given reference state
$q_{m,n}$	Quantity associated to the mode defined by the mth and nth harmonics of the fundamental spanwise wavenumber and frequency, respectively

1 Introduction

1.1 Atmospheric entry

During the past sixty years, the first steps in human space exploration have become a reality. The development of space science and technology has enabled humans to access outer space and orbit around the Earth, as well as giving birth to interplanetary travel through the solar system. Up to date, these advancements have led humans to land on the Moon, robotic rovers to land on Mars and space probes to visit other planets and asteroids, including landings on the surface of Venus and Saturn's moon Titan.

Whether crewed or not, space missions requiring landing on the surface of a planet with an atmosphere, including missions requiring a return to Earth, have to deal with the challenge of atmospheric entry. In this context, the term atmospheric entry refers to the movement of an object from outer space into and through the gas of a planet's atmosphere. While in outer space, spacecraft returning from orbit around a planet or arriving to it following an interplanetary trajectory, move at a very high speed relative to that of the gas in the planet's atmosphere. As an example, the International Space Station (ISS) orbits the Earth at an approximate velocity of 7.7 km/s (at a height of about 420 km). When a spacecraft docked to the ISS performs a deorbit burn to return to Earth, such as the Space Shuttle Orbiter or the Soyuz capsule, it begins to enter the Earth atmosphere at a speed near 7.7 km/s (Mach number near 24). Similarly, a spacecraft returning from Mars in a Mars-Earth transfer trajectory, would reach the Earth atmosphere at about

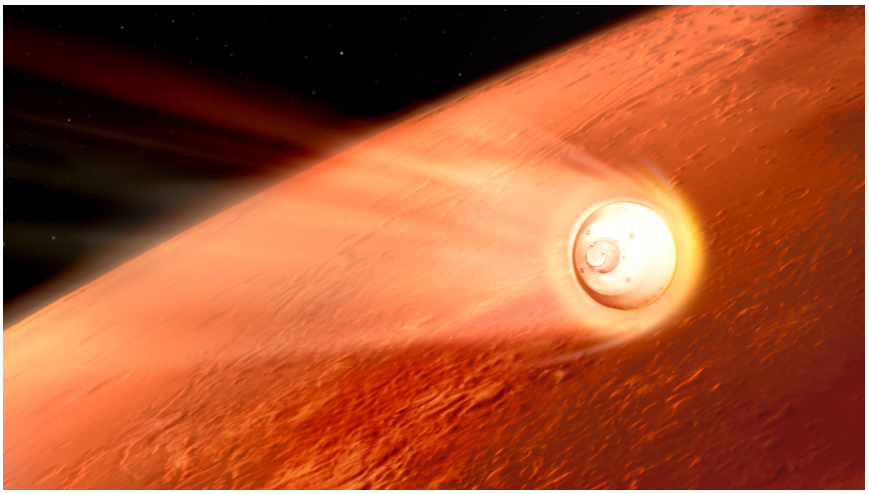

Figure 1.1: Artwork of the spacecraft carrying NASA's Perseverance rover decelerating in the atmosphere of Mars. Perseverance landed successfully on the surface of Mars on the 18th of February 2021. Credit: NASA.

15 km/s (approximately at Mach number 45). Traveling through the gas medium at such high velocity generates a large amount of atmospheric drag, caused both by the compression of the gas in front of the vehicle (pressure drag) and by the friction against the vehicle's surface (skin-friction drag). This force serves the purpose of slowing down the spacecraft but at the same time it induces strong aerothermodynamic loads on the surface of the vehicle, leading to enormous heat transfer rates.

At first glance, it might seem reasonable to think that other alternatives such as rocket propulsion or the use of parachutes could provide a controlled entry, descent and landing. Nevertheless, current propulsion technologies do not allow for this process to be efficient, as an enormous amount of fuel would be necessary on-board the spacecraft to provide the large amount of deceleration required. Similarly, currently existing materials are not able to withstand the stresses that would be encountered when deploying a parachute at such high speed. For these reasons, atmospheric entry at high speed is the only effective braking option available at present. It is important to note, however, that parachutes and rocket propulsion are often employed during the final phases of the descent and landing processes of non-lifting vehicles, such as Earth return capsules or Mars entry spacecraft (vehicles such as the Space Shuttle Orbiter do not require such technologies as they are capable of controlled gliding and landing on a runway). However, they are used only to further decrease the velocity of the spacecraft beyond its terminal velocity, so to ensure a safe impact against water or land. Most of the deceleration is in all

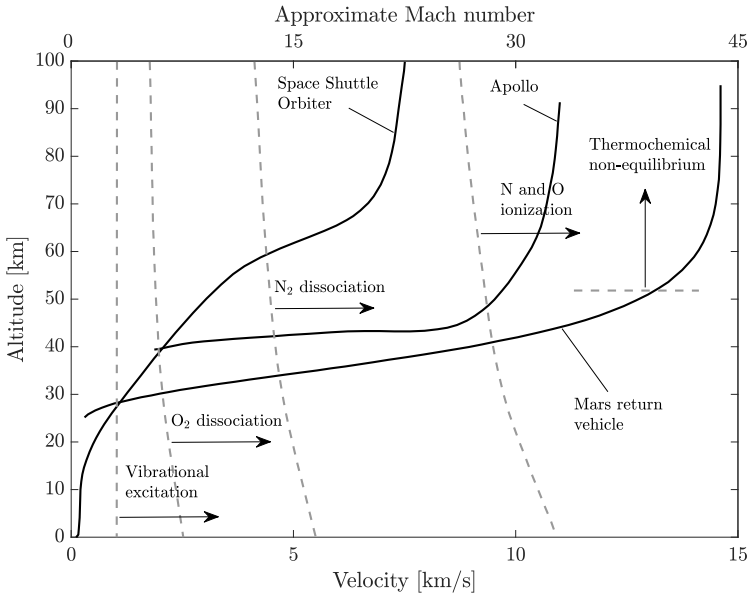

Figure 1.2: Velocity-altitude map illustrating the reentry trajectories of different spacecraft into Earth's atmosphere. The thresholds above which different high-enthalpy effects become important are denoted by dashed lines. Adapted from the map provided by Rivell [1].

cases achieved through atmospheric drag during the entry phase.

During the atmospheric entry process, the kinetic energy of the spacecraft is invested into heating up the gas around it. The physical mechanisms by which this conversion takes place are generally described by the theory of hypersonic and high-temperature gas dynamics, also commonly known as hypersonic aerodynamics. Although no rigorous definition of hypersonic flow exists, a flow is considered to be hypersonic when its Mach number is high enough so that certain physical flow phenomena become important (see Anderson [2]). The main phenomena that characterize hypersonic flows are thin shock layers, entropy layers, viscous interactions, low-density (rarefied) gas effects and high-enthalpy effects. The latter are a consequence of the high temperatures that can be reached by a gas flowing past a body at very high speed.

High-temperature flows are characterized by the coexistence of multiple physical phenomena, which include the excitation of the rotational, vibrational and electronic molecular energy modes, the dissociation of gas molecules into monoatomic species and, for very high temperatures, a ionization of such dissociated atoms. As a result, the analysis of high-enthalpy effects during the different stages of the atmospheric entry process is a complex matter that involves the coupling of several phenomena which often feature different characteristic time and length scales.

Figure 1.2 illustrates a velocity-altitude map showing the estimated trajectories for different spacecraft reentering the Earth atmosphere. Different regions of the plot highlight the different high-temperature phenomena encountered during the reentry trajectory. Note that vehicles entering the atmosphere from outside the Earth orbit feature a significantly higher entry velocity and consequently undergo much higher aerothermodynamic loads.

1.1.1 The problem of aerodynamic heating

The strong drag encountered during atmospheric entry results in big heat transfer rates on the surface of a vehicle. The need to accommodate all this heat in order to maintain the structural integrity of the spacecraft and to keep the temperature inside within the required limits constitutes what is known as the problem of aerodynamic heating [3].

The temperature of the gas in contact with the surface during entry typically ranges between 1500 and 2000 K[1]. For example, the leading edge surface temperature at the point of maximum heating during the nominal reentry trajectory of the Space Shuttle Orbiter is approximately 1800 K [4, 5]. Materials employed for aeronautical engineering applications are by no means capable of withstanding such strong thermal loads. For this reason, spacecraft designed to undergo atmospheric entry employ thermal protection systems (TPS), which are surface layers of heat-resistant materials specifically designed to maintain the structural integrity of the spacecraft. TPS can be reusable, such as in the case of the Space Shuttle Orbiter, or single-use, such as the ablative heat shields employed in reentry capsules like Apollo, Soyuz, Orion or Dragon. The left image in figure 1.3 depicts the Apollo command module after reentry, showing how the ablative material degraded during the process, leaving a rough surface. In contrast, the right image in figure 1.3 illustrates the thermal protection system of the Space Shuttle Atlantis near the nose region. In this case, the system mainly consists of reusable surface insulation tiles, together with a reinforced carbon-carbon (RCC) composite material in the nose cap and the wing leading edges, which are the regions exposed to the highest temperatures.

The complexity of the physical phenomena taking place during atmospheric entry makes it difficult to perform accurate predictions of the heat loads at which a vehicle will be exposed. For a given mission, these uncertainties lead to the need of using big safety factors during the design process, which generally result in oversized thermal protection systems. This, in turn, translates in a higher structural weight and a detriment in the payload capacity of the spacecraft, ultimately increasing the mission cost.

[1] It is important to note that this is the temperature of the gas immediately in contact with the surface. The temperature of the gas in the shock layer established between the bow shock wave in front of a vehicle and the surface can be as high as 11000 K [2].

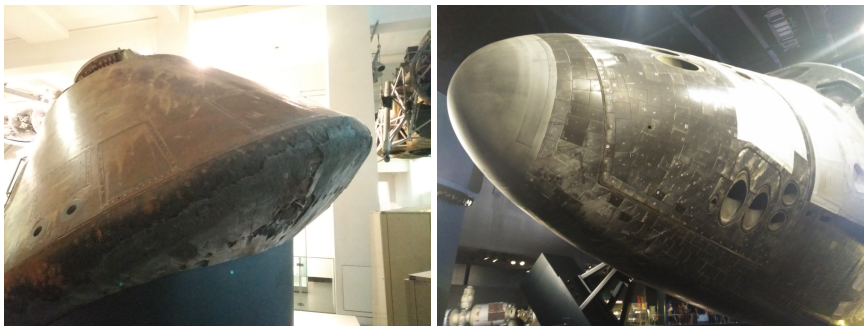

Figure 1.3: (left) Apollo command module on display at the Science Museum, London, 6 August 2019; (right) Front part of Space Shuttle Atlantis, on display at Kennedy Space Center, FL, USA, 12 January 2018. Pictures taken by I. Padilla Montero.

Perhaps the most important uncertainty originates from our current inability to predict the boundary-layer transition process in practical configurations. It is well known that when a boundary layer transitions from the laminar to the turbulent regime in hypersonic flow, the heat flux at the wall increases dramatically. During the transition process, the heat-transfer coefficient can surpass the laminar value by almost an order of magnitude [3], even overshooting the value in the fully developed turbulent regime, which in general is already several times higher than the laminar counterpart. For example, the turbulent heat-transfer coefficient on a flat plate in free flight at Mach 6 and at a Reynolds number of 10^7 is six times bigger than the respective laminar value [3]. It becomes clear, then, that a vehicle undergoing atmospheric entry in the turbulent regime will be exposed to significantly higher temperatures than in the laminar case. In the design process, conservative estimations are of paramount importance to ensure that safety remains the top priority. Given the uncertainties in transition prediction, this often implies the assumption of fully turbulent flow along the entire reentry trajectory.

To illustrate the importance of transition during reentry, the left plot in figure 1.4 shows the in-flight temperature signal recorded by one of the temperature sensors (thermocouples) located in the windward surface of the Space Shuttle Discovery during the reentry of STS-119, as reported by Berger *et al.* [5]. For this flight, different thermocouples were installed near the predicted wake region behind an artificial protuberance that was placed on a wing of the Orbiter to investigate boundary-layer transition, in the context of the project known as boundary-layer transition flight experiment (BLTFE). The temperature signal represented here corresponds to the thermocouple labeled TC1 in [5], which was intended to be located in the central wake region behind the protuberance. As it can be observed, a large increase in temperature is recorded at $t \approx 970$ s, which is attributed

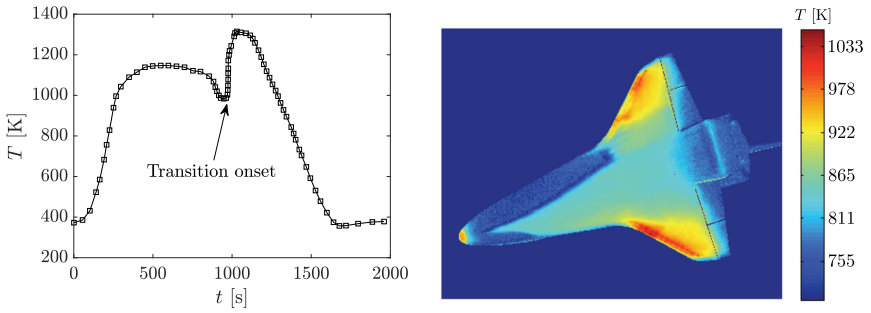

Figure 1.4: (left) Temperature signal recorded by a thermocouple (labeled as TC1) located in the wake behind a protuberance installed on a wing of the Space Shuttle Discovery (windward surface), during the reentry flight of STS-119. The data represented here has been manually extracted from the original signal shown in figure 9 of reference [5]. The uncertainty in the measurement is estimated to be ± 11 *K. Signal time is measured with respect to the time at which the Orbiter altitude is* 122 *km (*400000 *ft), known as the entry interface (EI); (right) Surface temperature map of Space Shuttle Endeavour during the reentry flight of STS-134, obtained by means of infrared thermography (flight Mach number* 5.8*, angle of attack* 28.8 *deg). Adapted from [6].*

to boundary-layer transition. The corresponding flight Mach number at that instant is estimated to be 15.6. Note that the surface temperature jump is about 330 K, that is, a 34% increase with respect to the laminar value before transition onset.

Similarly, the right plot in figure 1.4 shows a surface temperature map of the Space Shuttle Endeavour during its final reentry flight (STS-134), obtained by means of high-resolution infrared thermography measurements performed by Horvath *et al.* [6] in the framework of the hypersonic thermodynamic infrared measurements (HYTHIRM) project. The obtained temperature data shows that boundary-layer transition occurred in an asymmetric manner, starting shortly after the starboard rear corner of the nose landing gear door. Although a similar transition pattern was also observed in STS-119, its exact origin remains unknown. Horvath *et al.* [6] suggest that it is triggered by some form of isolated roughness originating from the nose landing gear door (such as a step or gap, for instance). In this case, the temperature difference between the laminar and the turbulent regions near the centerline of the Orbiter is about 120 K. Note that this measurement corresponds to a later time in the reentry trajectory than that of the transition onset depicted in the left plot of figure 1.4. For this measurement, the estimated flight Mach number is 5.8.

1.2 Boundary-layer transition in high-speed flow

As introduced in the previous section, boundary-layer transition from a laminar to a turbulent regime plays a crucial role in the problem of aerodynamic heating. As a consequence, it becomes a critical driver for the optimal design of hypersonic vehicles. Although hypersonic boundary-layer transition has been an active research topic for decades, the physical mechanisms involved in the process are not well understood yet. As a result, the existing transition prediction tools for practical hypersonic applications still rely heavily on engineering correlations with a high degree of empiricism, generally developed from wind tunnel experiments.

The boundary-layer transition process is known to be the result of the growth and interaction of perturbations that are generated inside the boundary-layer and/or introduced into it from the outside. Several sources of perturbations exist that can affect the boundary-layer (forcing), such as freestream disturbances, surface geometry and roughness, acoustic waves, structural vibrations, heat transfer or ablation. The effectiveness of such perturbations on the transition process depends on how receptive the boundary layer is to them (receptivity), and whether they are able to grow or not once evolving inside the boundary layer. Depending on the disturbance level to which the boundary-layer is exposed, the transition process can undergo different stages, or paths, the so-called paths to transition (see for example Morkovin *et al.* [7]), represented in figure 1.5.

In low-disturbance environments, path A usually prevails. This path begins with a linear mechanism in which the most unstable perturbations evolving in the boundary layer experience exponential growth, also known as eigenmode growth or modal growth. After reaching a certain amplitude, these perturbations develop secondary instabilities and interact with each other by means of non-linear mechanisms, rapidly triggering a breakdown to turbulence. For higher disturbance levels (paths B, C and D), the perturbations undergo transient growth directly after entering the boundary layer through the receptivity mechanisms. Transient growth, also known as non-modal growth, is a linear mechanism by which a given disturbance can undergo algebraic growth, even if all the perturbations in the boundary-layer are stable to modal amplification (see § 3.12). In path B, only a moderate level of transient growth is experienced by the perturbations, which then undergo a stage of exponential (modal) growth and follow a similar path to A, with the difference that in this case the amplitude at which modal interactions become important is reached before, owing to the additional algebraic growth induced in the prior non-modal stage. This usually translates in an upstream shift in the transition location with respect to path A.

When following path C, the perturbations are subject to a non-modal growth that is strong enough to trigger directly the non-linear interactions that produce a breakdown to turbulence, without the disturbances undergoing any eigenmode

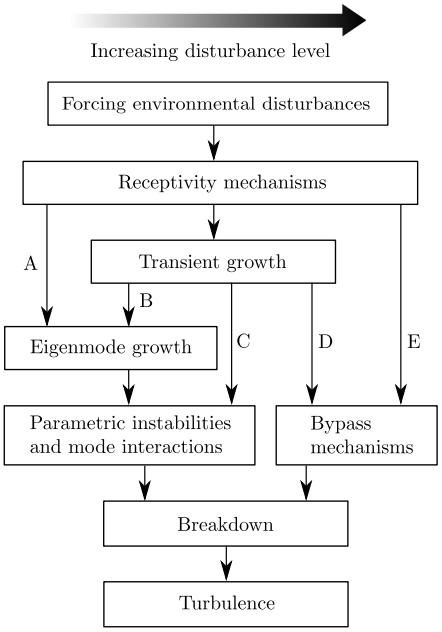

Figure 1.5: Different paths to transition depending on the disturbance level. Adapted from Morkovin et al. [7].

growth. By moving one step further in the disturbance level scale, perturbations that follow path D experience a very large transient growth, such that both the modal growth and modal interaction stages are bypassed, leading directly to breakdown. Finally, if the environmental disturbance level is very high, a bypass of all the different perturbation growth mechanisms can occur, immediately producing breakdown to turbulence, as depicted by path E.

An illustration of the different stages of the boundary-layer transition process in a low-disturbance environment, that is, following path A, is shown in the drawing displayed in figure 1.6 for a boundary-layer developing on a flat plate, as originally depicted by White [8]. In this case, the most unstable disturbance evolving inside the boundary layer takes the form of a Mack mode [10], or of a Tollmien-Schlichting (TS) wave in the realm of low-speed flows. As it can be observed, the transition process begins with the exponential growth of TS waves, in this case represented as two-dimensional waves with wave fronts parallel to the flat-plate leading edge. Then, as soon as the amplitude of the TS waves has grown significantly, secondary instabilities begin to develop and modal interactions begin to take place, introducing spanwise vorticity in the boundary layer and producing streamwise streaks that rapidly breakdown to generate turbulent spots, which eventually spread over the complete boundary layer leading to a fully turbulent flow.

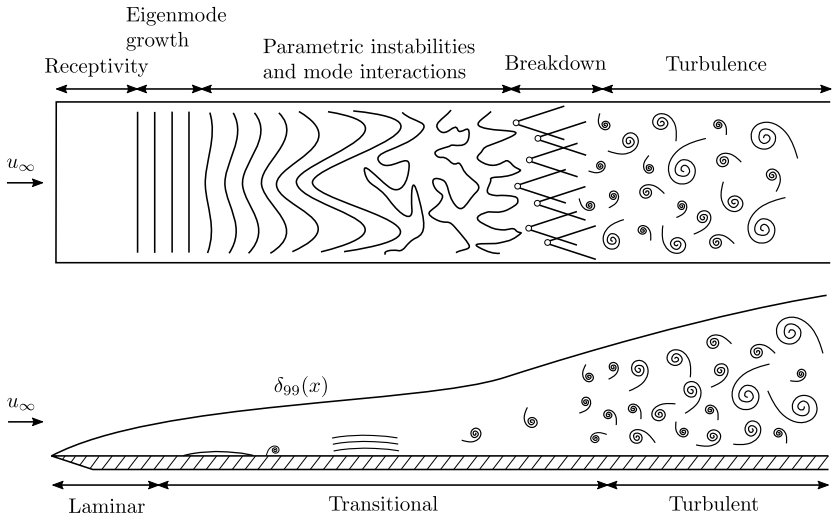

Figure 1.6: Stages of the transition process (not to scale) for a flat-plate boundary layer following path A (see figure 1.5). Adapted from White [8] and Miró Miró [9].

Although not shown to the respective scale in the figure, the eigenmode-growth stage is the longest part of the process in this case, and it is where most of the disturbance amplification takes place.

In order to improve the transition-prediction capabilities for the design of future high-speed applications, new methodologies able to take into account a higher degree of flow physics for each particular case should be developed. In particular, approaches that properly model the different stages of the transition paths described above are necessary [11]. The approach with the highest fidelity available is that of direct numerical simulation (DNS), which allows to evaluate the complete transition process by means of a numerical solution of the Navier-Stokes equations. Despite its very high computational cost, numerous DNS analyses in fundamental configurations have been performed in recent years, as the computational power available has increased significantly. Hand-in-hand with DNS analyses, hydrodynamic stability theory has become a very attractive and powerful tool nowadays, owing to its good degree of fidelity at a reduced computational cost compared to DNS, specially in its linear form [12]. In particular, linear stability theory allows to evaluate the eigenmode-growth stage of the low-disturbance-level transition process (path A), which, in many configurations of interest at flight conditions, is the longest stage and it is where most of the disturbance growth takes place. Additionally, for some applications such as a flat-plate boundary layer, the linear theory allows to provide an accurate prediction of transition location thanks to the e^N method (see § 3.7).

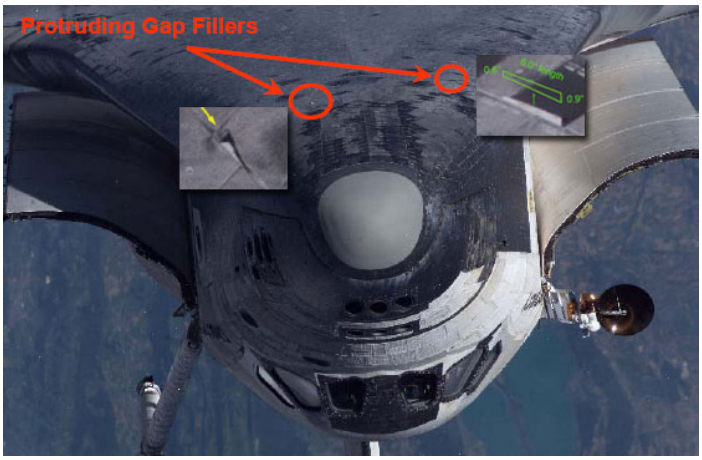

Figure 1.7: Gap fillers protruding from the thermal protection system of the Space Shuttle Discovery (STS-114). Photograph taken from the ISS, August 2005. Credit: NASA.

1.2.1 The role of isolated roughness elements on boundary-layer transition

One of the most important factors that are known to affect the boundary-layer transition process at high speed is the presence of localized or distributed roughness on the surface of a vehicle. Examples include damaged heat-shield tiles, gap fillers, ablated surfaces or remains of contaminants. For instance, the surface roughness of the Space Shuttle Orbiter was inherently defined by the placement and installation of the individual ceramic tiles and by any in-flight damage that altered the TPS surface. Tile gaps and misalignments resulted in discrete roughness that was scattered over the windward surface. In addition, the surface roughness could be further increased by post-launch damage in the form of tile cavities produced by debris impacts or gap fillers protruding between individual tiles due to structural vibrations [6]. Figure 1.7 illustrates two protruding gap fillers located on the windward surface of Space Shuttle Discovery photographed during mission STS-114, which were found during an inspection of the thermal protection system of the Orbiter prior to reentry. STS-114 was the first mission after the Space Shuttle Columbia disaster in 2003 [13]. For this reason, it was known as the Return to Flight mission. Since Columbia's accident, the concern regarding safety during reentry was particularly high. As a result, an extravehicular activity (EVA) was conducted by a crew member to remove the protruding gap fillers from the TPS.

The perturbations generated by surface roughness can enhance the growth of incoming disturbances and introduce additional instability mechanisms in the flow field, eventually leading to a premature occurrence of transition. Flight experiments such as BLTFE and HYTHIRM, introduced in the previous section, have

demonstrated the relevance of roughness-induced transition in the reentry of the Space Shuttle Orbiter. After analysis of data gathered during the HYTHIRM project, evidence was found that the observed transition pattern was most probably triggered by some form of isolated roughness located in proximity to the starboard rear corner of the nose landing gear door [6]. In the case of STS-119, computations went hand-in-hand with the flight experiments. Numerical analyses performed by Candler & Campbell [14], employing a turbulence model coupled with a boundary-layer tripping driven by the STS-119 flight measurements, were directly compared against the respective flight thermal imagery, displaying a good qualitative agreement. In parallel with flight experiments, numerous wind tunnel experimental investigations have also shown that laminar-turbulent transition can be dominated by roughness effects in a wide range of conditions (see for instance [15–19]).

The effects of two-dimensional discrete roughness elements on boundary-layer transition were investigated experimentally by Klebanoff & Tidstrom [15] for subsonic boundary layers, who found that the roughness geometry did not generate any additional instability mechanism in the flow, but rather it introduced modifications in the base flow which had a destabilizing influence on the already existing disturbances (Tollmien-Schlichting waves in this case). For the case of a Mach 4.8 boundary layer, Marxen *et al.* [20] studied the destabilizing effect introduced by a two-dimensional isolated roughness element on the evolution of a small disturbance by means of direct numerical simulation. The disturbance was generated by blowing and suction at the wall at a location upstream of the roughness element. The roughness was found to accelerate the transition process by introducing a stable mode in the flow which interfered with the upstream disturbance, effectively amplifying it in a given frequency range. Three-dimensional roughness elements with heights comparable to the local boundary-layer thickness usually have a stronger influence than two-dimensional elements on the transition process in supersonic and hypersonic flows. It has been shown both experimentally and numerically that these elements tend to induce counter-rotating streamwise vortices in the wake flow field (see for example [21–25]), which lift-up low-momentum fluid from the near-wall region and give rise to a series of high- and low-velocity streaks that are surrounded by regions of high shear and can support the growth of different instabilities [26–31].

Due to the numerous physical processes that come into play and the wide variety of geometrical configurations that are interesting in practice, roughness-induced transition is still not well understood. As reviewed by Schneider [19], current practical methodologies for the prediction of roughness effects on hypersonic boundary-layer transition rely mainly on empirical correlations and extensive wind tunnel testing. A physical parameter that has been found to play an important role in correlating different roughness-induced transition data is the roughness

Reynolds number, defined here as $Re_h = u_h h/\nu_h$, where u_h and ν_h are respectively the streamwise velocity and the kinematic viscosity of the fluid at the location and height (h) of the roughness element in a smooth boundary layer. As shown in the review of Reda [17], several existing roughness-dominated transition correlations could be modeled by a critical value of Re_h, above which boundary-layer transition would occur in a very short distance downstream of a roughness element, that is, by means of bypass mechanisms (paths D and E in figure 1.5).

DNS computations by Redford *et al.* [32] for supersonic flow over a flat plate with different isolated smooth roughness elements showed that the critical value of Re_h increases as the parameter $M_h T_\infty/T_w$ increases, with M_h being the Mach number at the roughness position and height in the undisturbed boundary layer and T_w is the wall-temperature, and found that a linear relation between $M_h T_\infty/T_w$ and Re_h (in particular, $M_h T_\infty/T_w = 3(Re_h - 300)/700$) successfully separated transitional from non-transitional cases in their DNS database. Later on, Bernardini *et al.* [33, 34] proposed a modified roughness Reynolds number definition ($Re_{h,w}$) by evaluating the dynamic viscosity at the wall instead of doing it at h, which allowed to account for the effect of wall-temperature. For a cuboidal roughness element, [34] found that a constant value of $Re_{h,w} = 460$ could successfully separate laminar from transitional cases in their DNS computations, therefore providing another bypass transition criterion based on the concept of a critical roughness Reynolds number. Additionally, Bernardini *et al.* [34] provided another roughness Reynolds number definition (Re_Q) that also includes the effect of the roughness shape by estimating the momentum deficit past a given obstacle, in this case issuing a critical roughness Reynolds number criterion that was approximately independent of the roughness shape and aspect ratio, namely, Re_Q between 200 and 280.

A physics-based correlation was proposed by Reshotko & Tumin [35] using results from transient-growth theory, suggesting that roughness-induced transient growth could be a relevant mechanism for boundary-layer transition in blunt bodies in the presence of distributed roughness. However, based on the joint efforts of Hein *et al.* [36], transient growth could not yet be conclusively linked to the onset of transition observed in blunt reentry capsules, whose physical mechanism still remains unknown.

In recent years, a significant number of researchers have focused their efforts on studying the stability characteristics of the wake induced by three-dimensional isolated roughness elements in high-speed flow, using both experimental and numerical techniques [26–31, 37–40]. Given the strong inhomogeneity of the wake flow field, numerical analyses based on stability theory employ two-dimensional amplitude functions, leading to two-dimensional local linear stability theory (2D-LST), also known as BiGlobal stability theory [12], or three-dimensional parabolized stability equations (3D-PSE) [41]. These studies have revealed that the

roughness wake supports the growth of sinuous and varicose instability modes that develop in the high-shear regions introduced by the counter-rotating vortex pair, and that these disturbances can undergo a substantial growth during the linear stages of the transition process. Groskopf *et al.* [26] performed temporal 2D-LST analyses in the wake behind isolated three-dimensional cuboidal roughness elements in a Mach 4.8 boundary layer and compared the amplitude functions against unsteady direct numerical simulations. The results showed the growth of an even (varicose) and an odd (sinuous) instability mode in the wake behind the element, reporting a good agreement of the disturbance amplitude shapes against the DNS data. Kegerise *et al.* [28] carried out experimental measurements of the disturbance amplitudes behind a diamond element in a flat plate at Mach 3.5, and compared them against the spatial amplitude signatures obtained from the 2D-LST analyses of Choudhari *et al.* [27] with satisfactory results, reinforcing the validity of the theory for the geometrical configurations considered. Their investigations revealed that, for a roughness Reynolds number of 426, the varicose mode was dominating the transition process, whereas for $Re_h = 319$ the sinuous instability was leading.

A sharp-edged cuboid geometry at Mach 2.5 was also studied by De Tullio *et al.* [29] using DNS as well as spatial 2D-LST and 3D-PSE stability theories. The two-dimensional eigenfunctions obtained from the 2D-LST computations and the growth rates extracted from the 3D-PSE simulations were respectively found to be in very good agreement with the DNS results. In that particular case, the varicose instability was found to drive the transition process until the breakdown to turbulence. The same geometrical configuration at Mach 6 was analyzed by De Tullio & Sandham [30] by means of direct numerical simulation. For a roughness element with a height of about half the local-boundary layer thickness, three different modes were found to govern the wake instability, namely, a sinuous mode and two varicose modes. The varicose modes featured a higher growth and their development persisted for a longer distance downstream. Two different mechanisms for the excitation of wake modes were identified. On the one hand, the sinuous instability was found to be excited by the interaction between the external disturbances introduced at the domain inflow and the recirculation regions induced by the roughness element. On the other hand, the varicose modes were excited by an interaction between the natural boundary-layer modes (Mack's first and second modes) and the roughness wake, leading to the hypothesis that a synchronization mechanism between the boundary-layer modes and the wake modes would lead to the continuous excitation of the wake modes as the boundary-layer modes grow downstream. Paredes *et al.* [42] performed stability computations using the laminar base flows of [30] and also reported good qualitative agreement with the DNS data for the 2D-LST amplitude functions and the 3D-PSE growth rates, respectively. However, a significant discrepancy was found between the 2D-LST and

3D-PSE growth rates, whose origin could not be identified.

Van den Eynde & Sandham [43] investigated different roughness geometries for a Mach 6 flow over a flat plate, showing that a smooth ramping of the rear portion of the roughness shape towards the wall could reduce significantly the growth of wake instabilities, due to a weakening of the three-dimensional shear layer surrounding the low-velocity streak. Additionally, the analyses of [43] confirmed that sharper-edged roughness elements are more effective in promoting transition than smooth elements. Later on, Groskopf & Kloker [31] considered the instabilities induced by skewed roughness elements on top of a flat plate in a Mach 4.8 freestream. In this case, a non-symmetric wake is established behind the elements, featuring a stronger low-speed streak than the symmetric counterpart. Local linear stability analyses and DNS results showed that at identical roughness height, a larger amplification is achieved for the eigenmodes in the oblique configuration.

A few recent works have also focused on roughness elements located on the heat shield of a reentry capsule. Theiss *et al.* [38] performed 2D-LST and 3D-PSE computations in the wake behind different isolated roughness geometries located on the forebody of a generic capsule at Mach 5.9. For all the cases considered, the varicose wake modes were the most amplified in terms of maximum N-factors, with the cylindrical roughness element being the most effective shape. In this case, in contrast to [42], the growth rates of the 2D-LST and the 3D-PSE computations were found to be in good qualitative agreement, with 3D-PSE providing higher growth rates. An important difference with respect to the flat-plate studies mentioned before is that, due to the strong bow shock in front of the capsule, the boundary-layer modes upstream of the roughness elements are highly stabilized, and as a result their interaction with wake modes is not present. Very recently, Di Giovanni & Stemmer [40] carried out linear stability and DNS computations for a patch of periodic distributed roughness and DNS computations for a patch of randomly distributed roughness on a blunt-capsule configuration at Mach 5.9. For the periodic case, the growth rates of the symmetric and antisymmetric wake modes were found to be in good agreement between 2D-LST, 3D-PSE and DNS. For the random case, the DNS results revealed a new type of roughness-induced cross-flow instability leading to breakdown to turbulence.

At present, currently available investigations do not yet provide a definitive answer on which are the mechanisms that lead to the excitation and dominance of a given type of roughness instability (varicose/sinuous) over another for a particular configuration. Similarly, the current understanding of the influence of boundary-layer disturbances on the roughness-induced wake instabilities is still very preliminary and deserves further analysis.

1.2.2 High-enthalpy effects on boundary-layer transition

The majority of the aforementioned numerical studies have assumed air to behave as a calorically perfect gas. However, one-dimensional local linear stability analyses in smooth flat-plate boundary layers have shown that this assumption must be abandoned when modeling high-enthalpy environments such as those encountered during atmospheric entry. Instead, flow assumptions accounting for the excitation of the internal energy modes and the dissociation of air molecules in the transition process are necessary.

High-temperature effects on the stability of hypersonic boundary layers were first studied by Malik & Anderson [44], who considered self-similar boundary-layer profiles in local thermodynamic equilibrium (LTE) to assess the influence of dissociation. Next, Stuckert & Reed [45] extended this analysis to boundary layers in chemical non-equilibrium and Hudson *et al.* [46] included also thermal non-equilibrium effects. The main findings from these studies showed a destabilization of the second Mack-mode instability in the presence of internal-energy-mode excitation and dissociation-driven base-flow cooling as well as a shift towards lower frequencies. Several authors have since investigated high-enthalpy effects on various configurations and test conditions, employing different stability theories and thermal and transport models [47–60]. A review of different high-enthalpy effects on boundary-layer transition can be found in the work of Miró Miró [9].

The investigations listed above are mainly restricted to second-mode instabilities in smooth configurations. Regarding the role of high-enthalpy effects on roughness-induced transition, little is known as very few studies are currently available. Groskopf *et al.* [61] analyzed the instability introduced by a discrete oblique roughness element in cold and hot hypersonic flow conditions, emulating the set-up of the BLTFE experiment flown in STS-119 (see the brief description in § 1.1.1). For the hot case, while their base-flow solutions were obtained by means of a solver modeling chemical non-equilibrium, only a thermally perfect gas model was available in the stability implementation, thus neglecting chemical reactions in the perturbation equations. The results showed a rather negligible influence of high-temperature effects on the growth rate of the modes developing in the roughness wake.

Stemmer *et al.* [62, 63] carried out direct numerical simulations for the flow field past a blunt wedge with a cuboidal roughness element mounted on top, at conditions replicating a point in the trajectory of the Hypersonic Boundary-Layer Transition (HyBoLT) experiment, namely, $M = 8.5$ at a height of 42.5 km. The evolution of disturbances behind the roughness element was studied for the calorically perfect gas, chemical equilibrium and chemical non-equilibrium flow assumptions. The results revealed a lower attenuation of the disturbances in the chemical equilibrium case with respect to the CPG solution, while in the chemical non-equilibrium case a region of amplification far dowstream of the obstacle

was observed, in contrast to the other two flow assumptions. Very recently, Di Giovanni & Stemmer [64, 65] performed direct numerical simulations on a hemispherical capsule-like geometry with a randomly distributed roughness patch including thermal and chemical non-equilibrium. They found that the inclusion of chemical non-equilibrium has a destabilizing effect on the evolution of unstable modes in the wake induced by the roughness patch.

The most recent analyses available suggest that internal-energy-mode excitation and chemical non-equilibrium may tend to destabilize roughness-induced instabilities. Whether this behavior could be attributed to the same physical reasons as the destabilization of second Mack-mode disturbances (i.e., base-flow cooling) deserves additional investigation.

1.3 Thesis scope and structure

Given the important role of isolated roughness elements on boundary-layer transition, the present doctoral thesis aims to improve our fundamental physical understanding of roughness-induced instabilities developing in a hypersonic boundary layer. Despite the numerous valuable experimental and numerical investigations available, described in the previous sections, the mechanisms by which three-dimensional discrete roughness elements influence boundary-layer transition are still far from being completely understood. Our current knowledge does not yet allow to predict which instabilities would dominate the transition process in a realistic scenario featuring discrete roughness. As a result, the presence of roughness elements on the surface of a body still remains an important source of uncertainty in our path towards an accurate prediction of laminar-turbulent transition. Like many of the works previously referenced, the intention of the present study is to move one step forward along that path, building upon the knowledge gathered from prior investigations.

In particular, this research focuses on high-speed flat-plate configurations with isolated roughness elements at subcritical roughness Reynolds numbers, in which modal disturbance growth is known to play a major role on the transition process. On first place, the attention is focused on cold hypersonic flow conditions, in which high-enthalpy effects are not important, allowing the use of a calorically perfect gas assumption. This is the case of most numerical and wind tunnel experimental studies currently available in the literature. In this regime, this work contributes to address the two following questions:

- *Which are the physical processes by which the roughness-induced instabilities extract their energy along the roughness wake?*
- *Is there a constructive interaction between the Mack-mode instabilities evolving in a flat-plate boundary layer and the roughness-induced wake instabil-*

ities?

For this purpose, two-dimensional local linear stability analyses are carried out, which allow to track the modal amplification of roughness-induced instabilities as well as that of Mack-mode perturbations, and a suitable disturbance energy evolution equation is derived, based on the disturbance energy formulation of Chu [66]. This allows to obtain a decomposition of the temporal growth rate of the roughness-induced instabilities into the different physical contributions that produce and dissipate the disturbance energy, extending the approach of Weder *et al.* [67] to perturbations that are inhomogeneous in two spatial directions.

On second place, flight conditions representative of those encountered during the Space Shuttle Orbiter reentry trajectory at an altitude of 65 km are considered and applied to a sharp flat-plate configuration at an angle of attack (equivalent to a sharp-wedge configuration). In this case, an oblique shock wave emanating at the leading edge compresses the hypersonic freestream to yield a high-temperature flow field, where molecular vibrational excitation, diffusion transport and dissociation in the boundary layer become important, requiring the use of the thermally perfect gas assumption and the need to account for chemical non-equilibrium. For these conditions, this doctoral work contributes to assess the following unknowns:

- *What is the effect of vibrational excitation and dissociation on the instabilities evolving in the wake behind an isolated roughness element?*
- *From the modeling point of view, how important is it to be consistent between the modeling assumptions introduced in the governing base-flow equations and those introduced in the governing stability equations for the case of roughness-induced instabilities?*

As in the CPG case, these questions are approached by means of two-dimensional local linear stability theory, employing stability equations that contain all the necessary terms to achieve a fully consistent computation when using base flows obtained from a solution of the TPG or CNE governing equations. Other high-enthalpy effects that are important during the reentry path of different vehicles (see figure 1.2), such as thermal non-equilibrium, ionization, surface catalysis or ablation-product injection are left out of the scope of this work.

This dissertation is structured as follows. Chapter 2 describes the governing equations used for each of the three different thermodynamic flow assumptions considered, together with the thermal, transport and chemical models employed. Chapter 3 is devoted to presenting the fundamentals of hydrodynamic stability theory, defining the linear stability formulation employed throughout this work and introducing the disturbance energy evolution equation developed for 2D-LST eigenmodes. The numerical methodology followed in order to solve the governing equations to obtain laminar base-flow solutions and to solve the linear stability problem is described in chapter 4. Next, chapter 5 presents the analysis of

roughness-induced instabilities in a calorically perfect gas, describing the topology of the stability spectrum behind the roughness element and the amplitude shape of the disturbances that develop in the roughness wake. For two different roughness geometries, the evolution of the different instabilities along the roughness-induced wake is explored and the mechanisms for the production and dissipation of disturbance energy are identified. The influence of the excitation of the vibrational molecular energy mode and the presence of chemical non-equilibrium on the behavior of roughness-induced disturbances is explored in chapter 6. Finally, concluding remarks and an outlook for future investigations are issued in chapter 7.

References

[1] Thomas Rivell. *Notes on Earth Atmospheric Entry for Mars Sample Return Missions*. Technical Report TP-2006-213486, NASA, 2006.

[2] John D. Anderson Jr. *Hypersonic and High Temperature Gas Dynamics*. American Institute of Aeronautics and Astronautics, Reston VA, second edition, 2006.

[3] E. R. van Driest. *The problem of aerodynamic heating*. Aeronautical Engineering Review, pages 26–41, 1956.

[4] S. D. Williams, Donald M. Curry, Dennis C. Chao, and Vuong T. Pham. *Ablation analysis of the shuttle orbiter oxidation protected reinforced carbon-carbon*. Journal of Thermophysics and Heat Transfer, 9(3):478–485, 1995.

[5] Karen T. Berger, Brian P. Anderson, Charles H. Campbell, Michael T. Garske, Luis A. Saucedo, and Gerald R. Kinder. *Boundary Layer Transition Flight Experiment Overview and In-Situ Measurements*. In 48th AIAA Aerospace Sciences Meeting Including the New Horizons Forum and Aerospace Exposition, volume 2010-240, Orlando, Florida, 2010. American Institute of Aeronautics and Astronautics.

[6] Thomas J. Horvath, Joseph N Zalameda, William A. Wood, Scott A. Berry, Richard J Schwartz, Ronald F Dantowitz, Thomas S Spisz, and Jeff C Taylor. *Global Infrared Observations of Roughness Induced Transition on the Space Shuttle Orbiter*. Technical report, RTO-MP-AVT-200, 27, NATO, 2012.

[7] M. V. Morkovin, E. Reshotko, and T. Herbert. *Transition in open flow systems - a reassessment*. Bulletin of the American Physical Society, 39(9):1882, 1994.

[8] Frank M. White. *Viscous Fluid Flow*. McGraw-Hill, New York NY, third edition, 2006.

[9] Fernando Miró Miró. *Numerical Investigation of Hypersonic Boundary-Layer Stability and Transition in the presence of Ablation Phenomena*. PhD thesis, Université Libre de Bruxelles and von Karman Insitute for Fluid Dynamics, 2020.

[10] Leslie M. Mack. *Boundary-Layer Linear Stability Theory*. In Special Course on Stability and Transition of Laminar Flow, AGARD-R-709, pages 3.1–3.81, 1984.

[11] Eli Reshotko. *Paths to Transition in Wall Layers*. In Advances in laminar-turbulent transition modeling, pages 1–8. von Karman Institute for Fluid Dynamics, 2008.

[12] Vassilios Theofilis. *Advances in global linear instability analysis of non-parallel and three-dimensional flows*. Progress in Aerospace Sciences, 39(4):249–315, 2003.

[13] Columbia accident investigation board. *Columbia accident investigation board report, volume 1*. Technical report, 2003.

[14] Graham V. Candler and Charles H. Campbell. *Hypersonic Navier-Stokes comparisons to orbiter flight data*. AIAA paper, 2010-455, 2010.

[15] P. S. Klebanoff and K. D. Tidstrom. *Mechanism by which a two-dimensional roughness element induces boundary-layer transition*. Physics of Fluids, 15(7):1173–1188, 1972.

[16] T. C. Corke, A. Bar-Sever, and Mark V. Morkovin. *Experiments on transition enhancement by distributed roughness*. Physics of Fluids, 29(10):3199–3213, 1986.

[17] Daniel C. Reda. *Review and Synthesis of Roughness-Dominated Transition Correlations for Reentry Applications*. Journal of Spacecraft and Rockets, 39(2):161–167, 2002.

[18] Keisuke Fujii. *Experiment of the two-dimensional roughness effect on hypersonic boundary-layer transition*. Journal of Spacecraft and Rockets, 43(4):731–738, jul 2006.

[19] Steven P. Schneider. *Effects of Roughness on Hypersonic Boundary-Layer Transition*. Journal of Spacecraft and Rockets, 45(2):193–209, 2008.

[20] Olaf Marxen, Gianluca Iaccarino, and Eric S.G. Shaqfeh. *Disturbance evolution in a mach 4.8 boundary layer with two-dimensional roughness-induced separation and shock*. Journal of Fluid Mechanics, 648:435–469, 2010.

[21] Ronald D. Joslin and Chester E. Grosch. *Growth characteristics downstream of a shallow bump: Computation and experiment*. Physics of Fluids, 7(12):3042–3047, 1995.

[22] Anatoli Tumin and Eli Reshotko. *Receptivity of a boundary-layer flow to a three-dimensional hump at finite Reynolds numbers*. Physics of Fluids, 17(9):1–8, 2005.

[23] Donald P Rizzetta and Miguel R Visbal. *Direct Numerical Simulations of Flow Past an Array of Distributed Roughness Elements*. AIAA Journal, 45(8):1967–1976, 2007.

[24] A. I. Ruban and M. A. Kravtsova. *Generation of steady longitudinal vortices in hypersonic boundary layer*. Journal of Fluid Mechanics, 729:702–731, 2013.

[25] Prahladh S. Iyer and Krishnan Mahesh. *High-speed boundary-layer transition induced by a discrete roughness element*. Journal of Fluid Mechanics, 729:524–562, 2013.

[26] Gordon Groskopf, Markus J. Kloker, and Olaf Marxen. *Bi-global crossplane stability analysis of high-speed boundary-layer flows with discrete roughness*. IUTAM Bookseries, 18:171–176, 2010.

[27] Meelan M. Choudhari, Fei Li, Chau-Lyan Chang, Jack Edwards, Michael Kegerise, and Rudolph A. King. *Laminar-Turbulent Transition behind Discrete Roughness Elements in a High-Speed Boundary Layer*. AIAA paper, 2010-1575, 2010.

[28] Michael A. Kegerise, Rudolph A. King, Lewis Owens, Meelan Choudhari, Andrew Norris, Fei Li, and Chau-Lyan Chang. *An Experimental and Numerical Study of Roughness-Induced Instabilities in a Mach 3.5 Boundary Layer*. Technical report, RTO AVT-200/RSM-030, 29, NATO, 2012.

[29] Nicola De Tullio, Pedro Paredes, Neil D. Sandham, and Vassilios Theofilis. *Laminar-turbulent transition induced by a discrete roughness element in a supersonic boundary layer*. Journal of Fluid Mechanics, 735:613–646, 2013.

[30] Nicola De Tullio and Neil D. Sandham. *Influence of boundary-layer disturbances on the instability of a roughness wake in a high-speed boundary layer*. Journal of Fluid Mechanics, 763:136–145, 2015.

[31] Gordon Groskopf and Markus J. Kloker. *Instability and transition mechanisms induced by skewed roughness elements in a high-speed laminar boundary layer*. Journal of Fluid Mechanics, 805:262–302, 2016.

[32] John A. Redford, Neil D. Sandham, and Graham T. Roberts. *Compressibility effects on boundary-layer transition induced by an isolated roughness element*. AIAA Journal, 48(12):2818–2830, 2010.

[33] M Bernardini, S Pirozzoli, Orlandi. P, and S. K. Lele. *Compressible boundary layer transition induced by isolated roughness elements*. In Centre for Turbulence Research, Proceedings of the Summer Program 2012, pages 15–24, 2012.

[34] Matteo Bernardini, Sergio Pirozzoli, Paolo Orlandi, and Sanjiva K. Lele. *Parameterization of boundary-layer transition induced by isolated roughness elements*. AIAA Journal, 52(10):2261–2269, 2014.

[35] Eli Reshotko and Anatoli Tumin. *Role of Transient Growth in Roughness-Induced Transition*. AIAA Journal, 42(4):766–770, 2004.

[36] Stefan J. Hein, Alexander Theiss, Antonio Di Giovanni, Christian Stemmer, Thomas Schilden, Wolfgang Schröder, Pedro Paredes, Meelan M. Choudhari, Fei Li, and Eli Reshotko. *Numerical investigation of roughness effects on transition on spherical capsules*. Journal of Spacecraft and Rockets, 56(2):388–404, 2019.

[37] Meelan M. Choudhari, Fei Li, Chau-Lyan Chang, Andrew Norris, and Jack Edwards. *Wake instabilities behind discrete roughness elements in high speed boundary layers*. AIAA paper, 2013-0081, 2013.

[38] Alexander Theiss, Stefan J. Hein, Syed Raza Christopher Ali, and Rolf Radespiel. *Wake flow instability studies behind discrete roughness elements on a generic re-entry capsule*. AIAA paper, 2016-4382, 2016.

[39] David Estruch-Samper, Richard Hillier, Leon Vanstone, and Bharathram Ganapathisubramani. *Effect of isolated roughness element height on high-speed laminar-turbulent transition*. Journal of Fluid Mechanics, 818:1–14, 2017.

[40] Antonio Di Giovanni and Christian Stemmer. *Cross-flow-type breakdown induced by distributed roughness in the boundary layer of a hypersonic capsule configuration*. Journal of Fluid Mechanics, 856:470–503, 2018.

[41] Pedro Paredes, Ardeshir Hanifi, Vassilis Theofilis, and Dan S. Henningson. *The Nonlinear PSE-3D Concept for Transition Prediction in Flows with a Single Slowly-varying Spatial Direction*. Procedia IUTAM, 14:36–44, 2015.

[42] Pedro Paredes, Nicola De Tullio, Neil D. Sandham, and Vassilios Theofilis. *Instability Study of the Wake Behind a Discrete Roughness Element in a Hypersonic Boundary-Layer*. Instability and Control of Massively Separated Flows, Fluid Mechanics and Its Applications, 107:91–96, 2015.

[43] Jeroen P.J.P. Van Den Eynde and Neil D. Sandham. *Numerical simulations of transition due to isolated roughness elements at Mach 6*. AIAA Journal, 54(1):53–65, 2016.

[44] Mujeeb R. Malik and E. C. Anderson. *Real gas effects on hypersonic boundary-layer stability*. Physics of Fluids, 803(3):803–821, 1991.

[45] Greg Stuckert and Helen L. Reed. *Linear Disturbances in Hypersonic, Chemically Reacting Shock Layers*. AIAA Journal, 32(7):1384–1393, 1994.

[46] Mary L. Hudson, Ndaona Chokani, and Graham V. Candler. *Linear stability of hypersonic flow in thermochemical nonequilibrium*. AIAA Journal, 35(6):958–964, 1997.

[47] Chau-Lyan Chang, H. Vinh, and Mujeeb R. Malik. *Hypersonic boundary-layer stability with chemical reactions using PSE*. AIAA paper, 1997-2012, 1997.

[48] Fabio P. Bertolotti. *The influence of rotational and vibrational energy relaxation on boundary-layer stability*. Journal of Fluid Mechanics, 372(1998):93–118, 1998.

[49] Heath B. Johnson, Trevor G. Seipp, and Graham V. Candler. *Numerical study of hypersonic reacting boundary layer transition on cones*. Physics of Fluids, 10(10):2676–2685, 1998.

[50] Mujeeb R. Malik. *Hypersonic Flight Transition Data Analysis Using Parabolized Stability Equations with Chemistry Effects*. Journal of Spacecraft and Rockets, 40(3):332–344, 2003.

[51] Jill Klentzman and Anatoli Tumin. *Stability and receptivity of high speed boundary layers in oxygen*. AIAA paper, 2013-2882, 2013.

[52] Olaf Marxen, Gianluca Iaccarino, and Thierry E. Magin. *Direct numerical simulations of hypersonic boundary-layer transition with finite-rate chemistry*. Journal of Fluid Mechanics, 755:35–49, 2014.

[53] N. P. Bitter and Joseph E. Shepherd. *Stability of highly cooled hypervelocity boundary layers*. Journal of Fluid Mechanics, 778:586–620, 2015.

[54] Clifton Mortensen and Xiaolin Zhong. *Real-Gas and Surface-Ablation Effects on Hypersonic Boundary-Layer Instability over a Blunt Cone*. AIAA Journal, 54(3):980–998, 2016.

[55] Ludovico Zanus, Fernando Miró Miró, and Fabio Pinna. *Weak Non-Parallel Effects on Chemically Reacting Hypersonic Boundary Layer Stability*. AIAA paper, 2019-2853, 2019.

[56] Fernando Miró Miró, Ethan S. Beyak, Fabio Pinna, and Helen L. Reed. *High-enthalpy models for boundary-layer stability and transition*. Physics of Fluids, 31(044101), 2019.

[57] Carleton P. Knisely and Xiaolin Zhong. *Significant supersonic modes and the wall temperature effect in hypersonic boundary layers*. AIAA Journal, 57(4):1552–1566, 2019.

[58] Fernando Miró Miró and Fabio Pinna. *Injection-gas-composition effects on hypersonic boundary-layer transition*. Journal of Fluid Mechanics, 890(R4), 2020.

[59] Fernando Miró Miró and Fabio Pinna. *Decoupling ablation effects on boundary-layer stability and transition*. Journal of Fluid Mechanics, 907:A14, jan 2021.

[60] Fernando Miró Miró, Ethan S. Beyak, Fabio Pinna, and Helen L. Reed. *Ionization and dissociation effects on boundary-layer stability*. Journal of Fluid Mechanics, 907:A13, 2021.

[61] Gordon Groskopf, Markus J. Kloker, K A Stephani, Olaf Marxen, and Gianluca Iaccarino. *Hypersonic flows with discrete oblique surface roughness and their stability properties*. In Center of Turbulence Research, Proceedings of the Summer Program, pages 405–422, 2010.

[62] Christian Stemmer, Marcel Birrer, and Nikolaus A. Adams. *Hypersonic boundary-layer flow with an obstacle in thermochemical equilibrium and nonequilibrium*. Journal of Spacecraft and Rockets, 54(4):899–915, 2017.

[63] Christian Stemmer, Marcel Birrer, and Nikolaus A. Adams. *Disturbance development in an obstacle wake in a reacting hypersonic boundary layer*. Journal of Spacecraft and Rockets, 54(4):945–960, 2017.

[64] Antonio Di Giovanni and Christian Stemmer. *Roughness-Induced Boundary-Layer Transition on a Hypersonic Capsule-Like Forebody Including Nonequilibrium*. Journal of Spacecraft and Rockets, 56(6):1795–1808, nov 2019.

[65] Antonio Di Giovanni and Christian Stemmer. *Roughness-induced crossflow-type instabilities in a hypersonic capsule boundary layer including nonequilibrium*. Journal of Spacecraft and Rockets, 56(5):1409–1423, sep 2019.

[66] Boa Teh Chu. *On the energy transfer to small disturbances in fluid flow (Part I)*. Acta Mechanica, 1(3):215–234, sep 1965.

[67] Mario Weder, Michael Gloor, and Leonhard Kleiser. *Decomposition of the temporal growth rate in linear instability of compressible gas flows*. Journal of Fluid Mechanics, 778:120–132, jul 2015.

2 Governing equations

This chapter summarizes the governing equations and gas-property models employed throughout this dissertation. No rarefied gas effects are considered, therefore the theoretical framework in use is restricted to the continuum regime.

2.1 Thermodynamic flow assumptions

All the different thermodynamic descriptions of a gas employed in this work are based on the assumption of a perfect gas. Here, the term perfect gas refers to a gas in which intermolecular forces are not important. The naming conventions employed follow the classification of gases given by Anderson [1]. See also Miró Miró [2].

The primitive thermodynamic variables of the gas are its density (ρ), pressure (p) and temperature (T). They are related by means of the perfect gas equation of state:

$$p = \rho R T, \tag{2.1}$$

where R is the specific gas constant, which can be evaluated as

$$R = \frac{\mathscr{R}}{\mathscr{M}}, \tag{2.2}$$

with $\mathscr{R} = 8.3144$ J/(mol K) being the universal gas constant and $\mathscr{M}$ the molar mass of the gas.

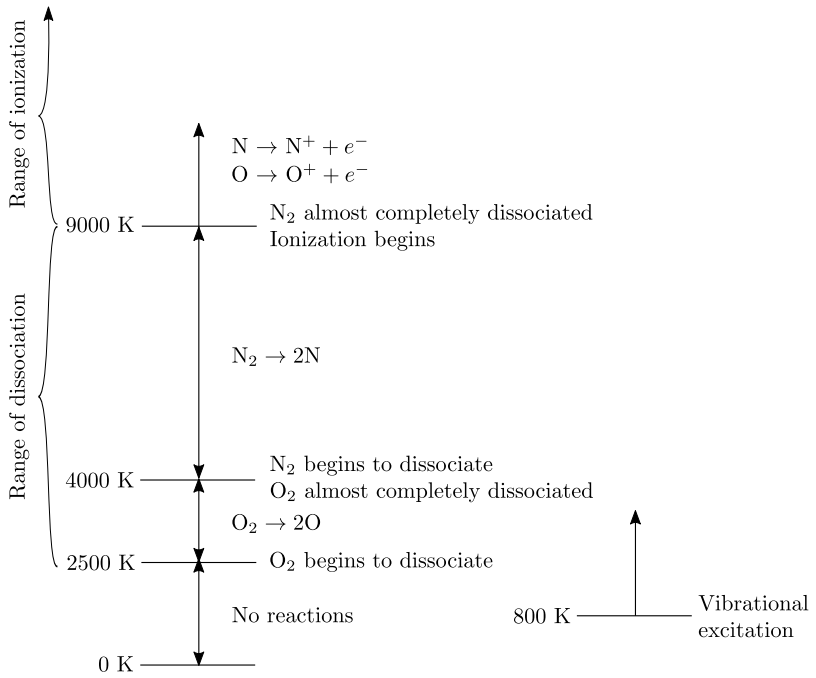

Figure 2.1: Temperature ranges of vibrational excitation, dissociation and ionization for air at $p = 101325$ Pa $= 1$ atm (standard state), including the corresponding reactions. Redrawn, original from [1].

2.1.1 Calorically perfect gas (CPG)

A calorically perfect gas is a perfect gas with constant specific heats, which implies a constant ratio of specific heats $\gamma = c_p/c_v$, with c_p and c_v being respectively the specific heat at constant pressure and at constant volume. This condition leads to simple linear functions that express the static enthalpy (h) and the internal energy (e) of the gas as a function of temperature only:

$$h = c_p T \quad \text{and} \quad e = c_v T. \tag{2.3}$$

Therefore, no specific modeling of the thermal properties c_p and c_v is required to describe the behavior of the gas. This flow assumption is suitable for gases at conditions for which the excitation of the vibrational energy mode of the gas molecules is not yet significant. For air at $p = 101325$ Pa, this is a good approximation for $T < 800$ K (see figure 2.1).

2.1.2 Thermally perfect gas (TPG)

A thermally perfect gas is a perfect gas in which the specific heats are a function of temperature only, that is

$$c_p = c_p(T) \quad \text{and} \quad c_v = c_v(T). \tag{2.4}$$

This flow assumption accounts for the excitation of the vibrational energy mode of the gas molecules as well as for the electronic energy associated with the motion of electrons in the atoms of the gas, but subject to the two following conditions. On the one hand, vibrational relaxation (represented by the time scale τ_{vib}) is assumed to take place considerably faster than the changes in the flow properties (represented by the time scale τ_{flow}), hence the flow can be considered to be in vibrational equilibrium (and hence also in thermal equilibrium since only the vibrational energy mode is considered to be excited). On the other hand, chemical reactions (represented by the time scale τ_{chem}) are assumed to occur substantially slower than the changes in the flow field, hence the gas can be considered to be chemically frozen. Therefore, for a thermally perfect gas $\tau_{vib} \ll \tau_{flow} \ll \tau_{chem}$, that is, a chemically frozen gas in vibrational equilibrium.

Under these considerations, the enthalpy and internal energy of the gas are also functions of temperature only, which can be expressed as

$$h = h(T) \quad \text{and} \quad e = e(T), \tag{2.5}$$

and their differential changes as

$$dh = c_p\, dT \quad \text{and} \quad de = c_v\, dT. \tag{2.6}$$

The function employed to describe the variation of the specific heats as a function of temperature depends on the chosen thermal model. Common models employed in hypersonic flows are the rigid-rotor harmonic oscillator (RRHO) model (see for example [3]), which assumes the molecules to behave as a rigid rotor and as a harmonic oscillator and the species to follow a Boltzmann distribution, and the polynomial curve fits developed by Thompson *et al.* [4]. In this work, the latter model is employed (see § 2.5.1). Since no chemical reactions are present, only two species are considered for the TPG thermal property modeling, namely, N_2 and O_2.

For air at atmospheric pressure, the TPG assumption constitutes a suitable choice up to approximately 2500 K, where the dissociation of oxygen molecules begins to be significant (see figure 2.1).

2.1.3 Mixture of perfect gases in chemical non-equilibrium (CNE)

The CNE thermodynamic flow assumption considers a multi-species chemically reacting gas in which chemical reactions take place at a similar rate as the changes in the flow field, but in which vibrational relaxation still occurs significantly faster, that is $\tau_{vib} \ll \tau_{chem} \sim \tau_{flow}$. Therefore, the CNE assumption can be described as a gas in chemical non-equilibrium yet in thermal equilibrium, such that all the energy modes of the gas mixture can be described by a single temperature.

Each species of the CNE mixture is assumed to behave by itself as a thermally perfect gas. However, in this case the thermal properties of the mixture depend not only on temperature but also on the instantaneous composition of the gas, that is

$$c_p = c_p(T, c_{N_2}, c_{O_2}, ..., c_s), \tag{2.7}$$

$$h = h(T, c_{N_2}, c_{O_2}, ..., c_s), \tag{2.8}$$

$$e = e(T, c_{N_2}, c_{O_2}, ..., c_s), \tag{2.9}$$

where c_s denotes the mass fraction of species s, defined as

$$c_s = \frac{\rho_s}{\rho}, \tag{2.10}$$

with ρ_s being the density of species s. The values of c_s describe the composition of the gas at a given position and instant.

Here, an air mixture consisting of five species is considered when accounting for chemical non-equilibrium, namely, N, O, NO, N_2 and O_2, also known as air-5. This mixture is able to model the dissociation of O_2 and N_2, as well as the formation and dissociation of NO. Therefore, at atmospheric pressure, this mixture is valid for temperatures up to 9000 K, where ionization becomes important (see figure 2.1). In order to model ionization, an eleven-species air mixture is required, commonly known as air-11. For a discussion on ionization effects on boundary-layer stability, which falls out of the scope of this study, the reader is referred to [2, 5].

Besides modeling the evolution of the thermal and transport properties of each species as a function of temperature, the CNE assumption also requires an appropriate modeling of the chemical interaction between the different species. This can be achieved by the law of mass action together with a list of chemical reactions, as described in § 2.5.3.

2.2 Navier-Stokes equations

The equations governing the problems studied in this work are the Navier-Stokes equations (see for instance [6]). They constitute a system of non-linear partial differential equations that express the conservation of mass, momentum and energy

of a fluid in space and time. As introduced before, the only fluid considered in this investigation is air, which is assumed to behave as a Newtonian fluid. This implies that there is a linear relationship between the viscous stresses of the fluid and its strain rate. Additionally, no body forces such as gravity are considered.

In the following, the Navier-Stokes equations are presented for each of the three different thermodynamic flow assumptions introduced before, expressed in a Cartesian coordinate system. In this reference frame, the instantaneous velocity of the fluid is denoted by the vector $\mathbf{V} = u\,\mathbf{e}_x + v\,\mathbf{e}_y + w\,\mathbf{e}_z$, where $\mathbf{e}_x$, $\mathbf{e}_y$ and $\mathbf{e}_z$ are unit vectors along the x, y and z directions, respectively.

2.2.1 Calorically perfect gas

For the case of a calorically perfect gas, the system of equations consists of the continuity equation, three momentum equations and the energy equation, expressed in non-conservation form as follows:

$$\frac{D\rho}{Dt} + \rho\nabla\cdot\mathbf{V} = 0, \tag{2.11a}$$

$$\rho\frac{Du}{Dt} + \frac{\partial p}{\partial x} - \frac{\partial \tau_{xx}}{\partial x} - \frac{\partial \tau_{yx}}{\partial y} - \frac{\partial \tau_{zx}}{\partial z} = 0, \tag{2.11b}$$

$$\rho\frac{Dv}{Dt} + \frac{\partial p}{\partial y} - \frac{\partial \tau_{xy}}{\partial x} - \frac{\partial \tau_{yy}}{\partial y} - \frac{\partial \tau_{zy}}{\partial z} = 0, \tag{2.11c}$$

$$\rho\frac{Dw}{Dt} + \frac{\partial p}{\partial z} - \frac{\partial \tau_{xz}}{\partial x} - \frac{\partial \tau_{yz}}{\partial y} - \frac{\partial \tau_{zz}}{\partial z} = 0, \tag{2.11d}$$

$$\begin{aligned}\rho\frac{De}{Dt} + p\nabla\cdot\mathbf{V} + \frac{\partial q_x}{\partial x} + \frac{\partial q_y}{\partial y} + \frac{\partial q_z}{\partial z}\\ - \tau_{xx}\frac{\partial u}{\partial x} - \tau_{yx}\frac{\partial u}{\partial y} - \tau_{zx}\frac{\partial u}{\partial z} - \tau_{xy}\frac{\partial v}{\partial x} - \tau_{yy}\frac{\partial v}{\partial y} - \tau_{zy}\frac{\partial v}{\partial z}\\ - \tau_{xz}\frac{\partial w}{\partial x} - \tau_{yz}\frac{\partial w}{\partial y} - \tau_{zz}\frac{\partial w}{\partial z} = 0,\end{aligned} \tag{2.11e}$$

where $D/Dt = \partial/\partial t + (\mathbf{V}\cdot\nabla)$ is the material derivative operator and $\nabla = \mathbf{e}_x\partial/\partial x + \mathbf{e}_y\partial/\partial y + \mathbf{e}_z\partial/\partial z$. Under the assumption of a Newtonian fluid, the viscous stresses are given by

$$\tau_{xx} = (2\mu+\lambda)\frac{\partial u}{\partial x} + \lambda\left(\frac{\partial v}{\partial y} + \frac{\partial w}{\partial z}\right), \tag{2.12a}$$

$$\tau_{yy} = (2\mu+\lambda)\frac{\partial v}{\partial y} + \lambda\left(\frac{\partial u}{\partial x} + \frac{\partial w}{\partial z}\right), \tag{2.12b}$$

$$\tau_{zz} = (2\mu+\lambda)\frac{\partial w}{\partial z} + \lambda\left(\frac{\partial u}{\partial x} + \frac{\partial v}{\partial y}\right), \tag{2.12c}$$

$$\tau_{xy} = \tau_{yx} = \mu\left(\frac{\partial u}{\partial y} + \frac{\partial v}{\partial x}\right), \tag{2.12d}$$

$$\tau_{xz} = \tau_{zx} = \mu\left(\frac{\partial u}{\partial z} + \frac{\partial w}{\partial x}\right), \tag{2.12e}$$

$$\tau_{yz} = \tau_{zy} = \mu\left(\frac{\partial v}{\partial z} + \frac{\partial w}{\partial y}\right), \tag{2.12f}$$

where μ is the dynamic viscosity of the fluid and λ is the bulk viscosity coefficient. Stokes' hypothesis is considered, such that

$$\lambda = -\frac{2}{3}\mu. \tag{2.13}$$

The conductive heat flux vector is modeled using Fourier's law of heat conduction, whose components are expressed as

$$q_x = -k\frac{\partial T}{\partial x}, \quad q_y = -k\frac{\partial T}{\partial y} \quad \text{and} \quad q_z = -k\frac{\partial T}{\partial z}, \tag{2.14}$$

where k denotes the thermal conductivity of the fluid. The system of equations is closed by means of the perfect gas equation of state (2.1).

For convenience in the derivation of the disturbance energy evolution equation (see § 3.10), the energy equation (2.11e) for a calorically perfect gas is formulated in terms of the total derivative of the internal energy. See for example [7] for different equivalent forms of the energy equation.

In this thermodynamic flow assumption, the transport properties μ and k are assumed to be functions of temperature only. They are modeled using either Sutherland's law or the Gupta-Wilke transport model (see § 2.5.2.2). To distinguish between the two choices, the acronyms CPGS and CPGGW are respectively adopted.

2.2.1.1 Non-dimensional form

For convenience in the derivation and the numerical solution of the disturbance governing equations (see § 3.1), the Navier-Stokes equations are also formulated in non-dimensional form. For the case of a calorically perfect gas, the dimensionless quantities employed are the following:

$$t' = \frac{tu_\infty}{l}, \quad x' = \frac{x}{l}, \quad u' = \frac{u}{u_\infty}, \quad v' = \frac{v}{u_\infty}, \quad w' = \frac{w}{u_\infty}, \quad \rho' = \frac{\rho}{\rho_\infty},$$
$$p' = \frac{p}{\rho_\infty u_\infty^2}, \quad T' = \frac{T}{T_\infty}, \quad e' = \frac{e}{u_\infty^2}, \quad \mu' = \frac{\mu}{\mu_\infty} \quad \text{and} \quad k' = \frac{k}{k_\infty}, \tag{2.15}$$

where $(\cdot)'$ denotes non-dimensional quantities and $(\cdot)_\infty$ denotes the dimensional reference quantities used for non-dimensionalization, which correspond to the

freestream flow conditions. The chosen reference length (l) is a boundary-layer length scale evaluated at the local streamwise coordinate of interest, defined as

$$l = \sqrt{\frac{\mu_\infty x}{\rho_\infty u_\infty}}. \tag{2.16}$$

This choice of dimensionless quantities leads to the following freestream non-dimensional numbers:

$$\text{Mach number:} \quad M = \frac{u_\infty}{a_\infty}, \tag{2.17a}$$

$$\text{Reynolds number:} \quad Re = \frac{\rho_\infty u_\infty l}{\mu_\infty}, \tag{2.17b}$$

$$\text{Prandtl number:} \quad Pr = \frac{c_p \mu_\infty}{k_\infty}, \tag{2.17c}$$

where a_∞ denotes the freestream speed of sound, which is defined for a calorically (or a thermally) perfect gas as

$$a_\infty = \sqrt{\gamma R T_\infty}. \tag{2.18}$$

The non-dimensional specific heats become

$$c_v' = \frac{1}{\gamma\left(\gamma - 1\right) M^2} \quad \text{and} \quad c_p' = \frac{1}{\left(\gamma - 1\right) M^2}, \tag{2.19}$$

such that

$$R' = c_p' - c_v' = \frac{1}{\gamma M^2}. \tag{2.20}$$

According to the quantities defined in (2.15), the non-dimensional form of the CPG Navier-Stokes equations can be written as

$$\frac{D\rho'}{Dt'} + \rho' \nabla' \cdot \mathbf{V}' = 0, \tag{2.21a}$$

$$\rho' \frac{Du'}{Dt'} + \frac{\partial p'}{\partial x'} - \frac{\partial \tau_{xx}'}{\partial x'} - \frac{\partial \tau_{yx}'}{\partial y'} - \frac{\partial \tau_{zx}'}{\partial z'} = 0, \tag{2.21b}$$

$$\rho' \frac{Dv'}{Dt'} + \frac{\partial p'}{\partial y'} - \frac{\partial \tau_{xy}'}{\partial x'} - \frac{\partial \tau_{yy}'}{\partial y'} - \frac{\partial \tau_{zy}'}{\partial z'} = 0, \tag{2.21c}$$

$$\rho' \frac{Dw'}{Dt'} + \frac{\partial p'}{\partial z'} - \frac{\partial \tau_{xz}'}{\partial x'} - \frac{\partial \tau_{yz}'}{\partial y'} - \frac{\partial \tau_{zz}'}{\partial z'} = 0, \tag{2.21d}$$

$$\rho' \frac{De'}{Dt'} + p' \nabla' \cdot \mathbf{V}' + \frac{\partial q'_x}{\partial x'} + \frac{\partial q'_y}{\partial y'} + \frac{\partial q'_z}{\partial z'} - \tau'_{xx} \frac{\partial u'}{\partial x'} - \tau'_{yx} \frac{\partial u'}{\partial y'} - \tau'_{zx} \frac{\partial u'}{\partial z'} - \tau'_{xy} \frac{\partial v'}{\partial x'} - \tau'_{yy} \frac{\partial v'}{\partial y'} - \tau'_{zy} \frac{\partial v'}{\partial z'} - \tau'_{xz} \frac{\partial w'}{\partial x'} - \tau'_{yz} \frac{\partial w'}{\partial y'} - \tau'_{zz} \frac{\partial w'}{\partial z'} = 0, \tag{2.21e}$$

with $D/Dt' = \partial/\partial t' + (\mathbf{V}' \cdot \nabla')$, $\nabla' = \mathbf{e}_x \partial/\partial x' + \mathbf{e}_y \partial/\partial y' + \mathbf{e}_z \partial/\partial z'$ and $\mathbf{V}' = u'\mathbf{e}_x + v'\mathbf{e}_y + w'\mathbf{e}_z$. The non-dimensional viscous stresses are given by

$$\tau'_{xx} = \frac{1}{Re}\left[(2\mu' + \lambda')\frac{\partial u'}{\partial x'} + \lambda'\left(\frac{\partial v'}{\partial y'} + \frac{\partial w'}{\partial z'}\right)\right], \tag{2.22a}$$

$$\tau'_{yy} = \frac{1}{Re}\left[(2\mu' + \lambda')\frac{\partial v'}{\partial y'} + \lambda'\left(\frac{\partial u'}{\partial x'} + \frac{\partial w'}{\partial z'}\right)\right], \tag{2.22b}$$

$$\tau'_{zz} = \frac{1}{Re}\left[(2\mu' + \lambda')\frac{\partial w'}{\partial z'} + \lambda'\left(\frac{\partial u'}{\partial x'} + \frac{\partial v'}{\partial y'}\right)\right], \tag{2.22c}$$

$$\tau'_{xy} = \tau'_{yx} = \frac{\mu'}{Re}\left(\frac{\partial u'}{\partial y'} + \frac{\partial v'}{\partial x'}\right), \tag{2.22d}$$

$$\tau'_{xz} = \tau'_{zx} = \frac{\mu'}{Re}\left(\frac{\partial u'}{\partial z'} + \frac{\partial w'}{\partial x'}\right), \tag{2.22e}$$

$$\tau'_{yz} = \tau'_{zy} = \frac{\mu'}{Re}\left(\frac{\partial v'}{\partial z'} + \frac{\partial w'}{\partial y'}\right), \tag{2.22f}$$

and the components of the non-dimensional heat flux vector as

$$q'_x = -\frac{k'}{(\gamma - 1)\, RePrM^2}\frac{\partial T'}{\partial x'}, \tag{2.23a}$$

$$q'_y = -\frac{k'}{(\gamma - 1)\, RePrM^2}\frac{\partial T'}{\partial y'}, \tag{2.23b}$$

$$q'_z = -\frac{k'}{(\gamma - 1)\, RePrM^2}\frac{\partial T'}{\partial z'}. \tag{2.23c}$$

Similarly, the perfect gas equation of state takes the following non-dimensional form:

$$p' = \frac{\rho' T'}{\gamma M^2}. \tag{2.24}$$

To avoid overloading the notation, in the remaining chapters of this work the use of the symbol $(\cdot)'$ to denote non-dimensional quantities is dropped. Each time the non-dimensional form of the governing equations is employed, it is specifically stated in the text. Results expressed in dimensional quantities are always accompanied by the corresponding SI units.

2.2.2 Thermally perfect gas

Under the assumption of a thermally perfect gas, the governing equations are essentially the same as for a calorically perfect gas. For convenience with the thermal property modeling, however, the energy equation used in this case is expressed in terms of the static enthalpy of the fluid instead of the internal energy, that is

$$\rho\frac{Dh}{Dt} - \frac{Dp}{Dt} + \frac{\partial q_x}{\partial x} + \frac{\partial q_y}{\partial y} + \frac{\partial q_z}{\partial z} - \tau_{xx}\frac{\partial u}{\partial x} - \tau_{yx}\frac{\partial u}{\partial y} - \tau_{zx}\frac{\partial u}{\partial z} - \tau_{xy}\frac{\partial v}{\partial x} - \tau_{yy}\frac{\partial v}{\partial y} - \tau_{zy}\frac{\partial v}{\partial z} - \tau_{xz}\frac{\partial w}{\partial x} - \tau_{yz}\frac{\partial w}{\partial y} - \tau_{zz}\frac{\partial w}{\partial z} = 0. \quad (2.25)$$

The difference with respect to the calorically perfect gas assumption resides in the evaluation of the enthalpy of the fluid. In this case, c_p is a function of temperature and therefore the enthalpy of the fluid must be evaluated using a model for the thermal properties.

2.2.3 Mixture in chemical non-equilibrium

For a gas in chemical non-equilibrium, the mass fraction of each species in the mixture becomes an unknown quantity. This is usually expressed by introducing the density of each species (ρ_s) as an independent quantity. Therefore, the vector of state variables in this case becomes: $\mathbf{q} = [\rho_s, u, v, w, T]^{\mathrm{T}}$, with $s \in \mathcal{S}$. This implies that additional relations are necessary to complete the system. Such additional governing equations are the species mass conservation equations (or species continuity equations). Furthermore, the transport of species mass by diffusion is also an active mechanism in this flow assumption. As a result, diffusion fluxes must be accounted for in the system.

The species mass conservation equations can be expressed as follows:

$$\rho\frac{Dc_s}{Dt} + \nabla \cdot \mathbf{j}_s - \dot{w}_s = 0, \quad (2.26)$$

where $\mathbf{j}_s$ is the species mass diffusion flux and $\dot{w}_s$ is the mass production rate of species s. The only diffusion-driving force considered in the scope of this work is the mass-fraction gradient (thermo- and barodiffusion processes are neglected). The species mass diffusion flux is then assumed to follow Fick's first law, which yields

$$\mathbf{j}_s = -\rho\mathcal{D}_{sm}\nabla c_s, \quad (2.27)$$

where $\mathcal{D}_{sm}$ is the multicomponent diffusion coefficient for the diffusion of species s into the mixture. An important property is that, for consistency, the sum of the diffusion fluxes $\mathbf{j}_s$ over all the species must be equal to zero. This brings the

possibility of substituting the mass-conservation equation of one of the species by the mixture continuity equation (preferably the one associated to the species with the largest mass fraction, often known as the bath species), which has the same form as equation (2.11a). This procedure has been found to improve the numerical behavior of the system when solving the linear stability problem (see Miró Miró & Pinna [8]). The diffusion coefficients employed here are modeled using a simplified, self-consistent diffusion model which relies on the definition of an effective diffusion coefficient (see § 2.5.2.3).

The net production rate of species mass is governed by the law of mass action as described in § 2.5.3.1.

Similarly to TPG, the energy equation for CNE is formulated in terms of the static enthalpy of the mixture. However, an additional term must be added to account for the transport of energy due to diffusion, that is

$$\rho\frac{Dh}{Dt} - \frac{Dp}{Dt} + \frac{\partial q_x}{\partial x} + \frac{\partial q_y}{\partial y} + \frac{\partial q_z}{\partial z} - \nabla\cdot\mathbf{J} - \tau_{xx}\frac{\partial u}{\partial x} - \tau_{yx}\frac{\partial u}{\partial y} - \tau_{zx}\frac{\partial u}{\partial z} - \tau_{xy}\frac{\partial v}{\partial x} - \tau_{yy}\frac{\partial v}{\partial y} - \tau_{zy}\frac{\partial v}{\partial z} - \tau_{xz}\frac{\partial w}{\partial x} - \tau_{yz}\frac{\partial w}{\partial y} - \tau_{zz}\frac{\partial w}{\partial z} = 0, \quad (2.28)$$

where $\mathbf{J}$ is the energy diffusion flux, defined as

$$\mathbf{J} = \sum_s h_s\,\mathbf{j}_s. \quad (2.29)$$

It is important to note that the energy equation does not contain an explicit term for the energy exchange due to chemical reactions because the heat of formation of each species, $(\Delta h_f)^0_s$, is contained within the absolute definition of h_s [1].

The mixture continuity equation and the momentum equations have a purely mechanical nature and are not affected by chemical reactions. Therefore, the system of governing equations for CNE consists of equation (2.11a), $N_s - 1$ equations like equation (2.26) and equations (2.11b), (2.11c), (2.11d) and (2.28). Additional relations that complete the system are the perfect gas equation of state and the following condition on the mass fractions:

$$\sum_s c_s = 1. \quad (2.30)$$

2.3 Boundary conditions

Prior to their solution, the governing equations presented in the previous section must be complemented with boundary conditions according to the physical problem under investigation. Four different types of boundaries are considered, namely, solid wall, inflow, outflow and symmetric boundaries, which are discussed next.

2.3.1 Wall boundary conditions

At solid-wall boundaries, the no-slip and no-penetration conditions are enforced on the flow velocity components, given by

$$u = v = w = 0. \tag{2.31}$$

In addition, a thermal wall condition is imposed, which either takes the form of an isothermal wall condition, expressed as

$$T = T_w, \tag{2.32}$$

where T_w denotes the temperature at the wall, or an adiabatic wall condition, defined as

$$\left.\frac{\partial T}{\partial n}\right|_w = 0, \tag{2.33}$$

where n is the coordinate normal to the wall and $(\partial T/\partial n)|_w$ is the wall-normal temperature gradient evaluated at the wall.

For a gas mixture in chemical non-equilibrium, a concentration condition is also imposed on the species mass fractions at the wall (which in turn determine the wall values of the species densities ρ_s). This condition results from the assumption that no chemical reactions take place at the wall boundary, and receives the name of non-catalytic wall condition, usually expressed for each species as

$$\left.\frac{\partial c_s}{\partial n}\right|_w = 0, \tag{2.34}$$

where $(\partial c_s/\partial n)|_w$ represents the wall-normal mass-fraction gradient evaluated at the wall.

2.3.2 Inflow boundary conditions

Two different kinds of inflow boundaries are considered in this dissertation, namely, freestream inflow boundaries at which the flow is supersonic, and inflow boundaries at which an inflow profile is given. In the former, all the primitive flow variables are prescribed to their respective freestream values. In the latter, two different approaches are used to respect the direction of propagation of information within the flow field, depending on whether the flow normal to the boundary is subsonic or supersonic. At the portions of the inflow profile where the flow is supersonic, all the primitive flow variables are prescribed to the values supplied by the inflow profile. At the portions of the inflow where the flow is subsonic, all primitive flow variables are prescribed except for the pressure, which is extrapolated from the interior of the domain.

As elaborated in chapter 5, the inflow profile condition is employed in this work to impose a boundary-layer profile at the inflow boundary.

2.3.3 Outflow boundary conditions

For the configurations studied in this work, only a supersonic outflow condition is considered. This implies that all the primitive flow variables are extrapolated from the interior of the domain along the entire outflow boundary, independently of whether the flow across the boundary is locally subsonic or supersonic.

This approach is a common practice in laminar high-speed flows with small streamwise gradients [7]. Since the Navier-Stokes equations have a mixed mathematical nature, it is in general better posed to use characteristic relations for each variable across the boundary, such that a different treatment is applied locally at the supersonic and subsonic portions of the boundary. Nonetheless, the nature of the governing equations in a steady and laminar boundary layer (such as that in the cases analyzed in this work) becomes nearly parabolic. In particular, in the limit in which the Navier-Stokes equations reduce to the boundary-layer equations, the mathematical nature of the problem becomes fully parabolic (see for instance [1, 7]). Since the outlet boundary in this study is always located far away from the roughness element, the flow field at the outflow boundary features a small dependence on the streamwise direction and therefore it is well approximated by the parabolized Navier-Stokes equations (PNS). Far outside of the roughness wake, where spanwise gradients become negligible, the flow field can also be described with good accuracy by the boundary-layer equations. According to these considerations, the nearly parabolic behavior of the problem allows this boundary condition (extrapolation from the interior) to be reasonably valid also in the subsonic part of the boundary layer. Any upstream propagation of information due to residual ellipticity (contained mainly in the streamwise pressure gradient term $\partial\bar{p}/\partial x$) at the subsonic portion of the outflow boundary is not believed to affect the quality of the base-flow solution.

2.3.4 Symmetry boundary conditions

At boundaries where the flow is symmetric in the direction normal to the boundary, symmetry boundary conditions are specified. All the scalar primitive flow variables are enforced to be mirror-imaged across the symmetry plane defined by the boundary, whereas the flow velocity vector is forced to be tangential to the boundary. This condition translates into a zero velocity component in the direction normal to the boundary.

2.4 Boundary-layer equations

For a wide range of analyses focused on the flow field inside the boundary layer, the governing equations can be simplified to a system known as the boundary-layer equations. The main assumptions leading to this simplification are that the boundary layer is very thin in comparison with the size of the body and that the Reynolds number is large. The boundary-layer equations can be obtained by introducing these assumptions into the Navier-Stokes equations and performing an order of magnitude analysis (see [1, 9, 10] for the details).

These assumptions are valid for the analysis of a flat plate boundary layer at high-speed, and hence the boundary-layer equations constitute a suitable simplified model for the stability analysis of hypersonic flat plate boundary layers. On the other hand, they are not valid for the analysis of a flat plate with discrete roughness elements whose size is of the order of the boundary-layer thickness. Nevertheless, as will become clearer in following chapters, the analysis of the smooth flat plate boundary layer (that is, without any roughness element) is essential for the understanding of the behavior of boundary-layer disturbances when a roughness element is introduced. For this reason, the steady boundary-layer equations and their solution are also considered in this work.

Since the current study is restricted to flat plate configurations that are oriented parallel to the freestream flow direction, in addition to the previously mentioned assumptions, two-dimensional flow is also considered. This removes the presence of crossflow terms into the resulting boundary-layer equations, which are otherwise essential for the analysis of swept configurations (refer to [2] for the complete form of the steady boundary-layer equations in the presence of different high-enthalpy phenomena).

2.4.1 Calorically and thermally perfect gas

Similarly to the Navier-Stokes equations, the boundary-layer equations for a calorically perfect gas are the same as those for a thermally perfect gas. Introducing the assumptions listed above into the Navier-Stokes system considered for a thermally perfect gas (equations (2.11a), (2.11b), (2.11c), (2.11d) and (2.25)), the resulting boundary-layer equations (valid for both CPG and TPG) can be written as

$$\frac{\partial(\rho u)}{\partial x} + \frac{\partial(\rho v)}{\partial y} = 0, \tag{2.35a}$$

$$\rho u \frac{\partial u}{\partial x} + \rho v \frac{\partial u}{\partial y} + \frac{\partial p}{\partial x} - \frac{\partial}{\partial y}\left(\mu \frac{\partial u}{\partial y}\right) = 0, \tag{2.35b}$$

$$\frac{\partial p}{\partial y} = 0, \tag{2.35c}$$

$$\rho u \frac{\partial h}{\partial x} + \rho v \frac{\partial h}{\partial y} - u \frac{\partial p}{\partial x} - \frac{\partial}{\partial y}\left(k \frac{\partial T}{\partial y}\right) - \mu \left(\frac{\partial u}{\partial y}\right)^2 = 0. \tag{2.35d}$$

Note that the wall-normal momentum equation (2.35c) simply states that the pressure is constant along the boundary-layer for a given x station. For this reason, the streamwise pressure derivate appearing in equations (2.35b) and (2.35d) is usually substituted by dp_e/dx, where p_e denotes the static pressure at the boundary-layer edge, which is only a function of x. The edge pressure is therefore directly imprinted on the wall. This is a reasonable assumption for hypersonic flows with moderately large Mach numbers such as the cases studied along this work (see [1]).

The same wall boundary conditions specified in § 2.3.1 apply to the system of boundary-layer equations. At the edge of the boundary layer, which can be considered as the wall-normal far-field boundary ($y \to \infty$), all primitive flow variables are prescribed to their respective edge values.

Equations (2.35) constitute a parabolic system of non-linear partial differential equations which can be solved by a marching procedure. Nevertheless, for certain cases they admit simplified solutions, known as self-similar solutions, which transform the system into a set of ordinary differential equations, reducing enormously the effort necessary to solve them. The case of a flat plate boundary layer is one of them, for which the solution is presented in the next section.

2.4.1.1 Self-similar solution for a flat plate

To derive a self-similar boundary-layer solution, an independent-variable transformation is applied to equations (2.35). The transformation, which in this case receives different names by different authors (for instance, Lees-Dorodnitsyn transformation by [1], Illingworth transformation by [9] or Levy-Lees transformation by [10]), is given by

$$\xi = \int_0^x \rho_e u_e \mu_e \, dx, \tag{2.36a}$$

$$\eta = \frac{u_e}{\sqrt{2\xi}} \int_0^y \rho \, dy \tag{2.36b}$$

where $\xi = \xi(x)$ and $\eta = \eta(x, y)$ denote the transformed coordinates and ρ_e, u_e and μ_e respectively refer to the density, streamwise velocity and dynamic viscosity at the edge of the boundary layer, which are functions of ξ only. In addition, the following non-dimensional quantities are introduced:

$$\frac{\partial f}{\partial \eta} = \frac{u}{u_e}, \quad g = \frac{h}{h_e}, \quad C = \frac{\rho \mu}{\rho_e \mu_e} \quad \text{and} \quad \mathrm{Pr} = \frac{c_p \mu}{k}, \tag{2.37}$$

where h_e is the static enthalpy at the boundary-layer edge. According to the relations stated in (2.36) and (2.37), and taking into account that the inviscid flow at the boundary-layer edge is governed by Euler's equation, namely

$$dp_e = -\rho_e u_e \, du_e, \tag{2.38}$$

the non-dimensional transformed boundary-layer equations become

$$\begin{aligned} \frac{\partial}{\partial \eta}\left(C\frac{\partial^2 f}{\partial \eta^2}\right) + f\frac{\partial^2 f}{\partial \eta^2} = \frac{2\xi}{u_e}\left[\left(\frac{\partial f}{\partial \eta}\right)^2 - \frac{\rho_e}{\rho}\right]\frac{du_e}{d\xi} \\ + 2\xi\left(\frac{\partial f}{\partial \eta}\frac{\partial^2 f}{\partial \xi \partial \eta} - \frac{\partial f}{\partial \xi}\frac{\partial^2 f}{\partial \eta^2}\right), \end{aligned} \tag{2.39a}$$

$$\frac{\partial p}{\partial \eta} = 0, \tag{2.39b}$$

$$\begin{aligned} \frac{\partial}{\partial \eta}\left(\frac{C}{\mathrm{Pr}}\frac{\partial g}{\partial \eta}\right) + f\frac{\partial g}{\partial \eta} + C\frac{u_e^2}{h_e}\left(\frac{\partial^2 f}{\partial \eta^2}\right)^2 = 2\xi\left(\frac{\partial f}{\partial \eta}\frac{\partial g}{\partial \xi}\right. \\ \left. + \frac{\partial f}{\partial \eta}\frac{g}{h_e}\frac{dh_e}{d\xi} - \frac{\partial g}{\partial \eta}\frac{\partial f}{\partial \xi} + \frac{\rho_e u_e}{\rho h_e}\frac{\partial f}{\partial \eta}\frac{du_e}{d\xi}\right). \end{aligned} \tag{2.39c}$$

Note that there is no continuity equation in the transformed system. This is due to the fact that by its definition, together with the coordinate transformation, f takes the form of a stream function, which implicitly satisfies the continuity equation [1].

For the solution to be self-similar, the dependency on ξ must vanish from the transformed equations. Restricting the attention to a flat plate case with constant conditions at the boundary-layer edge (that is u_e = const., ρ_e = const., μ_e = const. and h_e = const.) and with constant wall conditions (either isothermal or adiabatic), f and g become functions of η only (see for example [1]). Therefore, all the dependency upon ξ, contained in the right-hand side of equations (2.39a) and (2.39c), drops out and the equations become:

$$\frac{\partial}{\partial \eta}\left(C\frac{\partial^2 f}{\partial \eta^2}\right) + f\frac{\partial^2 f}{\partial \eta^2} = 0, \tag{2.40a}$$

$$\frac{\partial}{\partial \eta}\left(\frac{C}{\mathrm{Pr}}\frac{\partial g}{\partial \eta}\right) + f\frac{\partial g}{\partial \eta} + C\frac{u_e^2}{h_e}\left(\frac{\partial^2 f}{\partial \eta^2}\right)^2 = 0. \tag{2.40b}$$

This is a system of ordinary differential equations that represents the self-similar boundary-layer solution for a flat plate with constant edge and wall conditions. The boundary conditions that complete the system are three conditions at the wall ($\eta = 0$), namely

$$f(0) = 0, \quad \left.\frac{\partial f}{\partial \eta}\right|_{\eta=0} = 0, \tag{2.41}$$

$$g(0) = \frac{h_w}{h_e} \text{ (isothermal)} \quad \text{or} \quad \left.\frac{\partial g}{\partial \eta}\right|_{\eta=0} = 0 \text{ (adiabatic)}, \tag{2.42}$$

where h_w denotes the static enthalpy at the wall, and two conditions at the boundary-layer edge ($\eta \to \infty$):

$$\left.\frac{\partial f}{\partial \eta}\right|_{\eta\to\infty} = 1 \quad \text{and} \quad g(\eta \to \infty) = 1. \tag{2.43}$$

2.4.2 Mixture in chemical non-equilibrium

When accounting for chemical non-equilibrium, the mass conservation of each species as well as the energy transport due to diffusion within the boundary layer must also be considered. As in the case of CPG and TPG, the boundary-layer equations for CNE can be obtained by introducing the boundary-layer assumptions described before into the Navier-Stokes system for CNE (equations (2.11a), (2.11b), (2.11c), (2.11d), (2.28) and (2.26)). The resulting CNE boundary-layer equations consist of the same simplified momentum equations as for CPG/TPG (equations (2.35b) and (2.35c)) together with the following simplified energy and species continuity equations:

$$\begin{aligned} &\rho u \frac{\partial h}{\partial x} + \rho v \frac{\partial h}{\partial y} - u \frac{\partial p}{\partial x} - \frac{\partial}{\partial y}\left(k \frac{\partial T}{\partial y}\right) \\ &- \frac{\partial}{\partial y}\left(\rho \sum_s h_s \mathcal{D}_{sm} \frac{\partial c_s}{\partial y}\right) - \mu \left(\frac{\partial u}{\partial y}\right)^2 = 0, \end{aligned} \tag{2.44a}$$

$$\rho u \frac{\partial c_s}{\partial x} + \rho v \frac{\partial c_s}{\partial y} - \frac{\partial}{\partial y}\left(\rho \mathcal{D}_{sm} \frac{\partial c_s}{\partial y}\right) - \dot{w}_s = 0. \tag{2.44b}$$

To cast the previous system of equations into a more convenient form for its solution, the transformation given by (2.36) can also be applied when considering chemical non-equilibrium. However, in this case no self-similar solutions exist in practice. Chemical non-equilibrium processes also affect the conditions at the boundary-layer edge through the species mass source terms, which modify the composition of the mixture along the different streamwise stations. The main reason for the lack of similarity lies in the species mass production rates ($\dot{w}_s$), which, for self-similarity to be respected, must adopt a specific form which is not encountered in applications of interest. The precise requirements are detailed in appendix

D of reference [2]. As a result, the computation of solutions to the CNE boundary-layer equations must be carried out by solving (marching) the associated system of partial differential equations.

2.5 Modeling of gas properties

This section describes the different models employed in this study for the thermal, transport and chemical properties of the gas. It is important to emphasize that the choice of the different models has been partially constrained by the models available in the CFD++® package, which is the software used in this work to compute the three-dimensional base flow solutions for a flat plate in the presence of a discrete roughness element.

2.5.1 Thermal properties

The specific heat at constant pressure ($c_{p,s}$), the static enthalpy (h_s) and the Gibbs free energy per unit mass at atmospheric pressure (g_s^{atm}) of each individual species are modeled as a function of temperature by means of fourth-order least-squares polynomial curve fits developed by Thompson *et al.* [4] (see also Gupta *et al.* [11]), which are based on tabulated data. For a gas in thermal equilibrium, the following polynomial expressions are employed:

$$c_{p,s} = R_s \left(a_{1,s} + a_{2,s}T + a_{3,s}T^2 + a_{4,s}T^3 + a_{5,s}T^4\right), \tag{2.45a}$$

$$h_s = \int_{T_{\text{ref}}}^{T} c_{p,s}\, dT + \left(\Delta h_f\right)_s^{T_{\text{ref}}} = R_s \left[\left(a_{1,s} + \frac{a_{2,s}}{2}T + \frac{a_{3,s}}{3}T^2 + \frac{a_{4,s}}{4}T^3 + \frac{a_{5,s}}{5}T^4\right)T + b_{1,s}\right], \tag{2.45b}$$

$$g_s^{\text{atm}} = h_s - T\left[\int_{T_{\text{ref}}}^{T} \frac{c_{p,s}}{T}\, dT - R_s \ln\left(\frac{p_{\text{atm}}}{p_{\text{ref}}}\right) + s_{s,\text{ref}}\right] = R_s \left[a_{1,s}T\left(1 - \ln T\right) - \frac{a_{2,s}}{2}T^2 - \frac{a_{3,s}}{6}T^3 - \frac{a_{4,s}}{12}T^4 - \frac{a_{5,s}}{20}T^5 + b_{1,s} - b_{2,s}T\right], \tag{2.45c}$$

where R_s is the specific gas constant of species s, $p_{\text{atm}} = 101325$ Pa is the atmospheric pressure and $s_{s,\text{ref}}$ is the species reference entropy associated to the reference state defined by p_{ref} and T_{ref}. The coefficient $b_{1,s}$ is related to the species enthalpy of formation at the reference temperature, $\left(\Delta h_f\right)_s^{T_{\text{ref}}}$, whereas the coefficient $b_{2,s}$ is associated to the entropy contributions given by $\ln\left(p_{\text{atm}}/p_{\text{ref}}\right)$ and $s_{s,\text{ref}}$.

The values of the curve-fit coefficients a_{s1}, $b_{1,s}$, $a_{2,s}$ etc. are obtained from reference [4] and are summarized for the various species of interest in table 2.1. It is important to note that these curve fits are divided into five different temperature ranges, leading to a piecewise definition of the functions given in equation (2.45). The coefficients listed in table 2.1 correspond only to the temperature interval between 1000 and 6000 K, which constitutes the range of temperatures found within the high-enthalpy cases studied in this work (see chapter 6). When the flow field features a larger range of temperatures, the use of the coefficients corresponding to other intervals is required. However, since continuity between curve fits is not assured, this model generally introduces discontinuities in the derivatives of the thermal properties at the boundaries of each temperature interval. Therefore, for cases in which more than one temperature range needs to be considered, it is preferable to employ a different thermal model, such as the rigid-rotor and harmonic oscillator (RRHO) model, which offers a smooth continuous variation of the thermal properties (see for example [3]). The choice considered here is justified for the sake of consistency between the base flow solutions computed by the CFD++® package, which only incorporates the model described by equation (2.45), and the posterior stability analyses.

The thermal properties of the mixture are obtained from applying a mixing rule depending on the mass fraction of each species, that is

$$h = \sum_{s \in \mathcal{S}} c_s h_s, \tag{2.46}$$

$$c_p = \sum_{s \in \mathcal{S}} c_s c_{p,s}, \tag{2.47}$$

and analogously for e and c_v.

2.5.2 Transport properties

The transport properties of the gas are the viscosity μ, the thermal conductivity k and the diffusivity $\mathcal{D}$ (also known as the diffusion coefficient). The following transport property models are considered in this dissertation.

2.5.2.1 Sutherland's law

Sutherland's law [12] establishes that the dynamic viscosity of the mixture is given by

$$\mu = \mu_{\text{ref}} \left(\frac{T}{T_{\text{ref}}} \right)^{3/2} \frac{T_{\text{ref}} + S_\mu}{T + S_\mu}, \tag{2.48}$$

Species	$a_{1,s}$ [-]	$a_{2,s}$ [K^{-1}]	$a_{3,s}$ [K^{-2}]	$a_{4,s}$ [K^{-3}]
N	0.24820e+01	0.69258e-04	-0.63065e-07	0.18387e-10
O	0.25421e+01	-0.27551e-04	-0.31028e-08	0.45511e-11
NO	0.32047e+01	0.12705e-02	-0.46603e-06	0.75007e-10
N_2	0.32125e+01	0.10137e-02	-0.30467e-06	0.41091e-10
O_2	0.35949e+01	0.75213e-03	-0.18732e-06	0.27913e-10
Species	$a_{5,s}$ [K^{-4}]	$b_{1,s}$ [K]	$b_{2,s}$ [-]	
N	-0.11747e-14	0.56130e+05	0.42618e+01	
O	-0.43681e-15	0.29150e+05	0.49203e+01	
NO	-0.42314e-14	0.97640e+04	0.66867e+01	
N_2	-0.20170e-14	-0.10430e+04	0.43661e+01	
O_2	-0.15774e-14	-0.10440e+04	0.38353e+01	

Table 2.1: Coefficients from Thompson et al. [4] for the polynomial expressions of the thermal properties in equation (2.45) for $1000 \leq T \leq 6000$ K. Reference state $T_{ref} = 298.15$ K and $p_{ref} = 101325$ Pa.

where μ_{ref} denotes a reference dynamic viscosity at a reference temperature T_{ref} and S_μ is the Sutherland temperature for μ. This law provides an accurate model for the variation of viscosity with temperature up to approximately 1500 K, after which it significantly underpredicts it. This behavior is represented in figure 2.2, where the viscosity provided by Sutherland's law is compared against the evolution given by two more accurate transport models, namely, the Gupta-Wilke model (described in § 2.5.2.2) and the Chapman & Enskog molecular theory of gases [13]. As it can be observed, the Sutherland viscosity curve progressively deviates from the other two as temperature increases. Therefore, Sutherland's law is not an appropriate model for high-temperature flows. For this reason, here it is only employed together with the calorically perfect gas assumption, leading to the acronym CPGS.

The thermal conductivity in CPGS cases is either obtained from fixing a constant value of the Prandtl number, i.e.

$$k = \frac{c_p \mu}{Pr}, \tag{2.49}$$

or modeled with a Sutherland-type law for k as well, given by

$$k = k_{\text{ref}} \left(\frac{T}{T_{\text{ref}}} \right)^{3/2} \frac{T_{\text{ref}} + S_k}{T + S_k}, \tag{2.50}$$

μ_{ref} [kg/(m s)]	T_{ref} [K]	S_μ [K]	k_{ref} [W/(m K)]	S_k [K]
1.716e-05	273.15	111	2.41e-02	194

Table 2.2: Parameters used in Sutherland's law for the viscosity and thermal conductivity of air.

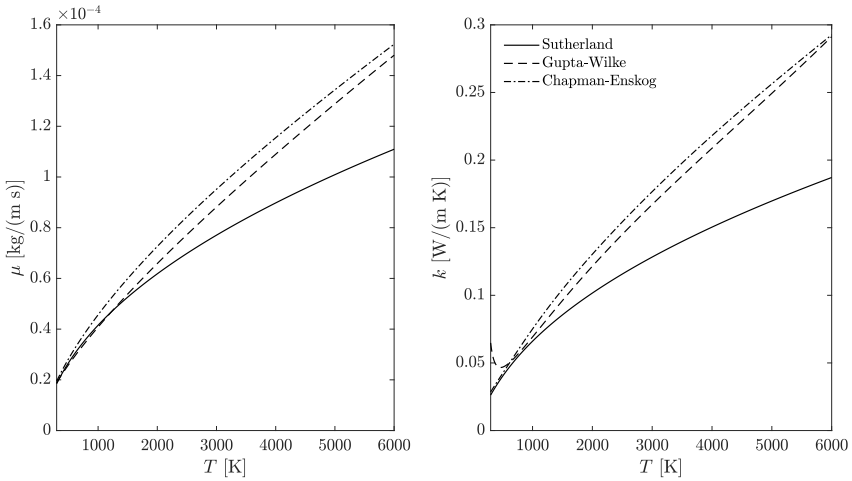

Figure 2.2: Viscosity and thermal conductivity for a two-species air mixture (N_2 and O_2) as a function of temperature using three different transport models ($p = 101325$ Pa, no dissociated species taken into account). Note that the prediction of k by the Gupta-Wilke model fails outside its range of applicability (i.e. when $T \leq 1000$ K).

where k_{ref} is a reference thermal conductivity at T_{ref} and S_k is the Sutherland temperature for k. The values considered for the different parameters appearing in equations (2.48) and (2.50) are summarized in table 2.2. As in the case of μ, Sutherland's law for k severely underpredicts the value of the thermal conductivity for temperatures higher than 1500 K (see figure 2.2).

2.5.2.2 Gupta-Wilke model

In this model, the viscosity and the thermal conductivity of each separate species are modeled as a function of temperature by means of polynomial-logarithmic expressions of the following form [11, 14]:

$$\mu_s = \exp\left[A_s^\mu \left(\ln T\right)^2 + B_s^\mu \ln T + C_s^\mu\right], \tag{2.51}$$

$$k_s = \exp\left[A_s^k \left(\ln T\right)^4 + B_s^k \left(\ln T\right)^3 + C_s^k \left(\ln T\right)^2 + D_s^k \ln T + E_s^k\right], \quad (2.52)$$

where the curve-fit parameters A_s^μ, A_s^k, B_s^μ etc. are obtained from Gupta *et al.* [11] and are summarized in tables 2.3 and 2.4. The properties of the gas mixture are then obtained from Wilke's mixing rule [15], given by

$$\mu = \sum_{s\in\mathcal{S}} \frac{X_s \mu_s}{\phi_s^\mu} \quad \text{and} \quad k = \sum_{s\in\mathcal{S}} \frac{X_s k_s}{\phi_s^\mu}, \quad (2.53)$$

where X_s is the species mole fraction and

$$\phi_s^\mu = \sum_{\ell\in\mathcal{S}} \frac{X_\ell}{\sqrt{8}} \left(1 + \frac{\mathscr{M}_s}{\mathscr{M}_\ell}\right)^{-1/2} \left[1 + \left(\frac{\mu_s}{\mu_\ell}\right)^{1/2} \left(\frac{\mathscr{M}_\ell}{\mathscr{M}_s}\right)^{1/4}\right]^2, \quad (2.54)$$

where $\mathscr{M}_s$ is the species molar mass. It is important to note that the Gupta-Wilke model is only valid for thermal equilibrium.

As it can be observed in figure 2.2, inside its range of applicability the Gupta-Wilke (GW) model is able to reproduce satisfactorily the viscosity and thermal conductivity evolution given by the Chapman & Enskog theory with an approximately constant error of about 6%. Chapman & Enskog's theory constitutes the most accurate transport model currently available but requires the solution of a linear matrix system at each point of the domain, hence resulting in a significant computational cost. Although efficient and more accurate models than GW exist, such as the Brokaw [16] and Yos' [17] simplifications of Chapman & Enskog's theory, the low computational cost and simplicity of the GW transport model make it a common choice in practice. For example, it is the model embedded in the CFD++® solver and thus it is employed in the high-temperature cases studied in this work. An evaluation of the accuracy of different transport models for 5 and 11-species air mixtures can be found in [2].

2.5.2.3 Constant Schmidt number diffusion model

The diffusion fluxes appearing in the species continuity equations and in the energy equation for CNE are modeled by means of a simple and widely used model (see for example [18, 19]), which consists in employing an effective diffusion coefficient identical for all the species in the mixture. The value of such effective coefficient is then determined through the assumption of a constant Schmidt number (Sc), that is

$$\mathcal{D}_{sm} = \mathcal{D}_{eff,s} = \frac{\mu}{Sc\,\rho}. \quad (2.55)$$

Species	A_s^μ	B_s^μ	C_s^μ
N	0.012	0.593	-14.6831
O	0.0205	0.4257	-13.8829
NO	0.0452	-0.0609	-11.7622
N_2	0.0203	0.4329	-14.1179
O_2	0.0484	-0.1455	-11.2257

Table 2.3: Viscosity coefficients for the Gupta-Wilke (GW) transport model (2.51) proposed by Gupta et al. [11] for $1000 \leq T \leq 30000$ *K. Note that the values of the coefficient* C_s^μ *have been adapted to yield the viscosity in SI units (kg/(m s)).*

Species	A_s^k	B_s^k	C_s^k	D_s^k	E_s^k
N	0	0	0.01619	0.55022	-6.8855
O	0	0	0.0331	0.22834	-5.5447
NO	0.02792	-0.87133	10.1797	-52.0347	94.707
N_2	0.03607	-1.075	11.9503	-57.9006	99.2543
O_2	0.07987	-2.5843	31.2596	-166.7627	327.7346

Table 2.4: Thermal conductivity coefficients for the Gupta-Wilke (GW) transport model (2.52) proposed by Gupta et al. [11] for $1000 \leq T \leq 30000$ *K. Note that the values of the coefficient* E_s^k *have been adapted to yield the thermal conductivity in SI units (W/(m K)).*

In the computations presented along this work, a value of $Sc = 0.7$ is always considered. Given that all the species diffusion coefficients are the same and that the species concentration gradients sum to zero, an important characteristic of this diffusion model is that it is self-consistent. This guarantees that the sum of the diffusion fluxes ($\mathbf{j}_s$) appearing in the governing equations is identically zero.

For an overview of different diffusion models and a discussion on their effect on boundary-layer stability, see Miró Miró *et al.* [20].

2.5.3 Chemical properties

The only chemical properties of the gas that require a specific modeling among the flow assumptions considered are the mass production rates of each species for a mixture in chemical non-equilibrium (CNE).

2.5.3.1 Law of mass action

Considering a set of reactions $\mathcal{R}$ between a set of species $\mathcal{S}$:

$$\sum_{s \in \mathcal{S}} \nu'_{s,r}\, s \underset{k_b}{\overset{k_f}{\rightleftharpoons}} \sum_{s \in \mathcal{S}} \nu''_{s,r}\, s, \quad \forall\, r \in \mathcal{R}\,, \tag{2.56}$$

the net mass production rate of each species can be approximated by the law of mass action [1, 21], given by

$$\dot{\omega}_s = \mathscr{M}_s \sum_{r \in \mathcal{R}} (\nu''_{s,r} - \nu'_{s,r}) \left[k_{f,r} \prod_{\ell \in \mathcal{S}} \left(\frac{\rho_\ell}{\mathscr{M}_\ell} \right)^{\nu'_{\ell,r}} - k_{b,r} \prod_{\ell \in \mathcal{S}} \left(\frac{\rho_\ell}{\mathscr{M}_\ell} \right)^{\nu''_{\ell,r}} \right], \tag{2.57}$$

where $\nu'_{s,r}$ and $\nu''_{s,r}$ represent the stoichiometric mole numbers of the reactants and products, respectively, and $k_{f,r}$ and $k_{b,r}$ are respectively the forward and backward reaction-rate constants of reaction r. The forward reaction-rate constants for a given temperature are modeled by means of the Arrhenius equation (see for instance [1]):

$$k_{f,r} = A^f_r T^{n^f_r} \exp\left(-T^f_r/T\right), \quad \forall r \in \mathcal{R}, \tag{2.58}$$

where the empirical parameters A^f_r, n^f_r and T^f_r for each reaction are obtained from Park *et al.* [22, 23] and Bose & Candler [24, 25], and are summarized in table 2.5. As introduced before, a five-species air mixture is considered in this investigation when assuming chemical non-equilibrium, for which the reaction mechanism consists of 17 elementary reactions (listed in table 2.5). The backward reaction-rate constants are obtained from the equilibrium constant for each reaction by means of the relation

$$k_{b,r} = \frac{k_{f,r}}{K^{eq}_{c,r}}, \quad \forall r \in \mathcal{R}, \tag{2.59}$$

where $K^{eq}_{c,r}$ is the equilibrium constant based on concentrations.

2.5.3.2 Calculation of the equilibrium constant

The equilibrium constant based on concentrations ($K^{eq}_{c,r}$) is expressed in terms of the equilibrium pressure constant ($K^{eq}_{p,r}$) by means of the equation of state, leading to the following relationship [1]:

$$K^{eq}_{c,r} = \frac{K^{eq}_{p,r}}{\prod_s (\mathscr{R}T)^{\nu''_{s,r} - \nu'_{s,r}}}, \quad \forall r \in \mathcal{R}. \tag{2.60}$$

The pressure-based equilibrium constant is then evaluated from classical thermodynamics as a function of the species Gibbs free energy at atmospheric pressure (g_s^{atm}, given by equation (2.45c)), that is

$$K_{p,r}^{eq} = \left(\prod_{s \in \mathcal{S}} p_{\text{atm}}^{\nu''_{s,r} - \nu'_{s,r}} \right) \exp\left[- \frac{\sum_s \left(\nu''_{s,r} - \nu'_{s,r} \right) g_s^{\text{atm}} \mathscr{M}_s}{\mathscr{R} T} \right], \quad \forall r \in \mathcal{R}\,. \tag{2.61}$$

Reaction	M	$A_r^f \left[\frac{1}{\text{s K}^{n_r^f}} \left(\frac{\text{m}^3}{\text{mol}} \right)^{\sum_s \nu'_{s,r} - 1} \right]$	n_r^f [-]	T_r^f [K]
$N_2 + M \rightleftharpoons 2N + M$	N	3.00e+16	-1.6	113200
	O	3.00e+16		
	NO	7.00e+15		
	N_2	7.00e+15		
	O_2	7.00e+15		
$O_2 + M \rightleftharpoons 2O + M$	N	1.00e+16	-1.5	59360
	O	1.00e+16		
	NO	2.00e+15		
	N_2	2.00e+15		
	O_2	2.00e+15		
$NO + M \rightleftharpoons N + O + M$	N	1.00e+11	0	75500
	O	1.00e+11		
	NO	1.00e+11		
	N_2	5.00e+09		
	O_2	5.00e+09		
$O + N_2 \rightleftharpoons N + NO$		5.69e+06	0.42	42938
$N + O_2 \rightleftharpoons NO + O$		2.49e+03	1.18	4005.5

Table 2.5: Empirical constants for the Arrhenius equation (2.58) used to model the forward reaction-rates of a 5-species air mixture, selected from the data provided by Park et al. [22, 23] and Bose & Candler [24, 25]. M denotes a collision partner.

References

[1] John D. Anderson Jr. *Hypersonic and High Temperature Gas Dynamics*. American Institute of Aeronautics and Astronautics, Reston VA, second edition, 2006.

[2] Fernando Miró Miró. *Numerical Investigation of Hypersonic Boundary-Layer Stability and Transition in the presence of Ablation Phenomena*. PhD thesis, Université Libre de Bruxelles and von Karman Insitute for Fluid Dynamics, 2020.

[3] James B. Scoggins. *Development of numerical methods and study of coupled flow, radiation, and ablation phenomena for atmospheric entry*. PhD thesis, Université Paris-Saclay and VKI, 2017.

[4] Richard A. Thompson, Kam-Pui Lee, and Roop N. Gupta. *Computer Codes For The Evaluation Of Thermodynamic Properties, Transport Properties, And Equilibrium Constants Of An 11-Species Air Model*. Technical Report TM-102602, NASA, 1990.

[5] Fernando Miró Miró, Ethan S. Beyak, Daniel Mullen, Fabio Pinna, and Helen L. Reed. *Ionization and Dissociation Effects on Hypersonic Boundary-Layer Stability*. In 31st ICAS Congress, Belo Horizonte, Brazil, 2018. International Council of the Aeronautical Sciences.

[6] John D. Anderson Jr. *Fundamentals of Aerodynamics*. McGraw-Hill, New York NY, fifth edition, 2011.

[7] John D. Anderson Jr. *Computational fluid dynamics: the basics with applications*. McGraw-Hill, New York NY, first edition, 1995.

[8] Fernando Miró Miró and Fabio Pinna. *Linear Stability Analysis of a Hypersonic Boundary Layer in Equilibrium and Non-Equilibrium*. AIAA paper, 2017-4518, 2017.

[9] Frank M. White. *Viscous Fluid Flow*. McGraw-Hill, 2nd edition, 1991.

[10] Hermann Schlichting and Klaus Gersten. *Boundary-Layer Theory*. Springer-Verlag, Berlin Heidelberg, ninth edition, 2017.

[11] Roop N. Gupta, Jerrold M. Yos, Richard A. Thompson, and Kam-Pui Lee. *A review of Reaction Rates and Thermodynamic and Transport Properties for an 11-Species Air Model for Chemical and Thermal Nonequilibrium Calculations to 30000K*. Technical Report RP-1232, NASA, 1990.

[12] William Sutherland. *The viscosity of gases and molecular force*. Philosophical Magazine Series 5, 36(223):507–531, 1893.

[13] S. Chapman and T.G. Cowling. *The Mathematical Theory of Non-uniform Gases: An Account of the Kinetic Theory of Viscosity, Thermal Conduction, and Diffusion in Gases*. The University Press, 1939.

[14] F. G. Blottner, M. Johnson, and M. Ellis. *Chemically Reacting Viscous Flow Program For Multi-Component Gas Mixtures*. Technical Report SC-RR-70-754, Sandia Laboratories, 1971.

[15] C. R. Wilke. *A Viscosity Equation for Gas Mixtures*. The Journal of Chemical Physics, 18(4):517–519, 1950.

[16] Richard S. Brokaw. *Approximate formulas for the viscosity and thermal conductivity of gas mixtures*. The Journal of Chemical Physics, 29(2):391–397, 1958.

[17] Jerrold M Yos. *Approximate equations for the viscosity and translational thermal conductivity of gas mixtures*. Technical Report AVSSD-0112-67-RM, Avco Corporation, 1967.

[18] Mary L. Hudson, Ndaona Chokani, and Graham V. Candler. *Linear stability of hypersonic flow in thermochemical nonequilibrium*. AIAA Journal, 35(6):958–964, 1997.

[19] Antonio Di Giovanni and Christian Stemmer. *Roughness-Induced Boundary-Layer Transition on a Hypersonic Capsule-Like Forebody Including Nonequilibrium*. Journal of Spacecraft and Rockets, 56(6):1795–1808, nov 2019.

[20] Fernando Miró Miró, Ethan S. Beyak, Fabio Pinna, and Helen L. Reed. *High-enthalpy models for boundary-layer stability and transition*. Physics of Fluids, 31(044101), 2019.

[21] Walter G. Vincenti and Charles H. Kruger. *Introduction to physical gas dynamics*. Huntington, N.Y. : Krieger, 1967.

[22] Chul Park. *Review of chemical-kinetic problems of future NASA missions. I - Earth entries*. Journal of Thermophysics and Heat Transfer, 7(3):385–398, 1993.

[23] Chul Park, Richard L. Jaffe, and Harry Partridge. *Chemical-Kinetic Parameters of Hyperbolic Earth Entry*. Journal of Thermophysics and Heat Transfer, 15(1):76–90, 2001.

[24] Deepak Bose and Graham V. Candler. *Thermal rate constants of the N2+O—NO+N reaction using ab initio 3A" and 3A' potential energy surfaces*. The Journal of Chemical Physics, 104(8):2825–2833, 1996.

[25] Deepak Bose and Graham V. Candler. *Thermal rate constants of the O2+N—NO+O reaction based on the A2' and A4' potential-energy surfaces*. The Journal of Chemical Physics, 107(16):6136–6145, 1997.

3

Hydrodynamic stability

Hydrodynamic stability refers to the study of the stability and the onset of instability of fluid flows. A fundamental aspect of hydrodynamic stability theory is the splitting of the instantaneous flow field (described by the vector of independent (state) variables $\mathbf{q}$) into a steady[1] component ($\bar{\mathbf{q}}$), known as base flow, and an unsteady perturbation field ($\tilde{\mathbf{q}}$) [2]:

$$\mathbf{q} = \bar{\mathbf{q}} + \tilde{\mathbf{q}}. \tag{3.1}$$

The base flow is considered a reference flow into which the perturbations develop. A fundamental requirement is that the base flow must satisfy the governing equations (their steady form in this case). Inserting the splitting given by equation (3.1) into the Navier-Stokes system (see § 2.2) leads to the most general form of the governing equations of stability theory, describing the dynamics of all three-dimensional non-linear perturbations ($\bar{\mathbf{q}} = \bar{\mathbf{q}}(x, y, z)$ and $\tilde{\mathbf{q}} = \tilde{\mathbf{q}}(x, y, z, t)$). These equations can be found for a calorically perfect gas in the appendix A of reference [3].

[1] The stability of time-periodic flows can also be studied by means of stability theory, involving the use of Floquet analysis. See for example Herbert [1] for details. All the base flows treated in this work are steady flows.

3.1 Linearized perturbation equations

As discussed in § 1.2, the most common paths to transition begin with a region of linear development of the perturbations. In many cases, such as for typical flat plate conditions as noted by Arnal [4], the streamwise extent of linear amplification can cover about 75 to 85% of the distance between the leading edge of the flat plate and the beginning of transition, which highlights the importance of analyzing linear perturbation growth.

The behavior of the disturbances during the linear stage is described by the linearized perturbation equations, which can be retrieved by assuming infinitesimally small perturbations, such that equation (3.1) becomes

$$\mathbf{q} = \bar{\mathbf{q}} + \epsilon\tilde{\mathbf{q}} + O(\epsilon^2), \tag{3.2}$$

with $\epsilon \ll 1$. This implies that terms of order $O(\epsilon^2)$ or higher in the general perturbation equations are negligibly small with respect to the linear terms. This simplification leads to the governing equations of linear stability theory, namely, the linearized perturbation equations, also known as the linearized Navier-Stokes equations (LNSE). These equations are reported in appendix A for a calorically perfect gas and for a base flow depending on y and z, i.e., $\bar{\mathbf{q}} = \bar{\mathbf{q}}(y, z)$. The direct solution of equations (A.1a) to (A.1e) without any further assumption on the perturbation quantities is usually known as linearized direct numerical simulation (LDNS).

3.2 Treatment of the perturbations of the dependent quantities

The dependent quantities appearing in the governing equations are also usually decomposed into a laminar base flow and a perturbation component following equation (3.2). Examples of dependent quantities include μ, k or h. Any perturbation variable associated to a dependent quantity must be expressed in terms of the perturbation variables associated to the independent quantities, denoted by the state vector $\tilde{\mathbf{q}}$, which are the unknowns for which the stability equations are solved. This is achieved by means of a Taylor expansion of the dependent perturbation quantities around zero. Denoting by $\tilde{Q}$ a perturbation quantity depending on a single independent quantity $\tilde{q}$, the expansion can be written as

$$\tilde{Q}(\tilde{q}) = \frac{d\bar{Q}}{d\bar{q}}\tilde{q} + \frac{1}{2}\frac{d^2\bar{Q}}{d\bar{q}^2}\tilde{q}^2 + \cdots + \frac{1}{n!}\frac{d^n\bar{Q}}{d\bar{q}^n}\tilde{q}^n, \tag{3.3}$$

where terms of order $O(\tilde{q}^2)$ or higher are neglected when a linear stability theory is considered. Equation (3.3) is suitable for dependent quantities in the CPG and

the TPG thermodynamic flow assumptions, which depend only on temperature. For CNE, however, the dependent perturbation quantities are not functions of $\tilde{T}$ only, but also of the composition of the mixture, described by the state variables $\tilde{\rho}_s$. Therefore, a multi-variable Taylor expansion is required in this case:

$$\tilde{Q}(\tilde{q}_1,\ldots,\tilde{q}_d) = \sum_{j=1}^{d} \frac{\partial \bar{Q}}{\partial \bar{q}_j}\tilde{q}_j + \frac{1}{2}\sum_{j=1}^{d}\sum_{l=1}^{d} \frac{\partial^2 \bar{Q}}{\partial \bar{q}_j \partial \bar{q}_l}\tilde{q}_j\tilde{q}_l + \cdots + \frac{1}{n!}\sum_{j1=1}^{d}\cdots\sum_{jn=1}^{d} \frac{\partial^n \bar{Q}}{\partial \bar{q}_{j1}\cdots\partial \bar{q}_{jn}}\tilde{q}_{j1}\cdots\tilde{q}_{jn}, \quad (3.4)$$

where d denotes the number of independent variables on which $\tilde{Q}$ depends. The use of this procedure in practice implies that the derivatives of the base-flow dependent quantities with respect to the thermodynamic state quantities must be known. This is usually a straightforward task for simple thermodynamic flow assumptions and property models, such as CPG and TPG. However, for more complex descriptions, such as CNE, symbolic expressions for the necessary derivatives are obtained by means of an automatic derivation tool and are subsequently implemented in different subroutines for their computation by means of an automatic implementation tool (see § 4.3.1). The reader is referred to reference [5] for details on the methodology employed for the automatic derivation of thermodynamic derivatives.

3.3 Fourier transformation of the perturbation quantities

For many applications of interest, the laminar base flows can be assumed to be two-dimensional in space. This leads to a system with constant coefficients with respect to the spatial direction of invariance. The same is true for the temporal dimension, as the base flow is assumed to be independent of time. This invariance of the system can be exploited given that the general solution to linear differential equations with constant coefficients can be decomposed into a sum of exponential functions. For this purpose, the problem can be Fourier-transformed in the directions of invariance. For example, given a base flow that depends on two arbitrary spatial dimensions, $\bar{\mathbf{q}} = \bar{\mathbf{q}}(y,z)$, the solution of the governing equations, that is, the perturbations of the independent quantities, can be expressed by means of the inverse Fourier transform as

$$\tilde{\mathbf{q}}(x,y,z,t) = \frac{1}{(2\pi)^2}\int_{-\infty}^{+\infty}\int_{-\infty}^{+\infty} \hat{\mathbf{q}}(y,z;\alpha,\omega)\,\mathrm{e}^{i(\alpha x-\omega t)}\,d\alpha\,d\omega, \quad (3.5)$$

where $\hat{\mathbf{q}}$ denotes the combination of the amplitude function of the perturbation in y and z and the Fourier transform of $\tilde{\mathbf{q}}$ in x and t, α is the wavenumber along x (streamwise wavenumber) and ω is the angular frequency. The choice of a negative sign for the angular frequency complex exponential term, $\exp(-i\omega t)$, is a convention commonly used in stability theory [6].

In addition to expressing the perturbations in terms of the Fourier transform, the solution is usually further simplified by assuming it to consist of a sum of discrete modes of the system. This is enforced by making each perturbation monochromatic in Fourier space or time, depending on whether the temporal or the spatial dynamics of the problem are considered. In the temporal case, one forces the solution to be monochromatic in space by fixing the wavenumber along each direction of invariance ($\alpha = \alpha_0$ in this case), and the problem is solved for ω. Similarly, in the spatial problem a fixed frequency is imposed ($\omega = \omega_0$) and the solution of the system provides the spatial evolution of the perturbations along one of the directions of invariance, in this case described by α. When there is more than one spatial direction of invariance, the wavenumber must also be prescribed along each direction except for the one for which the problem is being solved. The parameters fixed in each approach are normally chosen to be real, that is, a real perturbation frequency or a real wavenumber. For a temporal problem with a fixed streamwise wavenumber α_0, the vector $\hat{\mathbf{q}}$ can be written in terms of discrete modes as [7]:

$$\hat{\mathbf{q}}(y,z;\alpha,\omega) = \sum_k A_k \hat{\mathbf{q}}_k(y,z)\delta(\alpha-\alpha_0)\hat{\delta}(\omega-\mathscr{D}_k(\alpha)), \tag{3.6}$$

where A_k, $\hat{\mathbf{q}}_k$ and $\mathscr{D}_k$ are respectively the amplitude, the amplitude function and the dispersion relation of the discrete mode with index k, δ is the Dirac delta function and $\hat{\delta}$ is a delta function with similar properties to δ. For the purpose of this derivation, the behavior of $\hat{\delta}$ is equivalent to that of δ, that is, $\delta(\alpha-\alpha_0)=1$ if $\alpha = \pm\alpha_0$ and 0 otherwise and $\hat{\delta}(\omega-\mathscr{D}_k(\alpha)) = 1$ if $\omega = \pm\mathscr{D}_k(\alpha)$ and 0 otherwise. For the specific properties of $\hat{\delta}$, refer to the appendix A of reference [7]. It is implicitly assumed that A_k and $\hat{\mathbf{q}}_k$ are generally different for different values of α_0. Inserting equation (3.6) into equation (3.5) yields:

$$\begin{aligned}
&\tilde{\mathbf{q}}(x,y,z,t) = \\
&\frac{1}{(2\pi)^2}\int_{-\infty}^{+\infty}\int_{-\infty}^{+\infty}\left[\sum_k A_k\hat{\mathbf{q}}_k(y,z)\delta(\alpha-\alpha_0)\hat{\delta}(\omega-\mathscr{D}_k(\alpha))\right]\mathrm{e}^{i(\alpha x-\omega t)}\,d\alpha\,d\omega \\
&= \frac{1}{(2\pi)^2}\int_{-\infty}^{+\infty}\left[\sum_k A_k\hat{\mathbf{q}}_k(y,z)\hat{\delta}(\omega-\mathscr{D}_k(\alpha_0))\right]\mathrm{e}^{i(\alpha_0 x-\omega t)}\,d\omega + c.c.\,,
\end{aligned} \tag{3.7}$$

where $c.c.$ denotes the complex conjugate. For $\tilde{\mathbf{q}}$ to be a solution of the governing equations, the dispersion relation must be implicitly satisfied, meaning that for each mode $\omega = \mathscr{D}_k(\alpha_0)$. Therefore:

$$\tilde{\mathbf{q}}(x,y,z,t) = \frac{1}{(2\pi)^2}\sum_k A_k \hat{\mathbf{q}}_k(y,z)\,\mathrm{e}^{i[\alpha_0 x - \mathscr{D}_k(\alpha_0)t]} + c.c. \\ = \frac{1}{(2\pi)^2}\sum_k A_k \tilde{\mathbf{q}}_k(x,y,z,t) + c.c.\,. \quad (3.8)$$

Equation (3.8) is a form of the solution for the perturbation quantities written in terms of the discrete modes. Each $\tilde{\mathbf{q}}_k$ is a solution of the governing stability equations and represents the physical perturbation associated to the discrete mode with index k. It is important to note that in this formulation each $\tilde{\mathbf{q}}_k$ is independent of the others. This is very convenient in practice, because it implies that only those perturbations which are of interest for the physical problem under study can be considered.

In the literature, the solution is oftentimes presented in terms of the individual (discrete) modes of the system only, i.e., $\tilde{\mathbf{q}}_k$, usually formulated using the following perturbation ansatz (see for example [8]):

$$\tilde{\mathbf{q}}(x,y,z,t) = \hat{\mathbf{q}}(y,z)\exp\left[i\left(\alpha x - \omega t\right)\right] + c.c. = 2\Re\{\hat{\mathbf{q}}(y,z)\exp\left[i\left(\alpha x - \omega t\right)\right]\} \quad (3.9)$$

or the following compact form

$$\tilde{\mathbf{q}}(x,y,z,t) = \hat{\mathbf{q}}(y,z)\exp\left(i\Theta\right) + c.c.\,, \quad (3.10)$$

where Θ denotes the phase function of the perturbation. It is important to emphasize that these expressions correspond to a single mode only. The subindex k is dropped and the amplitude A_k and the factor $1/(2\pi)^2$ are not considered[2]. The usage of an ansatz like the one given by equation (3.9) is convenient for the derivation of stability equations. Substituting equation (3.9) into the linear perturbation equations leads to the governing stability equations for a single mode, which in this case take the form of a two-dimensional generalized eigenvalue problem (see § 3.6.1). For this reason, the discrete modes are often also known as eigenmodes or eigensolutions of the system. For simple incompressible flow configurations, it has been shown that the eigensolutions form a complete eigenfunction expansion basis, which consists of an infinite number of solutions (modes). For this

[2]Linear stability theories that lead to an eigenvalue problem are unable to provide an absolute value for the amplitude of the disturbances, as the computed amplitude functions (eigenvectors) are defined up to a complex multiplicative constant. Hence, leaving out the amplitude A_k and the factor $1/(2\pi)^2$ does not impact the physical meaning of the result.

reason, linear stability theory might be viewed as a means to obtain a basis for the eigenfunction expansion method (see the recent summary by Tumin [9]).

It is also important to stress that usually only a few eigensolutions become unstable and are of physical interest, thus reducing the problem to solving only for those individual modes which dominate the dynamics of the system. This clearly highlights one of the main advantages of stability analysis for the study of transition to turbulence.

3.4 Local linear stability theory

The first theoretical developments in linear stability theory considered base flows dependent only on a single spatial dimension other than the streamwise flow direction (in the case of a boundary-layer, $\bar{\mathbf{q}} = \bar{\mathbf{q}}(y)$ for example, with y being the wall-normal direction), leading to a one-dimensional local linear stability theory, also commonly known as linear stability theory or LST. Here, the term local refers to the fact that the base flow is not dependent on the streamwise direction and the perturbation solution at the local streamwise position where the analysis is carried out only depends on the base flow state at that location. As a result, the history of the perturbations is not taken into account. Only local information is necessary to solve the eigenvalue problem. This theory considers a perturbation ansatz of the form:

$$\tilde{\mathbf{q}}(x, y, z, t) = \hat{\mathbf{q}}(y) \exp\left[i\left(\alpha x + \beta z - \omega t\right)\right] + c.c.\,, \tag{3.11}$$

where β denotes the wavenumber along z (spanwise wavenumber). Introducing the ansatz (3.11) into the linearized perturbation equations leads to the governing equations of local linear stability theory, or the LST equations. For the case of a calorically perfect gas, these equations are reported in appendix C. An excellent review of local linear stability theory is given by Mack [6], which constitutes one of the most important reference texts for any reader interested in boundary-layer stability theory.

3.4.1 Parallel flow assumption

The assumption that the base flow depends only on one spatial direction represents a flow field that is parallel in two spatial directions and non-parallel in the third. In this case, the requirement for the base flow to satisfy the governing equations (the Navier-Stokes equations) brings additional implications on the base flow quantities. This can be illustrated as follows. The continuity equation governing a general three dimensional steady base flow can be written as

$$\frac{\partial(\bar{\rho}\bar{u})}{\partial x} + \frac{\partial(\bar{\rho}\bar{v})}{\partial y} + \frac{\partial(\bar{\rho}\bar{w})}{\partial z} = 0. \tag{3.12}$$

Assuming that the base flow depends only on the wall-normal direction, i.e. $\bar{\rho} = \bar{\rho}(y)$, $\bar{u} = \bar{u}(y)$, $\bar{v} = \bar{v}(y)$ and $\bar{w} = \bar{w}(y)$, yields

$$\frac{\partial(\bar{\rho}\bar{v})}{\partial y} = 0, \quad \text{or} \quad \bar{\rho}\bar{v} = \text{const.}. \tag{3.13}$$

At the wall ($y = 0$), the no-slip condition dictates that $\bar{v}|_{y=0} = 0$, therefore

$$\bar{\rho}\bar{v}|_{y=0} = 0 \implies \bar{\rho}\bar{v} = \text{const.} = 0 \implies \bar{v} = 0. \tag{3.14}$$

The assumption that $\bar{\mathbf{q}} = \bar{\mathbf{q}}(y)$ implies that the base flow wall-normal velocity must be zero for the continuity equation to be satisfied. Since $\bar{v}$ is the velocity component associated to the non-parallel part of the base flow, this means that any LST analysis only incorporates the physics associated to the parallel part of the base flow, and hence the use of ansatz (3.11) is sometimes also referred to as the parallel flow assumption. In the case of a boundary-layer base flow, for example, the parallel flow assumption neglects the local growth of the boundary layer, contained in $\rho\bar{v}$. In other words, LST analyses neglect non-parallel effects.

3.4.2 Temporal stability framework

In the temporal LST framework, both α and β are fixed to be real, that is $\alpha = \alpha_r$ and $\beta = \beta_r$, and the problem is solved for ω, which is complex in general ($\omega = \omega_r + i\omega_i$). The real part ω_r denotes the angular frequency of the perturbation and ω_i its associated temporal growth rate. A positive value of ω_i means that the perturbation is growing in time at a given location and spatial wavenumber vector (temporally unstable disturbance), whereas a negative value implies that it is decaying in time (temporally stable disturbance). Under these considerations, the following differential generalized eigenvalue problem is obtained:

$$\mathbf{A}_\omega \hat{\mathbf{q}} = \omega \mathbf{B}_\omega \hat{\mathbf{q}}, \tag{3.15}$$

where $\mathbf{A}_\omega$ and $\mathbf{B}_\omega$ are matrix operators that contain the coefficients of the system of governing equations (see appendix C) that respectively multiply the zeroth and the first powers of the eigenvalue ω.

3.4.3 Spatial stability framework

When the spatial evolution of the perturbations is desired, the frequency is fixed to be a real quantity ($\omega = \omega_r$). Since two spatial wavenumbers (α and β) are present in the LST framework, a further choice needs to be made on which of them is

fixed. In general, the interest focuses on the spatial growth of the perturbations along the streamwise direction, that is, β is fixed and the problem is solved for α. Typically β is fixed to be a real number, however, the problem can generally be solved for complex β as well. In this work, only cases with $\beta = \beta_r$ are considered, leaving $\alpha = \alpha_r + i\alpha_i$ as the only complex wave parameter. In this case, the real part of α represents the streamwise wavenumber of the perturbation and $-\alpha_i$ its spatial growth rate. Due to the sign convention adopted in the Fourier transform of the solution (see § 3.3), $\alpha_i < 0$ denotes spatial growth while $\alpha_i > 0$ indicates decay in space.

The previous assumptions lead once again to a differential generalized eigenvalue problem that can be expressed as

$$\mathbf{A}_\alpha \hat{\mathbf{q}} = \alpha \mathbf{B}_\alpha \hat{\mathbf{q}} + \alpha^2 \mathbf{C}_\alpha \hat{\mathbf{q}}, \tag{3.16}$$

where $\mathbf{A}_\alpha$, $\mathbf{B}_\alpha$ and $\mathbf{C}_\alpha$ are matrix operators that contain the coefficients of the system of LST equations that respectively multiply the zeroth, first and second powers of the eigenvalue. It is very important to note that in this case the problem is non-linear in the eigenvalue α, thus it cannot be solved by standard eigenvalue solvers. To convert the system to a linear generalized eigenvalue problem, the matrix companion method [10] is employed, which introduces auxiliary variables in the vector of amplitude functions of the form $\alpha\hat{\mathbf{q}}$. For example, in the case of CPG LST with a state vector given by $\hat{\mathbf{q}} = [\hat{u}, \hat{v}, \hat{w}, \hat{T}, \hat{p}]^{\mathrm{T}}$, the necessary auxiliary variables are $\alpha\hat{u}$, $\alpha\hat{v}$, $\alpha\hat{w}$ and $\alpha\hat{T}$, and the system of equations takes the form

$$\mathbf{A}^+_\alpha \hat{\mathbf{q}}^+ = \alpha \mathbf{B}^+_\alpha \hat{\mathbf{q}}^+, \tag{3.17}$$

with

$$\mathbf{A}^+_\alpha = \begin{bmatrix} \mathbf{A}_\alpha & -\mathbf{B}^{\hat{u}:\hat{T}}_\alpha \\ \mathbf{0} & \mathbf{I} \end{bmatrix}, \quad \mathbf{B}^+_\alpha = \begin{bmatrix} \mathbf{B}^{\hat{p}}_\alpha & \mathbf{C}^{\hat{u}:\hat{T}}_\alpha \\ \mathbf{I} & \mathbf{0} \end{bmatrix} \tag{3.18}$$

and

$$\hat{\mathbf{q}}^+ = [\hat{u}, \hat{v}, \hat{w}, \hat{T}, \hat{p}, \alpha\hat{u}, \alpha\hat{v}, \alpha\hat{w}, \alpha\hat{T}]^{\mathrm{T}}, \tag{3.19}$$

where $\mathbf{B}^{\hat{u}:\hat{T}}_\alpha$ and $\mathbf{C}^{\hat{u}:\hat{T}}_\alpha$ are non-square matrices which contain those columns from the respective matrix operators $\mathbf{B}_\alpha$ and $\mathbf{C}_\alpha$ that correspond to the variables $\hat{u}$, $\hat{v}$, $\hat{w}$ and $\hat{T}$. Similarly, $\mathbf{B}^{\hat{p}}_\alpha$ is a square matrix that contains only the columns from $\mathbf{B}_\alpha$ that correspond to the variable $\hat{p}$. The symbol $\mathbf{I}$ denotes the identity matrix. The auxiliary variable $\alpha\hat{p}$ is not necessary in this case as the system of LST equations for a calorically perfect gas does not feature second spatial derivatives of the pressure perturbation (see appendix C). It is important to emphasize that this procedure increases significantly the size of the system to be solved (in this particular case from 5 to 9 unknown variables) and therefore it has a large computational impact. The matrix companion method is also employed for the TPG and the CNE thermodynamic flow assumptions.

Finally, it is worth mentioning that the possibility also exists of fixing a complex wavenumber in the temporal approach or fixing a complex frequency in the spatial approach while solving for the other respective complex quantity in each framework. In this case, the approach receives the name of spatio-temporal analysis, which is widely employed in absolute instability studies [8].

3.4.4 Approximate relation between temporal and spatial growth rates

The perturbations analyzed in this work are waves that travel in a definite direction as their amplitude evolves downstream. Unstable disturbances of this type are known as convective instabilities, as opposed to absolute instabilities (see § 3.11). Each of them propagates at a given finite group velocity $c_g = \partial\omega/\partial\alpha$ which satisfies the dispersion relation dictated by the governing disturbance equations. For perturbations with $c_g \neq 0$, that is, convective perturbations, there exists an equivalence between temporal and spatial growth. This implies that a wave that features only a temporal amplification (as described by means of the temporal stability approach) can be transformed into a wave undergoing only a spatial growth, and vice versa.

An approximate relation between the temporal and spatial growth rates was derived by Gaster [11], given by

$$\alpha_i|_{\omega_i=0} = -\frac{\omega_i|_{\alpha_i=0}}{c_g} + O(\omega_i^2|_{\alpha_i=0}), \tag{3.20}$$

where $\alpha_i|_{\omega_i=0}$ denotes the spatial growth rate in the limit of $\omega_i = 0$, that is, for a wave with spatial growth only (as in the spatial approach), and $\omega_i|_{\alpha_i=0}$ represents the temporal growth rate in the limit of $\alpha_i = 0$, i.e. for a wave with temporal amplification only (as in the temporal approach). Equation (3.20), also known as the Gaster transformation, allows to convert the solution obtained by means of the temporal stability framework into an approximate solution of the spatial approach, and vice versa. The group velocity can be evaluated in either the temporal or the spatial limits as $c_g = \partial\omega_r/\partial\alpha_r$. It is important to note that Gaster's transformation is accurate up to second order in ω_i, meaning that it offers satisfactory conversions mainly for small growth rates (close to the neutral stability curve). In practice, however, the relation has been found to perform very well for a wide range of applications, including flat-plate boundary layers, secondary crossflow instabilities [12, 13] and roughness-induced disturbances [14, 15].

Given the increase in computational cost associated with the solution of the spatial eigenvalue problem, using Gaster's transformation to obtain spatial growth rates from the cheaper temporal solution constitutes a very advantageous approach in practice. Nevertheless, a verification of the validity of the transformation for the

problem under study is necessary. Section § 5.3.5.3 discusses its validity for some of the cases studied in this work.

3.5 Non-local linear stability theory: parabolized stability equations

With the aim of studying the role of non-parallel effects in convectively unstable flows, the LST parallel flow assumption can be relaxed by allowing a weak variation of the flow quantities in the streamwise direction. This can be achieved by means a parabolization of the linearized perturbation equations while introducing a streamwise dependency in the base flow ($\bar{\mathbf{q}} = \bar{\mathbf{q}}(x, y)$) and in the perturbation amplitude function ($\hat{\mathbf{q}} = \hat{\mathbf{q}}(x, y)$), giving birth to what is known as parabolized stability equations (PSE) [16, 17]. The fundamental assumption behind the PSE theory is a scale separation between the weak (or slow) variation of flow quantities along the streamwise direction (order $O(1/Re)$ for boundary-layer flows) and the strong variation along the wall-normal direction (order $O(1)$). The streamwise dependence of the base flow and of the perturbation quantities as well as the base flow wall-normal velocity component ($\bar{v}$) are assumed to scale with the small parameter $1/Re$, namely

$$\frac{\partial}{\partial x},\ \bar{v} \approx O(Re^{-1}), \tag{3.21}$$

whereas the remaining base flow quantities and their wall-normal derivative are assumed to be of unit order. Equivalently,

$$\frac{\partial}{\partial x} \ll \frac{\partial}{\partial y}, \quad \frac{\partial}{\partial z} = 0, \tag{3.22}$$

and, in turn, the second derivatives of $\bar{\mathbf{q}}$ and $\hat{\mathbf{q}}$ with respect to the streamwise direction are neglected for being of order $1/Re^2$.

The ansatz associated to the PSE assumption results from a WKB approximation and takes the following form

$$\tilde{\mathbf{q}}(x, y, z, t) = \hat{\mathbf{q}}(x, y) \exp\left[i \left(\int_{x_0}^{x} \alpha(\xi)\, d\xi + \beta z - \omega t \right) \right] + c.c.\,. \tag{3.23}$$

The parabolized stability equations can then be obtained by means of an order of magnitude analysis of the linearized disturbance equations, which removes terms of order $1/Re^2$, and the substitution of equation (3.23) into the resulting system of equations. These assumptions do not lead to an eigenvalue problem but to a streamwise marching problem instead, which can be expressed in matrix form as

$$\mathbf{L}\hat{\mathbf{q}} + \mathbf{M}\frac{\partial \hat{\mathbf{q}}}{\partial x} = \mathbf{0}, \tag{3.24}$$

where $\mathbf{L}$ and $\mathbf{M}$ are matrix operators that contain the coefficients of the PSE system of governing equations (see for instance [3]). The marching nature of the problem requires the use of upstream information in order to advance the solution downstream. In other words, the history of the perturbations is taken into account. In this sense, the PSE theory is non-local due to the fact that the disturbance solution at a given streamwise location is influenced by local as well as upstream flow conditions. The marching along the streamwise direction is usually carried out by means of a first or second-order backward Euler scheme.

The PSE ansatz features a streamwise dependency on both the amplitude function and the phase function. This introduces an ambiguity that can be resolved by means of an auxiliary condition, which usually takes the form of the following normalization condition:

$$\int_{y^-}^{y^+} \hat{\mathbf{q}}^* \frac{\partial \hat{\mathbf{q}}}{\partial x}\, dy = 0, \tag{3.25}$$

where y^- and y^+ respectively denote the lower and upper limits of integration along the y direction (the limits (boundaries) along y of the domain in which the analysis is performed) and $(\cdot)^*$ refers to the complex conjugate. This condition enforces the variation of the amplitude function to remain small enough to satisfy the $1/Re$ scaling of $\partial\hat{\mathbf{q}}/\partial x$. Note that the result of equation (3.25) is a scalar quantity.

It is important to emphasize that the PSE equations are not completely parabolic. A small ellipticity remains in the governing stability equations which allows for upstream propagation of information through the streamwise pressure gradient terms. This introduces oscillations in the marching solution when the streamwise step size is too small. Li & Malik [18] found the smallest theoretical stable step size to be

$$\Delta x_{min} = \frac{1}{|\alpha_r|} = \frac{|\lambda_x|}{2\pi}, \tag{3.26}$$

with λ_x being the streamwise wavelength. Hence, no more than 6 streamwise stations should be used for each streamwise wavelength. In practice, however, a convergence study with respect to Δx is often necessary to determine the step size limit for each particular application. On the other hand, stabilization techniques have also been developed which allow to relax the step size limitations, which include dropping the streamwise pressure derivative ($\partial\hat{p}/\partial x = 0$) or the addition of a stabilizing term to the system of equations [19].

3.5.1 Definition of growth rate

Given the non-local character of the PSE theory, the physical growth rate of a disturbance comes from two contributions, namely, the growth associated to the exponential part of the disturbance ($-\alpha_i$) and the growth associated to the streamwise variation of the amplitude function. Two different quantities are commonly employed to evaluate the second contribution (see for instance [8]). On the one hand, the streamwise variation of the amplitude function of any of the components of $\hat{\mathbf{q}}$ is used, yielding the following definition

$$\sigma = -\alpha_i + \Re\left\{\frac{1}{\hat{q}}\frac{\partial \hat{q}}{\partial x}\right\}\Bigg|_y, \tag{3.27}$$

where the second term is usually evaluated at the y coordinate where it reaches its maximum value. On the other hand, the disturbance kinetic energy $\hat{E}_K$ is often considered instead, leading to the following expression

$$\sigma = -\alpha_i + \frac{\partial}{\partial x}\left[\ln\left(\sqrt{\hat{E}_K}\right)\right], \tag{3.28}$$

with

$$\hat{E}_K = \int_{y^-}^{y^+} \bar{\rho}\left(\hat{u}\hat{u}^* + \hat{v}\hat{v}^* + \hat{w}\hat{w}^*\right) dy. \tag{3.29}$$

3.6 Extensions for base flows with additional inhomogeneous directions

In a large number of practical flow fields, the assumptions on the spatial base-flow dependency imposed by local (LST) or by non-local (PSE) linear stability theory are too restrictive for such theories to be able to appropriately describe the perturbation dynamics. Therefore, over the last four decades, different extensions have been developed to deal with flow fields that feature more than one inhomogeneous spatial direction as well as strong non-parallel effects [20–22]. Examples of such flows include the wake induced by isolated and/or distributed roughness, cross-flow vortices in swept-wing boundary layers, laminar separation bubbles, Görtler vortices and twin jets, among many others. The instability characteristics of these flow fields are still a state-of-the-art subject. As introduced in § 1.3, the first of them is the main focus of this work.

The most common theories currently in use for the analysis of base flows with more than one inhomogeneous direction are described next.

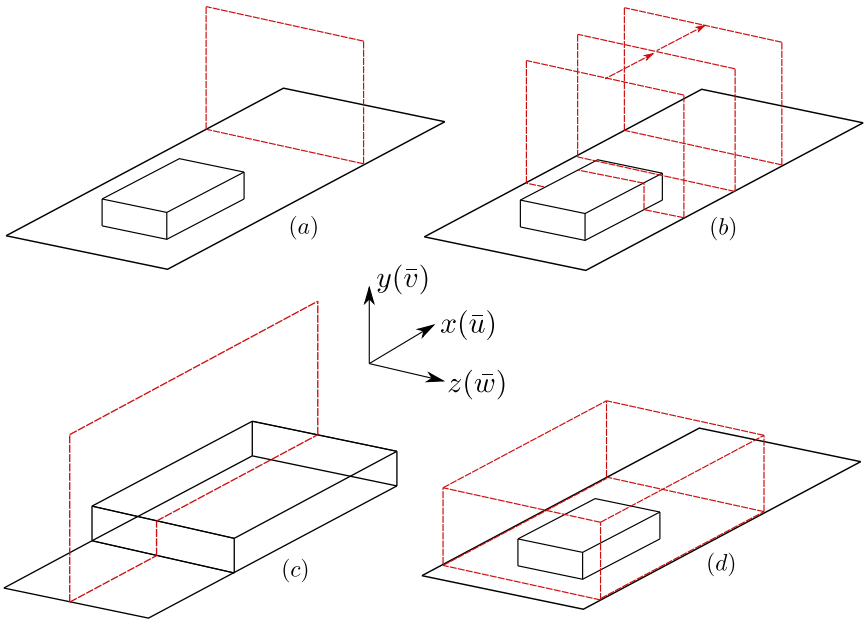

Figure 3.1: Example of the amplitude function domain (red-dotted line) for the different theories that consider more than one inhomogeneous direction: (a) *2D-LST;* (b) *3D-PSE;* (c) *Streamwise BiGlobal;* (d) *TriGlobal.*

3.6.1 Two-dimensional local linear stability theory

Two-dimensional local linear stability theory is a direct generalization of classical LST theory. It considers base flows and amplitude functions that depend on the two spatial directions other than the streamwise direction. If x is chosen to be the streamwise direction, 2D-LST theory assumes $\bar{\mathbf{q}} = \bar{\mathbf{q}}(y, z)$, such that the base flow is no longer required to be parallel along the spanwise direction as in LST (see figure 3.1(a)). The corresponding perturbation ansatz becomes:

$$\tilde{\mathbf{q}}(x, y, z, t) = \hat{\mathbf{q}}(y, z) \exp[i(\alpha x - \omega t)] + c.c. \,, \tag{3.30}$$

which was used as an example for the derivation described in § 3.3. Note that the spanwise wavenumber β is no longer part of the ansatz, reflecting the inhomogeneous character along z. The base flow and the perturbation amplitude function are then contained in a plane oriented perpendicularly to the streamwise flow direction, that is, a spanwise plane (yz). For this reason, this theory usually receives the name of spanwise BiGlobal stability theory [20, 21], where the term BiGlobal refers to the fact that there are two inhomogeneous directions embodied in the theory assumptions. This is the most common name currently encountered in the literature as it was the first terminology introduced. Later work by other au-

thors [23, 24], however, preferred to employ the 2D-LST designation to highlight its natural extension from classical LST theory and to reflect its local character in the sense that the solution at a given streamwise station still depends only on information at that location (i.e. the perturbation history is not taken into account). This is the nomenclature adopted in this dissertation. Another equivalent terminology, less common in the literature but that directly reflects the local behavior of this theory, is BiLocal stability theory [7]. It is also worth mentioning that, as already recognized by Theofilis [20], a potential source of confusion exists with respect to the meaning of the term "global" in the context of flow instability, which arises from the local/global nomenclature introduced by the high-impact work of Huerre & Monkewitz [25] to respectively denote the instability of a local profile or that of the entire flow field.

The ansatz for 2D-LST theory also leads to a (partial) differential generalized eigenvalue problem, in this case a two-dimensional eigenvalue problem, which can be stated in matrix form using the same expression as equation (3.15) for a temporal approach or the same expression as equation (3.16) for a spatial analysis. The 2D-LST equations for a calorically perfect gas can be found in appendix B.

Two-dimensional local linear stability theory becomes appropriate for flows which can be assumed to be parallel along the streamwise direction, but which however feature large variations along the wall-normal and spanwise directions. This is for instance the case of streamwise vortices, where the flow field in the yz plane is characterized by a strong vorticity but along x it undergoes a slow variation. As presented later in chapters 5 and 6, extensive use of 2D-LST theory is done in this work.

3.6.1.1 Parallel flow assumption revisited

The base flow assumption embedded in 2D-LST only requires the flow to be locally parallel along the streamwise direction. Recalling the continuity equation for a steady base flow (3.12), this assumption leads to the following relation:

$$\frac{\partial\left(\bar{\rho}\bar{v}\right)}{\partial y}+\frac{\partial\left(\bar{\rho}\bar{w}\right)}{\partial z}=0, \tag{3.31}$$

that is, the base flow momentum in the yz plane must be divergence-free. Therefore, unlike the case of one-dimensional local linear stability theory (see § 3.4.1), the parallel flow assumption in 2D-LST does not lead to the condition that $\bar{v}=0$. This means that 2D-LST allows in principle to incorporate the base flow wall-normal velocity field into the stability analysis.

It is important to mention that the condition imposed by equation (3.31) on the base flow field is not directly satisfied in the majority of practical problems of interest, since the solutions obtained from the Navier-Stokes equations do not generally yield $\partial\left(\bar{\rho}\bar{u}\right)/\partial x=0$ except in very specific cases. As a consequence, employing

a three-dimensional Navier-Stokes base flow into the governing equations for 2D-LST introduces a violation of condition (3.31). The impact of this inconsistency appears to be dependent on the particular problem under investigation. Bonfigli & Kloker [26] have investigated the effect of using three different representations of the base flow (primary state) in the case of the secondary instability of crossflow vortices. The three different descriptions employed consisted in either using the $\bar{v}$ and $\bar{w}$ velocity components directly from the solution of the Navier-Stokes equations, fixing only the $\bar{v}$ component from the Navier-Stokes solution and computing a modified $\bar{w}$ component by satisfying the 2D-LST continuity equation (3.31), or fixing the $\bar{w}$ component and obtaining a modified $\bar{v}$ component by once again satisfying the in-plane divergence-free condition. In all three cases, the 2D-LST theory failed to provide a successful agreement against the amplification rates provided by DNS, without showing an unequivocal advantage of using one of the three base flow representations over the others.

Other authors, instead, choose to neglect the base flow wall-normal velocity component in the 2D-LST calculations as a means to remove the growth of the flow field along the streamwise direction. Although this approach only leads to the fulfillment of equation (3.31) in the case that $\partial\left(\bar{\rho}\bar{w}\right)/\partial z = 0$ (such as for example in a flat plate boundary layer), it has been found for instance to provide a satisfactory agreement between 2D-LST and DNS results by Di Giovanni & Stemmer [24] in the case of the instabilities developing behind spanwise periodic roughness elements mounted on the forebody of a reentry capsule. This suggests, as noted by Groot [7], and in contrast to the observations by Bonfigli & Kloker [26], that the instability in this configuration is mainly governed by the $\bar{u}$ component and its respective gradients ($\partial\bar{u}/\partial y$ and $\partial\bar{u}/\partial z$), and only to a lesser extent by the in-plane velocity components $\bar{v}$ and $\bar{w}$, which are small in comparison.

At present, there is no consensus on which approach should be adopted in general. In this work, the assumption of Di Giovanni & Stemmer [24] is also followed, neglecting the base-flow wall-normal velocity component in the 2D-LST computations.

3.6.2 Streamwise BiGlobal stability theory

For the case of flow fields that are highly non-parallel along the streamwise direction, that is, which feature strong variations along x, another option considers base flows and amplitude functions that are inhomogeneous along the streamwise direction as well as along one of the other two spatial coordinates, while retaining a homogeneous character in the third. Possibilities for these requirements include $\bar{\mathbf{q}} = \bar{\mathbf{q}}(x, y)$ and $\hat{\mathbf{q}} = \hat{\mathbf{q}}(x, y)$ or $\bar{\mathbf{q}} = \bar{\mathbf{q}}(x, z)$ and $\hat{\mathbf{q}} = \hat{\mathbf{q}}(x, z)$. Such a theory receives the name of streamwise BiGlobal stability theory [20, 21], as the plane where the base flow and the amplitude functions live is oriented along the stream-

wise direction and the flow is non-local (see figure 3.1(c)). The ansatz for this theory can be written as

$$\tilde{\mathbf{q}}(x,y,z,t) = \hat{\mathbf{q}}(x,y)\exp[i(\beta z - \omega t)] + c.c.\,. \tag{3.32}$$

This theory is able to resolve the perturbation dynamics of any strongly non-parallel flow. Suitable applications include isolated laminar separation bubbles [27], the detached flow regions respectively located in front of a forward-facing step or behind a backward-facing step and the instabilities induced by two-dimensional bumps, gaps or indentations [28].

It is important to mention that in streamwise BiGlobal analyses, the proper imposition of boundary conditions at the inflow and outflow boundaries of the streamwise plane is a challenging problem which still remains a state-of-the-art topic. For details on the mathematical nature of this problem, the reader is referred to the recent work of Groot [7].

3.6.3 Three-dimensional parabolized stability equations

When weakly non-parallel flows in the streamwise direction are considered, a natural extension of the linear PSE theory consists in lifting the restriction for the flow to be inhomogeneous only along a single spatial direction, leading to a more general PSE theory commonly known as three-dimensional parabolized stability equations (3D-PSE) [29]. This theory assumes the base flow and the amplitude functions to be dependent in all three spatial directions but subject to the following condition

$$\frac{\partial}{\partial x} \ll \frac{\partial}{\partial y}, \frac{\partial}{\partial z}. \tag{3.33}$$

In a similar fashion to standard PSE, the ansatz for 3D-PSE becomes

$$\tilde{\mathbf{q}}(x,y,z,t) = \hat{\mathbf{q}}(x,y,z)\exp\left[i\left(\int_{x_0}^{x}\alpha(\xi)\,d\xi - \omega t\right)\right] + c.c.\,. \tag{3.34}$$

Hence, the flow field is allowed to be strongly inhomogeneous in the spanwise plane (yz) while retaining a small variation along x (see figure 3.1(b)). The deployment of ansatz (3.34) into the linearized perturbation equations leads to a marching problem analogous to equation (3.24), but with partial differential matrix operators defined in two spatial directions. The name plane-marching PSE is also sometimes employed to refer to 3D-PSE, which arises from the process of marching the solution contained in yz planes along the streamwise direction.

Similarly to classical PSE, a normalization condition is necessary, which for 3D-PSE usually takes the form

$$\int_{z^-}^{z^+} \int_{y^-}^{y^+} \hat{\mathbf{q}}^* \frac{\partial \hat{\mathbf{q}}}{\partial x} \, dy \, dz = 0, \tag{3.35}$$

where z^- and z^+ are the limits (boundaries) of the domain of analysis along the spanwise direction.

As it is the case between PSE and LST, 3D-PSE constitutes a more general theory than 2D-LST since it takes into account weak non-parallel effects in the streamwise direction.

It is also worth mentioning that another variation of the PSE theory exists which considers a weak evolution of the base-flow quantities along both the streamwise and the spanwise directions, which receives the name of surface-marching PSE [30, 31]. This theory is well suited for instance for the study of crossflow instabilities in swept wing configurations or the instabilities modulated by three-dimensional roughness elements with smooth shape variations along the streamwise and spanwise directions. It allows to take into account weakly non-parallel effects in both x and z while keeping only a single inhomogeneous direction, i.e., the wall-normal direction. Surface-marching PSE therefore requires a similar computational cost as the standard PSE theory.

Finally, for base flows with strong variations in the streamwise direction but which are parallel in the spanwise direction (such as the recirculating regions induced by forward- or backward-facing steps), it is interesting to note the existence of another methodology known as adaptive harmonic linearized Navier-Stokes (AHLNS) equations [32, 33]. The AHLNS formulation is also derived from the PSE approach by removing the assumption of slowly varying flow quantities in the streamwise direction, thus recovering the streamwise-related terms that are dropped in the PSE derivation and which bring a fully elliptic character to the equations. This technique is therefore a natural extension of the PSE methodology that enables the study of convective instabilities in the presence of large streamwise gradients. For the analysis of convective instabilities, AHLNS can provide a more efficient approach than the use of streamwise BiGlobal theory.

3.6.4 TriGlobal stability theory

TriGlobal stability theory deals with flow fields which are strongly inhomogeneous in all three spatial directions (see figure 3.1(d)). No assumptions are made on the spatial behavior of the instabilities, they are only assumed to be periodic in time. The TriGlobal perturbation ansatz reads

$$\tilde{\mathbf{q}}(x, y, z, t) = \hat{\mathbf{q}}(x, y, z) \exp\left(-i\omega t\right) + c.c. \, . \tag{3.36}$$

This form of the perturbation ansatz leads to a temporal eigenvalue problem in ω. Since no spatial wave-like behavior is imposed, the distinction between spatial and

temporal stability frameworks vanishes for this theory. The computational cost of solving the TriGlobal eigenvalue problem is prohibitively high except in very simple and fundamental configurations. In addition, the difficulties associated to the imposition of inflow/outflow boundary conditions at the streamwise boundaries, as introduced in § 3.6.2, are also present in this theory. Instead of solving the temporal eigenvalue problem, the application of TriGlobal stability theory to current practical configurations usually requires the use of time-stepping techniques (see for instance [22]).

3.7 The e^N method for transition prediction

Although linear stability theories describe the correct perturbation dynamics only during the linear stages of disturbance development, in several applications it is possible to correlate the linear amplification with the transition onset location observed experimentally. The methodology, introduced by van Ingen [34] and Smith & Gamberoni [35], is known as the e^N method.

The idea behind this method is that, under equivalent disturbance environments, transition takes place when the natural logarithm of the linearly determined perturbation amplitude (A) is increased by a given factor, commonly known as the N-factor, that is:

$$N(x) = \int_{x_0}^{x} \frac{1}{A}\frac{dA}{d\xi}\, d\xi = \ln\left[\frac{A(x)}{A(x_0)}\right], \tag{3.37}$$

where x_0 is the location at which the disturbance becomes unstable. For linear stability theories, the quantity inside the integral equals the growth rate of the perturbation, i.e.

$$\frac{dN}{dx} = \frac{1}{A}\frac{dA}{dx} = \sigma. \tag{3.38}$$

Therefore, for local linear stability theory (LST and 2D-LST), the N-factor can be evaluated as

$$N = \int_{x_0}^{x} -\alpha_i\, d\xi, \tag{3.39}$$

and similarly for PSE by employing equation (3.27) or (3.28).

For a quiet disturbance environment, that is, for a low freestream turbulence intensity, [34] and [35] observed that transition for typical flat-plate conditions occurs approximately at $N = 9$. Therefore, when any of the perturbations undergo a fixed linear amplification that amounts to $N = 9$, transition onset can be considered at that location. The key parameter for the e^N method to be effective in

practice is the particular value of N at transition onset for a given disturbance environment. If correctly calibrated by means of experimental investigations, the e^N method can become a powerful engineering tool for a given application. Under noisy wind tunnel conditions, smaller transitional values of N are to be expected. Typical values for noisy wind tunnels range between $N = 5$ and $N = 6$ [4].

In the context of flat plate boundary layers, the method has proved a notable prediction capability [4]. In particular, Mack [36] proposed a correlation for the transition N-factor in a flat-plate boundary layer as a function of the freestream turbulence intensity.

3.8 Accounting for non-linearities

Under many flow conditions, accounting for non-linearities is the only way to describe physical phenomena that lead to the correct computation of transition onset, which is otherwise not predictable by means of the e^N method coupled with linear theory. Without relying on the high computational cost of DNS simulations, a cheaper and direct way to model non-linearities in weakly non-parallel flows, such as flat-plate boundary layers, is to employ a non-linear version of the parabolized stability equations. For this purpose, the following perturbation ansatz is considered [16]:

$$\tilde{\mathbf{q}}(x,y,z,t) = \sum_{m=-N_m}^{N_m} \sum_{n=-N_n}^{N_n} A^0_{m,n} \hat{\mathbf{q}}_{m,n}(x,y) \exp\left[i \left(\int_{x_0}^{x} \alpha_{m,n}(\xi)\, d\xi + m\beta z - n\omega t \right) \right] + c.c.\,, \quad (3.40)$$

where $A^0_{m,n}$ denotes the initial amplitude of the mode defined by the mth and nth harmonics of the fundamental spanwise wavenumber (β) and frequency (ω), respectively, with N_m and N_n being the total number of harmonics considered. Upon substitution of equation (3.40) into the system of non-linear perturbation equations (that is, without neglecting terms of order $O(\epsilon^2)$ or higher), the system of governing equations for each mode in non-linear PSE (NPSE) theory is obtained, given by

$$\left(\mathbf{L}\hat{\mathbf{q}} + \mathbf{M}\frac{\partial \hat{\mathbf{q}}}{\partial x} \right)\Bigg|_{m,n} = \mathbf{f}_{m,n}, \quad (3.41)$$

where $\mathbf{f}_{m,n}$ denotes the forcing vector associated to mode (m,n), which contains the corresponding Fourier component of the total forcing vector $\mathbf{f}$, which comprises the non-linear terms belonging to the system of governing equations. When the number of modes in consideration is large enough, the computation of $\mathbf{f}_{m,n}$ from $\mathbf{f}$ is usually performed numerically by means of a fast Fourier transform

(FFT). However, if only a few modes are considered, the calculation is sometimes carried out in Fourier space through the convolution operator.

Finally, the same normalization condition employed for linear PSE theory also applies for each mode in the non-linear formulation, namely

$$\int_{y^-}^{y^+} \hat{\mathbf{q}}^*_{m,n} \frac{\partial \hat{\mathbf{q}}_{m,n}}{\partial x}\, dy = 0. \tag{3.42}$$

An equivalent non-linear extension follows as well for the three-dimensional parabolized stability equations, leading to 3D-NPSE theory. In this case, the perturbation ansatz involves only harmonics of the fundamental frequency (i.e. $n\omega$). See [3, 37] for further details.

The perturbation solution of non-linear PSE theory is then given by a combination of different modes (harmonics). This theory therefore accounts for the interaction between different modes, allowing to model more advanced stages of the transition process where linear theory fails to predict the correct dynamics of the instabilities. An example where non-linear theory succeeds to predict the correct disturbance behavior while linear theory does not is the case of crossflow instabilities developing in infinite swept-wing boundary layers (see for instance [38]).

3.9 Boundary conditions for the perturbation quantities

To complete the system of stability equations governing the disturbance dynamics for any of the theories introduced previously, appropriate boundary conditions must be imposed on the perturbation quantities. The nature of the eigenvalue problems resulting from the theoretical assumptions behind the LST, 2D-LST, streamwise BiGlobal and TriGlobal theories requires the imposition of homogeneous boundary conditions.

In this work, the stability equations are solved over physical domains that are oriented perpendicularly to the streamwise coordinate of flow development. Therefore, only boundary conditions along the wall-normal and the spanwise directions are considered here. For the treatment of boundary conditions at streamwise boundaries, see the work of Groot [7].

3.9.1 Wall boundary

In the same way as the base flow, perturbations at solid wall boundaries must also satisfy the no-slip and no-penetration conditions. This implies that, at the wall, all three components of the velocity perturbation vector must be zero. This condition is enforced by means of a homogeneous Dirichlet condition, that is

$$\hat{u} = \hat{v} = \hat{w} = 0. \tag{3.43}$$

If the disturbance under consideration is not stationary, i.e. $\omega > 0$, the thermal inertia of the wall generally prevents it from reacting to the rapid fluctuations associated with the temperature perturbation. For this reason, a homogeneous Dirichlet condition is usually imposed as well for the temperature perturbation at the wall ($\hat{T} = 0$).

The remaining independent perturbation quantities are forced to satisfy compatibility conditions at the wall, usually the wall-normal momentum perturbation equations (see [20, 22]). This ensures that all the quantities imposed at the boundary are compatible with (satisfy) the governing equations. For the CPG and TPG flow assumptions, wall-compatibility conditions are only required for the second thermodynamic state variable of the system, usually either $\hat{\rho}$ or $\hat{p}$. For example, the compatibility equation for $\hat{p}$ is usually derived from the wall-normal momentum equation (equation (B.2c) for 2D-LST theory). To obtain the associated compatibility condition at the wall, the following conditions are taken into account: the base flow and the perturbation velocity components are set to zero due to the no-slip and no-penetration conditions, the temperature perturbation is fixed to zero due to the reason described above, and the derivatives with respect to the spanwise direction (tangential to the wall) of the quantities that are zeroed by the homogeneous Dirichlet conditions become zero as well. With these considerations, a 2D-LST non-dimensional wall compatibility equation for $\hat{p}$ reads:

$$\begin{aligned}\frac{\partial \hat{p}}{\partial y} - \frac{1}{Re}\Bigg[\bar{\lambda}\left(i\alpha\frac{\partial \hat{u}}{\partial y} + \frac{\partial^2 \hat{v}}{\partial y^2} + \frac{\partial^2 \hat{w}}{\partial y \partial z}\right) + \bar{\mu}\left(i\alpha\frac{\partial \hat{u}}{\partial y} + 2\frac{\partial^2 \hat{v}}{\partial y^2} + \frac{\partial^2 \hat{w}}{\partial y \partial z}\right) \\ + \frac{d\bar{\lambda}}{d\bar{T}}\left(\frac{\partial \bar{T}}{\partial y}\frac{\partial \hat{v}}{\partial y} + \frac{\partial \hat{T}}{\partial y}\frac{\partial \bar{v}}{\partial y}\right) + \frac{d\bar{\mu}}{d\bar{T}}\left(2\frac{\partial \bar{T}}{\partial y}\frac{\partial \hat{v}}{\partial y} + 2\frac{\partial \hat{T}}{\partial y}\frac{\partial \bar{v}}{\partial y} + \frac{\partial \bar{T}}{\partial z}\frac{\partial \hat{w}}{\partial y}\right)\Bigg] = 0.\end{aligned} \tag{3.44}$$

It is important to mention that recent work by Theofilis [39] for incompressible flows has shown that, instead of employing the momentum compatibility equation at a given boundary, using the linearized pressure Poisson equation to provide a boundary closure for the pressure perturbation results in the absence of spurious modes in the stability spectrum, which are otherwise present when the momentum equation is considered. Therefore, using the Poisson equation for the pressure perturbation boundary condition is preferred over the momentum compatibility equation in incompressible flows. For compressible flows, the linearized Poisson equation derived by [39] might be extended to include the temperature dependency of the transport properties and employed as a boundary closure as well. Although the 2D-LST linearized pressure Poisson equation has not been implemented in this

work, its application to the problem under study deserves attention and should be investigated, as it is believed that its performance would also be superior than using the wall-normal momentum equation.

For the case of a mixture of perfect gases in chemical non-equilibrium, wall compatibility conditions are also required for each of the species density perturbations ($\hat{\rho}_s$). In this work, the approach developed by Miró Miró & Pinna [40] is followed (see also [5]), which employs the species momentum equation as a compatibility condition for each species density disturbance. The wall-normal momentum equation for a single species can be expressed as

$$\rho_s \frac{Dv}{Dt} + \frac{\partial p_s}{\partial y} - \frac{\partial \tau_{xy}}{\partial x} - \frac{\partial \tau_{yy}}{\partial y} - \frac{\partial \tau_{zy}}{\partial z} = 0, \tag{3.45}$$

where p_s denotes the partial pressure of species s, which satisfies Dalton's law of partial pressures [41], and the viscous stresses follow the same definitions given by equations (2.12b), (2.12d) and (2.12f). It is important to note that due to the lack of an accurate mixture rule for viscosity, the mixture viscosity (μ) is employed in equation (3.45) instead of the species viscosity. Applying the splitting and linearization described by equation (3.2) to equation (3.45), and substituting the ansatz associated with the stability theory in use, the compatibility equations for the species partial density perturbations are obtained.

From the numerical point of view, it has been shown [42] that using $N_s - 1$ species wall-normal momentum equations together with the mixture wall-normal momentum equation (2.11c) improves the conditioning of the system of equations with respect to the use of N_s species momentum equations. For this purpose, the bath species is usually chosen to be the one without a dedicated momentum equation.

3.9.2 Wall-normal far-field boundary

For the majority of boundary-layer base flows, the discrete perturbations of interest decay exponentially to zero when moving far away from the wall. Therefore, appropriate boundary conditions at the wall-normal far-field boundary usually consist of homogeneous Dirichlet conditions. Similarly to the procedure described in the previous section for the solid wall boundary, homogeneous Dirichlet conditions are applied at the wall-normal far-field boundary for all three components of the velocity perturbation vector as well as for the temperature disturbance. To ensure consistency with the governing equations, the remaining thermodynamic independent variables that compose the state vector are once again enforced to follow compatibility conditions also at this boundary. If the far-field boundary is far enough, the compatibility conditions ensure that the remaining perturbation quantities vanish as well without explicitly forcing their value to be zero.

As discussed previously, the linearized pressure Poisson equation might also be considered as a boundary closure for the pressure perturbation at the wall-normal far-field boundary.

3.9.3 Periodic spanwise boundaries

For physical problems where the base flow field features a spanwise periodicity, the perturbations developing in the domain can also be made periodic with respect to the spanwise direction by means of periodic boundary conditions. This is achieved by forcing the value of the perturbation quantities and their first derivative normal to the boundary to be equal at both spanwise boundaries. Therefore, periodic boundary conditions impose two conditions on $\hat{\mathbf{q}}$, namely

$$\hat{\mathbf{q}}|_{z^-} = \hat{\mathbf{q}}|_{z^+}\,, \tag{3.46a}$$

$$\left.\frac{\partial \hat{\mathbf{q}}}{\partial z}\right|_{z^-} = \left.\frac{\partial \hat{\mathbf{q}}}{\partial z}\right|_{z^+}. \tag{3.46b}$$

These conditions are also applicable to base flows which are symmetric (not periodic) with respect to the spanwise direction, such as in the cases investigated in this dissertation.

3.9.4 Symmetric spanwise boundaries

In the case of base flows which have a spanwise symmetry, only half of the physical domain in the spanwise direction can be considered to perform the stability analysis. Perturbations at the symmetry boundary can be assumed to behave as symmetric or antisymmetric disturbances by imposing symmetry or antisymmetry boundary conditions. In the case of symmetry conditions, the first derivative of all perturbation quantities in the direction normal to the boundary is set to zero except for the spanwise velocity perturbation, whose value is set to zero at the boundary. Then, homogeneous Neumann conditions are employed for all the independent perturbation quantities except for $\hat{w}$, for which a homogeneous Dirichlet condition is imposed. In the case of antisymmetry conditions, these specifications are inverted, homogeneous Dirichlet conditions are imposed for all quantities except for $\hat{w}$, for which a homogeneous Neumann condition is used. As an example, symmetric boundary conditions for CPG can be expressed as follows:

$$\frac{\partial \hat{u}}{\partial z} = \frac{\partial \hat{v}}{\partial z} = \frac{\partial \hat{T}}{\partial z} = \frac{\partial \hat{p}}{\partial z} = 0, \quad \hat{w} = 0, \tag{3.47}$$

and antisymmetric boundary conditions as

$$\hat{u} = \hat{v} = \hat{T} = \hat{p} = 0, \quad \frac{\partial \hat{w}}{\partial z} = 0. \tag{3.48}$$

At the other spanwise boundary of the domain, appropriate boundary conditions depend on the nature of the disturbance under investigation. If the perturbation develops only in a small, well-defined region of the domain, such as the disturbances associated with streamwise vortices developing inside a boundary layer, it can be forced to decay towards zero at the spanwise far-field boundary by means of homogeneous Dirichlet and compatibility conditions. On the other hand, if the perturbation is a boundary-layer disturbance, which develops over all the spanwise domain of analysis, symmetry/antisymmetry conditions should be employed at both spanwise boundaries.

In practice, the use of symmetry/antisymmetry boundary conditions reduces the computational effort necessary to obtain a given solution for the perturbation quantities since only half of the spanwise domain needs to be considered. However, the imposition of symmetry or antisymmetry conditions at a boundary implies that only those perturbations which satisfy the imposed symmetry conditions will be obtained when solving the stability eigenvalue problem. For instance, if both symmetric and antisymmetric perturbations are desired, two different solutions of the eigenvalue problem are required, one for symmetric perturbations and another for antisymmetric ones. On the other hand, with the use of periodic boundary conditions, both types of perturbations can be obtained at once in the same solution, at the expense of employing the full spanwise domain. Therefore, both options have advantages and disadvantages, and the most appropriate configuration depends on the problem under study. As will be shown later (see chapter 5), in the case of roughness-induced wake instabilities developing on a flat plate, both symmetric and antisymmetric perturbations as well as wake and boundary-layer disturbances coexist in the 2D-LST spectrum. As a result, the use of periodic boundary conditions is preferable for this particular problem.

3.10 Disturbance energy evolution equation for a calorically perfect gas

The analysis of the energy in a disturbance can provide an additional level of understanding of the energy-exchange mechanisms between the base flow and the instabilities. The derivation and evaluation of an appropriate disturbance energy equation therefore constitutes a very attractive tool from the theoretical point of view. Nowadays, however, no complete consensus exists on which is the most adequate definition of the energy in a disturbance (see for instance George & Sujith [43]).

An evolution equation for the total energy of a disturbance in a calorically perfect gas was originally derived by Chu [44] for two-dimensional perturbations developing in base flows that depend only on one spatial dimension ($\bar{\mathbf{q}} = \bar{\mathbf{q}}(y)$

and $\tilde{\mathbf{q}} = \tilde{\mathbf{q}}(x, y, t)$). This derivation was recently extended by Tritarelli [45], Weder [46] and Weder *et al.* [47] to account also for non-vanishing disturbances at the domain boundaries, which introduced additional flux terms in the resulting evolution equation.

The disturbance energy definition resulting from the evolution equation of Chu is equivalent to the energy norm considered by Mack [48] and Hanifi *et al.* [49]. This definition of perturbation energy is also adopted in this work, as described in the following paragraphs.

3.10.1 The disturbance energy definition of Chu

According to Chu [44], a disturbance energy equation can be obtained by adding all five non-dimensional linearized perturbation equations (equations (A.1a) to (A.1e)) together, each of them multiplied by a specific factor, and then integrating the resulting sum over an arbitrary time-dependent domain. The multiplicative factors selected by Chu for each equation (calorically perfect gas) are: $\bar{T}\tilde{\rho}/(\gamma M^2 \bar{\rho})$ for the continuity equation (A.1a), $\tilde{u}$ for the x-momentum equation (A.1b), $\tilde{v}$ for the y-momentum equation (A.1c), $\tilde{w}$ for the z-momentum equation (A.1d) and $\tilde{T}/\bar{T}$ for the energy equation (A.1e).

This formulation leads to a definition of the total disturbance energy which satisfies two fundamental requirements, namely, that the disturbance energy must be a positive definite quantity, and that in the absence of energy sources, the energy of the disturbance must be a monotone non-increasing function of time. However, as Chu [44] points out, it is not obvious whether these two properties are sufficient to define uniquely the energy in a disturbance. A later work by Hanifi *et al.* [49] shows that this formulation of the disturbance energy is actually not unique, and that the choice of the multiplicative factors for each governing equation is rather arbitrary as long as the resulting disturbance energy quantity satisfies the desired properties. A formal proof of the non-uniqueness of Chu's disturbance energy norm is provided by George & Sujith [43], who show that Chu's definition is only one among a family of positive definite disturbance energy norms that do not exhibit unphysical growth or decay in the absence of energy sources or sinks.

Depending on the purpose for which this disturbance energy formulation is employed, it is very important to bear in mind the implications of the inherent non-uniqueness that arises when defining the disturbance energy in this manner. On the one hand, if the disturbance energy is used as a measure of the size (amplitude) of the perturbations to evaluate non-modal disturbance growth, such as done by [49] (see also § 3.12), then the current formulation is valid. George & Sujith [43, 50] have shown that Chu's energy norm does not lead to spurious transient energy growth when the disturbance amplitude remains constant (or equivalently, in the absence of energy sources or sinks), which demonstrates its suitability for this

purpose.

On the other hand, if the objective is to compare different constituting parts of the total disturbance energy, this formulation is not appropriate. In particular, it is not meaningful to compare different energy contributions that originate from different equations of the governing system, since the relative magnitudes of these contributions depend on the chosen multipliers. For instance, for different choices of the multiplicative factors, the relative magnitudes of the terms derived from the momentum equation (kinetic energy) and those derived from the energy equation (internal energy) are different.

Taking into account the previous considerations, in this dissertation Chu's disturbance energy definition is employed to gain understanding on which are the mechanisms with which roughness-induced instabilities extract energy from the base-flow quantities.

3.10.1.1 Chu's disturbance energy evolution equation for base flows depending on y and z

In this study, the derivation of Chu [44] is generalized to three-dimensional perturbations developing in base flows that depend on two spatial directions ($\bar{\mathbf{q}} = \bar{\mathbf{q}}(y,z)$ and $\tilde{\mathbf{q}} = \tilde{\mathbf{q}}(x,y,z,t)$). This leads to a framework that is compatible with the perturbations computed by means of 2D-LST. Let $d\mathcal{V} = dx\,dy\,dz$ denote an infinitesimal volume element belonging to the integration domain Ω, and dS denote an infinitesimal surface element belonging to the integration boundary Γ. According to the total perturbation energy definition of Chu, the following non-dimensional power equation, which describes the temporal evolution of the disturbance energy in base flows depending on y and z, can be retrieved:

$$\frac{d\tilde{E}}{dt} = -\int_\Omega \bar{\rho}\tilde{u}\tilde{v}\frac{\partial \bar{u}}{\partial y}\,d\mathcal{V} - \int_\Omega \bar{\rho}\tilde{u}\tilde{w}\frac{\partial \bar{u}}{\partial z}\,d\mathcal{V} - \int_\Omega \bar{\rho}\tilde{v}^2\frac{\partial \bar{v}}{\partial y}\,d\mathcal{V} \tag{3.49a-c}$$

$$-\int_\Omega \bar{\rho}\tilde{v}\tilde{w}\frac{\partial \bar{v}}{\partial z}\,d\mathcal{V} - \int_\Omega \bar{\rho}\tilde{w}\tilde{v}\frac{\partial \bar{w}}{\partial y}\,d\mathcal{V} - \int_\Omega \bar{\rho}\tilde{w}^2\frac{\partial \bar{w}}{\partial z}\,d\mathcal{V} \tag{3.49d-f}$$

$$-\int_\Omega \tilde{\rho}\tilde{u}\bar{v}\frac{\partial \bar{u}}{\partial y}\,d\mathcal{V} - \int_\Omega \tilde{\rho}\tilde{u}\bar{w}\frac{\partial \bar{u}}{\partial z}\,d\mathcal{V} - \int_\Omega \tilde{\rho}\tilde{v}\bar{v}\frac{\partial \bar{v}}{\partial y}\,d\mathcal{V} \tag{3.49g-i}$$

$$-\int_\Omega \tilde{\rho}\tilde{v}\bar{w}\frac{\partial \bar{v}}{\partial z}\,d\mathcal{V} - \int_\Omega \tilde{\rho}\tilde{w}\bar{v}\frac{\partial \bar{w}}{\partial y}\,d\mathcal{V} - \int_\Omega \tilde{\rho}\tilde{w}\bar{w}\frac{\partial \bar{w}}{\partial z}\,d\mathcal{V} \tag{3.49j-l}$$

$$-\int_\Omega \bar{\rho}\tilde{v}\tilde{s}\frac{\partial \bar{T}}{\partial y}\,d\mathcal{V} - \int_\Omega \bar{\rho}\tilde{w}\tilde{s}\frac{\partial \bar{T}}{\partial z}\,d\mathcal{V} + \int_\Omega \tilde{Q}\frac{\tilde{T}}{\bar{T}}\,d\mathcal{V} \tag{3.49m-o}$$

$$-\int_\Omega \frac{\tilde{\rho}\tilde{v}}{\bar{\rho}}\frac{\partial \bar{p}}{\partial y}\,d\mathcal{V} - \int_\Omega \frac{\tilde{\rho}\tilde{w}}{\bar{\rho}}\frac{\partial \bar{p}}{\partial z}\,d\mathcal{V} \tag{3.49p,q}$$

$$-\int_\Omega \frac{\tilde{p}\tilde{T}}{\bar{T}}\frac{\partial \bar{v}}{\partial y}\,d\mathcal{V} - \int_\Omega \frac{\tilde{p}\tilde{T}}{\bar{T}}\frac{\partial \bar{w}}{\partial z}\,d\mathcal{V} - \int_\Omega \bar{p}\frac{\tilde{\rho}^2}{\bar{\rho}^2}\frac{\partial \bar{v}}{\partial y}\,d\mathcal{V} - \int_\Omega \bar{p}\frac{\tilde{\rho}^2}{\bar{\rho}^2}\frac{\partial \bar{w}}{\partial z}\,d\mathcal{V} \quad \text{(3.49r-u)}$$

$$-\int_\Omega \frac{1}{\gamma(\gamma-1)M^2}\frac{\bar{v}}{\bar{T}}\tilde{\rho}\tilde{T}\frac{\partial \bar{T}}{\partial y}\,d\mathcal{V} - \int_\Omega \frac{1}{\gamma(\gamma-1)M^2}\frac{\bar{w}}{\bar{T}}\tilde{\rho}\tilde{T}\frac{\partial \bar{T}}{\partial z}\,d\mathcal{V} \quad \text{(3.49v,w)}$$

$$\begin{aligned}-\int_\Omega \Bigg[&\tilde{\tau}_{xx}\frac{\partial \tilde{u}}{\partial x} + \tilde{\tau}_{yy}\frac{\partial \tilde{v}}{\partial y} + \tilde{\tau}_{zz}\frac{\partial \tilde{w}}{\partial z} + \tilde{\tau}_{xy}\left(\frac{\partial \tilde{u}}{\partial y} + \frac{\partial \tilde{v}}{\partial x}\right)\\ &+\tilde{\tau}_{xz}\left(\frac{\partial \tilde{u}}{\partial z} + \frac{\partial \tilde{w}}{\partial x}\right) + \tilde{\tau}_{yz}\left(\frac{\partial \tilde{v}}{\partial z} + \frac{\partial \tilde{w}}{\partial y}\right)\Bigg]\,d\mathcal{V}\end{aligned} \quad \text{(3.49x)}$$

$$+\int_\Omega \frac{1}{\bar{T}}\left(\tilde{q}_x\frac{\partial}{\partial x} + \tilde{q}_y\frac{\partial}{\partial y} + \tilde{q}_z\frac{\partial}{\partial z}\right)\tilde{T}\,d\mathcal{V} \quad \text{(3.49y)}$$

$$\begin{aligned}+\int_\Gamma \big[&\tilde{\tau}_{xx}\tilde{u}n_x + \tilde{\tau}_{yy}\tilde{v}n_y + \tilde{\tau}_{zz}\tilde{w}n_z + \tilde{\tau}_{xy}\left(\tilde{u}n_y + \tilde{v}n_x\right)\\ &+\tilde{\tau}_{xz}\left(\tilde{u}n_z + \tilde{w}n_x\right) + \tilde{\tau}_{yz}\left(\tilde{v}n_z + \tilde{w}n_y\right)\big]\,dS\end{aligned} \quad \text{(3.49z)}$$

$$-\int_\Gamma \left(\tilde{q}_x n_x + \tilde{q}_y n_y + \tilde{q}_z n_z\right)\frac{\tilde{T}}{\bar{T}}\,dS - \int_\Gamma \tilde{p}\left(\tilde{u}n_x + \tilde{v}n_y + \tilde{w}n_z\right)dS \quad \text{(3.49aa,bb)}$$

$$+\frac{1}{Re}\int_\Omega \frac{\partial}{\partial y}\left(\tilde{u}\tilde{T}\frac{d\bar{\mu}}{d\bar{T}}\frac{\partial \bar{u}}{\partial y}\right)d\mathcal{V} + \frac{1}{Re}\int_\Omega \frac{\partial}{\partial z}\left(\tilde{u}\tilde{T}\frac{d\bar{\mu}}{d\bar{T}}\frac{\partial \bar{u}}{\partial z}\right)d\mathcal{V} \quad \text{(3.49cc,dd)}$$

$$+\frac{1}{Re}\int_\Omega \frac{\partial}{\partial x}\left(\tilde{v}\tilde{T}\frac{d\bar{\mu}}{d\bar{T}}\frac{\partial \bar{u}}{\partial y}\right)d\mathcal{V} + \frac{1}{Re}\int_\Omega \frac{\partial}{\partial x}\left(\tilde{w}\tilde{T}\frac{d\bar{\mu}}{d\bar{T}}\frac{\partial \bar{u}}{\partial z}\right)d\mathcal{V} \quad \text{(3.49ee,ff)}$$

$$+\frac{1}{Re}\int_\Omega \frac{\partial}{\partial z}\left(\tilde{v}\tilde{T}\frac{d\bar{\mu}}{d\bar{T}}\frac{\partial \bar{v}}{\partial z}\right)d\mathcal{V} + \frac{1}{Re}\int_\Omega \frac{\partial}{\partial y}\left(\tilde{w}\tilde{T}\frac{d\bar{\mu}}{d\bar{T}}\frac{\partial \bar{v}}{\partial z}\right)d\mathcal{V} \quad \text{(3.49gg,hh)}$$

$$+\frac{1}{Re}\int_\Omega \frac{\partial}{\partial z}\left(\tilde{v}\tilde{T}\frac{d\bar{\mu}}{d\bar{T}}\frac{\partial \bar{w}}{\partial y}\right)d\mathcal{V} + \frac{1}{Re}\int_\Omega \frac{\partial}{\partial y}\left(\tilde{w}\tilde{T}\frac{d\bar{\mu}}{d\bar{T}}\frac{\partial \bar{w}}{\partial y}\right)d\mathcal{V} \quad \text{(3.49ii,jj)}$$

$$+\frac{2}{Re}\int_\Omega \frac{\partial}{\partial y}\left(\tilde{v}\tilde{T}\frac{d\bar{\mu}}{d\bar{T}}\frac{\partial \bar{v}}{\partial y}\right)d\mathcal{V} + \frac{2}{Re}\int_\Omega \frac{\partial}{\partial z}\left(\tilde{w}\tilde{T}\frac{d\bar{\mu}}{d\bar{T}}\frac{\partial \bar{w}}{\partial z}\right)d\mathcal{V} \quad \text{(3.49kk,ll)}$$

$$+\frac{1}{Re}\int_\Omega \frac{\partial}{\partial x}\left(\tilde{u}\tilde{T}\frac{d\bar{\lambda}}{d\bar{T}}\frac{\partial \bar{v}}{\partial y}\right)d\mathcal{V} + \frac{1}{Re}\int_\Omega \frac{\partial}{\partial y}\left(\tilde{v}\tilde{T}\frac{d\bar{\lambda}}{d\bar{T}}\frac{\partial \bar{v}}{\partial y}\right)d\mathcal{V} \quad \text{(3.49mm,nn)}$$

$$+\frac{1}{Re}\int_\Omega \frac{\partial}{\partial z}\left(\tilde{w}\tilde{T}\frac{d\bar{\lambda}}{d\bar{T}}\frac{\partial \bar{v}}{\partial y}\right)d\mathcal{V} + \frac{1}{Re}\int_\Omega \frac{\partial}{\partial x}\left(\tilde{u}\tilde{T}\frac{d\bar{\lambda}}{d\bar{T}}\frac{\partial \bar{w}}{\partial z}\right)d\mathcal{V} \quad \text{(3.49oo,pp)}$$

$$+\frac{1}{Re}\int_\Omega \frac{\partial}{\partial y}\left(\tilde{v}\tilde{T}\frac{d\bar{\lambda}}{d\bar{T}}\frac{\partial \bar{w}}{\partial z}\right)d\mathcal{V} + \frac{1}{Re}\int_\Omega \frac{\partial}{\partial z}\left(\tilde{w}\tilde{T}\frac{d\bar{\lambda}}{d\bar{T}}\frac{\partial \bar{w}}{\partial z}\right)d\mathcal{V} \quad \text{(3.49qq,rr)}$$

$$-\frac{1}{2}\int_\Omega \frac{\partial}{\partial x}\left[\bar{u}\bar{p}\frac{\tilde{\rho}^2}{\bar{\rho}^2} + \frac{\bar{u}\bar{p}}{\gamma-1}\frac{\tilde{T}^2}{\bar{T}^2} + \bar{u}\bar{\rho}\left(\tilde{u}^2+\tilde{v}^2+\tilde{w}^2\right)\right]d\mathcal{V} \quad \text{(3.49ss)}$$

$$-\frac{1}{2}\int_\Omega \left[\bar{v}\frac{\bar{p}}{\bar{\rho}^2}\frac{\partial \tilde{\rho}^2}{\partial y} + \frac{\bar{v}\bar{p}}{(\gamma-1)\bar{T}^2}\frac{\partial \tilde{T}^2}{\partial y} + \bar{v}\bar{\rho}\frac{\partial}{\partial y}\left(\tilde{u}^2+\tilde{v}^2+\tilde{w}^2\right)\right]d\mathcal{V}, \quad \text{(3.49tt)}$$

$$-\frac{1}{2}\int_{\Omega}\left[\bar{w}\frac{\bar{p}}{\bar{\rho}^2}\frac{\partial\tilde{\rho}^2}{\partial z}+\frac{\bar{w}\bar{p}}{(\gamma-1)\bar{T}^2}\frac{\partial\tilde{T}^2}{\partial z}+\bar{w}\bar{\rho}\frac{\partial}{\partial z}\left(\tilde{u}^2+\tilde{v}^2+\tilde{w}^2\right)\right]d\mathcal{V}, \quad (3.49uu)$$

where $\tilde{E}$ is the total disturbance energy, defined as

$$\tilde{E}=\frac{1}{2}\int_{\Omega}\left[\bar{\rho}\left(\tilde{u}^2+\tilde{v}^2+\tilde{w}^2\right)+\frac{\bar{T}\tilde{\rho}^2}{\gamma M^2\bar{\rho}}+\frac{\bar{\rho}\tilde{T}^2}{\gamma(\gamma-1)M^2\bar{T}}\right]d\mathcal{V}. \quad (3.50)$$

The previous expression for the total perturbation energy (3.50) is directly obtained by collecting all the time derivative terms appearing when building (3.49). According to [44], the first term inside the integral of equation (3.50) represents the kinetic energy in the disturbance per unit volume, whereas the second and third terms together can be interpreted as the generalized potential disturbance energy per unit volume.

The components of the outward unit vector normal to Γ are denoted by n_x, n_y and n_z. The quantity $\tilde{s}$ is the specific disturbance entropy, which can be expressed as a function of the density and temperature of the perturbation through the following relation:

$$\tilde{s}=\frac{1}{\gamma M^2}\left[\frac{1}{\gamma-1}\left(\frac{\tilde{T}}{\bar{T}}\right)-\frac{\tilde{\rho}}{\bar{\rho}}\right]. \quad (3.51)$$

Equation (3.51) can be derived from the thermodynamic relationship that quantifies the non-dimensional change in entropy in a calorically perfect gas (see for instance [51]), i.e.,

$$s-s_{ref}=\frac{1}{\gamma M^2}\left[\frac{1}{\gamma-1}\ln\left(\frac{T}{T_{ref}}\right)+\ln\left(\frac{\rho_{ref}}{\rho}\right)\right], \quad (3.52)$$

together with the assumption of small perturbations, requiring a Taylor expansion of $\ln(1+\tilde{T}/\bar{T})$ and $\ln(1+\tilde{\rho}/\bar{\rho})$ around 0. Refer to appendix D.1 for the complete derivation of equation (3.51).

The disturbance viscous stresses are given by

$$\tilde{\tau}_{xx}=\frac{1}{Re}\left[\left(2\bar{\mu}+\bar{\lambda}\right)\frac{\partial\tilde{u}}{\partial x}+\bar{\lambda}\left(\frac{\partial\tilde{v}}{\partial y}+\frac{\partial\tilde{w}}{\partial z}\right)\right], \quad (3.53a)$$

$$\tilde{\tau}_{yy}=\frac{1}{Re}\left[\left(2\bar{\mu}+\bar{\lambda}\right)\frac{\partial\tilde{v}}{\partial y}+\bar{\lambda}\left(\frac{\partial\tilde{u}}{\partial x}+\frac{\partial\tilde{w}}{\partial z}\right)\right], \quad (3.53b)$$

$$\tilde{\tau}_{zz}=\frac{1}{Re}\left[\left(2\bar{\mu}+\bar{\lambda}\right)\frac{\partial\tilde{w}}{\partial z}+\bar{\lambda}\left(\frac{\partial\tilde{u}}{\partial x}+\frac{\partial\tilde{v}}{\partial y}\right)\right], \quad (3.53c)$$

$$\tilde{\tau}_{xy}=\frac{\bar{\mu}}{Re}\left(\frac{\partial\tilde{u}}{\partial y}+\frac{\partial\tilde{v}}{\partial x}\right), \quad (3.53d)$$

$$\tilde{\tau}_{xz} = \frac{\bar{\mu}}{Re}\left(\frac{\partial \tilde{u}}{\partial z} + \frac{\partial \tilde{w}}{\partial x}\right), \tag{3.53e}$$

$$\tilde{\tau}_{yz} = \frac{\bar{\mu}}{Re}\left(\frac{\partial \tilde{v}}{\partial z} + \frac{\partial \tilde{w}}{\partial y}\right), \tag{3.53f}$$

and the components of the perturbation conductive heat flux vector by

$$\tilde{q}_x = -\frac{\bar{k}}{(\gamma-1)\,RePrM^2}\frac{\partial \tilde{T}}{\partial x}, \tag{3.54a}$$

$$\tilde{q}_y = -\frac{\bar{k}}{(\gamma-1)\,RePrM^2}\frac{\partial \tilde{T}}{\partial y}, \tag{3.54b}$$

$$\tilde{q}_z = -\frac{\bar{k}}{(\gamma-1)\,RePrM^2}\frac{\partial \tilde{T}}{\partial z}. \tag{3.54c}$$

The quantity $\tilde{Q}$ denotes the specific disturbance heat source, expressed as

$$\begin{aligned}
\tilde{Q} = {} & \frac{1}{Re}\left(2\bar{\mu} - \frac{d\bar{\mu}}{d\bar{T}}\bar{T}\right)\left[\frac{\partial \bar{u}}{\partial y}\left(\frac{\partial \tilde{u}}{\partial y} + \frac{\partial \tilde{v}}{\partial x}\right) + \frac{\partial \bar{u}}{\partial z}\left(\frac{\partial \tilde{u}}{\partial z} + \frac{\partial \tilde{w}}{\partial x}\right)\right. \\
& \left. + 2\frac{\partial \bar{v}}{\partial y}\frac{\partial \tilde{v}}{\partial y} + \left(\frac{\partial \bar{v}}{\partial z} + \frac{\partial \bar{w}}{\partial y}\right)\left(\frac{\partial \tilde{v}}{\partial z} + \frac{\partial \tilde{w}}{\partial y}\right) + 2\frac{\partial \bar{w}}{\partial z}\frac{\partial \tilde{w}}{\partial z}\right] \\
& + \frac{1}{Re}\left(2\bar{\lambda} - \frac{d\bar{\lambda}}{d\bar{T}}\bar{T}\right)\left(\frac{\partial \bar{v}}{\partial y} + \frac{\partial \bar{w}}{\partial z}\right)\left(\frac{\partial \tilde{u}}{\partial x} + \frac{\partial \tilde{v}}{\partial y} + \frac{\partial \tilde{w}}{\partial z}\right) \\
& + \frac{1}{(\gamma-1)\,RePrM^2}\frac{\bar{k}}{\bar{T}}\left(\frac{\partial \bar{T}}{\partial y}\frac{\partial \tilde{T}}{\partial y} + \frac{\partial \bar{T}}{\partial z}\frac{\partial \tilde{T}}{\partial z}\right) \\
& + \frac{1}{Re}\tilde{T}\frac{d\bar{\mu}}{d\bar{T}}\left[\left(\frac{\partial \bar{u}}{\partial y}\right)^2 + \left(\frac{\partial \bar{u}}{\partial z}\right)^2 + 2\left(\frac{\partial \bar{v}}{\partial y}\right)^2 + \left(\frac{\partial \bar{v}}{\partial z}\right)^2 + \left(\frac{\partial \bar{w}}{\partial y}\right)^2\right. \\
& \left. + 2\left(\frac{\partial \bar{w}}{\partial z}\right)^2 + 2\frac{\partial \bar{v}}{\partial z}\frac{\partial \bar{w}}{\partial y}\right] + \frac{1}{Re}\tilde{T}\frac{d\bar{\lambda}}{d\bar{T}}\left[\left(\frac{\partial \bar{v}}{\partial y}\right)^2 + \left(\frac{\partial \bar{w}}{\partial z}\right)^2 + 2\frac{\partial \bar{v}}{\partial y}\frac{\partial \bar{w}}{\partial z}\right] \\
& + \frac{1}{(\gamma-1)\,RePrM^2}\left[\frac{\partial}{\partial y}\left(\tilde{T}\frac{d\bar{k}}{d\bar{T}}\frac{\partial \bar{T}}{\partial y}\right) + \frac{\partial}{\partial z}\left(\tilde{T}\frac{d\bar{k}}{d\bar{T}}\frac{\partial \bar{T}}{\partial z}\right)\right].
\end{aligned} \tag{3.55}$$

A considerable amount of intermediate steps are necessary to cast equation (3.49) into it's final form. Besides introducing the disturbance entropy (3.51), integration by parts in space is applied to the terms that contain second derivatives of the perturbation variables. This procedure introduces the surface terms (3.49z) and (3.49aa,bb). In addition, unlike [44] and [47], a zero wall-normal pressure gradient is not assumed, which leads to the presence of the first term in (3.49p,q). The different steps followed in the derivation of equation (3.49) are described in appendix D.

3.10.1.2 Chu's total disturbance energy definition in terms of $\tilde{p}$ and $\tilde{s}$

As noted by Chu [44], the generalized disturbance potential energy can also be expressed as a function of the pressure and entropy fluctuations. For this purpose, the disturbance entropy definition given by equation (3.51) can be expressed in terms of $\tilde{T}$ and $\tilde{p}$ and in terms of $\tilde{\rho}$ and $\tilde{p}$, yielding the following relationships:

$$\frac{\tilde{T}}{\bar{T}} = \frac{\gamma - 1}{\gamma}\left(\frac{\tilde{p}}{\bar{p}} + \gamma M^2 \tilde{s}\right), \tag{3.56a}$$

$$\frac{\tilde{\rho}}{\bar{\rho}} = \frac{1}{\gamma}\frac{\tilde{p}}{\bar{p}} - (\gamma - 1) M^2 \tilde{s}. \tag{3.56b}$$

These relations can then be employed to rewrite the generalized potential energy per unit volume as

$$\frac{1}{2}\frac{\bar{T}\tilde{\rho}^2}{\gamma M^2 \bar{\rho}} + \frac{1}{2}\frac{\bar{\rho}\tilde{T}^2}{\gamma(\gamma-1)M^2\bar{T}} = \frac{1}{2}\frac{\bar{\rho}\bar{T}}{M^2}\left(\frac{\tilde{p}}{\gamma\bar{p}}\right)^2 + \frac{1}{2}\frac{\gamma-1}{\gamma}\bar{p}\left(\frac{\tilde{s}}{R}\right)^2, \tag{3.57}$$

where R is given in non-dimensional form by equation (2.20). Therefore, the disturbance generalized potential energy consists of two contributions, namely, that resulting from compression work (pressure fluctuations), and that associated with heat exchange (entropy fluctuations). Hence, an alternative way to express the total disturbance energy (3.50) is:

$$\tilde{E} = \frac{1}{2}\int_{\Omega}\left[\bar{\rho}\left(\tilde{u}^2 + \tilde{v}^2 + \tilde{w}^2\right) + \frac{\bar{\rho}\bar{T}}{M^2}\left(\frac{\tilde{p}}{\gamma\bar{p}}\right)^2 + \frac{\gamma-1}{\gamma}\bar{p}\left(\frac{\tilde{s}}{R}\right)^2\right] d\mathcal{V}. \tag{3.58}$$

As it can be deduced from equation (3.58), it is important to stress that entropy fluctuations lead to a change in the generalized potential energy of the disturbance rather than to a change in the internal disturbance energy only.

3.10.2 Decomposition of the temporal growth rate for two-dimensional local linear stability theory

The substitution of the perturbation ansatz (3.30) into the disturbance energy equation (3.49) allows to obtain a decomposition of the temporal growth rate [47] into the different terms that contribute to an increase or decrease in the amplitude of a perturbation, which are directly linked to the production and the dissipation of disturbance energy. To derive this decomposition, a temporal stability framework is employed, such that the disturbances are periodic in the streamwise direction (real streamwise wavenumber $\alpha = \alpha_r$) but allowed to grow or decay in time (complex angular frequency $\omega = \omega_r + i\omega_i$).

It is worth noting that all the integrands in equation (3.49) involve products of two disturbance quantities. The product of two generic perturbation quantities $\tilde{f}$ and $\tilde{g}$ described by the 2D-LST ansatz (3.30) can be expressed as

$$\begin{aligned}\tilde{f}\tilde{g} &= 4\Re\left\{\hat{f}\mathrm{e}^{i(\alpha_r x-\omega t)}\right\}\Re\left\{\hat{g}\mathrm{e}^{i(\alpha_r x-\omega t)}\right\}\\ &= 4\Re\left\{|\hat{f}|\mathrm{e}^{i\psi_{\hat{f}}}\mathrm{e}^{\omega_i t}\mathrm{e}^{i(\alpha_r x-\omega_r t)}\right\}\Re\left\{|\hat{g}|\mathrm{e}^{i\psi_{\hat{g}}}\mathrm{e}^{\omega_i t}\mathrm{e}^{i(\alpha_r x-\omega_r t)}\right\}\\ &= 4\mathrm{e}^{2\omega_i t}|\hat{f}||\hat{g}|\cos(\alpha_r x-\omega_r t+\psi_{\hat{f}})\cos\left(\alpha_r x-\omega_r t+\psi_{\hat{g}}\right)\\ &= 2\mathrm{e}^{2\omega_i t}|\hat{f}||\hat{g}|\left[\cos(\psi_{\hat{f}}-\psi_{\hat{g}})+\cos(2\alpha_r x-2\omega_r t+\psi_{\hat{f}}+\psi_{\hat{g}})\right], \quad (3.59)\end{aligned}$$

where $\psi_{\hat{f}}$ and $\psi_{\hat{g}}$ are respectively the arguments of the complex amplitude functions $\hat{f}$ and $\hat{g}$. Following Weder *et al.* [47], the domain size in the streamwise direction is chosen to be equal to a single wavelength, that is $2\pi/\alpha_r$, which allows simplifying the streamwise integration of disturbance products (see also [46]) as follows

$$\begin{aligned}&\int_0^{2\pi/\alpha_r}\tilde{f}\tilde{g}\,dx\\ &= 2\mathrm{e}^{2\omega_i t}|\hat{f}||\hat{g}|\int_0^{2\pi/\alpha_r}\left[\cos(\psi_{\hat{f}}-\psi_{\hat{g}})+\cos(2\alpha_r x-2\omega_r t+\psi_{\hat{f}}+\psi_{\hat{g}})\right]dx\\ &= 2\mathrm{e}^{2\omega_i t}|\hat{f}||\hat{g}|\left[\cos(\psi_{\hat{f}}-\psi_{\hat{g}})x+\frac{1}{2\alpha_r}\sin(2\alpha_r x-2\omega_r t+\psi_{\hat{f}}+\psi_{\hat{g}})\right]_0^{2\pi/\alpha_r}\\ &= \frac{4\pi}{\alpha_r}\mathrm{e}^{2\omega_i t}|\hat{f}||\hat{g}|\cos(\psi_{\hat{f}}-\psi_{\hat{g}}) = \frac{4\pi}{\alpha_r}\exp(2\omega_i t)\langle\hat{f},\hat{g}\rangle, \quad (3.60)\end{aligned}$$

where

$$\langle\hat{f},\hat{g}\rangle = \frac{\hat{f}^*\hat{g}+\hat{f}\hat{g}^*}{2} = \hat{f}_r\hat{g}_r+\hat{f}_i\hat{g}_i, \quad (3.61)$$

with $\hat{f}_r$ and $\hat{f}_i$ being the respective real and imaginary parts of $\hat{f}$, and similarly for $\hat{g}$. In addition, due to streamwise periodicity, all the terms with volume integrals of the form $\int_\Omega \partial(\cdot)/\partial x\,d\mathcal{V}$ or with surface integrals of the form $\int_\Gamma(\cdot)n_x\,dS$ become zero. Using (3.60), the disturbance energy can be expressed in terms of the amplitude function of the primitive variables as

$$\tilde{E} = \frac{4\pi}{\alpha_r}\exp(2\omega_i t)\frac{1}{2}\int_{z^-}^{z^+}\int_{y^-}^{y^+}\left[\bar{\rho}\left(\langle\hat{u},\hat{u}\rangle+\langle\hat{v},\hat{v}\rangle+\langle\hat{w},\hat{w}\rangle\right)+\frac{\bar{T}}{\gamma M^2\bar{\rho}}\langle\hat{\rho},\hat{\rho}\rangle\right.$$

$$+\frac{\bar{\rho}}{\gamma(\gamma-1)M^2\bar{T}}\langle\hat{T},\hat{T}\rangle\Big]\,dy\,dz=\frac{4\pi}{\alpha_r}\exp(2\omega_i t)\hat{E}, \quad (3.62)$$

where $\hat{E}$ denotes the perturbation energy amplitude function. Making use of relation (3.62), the left-hand side of equation (3.49) becomes

$$\frac{d\tilde{E}}{dt}=\frac{4\pi}{\alpha_r}\exp(2\omega_i t)2\omega_i\hat{E}. \quad (3.63)$$

Employing (3.60) in all the remaining terms of the disturbance energy equation (3.49) and noting that the factor $4\pi/\alpha_r\exp(2\omega_i t)$ is common to all terms and cancels out, the following decomposition of the temporal growth rate is obtained

$$\omega_i=\frac{1}{2\hat{E}}\left(\hat{P}+\hat{D}+\hat{F}\right), \quad (3.64)$$

where $\hat{P}$ contains the growth-rate contributions of the energy production terms, which can be either positive or negative depending on the particular conditions, $\hat{D}$ encloses the contributions of the energy dissipation terms, which are always negative, and $\hat{F}$ comprises the contributions due to the energy fluxes across the domain boundary Γ. Here, the following classification of terms is adopted

$$\hat{P}=\hat{P}_{RS}+\hat{P}_s+\hat{P}_Q+\hat{P}_{mom}+\hat{P}_{\nabla p}+\hat{P}_{dil}+\hat{P}_{s,T}+\hat{P}_{con}, \quad (3.65a)$$

$$\hat{D}=\hat{D}_\mu+\hat{D}_k, \quad (3.65b)$$

$$\hat{F}=\hat{F}_p+\hat{F}_\mu+\hat{F}_k+\hat{F}_{d\mu/dT}, \quad (3.65c)$$

with

$$\begin{aligned}\hat{P}_{RS}=&-\int_{z^-}^{z^+}\int_{y^-}^{y^+}\bar{\rho}\langle\hat{u},\hat{v}\rangle\frac{\partial\bar{u}}{\partial y}\,dy\,dz-\int_{z^-}^{z^+}\int_{y^-}^{y^+}\bar{\rho}\langle\hat{u},\hat{w}\rangle\frac{\partial\bar{u}}{\partial z}\,dy\,dz\\&-\int_{z^-}^{z^+}\int_{y^-}^{y^+}\bar{\rho}\langle\hat{v},\hat{v}\rangle\frac{\partial\bar{v}}{\partial y}\,dy\,dz-\int_{z^-}^{z^+}\int_{y^-}^{y^+}\bar{\rho}\langle\hat{v},\hat{w}\rangle\frac{\partial\bar{v}}{\partial z}\,dy\,dz\\&-\int_{z^-}^{z^+}\int_{y^-}^{y^+}\bar{\rho}\langle\hat{w},\hat{v}\rangle\frac{\partial\bar{w}}{\partial y}\,dy\,dz-\int_{z^-}^{z^+}\int_{y^-}^{y^+}\bar{\rho}\langle\hat{w},\hat{w}\rangle\frac{\partial\bar{w}}{\partial z}\,dy\,dz,\end{aligned} \quad (3.66a)$$

$$\hat{P}_s=-\int_{z^-}^{z^+}\int_{y^-}^{y^+}\bar{\rho}\langle\hat{v},\hat{s}\rangle\frac{\partial\bar{T}}{\partial y}\,dy\,dz-\int_{z^-}^{z^+}\int_{y^-}^{y^+}\bar{\rho}\langle\hat{w},\hat{s}\rangle\frac{\partial\bar{T}}{\partial z}\,dy\,dz, \quad (3.66b)$$

$$\hat{P}_Q=\int_{z^-}^{z^+}\int_{y^-}^{y^+}\frac{\langle\hat{Q},\hat{T}\rangle}{\bar{T}}\,dy\,dz, \quad (3.66c)$$

$$\hat{P}_{mom} = -\int_{z^-}^{z^+}\int_{y^-}^{y^+} \langle\hat{\rho},\hat{u}\rangle\bar{v}\frac{\partial\bar{u}}{\partial y}\,dy\,dz - \int_{z^-}^{z^+}\int_{y^-}^{y^+} \langle\hat{\rho},\hat{u}\rangle\bar{w}\frac{\partial\bar{u}}{\partial z}\,dy\,dz$$
$$- \int_{z^-}^{z^+}\int_{y^-}^{y^+} \langle\hat{\rho},\hat{v}\rangle\bar{v}\frac{\partial\bar{v}}{\partial y}\,dy\,dz - \int_{z^-}^{z^+}\int_{y^-}^{y^+} \langle\hat{\rho},\hat{v}\rangle\bar{w}\frac{\partial\bar{v}}{\partial z}\,dy\,dz$$
$$- \int_{z^-}^{z^+}\int_{y^-}^{y^+} \langle\hat{\rho},\hat{w}\rangle\bar{v}\frac{\partial\bar{w}}{\partial y}\,dy\,dz - \int_{z^-}^{z^+}\int_{y^-}^{y^+} \langle\hat{\rho},\hat{w}\rangle\bar{w}\frac{\partial\bar{w}}{\partial z}\,dy\,dz, \tag{3.66d}$$

$$\hat{P}_{\nabla p} = -\int_{z^-}^{z^+}\int_{y^-}^{y^+} \frac{\langle\hat{\rho},\hat{v}\rangle}{\bar{\rho}}\frac{\partial\bar{p}}{\partial y}\,dy\,dz - \int_{z^-}^{z^+}\int_{y^-}^{y^+} \frac{\langle\hat{\rho},\hat{w}\rangle}{\bar{\rho}}\frac{\partial\bar{p}}{\partial z}\,dy\,dz, \tag{3.66e}$$

$$\hat{P}_{dil} = -\int_{z^-}^{z^+}\int_{y^-}^{y^+} \frac{\langle\hat{p},\hat{T}\rangle}{\bar{T}}\frac{\partial\bar{v}}{\partial y}\,dy\,dz - \int_{z^-}^{z^+}\int_{y^-}^{y^+} \frac{\langle\hat{p},\hat{T}\rangle}{\bar{T}}\frac{\partial\bar{w}}{\partial z}\,dy\,dz$$
$$- \int_{z^-}^{z^+}\int_{y^-}^{y^+} \frac{\langle\hat{\rho},\hat{\rho}\rangle}{\bar{\rho}^2}\bar{p}\frac{\partial\bar{v}}{\partial y}\,dy\,dz - \int_{z^-}^{z^+}\int_{y^-}^{y^+} \frac{\langle\hat{\rho},\hat{\rho}\rangle}{\bar{\rho}^2}\bar{p}\frac{\partial\bar{w}}{\partial z}\,dy\,dz, \tag{3.66f}$$

$$\hat{P}_{s,T} = -\frac{1}{\gamma\,(\gamma-1)\,M^2}\int_{z^-}^{z^+}\int_{y^-}^{y^+} \frac{\langle\hat{\rho},\hat{T}\rangle}{\bar{T}}\bar{v}\frac{\partial\bar{T}}{\partial y}\,dy\,dz$$
$$- \frac{1}{\gamma\,(\gamma-1)\,M^2}\int_{z^-}^{z^+}\int_{y^-}^{y^+} \frac{\langle\hat{\rho},\hat{T}\rangle}{\bar{T}}\bar{w}\frac{\partial\bar{T}}{\partial z}\,dy\,dz, \tag{3.66g}$$

$$\hat{P}_{con} = -\int_{z^-}^{z^+}\int_{y^-}^{y^+} \left[\frac{\bar{v}\bar{p}}{\bar{\rho}^2}\langle\hat{\rho},\partial\hat{\rho}/\partial y\rangle + \frac{\bar{v}\bar{p}}{(\gamma-1)\bar{T}^2}\langle\hat{T},\partial\hat{T}/\partial y\rangle\right.$$
$$\left. + \bar{v}\bar{\rho}\,(\langle\hat{u},\partial\hat{u}/\partial y\rangle + \langle\hat{v},\partial\hat{v}/\partial y\rangle + \langle\hat{w},\partial\hat{w}/\partial y\rangle)\right]\,dy\,dz$$
$$- \int_{z^-}^{z^+}\int_{y^-}^{y^+} \left[\frac{\bar{w}\bar{p}}{\bar{\rho}^2}\langle\hat{\rho},\partial\hat{\rho}/\partial z\rangle + \frac{\bar{w}\bar{p}}{(\gamma-1)\bar{T}^2}\langle\hat{T},\partial\hat{T}/\partial z\rangle\right.$$
$$\left. + \bar{w}\bar{\rho}\,(\langle\hat{u},\partial\hat{u}/\partial z\rangle + \langle\hat{v},\partial\hat{v}/\partial z\rangle + \langle\hat{w},\partial\hat{w}/\partial z\rangle)\right]\,dy\,dz, \tag{3.66h}$$

$$\hat{D}_{\mu} = -\int_{z^-}^{z^+}\int_{y^-}^{y^+} (\langle\hat{\tau}_{xx}, i\alpha\hat{u}\rangle + \langle\hat{\tau}_{yy},\partial\hat{v}/\partial y\rangle + \langle\hat{\tau}_{zz},\partial\hat{w}/\partial z\rangle$$
$$+\langle\hat{\tau}_{xy},\partial\hat{u}/\partial y\rangle + \langle\hat{\tau}_{xy}, i\alpha\hat{v}\rangle + \langle\hat{\tau}_{xz},\partial\hat{u}/\partial z\rangle + \langle\hat{\tau}_{xz}, i\alpha\hat{w}\rangle$$
$$+\langle\hat{\tau}_{yz},\partial\hat{v}/\partial z\rangle + \langle\hat{\tau}_{yz},\partial\hat{w}/\partial y\rangle)\,dy\,dz, \tag{3.66i}$$

$$\hat{D}_{k} = \int_{z^-}^{z^+}\int_{y^-}^{y^+} \frac{\langle\hat{q}_x, i\alpha\hat{T}\rangle + \langle\hat{q}_y,\partial\hat{T}/\partial y\rangle + \langle\hat{q}_z,\partial\hat{T}/\partial z\rangle}{\bar{T}}\,dy\,dz, \tag{3.66j}$$

$$\hat{F}_p = -\int_{z^-}^{z^+} \langle\hat{p},\hat{v}\rangle|_{y^-}^{y^+}\,dz - \int_{y^-}^{y^+} \langle\hat{p},\hat{w}\rangle|_{z^-}^{z^+}\,dy, \tag{3.66k}$$

$$\hat{F}_{\mu} = \int_{z^-}^{z^+} \langle\hat{\tau}_{yy},\hat{v}\rangle|_{y^-}^{y^+}\,dz + \int_{y^-}^{y^+} \langle\hat{\tau}_{zz},\hat{w}\rangle|_{z^-}^{z^+}\,dy + \int_{z^-}^{z^+} \langle\hat{\tau}_{xy},\hat{u}\rangle|_{y^-}^{y^+}\,dz$$
$$+ \int_{y^-}^{y^+} \langle\hat{\tau}_{xz},\hat{u}\rangle|_{z^-}^{z^+}\,dy + \int_{z^-}^{z^+} \langle\hat{\tau}_{yz},\hat{w}\rangle|_{y^-}^{y^+}\,dz + \int_{y^-}^{y^+} \langle\hat{\tau}_{yz},\hat{v}\rangle|_{z^-}^{z^+}\,dy, \tag{3.66l}$$

$$\hat{F}_k = -\int_{z^-}^{z^+} \frac{\langle \hat{q}_y, \hat{T} \rangle}{\bar{T}} \bigg|_{y^-}^{y^+} dz - \int_{y^-}^{y^+} \frac{\langle \hat{q}_z, \hat{T} \rangle}{\bar{T}} \bigg|_{z^-}^{z^+} dy, \tag{3.66m}$$

$$\begin{aligned}
\hat{F}_{d\mu/dT} = {} & \frac{1}{Re} \int_{z^-}^{z^+} \langle \hat{u}, \hat{T} \rangle \frac{d\bar{\mu}}{d\bar{T}} \frac{\partial \bar{u}}{\partial y} \bigg|_{y^-}^{y^+} dz + \frac{1}{Re} \int_{y^-}^{y^+} \langle \hat{u}, \hat{T} \rangle \frac{d\bar{\mu}}{d\bar{T}} \frac{\partial \bar{u}}{\partial z} \bigg|_{z^-}^{z^+} dy \\
& + \frac{1}{Re} \int_{y^-}^{y^+} \langle \hat{v}, \hat{T} \rangle \frac{d\bar{\mu}}{d\bar{T}} \frac{\partial \bar{v}}{\partial z} \bigg|_{z^-}^{z^+} dy + \frac{1}{Re} \int_{z^-}^{z^+} \langle \hat{w}, \hat{T} \rangle \frac{d\bar{\mu}}{d\bar{T}} \frac{\partial \bar{w}}{\partial z} \bigg|_{y^-}^{y^+} dz \\
& + \frac{1}{Re} \int_{y^-}^{y^+} \langle \hat{v}, \hat{T} \rangle \frac{d\bar{\mu}}{d\bar{T}} \frac{\partial \bar{v}}{\partial y} \bigg|_{z^-}^{z^+} dy + \frac{1}{Re} \int_{z^-}^{z^+} \langle \hat{w}, \hat{T} \rangle \frac{d\bar{\mu}}{d\bar{T}} \frac{\partial \bar{w}}{\partial y} \bigg|_{y^-}^{y^+} dz \\
& + \frac{2}{Re} \int_{z^-}^{z^+} \langle \hat{v}, \hat{T} \rangle \frac{d\bar{\mu}}{d\bar{T}} \frac{\partial \bar{v}}{\partial y} \bigg|_{y^-}^{y^+} dz + \frac{2}{Re} \int_{y^-}^{y^+} \langle \hat{w}, \hat{T} \rangle \frac{d\bar{\mu}}{d\bar{T}} \frac{\partial \bar{w}}{\partial z} \bigg|_{z^-}^{z^+} dy \\
& + \frac{1}{Re} \int_{z^-}^{z^+} \langle \hat{v}, \hat{T} \rangle \frac{d\bar{\lambda}}{d\bar{T}} \frac{\partial \bar{v}}{\partial y} \bigg|_{y^-}^{y^+} dz + \frac{1}{Re} \int_{y^-}^{y^+} \langle \hat{w}, \hat{T} \rangle \frac{d\bar{\lambda}}{d\bar{T}} \frac{\partial \bar{v}}{\partial y} \bigg|_{z^-}^{z^+} dy \\
& + \frac{1}{Re} \int_{z^-}^{z^+} \langle \hat{v}, \hat{T} \rangle \frac{d\bar{\lambda}}{d\bar{T}} \frac{\partial \bar{w}}{\partial z} \bigg|_{y^-}^{y^+} dz + \frac{1}{Re} \int_{y^-}^{y^+} \langle \hat{w}, \hat{T} \rangle \frac{d\bar{\lambda}}{d\bar{T}} \frac{\partial \bar{w}}{\partial z} \bigg|_{z^-}^{z^+} dy.
\end{aligned} \tag{3.66n}$$

The production term $\hat{P}_{RS}$ represents the work done by the disturbance Reynolds stresses against the velocity shear layers present in the base flow. Term $\hat{P}_s$ describes the energy produced due to the transport of entropy spottiness across the base-flow temperature gradients. The next term, $\hat{P}_Q$, refers to the production of disturbance energy due to the heat source $\hat{Q}$, which is generated by transport phenomena, including the variation of the transport properties with temperature. The contribution denoted by $\hat{P}_{mom}$ encloses the energy produced as a result of the convection of disturbance momentum across the base flow velocity shear layers. The presence of a non-negligible pressure gradient in the base flow brings an additional energy production term, labeled as $\hat{P}_{\nabla p}$, which can be interpreted as a form of pressure work. Another source of energy production arises from the interaction between pressure and the divergence of the velocity field, which adopts the shape of a pressure dilatation term, $\hat{P}_{dil}$. Term $\hat{P}_{s,T}$ results from the material derivative of the internal energy fluctuation. The last contribution to the disturbance energy production is comprised inside the term $\hat{P}_{con}$, which represents a part of the convective derivative of the total disturbance energy.

The dissipation of perturbation energy due to friction and thermal conduction is contained in the dissipation terms $\hat{D}_\mu$ and $\hat{D}_k$, respectively. Regarding the disturbance energy flux, term $\hat{F}_p$ describes the rate of work done on the domain due to the disturbance pressure force. The terms $\hat{F}_\mu$ and $\hat{F}_k$ respectively embody the net flux of mechanical and thermal energy convected across the domain boundary owing to friction and thermal conduction. Finally, the disturbance energy flux con-

tribution given by $\hat{F}_{d\mu/dT}$ appears as a result of the dependence of viscosity with temperature.

The term $\hat{P}_Q$ is a clear example of how the transport processes of viscous friction and thermal conduction can also have a destabilizing influence on the perturbations. Although this is a counter-intuitive result, as friction and thermal conduction are commonly associated with energy dissipation, it complements the well-known destabilizing role of the disturbance Reynolds stresses (term $\hat{P}_{RS}$), which explained the existence of viscous instabilities (TS waves) in low-speed flows [52, 53].

3.11 Convective and absolute instabilities

In general, instability waves can grow or decay in both space and in time. Depending on its behavior, each unstable wave can be classified as a convective or an absolute perturbation. The difference between the two can be illustrated by considering the impulse response of a given base flow field [8]. The impulse response is the evolution of the wavepacket that results from an impulse that excites every wave simultaneously at $x = 0$ and $t = 0$. For a given flow field, only those waves that satisfy the dispersion relation dictated by the governing equations are allowed to propagate. Each wave propagates away from the point of impulse at a different velocity, defined by its associated group velocity ($c_g = \partial\omega/\partial\alpha$), and grows or decays at a different rate, given by its growth rate.

If all the developing waves decay in time, the flow is stable, whereas if any of the waves grows in time, the flow is unstable. For unstable flows, a further distinction on the nature of each unstable wave is necessary. For a long time after the impulse, the only wave that remains at the point of impulse ($x = 0$) is the one that features a zero group velocity. If such a wave decays in time, then the impulse response decays to zero at the point of impulse, and the flow is known as a convectively unstable flow. All the unstable waves that propagate away from the impulse location are known as convective instabilities. On the other hand, if the wave with zero group velocity grows in time, then the impulse response grows to infinity. In this case, the flow is called absolutely unstable, and the wave with $c_g = 0$ is known as an absolute instability.

In practice, to determine whether a given flow field is absolutely unstable or not, a spatio-temporal analysis is employed, in which both spatial and temporal growth is allowed. Within the framework of local linear stability theory, this is achieved by letting both ω and α (or β) be complex quantities. The solution of the eigenvalue problem for a set of different complex wavenumbers and frequencies allows to identify conditions for which zero group velocity waves exist, known as saddle points in the complex plane. The Briggs-Bers criterion [25] is then employed to analyze the behavior of the different saddle points and determine whether

they correspond to an absolute instability or not.

In this work, only convective instabilities are investigated.

3.12 Non-modal growth

Theoretical research in laminar-turbulent transition has traditionally focused on the study of small-amplitude disturbances undergoing exponential growth based on the mechanisms predicted by linear modal stability theory. However, this scenario of modal growth does not always provide a satisfactory explanation for the occurrence of transition encountered in experimental and in-flight observations. As introduced in § 1.2, different paths to transition exist in which eigenmode growth does not play a dominant role. Probably, the most notable example of this situation is the so-called blunt-body paradox, which makes reference to the occurrence of transition observed in blunt bodies at conditions at which the boundary layer is stable to modal perturbations, usually corresponding to high freestream Mach numbers. In view of the need of an alternative explanation, non-modal growth, also known as transient growth, has emerged as a possible mechanism leading to a different path to transition [54, 55].

The first application of the theoretical transient-growth framework to compressible flat-plate boundary layers is due to Hanifi *et al.* [49], who employed a singular value decomposition of the linearized evolution operator based on temporal local linear stability theory. They showed that a significant transient growth can take place over a wide range of parameter values for compressible flow, and that the optimal initial perturbations for the compressible case are found to be streamwise vortices generated by the lift-up effect. Tumin & Reshotko [56] later extended the same analysis to spatially growing disturbances. Building upon this work, Reshotko & Tumin [55] developed a correlation for roughness-induced transition based on spatial transient growth results which is able to reproduce transition trends observed experimentally, giving weight to the idea that transient growth could be a plausible mechanism for early transition due to distributed surface roughness.

A different theoretical approach was independently developed by Andersson *et al.* [57] and Luchini [58] to quantify the spatial transient energy growth in boundary layers including non-parallel effects. This technique is based on the parabolized stability equations and consists in an optimization marching procedure in which the disturbance energy over a given spatial extent is maximized. Recently, by employing this methodology, Paredes and co-authors [59] have extended the current body of results for optimal non-modal disturbance growth in boundary-layer flows to the hypersonic Mach number regime. Additionally, Paredes *et al.* [60] have revisited the blunt-body paradox using an improved transient-growth framework, leading to some modifications of the Reshotko-Tumin correlation but

at the same time highlighting the need to further investigate the optimal-growth criterion underlying this correlation. Similarly, Hein *et al.* [61] have investigated the disturbance growth in the wake of a roughness patch mounted on the forebody of a reentry capsule at Mach 5.9, for which the onset of transition is observed experimentally. Nevertheless, no evidence of important modal or non-modal growth could be found in that study. Despite these efforts, transient growth is not yet conclusively linked to the measured onset of transition over blunt-body configurations.

3.12.1 Formulation according to the 2D-LST initial value problem

The solution of the eigenvalue problem presented in previous sections describes the linear disturbance evolution in the limit of $t \to \infty$. To compute the perturbation dynamics at $t \to 0$, the initial value problem represented by the linearized perturbation equations must be considered (see § 3.1). For this purpose, only a spatial Fourier transformation of the perturbation quantities is applied for simplification, that is

$$\tilde{\mathbf{q}}(x, y, z, t) = \check{\mathbf{q}}(y, z, t) \exp(i\alpha x) + c.c. \tag{3.67}$$

for the case of two inhomogeneous spatial directions. The initial value problem (IVP) governing the temporal linear evolution of the disturbances can then be expressed in matrix form as

$$\mathbf{B}\frac{\partial \check{\mathbf{q}}}{\partial t} = \mathbf{A}\check{\mathbf{q}}, \tag{3.68}$$

where the matrix operators $\mathbf{A}$ and $\mathbf{B}$ are associated with the spatial discretization of the system of governing equations. In general, the matrix $\mathbf{B}$ is non-singular, which allows rewriting equation (3.68) as

$$\frac{\partial \check{\mathbf{q}}}{\partial t} = \mathbf{C}\check{\mathbf{q}}, \tag{3.69}$$

with $\mathbf{C} = \mathbf{B}^{-1}\mathbf{A}$. The solution of system (3.69) can be written explicitly as follows:

$$\check{\mathbf{q}}(t) = \exp\left(\mathbf{C}t\right)\check{\mathbf{q}}(0), \tag{3.70}$$

where $\check{\mathbf{q}}(0) = \check{\mathbf{q}}(t = 0)$ is an initial condition and the matrix exponential $\exp(\mathbf{C}t)$ is usually known as the propagator (or evolution) operator. If this operator features some degree of non-normality, as it is usually the case in flow fields of interest, transient algebraic disturbance growth can be experienced even if the system has a stable asymptotic time response. It can be shown that the optimal transient growth of disturbance energy ($G(t)$), optimized for all possible initial conditions, is given

by the square of the norm of the matrix exponential (see for instance Schmid & Henningson [2, 62]), that is

$$G(t) = ||\exp(\mathbf{C}t)||_E^2 = \max_{\check{\mathbf{q}}(0)} \frac{||\check{\mathbf{q}}(t)||_E^2}{||\check{\mathbf{q}}(0)||_E^2}, \tag{3.71}$$

where the subindex E denotes an energy norm. It is important to note that the definition of an inner product and its associated norm is implicit in equation (3.71).

Following the results obtained from a solution of the eigenvalue problem associated with linear stability theory, the quantity $G(t)$ can be computed by evaluating the orthogonality of the different eigenfunctions that compose the eigenfunction expansion basis as well as the size of the associated perturbations. The first can be achieved by the definition of an inner product and the second by an associated norm.

The first application of this framework to compressible boundary layers is due to Hanifi *et al.* [49], who re-derived the disturbance energy definition introduced by Chu [44] (already presented before as equation (3.50)) to obtain an appropriate energy norm. In this work, the same norm as [49] is adopted, given by

$$||\check{\mathbf{q}}||_E^2 = (\check{\mathbf{q}}, \check{\mathbf{q}})_E = 2\check{E}, \tag{3.72}$$

with[3]

$$\check{E} = \frac{1}{2}\int_{z^-}^{z^+}\int_{y^-}^{y^+} \left[\bar{\rho}\left(\check{u}^*\check{u} + \check{v}^*\check{v} + \check{w}^*\check{w}\right) + \frac{\bar{T}}{\gamma M^2 \bar{\rho}}\check{\rho}^*\check{\rho} + \frac{\bar{\rho}}{\gamma\left(\gamma-1\right)M^2\bar{T}}\check{T}^*\check{T}\right] dy\, dz, \tag{3.73}$$

where, as in § 3.10.2, the integral along a single streamwise wavelength is considered without loss of generality. The associated inner product for a given pair of amplitude functions is therefore expressed as

$$(\check{\mathbf{q}}_f, \check{\mathbf{q}}_g)_E = \int_{z^-}^{z^+}\int_{y^-}^{y^+} \check{\mathbf{q}}_f^H \mathbf{M}\, \check{\mathbf{q}}_g \, dy\, dz, \tag{3.74}$$

where the superscript H refers to the Hermitian transpose (conjugate transpose) and the matrix $\mathbf{M}$ is defined as

$$\mathbf{M} = \text{diag}\left[\bar{\rho}, \bar{\rho}, \bar{\rho}, \frac{\bar{T}}{\gamma M^2 \bar{\rho}}, \frac{\bar{\rho}}{\gamma\left(\gamma-1\right)M^2\bar{T}}\right]. \tag{3.75}$$

After a choice on the inner product and the associated norm has been made, the eigenfunction expansion of the time-dependent amplitude function is considered.

[3] Note that, according to (3.61), $\langle\check{u}, \check{u}\rangle = \check{u}^*\check{u}$ (and similarly for the other perturbation quantities).

Denoting the first K eigenvalues and eigenvectors obtained from the solution of the temporal eigenvalue problem by ω_k and $\hat{\mathbf{q}}_k$, respectively, the vector $\check{\mathbf{q}}$ can be expanded as

$$\check{\mathbf{q}}(y,z,t) = \sum_{k=1}^{K} a_k(t)\hat{\mathbf{q}}_k(y,z) \tag{3.76}$$

with

$$a_k(t) = a_k(0)\exp(-i\omega_k t), \tag{3.77}$$

or in matrix form as

$$\check{\mathbf{q}}(y,z,t) = \mathbf{Q}\,\mathbf{a}(t), \tag{3.78}$$

with

$$\mathbf{a}(t) = \mathbf{\Lambda}\,\mathbf{a}(0) \quad \text{and} \quad \mathbf{\Lambda} = \text{diag}\left[\exp(-i\omega_1 t), ..., \exp(-i\omega_K t)\right], \tag{3.79}$$

where $\mathbf{Q}$ is a matrix whose columns contain the eigenvectors $\hat{\mathbf{q}}_k$ and the vector $\mathbf{a}(0) = [a_1(0), ..., a_K(0)]^{\mathrm{T}}$ contains the initial expansion coefficients that determine the individual contribution of each eigenmode to the transient response. By employing the inner product defined by equation (3.74) together with the expansion in equation (3.78), the following relationship can be found between the energy-norm inner product and the L_2-norm inner product:

$$\begin{aligned}(\check{\mathbf{q}}_f, \check{\mathbf{q}}_g)_E = (\mathbf{Q}\,\mathbf{a}_f, \mathbf{Q}\,\mathbf{a}_g)_E &= \int_{z^-}^{z^+}\int_{y^-}^{y^+} \mathbf{a}_f^H \mathbf{Q}^H \mathbf{M}\,\mathbf{Q}\,\mathbf{a}_g\, dy\, dz \\ &= \mathbf{a}_f^H \mathbf{D}\,\mathbf{a}_g = \mathbf{a}_f^H \mathbf{F}^H \mathbf{F}\,\mathbf{a}_g = (\mathbf{F}\,\mathbf{a}_f, \mathbf{F}\,\mathbf{a}_g)_2\,,\end{aligned} \tag{3.80}$$

where the subscript 2 denotes the L_2-norm

$$||\check{\mathbf{q}}||_2^2 = (\check{\mathbf{q}}, \check{\mathbf{q}})_2 = \check{\mathbf{q}}^H \check{\mathbf{q}} \tag{3.81}$$

and the matrix $\mathbf{F}$ is the Cholesky decomposition of the Hermitian and positive-definite matrix $\mathbf{D}$, that is, $\mathbf{D} = \mathbf{F}^H\mathbf{F}$, which is defined element-wise as

$$\mathbf{D}_{fg} = \int_{z^-}^{z^+}\int_{y^-}^{y^+} \hat{\mathbf{q}}_f^H \mathbf{M}\,\hat{\mathbf{q}}_g\, dy\, dz. \tag{3.82}$$

The relation given by equation (3.80) allows to rewrite the disturbance energy norm in terms of the L_2-norm as follows:

$$||\check{\mathbf{q}}(t)||_E^2 = ||\mathbf{F}\,\mathbf{a}(t)||_2^2. \tag{3.83}$$

Inserting equation (3.83) into the definition of the maximum transient energy growth (equation (3.71)) yields

$$\begin{aligned} G(t) = \max_{\check{\mathbf{q}}(0)} \frac{||\check{\mathbf{q}}(t)||_E^2}{||\check{\mathbf{q}}(0)||_E^2} &= \max_{\check{\mathbf{q}}(0)} \frac{||\mathbf{F}\,\mathbf{a}(t)||_2^2}{||\mathbf{F}\,\mathbf{a}(0)||_2^2} \\ &= \max_{\check{\mathbf{q}}(0)} \frac{||\mathbf{F}\boldsymbol{\Lambda}\mathbf{F}^{-1}\mathbf{F}\,\mathbf{a}(0)||_2^2}{||\mathbf{F}\,\mathbf{a}(0)||_2^2} = ||\mathbf{F}\boldsymbol{\Lambda}\mathbf{F}^{-1}||_2^2. \end{aligned} \tag{3.84}$$

The L_2-norm of matrix $\mathbf{S} = \mathbf{F}\boldsymbol{\Lambda}\mathbf{F}^{-1}$ can be evaluated by means of singular value decomposition (SVD). The value of $G(t)$ is then given by the square of the largest singular value of matrix $\mathbf{S}$. The optimal initial conditions giving rise to the maximum transient growth can be computed via the right singular eigenvector $\mathbf{r}$ associated to the largest singular value of matrix $\mathbf{S}$, that is

$$\mathbf{a}(0) = \mathbf{F}^{-1}\mathbf{r}. \tag{3.85}$$

In practice, the application of the methodology just introduced requires knowledge of a large number of eigenmodes in order to properly describe the eigenfunction expansion basis. Equivalently, this implies that enough modes from the stability spectrum must be known prior to the evaluation of G. For local linear stability theory (LST), the size of the eigenvalue problem allows to compute all the eigenmodes that belong to the spectrum for a given discretization with a very affordable computational cost. However, this task becomes very expensive from the computational point of view for theories dealing with more than one inhomogeneous spatial direction, such as 2D-LST. For this reason, only few works exist in literature that employ the formulation presented above to evaluate transient growth using 2D-LST. Very recently, Quintanilha *et al.* [63] have performed temporal transient-growth computations on the HIFiRE-5 elliptic cone model in hypersonic flow, using two-dimensional linear stability theory. The results show that a significant amount of transient growth can take place at short times, after which modal unstable perturbations take the lead and the growth becomes exponential. This suggests the possibility that this configuration follows a transition scenario like that of path B in figure 1.5.

With the interest of exploring the potential for non-modal growth in the instabilities induced by an isolated roughness element, in this work a transient-growth solver has been implemented in VESTA toolkit based on LST and 2D-LST eigenmodes. However, a successful application of the methodology has only been achieved for a smooth flat-plate boundary layer. Appendix H shows a verification

of the solver applied to a supersonic flat-plate boundary layer and details difficulties encountered when applying the methodology to the case of roughness-induced instabilities, providing recommendations for future work in this regard.

3.13 Pseudospectra

As introduced in the previous section, for many relevant problems such as flat plate boundary layers, the linear evolution operator for infinitesimal disturbances is of non-normal type, i.e. its associated eigenfunctions are non-orthogonal. This implies that the information provided by the eigenvalue spectrum is limited to the behavior of the disturbances for large times. To resolve the short-time, transient behavior of the non-normal operator, a generalization of the concept of spectra is usually employed [62], usually known as pseudospectra, as introduced by Trefethen [64, 65].

A complex number z lies in the ϵ-pseudospectrum of a matrix $\mathbf{A}$ if either of the two following equivalent conditions is satisfied: z is an eigenvalue of $\mathbf{A}' = \mathbf{A} + \mathbf{E}$ for some random perturbation matrix $\mathbf{E}$, with $||\mathbf{E}|| \leq \epsilon$, or the norm of the resolvent at z is larger or equal than $1/\epsilon$, that is

$$||(z\mathbf{I} - \mathbf{A})|| \geq \epsilon^{-1}. \tag{3.86}$$

The norm of the resolvent is continuously defined in the complex plane with the exception of the spectrum of $\mathbf{A}$. Its computation can be carried out by means of singular value decomposition in a similar fashion to the calculation of G presented in the previous section, requiring a transformation of the resolvent norm into the L_2-norm.

The evaluation of pseudospectra is interesting in practice because it provides a measure of the sensitivity of the eigenvalues to a small perturbation of the operator (see [65, 66]). Large transient growth is often associated with a high sensitivity of the spectrum and can occur even if the spectrum predicts disturbance decay in the limit of $t \to \infty$. A quantitative link between transient growth and the ϵ-pseudospectrum is given by the Hille-Yosida theorem (see [62, 67] for details).

3.14 Data-driven analysis of flow instabilities

When instantaneous flow-field data are available, generally in the form of a time series of flow snapshots computed by means of DNS or obtained by means of experimental visualization/measurement techniques such as time-resolved particle image velocimetry (PIV), some data-driven techniques may be employed to extract dynamic information that can be used to obtain a description of the coherent structures present in the flow field.

The most widely used technique for extracting coherent features from flow data is known as proper orthogonal decomposition (POD) [68], which provides a set of deterministic modes that correspond to the most energetic flow structures of an ensemble of stochastic flow data. In particular, the frequency domain form of POD, known as spectral POD (SPOD), has been shown to be able to represent the evolution of coherent flow structures in both space and time [69]. Recent work by Lefieux [70] constitutes an example of SPOD applied to the analysis of roughness-induced instabilities in a high-speed boundary layer, based on data originating from DNS computations. The most energetic modes identified by means of the SPOD analysis reveal convective shear-layer instabilities that evolve in the central wake region as well as in the horseshoe vortex system, closely resembling the global flow instabilities reported in similar literature cases.

Recently, another technique known as dynamic mode decomposition (DMD) [71] has also been developed as an alternative to POD. In this case, by means of a direct analysis of a time series of flow snapshots, the flow dynamics are obtained as a set of dynamic modes, which describe the evolution of the flow from one time instant to the next. In the case of a linearly perturbed flow, the modes extracted by means of DMD are equivalent to those resulting from linear stability analysis. An example of the DMD technique applied to hypersonic roughness-induced transition can be found in the work of Subbareddy *et al.* [72], which reported similar findings as [70].

Although experimental flow fields have also been employed as base flows for linear stability analysis, see for instance [73], difficulties arise in defining a good quality base-flow field in this case that can satisfy the governing equations with satisfactory accuracy. The main advantage of data-driven techniques is that they can be directly applied to experimental data sets to obtain useful information on the instability characteristics of a given flow field, without the need of an underlying flow model such as the governing flow equations. Additionally, the resulting dynamical information obtained can be exploited to reduce the degrees of freedom of the system under analysis, opening the possibility to develop reduced-order models from the available data [74]. On the other hand, it is important to mention that the application of the aforementioned data-driven techniques does not generally provide access to the complete stability spectrum. As a result, not all the relevant information on the flow instability features might be available if the coherent structures to be expected are not known beforehand. Therefore, for systems whose instability characteristics are completely unknown, stability theory can still provide a deeper level of understanding of the dominant amplification mechanisms in the flow.

3.15 Modal instabilities evolving in a smooth flat-plate boundary layer at high speed

The most studied fundamental configuration since the birth of hydrodynamic stability theory up to the present day is that of a smooth flat plate boundary layer. Historically, the first studies in flow stability theory were focused on inviscid instabilities only, as the effect of viscosity was believed to always have a stabilizing (dissipative) effect. The work of Lord Rayleigh [75] was the first to provide a criterion for the existence of an inviscid instability in an incompressible boundary layer, known as the inflection-point criterion. However, this criterion was not able to explain the transition onset observed experimentally in incompressible boundary layers, which are stable to inviscid instabilities. It was not until some years later that the destabilizing role of viscosity began to be understood through the investigations of Taylor [76] and Prandtl [77], giving rise to the development of a viscous theory of boundary-layer instability. The studies of Tollmien [52] and Schlichting [53] led to the discovery of a viscous instability responsible for transition in incompressible smooth flat plate boundary layers, known as Tollmien-Schlichting waves. The most unstable TS waves for an incompressible boundary-layer are always two-dimensional waves, i.e. they do not present a spanwise wavenumber ($\beta = 0$). Squire proved the previous statement in the form of a theorem [78].

When compressibility effects become important, the boundary-layer becomes unstable to inviscid instabilities as well. Therefore, compressible boundary layers are unstable to both viscous and inviscid instabilities. The dominant waves in compressible flow are usually no longer two-dimensional but three dimensional ($\beta > 0$), see for instance [4]. The extensive work of Mack [6, 48] investigated the instability of compressible boundary layers ranging from moderate Mach numbers to supersonic and hypersonic Mach numbers, showing that while in incompressible theory there is a unique relation between the wavenumber and phase velocity, in the compressible case there is an infinite sequence of wavenumbers for each phase velocity whenever the base flow relative to the phase velocity is supersonic (occurring at $M > 2.2$ for an adiabatic flat plate). Mack named these additional solutions higher modes, each one of them in the sequence respectively being referred to as second (Mack) mode, third (Mack) mode etc. With this nomenclature, the original mode prior to the appearance of higher modes received the name of first mode or first Mack mode.

First-mode instabilities have a mixed viscous-inviscid nature. At low Mach numbers, the instability behaves mostly as a viscous disturbance. However, as the Mach number increases, its nature gradually changes from a viscous to an inviscid type. When the boundary-layer edge Mach number becomes approximately 4, the mode becomes completely inviscid in character.

Second-mode instabilities are very important in high-speed boundary layers

because they become the most unstable disturbances at hypersonic Mach numbers, usually for $M > 4$ [6]. For this reason, they have been extensively studied in the context of hypersonic boundary-layer transition. Unlike the first Mack mode, second and higher Mack modes are most unstable when behaving as two-dimensional waves, owing to the fact that it is in this configuration that the region of relative supersonic speed is of maximum extent. The two-dimensional second Mack mode is the responsible for transition onset in most hypersonic smooth flat plate boundary layers.

It is important to note that, depending on the particular conditions considered, the dominant boundary-layer instability for a given wavenumber/frequency at a given streamwise location can manifest itself either as a first Mack mode, a second Mack mode, a third Mack mode etc. First- and second-mode instabilities do not coexist as separate modes in the same spectrum. The same is true for the different higher modes. As pointed out by Fedorov & Tumin [79], it is important to emphasize that the first, second and higher Mack modes are not completely separate instabilities, rather they are different manifestations of the same disturbance, which changes its properties by means of synchronization processes (energy exchange) with different fast acoustic modes (see also Ma & Zhong [80]).

3.15.1 Topology of first- and second-mode instabilities in the 2D-LST spectrum

When performing two-dimensional local linear stability analyses of high-speed flat-plate boundary layers, the resulting stability spectrum contains multiple modes associated with the boundary-layer instability. It is important to identify the arrangement of these modes in the spectrum for each particular case. The family of modes associated to the boundary-layer instability corresponds to the different spanwise wavenumbers that fit within the domain of analysis along the spanwise direction. Therefore, a first-mode instability or a higher-mode instability always manifests itself as a branch of modes in the 2D-LST spectrum. The shape of this branch is different whether the instability behaves as a first Mack mode or as a second or higher Mack mode. Recalling the previous discussion, the most unstable first-mode disturbance is three-dimensional. This means that there is a spanwise wavenumber different from zero for which the instability features the maximum growth rate. In this case, the corresponding branch in the 2D-LST spectrum has a hook-like shape. On the other hand, the most unstable second (or higher) Mack mode disturbance is the two-dimensional one. This implies that the shape of the branch becomes a diagonal line.

The two scenarios are illustrated in figure 3.2, which shows an example 2D-LST spectrum for a boundary layer at Mach 6 at two different streamwise wavelengths (λ_x). Starting at the mode with $\beta = 0$ and moving in the direction of

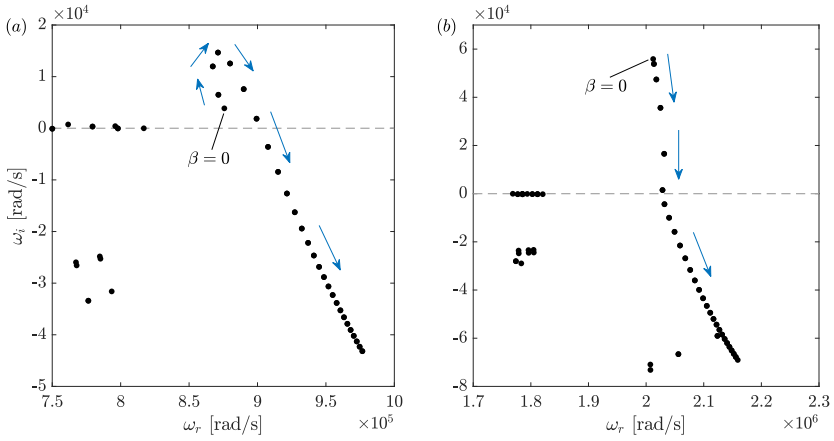

Figure 3.2: Portion of the temporal 2D-LST stability spectrum containing the boundary layer instability for an isothermal flat plate at $M = 6$ at a streamwise distance of $x = 0.1$ m from the leading edge (freestream static pressure $p_\infty = 1963.42$ Pa, temperature $T_\infty = 60.98$ K, wall temperature $T_w = 300$ K): (a) $\lambda_x = 0.006$ m (first-mode instability); (b) $\lambda_x = 0.0027$ m (second-mode instability). Arrows denote the direction of increasing spanwise wavenumber.

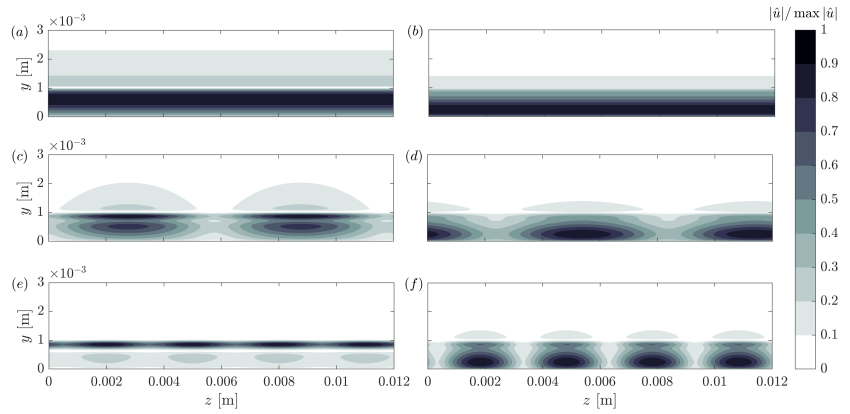

Figure 3.3: Normalized contours of the magnitude of the streamwise velocity amplitude function ($\hat{u} = \hat{u}(y, z)$) for the first three modes belonging to the instability branch presented in figure 3.2: (a, c, e) first-mode instability; (b, d, f) second-mode instability.

increasing spanwise wavenumber (as indicated by the arrows), the branch in each solution describes a different shape. In the case of the first-mode instability, the growth rate of the modes belonging to the branch first increases progressively until reaching the value of β for maximum amplification. From there on, the growth rate of the modes progressively decreases with increasing β. Overall, a hook shape

is described when following the branch. In the case of the second-mode instability, the growth rate is maximum for the first mode of the branch ($\beta = 0$) and it progressively decreases when moving along the direction of increasing spanwise wavenumber, describing a diagonal line. The shape of the branch can therefore be used as a qualitative criterion to determine whether the boundary-layer instability behaves as a first or a second mode. For the sake of clarity, figure 3.3 depicts the two-dimensional streamwise velocity amplitude functions of the first three modes located in the branch for each case. The first mode of the branch is constant along the spanwise direction ($\beta_1 = 0$), the second one has a spanwise wavelength equal to the spanwise domain size, denoted by z_∞, hence $\beta_2 = 2\pi/z_\infty$, and the third one features a spanwise wavelength equal to half of the spanwise domain size, that is $\beta_3 = 4\pi/z_\infty$.

References

[1] Thorwald Herbert. *Secondary Instability Of Boundary Layers*. Annual Review of Fluid Mechanics, 20(1):487–526, 1988.

[2] Peter J. Schmid and Dan S. Henningson. *Stability and Transition in Shear Flows*. Springer-Verlag, New York, NY, 2001.

[3] Pedro Paredes. *Advances in global instability computations: From incompressible to hypersonic flow*. PhD thesis, Universidad Politécnica de Madrid, Escuela Técnica Superior de Ingenieros Aeronáuticos, 2014.

[4] Daniel Arnal. *Boundary layer transition: predictions based on linear theory*. In Special Course on Progress in Transition Modelling, AGARD-R-793, pages 2.1–2.63. 1993.

[5] Fernando Miró Miró. *Numerical Investigation of Hypersonic Boundary-Layer Stability and Transition in the presence of Ablation Phenomena*. PhD thesis, Université Libre de Bruxelles and von Karman Insitute for Fluid Dynamics, 2020.

[6] Leslie M. Mack. *Boundary-Layer Linear Stability Theory*. In Special Course on Stability and Transition of Laminar Flow, AGARD-R-709, pages 3.1–3.81, 1984.

[7] Koen J. Groot. *BiGlobal Stability of Shear Flows Spanwise & Streamwise Analyses*. PhD thesis, TU Delft and von Karman Institute for Fluid Dynamics, 2018.

[8] Matthew P. Juniper, Ardeshir Hanifi, and Vassilios Theofilis. *Modal stability theory*. Applied Mechanics Reviews, 66(2), 2014.

[9] Anatoli Tumin. *LST and the Eigenfunction Expansion Method for Linearized Navier-Stokes Equations – a Summary*. AIAA paper, 2020-0105, 2020.

[10] T J Bridges and P. J. Morris. *Differential eigenvalue problems in which the parameter appears nonlinearly*. Journal of Computational Physics, 55(3):437–460, 1984.

[11] M Gaster. *A note on the relation between temporally-increasing and spatially-increasing disturbances in hydrodynamic stability*. Journal of Fluid Mechanics, 14(2):222–224, 1962.

[12] Werner Koch, Fabio P. Bertolotti, Andreas Stolte, and Stefan J. Hein. *Nonlinear equilibrium solutions in a three-dimensional boundary layer and their secondary instability*. Journal of Fluid Mechanics, 406:131–174, 2000.

[13] Koen J. Groot, Jacopo Serpieri, Fabio Pinna, and Marios Kotsonis. *Secondary crossflow instability through global analysis of measured base flows*. Journal of Fluid Mechanics, 846:605–653, 2018.

[14] Gordon Groskopf, Markus J. Kloker, K A Stephani, Olaf Marxen, and Gianluca Iaccarino. *Hypersonic flows with discrete oblique surface roughness and their stability properties*. In Center of Turbulence Research, Proceedings of the Summer Program, pages 405–422, 2010.

[15] Gordon Groskopf and Markus J. Kloker. *Instability and transition mechanisms induced by skewed roughness elements in a high-speed laminar boundary layer*. Journal of Fluid Mechanics, 805:262–302, 2016.

[16] F. P. Bertolotti. *Linear and nonlinear stability of boundary layers with streamwise varying properties*. PhD thesis, The Ohio-State University, 1991.

[17] Thorwald Herbert. *Parabolized Stability Equations*. Annual Review of Fluid Mechanics, 29(1):245–283, 1997.

[18] Fei Li and Mujeeb R Malik. *Mathematical Nature of Parabolized Stability Equations*. In Ryoji Kobayashi, editor, Laminar-Turbulent Transition, pages 205–212, Berlin, Heidelberg, 1995. Springer Berlin Heidelberg.

[19] P. Andersson, D. S. Henningson, and A. Hanifi. *On a stabilization procedure for the parabolic stability equations*. Journal of Engineering Mathematics, 33(3):311–332, 1998.

[20] Vassilios Theofilis. *Advances in global linear instability analysis of nonparallel and three-dimensional flows*. Progress in Aerospace Sciences, 39(4):249–315, 2003.

[21] Vassilios Theofilis. *Global Linear Instability*. Annual Review of Fluid Mechanics, 43(1):319–352, 2011.

[22] F. Gómez, Soledad Le Clainche, Pedro Paredes, Miguel Hermanns, and Vassilios Theofilis. *Four decades of studying global linear instability: Problems and challenges*. AIAA Journal, 50(12):2731–2743, 2012.

[23] Alexander Theiss, Stefan J. Hein, Syed Raza Christopher Ali, and Rolf Radespiel. *Wake flow instability studies behind discrete roughness elements on a generic re-entry capsule*. AIAA paper, 2016-4382, 2016.

[24] Antonio Di Giovanni and Christian Stemmer. *Cross-flow-type breakdown induced by distributed roughness in the boundary layer of a hypersonic capsule configuration*. Journal of Fluid Mechanics, 856:470–503, 2018.

[25] Patrick Huerre and Peter A. Monkewitz. *Local and global instabilities in spatially developing flows*. Annual Review of Fluid Mechanics, 22(1):473–537, 1990.

[26] Giuseppe Bonfigli and Markus J. Kloker. *Secondary instability of crossflow vortices: Validation of the stability theory by direct numerical simulation*. Journal of Fluid Mechanics, 583:229–272, 2007.

[27] Daniel Rodríguez, Elmer M. Gennaro, and Matthew P. Juniper. *The two classes of primary modal instability in laminar separation bubbles*. Journal of Fluid Mechanics, 734:1–11, 2013.

[28] Thibaut Appel, Mohammed S. Mughal, and Richard Ashworth. *Global Stability Analysis of a Boundary Layer with Surface Indentations*. AIAA Paper, 2019-3537, 2019.

[29] Nicola De Tullio, Pedro Paredes, Neil D. Sandham, and Vassilios Theofilis. *Laminar-turbulent transition induced by a discrete roughness element in a supersonic boundary layer*. Journal of Fluid Mechanics, 735:613–646, 2013.

[30] Thorwald Herbert. *On the stability of 3D boundary layers*. 28th Fluid Dynamics Conference, AIAA paper 1997-1961, 1997.

[31] Chau Lyan Chang. *LASTRAC.3d: Transition prediction in 3D boundary layers*. 34th AIAA Fluid Dynamics Conference and Exhibit, AIAA paper 2004-2542, 2004.

[32] Juan Alberto Franco Sumariva and Stefan J. Hein. *Adaptive Harmonic Linearized Navier-Stokes equations used for boundary layer instability analysis in the presence of large streamwise gradients*. AIAA paper, 2018-1548, 2018.

[33] Juan Alberto Franco Sumariva, Stefan Hein, and Eusebio Valero. *On the influence of two-dimensional hump roughness on laminar-turbulent transition*. Physics of Fluids, 32(3), 2020.

[34] J. L. van Ingen. *A suggested semi-empirical method for the calculation of the boundary layer transition region*. Technical Report VTH-74, Technische Hogeschool Delft, Vliegtuigbouwkunde, 1956.

[35] A. M. O. Smith and N. Gamberoni. *Transition, pressure gradient and stability theory*. Technical Report ES 26388, Douglas Aircraft Co., El Segundo, California, 1956.

[36] Leslie M. Mack. *Transition and Laminar Instability*. Technical report, Jet Propulsion Lab., 1977.

[37] Pedro Paredes, Nicola De Tullio, Neil D. Sandham, and Vassilios Theofilis. *Instability Study of the Wake Behind a Discrete Roughness Element in a Hypersonic Boundary-Layer*. Instability and Control of Massively Separated Flows, Fluid Mechanics and Its Applications, 107:91–96, 2015.

[38] Tim S. Haynes and Helen L. Reed. *Simulation of swept-wing vortices using nonlinear parabolized stability equations*. Journal of Fluid Mechanics, 405:325–349, 2000.

[39] Vassilis Theofilis. *The linearized pressure Poisson equation for global instability analysis of incompressible flows*. Theoretical and Computational Fluid Dynamics, 31(5-6):623–642, 2017.

[40] Fernando Miró Miró and Fabio Pinna. *Linear Stability Analysis of a Hypersonic Boundary Layer in Equilibrium and Non-Equilibrium*. AIAA paper, 2017-4518, 2017.

[41] John D. Anderson Jr. *Hypersonic and High Temperature Gas Dynamics*. American Institute of Aeronautics and Astronautics, Reston VA, second edition, 2006.

[42] Greg Stuckert and Helen L. Reed. *Linear Disturbances in Hypersonic, Chemically Reacting Shock Layers*. AIAA Journal, 32(7):1384–1393, 1994.

[43] K. Joseph George and R. I. Sujith. *Disturbance energy norms: A critical analysis*. Journal of Sound and Vibration, 331(7):1552–1566, 2012.

[44] Boa Teh Chu. *On the energy transfer to small disturbances in fluid flow (Part I)*. Acta Mechanica, 1(3):215–234, sep 1965.

[45] R. C. Tritarelli. *Modal and Non-modal Energy Evolution in Hypersonic Boundary Layers Over Porous Coatings*. Master's thesis, Institute of Fluid Dynamics, ETH Zurich, 2011.

[46] Mario Weder. *Linear Stability and Acoustics of a Subsonic Plane Jet Flow*. Master's thesis, Institute of Fluid Dynamics, ETH Zurich, 2012.

[47] Mario Weder, Michael Gloor, and Leonhard Kleiser. *Decomposition of the temporal growth rate in linear instability of compressible gas flows*. Journal of Fluid Mechanics, 778:120–132, jul 2015.

[48] Leslie M. Mack. *Boundary-Layer Stability Theory*. Jet Propulsion Laboratory, California Institute of Technology, Report 900-277, 1969.

[49] Ardeshir Hanifi, Peter J. Schmid, and Dan S. Henningson. *Transient growth in compressible boundary layer flow*. Physics of Fluids, 8(3):826–837, 1996.

[50] K. Joseph George and R. I. Sujith. *On Chu's disturbance energy*. Journal of Sound and Vibration, 330(22):5280–5291, 2011.

[51] John D. Anderson Jr. *Fundamentals of Aerodynamics*. McGraw-Hill, New York NY, fifth edition, 2011.

[52] W. Tollmien. *Über die Entstehung der Turbulenz (in German)*. ZAMM Journal of Applied Mathematics and Mechanics / Zeitschrift für Angewandte Mathematik und Mechanik, 11(6):407–409, 1931.

[53] H. Schlichting. *Zur Enstehung der Turbulenz bei der Plattenstrmung (in German)*. Nachrichten von der Gesellschaft der Wissenschaften zu Gttingen, Mathematisch-Physikalische Klasse, pages 181–208, 1933.

[54] Eli Reshotko and Anatoli Tumin. *The Blunt Body Paradox — A Case for Transient Growth*. In Hermann F Fasel and William S Saric, editors, Laminar-Turbulent Transition, pages 403–408, Berlin, Heidelberg, 2000. Springer Berlin Heidelberg.

[55] Eli Reshotko and Anatoli Tumin. *Role of Transient Growth in Roughness-Induced Transition*. AIAA Journal, 42(4):766–770, 2004.

[56] Anatoli Tumin and Eli Reshotko. *Spatial theory of optimal disturbances in boundary layers*. Physics of Fluids, 13(7):2097–2104, 2001.

[57] Paul Andersson, Martin Berggren, and Dan S. Henningson. *Optimal disturbances and bypass transition in boundary layers*. Physics of Fluids, 11(1):134–150, 1999.

[58] Paolo Luchini. *Reynolds-number-independent instability of the boundary layer over a flat surface: optimal perturbations*. Journal of Fluid Mechanics, 404:289–309, feb 2000.

[59] Pedro Paredes, Meelan M. Choudhari, Fei Li, and Chau Lyan Chang. *Optimal growth in hypersonic boundary layers*. AIAA Journal, 54(10):3050–3061, 2016.

[60] Pedro Paredes, Meelan M. Choudhari, and Fei Li. *Blunt-body paradox and improved application of transient-growth framework*. AIAA Journal, 56(7):2604–2614, 2018.

[61] Stefan J. Hein, Alexander Theiss, Antonio Di Giovanni, Christian Stemmer, Thomas Schilden, Wolfgang Schröder, Pedro Paredes, Meelan M. Choudhari, Fei Li, and Eli Reshotko. *Numerical investigation of roughness effects on transition on spherical capsules*. Journal of Spacecraft and Rockets, 56(2):388–404, 2019.

[62] Peter J. Schmid and Dan S. Henningson. *Optimal energy density growth in Hagen-Poiseuille flow*. Journal of Fluid Mechanics, 277(2):197–225, 1994.

[63] Helio Ricardo Quintanilha Junior, Vassilis Theofilis, and Ardeshir Hanifi. *Global Transient-Growth Analysis of Hypersonic Flow on the HIFiRE-5 Elliptic Cone Model*. AIAA Paper, 2019-2148, jan 2019.

[64] Lloyd N. Trefethen. *Pseudospectra of matrices*. In D. F. Griffiths and G. A. Watson, editors, Numerical analysis 1991, Harlow, Essex, UK, 1992. Longman Scientific & Technical.

[65] Lloyd N. Trefethen. *Computation of pseudospectra*. Acta Numerica, 8:247–295, 1999.

[66] Peter J. Schmid, Dan S. Henningson, Mehdi R. Khorrami, and Mujeeb R. Malik. *A study of eigenvalue sensitivity for hydrodynamic stability operators*. Theoretical and Computational Fluid Dynamics, 4(5):227–240, 1993.

[67] Satish C Reddyt, Peter J. Schmid, and Dan S Henningson. *Pseudospectra of the Orr-Sommerfeld operator*. Technical Report 1, 1993.

[68] John L. Lumley. *Stochastic Tools in Turbulence*. Academic Press, New York, 1970.

[69] Aaron Towne, Oliver T. Schmidt, and Tim Colonius. *Spectral proper orthogonal decomposition and its relationship to dynamic mode decomposition and resolvent analysis*. Journal of Fluid Mechanics, 847:821–867, 2018.

[70] Julien Lefieux. *DNS study of roughness-induced transition in hypersonic flows*. PhD thesis, Université Paris-Saclay, 2021.

[71] Peter J. Schmid. *Dynamic mode decomposition of numerical and experimental data*. Journal of Fluid Mechanics, 656:5–28, 2010.

[72] Pramod K. Subbareddy, Matthew D. Bartkowicz, and Graham V. Candler. *Direct numerical simulation of high-speed transition due to an isolated roughness element*. Journal of Fluid Mechanics, 748(3):848–878, 2014.

[73] Koen J. Groot, Fernando Miró Miró, Ethan S. Beyak, Alexander J. Moyes, Fabio Pinna, and Helen L. Reed. *DEKAF: spectral multi-regime basic-state solver for boundary-layer stability*. AIAA paper, 2018-3380, 2018.

[74] Gilles Tissot, Laurent Cordier, Nicolas Benard, and Bernd R. Noack. *Model reduction using Dynamic Mode Decomposition*. Comptes Rendus - Mecanique, 342(6-7):410–416, 2014.

[75] Lord Rayleigh. *On the Stability, or Instability, of certain Fluid Motions*. Proceedings of the London Mathematical Society, s1-11(1):57–72, 1879.

[76] G. I. Taylor. *Eddy Motion in the Atmosphere*. Philosophical Transactions of the Royal Society A: Mathematical, Physical and Engineering Sciences, 215:1–26, 1915.

[77] Ludwig Prandtl. *Bemerkungen über die Enstehund der Turbulenz (in German)*. ZAMM, 1:431–436, 1921.

[78] Herbert Brian Squire. *On the stability for three-dimensional disturbances of viscous fluid flow between parallel walls*. Proceedings of the Royal Society of London. Series A, Containing Papers of a Mathematical and Physical Character, 142(847):621–628, nov 1933.

[79] Alexander V. Fedorov and Anatoli Tumin. *High-Speed Boundary-Layer Instability: Old Terminology and a New Framework*. AIAA Journal, 49(8):1647–1657, 2011.

[80] Yanbao Ma and Xiaolin Zhong. *Receptivity of a supersonic boundary layer over a flat plate. Part 1. Wave structures and interactions*. Journal of Fluid Mechanics, 488:31–78, 2003.

4

Numerical methodology

This chapter describes the numerical methodology employed to compute the laminar base-flow solutions that serve as a reference state to the stability analysis as well as the numerical techniques used for the solution of the linearized governing stability equations.

4.1 Base-flow computation

The main physical problem under study in this work consists of a three-dimensional isolated roughness element mounted on top of a flat plate inside a hypersonic freestream. The required base flow fields for the stability analysis of such configuration are laminar and steady solutions of the three-dimensional compressible Navier-Stokes equations (see § 2.2).

For the analysis of the smooth flat-plate boundary layer, that is, with no roughness element, a laminar solution of the boundary-layer equations (see § 2.4) is considered instead. The base-flow solution of the smooth flat-plate boundary layer serves two main purposes. On the one hand, the boundary-layer profiles can be used as an inflow to the more complex, three-dimensional Navier-Stokes simulation in cases in which the flat-plate leading edge is assumed to be infinitely sharp, as described in § 5.1. On the other hand, the stability analysis of the smooth configuration is important to understand the instability characteristics of the boundary layer prior to introducing the roughness element, and allows to quantify the potential destabilizing effect associated to the obstacle.

4.1.1 Solution of the boundary-layer equations

Due to their parabolic nature, the general solution of the boundary-layer equations can be carried out by means of a marching procedure along the streamwise direction. However, as presented previously in § 2.4, depending on the thermodynamic flow assumption considered, the boundary-layer equations for the case of a flat-plate geometry can have a self-similar solution, which simplifies the equations to be solved to a system of ordinary differential equations (ODE). This is the case for the CPG and the TPG assumptions, see § 2.4.1.1.

Standard numerical solutions of the self-similar boundary layer equations usually employ Runge-Kutta schemes of 4th or 5th-order to integrate the system of ordinary differential equations, together with a shooting technique that iteratively converges the solution to make it compatible with the desired boundary conditions (see for instance [1]). Marching solutions of the complete boundary-layer equations often combine Runge-Kutta discretizations along the wall-normal direction coupled with first or second-order finite difference discretizations along the streamwise (marching) direction.

In the context of stability analysis, it is important to employ base-flow fields with a significant degree of accuracy. For this reason, high-order numerical solutions are desirable. It is important to mention that high-order numerical solutions of the full Navier-Stokes equations in high-speed flows are a state-of-the-art topic, mainly due to the challenges posed by flow discontinuities such as shock waves [2]. As a consequence, such solutions are not yet common in practice. However, high-order numerical solutions of the boundary-layer equations, which exclude discontinuities in the flow, are less challenging and can be routinely obtained. In this work, the solution of the boundary-layer equations for all flow assumptions considered is carried out by means of the flow solver DEKAF, presented in the next section.

4.1.2 The DEKAF flow solver

The DEKAF flow solver [3–5] was developed with the objective of computing numerical solutions of the boundary-layer equations with a high degree of accuracy. This is specially suited for minimizing the numerical errors introduced in stability computations, owing to the high sensitivity of the disturbances to the smoothness and the numerical convergence of the base flow field [6].

DEKAF consists of a boundary-layer solver coupled with inviscid solvers for simple geometries which incorporates a high-fidelity thermophysical modeling, allowing the computation of boundary-layer profiles in the presence of a wide range of high-enthalpy effects. At its core lies a Chebyshev spectral collocation method (see § 4.2.1.1) employed for discretization along the wall-normal direction, together with a variable-order forward finite-difference scheme for discretization

along the marching direction. The solution of the system of governing equations at each marching station is computed iteratively by means of a Newton-Raphson method built on the linearized boundary-layer equations.

The inviscid solvers incorporated in DEKAF include the shock-jump relations for wedge and conical surfaces as well as an inviscid non-equilibrium solver in one dimension. The coupling between the inviscid- and viscous-flow regions is of 0th-order [7]. For further details on the solver, including several verification cases in different regimes and thermodynamic flow assumptions, the reader is referred to references [4, 5].

Results presented in chapter 5 employ boundary-layer profiles for a calorically perfect gas obtained with DEKAF, and results presented in chapter 6 also use profiles for a thermally perfect gas and for a mixture of gases in chemical equilibrium computed by DEKAF as well. Due to the spectral order of the discretization technique in use, a small number of grid points (collocation points in this case) is required to obtain a converged boundary-layer solution, usually on the order of 100 points.

4.1.3 Solution of the Navier-Stokes equations

Obtaining base-flow solutions for the flat-plate configuration with a roughness element requires the solution of the full compressible Navier-Stokes equations. Since a laminar solution is required, the equations are directly solved without any turbulence modeling. In this sense, the base-flow solutions obtained are equivalent to direct numerical simulations. However, it is important to note that no artificial disturbances are explicitly introduced in the computational domain other than the flow distortion induced by the presence of the roughness element.

Although a steady base-flow solution is desired, the optimal numerical solution strategy consists in evolving the time-dependent equations until convergence to steady state is achieved, starting from a given initial flow field. This remains a valid approach as long as there are no unsteady physical phenomena taking place in the flow field, which is the case for all the base-flow solutions studied in this work.

To carry out the solution of the Navier-Stokes equations, the commercial software suite CFD++® (see [8, 9]) is employed, which provides a unified physics framework which enables the solution of compressible flows at different Mach numbers and at a wide range of temperatures.

4.1.3.1 The Navier-Stokes solver in CFD++®

CFD++® provides a solver for the numerical solution of the Navier-Stokes equations which allows to account for different high-enthalpy phenomena, including the effects considered in this dissertation: vibrational-energy-mode excitation and

chemical non-equilibrium. The spatial discretization is based on a second-order upwind finite volume scheme. The scheme employs a limited total variation diminishing (TVD) multi-dimensional linear flux interpolation combined with the Harten-Lax-van Leer contact (HLLC) approximate Riemann solver [10, 11], which together contribute to minimize numerical oscillations as well as numerical dissipation in the vicinity of flow discontinuities, thus enabling good shock-capturing capabilities.

The time integration is performed with a point-implicit scheme (backward Euler) that incorporates multigrid acceleration and residual smoothing. The implicit nature of the method allows the use of larger time steps to enhance the convergence to steady state.

In the case of the TPG and CNE thermodynamic frameworks, the thermal, transport and chemistry models described in § 2.5.1, § 2.5.2 and § 2.5.3 are employed by the solver.

4.1.3.2 Grid generation

The grids used for computing the Navier-Stokes base flows are block-structured and consist of hexahedral cells. Due to the rather simple geometrical configuration studied in this work, namely, a flat plate with a sharp-edged roughness element on top (see § 5.1), the generation of the grids is performed by means of OpenFOAM's blockMesh [12] utility.

The use of blockMesh enables to script the grid generation process, thus allowing to perform quick changes in the geometry and the blocking structure without the need of a graphical interface, only requiring a change of the mesh generation script. Additionally, it allows to control precisely the grid stretching applied along the different directions. For a given block edge, the grading in the grid spacing is achieved by means of a constant expansion ratio (r_E) between consecutive cells, that is, $r_E = \delta_{j+1}/\delta_j$, where δ_j denotes the cell spacing of the jth cell along the edge. For a given edge with length l_E, the expansion ratio can be obtained by finding the roots of the following polynomial equation:

$$\delta_0 \sum_{k=0}^{N_E-1} r_E^k = l_E, \tag{4.1}$$

where δ_0 is the size of the first cell along the edge and N_E is the number of cells along the edge. The roots can be obtained by computing the eigenvalues of the companion matrix associated to the polynomial. The value of r_E is given by the only real and positive root bigger than zero. Therefore, given a desired first cell size and a desired number of cells, the relationship expressed by equation (4.1) uniquely defines the necessary grading to be imposed on the edge so that a constant expansion ratio in the cell size is achieved.

The grading law given by equation (4.1) allows to perform a desired continuous grid stretching in a single direction along the edge. However, in many cases it is desirable to have different gradings along the same edge, such as for instance a clustering of grid points towards both ends of an edge. Here, this is achieved by splitting the edge into different segments for which a single grading is applied following the relation introduced above. In this case, the number of cells employed into each segment is carefully adapted to keep the cell spacing as continuous as possible between the different grading regions.

By fixing the first cell size along a given edge to be the same as the last cell size of the adjacent edge, the transitions in cell size between different blocks are kept continuous. This ensures that the cell spacing function along a given direction is at least of class C^0. This requirement is found to be sufficient for the base-flow computations performed in this work, as they are based on a second-order discretization scheme. In the case of direct numerical simulations that resolve the evolution of disturbances and the breakdown to turbulence, high-order discretization schemes are usually employed. In these cases, the cell spacing functions might be required to be continuous up to the fourth derivative (C^4) to achieve the desired quality in the solution, see for instance [13, 14].

Illustrations of some of the base-flow grids employed in this work can be found in figures 5.5 and 5.18.

An observation that is worth mentioning regarding the behavior of blockMesh concerns the case of long trapezoidal blocks. When a given edge grading is imposed along the vertical edges of a trapezoidal block elongated along the horizontal direction, it has been found that the imposed grid stretching is not perfectly respected in the interior vertical grid lines of the block. This can lead to small discontinuities in the cell spacing between two adjacent blocks. In order to minimize this issue, the elongated trapezoidal blocks can be split into smaller blocks such that the aspect ratio of the blocks becomes close to 1.

4.2 Stability analysis

In the following sections, the numerical methods employed for the discretization and the solution of the generalized eigenvalue problem that originates from local linear stability theory with one (LST) and two (2D-LST) inhomogeneous directions is presented.

4.2.1 Spatial discretization techniques

The governing equations for local linear stability theory are partial-differential equations which lead to a partial-differential eigenvalue problem. Therefore, spatial discretization techniques are required for the numerical solution of the eigen-

value problem. Given the strong inhomogeneity of the perturbations evolving in a boundary layer, high-order numerical methods are generally employed for this purpose. For one-dimensional local linear stability theory, the Chebyshev collocation method has been widely applied owing to its spectral accuracy. However, for the analysis of base flows with two inhomogeneous directions, requiring the use of 2D-LST, the Chebyshev collocation method often results in a very high computational cost. As a result, high-order finite difference methods are usually considered instead, which still benefit from high accuracy at a reduced computational cost.

The two spatial discretization techniques employed for the stability analysis performed in this work are briefly described next.

4.2.1.1 Chebyshev collocation method

The Chebyshev collocation method is a spectral discretization technique that employs a nodal basis consisting of characteristic Lagrange polynomials, which are defined in a set of pre-established locations (nodes) known as collocation points. A complete description of the method including its derivation can be found in the work of Canuto *et al.* [15] and Trefethen [16], for instance. Here, the attention is focused on the definition of the coordinates of the collocation points and the associated differentiation matrices, which are the elements required in practice for applying the discretization method in the scope of this work.

The coordinates of the collocation points, also commonly known as Chebyshev-Gauss-Lobatto (CGL) points (among others), are defined by the extrema of Chebyshev polynomials in the interval $\xi \in [-1, 1]$ (usually referred to as the transformed or computational space), and are given by

$$\xi_j = \cos \frac{(j-1)\pi}{N_\xi - 1}, \quad j = 1, ..., N_\xi, \tag{4.2}$$

where N_ξ denotes the number of collocation points. This particular distribution of grid points is found to decrease the error introduced by the discretization thanks to the clustering of points towards the boundaries of the domain, thus helping to reduce the problem known as Runge phenomenon [16]. It is important to mention that the coordinates of the resulting points are ordered from right to left (or in decreasing order), that is, from $\xi_1 = 1$ to $\xi_{N_\xi} = -1$. Given this set of collocation points, a generic function f can be discretized by means of the Chebyshev collocation method as follows:

$$f(\xi) = \sum_{j=1}^{N_\xi} f_j \psi_j(\xi), \tag{4.3}$$

where f_j is the value of the function at the jth collocation point and ψ_j is the characteristic Lagrange polynomial associated with the jth collocation point, which

can be expressed as

$$\psi_j(\xi) = \prod_{\substack{k=1 \\ k \neq j}}^{N_\xi} \frac{\xi - \xi_k}{\xi_j - \xi_k}, \quad j = 1, ..., N_\xi. \tag{4.4}$$

Equation (4.4) can also be expressed in a more compact way in terms of the Chebyshev polynomials, see for example [15]. It is important to mention that the Lagrange polynomials are defined in the entire ξ domain, i.e., they are not piecewise polynomials. This is what gives a spectral character to this method, in the sense that all polynomials intervene in the evaluation of the function at a given point.

Once the discrete representation of f has been defined (equation (4.3)), its derivative can be discretized through the derivative of the basis functions (the Lagrange polynomials in this case), that is

$$\frac{df(\xi)}{d\xi} = \sum_{j=1}^{N_\xi} f_j \frac{d\psi_j(\xi)}{d\xi}, \tag{4.5}$$

where $d\psi_j(\xi)/\,d\xi$ is known analytically. At this point, it is useful to introduce a matrix form to express the discretization of the derivative evaluated at the collocation points, given by

$$\mathbf{d} = \mathbf{D}_\xi \mathbf{f}, \tag{4.6}$$

where $\mathbf{d} = [df(\xi_1)/\,d\xi, ..., df(\xi_{N_\xi})/\,d\xi]^{\mathrm{T}}$, $\mathbf{f} = [f_1, ..., f_{N_\xi}]^{\mathrm{T}}$ and $\mathbf{D}_\xi$ is the so-called pseudo-spectral differentiation matrix, or simply differentiation matrix, whose entries can be written as

$$D_{\xi,jk} = \begin{cases} \dfrac{2\left(N_\xi - 1\right)^2 + 1}{6} & \text{if } j = k = 1 \\ -\dfrac{2\left(N_\xi - 1\right)^2 + 1}{6} & \text{if } j = k = N_\xi \\ -\dfrac{\xi_j}{2\left(1 - \xi_j^2\right)} & \text{if } j = k = 2, ..., N_\xi - 1 \\ \dfrac{c_j}{c_k} \dfrac{(-1)^{j+k}}{(\xi_j - \xi_k)} & \text{if } j \neq k, \quad j, k = 2, ..., N_\xi - 1 \end{cases}, \tag{4.7}$$

with

$$c_j = \begin{cases} 2 & \text{if } j = 1, N_\xi \\ 1 & \text{if } j = 2, ..., N_\xi - 1 \end{cases}. \tag{4.8}$$

Each row of the differentiation matrix can be interpreted as a vector that contains the coefficients of a stencil that is used to evaluate the derivative of the function at that collocation point. In this method, the resulting stencils employ information from all the collocation points, meaning that each row of the differentiation matrix contains no zeros. As a result, $\mathbf{D}_\xi$ is a dense matrix. This has direct implications in the computational cost of the discretization method, as it leads to dense matrices describing the generalized eigenvalue problem (see § 3.4).

A direct advantage of expressing the discretization of the derivative in matrix form is that the differentiation matrices for higher derivatives can be directly obtained by computing powers of the first-derivative differentiation matrix. For instance, the second-derivative differentiation matrix is obtained by squaring the first-derivative differentiation matrix, i.e., $\mathbf{D}_{\xi\xi} = \mathbf{D}_\xi^2$.

In this work, the base flows of interest are inhomogeneous in two spatial dimensions. Therefore, the discretization is performed with a two-dimensional collocation grid defined in the transformed domain $(\xi, \eta) \in [-1, 1] \times [-1, 1]$. In this method, the discretization given by equation (4.3) is directly extended to two dimensions as

$$f(\xi, \eta) = \sum_{j=1}^{N_\xi} \sum_{k=1}^{N_\eta} f_{kj} \psi_{kj}(\xi, \eta), \tag{4.9}$$

where $\psi_{kj}(\xi, \eta)$ are two-dimensional characteristic Lagrange polynomials, which can be obtained by multiplying the respective one-dimensional polynomials along each direction (see for example Groot [17]). For convenience, the discrete function $f_{kj} = f(\xi_j, \eta_k)$ may be represented in matrix form as a matrix of N_η rows by N_ξ columns, such that η is interpreted as the vertical direction of the computational domain and ξ as the horizontal one. This representation is usually known as a tensor-product grid [16].

In the context of local linear stability theory, f represents the amplitude function of a perturbation quantity, which in turn is one of the components of the full eigenvector $\hat{\mathbf{q}}$ of the system (see for instance equation (3.15)). From the computational point of view, f_{kj} is generally represented as a single vector instead of a matrix. Here, this is achieved by stacking all the columns of f_{kj} in its matrix form, such that a vector of $N_\eta N_\xi$ elements is obtained, given by

$$\mathbf{f}_: = [f_{11}, ..., f_{N_\eta 1}, f_{12}, ..., f_{N_\eta 2}, ..., f_{1N_\xi}, ..., f_{N_\eta N_\xi}]^{\mathrm{T}}. \tag{4.10}$$

Therefore, the computational representation of $\hat{\mathbf{q}}$ consists of a single vector composed of different sub-vectors of size $N_\eta N_\xi$, one per state variable in the system. In practice, the length of the stacked vector $\hat{\mathbf{q}}$ yields the number of rows/columns of the square matrices that define the discrete generalized eigenvalue problem.

By extension of equation (4.5), partial derivatives of the two-dimensional function $f(\xi,\eta)$ can be obtained by evaluating the partial derivatives of the associated two-dimensional Lagrange polynomials, that is

$$\frac{\partial f(\xi,\eta)}{\partial \xi} = \sum_{j=1}^{N_\xi}\sum_{k=1}^{N_\eta} f_{kj}\frac{\partial \psi_{kj}(\xi,\eta)}{\partial \xi}, \quad \frac{\partial f(\xi,\eta)}{\partial \eta} = \sum_{j=1}^{N_\xi}\sum_{k=1}^{N_\eta} f_{kj}\frac{\partial \psi_{kj}(\xi,\eta)}{\partial \eta}. \tag{4.11}$$

In matrix form, the calculation of the partial derivatives at the collocation points can also be achieved by employing the respective differentiation matrix along each direction, similarly to equation (4.6). However, in this case it is important to emphasize that the dimension of the stacked vector $\mathbf{f}_{:}$ is no longer the same as the dimension of the differentiation matrices defined as in equation (4.7). In order to obtain a differentiation matrix that can be applied to the vector $\mathbf{f}_{:}$, the standard differentiation matrices $\mathbf{D}_\xi$ and $\mathbf{D}_\eta$ can be extended by applying the Kronecker product ($\otimes$) with the identity matrix [16], such that

$$\mathbf{D}_{\xi:} = \mathbf{D}_\xi \otimes \mathbf{I}_{N_\eta}, \tag{4.12a}$$

$$\mathbf{D}_{\eta:} = \mathbf{I}_{N_\xi} \otimes \mathbf{D}_\eta, \tag{4.12b}$$

where $\mathbf{I}_{N_\xi}$ and $\mathbf{I}_{N_\eta}$ are identity matrices of size $N_\xi \times N_\xi$ and $N_\eta \times N_\eta$, respectively, and $\mathbf{D}_{\xi:}$ and $\mathbf{D}_{\eta:}$ are differentiation matrices of size $N_\eta N_\xi \times N_\eta N_\xi$, which can operate on the discrete vector $\mathbf{f}_{:}$ to produce a discrete stacked vector of partial derivatives.

Finally, the second-derivative differentiation matrices for the two-dimensional case can also be obtained by employing the Kronecker product with the identity matrix, i.e., $\mathbf{D}_{\xi\xi:} = \mathbf{D}_\xi^2 \otimes \mathbf{I}_{N_\eta}$ and $\mathbf{D}_{\eta\eta:} = \mathbf{I}_{N_\xi} \otimes \mathbf{D}_\eta^2$. Nonetheless, in the multidimensional case, cross derivatives also need to be discretized. For the purpose of this work, only the cross-derivative differentiation matrix $\mathbf{D}_{\xi\eta:}$ needs to be considered, which can be obtained as

$$\mathbf{D}_{\xi\eta:} = \mathbf{D}_\xi \otimes \mathbf{D}_\eta. \tag{4.13}$$

For further details regarding the computational formation of the discrete matrices that define the LST or the 2D-LST eigenvalue problems, the reader is referred to [17, 18].

4.2.1.2 High-order finite difference method by Hermanns & Hernández [19]

A high-order finite difference method recently developed by Hermanns & Hernández [19] has become widely used in hydrodynamic stability studies [20–22] due to its

excellent trade-off between accuracy and computational cost, specially for problems which feature more than one inhomogeneous direction. The main idea behind this discretization method is to construct a finite difference scheme on a non-uniform grid, where the coordinates of the points are defined following the same philosophy as the Chebyshev-Gauss-Lobatto collocation points, thus allowing to minimize interpolation errors by distributing the grid points in a specific way. However, in contrast to the Chebyshev collocation technique, this method is based on a piecewise polynomial interpolation.

For a given distribution of grid points ξ_j defined in the transformed domain $\xi \in [-1, 1]$, a piecewise polynomial interpolant is constructed so that it matches the discrete values of a function (f_j) at each grid point. Each of the individual interpolating polynomials ($I_j(\xi)$) is only valid inside the subdomain comprised between $\xi_{j-1/2}$ and $\xi_{j+1/2}$. The union of all the subdomains is then equal to the whole domain of the problem $[-1, 1]$. Similarly to the Chebyshev collocation method, the interpolating polynomials are obtained by means of a Lagrange interpolation formula, which allows to express the piecewise discretization as

$$I_j(\xi) = \sum_{k=s_j}^{s_j+q_p} f_k \psi_{jk}(\xi), \quad \psi_{jk}(\xi) = \prod_{\substack{m=0 \\ s_j+m\neq k}}^{q_p} \frac{\xi - \xi_{s_j+m}}{\xi_k - \xi_{s_j+m}}, \tag{4.14}$$

where q_p is the polynomial degree, which must satisfy $q_p \leq N_\xi - 1$, with N_ξ being the number of grid points, and s_j denotes the index of the leftmost grid point involved in the construction of the interpolant $I_j(\xi)$. For the case of an even polynomial degree (which is always the choice throughout this work), a centered finite difference scheme is obtained, for which s_j is given by

$$s_j = \begin{cases} 0 & \text{if } j = 1, ..., q_p/2 \\ j - q_p/2 - 1 & \text{if } j = q_p/2 + 1, ..., N_\xi - q_p/2 \\ N_\xi - q_p - 1 & \text{if } j = N_\xi - q_p/2 + 1, ..., N_\xi \end{cases}, \tag{4.15}$$

From equation (4.14), it can be noted that the higher the polynomial degree, the larger the number of points involved in the construction of each individual interpolant. This is a very important feature of this discretization method, as it allows to control the order of the discretization according to the needs of a particular problem. Following this line of reasoning, the term FD-q was introduced by Paredes *et al.* [21] to refer to this discretization technique. The resulting stencils of the individual polynomials lead to centered finite difference formulas for interior points that are sufficiently far away from the domain boundaries. Close to the boundaries, however, the stencils become biased to keep using the necessary number of existing grid points ($q_p + 1$ grid points). A visualization of the resulting stencils can be found in figure 1 from reference [19].

Having defined the piecewise interpolation, the particular choice of the grid points for this technique remains to be discussed. As mentioned previously, the distribution of collocation points in the grid plays an important role in the error of the interpolation. For a given number of grid points and polynomial degree, Hermanns & Hernández compute the optimal distribution of grid points that makes the interpolation error uniform across the domain (the details of the algorithm can be found in [19]). Therefore, for each pair of N_ξ and q_p, a different distribution of grid points is obtained such that the error of the interpolation remains uniform. As in the case of CGL points, the resulting grids tend to be clustered towards the domain boundaries to control the interpolation error. This feature constitutes the key advantage of the FD-q technique over other finite-difference methods, such as standard centered finite differences, compact finite-difference schemes, dispersion-relation-preserving finite differences or summation-by-parts operators. The particular distribution of collocation points for a given order q_p enables FD-q to yield a smaller error than the aforementioned finite-difference methods for the same discretization order (see [21]).

The discretization of derivatives by means of the FD-q method can be performed in the same way as for the Chebyshev collation technique, namely, by means of differentiation matrices as described in 4.2.1.1. For the two-dimensional case, the same expansion of the differentiation matrices by means of the Kronecker product also applies in this technique. In practice, this is very convenient as it allows to use the same implementation for both discretization techniques, with the only differences being the coordinates of the collocation points and the elements of the differentiation matrices. Furthermore, in the limit of $q_p = N_\xi - 1$, the FD-q discretization becomes equivalent to the Chebyshev collocation method, that is, the CGL collocation points are retrieved. This means that the spectral discretization of the Chebyshev collocation method can also be performed with the FD-q routines.

From the computational point of view, besides its unified implementation with the Chebyshev collocation technique, a very important advantage of using the FD-q discretization method lies in the degree of sparsity introduced in the discretized system matrices when $q_p \ll N_\xi - 1$. This has a large impact on the computational cost of the solution of the eigenvalue problem, as a decrease in the computational cost of multiple orders of magnitude can be achieved while maintaining an excellent accuracy (see the analysis of Paredes *et al.* [21]). Such a reduction in the solution cost is of paramount importance for the solution of the 2D-LST eigenvalue problem, for which the computational cost associated with spectral discretizations is very high. In the context of local linear stability theory, [20, 21] show the excellent performance of the FD-q method in resolving the eigenspectrum for a self-similar boundary layer. For a value of q_p on the order of 8, the entire discrete spectrum is retrieved by the FD-q discretization as reliably as by the Chebyshev

collocation method. Particularly interesting is their observation that for a given value of N_ξ, there is an optimal value of $q_p < N_\xi - 1$ for which the error in the discretization of the continuous part of the spectrum is minimum.

Owing to the advantages outlined above, the FD-q technique is nowadays employed in many 2D-LST and 3D-PSE stability analyses, typically using polynomial degrees that range between $q_p = 6$ and $q_p = 12$ (see for example [13, 23–27]). As shown in chapters 5 and 6, this method is also the choice for most of the 2D-LST computations presented in this work.

4.2.2 Mapping techniques

In the majority of physical problems of interest, the transformed space in which the discretization techniques described in § 4.2.1 define the collocation grid points does not coincide with the physical domain of study. As a result, coordinate transformations are necessary to map the computational domain to the physical one. These transformations generally receive the name of mapping techniques. In the following, the two mapping methods employed in this work are presented.

4.2.2.1 Mapping proposed by Malik [28]

A widely used mapping technique is the transformation introduced by Malik [28], which allows to place half of the grid points below a desired coordinate. Considering the wall-normal direction, for instance, the wall-normal coordinate in the transformed space (η) is mapped to the physical space (y) as

$$y = \frac{y_i y_{max}(1+\eta)}{y_{max} - \eta(y_{max} - 2y_i)}, \tag{4.16}$$

where y_{max} is the maximum wall-normal coordinate (location of the wall-normal far-field boundary) and y_i denotes the coordinate at which the number of grid points is split into two halves. This mapping technique is very convenient for the study of boundary layers, as it allows to concentrate a higher number of points near the wall, hence contributing to increase the accuracy of the discretization in the region of interest. In the stability analyses performed in this dissertation, equation (4.16) is always employed along the wall-normal direction. Additionally, when spanwise symmetry is considered in the stability analysis, as described in § 3.9.4, this transformation is also employed along the spanwise direction to increase the grid resolution near the roughness spanwise symmetry plane (see § 5.1). Figure 4.1(a) illustrates an example of a collocation grid mapped using equation (4.16) in both y and z directions.

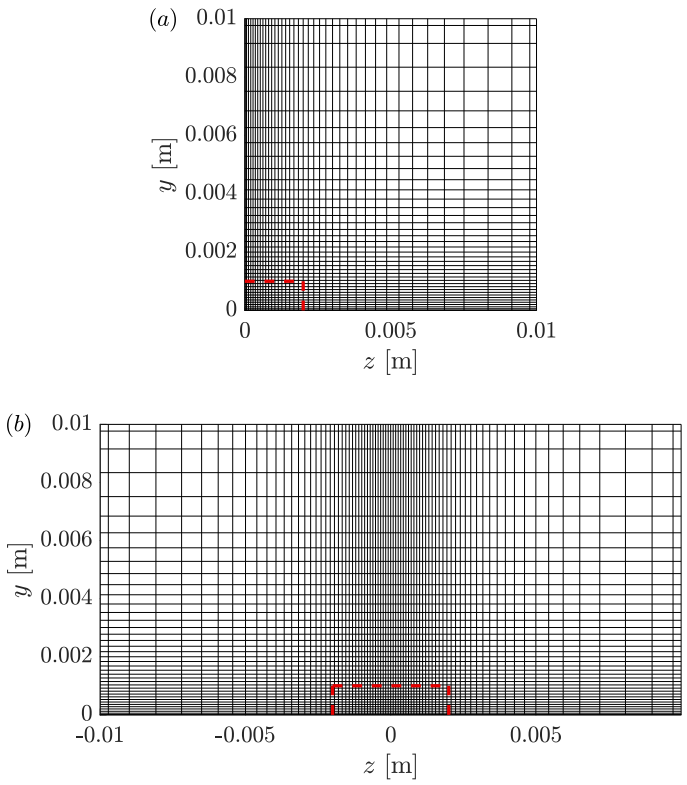

Figure 4.1: Examples of two different collocation grids mapped to the physical domain (FD-q8): (a) $N_\eta = 41$, $N_\xi = 41$, mapping (4.16) applied in both directions, with $y_i = z_i = 0.002$ m; (b) $N_\eta = 41$, $N_\xi = 81$, mapping (4.16) applied in the wall-normal direction ($y_i = 0.002$ m) and mapping (4.17) applied along the spanwise direction ($z_{i1} = -0.002$ m and $z_{i2} = 0.002$ m). The red dashed lines denote a projection of a generic roughness element shape, behind which the roughness wake would be located.

4.2.2.2 Biquadratic mapping

A generalization of the mapping technique proposed by Malik (see § 4.2.2.1) consists in dividing the domain in three different regions and placing one-third of the grid points in each of them, thus allowing to increase the grid resolution not only towards the domain boundaries if desired, but also in a given confined region of interest inside the domain. This transformation, developed together by Esposito [29] and Groot [17, 30], receives the name of biquadratic mapping. For the spanwise

direction, for example, the biquadratic transformation is given by

$$z = \frac{a\xi^2 + b\xi + c}{d\xi^2 + f}, \tag{4.17a}$$

$$a = 2z_{max}(z_{i2} - 3z_{i1}) - 2z_{min}(3z_{i2} - z_{i1}), \tag{4.17b}$$

$$b = -3(z_{i1} - z_{i2})(z_{max} - z_{min}), \tag{4.17c}$$

$$c = z_{i1}(3z_{max} - z_{min}) + z_{i2}(z_{max} - 3z_{min}), \tag{4.17d}$$

$$d = 8(z_{i2} - z_{i1}) - 4(z_{max} - z_{min}), \tag{4.17e}$$

$$f = 2(z_{i1} - z_{i2}) + 4(z_{max} - z_{min}), \tag{4.17f}$$

where $\xi \in [-1, 1]$ denotes the spanwise coordinate in the collocation grid, z_{min} and z_{max} are respectively the minimum and maximum spanwise coordinates of the physical domain (location of the spanwise far-field boundaries), and $z_{i,1}$, $z_{i,2}$ are the spanwise locations which divide the domain in three different regions. This transformation concentrates one-third of the grid points in each of the three regions comprised between $z_{min} < z_{i1} < z_{i2} < z_{max}$. It is is important to mention that to ensure a regular monotonic behavior in the grid spacing, the following requirements must be satisfied [29]:

$$z_{i2} > z_{i1}, \tag{4.18a}$$

$$z_{i2} \leq 9z_{i1} + 8z_{min}, \tag{4.18b}$$

$$z_{i2} \leq \frac{z_{i1}}{9} + \frac{8}{9}z_{max}. \tag{4.18c}$$

In this work, the biquadratic mapping is employed along the spanwise direction in cases where spanwise symmetry conditions are not applied but the complete spanwise domain is considered instead, using periodic boundary conditions on the perturbation variables (see § 3.9.3). This allows to compute symmetric and antisymmetric perturbations from the solution of the same eigenvalue problem. Figure 4.1(b) shows an example of a collocation grid mapped using the biquadratic mapping along the spanwise direction and the mapping given by equation (4.16) along the wall-normal direction. Note that the grid resolution increases towards the central region of the domain along the span, where the roughness element wake is contained.

4.2.2.3 Transformation of the differentiation matrices to the physical domain

The mapping of the discretization from the transformed space to the physical space also requires a transformation of the associated differentiation matrices through the

corresponding metrics. According to the chain rule, the first and second derivatives of a function in physical space can be expressed in terms of the respective derivatives in the transformed space as

$$\frac{\partial f}{\partial y} = \frac{\partial f}{\partial \eta}\frac{d\eta}{dy}, \quad \frac{\partial^2 f}{\partial y^2} = \frac{\partial^2 f}{\partial \eta^2}\left(\frac{d\eta}{dy}\right)^2 + \frac{\partial f}{\partial \eta}\frac{d^2\eta}{dy^2}, \tag{4.19}$$

where the wall-normal direction has been chosen as an example. Since the mapping relations are generally expressed as $y = y(\eta)$, the derivatives of the reciprocal function $\eta = \eta(y)$ can be obtained as

$$\frac{d\eta}{dy} = \frac{1}{dy/d\eta}, \quad \frac{d^2\eta}{dy^2} = -\frac{d^2y}{d\eta^2}\left(\frac{d\eta}{dy}\right)^3. \tag{4.20}$$

Making use of these relations, the differentiation matrices can be transformed to the physical domain by means of diagonal matrices that contain the metrics of the transformation at each collocation point [31], that is

$$\mathbf{D}_y = \mathbf{D}_\eta \,\mathrm{diag}\left(\frac{1}{dy(\eta_j)/d\eta}\right), \quad j = 1, ..., N_\eta, \tag{4.21}$$

$$\mathbf{D}_{yy} = \mathbf{D}_{\eta\eta}\,\mathrm{diag}\left(\frac{1}{[dy(\eta_j)/d\eta]^2}\right) - \mathbf{D}_\eta\,\mathrm{diag}\left(\frac{d^2y(\eta_j)/d\eta^2}{[dy(\eta_j)/d\eta]^3}\right), \; j = 1, ..., N_\eta. \tag{4.22}$$

An equivalent process can be applied along the spanwise direction. Finally, it is worth mentioning that the transformed matrices can also be directly extended for two-dimensional cases by means of the Kronecker products introduced in § 4.2.1.1.

4.2.2.4 Interpolation of base-flow quantities on the mapped collocation grid

Even though the mapping techniques transform the collocation grid to the physical domain, the mapped grid defined by the Chebyshev collocation or the FD-q discretization methods does not generally coincide with the mesh employed to obtain the base-flow solutions (see § 4.1.3.2). As a consequence, before evaluating the coefficients of the governing stability equations according to the chosen high-order discretization, the necessary base-flow quantities must be interpolated on the collocation grid. In the computations presented in this dissertation, a cubic spline interpolation which uses not-a-knot end conditions is employed for this purpose, see for example [32]. The interpolation is carried out using the built-in MATLAB functions `interp1` (for base-flow quantities depending on a single spatial dimension, such in LST) and `interp2` (for base-flow quantities depending on two spatial dimensions, such as in 2D-LST).

4.2.3 Integration techniques

In order to compute certain quantities of interest, the spatial integration of functions defined in the collocation grid is required. Examples include the evaluation of the disturbance energy or the computation of the different contributions that constitute the decomposition of the temporal growth rate given by equation (3.64). The most straightforward approach to evaluate such integrals is to employ a simple trapezoidal integration rule. However, this method leads to poor accuracy since the collocation grids are generally characterized by a small number of points. In order to integrate a function while keeping the high-order accuracy of the Chebyshev collocation or the FD-q discretizations, different high-order integration techniques exist (see for example Trefethen [16]). The two methodologies considered in this study are described next.

4.2.3.1 Integration by means of Chebyshev integral weight functions

When evaluating the integral of a function discretized with the Chebyshev collocation method, the function can be integrated with spectral accuracy by means of the Chebyshev integral weight function derived by Hanifi *et al.* [33]. For example, to compute the integral of a generic function f along the wall-normal direction, the following relation can be employed in the transformed space (η):

$$\int_{-1}^{1} f(\eta)\, d\eta = \sum_{j=0}^{N_\eta - 1} f(\eta_j) \mathcal{W}(\eta_j), \tag{4.23}$$

where η_j denotes the coordinates of the Chebyshev-Gauss-Lobatto collocation points, given by equation (4.2), and $\mathcal{W}$ is the Chebyshev weight function in the transformed space, given by

$$\mathcal{W}(\eta_j) = \frac{b_j}{N_\eta - 1} \left\{ 2 + \sum_{n=2}^{N_\eta - 1} c_n \frac{[1 + (-1)^n]}{(1 - n^2)} \cos\left(\frac{nj\pi}{N_\eta - 1} \right) \right\}, \tag{4.24}$$

where $b_0 = b_{N_\eta - 1} = 1/2$, $b_j = 1$ for $0 < j < N_\eta - 1$, $c_0 = c_{N_\eta - 1} = 1$ and $c_n = 2$ for $0 < n < N_\eta - 1$. If a mapping is used to transform the collocation grid to the physical domain, the integral can be evaluated in the mapped domain as

$$\int_{y^-}^{y^+} f(y)\, dy = \sum_{j=0}^{N_\eta - 1} f(y_j) W(y_j), \tag{4.25}$$

where W is the Chebyshev weight function in the physical domain, which can be computed as

$$W(y_j) = \frac{b_j}{N_\eta - 1} \sum_{n=0}^{N_\eta - 1} c_n \cos\left(\frac{nj\pi}{N_\eta - 1}\right) \int_{-1}^{1} T_n(\eta) \frac{dy}{d\eta}\, d\eta, \tag{4.26}$$

where $dy/\,d\eta$ is the metric of the chosen mapping transformation (see § 4.2.2.3) and T_n denotes the nth Chebyshev polynomial, given by

$$T_n(\eta) = \cos\left(n \arccos\left(\eta\right)\right). \tag{4.27}$$

If the metric $dy/\,d\eta$ is known analytically, as it is usually the case for the majority of mapping techniques, the integral in equation (4.26) can be evaluated with high accuracy using equation (4.23) in a fine collocation grid of choice.

By direct extension, surface and volume integrals can be computed with spectral accuracy by employing the respective weight functions along each direction. For example, integration over the spanwise plane (yz) can be expressed as follows:

$$\int_{z^-}^{z^+} \int_{y^-}^{y^+} f(y,z)\, dy\, dz = \sum_{k=0}^{N_\xi - 1} \left(\sum_{j=0}^{N_\eta - 1} f(y_j, z_k) W(y_j) \right) W(z_k). \tag{4.28}$$

Here, this integration method has been employed for all the computations performed using the Chebyshev collocation method.

4.2.3.2 Integration using the inverse of part of the differentiation matrices

As described by Trefethen [16], a simple method for computing the integral of a function discretized in a grid of collocation points ($\eta \in [-1, 1]$), such as

$$I = \int_{-1}^{1} f(\eta)\, d\eta, \tag{4.29}$$

arises naturally from the solution of the following ODE-based initial value problem:

$$\frac{dF(\eta)}{d\eta} = f(\eta), \quad F(-1) = 0, \quad \eta > -1, \tag{4.30}$$

where $I = F(1)$. The problem (4.30) can then be discretized and solved by means of the desired collocation method employing the corresponding differentiation matrix ($\mathbf{D}_\eta$). In order to impose the homogeneous Dirichlet condition at $\eta = \eta_{N_\eta} = -1$, the last row and column of the differentiation matrix are removed, producing a reduced square matrix $\tilde{\mathbf{D}}_\eta$. Therefore, the initial value problem can be expressed in matrix form as

$$\tilde{\mathbf{D}}_\eta \mathbf{F} = \mathbf{f}, \tag{4.31}$$

with $\mathbf{F} = [F(\eta_1), ..., F(\eta_{N_\eta - 1})]^{\mathrm{T}}$ and $\mathbf{f} = [f(\eta_1), ..., f(\eta_{N_\eta - 1})]^{\mathrm{T}}$. Note that to compute $I = F(1) = F(\eta_1)$, only the first row of the matrix $\tilde{\mathbf{D}}_\eta^{-1}$ is necessary, denoted by $\mathbf{w}^{\mathrm{T}}$. Hence, the integration can be expressed as

$$I = \int_{-1}^{1} f(\eta)\, d\eta = \mathbf{w}^{\mathrm{T}} \mathbf{f}. \tag{4.32}$$

To compute the integral in the physical domain, the same procedure is directly applicable, simply exchanging the differentiation matrix by the corresponding one in the mapped domain, as described in § 4.2.2.3. This integration method also maintains the order of accuracy of the discretization scheme and it is easy to implement from the computational point of view. Its extension to multi-dimensional integration is straightforward by making use of the differentiation matrices along each spatial direction. In this work, this is the integration method employed for all the computations performed using the FD-q discretization technique.

4.2.4 Calculation of base-flow derivatives

The solution of the governing stability equations requires a significant number of first and second base-flow derivatives to be known. This presents an additional challenge specially when employing Navier-Stokes base-flow solutions obtained by means of low-order discretization schemes, such as the second-order finite volume methods commonly used in CFD. In general, providing the spatial derivatives of the flow variables in the solution is usually not a priority in CFD, in particular second derivatives. As a result, most commercial CFD softwares do not integrate the functionality to provide all the derivatives required for stability analysis. In the case of CFD++®, the first spatial derivatives of the primitive variables $\bar{\rho}$, $\bar{u}$, $\bar{v}$, $\bar{w}$, $\bar{T}$ and $\bar{p}$ are provided as part of the solution.

In this work, two different methodologies are considered for the computation of the necessary spatial base-flow derivatives. The first method is based on conventional finite difference stencils which are derived for arbitrarily spaced grids in one dimension. The derivation of the stencil coefficients (weights) to evaluate the derivative of a function at a given grid point is based on a Taylor series expansion of the function at each of the points involved in the stencil. For a given stencil of N_s points, denoted by $\mathbf{s} = [s_1, ..., s_j, ..., s_{N_s}]^{\mathrm{T}}$, the coefficients of the finite difference equations for all derivatives with order $d < N_s$ can be computed by solving the following linear system:

$$\begin{bmatrix} s_1^0 & \cdots & s_{N_s}^0 \\ \vdots & \ddots & \vdots \\ s_1^{N_s-1} & \cdots & s_{N_s}^{N_s-1} \end{bmatrix} \begin{bmatrix} c_{1,0} & \cdots & c_{1,N_s-1} \\ \vdots & \ddots & \vdots \\ c_{N_s,0} & \cdots & c_{N_s,N_s-1} \end{bmatrix} = \begin{bmatrix} \frac{0!}{\Delta y^0} & \cdots & 0 \\ \vdots & \ddots & \vdots \\ 0 & \cdots & \frac{(N_s-1)!}{\Delta y^{N_s-1}} \end{bmatrix}, \tag{4.33}$$

where $c_{j,k}$ is the coefficient of the jth stencil point for the finite difference formula of the kth derivative and Δy is a reference grid spacing that defines the values of the stencil, which are given by

$$s_j = \frac{y_j - y_0}{\Delta y}, \quad j = 1, ..., N_s, \tag{4.34}$$

where $\mathbf{y} = [y_1, ..., y_j, ..., y_{N_s}]^{\mathrm{T}}$ are the coordinates of the grid points in ascending order and y_0 is the grid point at which the derivative is to be computed. Here, the value of Δy is taken to be the minimum distance between two consecutive grid points.

The second approach considered to compute base-flow derivatives is to employ the differentiation matrices of the discretization method employed for the solution of the eigenvalue problem (see § 4.2.1). This requires a previous interpolation of the base-flow quantities to be differentiated on the collocation grid, as described in § 4.2.2.4. Due to the fact that the differentiation matrices are already required for the discretization of the derivatives of the perturbation quantities and that the interpolation on the collocation grid also needs to be performed for non-derivative base-flow quantities, this strategy has the advantage of being more efficient and straightforward to implement than the calculation of derivatives in the base-flow grid.

When considering a calorically perfect gas, the first spatial derivatives of the primitive base-flow quantities provided by CFD++® are employed for the stability analysis. The second and cross spatial derivatives of the primitive quantities are then evaluated on the base-flow grid by differentiating the first derivative fields given by CFD++®. This is done by means of fourth-order finite differences with stencil coefficients given according to equation (4.33). To compute the first derivative of a quantity f at a given point y_0 with fourth-order accuracy, a stencil of five points is considered and the resulting finite difference formula can be expressed as

$$\frac{\partial f}{\partial y}(y_0) = c_{1,1} f(y_1) + c_{2,1} f(y_2) + c_{3,1} f(y_3) + c_{4,1} f(y_4) + c_{5,1} f(y_5). \tag{4.35}$$

At interior grid points, centered stencils are always considered, while near the boundaries of the domain, uncentered stencils are employed to adjust the coefficients while maintaining the order of accuracy of the differentiation. The base-flow

derivative fields computed following this approach are then interpolated on the collocation grid used for the discretization of the eigenvalue problem. In this study, this method was found to yield very similar results to the use of the FD-q differentiation matrices to compute the second derivatives directly on the collocation grid.

An example that illustrates both methodologies is shown in figure 4.2, which compares the second derivative obtained from the first derivative provided by CFD++® by using the finite difference stencil of equation (4.35) against those using the differentiation matrices of the Chebyshev collocation and FD-q discretization methods. To show from which profile the second derivative comes from, the profile considered for this example and its first derivative are also shown in figure 4.2(a, b). As it can be observed in figure 4.2(d), the use of the 4th-order finite difference stencil (labeled FD4) and the FD-q method with $q_p = 8$ (labeled FDq8) yield almost indistinguishable results. However, when the Chebyshev differentiation matrices are employed (labeled CGL, see figure 4.2(c)), significant spurious oscillations are retrieved in the second derivative, which are found to increase near the domain boundaries. These oscillations are also observed using the FD-q method when the value of q_p becomes large, and are seen to increase as q_p approaches the CGL limit ($q_p = N_\eta - 1$). These oscillations are argued to be the result of the order of discretization of the function to be differentiated (in this case a function computed by a second-order finite volume method) being much lower than that of the discretization method chosen for the stability analysis. Therefore, the second approach to evaluate CFD base-flow derivatives should only be used when the stability problem is discretized using $q_p \ll N_\eta$, such as shown in figure 4.2(d).

The use of the finite difference stencils defined by equation (4.33) is found to provide a slightly more consistent discretization with the first derivatives provided by CFD++®. By computing the first derivatives using the fourth-order finite difference stencil, the resulting values are closer to the actual first derivative provided by CFD++® than when computing it by FD-q. For this reason, although both methods are equally valid for the purpose of this analysis, the first approach is chosen in CPG as it leads to a more consistent discretization between first and second derivatives.

In the case of CPG base flows, the spatial derivatives of the dependent variables are always expressed in terms of the spatial derivatives of the independent variables on which they depend upon by means of the chain rule (see equation (A.4)). In this case, the dependent variables are the transport properties $\bar{\mu}$, $\bar{\lambda}$ and $\bar{k}$ as well as their first derivative with respect to temperature ($d\bar{\mu}/d\bar{T}$, $d\bar{\lambda}/d\bar{T}$ and $d\bar{k}/d\bar{T}$), which appear due to the Taylor expansion[1] of the perturbation quantities

[1] It is important to emphasize that $d\bar{\mu}/d\bar{T}$, $d\bar{\lambda}/d\bar{T}$ and $d\bar{k}/d\bar{T}$ appear in the linearized perturbation equations even if the chain rule is not applied on the transport properties. They appear due to the lin-

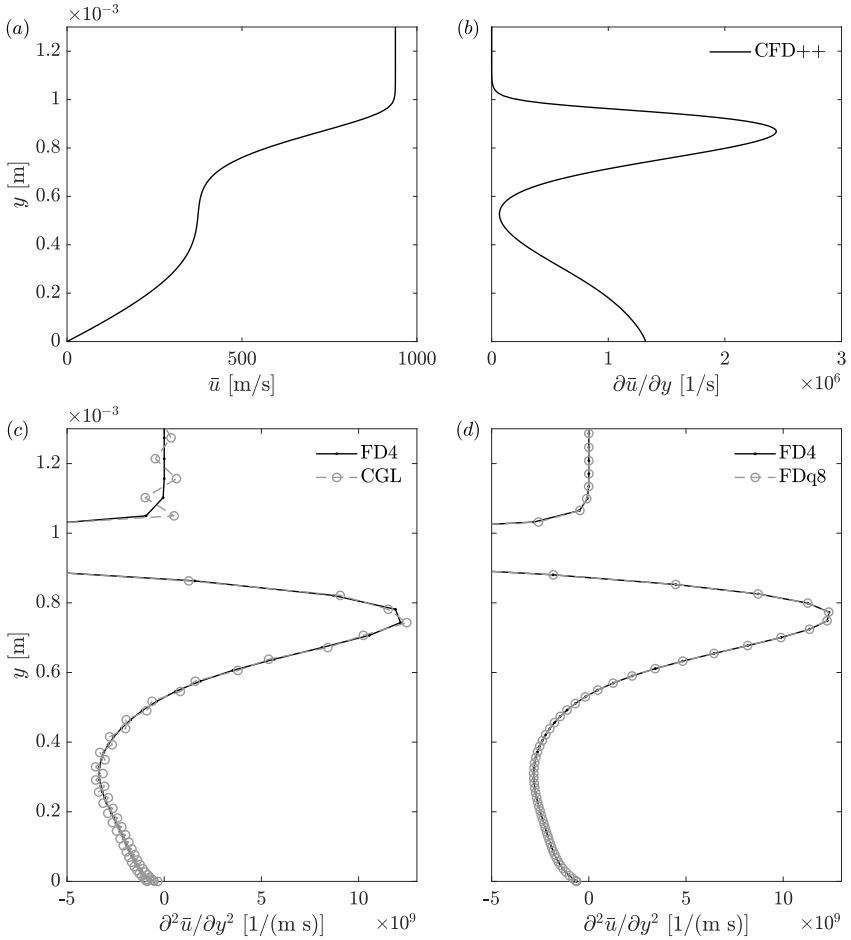

Figure 4.2: Comparison of different methods to compute the second derivative of a given streamwise velocity base-flow profile: (a) streamwise velocity profile obtained from CFD++; (b) first derivative of the profile obtained from CFD++; (c) second derivative of the profile obtained using a fourth-order finite difference stencil (equation (4.35)) on the first derivative provided by CFD++ and then interpolated on a CGL grid with $N_\eta = 121$ (labeled FD4), compared to the second derivative computed by using the Chebyshev differentiation matrices on the interpolated first derivative provided by CFD++ (labeled CGL); (d) same as (c) but using a collocation grid based on FD-q ($N_\eta = 121$ and $q_p = 8$). This streamwise velocity profile originates from the central wake region behind an isolated roughness element. It is used here as an example. It has been extracted from the base-flow solution presented in § 5.3 for the ramp-shaped roughness element, and corresponds to $x \approx 0.08$ m and $z \approx 10^{-4}$ m.

as described in § 3.2. In CPG all these quantities are themselves a function of temperature only, and therefore their spatial derivatives can be expressed in terms of the spatial derivative of temperature, as in the examples given in equation (A.4). Furthermore, note that since for CPG the variation of the transport properties with temperature is defined by Sutherland's law (see § 2.5.2.1), the necessary first and second derivatives of the transport properties with respect to temperature can be computed analytically.

When considering the CNE flow assumption, however, the number of dependent variables becomes significantly high. In this case, expanding their derivatives in terms of the spatial derivatives of the independent quantities through the chain rule leads to a very large number of derivatives to be evaluated (see Miró Miró [4, § 8.1.2]). For this reason, the spatial derivatives of the dependent quantities are directly computed in this case, i.e., quantities like $\partial\bar{\mu}/\partial y$ or $\partial\left(\partial\bar{\mu}/\partial\bar{T}\right)/\partial y$ are directly calculated numerically without expressing them in terms of the derivatives of the independent quantities. Despite this consideration, the number of necessary derivatives to evaluate remains important due to the significant number of dependent quantities to be treated (about 80 dependent quantities for the formulation considered here). In these cases, the second approach is employed to compute the necessary spatial derivatives based on FD-q differentiation matrices. Furthermore, for this flow assumption, all the necessary first derivatives are not provided by CFD++®, as it is otherwise done in CPG. Therefore, for consistency, both first and second derivatives are computed in the collocation grid by employing the first and second derivative differentiation matrices, respectively. This proves to be significantly more efficient than calculating the derivatives on the base-flow grid by the finite difference stencils, given the large number of derivatives that need to be evaluated. For the TPG assumption, the same methodology as for the CNE assumption has been employed in this work. However, in this case the number of dependent quantities remains similar to the CPG assumption so the two approaches presented in this section could be applied without major difficulties in practice.

Finally, it is worth mentioning that in the case of base-flows coming from the solution of the boundary-layer equations, the DEKAF solver provides all the derivatives required for the stability analysis evaluated in the same collocation grid in which the boundary-layer solution is computed (see [5]).

4.2.5 Numerical implementation of boundary conditions for the perturbation quantities

Before carrying out the solution of the stability problem, the algebraic equations resulting from the discretization of the partial-differential eigenvalue problem must

earized Taylor expansions for $\tilde{\mu}$, $\tilde{\lambda}$ and $\tilde{k}$. For this reason, they are also treated explicitly as dependent quantities.

be completed with the necessary boundary conditions. The different boundary conditions considered for the perturbation quantities are described in § 3.9.

In this work, the implementation of boundary conditions in the system matrices is carried out through the following steps. First, all the entries of the matrices that form the discretized eigenvalue problem are computed in the entire domain. Next, the discretized boundary conditions corresponding to each of the grid points that belong to the domain boundaries are added to the system as additional rows which are appended at the end of the original system matrices. Finally, before transferring the matrices to the eigenvalue solver, all the rows and columns corresponding to original boundary positions are removed from the system. This leads to a structure of the matrices where all the boundary conditions are found together in the last rows. By keeping track of the original position of each boundary point in the matrices, the complete eigenvector solutions are reconstructed once the eigenvalue solver has finished.

In the following, the discrete formulation of the different types of boundary conditions employed in the 2D-LST eigenvalue problem is introduced, considering a tensor-product grid defined in the yz plane.

4.2.5.1 Homogeneous Dirichlet conditions

The Dirichlet conditions directly impose the value of the solution vector (eigenvector) at the designated boundaries. In this case, no specific numerical treatment is required. The rows and columns of the system matrices that correspond to those grid points where homogeneous Dirichlet boundary conditions are applied are removed from the system prior to solving the eigenvalue problem.

4.2.5.2 Homogeneous Neumann conditions

The homogeneous Neumann conditions enforce the first derivative of the eigenvector to be equal to zero in the direction normal to the boundary. In the discrete system, this is expressed employing the first derivative differentiation matrix. For example, in the case of a spanwise boundary aligned with the wall-normal direction, such as $\xi = -1$ ($z = z^-$), the homogeneous Neumann condition on $\hat{u}$ can be expressed as

$$\sum_{j=1}^{N_\xi} D_{z,jN_\xi} \hat{u}_{kj} = 0, \quad k = 1, ..., N_\eta, \tag{4.36}$$

where D_{z,jN_ξ} denotes the element in the jth row and the N_ξth column of the mapped differentiation matrix $\mathbf{D}_z$ (see § 4.2.2.3). An equivalent expression can be found for a homogeneous Neumann condition imposed on a wall-normal boundary aligned with the spanwise direction, in this case employing the entries of the differentiation matrix $\mathbf{D}_y$.

Note that for the computation of the derivative at a given boundary point, such as the point at y_k and z_{N_ξ}, multiple grid points are involved. This can be interpreted as a stencil resulting from the discretization of the derivative. For the Chebyshev collocation method, the stencil involves all the grid points, whereas for the FD-q method the number of points included depends on the value of q_p, which controls the number of non-zero entries in the differentiation matrices.

Given a spanwise boundary at which Neumann conditions are imposed, for example, N_η rows are appended at the end of the system matrices. Each of these rows contains the coefficients that multiply the solution vector to evaluate the Neumann condition at the kth boundary point, as given by equation (4.36), for all the perturbation quantities for which a Neumann condition is applied. A representation of the position of these coefficients in the structure of a system matrix block of size $N_\xi N_\eta \times N_\xi N_\eta$, corresponding to a single perturbation variable, can be found in [18, § 5.7.2].

4.2.5.3 Periodic conditions

In the case of periodic conditions at spanwise boundaries ($\xi = \pm 1$, or $z = z^-, z^+$), the solution values at the grid points corresponding to opposite boundaries as well as their derivative normal to the boundary are required to be equal. Taking once again the streamwise velocity perturbation for purposes of illustration, the first condition can be expressed as follows:

$$\hat{u}_{kN_\xi} - \hat{u}_{k1} = 0, \quad k = 1, ..., N_\eta, \tag{4.37}$$

while the second one, recalling the notation introduced in equation (4.36), is given by

$$\sum_{j=1}^{N_\xi} D_{z,jN_\xi} \hat{u}_{kj} - \sum_{j=1}^{N_\xi} D_{z,j1} \hat{u}_{kj} = 0, \quad k = 1, ..., N_\eta. \tag{4.38}$$

Note that this boundary condition requires two different equations to be satisfied for a given pair of grid points. Here, it is chosen to impose condition (4.37) on the grid points belonging to the boundary at $\xi = 1$ while condition (4.38) is applied on the grid points at $\xi = -1$. This choice does not influence the solution. Therefore, spanwise periodic conditions are applied by appending $2N_\eta$ additional rows at the end of the system matrices. An illustration of these conditions imposed on a matrix block of size $N_\xi N_\eta \times N_\xi N_\eta$ is provided in [18, § 5.7.4].

4.2.5.4 Compatibility conditions

The discretization of the equations employed for the compatibility conditions (see for instance equation (3.44)) follows the same treatment as the discretization of

the governing stability equations at interior collocation points. In particular, each of the compatibility conditions are built separately as non-square matrices which have a size equal to $N_\xi N_\eta \times N_\xi N_\eta N_{ind}$, where N_{ind} denotes the number of independent perturbation variables. Then, these matrices are appended at the end of the main system matrices.

It is important to mention that when the rows and columns corresponding to Dirichlet boundary conditions are removed from the system, the corresponding terms from the compatibility equations that involve perturbation variables which have a Dirichlet condition imposed are automatically set to zero. This ensures a consistent application of the two conditions for a given boundary.

4.2.5.5 Treatment at domain corners

At the corner grid points of the two-dimensional collocation grid, an overlap of two different boundary conditions is encountered. As a consequence, a criterion should be established on which conditions to keep at those points. At the corner points located at $\eta = -1$ ($y = y^-$), which for the cases studied here correspond to the flat-plate wall, the wall conditions described in § 3.9.1 are chosen to prevail over any other boundary condition imposed at the spanwise boundaries. At the corner points located at $\eta = 1$ ($y = y^+$), which correspond to the wall-normal far-field boundary, the far-field conditions described in § 3.9.2 are given priority over any other condition imposed at the spanwise boundaries.

4.2.6 Algorithms for the solution of the generalized eigenvalue problem

When using one- or two-dimensional local linear stability theory, the spatial discretization of equations (3.15) or (3.16) together with the associated boundary conditions yields an algebraic generalized eigenvalue problem defined by matrices $\mathbf{A}$ and $\mathbf{B}$. For the governing equations considered (see chapter 2), the resulting matrices $\mathbf{A}$ and $\mathbf{B}$ are generally complex and non-Hermitian. The two algorithms employed in this work to compute eigenvalues and eigenvectors of the system are described next.

4.2.6.1 QZ algorithm

The most common method for solving generalized non-Hermitian eigenvalue problems is the QZ algorithm, originally developed by Moler & Stewart [34]. This direct method is the analogous of the QR algorithm for generalized eigenvalue problems. It allows to compute all the eigenvalues of the system as well as the right and left eigenvectors if desired. For a description of the algorithm, the reader is referred to Golub & Van Loan [35].

In this work, the QZ algorithm is performed by means of LAPACK [36] routines which are called from MATLAB through the built-in function `eig`. Although the algorithm allows to obtain the complete stability spectrum, its computational cost is significantly high. It requires approximately $30n^3$ floating point operations to compute the eigenvalues and an additional $16n^3$ operations to obtain the right eigenvectors [35, 37], where n denotes the number of rows or columns of the square matrices that define the problem. This implies a computational cost of $O(n^3)$ floating point operations. In the temporal stability case, n is equal to the number of grid points times the number of independent variables in the system, while in the spatial case its value is almost doubled according to the extension of the system necessary to linearize the eigenvalue problem (see § 3.4.3).

Due to its computational cost, the QZ algorithm is usually employed only for the solution of the LST eigenvalue problem. For computing eigenvalues of large-scale problems such as in the case of the 2D-LST system, other techniques are generally considered, such as the implicitly restarted Arnoldi method, discussed in the next section. In the 2D-LST eigenvalue problem, the number of rows/columns of the square matrices that define the generalized eigenvalue problem is given by $N_\xi N_\eta N_{ind}$, where N_{ind} denotes the number of independent variables in the system (number of flow quantities in $\hat{\mathbf{q}}$). As an example, for a typical collocation grid with $N_\xi = 181$ and $N_\eta = 141$ in CPG ($N_{ind} = 5$), the number of rows/columns of the matrices that from the temporal stability problem is about 127600, that is $O(10^5)$. For such large matrices, the computational cost of the QZ algorithm becomes too high to enable its extensive use in practice nowadays.

It is also important to mention that the QZ algorithm does not benefit from the sparsity introduced by non-spectral discretization methods such as FD-q, hence resulting in a similar computational cost for both the Chebyshev collocation method and the FD-q technique for the same number of grid points.

4.2.6.2 Implicitly restarted Arnoldi method

Given the expensive computational requirements of the QZ method, a big step forward in the calculation of eigenvalues for large-scale problems was achieved with the development of the so-called implicitly restarted Arnoldi method (IRAM) [38, 39]. The IRAM is an iterative algorithm that allows an efficient computation of a given set of eigenvalues and eigenvectors of a large system. It is based on the Arnoldi iteration (see for example Trefethen & Bau [40] and Lehoucq *et al.* [41]), also known as Arnoldi factorization, which is an orthogonal projection method for approximating a subset of the eigensystem of a general square matrix. This method exploits the information contained in the sequence of vectors produced by the classical power iteration method (employed to obtain a single eigenvalue-eigenvector pair [40]) in order to enable convergence to additional eigenvectors. This is achieved by constructing linear combinations of the vectors that arise dur-

ing the power sequence, which is formally equivalent to considering a Krylov subspace.

When the problem under study has a wide range of eigenvalues but the eigenvalues of interest are clustered in a given region, it is not possible to know in advance how many iterations would be required for the Arnoldi method to produce a satisfactory approximation to the desired eigenvalues. If a large number of iterations is required, difficulties arise which hinder the practical use of the standard Arnoldi factorization (see for instance [41]). On the one hand, the computational cost of the algorithm becomes significantly high, both in terms of floating point operations and memory requirements. On the other hand, numerical difficulties are encountered to maintain the orthogonality of the computed vectors, which can lead to spurious copies of the approximate eigenvalues produced by the method.

These difficulties motivated the development of restarting schemes for the Arnoldi iteration, leading, among others, to the implicitly restarting Arnoldi method. Restarting the algorithm provides a means to extract and exploit interesting information from large Krylov subspaces while avoiding the high storage requirements and numerical difficulties of doing so in the standard Arnoldi method. The philosophy of restarting the method is to employ the information that can be obtained from a partial application of the algorithm to define a new starting vector enhanced in the direction of the desired eigenvectors, which is then employed to start a new run of the Arnoldi iteration, thus accelerating the convergence of the method. A detailed description of the IRAM algorithm can be found in [35, 37, 41].

The Arnoldi iteration converges first to the eigenvalues of largest magnitude, which generally correspond to extreme eigenvalues, that is, eigenvalues located near the boundaries of the spectrum. In the majority of situations, these are not the eigenvalues of interest. In order to enhance the convergence of the method for computing eigenvalues in a given region of interest, a spectral transformation of the eigenvalue problem can be employed. Here, a shift-invert transformation is applied, given by

$$\left(\mathbf{A}_\omega - \sigma \mathbf{B}_\omega\right)^{-1} \mathbf{B}_\omega \hat{\mathbf{q}} = \nu \hat{\mathbf{q}}, \quad \text{with} \quad \nu = \frac{1}{\omega - \sigma}, \tag{4.39}$$

where σ denotes the shift-invert parameter and ν is the eigenvalue of the transformed system. Equation (4.39) is expressed in terms of the matrices that define the temporal stability problem, however, an identical transformation applies to the spatial problem. This transformation maps the eigenvalues close to the shift-invert parameter to the eigenvalues of largest magnitude in the transformed system, thus allowing the IRAM to converge first to the eigenvalues of interest. It is important to note that if σ is chosen to be very close to an actual eigenvalue of the system, the problem can become ill-conditioned. Therefore, care should be taken when selecting appropriate values of the shift-invert parameter.

In the case of LST and 2D-LST analyses on compressible boundary-layer base flows, a good choice for σ is usually a value in the real axis of the spectrum that is near the merged vertical continuous branch which contains entropy and vorticity disturbances. These waves travel at a phase speed equal to the freestream velocity and therefore the continuous branch is located at a non-dimensional value of $\omega_r = \alpha_r$ (see the treatment of Balakumar & Malik [42]). In this work, typical values of the shift-invert parameter employed are $\sigma = 0.9\alpha_r$ in the temporal case and $\sigma = 1.1\omega_r$ in the spatial case, where α_r and ω_r respectively refer to the fixed real value of the non-dimensional wavenumber and angular frequency.

Another important parameter that influences the convergence of the implicitly restarted Arnoldi algorithm is the number of linear combinations of the vectors resulting from the power sequence that are considered, that is, the size of the Krylov subspace. In general, the larger the dimension of the Krylov subspace the higher the memory requirements and computational cost but also the faster is the convergence of the IRAM. Therefore, in practice, an optimal subspace dimension can be found for a given problem which provides the best trade-off between the computational cost per iteration and the number of iterations necessary for the algorithm to converge to the desired eigenvalues. For the computations performed in this work, a subspace dimension that is equal to 4 times the number of desired eigenvalues is used.

For the majority of results presented in this dissertation, the implicitly restarted Arnoldi method has been performed employing ARPACK [41] routines which are interfaced through MATLAB's built-in function `eigs`. However, for the results presented in § 5.2, which are based on the Chebyshev collocation method, a parallel implementation of the ARPACK routines (see P_ARPACK [43])) was used via an in-house MATLAB-Fortran interface developed by Naddei [44]. This was necessary due to the high memory requirements of the solver in these cases, owing to the dense structure of the spectrally discretized matrices. These requirements could not be met with a high-end desktop workstation and therefore the solution of the problem was moved to a computer cluster.

As already pointed out by Groot [18], a particular observation in the behavior of the memory requirements of MATLAB's built-in function `eigs` deserves special mention. When executing the IRAM algorithm, one of the first steps performed by the `eigs` function is a lower-upper (LU) factorization of the matrix $\mathbf{A} - \sigma\mathbf{B}$. In MATLAB, this is carried out by a non-symmetric multifrontal method based on UMFPACK [45] routines, which are able to exploit any sparsity present in the system. However, when transferring the LU decomposition from UMFPACK routines to ARPACK routines, an important increase in memory usage is observed to take place, which is on the order of twice the memory required for the actual LU factorization. This behavior limits considerably the size of the problem that can be solved by means of the `eigs` function in a given machine. For this

reason, here the implicitly restarted Arnoldi iteration of the eigenvalue problem discretized by means of the Chebyshev collocation method is performed outside MATLAB with the P_ARPACK library, for which the LU factorization is carried out by means of the ScaLAPACK library [46] (see [44] for additional details). It is important to note, nevertheless, that the ScaLAPACK routines are designed to work with dense matrices only, and therefore they do not take advantage of any sparsity present in the system. This is not a detrimental factor in the solution of problems discretized with spectral methods, but for problems discretized using for instance the FD-q technique, where a high degree of sparsity is achieved, the use of MATLAB's `eigs` utility is much more efficient both in terms of memory and floating point operations.

4.2.7 Algorithms to compute the evolution of a single eigenvalue/eigenvector pair

In order to compute the evolution of a given eigenmode for relatively small changes in the matrices that form the generalized eigenvalue problem, such as for small shifts in the disturbance frequency or wavenumber, or small variations in the base-flow fields, iterative methods also exist that are dedicated to the calculation of a single eigenvalue-eigenvector pair, given an initial guess for both of them. Although the evolution of a single eigenmode can also be tracked by means of the implicitly restarted Arnoldi algorithm, these single eigenvalue solvers prove to be more robust in the majority of situations in which a good initial guess of the eigenvalue is known beforehand, avoiding the need to find an appropriate eigenvalue shift (σ) to achieve a satisfactory convergence of the IRAM. This is particularly important in cases where several eigenmodes are close in the spectrum, such as in the base-flow solutions analyzed in chapter 5. In these situations, it can become difficult to discern between different eigenmodes and therefore difficult to select a good shift-invert parameter for the next run of the IRAM. Hence, by performing a tracking of a particular mode by means of an individual eigenvalue solver, the difficulties that arise in the presence of multiple modes might be circumvented. To start the individual tracking, a good initial guess can then be provided by means of the implicitly restarted Arnoldi algorithm.

Two different iterative algorithms for computing the evolution of a single eigenmode are presented next. It is important to mention that these individual eigenvalue algorithms still require the solution of a linear system of equations at each iteration, whose dimension is of the same order as the size of the matrices defining the eigenvalue problem. As a result, these iterative methods are in general not faster than the IRAM when the latter is performed for a small number of eigenmodes. Their main advantage lies in their ability to keep track of the same eigenvalue-eigenvector pair without the need to define a search region.

4.2.7.1 Newton-Raphson iteration

An iterative method to compute an eigenvalue and its associated eigenvector when a sufficiently close initial guess is known can be built by means of a Newton-Raphson method, as implemented by Pinna [31]. The problem for which a root is sought in this case can be expressed as a system of two equations. For the temporal stability approach, for example, it can be written as

$$\mathbf{F}(\omega, \hat{\mathbf{q}}) = \begin{bmatrix} (\mathbf{A}_\omega - \omega \mathbf{B}_\omega)\, \hat{\mathbf{q}} \\ \hat{\mathbf{q}}^H \hat{\mathbf{q}} - 1 \end{bmatrix}, \tag{4.40}$$

where the relation $\hat{\mathbf{q}}^H \hat{\mathbf{q}} - 1 = 0$ is a normalization condition on the eigenvector. Therefore, the roots of the system are the eigenvalue ω and the eigenvector $\hat{\mathbf{q}}$. The Newton-Raphson iteration is then given by

$$\mathbf{s}_{j+1} = \mathbf{s}_j - \mathbf{J}_F^{-1}(\omega_j, \hat{\mathbf{q}}_j)\mathbf{F}(\omega_j, \hat{\mathbf{q}}_j), \tag{4.41}$$

where $\mathbf{s} = [\hat{\mathbf{q}}, \omega]^{\mathrm{T}}$ and $\mathbf{J}_F$ is the Jacobian of the system, which in this case can be determined analytically, resulting in the following expression:

$$\mathbf{J}_F(\omega, \hat{\mathbf{q}}) = \begin{bmatrix} \mathbf{A}_\omega - \omega \mathbf{B}_\omega & -\mathbf{B}_\omega \hat{\mathbf{q}} \\ \hat{\mathbf{q}}^H & 0 \end{bmatrix}. \tag{4.42}$$

At every iteration, the correction $\mathbf{c} = [\Delta\hat{\mathbf{q}}, \Delta\omega]^{\mathrm{T}} = \mathbf{J}_F^{-1}(\omega_j, \hat{\mathbf{q}}_j)\mathbf{F}(\omega_j, \hat{\mathbf{q}}_j)$ has to be computed. Nonetheless, it is important to note that the inverse of $\mathbf{J}_F$ does not need to be calculated explicitly. Instead, the correction can be obtained from the numerical solution of the following linear system of size $n+1 \times n+1$ (with n being the number of rows/columns of the matrices that define the eigenvalue problem):

$$\mathbf{J}_F(\omega_j, \hat{\mathbf{q}}_j)\, \mathbf{c} = \mathbf{F}(\omega_j, \hat{\mathbf{q}}_j). \tag{4.43}$$

This method, being based on a Newton-Raphson iteration, has a quadratic convergence, so typically only a small number of iterations (less than 10) suffices to achieve a good degree of convergence. The convergence criterion considered in this work to stop the iteration is based on the infinity norm of the correction, that is $||\mathbf{c}||_\infty = \max(|\mathbf{c}|)$. In the case of a spatial stability analysis, the same iterative method can be applied by replacing the eigenvalue by α, the eigenvector by $\hat{\mathbf{q}}^+$ and the system matrices by $\mathbf{A}_\alpha^+$ and $\mathbf{B}_\alpha^+$ (see § 3.4.3).

4.2.7.2 Generalized Rayleigh quotient iteration

A well-known iterative eigenvalue algorithm is the Rayleigh quotient iteration (RQI), see for instance Trefethen & Bau [40]. This algorithm combines the inverse power method, usually employed to obtain an eigenvector estimate when an

approximation to the associated eigenvalue is known, with the Rayleigh quotient, usually employed to obtain an eigenvalue estimate when an approximation to the associated eigenvector is known. The result is an iterative method that allows to obtain an approximation to both an eigenvalue and a corresponding eigenvector with a single algorithm.

The RQI algorithm computes an increasingly accurate approximation to the eigenvector-eigenvalue pair by means of two steps in each iteration. For the case of the temporal stability approach, the steps of the algorithm can be expressed as follows. First, the next estimate to the eigenvector ($\hat{\mathbf{q}}_{j+1}$) is computed by solving the linear system

$$\left(\mathbf{A}_\omega - \omega_j \mathbf{B}_\omega\right) \hat{\mathbf{q}}_{j+1} = \mathbf{B}_\omega \hat{\mathbf{q}}_j \tag{4.44}$$

for $\hat{\mathbf{q}}_{j+1}$ and normalizing it with respect to its L_2 norm, that is

$$\hat{\mathbf{q}}_{j+1} = \frac{\left(\mathbf{A}_\omega - \omega_j \mathbf{B}_\omega\right)^{-1} \mathbf{B}_\omega \hat{\mathbf{q}}_j}{|| \left(\mathbf{A}_\omega - \omega_j \mathbf{B}_\omega\right)^{-1} \mathbf{B}_\omega \hat{\mathbf{q}}_j ||_2}. \tag{4.45}$$

Second, the next approximation to the eigenvalue is obtained by means of the Rayleigh quotient. For linear stability theory, a generalized form of the Rayleigh quotient is employed [47], given by

$$\omega_{j+1} = \frac{\hat{\mathbf{q}}_{j+1}^H \mathbf{B}_\omega^H \mathbf{A}_\omega \hat{\mathbf{q}}_{j+1}}{\hat{\mathbf{q}}_{j+1}^H \mathbf{B}_\omega^H \mathbf{B}_\omega \hat{\mathbf{q}}_{j+1}}. \tag{4.46}$$

Equations (4.45) and (4.46) are iterated until a desired degree of convergence is achieved. In this work, the convergence criterion chosen for this algorithm is based on the relative error in the eigenvalue, i.e., $\varepsilon_r = |\omega_{j+1} - \omega_j|/|\omega_{j+1}|$. If a spatial stability framework is considered, the same algorithmic steps are applied, once again replacing the eigenvalue by α, the eigenvector by $\hat{\mathbf{q}}^+$ and the system matrices by $\mathbf{A}_\alpha^+$ and $\mathbf{B}_\alpha^+$.

The Rayleigh quotient iteration is specially well suited for Hermitian or symmetric matrices, for which a cubic convergence is guaranteed if the initial eigenvector-eigenvalue pair is sufficiently close to an actual pair of the system [40]. Nevertheless, the matrices originating from the governing equations of the linear stability problem do not satisfy this property, and as a result cubic convergence is usually not achieved in this case. Despite this fact, the performance of the algorithm for the cases studied in this work has been found to be very satisfactory, typically requiring one less iteration than the Newton-Raphson algorithm introduced previously. On average, 5 iterations were found to be sufficient to achieve a convergence tolerance of 10^{-10} with the generalized RQI. Therefore, this algorithm has been employed for the 2D-LST analyses presented in this dissertation.

4.3 VESTA toolkit

The stability analyses presented in this work have been performed by means of the **V**KI **E**xtensible **S**tability and **T**ransition **A**nalysis (VESTA) toolkit, originally developed by Pinna [48]. VESTA is a set of computational tools for the derivation, implementation and solution of the governing equations originating from different hydrodynamic stability theories, for different thermodynamic flow assumptions and coordinate systems. At present, VESTA mainly supports the derivation, implementation and solution of the equations for LST, 2D-LST, streamwise BiGlobal, PSE and NPSE theories for a wide range of flow assumptions, which include CPG, TPG, LTE, CNE and thermo-chemical non-equilibrium (TCNE), among others (see [4, Chapter 8] for a complete description). A preliminary implementation of the 3D-PSE theory in CPG is also available [49].

Three different main solvers are available for the respective solution of the LST [4, 31, 50–54], the 2D-LST/BiGlobal [18, 44, 55–57] and the PSE/NPSE problems [58–61], which share a unified data structure and a common module for the implementation of the discretized governing equations (see § 4.3.1) and the associated boundary conditions. These solvers are complemented with numerous pre- and post-processing tools. Pre-processing functionalities comprise structured mesh generation for CFD base-flow computations in simple geometries, the extraction of base-flow data from CFD solutions and the manipulation of base-flow fields to make them suitable for stability analysis, involving the computation of necessary base-flow derivatives as described in § 4.2.4. Post-processing utilities enable the analysis of absolute instabilities [62, 63], transition prediction by means of the e^N method or skin friction deviation in NPSE computations, the evaluation of non-modal growth by means of singular value decomposition of the (2D)LST operator [64] and the analysis of the production and dissipation mechanisms of the total disturbance energy in a calorically perfect gas [56]. In addition, a module to estimate N-factor envelope curves in high-speed boundary layers by means of a neural network is also available (see [65]).

A summary of different problems on which VESTA toolkit has recently been applied to study the stability of hypersonic and high-enthalpy shear flows can be found in the work of Pinna *et al.* [66].

4.3.1 Automatic derivation and implementation tool (ADIT)

At the heart of VESTA solvers lies a database of scripts that build the matrices of the stability problem for a given stability theory, thermodynamic flow assumption and coordinate system. These scripts, referred to as build scripts, are automatically generated by means of a module known as the Automatic Derivation and Implementation Tool (ADIT).

When deriving the governing stability equations in the compressible regime,

the number of resulting terms becomes significant. This can be appreciated from the CPG equations listed in appendices B and C. As a consequence, the manual derivation and posterior implementation of such equations is subject to human error. For this reason, having a computational tool that is able to perform these tasks automatically is highly desirable. This motivated the development of the original ADIT module in VESTA (see [18, 31, 67]). When more elaborated flow assumptions such as CNE are considered, the equation complexity significantly increases, and the resulting number of terms in a given equation can increase by multiple orders of magnitude. For example, the 2D-LST energy equation for CPG has 51 terms (B.1e), while the 2D-LST energy equation in CNE features about 3000 terms. In these cases, an automatic derivation and implementation of the equations is a necessity. For this reason, a generalization of the tool was performed by Miró Miró [4] to include a complete derivation of the governing stability equations in multiple flow assumptions, which was further extended by Zanus [60, 68, 69] for the case of non-linear equations (NPSE).

The derivation side of the tool is based on the computer algebra system (CAS) known as Maxima [70], which provides a powerful framework for the symbolic manipulation of the governing equations. The steps followed during the derivation process of the stability equations are detailed in [4, Chapter 8]. They are essentially the same steps that are required for a manual derivation of the equations. In addition to the derivation of the governing stability equations, the ADIT module was also extended by Miró Miró [4] to allow for the automatic derivation of the thermodynamic derivatives of the base-flow properties (i.e., quantities such as $\partial\bar{\mu}/\partial\bar{T}$) for all the different thermodynamic flow assumptions available. As introduced in § 4.2.4, these derivatives are required in the stability equations because of the Taylor expansion of the perturbation variables associated to the dependent flow quantities. In the case of thermodynamic assumptions such as CNE or TCNE, obtaining analytical expressions for the large number of thermodynamic derivatives that need to be evaluated is a challenging task, in part owing to the complex expressions resulting from many of the thermal, transport and chemical models that are usually employed in practice. Therefore, a manual derivation of the necessary expressions becomes an error-prone process once again. For this reason, a symbolic differentiation of the required functions is also performed automatically by means of Maxima.

The implementation part of the tool translates the symbolic expressions derived by Maxima into MATLAB scripts (build scripts) that are then used to evaluate those expressions when building the matrices of the stability problem. In the case of the stability equations, this is achieved by means of the following process. First, once the derivation of the equations is complete, the various terms appearing in the equations are grouped according to the independent perturbation quantity they involve as well as the wave parameters (α, β, ω). This associates the terms to the

different matrices and submatrices of the system. Next, the expressions inside each of these groups are written by Maxima into text files that can be read by MATLAB. Then, specific MATLAB functions read the text files and write the expressions into the build scripts, translating the symbolic variable names into the names of the data structures employed by the VESTA solvers.

In the case of the expressions for the thermodynamic derivatives, the implementation process follows the same philosophy, ultimately generating a set of build scripts containing MATLAB functions that evaluate the necessary derivatives required by the stability equations. However, in this case the translation of the symbolic expressions into MATLAB functions is more complex, as summations and products are involved (which need to be translated into loops) and, in some cases, the solution of linear systems of equations are required by the models. The reader is referred to [4, Chapter 8] for a more detailed description of the implementation procedure.

All the build scripts generated by the ADIT module employ the same unified data structure which is shared among the different VESTA solvers. For a given combination of stability theory, thermodynamic flow assumption, coordinate system and thermodynamic- and transport-property models, the solvers search for the necessary build scripts in a common database. As a result, all solvers build the matrices of the stability problem in the same manner, using a unified implementation of build scripts for any desired configuration.

4.3.2 The 2D-LST/BiGlobal solver

This work makes extensive use of the 2D-LST/BiGlobal solver implemented in VESTA toolkit. This solver was originally developed by Groot [18] for incompressible and compressible CPG flows in different coordinate systems. By the choice of the two spatial directions in which the base flow is assumed to be inhomogeneous, the solver implements the respective equations that lead either to the 2D-LST formulation or the streamwise BiGlobal formulation (see § 3.6.2) in the chosen coordinate system.

The original solver was based on a discretization by means of the Chebyshev collocation method, which was found to limit considerably the size of the two-dimensional collocation grid that could be employed in practice, owing to the associated computational cost to be handled by the MATLAB implementation. Later on, Naddei [44] introduced a MATLAB-Fortran interface for a parallel implementation of the implicitly restarted Arnoldi algorithm, to allow for the solution of the resulting dense, large-scale eigenvalue problem outside MATLAB, as described in § 4.2.6.2.

In this work, the original solver has been significantly modified to allow for a more efficient solution of the two-dimensional generalized eigenvalue problem

and to extend its capabilities to the analysis of high-enthalpy flows. On the one hand, the solver has been adapted to use the FD-q discretization technique (see § 4.2.1.2). Most importantly, it has been modified to exploit the sparsity introduced in the system matrices when this method is applied, which has reduced dramatically the computational cost of solving the 2D-LST eigenvalue problem. On the other hand, the data structure of the solver has been made consistent with the other VESTA solvers in order to benefit from the unified build script database, directly extending the capabilities of the solver to other thermodynamic flow assumptions. In addition, the boundary-condition implementation has also been updated according to the description given in § 4.2.5, allowing also a unified treatment of boundary conditions with the other solvers. These modifications have enabled the 2D-LST analyses presented in § 5.3, which require a significant grid resolution in the spanwise direction, and the 2D-LST computations in TPG and CNE presented in chapter 6.

Verifications of the original solver in CPG smooth boundary-layer flows are available in the work of Groot [18]. A verification of the solver for the instabilities evolving behind a discrete roughness element is presented in appendix F, which shows a comparison of the stability spectrum obtained by the VESTA solver against the DLR solver of Theiss *et al.* [24, 71]. Finally, a verification of the 2D-LST solver in the case of the TPG and CNE flow assumptions is provided in § 6.3, which is performed against the extensively verified LST solver in VESTA [4].

References

[1] John D. Anderson Jr. *Hypersonic and High Temperature Gas Dynamics*. American Institute of Aeronautics and Astronautics, Reston VA, second edition, 2006.

[2] E. F. Toro. *Riemann solvers and numerical methods for fluid dynamics*. Springer-Verlag Berlin Heidelberg, third edition, 2009.

[3] Koen J. Groot, Fernando Miró Miró, Ethan S. Beyak, Alexander J. Moyes, Fabio Pinna, and Helen L. Reed. *DEKAF: spectral multi-regime basic-state solver for boundary-layer stability*. AIAA paper, 2018-3380, 2018.

[4] Fernando Miró Miró. *Numerical Investigation of Hypersonic Boundary-Layer Stability and Transition in the presence of Ablation Phenomena*. PhD thesis, Université Libre de Bruxelles and von Karman Insitute for Fluid Dynamics, 2020.

[5] Fernando Miró Miró, Koen Groot, Ethan S. Beyak, Alexander J. Moyes, Fabio Pinna, and Helen L. Reed. *DEKAF: an open source spectral boundary-layer solver*. Technical Report VKI Technical Memorandum 56, von Karman Institute for Fluid Dynamics, 2020.

[6] Helen L. Reed, William S. Saric, and Daniel Arnal. *Linear Stability Theory Applied to Boundary Layers*. Annual Reviews of Fluid Mechanics, 28:389–428, 1996.

[7] J. Ph. Brazier, B. Aupoix, and Jean Cousteix. *Second-Order Effects in Hypersonic Laminar Boundary Layers*. In T.K.S. Murthy, editor, Computational Methods in Hypersonic Aerodynamics. Kluwer Academic, 1991.

[8] Sukumar Chakravarthy, Oshin Peroomian, Uriel Goldberg, and Sampath Palaniswamy. *The CFD++ Computational fluid dynamics software suite*. AIAA paper, 1998-5564, 1998.

[9] Metacomp Technologies. *CFD++ User Manual*, 2015.

[10] E. F. Toro, M. Spruce, and W. Speares. *Restoration of the contact surface in the HLL-Riemann solver*. Shock Waves, 4(1):25–34, 1994.

[11] E. F. Toro. *The HLLC Riemann solver*. Shock Waves, 29(8):1065–1082, 2019.

[12] CFD Direct. *OpenFOAM v6 User Guide: 5.3 Mesh generation with blockMesh*, 2018.

[13] Nicola De Tullio, Pedro Paredes, Neil D. Sandham, and Vassilios Theofilis. *Laminar-turbulent transition induced by a discrete roughness element in a supersonic boundary layer*. Journal of Fluid Mechanics, 735:613–646, 2013.

[14] Nicola De Tullio. *Receptivity and transition to turbulence of supersonic boundary layers with surface roughness*. PhD thesis, University of Southampton, 2013.

[15] C. Canuto, A. Quarteroni, Y. M. Hussaini, and T. A. Zang. *Spectral methods. Fundamentals in single domains*. Springer-Verlag Berlin Heidelberg, first edition, 2006.

[16] Lloyd N. Trefethen. *Spectral Methods in MATLAB*. SIAM, 2000.

[17] Koen J. Groot. *BiGlobal Stability of Shear Flows Spanwise & Streamwise Analyses*. PhD thesis, TU Delft and von Karman Institute for Fluid Dynamics, 2018.

[18] Koen J. Groot. *Derivation of and Simulations with BiGlobal Stability Equations*. Technical Report AE5110, VKI and TU Delft, 2013.

[19] Miguel Hermanns and Juan Antonio Hernández. *Stable high-order finite-difference methods based on non-uniform grid point distributions*. International Journal for Numerical Methods in Fluids, 56:233–255, 2008.

[20] F. Gómez, Soledad Le Clainche, Pedro Paredes, Miguel Hermanns, and Vassilios Theofilis. *Four decades of studying global linear instability: Problems and challenges*. AIAA Journal, 50(12):2731–2743, 2012.

[21] Pedro Paredes, Miguel Hermanns, Soledad Le Clainche, and Vassilis Theofilis. *Order 10^4 speedup in global linear instability analysis using matrix formation*. Computer Methods in Applied Mechanics and Engineering, 253:287–304, 2013.

[22] Pedro Paredes. *Advances in global instability computations: From incompressible to hypersonic flow*. PhD thesis, Universidad Politécnica de Madrid, Escuela Técnica Superior de Ingenieros Aeronáuticos, 2014.

[23] Pedro Paredes, Nicola De Tullio, Neil D. Sandham, and Vassilios Theofilis. *Instability Study of the Wake Behind a Discrete Roughness Element in a Hypersonic Boundary-Layer*. Instability and Control of Massively Separated Flows, Fluid Mechanics and Its Applications, 107:91–96, 2015.

[24] Alexander Theiss, Stefan J. Hein, Syed Raza Christopher Ali, and Rolf Radespiel. *Wake flow instability studies behind discrete roughness elements on a generic re-entry capsule*. AIAA paper, 2016-4382, 2016.

[25] Pedro Paredes, Meelan M. Choudhari, and Fei Li. *Instability wave-streak interactions in a supersonic boundary layer*. Journal of Fluid Mechanics, 831:524–553, 2017.

[26] Stefan J. Hein, Alexander Theiss, Antonio Di Giovanni, Christian Stemmer, Thomas Schilden, Wolfgang Schröder, Pedro Paredes, Meelan M. Choudhari, Fei Li, and Eli Reshotko. *Numerical investigation of roughness effects on transition on spherical capsules*. Journal of Spacecraft and Rockets, 56(2):388–404, 2019.

[27] Pedro Paredes, Meelan M. Choudhari, and Fei Li. *Instability wave-streak interactions in a high Mach number boundary layer at flight conditions*. Journal of Fluid Mechanics, 858:474–499, 2019.

[28] Mujeeb R. Malik. *Numerical methods for hypersonic boundary layer stability*. Journal of Computational Physics, 86(2):376–413, 1990.

[29] Alfonsina Esposito. *Development and analysis of mapping and domain decomposition techniques for compressible shear flow stability calculations*. Technical Report VKI SR 2016-16, von Karman Institute for Fluid Dynamics, 2016.

[30] Koen J. Groot, Jacopo Serpieri, Fabio Pinna, and Marios Kotsonis. *Secondary crossflow instability through global analysis of measured base flows*. Journal of Fluid Mechanics, 846:605–653, 2018.

[31] Fabio Pinna. *Numerical study of stability of flows from low to high Mach number*. PhD thesis, Università degli Studi di Roma La Sapienza, 2012.

[32] Carl de Boor. *A practical guide to splines*. Springer, revised edition, 1978.

[33] Ardeshir Hanifi, Peter J. Schmid, and Dan S. Henningson. *Transient growth in compressible boundary layer flow*. Physics of Fluids, 8(3):826–837, 1996.

[34] C. B. Moler and G. W. Stewart. *An Algorithm for Generalized Matrix Eigenvalue Problems*. SIAM Journal on Numerical Analysis, 10(2):241–256, apr 1973.

[35] G. H. Golub and C. F. Van Loan. *Matrix computations*. The Johns Hopkins University Press, fourth edition, 2013.

[36] E. Anderson, Z. Bai, C. Bischof, S. Blackford, J. Demmel, J. Dongarra, J. Du Croz, A. Greenbaum, S. Hammarling, A. McKenney, and D. Sorensen. *LAPACK Users' Guide*. Society for Industrial and Applied Mathematics, Philadelphia, PA, third edition, 1999.

[37] Z. Bai, J. Demmel, J. Dongarra, A. Ruhe, and H. van der Vorst. *Templates for the solution of algebraic eigenvalue problems: a practical guide*. Society for Industrial and Applied Mathematics, Philadelphia, PA, first edition, 2000.

[38] D. C. Sorensen. *Implicit Application of Polynomial Filters in a k -Step Arnoldi Method*. SIAM Journal on Matrix Analysis and Applications, 13(1):357–385, jan 1992.

[39] R. B. Lehoucq and D C Sorensen. *Deflation techniques for an implicitly restarted Arnoldi iteration*. SIAM Journal on Matrix Analysis and Applications, 17(4):789–821, 1996.

[40] Lloyd N. Trefethen and David Bau. *Numerical linear algebra*. Society for Industrial and Applied Mathematics, first edition, 1997.

[41] R. B. Lehoucq, D. C. Sorensen, and C. Yang. *ARPACK Users' Guide: solution of large scale eigenvalue problems with implicitly restarted Arnoldi methods*. 1997.

[42] Ponnampalam Balakumar and Mujeeb R. Malik. *Discrete modes and continuous spectra in supersonic boundary layers*. Journal of Fluid Mechanics, 239:631–656, 1992.

[43] K. J. Maschhoff and D. C. Sorensen. *P_ARPACK: An efficient portable large scale eigenvalue package for distributed memory parallel architectures*. pages 478–486. 1996.

[44] Fabio Naddei. *Parallel computation of global eigenmodes for space propulsion systems*. Technical Report VKI SR 2016-15, von Karman Institute for Fluid Dynamics, 2016.

[45] Timothy A. Davis. *Algorithm 832: UMFPACK V4.3 - an unsymmetric-pattern multifrontal method*. ACM Transactions on Mathematical Software, 30(2):196–199, jun 2004.

[46] L. S. Blackford, J. Choi, A. Cleary, E. D'Azevedo, J. Demmel, I. Dhillon, J. Dongarra, S. Hammarling, G. Henry, A. Petitet, K. Stanley, D. Walker, and R. C. Whaley. *ScaLAPACK Users' Guide*. Society for Industrial and Applied Mathematics, 1997.

[47] Melina A. Freitag and Alastair Spence. *Convergence theory for inexact inverse iteration applied to the generalised nonsymmetric eigenproblem*. Electronic Transactions on Numerical Analysis, 28:40–64, 2007.

[48] Fabio Pinna. *VESTA toolkit: a Software to Compute Transition and Stability of Boundary Layers*. AIAA paper, 2013-2616, 2013.

[49] Giacomo Zuccarino. *Development and implementation of a 3D solver for Parabolized Stability Equations*. Technical Report PR 2019-32, von Karman Institute for Fluid Dynamics, Brussels, Belgium, 2019.

[50] Fernando Miró Miró and Fabio Pinna. *Effect of uneven wall blowing on hypersonic boundary-layer stability and transition*. Physics of Fluids, 30(084106), 2018.

[51] Fernando Miró Miró, Ethan S. Beyak, Fabio Pinna, and Helen L. Reed. *High-enthalpy models for boundary-layer stability and transition*. Physics of Fluids, 31(044101), 2019.

[52] Fernando Miró Miró and Fabio Pinna. *Injection-gas-composition effects on hypersonic boundary-layer transition*. Journal of Fluid Mechanics, 890(R4), 2020.

[53] Fernando Miró Miró and Fabio Pinna. *Decoupling ablation effects on boundary-layer stability and transition*. Journal of Fluid Mechanics, 907:A14, jan 2021.

[54] Fernando Miró Miró, Ethan S. Beyak, Fabio Pinna, and Helen L. Reed. *Ionization and dissociation effects on boundary-layer stability*. Journal of Fluid Mechanics, 907:A13, 2021.

[55] Iván Padilla Montero and Fabio Pinna. *BiGlobal stability analysis of the wake behind an isolated roughness element in hypersonic flow*. Proceedings of the Institution of Mechanical Engineers, Part G: Journal of Aerospace Engineering, 234(1):5–19, jan 2020.

[56] Iván Padilla Montero and Fabio Pinna. *Analysis of the instabilities induced by an isolated roughness element in a laminar high-speed boundary layer*. Journal of Fluid Mechanics, 915:A90, 2021.

[57] Iván Padilla Montero, Fernando Miró Miró, and Fabio Pinna. *Influence of high-temperature effects on the stability of the wake behind an isolated roughness element in hypersonic flow*. Laminar-Turbulent Transition, IUTAM Bookseries 38:–, 2021.

[58] Ludovico Zanus, Fernando Miró Miró, and Fabio Pinna. *Parabolized stability analysis of chemically reacting boundary layer flows in equilibrium conditions*. Proceedings of the Institution of Mechanical Engineers, Part G: Journal of Aerospace Engineering, 234(1):79–95, 2020.

[59] Ludovico Zanus, Fernando Miró Miró, and Fabio Pinna. *Weak Non-Parallel Effects on Chemically Reacting Hypersonic Boundary Layer Stability*. AIAA paper, 2019-2853, 2019.

[60] Ludovico Zanus, Fernando Miró Miró, and Fabio Pinna. *Nonlinear PSE Transition Predictions in Hypersonic Boundary-Layers with Finite-Rate Chemical Reactions*. In IUTAM Bookseries, page In publication, 2019.

[61] Ludovico Zanus, Carleton P. Knisely, Fernando Miró Miró, and Fabio Pinna. *Multiple-Tool Stability Analysis of Supersonic Modes in Thermo-Chemical Nonequilibrium Boundary Layers*. AIAA paper, 2020-3067, 2020.

[62] S. Demange, O. Chazot, and F. Pinna. *Local analysis of absolute instability in plasma jets*. Journal of Fluid Mechanics, 903:A51, nov 2020.

[63] S. Demange and F. Pinna. *On the role of thermo-transport properties in the convective/absolute transition of heated round jets*. Physics of Fluids, 32(12):124104, dec 2020.

[64] Iván Padilla Montero and Fabio Pinna. *Transient growth analysis of a compressible boundary layer using two-dimensional linear stability theory*. In 8th European Conference for Aeronautics and Aerospace Sciences, Madrid, Spain, 1-4 July 2019, EUCASS2019-591.

[65] Florian Danvin, M. Olazabal-Loume, and Fabio Pinna. *Laminar to turbulent transition prediction in hypersonic flows with metamodels*. AIAA Aviation 2019 Forum, 2019-2837, 2019.

[66] Fabio Pinna, Fernando Miró Miró, Ludovico Zanus, Iván Padilla Montero, and Simon Demange. *Automatic Derivation of Stability Equations and their Application to Hypersonic and High-Enthalpy Shear Flows*. In International Conference for Flight Vehicles, Aerothermodynamics and Re-entry Missions & Engineering, Monopoli, Italy, 2019.

[67] Fabio Pinna and Koen J. Groot. *Automatic derivation of stability equations in arbitrary coordinates and different flow regimes*. AIAA paper, 2014-2634, 2014.

[68] Ludovico Zanus, Fernando Miró Miró, and Fabio Pinna. *Nonlinear Parabolized Stability Analysis of Hypersonic Flows in Presence of Curvature Effects*. AIAA paper, 2018-2087, 2018.

[69] Ludovico Zanus and Fabio Pinna. *Stability Analysis of Hypersonic Flows in Local Thermodynamic Equilibrium Conditions by Means of Nonlinear PSE*. AIAA paper, 2018-3696, 2018.

[70] *Maxima Manual Version 5.42.0*, 2018.

[71] Alexander Theiss and Stefan J. Hein. *Investigation on the wake flow instability behind isolated roughness elements on the forebody of a blunt generic reentry capsule*. Progress in Flight Physics, 9:451–480, 2017.

5

Stability analysis of the wake behind an isolated roughness element in a calorically perfect gas

5.1 Problem description

The first problem analyzed in this work consists of a sharp-edged roughness element mounted on top of a flat plate inside a cold hypersonic freestream. The freestream values considered correspond to the high-Reynolds number test conditions of the von Karman Institute H3 hypersonic wind tunnel (see for example the work of Tirtey [1]), which are summarized in table 5.1. The total temperature associated to these conditions is $T_0 = T_\infty \left[1 + M_\infty^2 \left(\gamma - 1\right)/2\right] = 500$ K. For this range of temperatures, no significant excitation of the vibrational molecular energy mode is expected in the flow field[1], hence the assumption of a calorically perfect gas for these conditions is an appropriate choice. Depending on the case, the flat plate wall is considered to be either isothermal, with a fixed wall temperature of $T_w = 300$ K, or adiabatic. The former option is a more reasonable approximation of the situation encountered in the wind tunnel owing to its short operating times.

The geometrical configuration studied in this chapter is represented in figure 5.1. The roughness element is mounted on top of a flat plate and is located inside

[1] The temperature at which vibrational excitation becomes important in air is practically not influenced by pressure [2]. According to figure 2.1, vibrational excitation can be neglected for temperatures below 800 K.

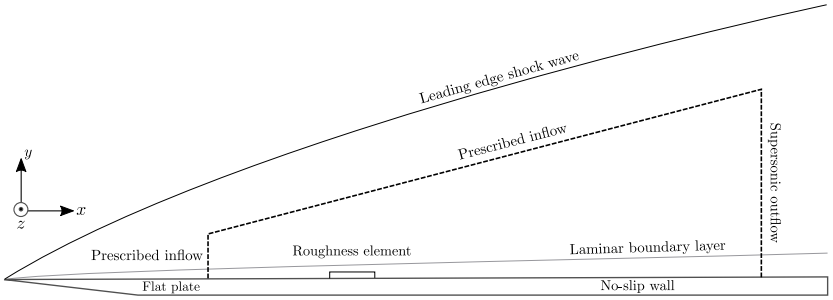

Figure 5.1: Geometrical configuration considered to study the instabilities induced by an isolated roughness element in a calorically perfect gas. The dashed lines represent a slice along the xy roughness symmetry plane ($z = 0$) of the computational domain used for obtaining the base-flow solutions. Not to scale.

M_∞	u_∞ [m/s]	T_∞ [K]	p_∞ [Pa]	ρ_∞ [kg/m^3]	Re_∞/l [1/m]
6	939.45	60.98	1963.42	0.1121	2.61e+07

Table 5.1: Summary of the freestream conditions used in the calorically perfect gas analyses (VKI H3 wind tunnel [1]).

the laminar boundary layer developing along the plate. Unless otherwise stated, the flat plate is assumed to be infinitely sharp. Due to a hypersonic viscous-inviscid interaction at the flat-plate leading edge, a weak shock wave is induced at the leading edge. The computational domain is located inside the shock layer established between the surface and the weak shock wave originating at the flat-plate leading edge. This approach reduces the computational effort necessary to obtain a base-flow solution while adding flexibility to test different inflow conditions on the same grid. For these reasons, it has already been employed in similar studies in the literature (see for example [3–6]). The top boundary of the domain has an angle to prevent roughness-induced compression waves and weak shock waves to impinge on it, thus avoiding potential spurious reflections back into the boundary layer.

The primitive flow variables are prescribed at the inlet and the top boundaries of the domain, using quantities that are either obtained from a Navier-Stokes solution in a bigger domain without the roughness element, or from a self-similar boundary-layer computation. Note that when no roughness is present, the flow field is constant along the spanwise direction and the problem becomes two-dimensional, so that the values to prescribe can be computed through a 2D Navier-Stokes simulation. This is an additional advantage of using a subdomain with prescribed inflow data. At the roughness symmetry plane ($z = 0$) and at the

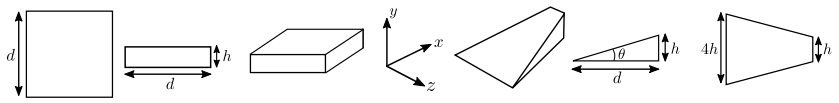

Figure 5.2: Roughness geometries considered. Not to scale.

xy far-field plane ($z = z_\infty$), symmetry conditions are specified. At the wall, a no-slip condition is enforced. The wall thermal boundary condition depends on each particular case, and is defined in the following sections. Finally, at the outlet boundary, a supersonic outflow condition is specified, in which all the primitive flow variables are extrapolated from the interior of the domain. For a description of these boundary conditions, see § 2.3.

With respect to the initial conditions, the flow field is initialized with the freestream values and the system is integrated in time until a decrease of at least eight orders of magnitude in the averaged system residual is achieved.

5.1.1 Roughness geometries

Two different roughness geometries are considered in this chapter, which are depicted in figure 5.2. The first geometry is a sharp-edged cuboidal element with a square planform shape. The second one consists in a three-dimensional sharp-edged ramp geometry, which is inspired by popular passive flow control devices employed to promote boundary layer transition. An example is the design developed by the Hypersonic Airbreathing Propulsion Branch at NASA Langley Research Center (see for instance [7]), who explored the possibility of using wall-mounted ramp fuel injectors in scramjet combustors. Ramp-shaped injectors shed vortices and produce local flow separation which can enhance mixing and flame holding.

The spanwise symmetry of these roughness geometries is exploited in the base-flow computations by considering only half of the roughness element width, and therefore only half of the computational domain width.

5.2 Instabilities induced by a cuboidal roughness element at a fixed streamwise location and frequency

The first analysis presented in this chapter focuses on the wake instabilities behind a sharp-edged cuboidal roughness geometry such as the one illustrated in figure 5.2. The wake instabilities are examined by means of 2D-LST theory at a given streamwise position (yz plane) and at a given frequency.

x_{in} [mm]	x_{out} [mm]	y_{in} [mm]	y_{out} [mm]	z_∞ [mm]
20.28	67.59	1.26	9.60	6.31

Table 5.2: Dimensions of the first computational domain considered in this chapter. The origin is located at the flat-plate leading edge.

5.2.1 Geometrical parameters and definition of different test cases

The height and location of the roughness element in this case are determined following the approach presented by De Tullio *et al.* [3] and De Tullio & Sandham [4]. In this approach, the roughness has a height (h) equal to the displacement thickness (δ_1) of the flat-plate self-similar boundary layer at a given reference position, denoted by x_{δ_1}. This reference location is defined by fixing the displacement thickness Reynolds number, $Re_{\delta_1} = \rho_\infty u_\infty \delta_1 / \mu_\infty$, and the freestream conditions, so that δ_1 is uniquely determined. The value of Re_{δ_1} employed here is the same one used by De Tullio & Sandham [4], namely $Re_{\delta_1} = 8200$. This value, together with the freestream parameters considered in this chapter (see table 5.1) and the assumption of an isothermal flat-plate wall with $T_w = 300$ K, results in a roughness height of $h = \delta_1 = 0.315$ mm and a reference position of $x_{\delta_1} = 15.24$ mm with respect to the flat-plate leading edge. The planform shape of the roughness element is a square with edge length $d = 6h$.

Following De Tullio & Sandham [4], the inlet of the computational domain is located at a streamwise distance of $16h$ downstream of x_{δ_1}, that is $x_{in} = 20.28$ mm with respect to the flat-plate leading edge. The leading edge of the roughness element is placed at a streamwise distance of $34h$ downstream of the inlet of the computational domain. Therefore, the roughness element is placed at a streamwise position of $x_h = 31$ mm with respect to the flat-plate leading edge.

Regarding the size of the computational domain, table 5.2 lists the x and y coordinates (streamwise position and height) of the inflow and outflow planes of the domain as well as half of the domain width, denoted by z_∞. Note that owing to spanwise symmetry, only half of the span is considered ($0 \leq z \leq z_\infty$). Therefore, z_∞ is the actual spanwise size of the computational domain employed for the baseflow calculations. The angle of the top boundary of the domain with respect to the flat-plate wall is 10 degrees.

A summary of the different cases investigated in this set-up is provided in table 5.3. All these cases assume a constant value of the Prandtl number equal to $Pr = 0.72$. The parameter Re_h denotes the roughness Reynolds number, defined as

Case	Thermal BC[a]	Re_h	$Re_{h,w}$	h/δ_{99}	Inflow profile
1	Isothermal	324	278	0.54	Self-similar boundary layer
2	Isothermal	352	301	0.54	NS[b] sharp leading edge
3	Isothermal	290	273	0.36	NS circular leading edge ($r = 0.5$ mm)
4	Adiabatic	137	119	0.44	Self-similar boundary layer

[a]BC stands for boundary condition
[b]NS stands for Navier-Stokes

Table 5.3: Summary of the different cases analyzed. Isothermal cases have a fixed wall temperature of $T_w = 300$ K.

$$Re_h = \frac{\rho_h u_h h}{\mu_h}, \tag{5.1}$$

where ρ_h, u_h and μ_h are the density, streamwise velocity and dynamic viscosity of the fluid evaluated at the streamwise location of the roughness leading edge and at a height of $y = h$ in the corresponding smooth flat-plate boundary layer (i.e. without roughness element). The quantity $Re_{h,w}$ refers to the modified roughness Reynolds number definition of Bernardini *et al.* [8, 9], which also accounts for wall-temperature effects by evaluating the dynamic viscosity at the wall, that is

$$Re_{h,w} = \frac{\rho_h u_h h}{\mu_w}. \tag{5.2}$$

The value of h/δ_{99} describes the ratio between the roughness height and the local boundary layer thickness at the streamwise position of the leading edge of the roughness element, denoted by δ_{99}. The value of δ_{99} is determined by means of the total enthalpy criterion $h_0/h_{0,\infty} = 0.995$ [10], using once again the smooth flat-plate boundary layer profiles associated to each particular case. This criterion is well suited for high Mach number flows and can also provide a good estimation of the boundary-layer thickness in cases where an entropy layer is present.

Typical values of Re_h reported in literature above which transition occurs shortly after the roughness element (usually known as the critical roughness Reynolds number) at the Mach number under study range between $Re_h \approx 300$–600 (see Redford *et al.* [11]). Redford and coworkers found the line $M_h T_\infty / T_w = 3(Re_h - 300)/700$ to successfully divide transitional and non-transitional cases in their database, therefore proposing it as a critical roughness Reynolds number correlation which takes into account compressibility effects. It is important to mention, however, that this correlation does not take into account the roughness shape, the wall temperature or the disturbance environment, but it constitutes a

good starting reference for calibrating the design of a particular case in terms of roughness position and height. The modified roughness Reynolds number definition of Bernardini *et al.* [9] was found to provide a critical value of the roughness Reynolds number that was independent of the parameter $M_h T_\infty / T_w$ for a given roughness shape and disturbance environment, therefore providing a further simplified correlation. According to [9], the critical value of $Re_{h,w}$ ranges between $Re_{h,w} \approx 400$–700 depending on the shape of the obstacle. For a cube-shaped roughness element, [9, 12] report a critical value of $Re_{h,w} = 460$.

In supercritical cases (cases with a roughness Reynolds number above the critical value), transition is to be expected in a very short distance downstream of the roughness element, in many cases bypassing any linear growth mechanisms and triggering bypass transition (see for instance [13, 14]). On the other hand, in subcritical cases, the onset of transition is no longer completely governed by roughness-induced perturbations. Nonetheless, it is important to note that this does not imply that transition is not accelerated by the presence of the roughness element anymore, or that the roughness element no longer influences transition. In particular, for values of the roughness Reynolds number which are not too far under the critical value, the roughness element is still expected to play an important role on the transition process, in such a way that there is an extensive region of roughness-induced linear disturbance amplification. These cases are the main focus of this dissertation, where linear stability theory can provide additional physical understanding.

Figure 5.3 shows where the current cases fall in the criteria provided by [11] and [9]. As it can be noticed, all four cases lie in the subcritical regime. For cases 1 and 2, the chosen configuration yields a value of the roughness Reynolds number that is slightly under the critical Re_h threshold, and further below the critical $Re_{h,w}$ value. This allows to investigate the growth of roughness-induced instabilities in a transition scenario governed by significant linear amplification. In addition, these values of the roughness Reynolds number are low enough so that global instabilities are not present in the flow field (see [3, 4, 15]), allowing to focus the analysis on purely convective instabilities and enabling the use of a local linear stability theory. For the analysis of three-dimensional global instabilities induced by an isolated roughness element, see the works of Loiseau *et al.* [16] and Bucci *et al.* [17].

Cases 1, 2 and 3 are used to study the effect of the flat plate leading edge on the instability of the wake. The only difference between them is the inflow data that is prescribed at the inlet and the top boundaries of the domain, namely, a self-similar boundary-layer profile in case 1, the boundary-layer resulting from a two-dimensional Navier-Stokes simulation considering a flat plate with a sharp leading edge (thus accounting for the viscous-inviscid interaction at the flat plate leading edge) in case 2, and the boundary-layer resulting from another two-dimensional

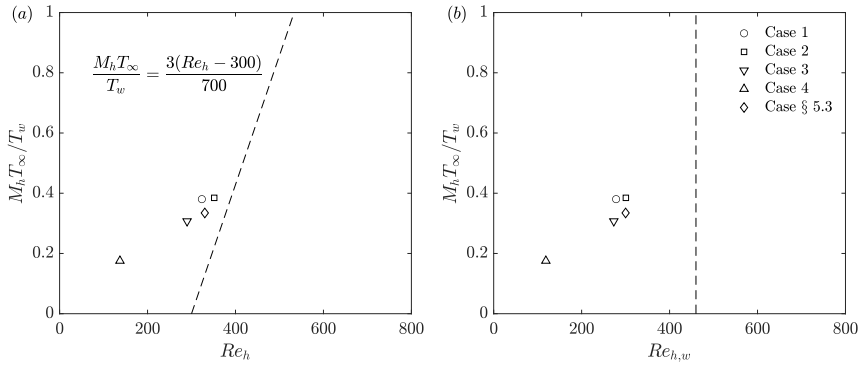

Figure 5.3: Critical roughness Reynolds number criteria of Redford et al. [11] (a) and Bernardini et al. [9] (b) applied to the cases studied in this chapter. Supercritical cases are located at the right side of the dashed line; subcritical cases at the left side. The symbol labeled Case § 5.3 refers to the set-up analyzed in § 5.3.

Navier-Stokes computation assuming a flat plate with a circular leading edge of radius $r = 0.5$ mm in case 3. On the other hand, case 4 is used to assess the influence of the thermal wall boundary condition on the instability characteristics of the roughness wake. In case 4, the wall is assumed to be adiabatic while keeping the rest of the parameters identical to those of case 1. The adiabatic wall temperature of the self-similar boundary layer can be estimated through the following approximate relation [2]:

$$\frac{T_{ad}}{T_\infty} = 1 + Pr^{1/2}\left[(\gamma - 1)/2\right] M_\infty^2. \tag{5.3}$$

With the freestream parameters considered here, equation (5.3) yields a value of $T_{ad} \approx 434$ K. Therefore, the use of the temperature $T_w = 300$ K in the other three cases corresponds to a cold wall boundary condition.

The difference between the roughness Reynolds number in cases 1 and 2 is mainly due to differences in the density profile, which arise as a consequence of assuming that the pressure at the boundary-layer edge (p_e) is equal to the freestream pressure in case 1 (similarity solution). In case 2, the boundary-layer profile employed to estimate the roughness Reynolds number comes from a solution of the Navier-Stokes equations. Therefore, it accounts for the weak shock wave that originates at the sharp flat-plate leading edge due to a hypersonic viscous-inviscid interaction. In case 1, the self-similar boundary-layer profile is considered instead, which neglects the leading edge shock wave and as a result assumes that $p_e = p_\infty$. This simplification results in a 6% difference in the static pressure level across the boundary layer, which translates into a deviation in the density profile that leads to the observed difference in Re_h.

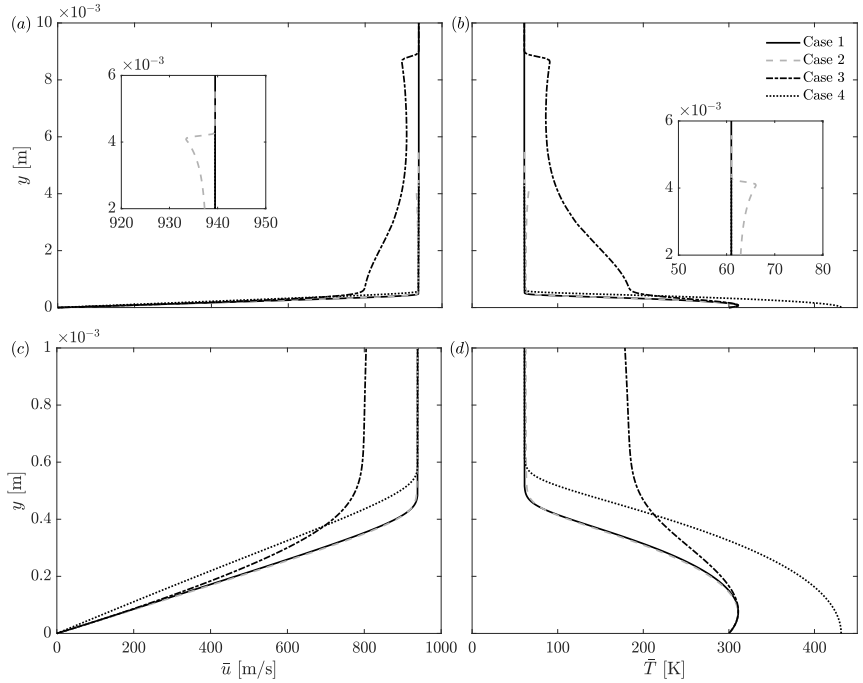

Figure 5.4: Inflow boundary-layer profiles for each of the cases presented in table 5.3: (a) complete streamwise velocity profiles; (b) complete temperature profiles; (c) detail of streamwise velocity profiles near the wall; (d) detail of temperature profiles near the wall.

The inflow boundary-layer profiles employed for each case are represented in figure 5.4. The differences between cases 1 and 2 are small, as the viscous-inviscid interaction taking place at the sharp flat-plate leading edge is weak and is mostly significant near the leading edge. Nevertheless, the effect of the leading edge shock wave is still noticeable in the inflow profiles (see the small jump at $y \approx 4$ mm depicted in the inserts in figures 5.4(a, b)), which reflects the presence of a small entropy layer in the flow field. A much larger difference is found for case 3. In this case, the blunt leading edge induces a strong bow shock that generates a large entropy layer over the flat plate, which persists a long distance downstream. At the domain inflow, the profiles still display a significant jump due to the bow shock propagating from the leading edge, and feature important velocity and temperature variations outside of the boundary layer. Such variations are a consequence of the entropy layer established between the bow shock and the flat-plate wall. Finally, the adiabatic wall condition imposed in case 4 leads to a thicker inflow boundary layer as a result of the higher wall-temperature. The larger boundary-layer thickness combined with the higher temperature at the roughness

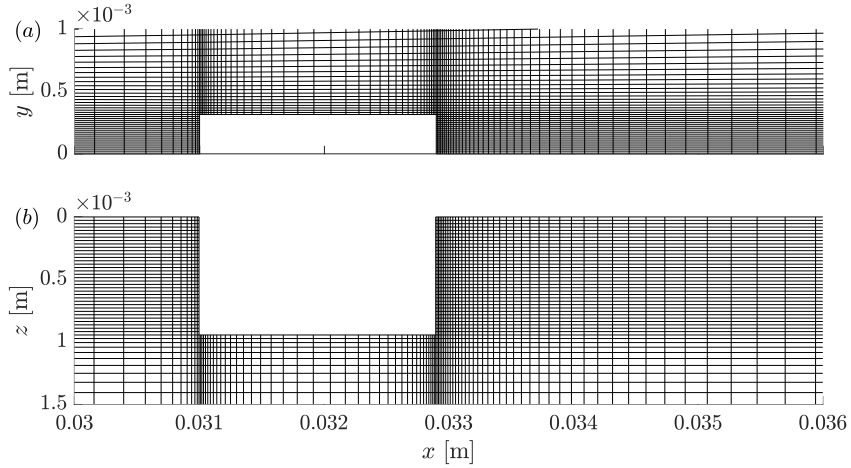

Figure 5.5: Detail of the computational grid used to obtain the base-flow solutions in the region near the roughness element: (a) xy plane at $z = 0$; (b) xz plane at $y = 0$. Only every four grid points in the streamwise and spanwise directions and every six in the wall-normal direction are shown.

height result in a much smaller roughness Reynolds number for case 4 with respect to the other cases.

5.2.2 Computational grid employed for the base flow calculations

An overview of the numerical grid employed to calculate the base-flow solutions in this analysis is represented in figure 5.5, which shows the region surrounding the roughness element. In order to maintain a reasonable computational effort, the mesh is clustered towards the element in all directions. The cell spacing is uniform up to the roughness height in the wall-normal direction and up to the roughness width in the spanwise coordinate. From then on, a constant expansion ratio is applied until the domain boundary, always keeping a continuity in the cell sizes between the uniform and the expansion regions. In the streamwise direction, the grid is respectively clustered towards the leading and trailing edges of the roughness, also employing a constant expansion ratio. The ratios are uniquely defined by the number of cells desired on a given edge and the length of that edge, according to the bunching law given by equation (4.1). The number of grid points employed along the streamwise, wall-normal and spanwise directions in this configuration is 561, 341 and 241, respectively, yielding a total count of approximately 43 million points.

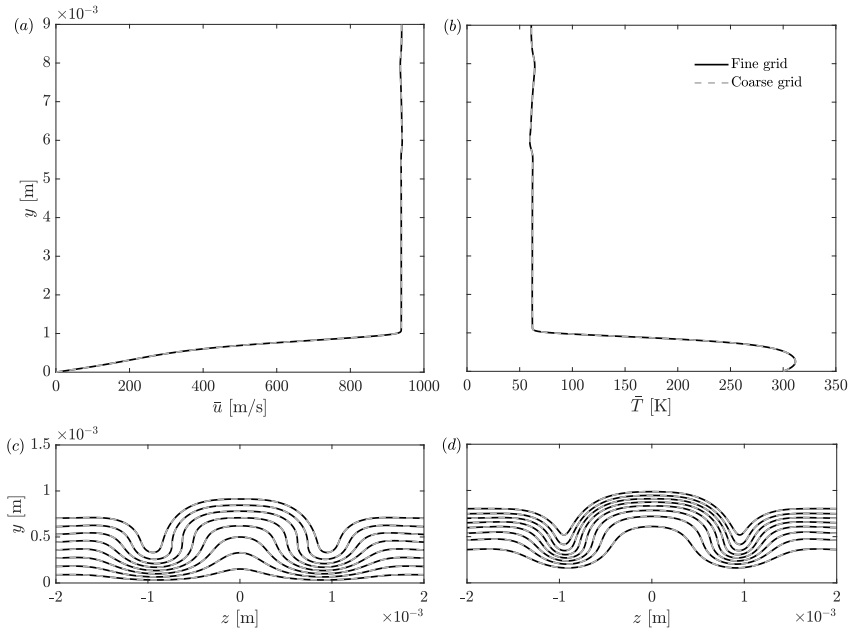

Figure 5.6: Comparison of the base flow obtained for case 1 employing the designed grid and a finer grid with a 25% increase in the number of cells in the streamwise and wall-normal directions: (a, b) *boundary-layer velocity and temperature profiles at the roughness centerline* ($z = 0$) *and at the domain outlet* ($x = 0.0676$ *m); contours of streamwise velocity* (c) *and temperature* (d) *at the outlet* yz *plane.*

In order to check the grid convergence of the base-flow solution, an additional computation has been carried out on a finer mesh generated by increasing the number of points in the streamwise and wall-normal directions by 25%, reaching a total of 70 million grid points. For case 1, figure 5.6 shows a comparison of the boundary-layer profiles at the roughness centerline and the streamwise velocity and temperature contours on a spanwise plane, all of them evaluated at the domain outlet for the two different meshes. It can be seen that both grids deliver the same base-flow solution. As a result, the coarser mesh has been employed for the other three cases reported in this set-up.

5.2.3 Base-flow solutions

The main features of the base flow are depicted in figure 5.7, which shows results for case 1. The cuboidal roughness element generates two regions of separated flow, located immediately upstream and downstream of it. The flow in these regions is similar to the recirculation bubbles induced by a forward and a backward

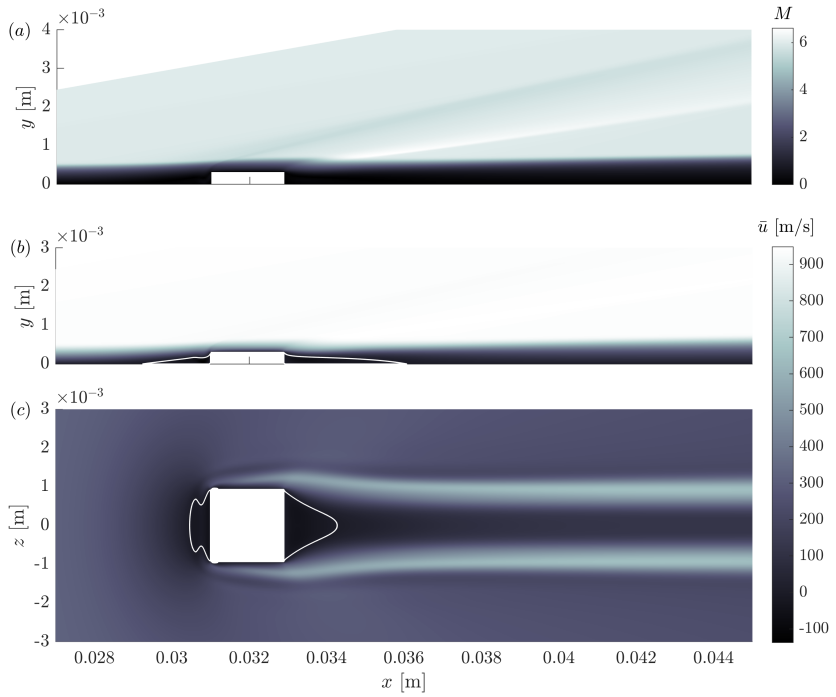

Figure 5.7: Base flow results for case 1: (a) Mach number contours on the streamwise (xy) plane at the roughness centerline ($z = 0$), showing the roughness-induced shock and expansion waves; (b) streamwise velocity contours at the roughness center plane; (c) streamwise velocity contours on a xz plane at $y = 0.5h$. The white lines represent isolines of $\bar{u} = 0$, delimiting regions of separated flow.

facing steps, respectively. The non-homogeneous shape of the upstream recirculation bubble, as it can be observed in figure 5.7(c), indicates the presence of a pair of horseshoe vortices wrapped around the roughness.

The Mach number contours shown in figure 5.7(a) illustrate that the roughness element induces a displacement of the boundary layer which leads to a viscous-inviscid interaction and generates a set of compression waves. The oblique shock wave relations (see for example [18]) reveal that, in the current configuration, this upstream compression is not strong enough to form an oblique shock wave. As the flow reaches the trailing edge of the roughness element, it turns and detaches, giving rise to an expansion fan that accelerates the flow above the boundary-layer edge. This expansion fan can be satisfactorily modeled as a Prandtl-Meyer expansion wave. Shortly after, the separated trailing-edge flow progressively reattaches downstream of the obstacle, in this case generating an actual oblique shock wave. Note that such an oblique shock is weak because of the small effective deflection

angle experienced by the flow (approximately 3 degrees), which results in a wave angle of about 9 degrees. The resulting jump in Mach number across the shock in this case is $M_2/M_1 \approx 0.94$, with M_1 denoting the Mach number upstream of the shock wave and M_2 denoting the Mach number downstream.

Figure 5.7(c) depicts the topology of the streamwise velocity streaks that characterize the wake behind the roughness element. A pair of strong counter-rotating streamwise vortices is generated at the side edges of the element, due to a pressure gradient between the top and the lateral surfaces (see the similar analysis of De Tullio & Sandham [19]). These vortices lift up low-momentum fluid near the flat plate wall at the roughness symmetry plane and pull down high-momentum fluid located above the boundary-layer edge towards the sides of the roughness wake. In this process, a low-velocity streak is induced at the center of the wake, surrounded by two high-velocity streaks at the sides.

A more detailed representation of the separated-flow regions can be obtained by looking at the skin friction coefficient (c_f) and the Stanton number (St) distributions along the flat-plate wall. Here, the following definitions are employed [2]:

$$c_f = \frac{\bar{\tau}_w}{\frac{1}{2}\rho_\infty u_\infty^2}, \tag{5.4}$$

$$St = \frac{\bar{q}_w}{u_\infty \rho_\infty c_p (T_{ad} - T_w)}, \tag{5.5}$$

where $\bar{\tau}_w$ and $\bar{q}_w$ are respectively the viscous shear stress and the magnitude of the heat flux at the flat-plate wall. Note that at the flat-plate wall, only the wall-normal derivatives are different from zero in the current configuration. Therefore:

$$\bar{\tau}_w = \bar{\mu}_w \left.\frac{\partial \bar{u}}{\partial y}\right|_w \quad \text{and} \quad \bar{q}_w = \bar{k}_w \left.\frac{\partial \bar{T}}{\partial y}\right|_w. \tag{5.6}$$

The value of the adiabatic wall temperature (T_{ad}) employed here to evaluate the Stanton number is that given by equation (5.3).

Figure 5.8 represents the skin friction coefficient and Stanton number distributions along the flat-plate wall and at the roughness centerline for the different cases under consideration. Negative values of the skin friction coefficient delimit the extent of the upstream and downstream detached flow regions. Both quantities feature a strong peak in the upstream recirculation bubble generated in front of the roughness, which is a consequence of the significant blockage produced by the element and denotes a region of strong viscous dissipation. The downstream recirculation bubble, on the other hand, presents much lower values of skin friction as well as the lowest values of the Stanton number.

By comparing the skin friction coefficient curves for the different cases, it can be observed that the negative peak in c_f in front of the element is significantly smaller for cases 3 and 4 than for cases 1 and 2. This is a consequence of the

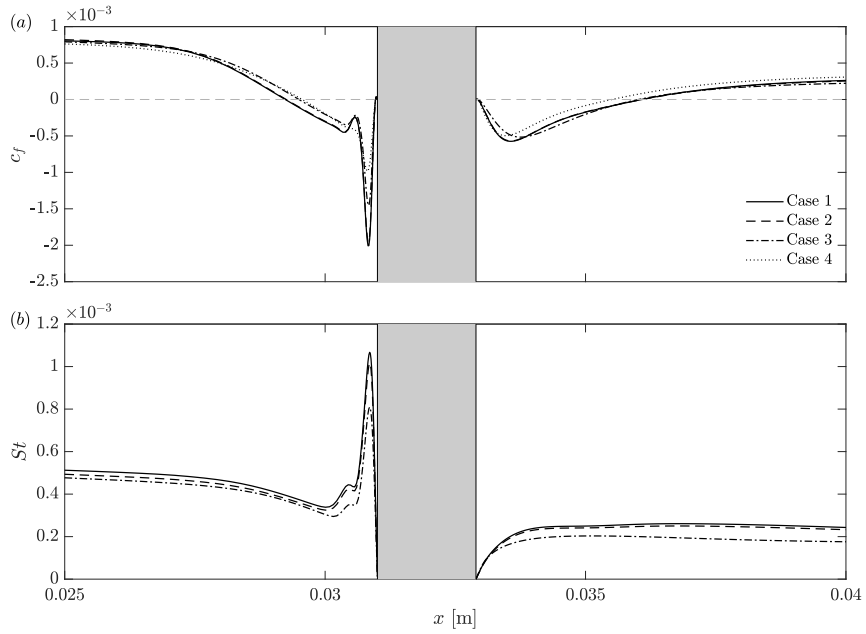

Figure 5.8: Skin friction coefficient (a) and Stanton number (b) distributions along the flat-plate wall at the roughness centerline ($z = 0$) for each case. The Stanton number distribution is only represented for the cases with an isothermal wall. The shaded rectangular bands represent the position and streamwise extent of the roughness element.

smaller blockage introduced by the obstacle owing to the smaller ratio h/δ_{99} (see table 5.3) in cases 3 and 4. This is also reflected in the smaller size of the upstream recirculation bubble for cases 3 and 4. In regard to the downstream recirculation region, its size is also smaller for case 4 with respect to the other three cases, for which it features a very similar length. Owing to the similarities in the conditions between cases 1 and 2, the evolution of the skin friction coefficient is also very similar for the two cases along the entire streamwise range. Comparing the Stanton number evolution for the different isothermal-wall cases, it is worth mentioning that case 3 shows a smaller heat transfer for all the streamwise region considered. The decrease is specially significant at the peak in front of the roughness element, similarly to what is observed for the skin friction coefficient.

To better illustrate the flow structure inside the wake behind the elements, two additional quantities are represented in cross-flow (y-z) planes in figures 5.9 and 5.10. Figure 5.9 shows contour plots of the streamwise shear magnitude, defined as

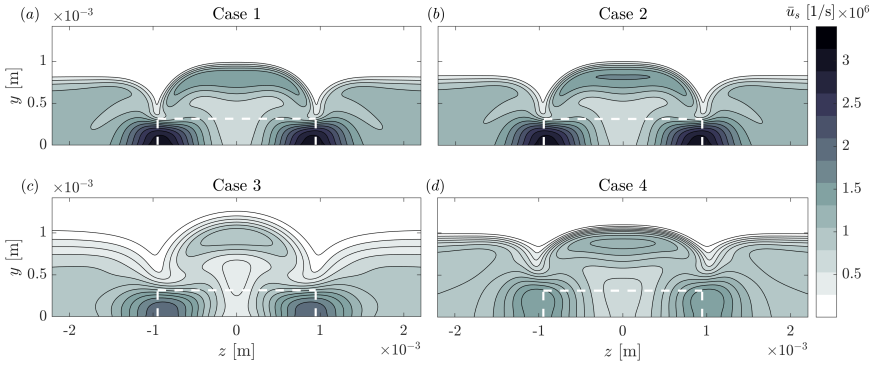

Figure 5.9: Contours of streamwise shear magnitude (equation (5.7)) in a spanwise plane located at $x = 0.0643$ m. The white dashed lines represent a projection of the roughness element.

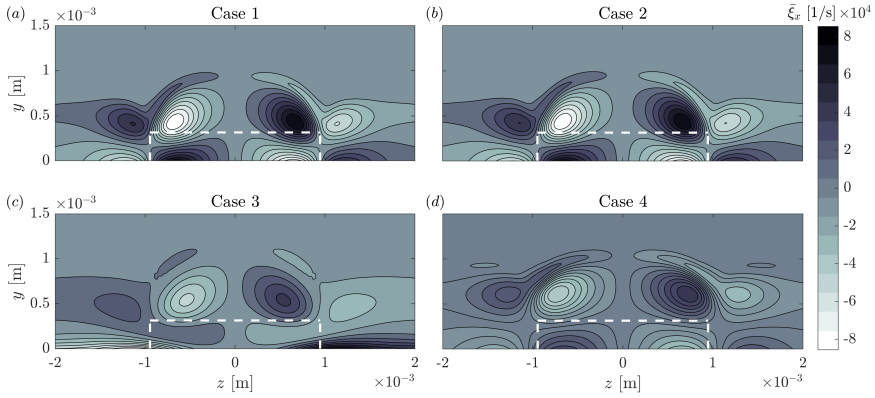

Figure 5.10: Contours of streamwise vorticity (equation (5.8)) in a spanwise plane located at $x = 0.0643$ m. The white dashed lines represent a projection of the roughness element.

$$\bar{u}_s = \sqrt{\left(\frac{\partial \bar{u}}{\partial y}\right)^2 + \left(\frac{\partial \bar{u}}{\partial z}\right)^2}, \tag{5.7}$$

on a plane located at a distance of $x = 0.0643$ m with respect to the flat-plate leading edge, which is equivalent to a distance of $100h$ downstream of the roughness trailing edge. Similarly, figure 5.10 displays contours of the streamwise vorticity at the same streamwise location, given by

$$\bar{\xi}_x = \frac{\partial \bar{w}}{\partial y} - \frac{\partial \bar{v}}{\partial z}. \tag{5.8}$$

Two regions of large shear magnitude can be identified near the flat plate-wall at the side edges of the roughness element (see figure 5.9). These regions are located between the wall and the high-velocity streaks established in the roughness wake. The large shear values attained at these locations can be explained due to the big velocity gradient that exists between the high-velocity fluid traveling inside the streaks and the zero-velocity fluid at the flat plate wall. In between these two areas, another region of low shear is found, which corresponds to the origin of the central low-velocity streak where the lift-up effect takes place. The low-momentum fluid that is pulled up in this region gives rise to the mushroom-shaped structure that characterizes the central part of the wake. Owing to the large velocity gradient established between the low-velocity fluid inside the central streak and the outer flow-field above the boundary layer, the region surrounding the low-velocity streak features a layer of high shear magnitude. The streamwise vorticity contours (see figure 5.10) clearly illustrate the location and shape of the counter-rotating vortex pair. These contours also reveal that two additional small and opposite vortices are respectively induced at each side of the counter-rotating pair.

Cases 1 and 2 display very similar shear magnitude and streamwise vorticity signatures, with case 2 showing slightly larger values of $\bar{u}_s$ at the top of the central streak. Cases 3 and 4 feature significantly smaller values for both quantities compared to cases 1 and 2 for the same streamwise location behind the element. For case 4, this is attributed to the higher boundary-layer thickness associated to this configuration, which leads to weaker counter-rotating vortices as reflected in figure 5.10(d). The larger boundary-layer thickness is a result of the higher temperature inside the boundary layer (see figure 5.4). Because the pressure is the same in both the adiabatic and isothermal wall cases, the density of the fluid in the boundary layer is much lower in the adiabatic solution. Therefore, a larger volume of fluid is required to accommodate the same mass flow within the boundary layer [18, Chapter 18], resulting in a thickening of the boundary layer. In case 3, although the thicker boundary layer also leads to a weaker counter-rotating vortex pair, the main reason for the reduced shear in this case is the smaller velocity present in the inviscid flow region above the boundary-layer (see figure 5.4), which is due to the presence of the large entropy layer that characterizes the flow field in this configuration.

5.2.4 Spatial stability spectrum

This section presents the results of a spatial stability analysis performed in the wake behind the roughness element at given streamwise location and frequency. All the calculations are performed at a frequency $f = 417.1$ kHz, which corresponds to a non-dimensional frequency of $F = fh/u_\infty = 0.14$, and at a streamwise location of $x = 0.0643$ m, which is equivalent to a distance of $140h$ down-

stream of the domain inflow ($100h$ downstream of the roughness trailing edge). These values have been chosen following the DNS results of De Tullio & Sandham [4] for a very similar configuration, for which this frequency is the one featuring the highest linear disturbance growth and the plane is located at a streamwise distance where a significant linear development of the dominant instability modes has been attained (see also the 2D-LST analysis of Paredes *et al.* [20]).

The Chebyshev collocation method is employed for the discretization of the 2D-LST eigenvalue problem. Symmetry/antisymmetry boundary conditions are imposed along the spanwise direction in order to resolve only half of the domain width in each computation. Therefore, all the spectra shown in this section contain the merged results from the solution of two different eigenvalue problems for each case, namely, the eigenvalues obtained with symmetry boundary conditions at both spanwise boundaries and the eigenvalues obtained with the antisymmetric counterpart. The collocation grid is mapped to the physical domain employing the transformation given by equation (4.16) along each spatial direction, considering the following mapping parameters: $y_{max} = 16h$, $z_{max} = 10h$, $y_i = 2.5h$ and $z_i = 2h$. The implicitly restarted Arnoldi algorithm is employed for computing 200 eigenmodes for each spanwise boundary condition specification (symmetry/antisymmetry), using a non-dimensional shift-invert parameter of $\sigma = 0.95$.

Results of the stability calculation for case 1 are mainly presented in figures 5.11 and 5.12. Figure 5.11 shows the spatial 2D-LST spectrum and figure 5.12 illustrates the two-dimensional streamwise velocity amplitude functions of the most unstable discrete modes obtained at the specified streamwise location and frequency. In addition, to provide an idea of the approximate three-dimensional shape of the most relevant perturbations under analysis, figures 5.13 and 5.14 display contour plots of the streamwise velocity perturbation ($\tilde{u}$) on xy and xz planes along a streamwise region comprised between $x \approx 0.061$ m and $x \approx 0.067$ m. It is very important to emphasize that these two figures were produced by employing the information obtained from the 2D-LST computation at $x = 0.0643$ m only. The three-dimensional function $\tilde{u} = \tilde{u}(x, y, z, t)$ for each instability was obtained by evaluating the perturbation ansatz defined by equation (3.30), using the respective values of α and $\hat{u}$ computed by means of the 2D-LST solution at the selected location and frequency and for $t = 0$ s. The actual shape of the perturbations is slightly different because their growth rate and wavenumber are different at each streamwise station.

Different grids have been tested in order to check the convergence of the spectrum with respect to the number of collocation points in both the spanwise (N_z) and the wall-normal (N_y) directions, providing at the same time a direct visualization of the location of continuous, discrete and spurious numerical modes in the stability spectrum (see figure 5.11). A discretized vertical continuous branch located at $\alpha_r = \omega_r / \bar{u}_\infty$ can be observed, which is composed of modes that represent

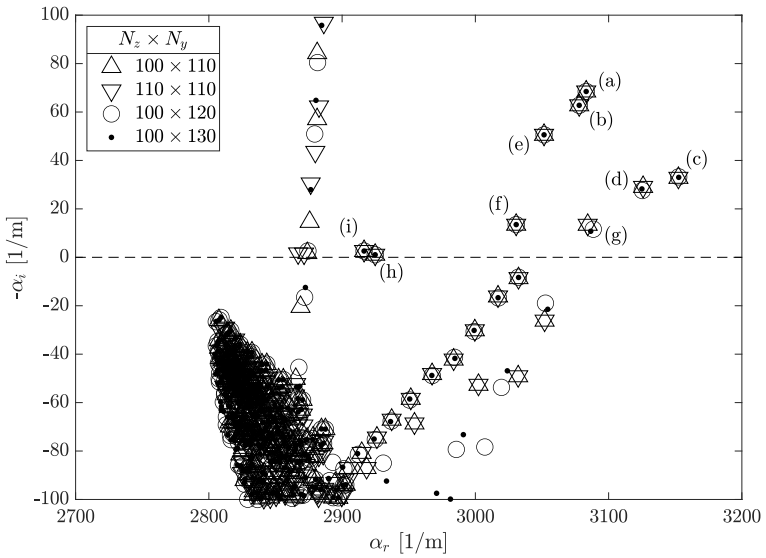

Figure 5.11: Spatial 2D-LST spectrum for case 1 at $f = 417.1$ kHz and $x = 0.0643$ m. The letters between parentheses label the different discrete unstable modes present in the spectrum and associate each of them with the corresponding amplitude function represented in figure 5.12.

entropy and vorticity waves and travel with a phase speed equal to the freestream velocity (see Balakumar & Malik [21]). Although not shown in the figure, two additional horizontal continuous branches located in the real axis respectively at the right and left of the vertical branch can also be found in the spectrum. These branches are associated to the supersonic nature of the flow, and in this case represent acoustic waves. It has been checked that such branches can actually be retrieved when changing the shift of the transformed GEVP and/or solving for a larger number of eigenvalues. Several spurious modes appear scattered along the imaginary axis at a nearly constant wavenumber of about $\alpha_r = 2880$ m^{-1}, which do not show any grid convergence. Their unphysical nature has been further confirmed by looking at the associated amplitude functions. The discrete, and physically interesting, eigenvalues are located at the right of the continuous branch, spanning different wavenumbers in the range approximately between $\alpha_r = 2900$ m^{-1} and $\alpha_r = 3200$ m^{-1}. These modes are completely converged with respect to N_z, while convergence is close with respect to N_y, specially for the unstable eigenvalues. In the remaining stability calculations shown in this section, a grid resolution of $N_z \times N_y = 100 \times 110$ is employed.

Nine unstable discrete modes are identified in the spectrum, labeled with letters

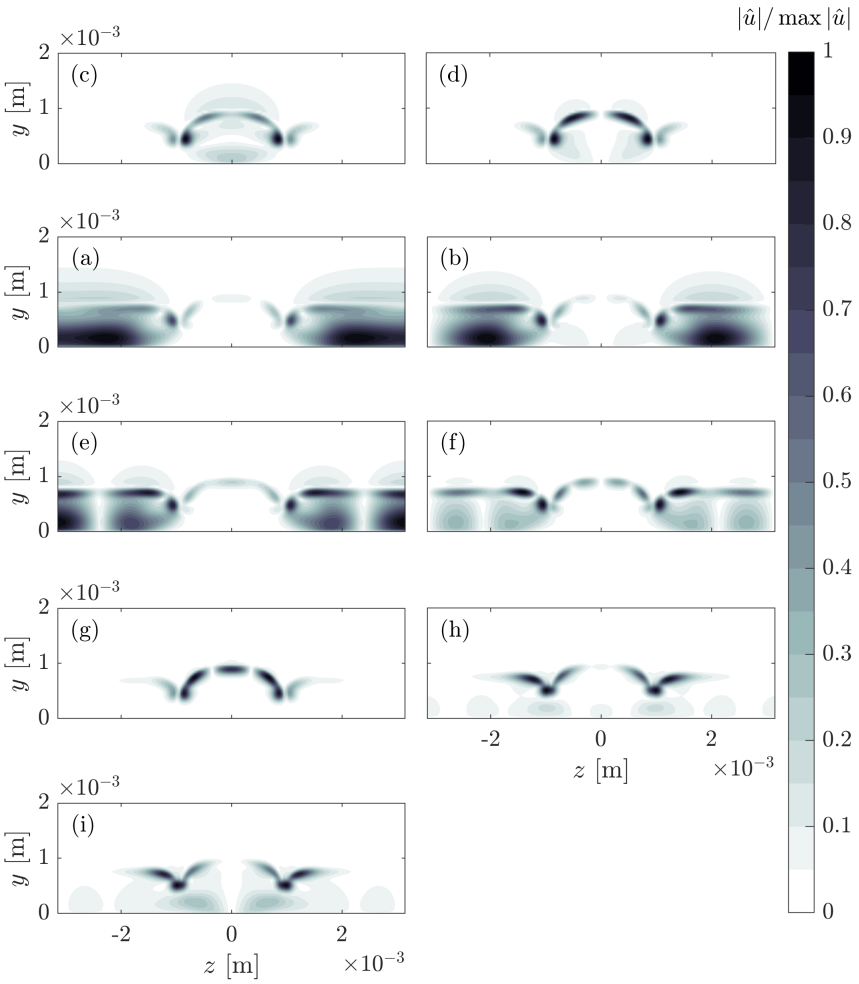

Figure 5.12: Contours of the normalized magnitude of the streamwise velocity eigenfunctions for case 1 ($f = 417.1$ kHz and $x = 0.0643$ m). The letters inside parentheses denote the corresponding discrete instability mode in the spectrum (figure 5.11). The eigenfunctions represented correspond to a grid resolution of 100×110 *collocation points.*

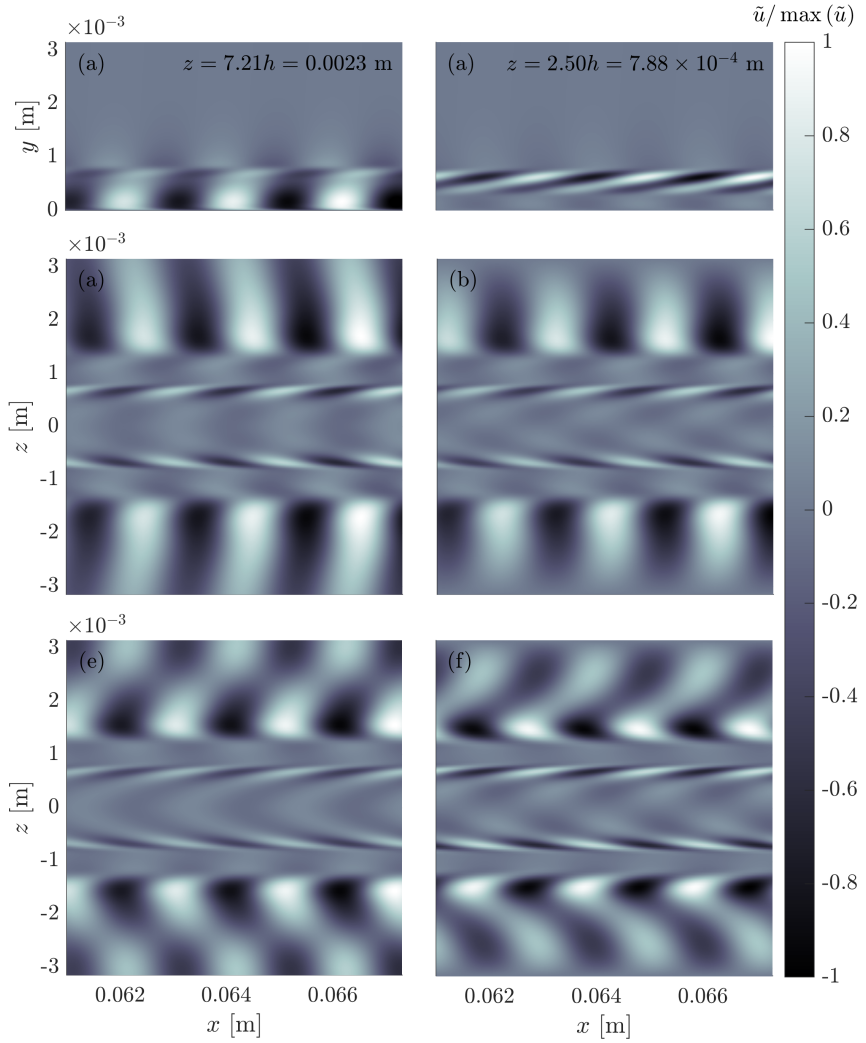

Figure 5.13: Contours of the normalized streamwise velocity perturbation on streamwise (xy) and wall-normal (xz) planes for the instabilities associated to the Mack-mode family in case 1. The letters inside parentheses indicate the corresponding mode according to figure 5.11. The xz plots correspond to a height of $y = 2.44h = 7.69 \times 10^{-4}$ m. Note that these contours are generated by evaluating the three-dimensional perturbation function given by the 2D-LST ansatz (3.30) at $t = 0$ s, using the amplitude function and growth rate computed for each mode at $x = 0.0643$ m only.

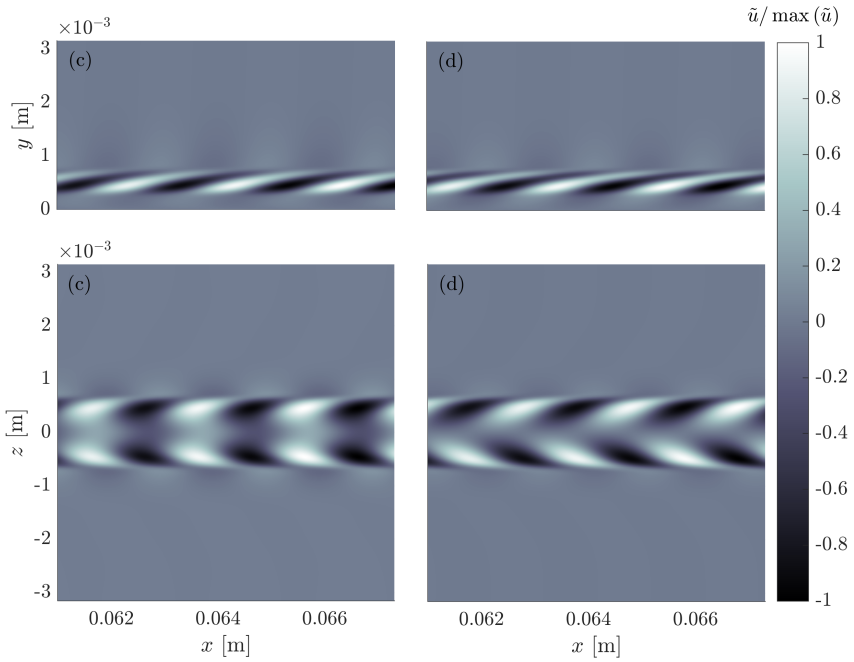

Figure 5.14: Contours of the normalized streamwise velocity perturbation on streamwise (xy) and wall-normal (xz) planes for the most unstable sinuous and varicose wake instabilities in case 1. The letters inside parentheses indicate the corresponding mode according to figure 5.11. The xy plots correspond to a cut at $z = 2.50h = 7.88 \times 10^{-4}$ m and the xz plots to $y = 2.69h = 8.48 \times 10^{-4}$ m. Note that these contours are generated by evaluating the three-dimensional perturbation function given by the 2D-LST ansatz (3.30) at $t = 0$ s, using the amplitude function and growth rate computed for each mode at $x = 0.0643$ m only.

ranging from (a) to (i). These letters are respectively associated to the contour plots of the streamwise velocity amplitude functions displayed in figures 5.12, 5.13 and 5.14. For the particular conditions considered, the leading instability mode (a) is the two-dimensional Mack mode, which mainly develops in the boundary layer starting at the sides of the roughness element and spanning the complete computational domain in the spanwise direction. The nature of this boundary-layer mode is not associated to the presence of the roughness and therefore it can also be retrieved both by means of LST or 2D-LST considering a smooth flat plate, i.e., without the roughness element. Nevertheless, in this case the wake induced by the obstacle strongly modulates the Mack-mode perturbation, as can be observed in the xz plots and in the cut plane at $z/h = 2.50$ in figure 5.13.

The second dominant instability mode (b) also peaks at the sides of the element, with an antisymmetric shape function showing a similar amplitude distri-

bution to that of the Mack mode. The same is true for modes (e) and (f). It is argued that modes (b), (e) and (f) are oblique perturbations of the same family as the Mack mode, with an increasing spanwise wavenumber β ($\beta_{(b)} < \beta_{(e)} < \beta_{(f)}$). Their diagonal-like distribution along the spectrum and the perturbation functions shown in figure 5.13 further support this argument. On the other hand, modes (c) and (d) respectively correspond to the most unstable varicose and sinuous deformations of the low-velocity streak, whose amplitude functions are maximum in the high-shear layer surrounding the mushroom-shaped structure. These are the most unstable perturbations developing inside the wake behind the roughness element, with the varicose mode showing a slightly higher growth rate in this case. Figure 5.14 shows the even and odd perturbation functions respectively associated with the varicose and sinuous instabilities. Their region of development is concentrated inside the roughness wake and in the shear layer around the central streak.

The wake of the element also sustains the growth of two additional modes, denoted by (h) and (i), which have very small growth rates and their amplitude peaks are located at the interface between the streamwise counter-rotating vortices and the boundary layer at the sides of the roughness element. It is worth noting that, as could be expected, the regions where the amplitude functions of the wake modes are higher mainly correspond to the areas with larger shear magnitude gradients. Finally, mode (g) is argued to be related to the leading wake fluctuations (c) and (d). Similarly to perturbations (b), (e) and (f) in the case of the Mack mode, this mode seems to correspond to an instability of the same family as the varicose and sinuous modes, featuring additional peak and valley regions distributed along the high-shear layer that surrounds the low-velocity streak, as can be observed by its amplitude function. The remaining discrete stable modes located in the diagonal line at the right of the vertical continuous branch are oblique variations belonging to the Mack-mode family, with increasing β when moving towards lower growth rates (see § 3.15.1).

These results agree qualitatively well with the 2D-LST analysis of Paredes *et al.* [20], performed at the same frequency and streamwise position on a base flow with the same roughness geometry and size but at different freestream and wall-temperature conditions. In that study, the Mack mode is also the most unstable disturbance at the particular conditions considered, followed by the same antisymmetric perturbation here denoted by mode (b) and the varicose mode, although no sinuous instability is reported. In this work, the relationship between Mack-mode instabilities and the wake sinuous and varicose modes induced by the roughness is elaborated in § 5.3.

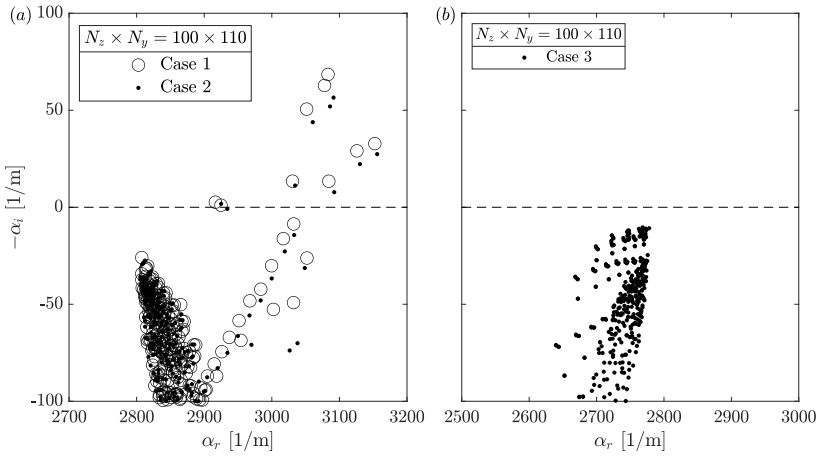

Figure 5.15: Spatial 2D-LST spectra for $f = 417.1$ kHz at $x = 0.0643$ m: (a) comparison between cases 1 and 2; (b) spectrum for case 3. For clarity, spurious numerical modes are not shown.

5.2.4.1 Effect of the self-similar boundary-layer assumption at the domain inflow

The self-similar boundary-layer profile imposed at the domain inflow in case 1 neglects the viscous-inviscid interaction that takes place at the sharp flat-plate leading edge, which induces a weak curved shock wake (see for example [2, Chapter 7]). Although small, the influence of this shock wave is still noticeable at the location of the domain inflow, as shown in the boundary-layer profiles for case 2 represented in figure 5.4. As discussed previously, figures 5.9 and 5.10 reveal that the base flow behind the roughness element is very similar for cases 1 and 2, but small differences can nonetheless be observed, with case 2 resulting in a slightly higher local boundary-layer thickness.

In order to examine the effect of the viscous-inviscid interaction that takes place at the sharp flat-plate leading edge on the stability of the roughness wake, the spatial stability spectra obtained for cases 1 and 2 are compared in figure 5.15(a). It can be seen that the weak shock induced at the flat-plate leading edge leads to a mild stabilization of the boundary layer as well as a small shift towards higher wavenumbers. Although the topology of the spectrum remains the same in both cases, all the discrete modes in case 2 have a lower growth rate than in case 1. Therefore, even if the leading-edge shock is weak, it induces a small entropy gradient that has a non-negligible impact on the stability of the flow field far downstream of the roughness element.

5.2.4.2 Effect of the flat plate leading-edge bluntness

A local analysis of the wake instability for case 3 allows to have a preliminary assessment of the influence of considering a blunt flat-plate leading edge. In this case, a large entropy layer is present in the flow field, which extends for a long distance downstream and severely affects the inviscid flow region above the boundary-layer edge (see the inflow profile represented in figure 5.4). Figure 5.15(b) presents the resulting spectrum obtained from the 2D-LST analysis at $f = 417.1$ kHz and $x = 0.0643$ m for case 3. No unstable modes have been retrieved for this particular configuration. As can be noticed in figures 5.9(c) and 5.10(c), the streamwise shear and the streamwise vorticity found behind the element in case 3 are signicantly smaller than in the other cases, already suggesting that the wake instability mechanisms might be considerably weaker. In order to confirm this result, on one side, a larger area of the 2D-LST spectrum has been scanned by performing stability computations with different shifts at a smaller resolution. On the other side, a LST analysis has been carried out for the boundary-layer profile far away from the roughness wake. None of the calculations have revealed unstable modes, so it is argued that the flow field is stable for this case at the particular frequency and streamwise position considered.

It is important to note that in order to characterize the effect of leading edge bluntness on the roughness wake instability, a complete study considering the streamwise and frequency evolution of the growth rate of the wake and boundary-layer modes would be necessary. This analysis has been left out of the scope of this work. The effect of the entropy layer on the linear stability of supersonic boundary layers over smooth blunt flat plates and wedges has been investigated for example by Balakumar [22]. The reported findings show that the entropy layer that induced by the bow shock generated in front of the blunt leading edge persists for a long distance downstream and leads to a strong stabilization of the boundary layer. For large nose-tip bluntness, however, experiments on blunt cones at high speed reveal an upstream movement of the transition location with increasing nose-tip radius (see Stetson [23]), known as transition reversal. The reasons for this behavior are not yet fully understood, and the study of transition mechanisms that could explain the early breakdown to turbulence observed in experimental investigations on blunt cones at hypersonic speeds remains a state-of-the-art topic, see for instance Paredes *et al.* [24].

5.2.4.3 Effect of the thermal wall boundary condition

The base flow obtained when considering an adiabatic flat plate (case 4) presents substantial differences with respect to the isothermal solution (case 1). As described before, the boundary layer is considerably thicker when the wall is assumed to be adiabatic (see figures 5.9(d) and 5.10(d)), leading to a smaller ratio

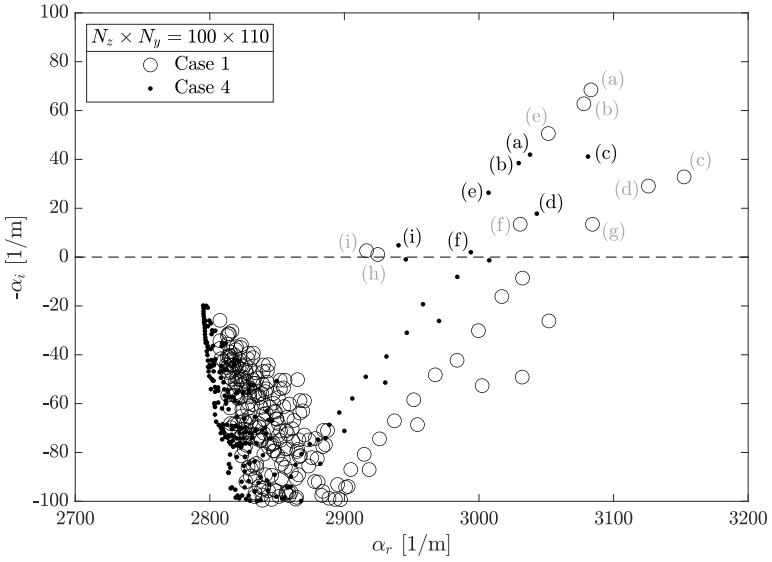

Figure 5.16: Comparison of the spatial 2D-LST spectra between case 1 and case 4 ($f = 417.1$ kHz, $x = 0.0643$ m). The letters inside parentheses label the different discrete unstable modes present in the spectrum and associate each of them with the corresponding amplitude function shown in figures 5.12 and 5.17. Letters in grey refer to case 1 whereas letters in black label the equivalent instability modes for case 4. Spurious numerical modes are not shown.

of roughness height to boundary-layer thickness as well as to a smaller roughness Reynolds number. The resulting shear magnitude and vorticity found within the roughness wake are significantly reduced with respect to the isothermal wall case. These differences are expected to yield a more stable wake with respect to case 1.

The results of the stability analysis performed for case 4 at $f = 417.$ kHz and $x = 0.0643$ m are displayed in figures 5.16 and 5.17, which respectively show a comparison of the spectra between cases 1 and 4 and the amplitude functions of the different unstable discrete modes obtained for case 4. As before, the letters in parenthesis identify the different unstable disturbances. The topology of the spectrum for the adiabatic wall configuration is similar to the isothermal case, but the relative importance between the dominant instability modes presents some differences. In general terms, the boundary layer is more stable in case 4, as expected owing to the smaller shear present in the wake, and there is a shift to smaller wavenumbers for almost all the instabilities. Focusing on the individual disturbances, the Mack mode (a) is once again the dominant perturbation, although with a lower growth rate than in case 1. This is consistent with the results of linear

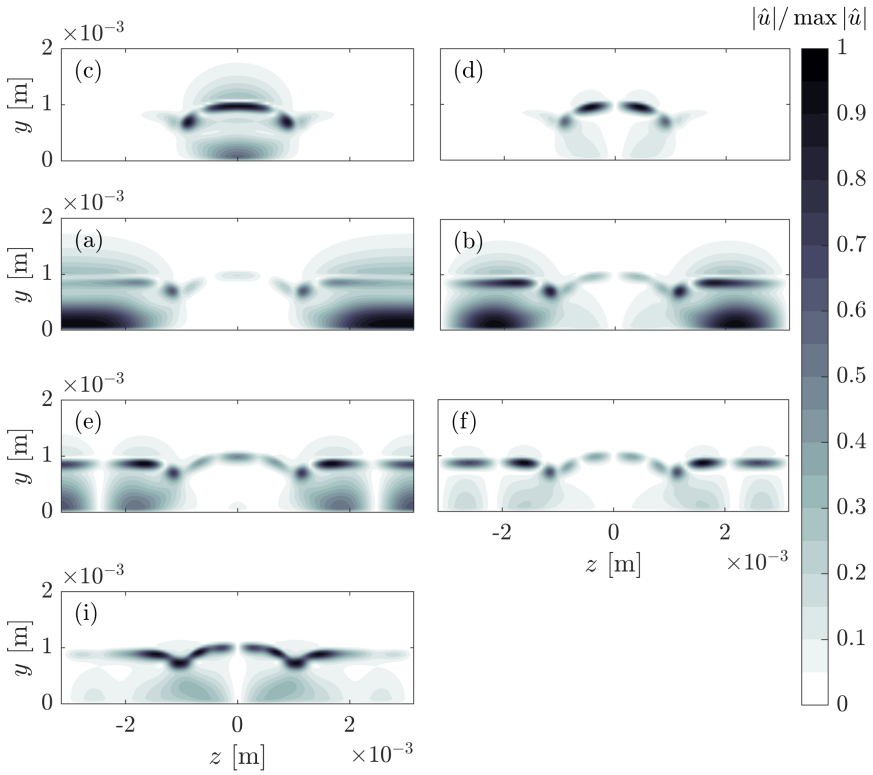

Figure 5.17: Contours of the normalized magnitude of the streamwise velocity eigenfunctions for case 4 ($f = 417.1$ kHz, $x = 0.0643$ m). The letters inside parentheses indicate the corresponding instability mode in the spectrum, as illustrated by the black labels in figure 5.16.

stability theory in smooth flat-plate configurations, see for instance Mack [25], for which it is well known that boundary-layer heating has a stabilizing effect on Mack's second mode.

The varicose mode (c), however, is found to be more unstable than in the isothermal case, this time featuring a very similar growth rate to that of the Mack mode, making it the second most unstable disturbance for this particular configuration. This behavior of the varicose mode is argued to be correlated with its region of amplitude development near the wall, as can be observed in figure 5.17. As suggested by De Tullio & Sandham [4] and further reported by Groskopf & Kloker [15], two distinct frequency ranges in which the varicose instability undergoes large amplification can be found in the roughness wake, which seem to respectively correlate with the frequency bands associated to the amplification of

Mack's first- and second-mode instabilities. When the amplitude function of the varicose mode features a region of high amplitude near the flat-plate wall, its range of amplification is found to be similar to that of Mack's second mode. In particular, the varicose mode at these conditions is found to be tuned with the boundary-layer thickness (see the behavior of mode VC (varicose-central) reported in [4]), in the same manner as Mack's second mode evolving in the flat plate boundary layer. Therefore, the thickening of the boundary layer when assuming adiabatic wall conditions has a significant impact on the varicose disturbance for the frequency under consideration. Nevertheless, it is important to mention that the varicose instability is found to behave in the opposite way to the second Mack mode with respect to base-flow heating, i.e., it becomes destabilized for higher boundary-layer temperatures. This is the same behavior observed by De Tullio & Sandham [4] for the varicose-central mode found in their analysis. In this work, the two different frequency ranges of development of the varicose mode are identified and discussed in § 5.3.

In contrast to the varicose perturbation, the sinuous mode (d) becomes less unstable than when considering an isothermal wall, following a similar trend to the majority of the instabilities found in the spectrum. Modes (b), (e) and (f) once again correspond to oblique disturbances of increasing spanwise number that are associated to the Mack mode. The last mode (i) is of the same kind as modes (h) and (i) in case 1, namely, a disturbance peaking at the interface between the streak, the roughness-induced vortices and the boundary layer at the sides of the roughness wake.

It is important to mention that the adiabatic wall configuration considered here does not employ a scaled roughness element height to maintain a constant Re_h. As a result, a considerably smaller Re_h is obtained in this case (see table 5.3), leading to a lower amplification of the instabilities. This means that in the comparison of cases 1 and 4, two different effects are present, namely, the influence of the wall-temperature condition and the effect of a lower roughness Reynolds number. To have an assessment of pure wall-temperature effects, the roughness size should be increased to keep Re_h constant, as done for instance by De Tullio & Sandham [4]. Nonetheless, the effect of decreasing Re_h is believed to be purely stabilizing for the disturbances, while the effect of using a different wall-temperature condition is the responsible for the varicose-mode destabilization described above. The effect of the boundary-layer heating on the other wake modes, such as the sinuous mode (d) cannot be distinguished from the effect of having a different Re_h in this analysis.

5.3 Streamwise evolution of the instabilities induced by a cuboidal and a ramp-shaped roughness element

The second analysis presented in this chapter considers the streamwise evolution of instabilities along the wake induced by an isolated roughness element. Although the same geometrical configuration as in the previous cases is considered, different dimensions and roughness location are used here, yielding a slightly different roughness Reynolds number. The previously described analysis constitutes a test case for establishing and verifying the methodology for performing 2D-LST stability computations behind a discrete roughness element, and describes the topology of the instabilities and their sensitivity to different factors at a fixed streamwise station and frequency. However, it does not allow to issue concluding remarks on which are the instabilities governing the transition process in terms of integrated amplification factors. The study presented in the following discusses the evolution of the leading disturbances in the roughness wake and examines the energy extraction mechanisms that lead to their excitation.

5.3.1 Geometrical parameters and case definition

For this analysis, the two different roughness geometries presented in figure 5.2 are considered and compared, namely, a cuboidal roughness element and a ramp-shaped roughness element. The dimensions of the computational domain are the same for both roughness geometries and are summarized in table 5.4, which lists the streamwise coordinate and height of the inlet (x_{in}, y_{in}) and outlet (x_{out}, y_{out}) planes of the domain, as well as the spanwise domain size (z_∞), which is constant. Both roughness elements have a height of $h = 0.4$ mm and their leading edge is located at a streamwise distance of $x_h = 60$ mm from the flat-plate leading edge. Their length is determined according to the ramp angle θ as $d = h/\tan(\theta)$, with $\theta = 10$ degrees. The resulting roughness Reynolds number for this configuration, based on a self-similar boundary-layer profile at x_h, is $Re_h = 330$ ($Re_{h,w} = 300$). The corresponding ratio of roughness height to local boundary layer thickness is $h/\delta_{99} = 0.59$, where δ_{99} is once again estimated by applying the total enthalpy criterion ($h_0/h_{0,\infty} = 0.995$) in the self-similar boundary-layer profile. The Reynolds number based on the displacement thickness of the boundary layer at the domain inflow is $Re_{\delta_1} = 14847$.

The chosen roughness Reynolds number is almost identical to the one used in the DNS analysis of De Tullio & Sandham [4], which considers a cuboidal roughness. The present cuboid configuration is therefore very similar to that of [4], the main difference being the freestream and wall-temperature employed. In the current case, the wall is chosen to be isothermal with $T_w = 300$ K, whereas in De

x_{in} [mm]	x_{out} [mm]	y_{in} [mm]	y_{out} [mm]	z_∞ [mm]
50	400	7.69	88.49	15

Table 5.4: Dimensions of the second computational domain considered in this chapter. The origin is located at the flat-plate leading edge.

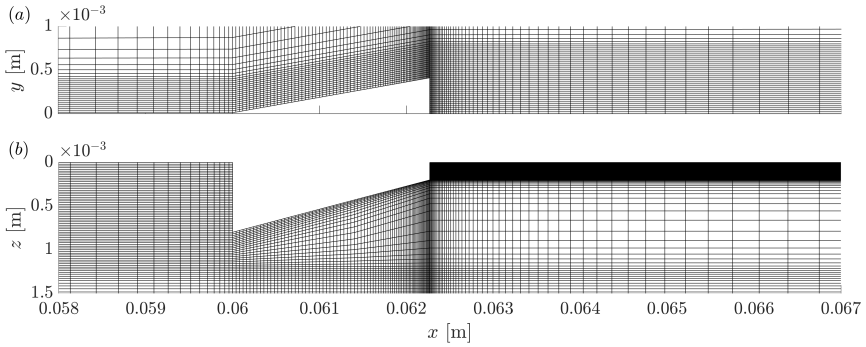

Figure 5.18: Computational grid employed for the ramp roughness geometry: (a) xy plane at $z = 0$; (b) xz plane at $y = 0$. For representation purposes, only every eight grid points are shown along the wall-normal direction, and every two points along the streamwise and spanwise directions.

Tullio & Sandham [4] it is fixed to $T_w = T_{ad} = 1942$ K, which corresponds to the adiabatic wall temperature according to the conditions chosen in their work. Despite the different thermal wall boundary condition, the similarity in the roughness geometry and roughness Reynolds number allows for qualitative comparison between both cases, similarly to the results presented in § 5.2.

The base flows studied in the remaining part of this chapter employ a non-constant Prandtl number, which is obtained as a result of applying Sutherland's law for both viscosity and thermal conductivity as described in § 2.5.2.1.

5.3.2 Computational grids

The computational grids used to obtain the base-flow solutions in the current configuration are also block-structured and consist of hexahedral cells. As in the previous cases analyzed, for both roughness geometries the grid is clustered towards the element in all directions as well as towards the flat plate wall. The reference grid resolution employed for each case in every direction is summarized in table 5.5, resulting in a total number of 65 million cells for the cuboid element and 76 million cells for the ramp geometry. The grid near the cuboidal roughness is almost identical to the one shown in figure 5.5. The grid in the vicinity of the

Roughness geometry	Reference			Coarse		
	N_x	N_y	N_z	N_x	N_y	N_z
Cuboid	1001	351	191	751	264	144
Ramp	841	421	231	632	316	174

Table 5.5: Grid resolution employed for the base-flow computations. The quantities N_x, N_y and N_z denote the number of grid points along each spatial direction.

ramp element is illustrated in figure 5.18. It important to emphasize that the side surface of the ramp geometry is a triangle. In order to mesh this surface employing quadrilaterals, the triangle is split into three quadrilaterals at its centroid.

In order to check for grid convergence, the numerical base-flow solutions are also computed on coarser grids generated by reducing by one-fourth the number of points in each direction (along every edge of the block structure). The coarser grid resolution is also reported in table 5.5. Results for both grid resolutions are compared in figure 5.19. A very good agreement is obtained between the quantities computed with both grids for each roughness geometry, indicating a satisfactory grid convergence of the base-flow solutions. The analyses presented further below have been carried out employing the Navier-Stokes solutions obtained in the finer (reference) grid for each roughness.

5.3.3 Base-flow solutions

The main features of the base-flow solutions computed for each roughness geometry are displayed in figure 5.20. These flow fields bear strong resemblance to those presented in § 5.2.3, therefore most of their relevant physical characteristics have already been described. In this section, the attention is mainly focused on the differences between both roughness geometries.

Owing to the planform shape of the ramp geometry (see figure 5.2), the roughness width at the trailing edge is one-fourth of that at the leading edge. This variation results in a small region of recirculating fluid downstream of the obstacle and, as a consequence, the size of the downstream recirculation bubble is much larger for the cuboid geometry than for the ramp. Upstream of the roughness element, only the cuboidal geometry induces a separation region. The ramp-shaped element leads to a much weaker compression of the flow and no upstream detachment occurs.

The Mach number contours shown in figures 5.20(a, c) illustrate that both elements generate a very similar system of compression and expansion waves. The oblique shock relations confirm once again that the reattachment compressive wave induced downstream of the elements is an actual weak oblique shock for both roughness geometries. Figures 5.20(b, d) depict the topology of the stream-

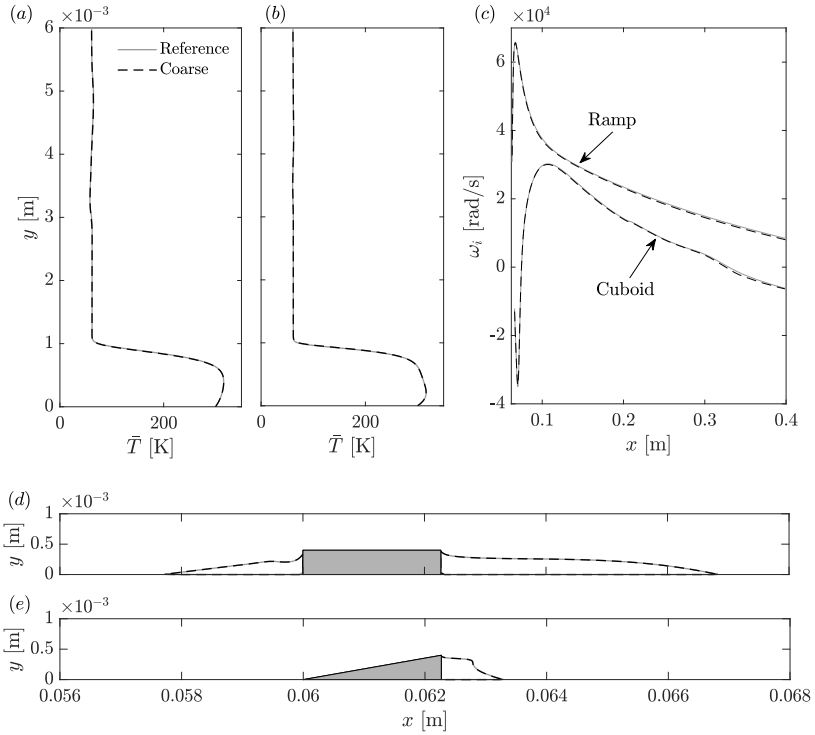

Figure 5.19: Convergence of results with respect to the base-flow grid resolution: temperature profiles at $x = 0.1$ m and at the roughness symmetry plane ($z = 0$) for (a) the cuboid and (b) the ramp roughness geometries; (c) temporal growth rate as a function of the streamwise direction for a sinuous wake instability of wavelength $\lambda_x = 0.325$ cm (cuboid) and $\lambda_x = 0.86$ cm (ramp); shape of the recirculation bubbles induced by (d) the cuboid and (e) the ramp element at the roughness symmetry plane, represented as isolines of $\bar{u} = 0$.

wise velocity streaks that characterize the wake behind the roughness elements. Comparing both roughness shapes, the lateral angle of the ramp geometry leads to a narrower low-velocity streak as compared with that of the cuboid. The two high-velocity streaks originating at the sides of the elements become very close to each other in the case of the ramp configuration.

To better illustrate the differences in the flow structure inside the wake behind the elements, the streamwise shear magnitude, defined in equation (5.7), and the streamwise vorticity, given by equation (5.8), are also examined in cross-flow (y-z) planes. Figures 5.21 and 5.22 respectively display contour plots of these two parameters at three different streamwise locations for each roughness geometry. Both geometries induce a counter-rotating vortex pair that generates a three-dimensional

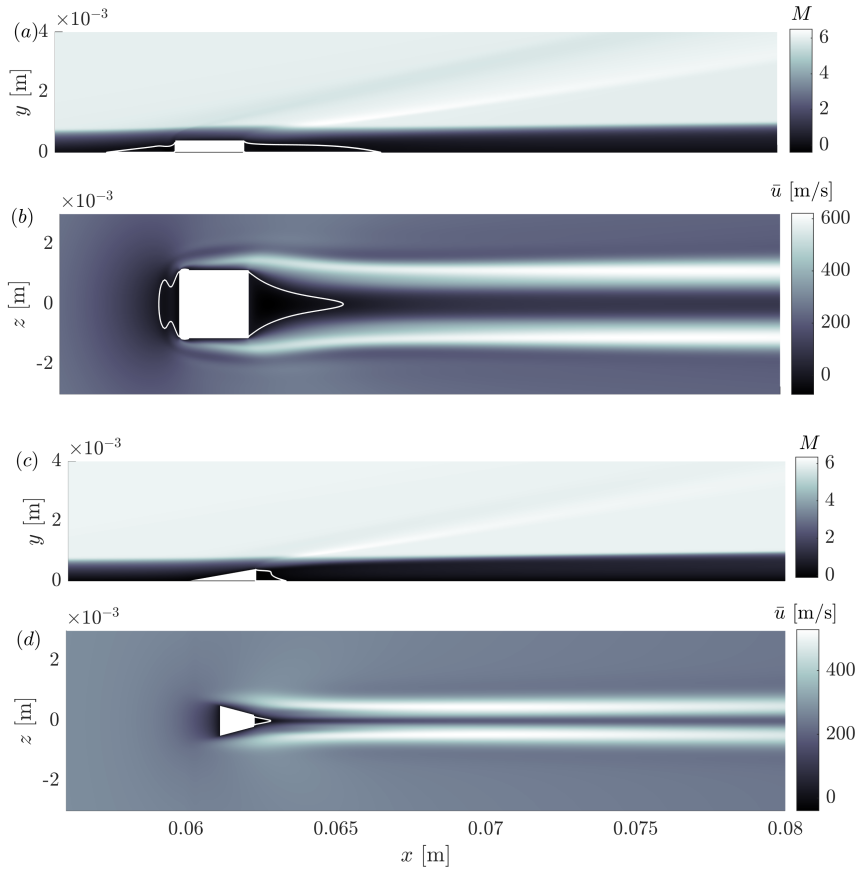

Figure 5.20: Main features of the laminar base-flow solution obtained for each roughness element: (a, c) Mach number contours at the roughness symmetry plane ($z = 0$); (b, d) streamwise velocity contours in the x-z plane located at half of the roughness element height ($y = h/2$). The white solid lines indicate isolines of $\bar{u} = 0$, which delimit regions of separated flow.

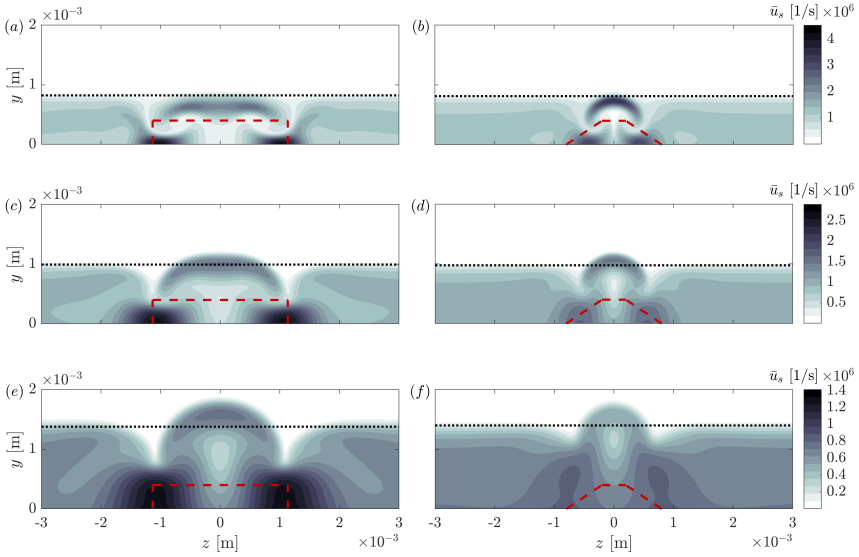

Figure 5.21: Contours of base-flow streamwise shear magnitude for the cuboid (a, c, e) and the ramp (b, d, f) roughness geometries at three different streamwise locations: (a, b) $x = 0.07$ m; (c, d) $x = 0.1$ m; (e, f) $x = 0.2$ m. The dashed lines represent a projection of the roughness element and the dotted lines denote the local boundary-layer thickness.

high-shear layer that surrounds the central, low-velocity streak, as described in § 5.2.3. The thickness of the low-velocity streak is found to grow with the boundary layer. As a consequence, the shear that surrounds it progressively decreases in magnitude downstream, as the vortices lose strength due to dissipation and the differences in velocity between the streaks and the outer flow become smaller. At a streamwise station of $x = 0.2$ m, the shear in the layer surrounding the central streak has already become approximately of the same magnitude as the shear developing in the boundary layer outside of the roughness wake for both roughness geometries (see figures 5.21(e, f)).

An important observation is that the ramp element induces a three-dimensional shear layer around the central streak which features the same shear magnitude as the high-shear regions near the wall (see figures 5.21(b, d)). This is in contrast to the cuboidal geometry, for which the shear enclosing the low-velocity streak is of smaller magnitude than that close to the wall, as illustrated in figures 5.21(a, c, e), despite the maximum values of $\bar{u}_s$ being higher for the cuboid configuration. This suggests that the lift-up effect is stronger for the ramp case, which could be explained by the fact that the counter-rotating vortices are closer to each other due to the smaller spanwise extent of the ramp geometry. The regions of development of streamwise vorticity shown in figure 5.22 further support this argument, i.e., for

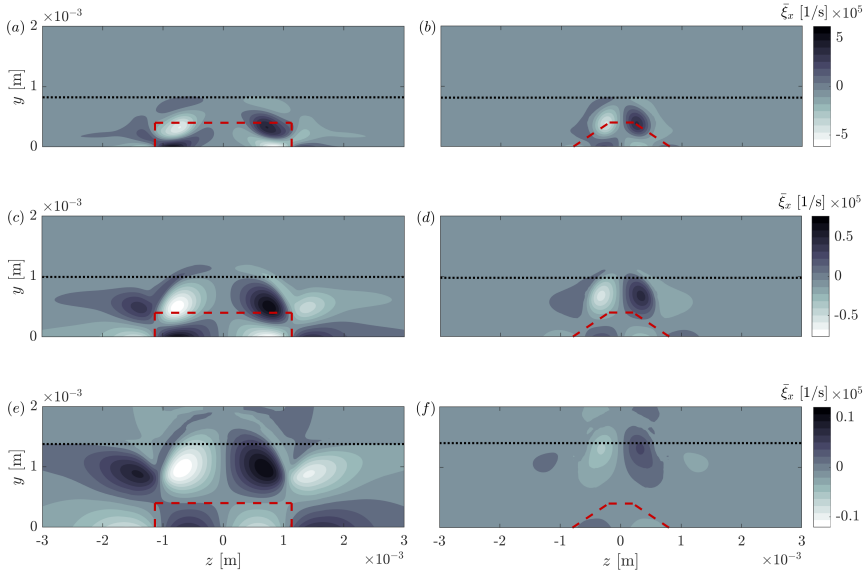

Figure 5.22: Contours of base-flow streamwise vorticity for the cuboid (a, c, e) and the ramp (b, d, f) roughness geometries at three different streamwise locations: (a, b) $x = 0.07$ m; (c, d) $x = 0.1$ m; (e, f) $x = 0.2$ m. The dashed lines represent a projection of the roughness element and the dotted lines denote the local boundary-layer thickness.

the ramp case these regions are concentrated in a narrower area, and the vortical structures are more elongated.

A comparison of the strength of the roughness wake along the streamwise direction for both obstacle geometries is provided in figure 5.23, which shows the evolution of the local in-plane maxima of relevant flow quantities. The maximum streamwise vorticity, represented in figure 5.23(a), decreases very fast in the vicinity of the roughness elements and then follows an exponential decay. In line with the contour plots represented in figure 5.22, the counter-rotating vortex pair induced by the cuboid geometry features a higher streamwise vorticity than that of the ramp. Figure 5.23(b) shows the evolution of the streak amplitude, which is a measure of the strength of the low-velocity streak developing in the wake. In the figure, the same definition used by [4] is employed, given by

$$\Delta\bar{u}_{st}(x) = \max_{y}[\bar{u}(x, y, z_\infty) - \bar{u}(x, y, 0)]. \tag{5.9}$$

For the cuboidal roughness, it can be noticed that although the wake streamwise vorticity decreases monotonically, the streak amplitude undergoes an increase right after the trailing edge separation bubble. This behavior could be interpreted according to the development of the lift-up effect. As the streamwise counter-rotating

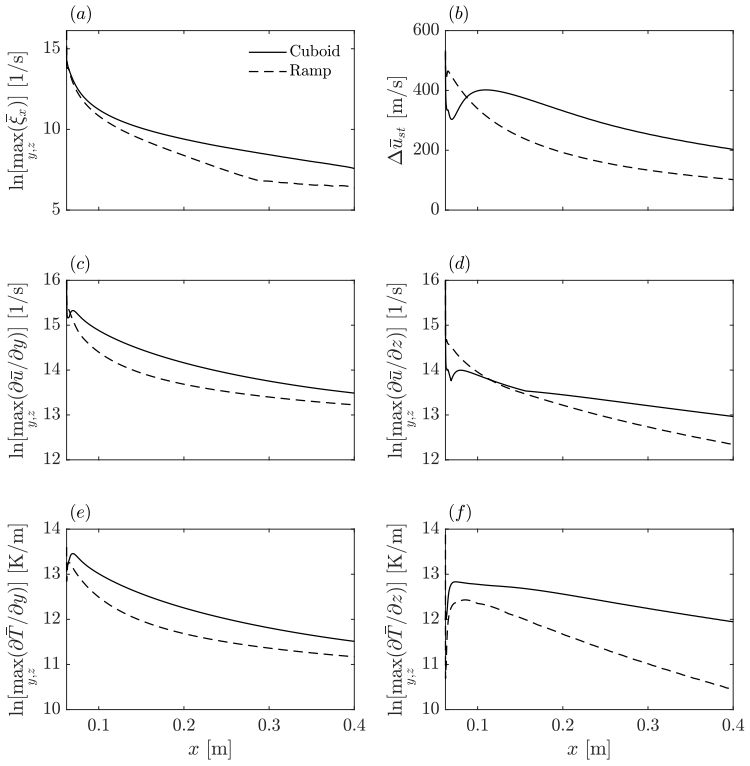

Figure 5.23: Streamwise evolution of different base-flow quantities along the wake for both roughness geometries: (a) maximum streamwise vorticity at each y-z plane; (b) streak amplitude as given by equation (5.9); (c, d) maximum wall-normal and spanwise gradients of the streamwise velocity at every cross-flow plane; (e, f) maximum wall-normal and spanwise temperature gradients at each y-z plane. The initial streamwise location corresponds to the trailing edge of the roughness elements.

vortices are forming, the lift-up progressively increases until reaching a maximum strength. Then, as the dissipation of the vortex intensity becomes more significant, its effect is progressively reduced and the streak amplitude starts to decrease at a nearly constant rate. For the ramp geometry, the streak amplitude begins to decay almost immediately after the roughness trailing edge and does not feature the transient-growth behavior observed for the cuboid. Using this definition of the streak amplitude, the resulting streak strength for the ramp obstacle is higher than for the cuboid up to a streamwise distance of $x \approx 0.1$ m. The $\Delta\bar{u}_{st}$ signature obtained for the cuboid geometry features a strong similarity with that reported by De Tullio & Sandham [4]. Note, however, that the curve reported in [4] covers a

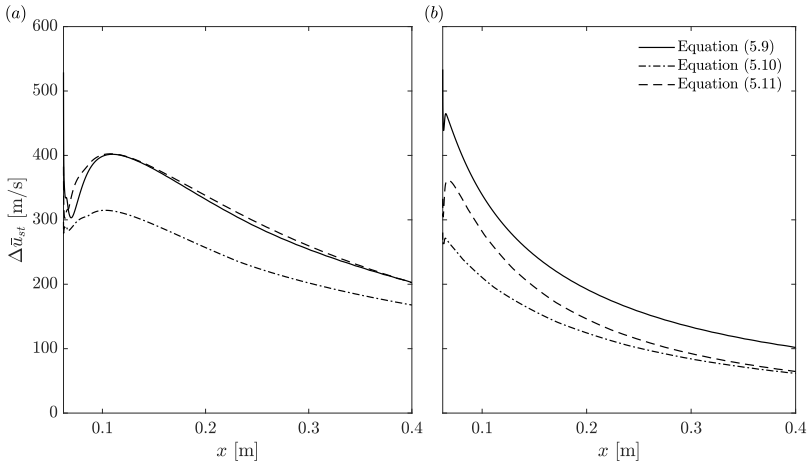

Figure 5.24: Streamwise evolution of the streak amplitude for the cuboid (a) *and the ramp* (b) *roughness geometries using the three different definitions given by equations* (5.9)*,* (5.10) *and* (5.11)*.*

much smaller streamwise range (approximately 18 times the roughness length, i.e. up to $x \approx 0.1$ m) than the one shown in figure 5.23(b).

The maximum wall-normal shear, displayed in figure 5.23(c), also decreases monotonically downstream of the trailing edge recirculation bubble for both elements, progressively adopting an exponential decay rate as the wake evolves downstream. The cuboid shape features larger values than the ramp in this case. On the other hand, the maximum spanwise shear (figure 5.23(d)) is initially larger for the ramp element but undergoes a faster decrease than the cuboid. The maximum wall-normal temperature gradient follows the same trend as the wall-normal shear, as shown in figure 5.23(e). The maximum spanwise temperature gradient (figure 5.23(f)) features an algebraic growth immediately behind the roughness trailing edge in both cases and once again adopts an exponential decrease further downstream, remaining larger for the cuboid element along all the wake region investigated. It is worth noting that for the ramp obstacle, the maximum spanwise gradients decay at a higher rate than the respective wall-normal derivatives.

Other authors employ different definitions for $\Delta\bar{u}_{st}$, which are based on the difference between the local maximum and minimum deviations of $\bar{u}$ instead of considering only the maximum deviation. For instance, De Tullio *et al.* [3] evaluate the streak amplitude according to the difference between the local maximum and minimum in $\bar{u}$ with respect to the roughness symmetry plane, that is

$$\Delta\bar{u}_{st}(x) = \frac{1}{2}\left\{\max_{y,z}[\bar{u}(x,y,z) - \bar{u}(x,y,0)] - \min_{y,z}[\bar{u}(x,y,z) - \bar{u}(x,y,0)]\right\}. \tag{5.10}$$

Similarly, the definition used by Theiss *et al.* [5] and Stemmer *et al.* [26] relies on the difference between local maxima and minima compared to the undisturbed flow, which in this case can be assumed to be the flow far outside of the roughness wake, i.e.,

$$\Delta\bar{u}_{st}(x) = \frac{1}{2}\left\{\max_{y,z}[\bar{u}(x,y,z) - \bar{u}(x,y,z_\infty)] - \min_{y,z}[\bar{u}(x,y,z) - \bar{u}(x,y,z_\infty)]\right\}. \tag{5.11}$$

The resulting streak amplitudes using each of the three different definitions presented are compared for each roughness geometry in figure 5.24. The definition given by equation (5.10) leads to a smaller streak amplitude over all the domain for both roughness geometries, but the trend of the curves is preserved with respect to the results obtained with the definition (5.9). On the other hand, equation (5.11) leads to a very similar signature as equation (5.9) for the cuboid but to a smaller streak strength for the ramp, once again preserving the same trend. The magnitude of the streak amplitude for the ramp case using (5.11) lies between that provided by the other two definitions.

5.3.4 Temporal stability spectrum

This section and the remaining ones in this chapter present the results obtained from the stability analysis and the temporal growth-rate decomposition of the instabilities developing in the wake induced behind the two isolated roughness element geometries considered. All the stability results shown in the following have been computed employing the FD-q discretization technique introduced in § 4.2.1.2, using a polynomial order of $q_p = 8$, which is deemed to provide an appropriate trade-off between accuracy and computational cost for the problem under consideration (see for instance [3, 5]). For this study, periodic boundary conditions are imposed on the spanwise domain boundaries to allow for the computation of symmetric and antisymmetric disturbances from the solution of the same eigenvalue problem. Therefore, the complete spanwise domain is considered in the 2D-LST calculations.

Along the spanwise direction, the biquadratic mapping presented in § 4.2.2.2 is employed, whereas along the wall-normal coordinate the transformation introduced by Malik (see equation (4.16)) is used. According to the obtained base-flow

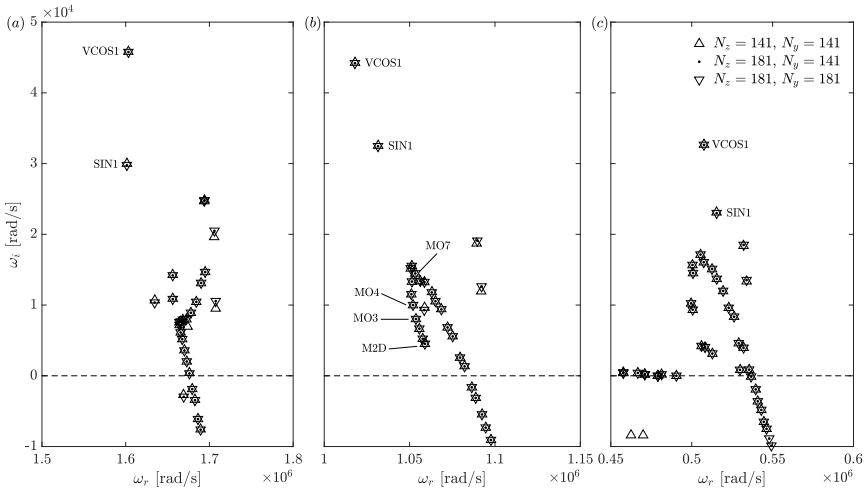

Figure 5.25: Most relevant region of the temporal 2D-LST spectrum for the cuboid roughness geometry at $x = 0.1$ m for three different streamwise wavelengths: (a) $\lambda_x = 0.325$ cm; (b) $\lambda_x = 0.5$ cm; (c) $\lambda_x = 1$ cm.

solutions, the following mapping parameters are selected for the stability analyses: $y_{max} = y_\infty$ and $y_i = 20l$ for both roughness geometries, $z_{max} = -z_{min} = 25h$ and $z_{i2} = -z_{i1} = 10h$ for the cuboid configuration and $z_{max} = -z_{min} = 17.64h$ and $z_{i2} = -z_{i1} = 7.05h$ for the ramp element. The quantity y_∞ denotes the domain height of the computational domain used to obtain the base-flow solution at each streamwise location. Since the width of the roughness wake remains constant along the entire domain length, the spanwise parameters are kept fixed along the streamwise direction. On the other hand, the parameter y_i is set to be proportional to the length scale l (see equation (2.16)) in the wall-normal direction to account for the boundary-layer growth along x. The value of y_{max} also evolves along the streamwise direction, and ranges between $y_{max} = 28.45h$ at the first location analysed behind the roughness elements and $y_{max} = 92.94h$ at the end of the domain.

The temporal spectra shown in this section have been obtained by means of the implicitly restarted Arnoldi algorithm, computing 50 eigenmodes for each case and using non-dimensional values of the shift-invert parameter ranging between $\sigma = 0.85\alpha_r$ and $\sigma = 0.95\alpha_r$.

In the first place, the temporal stability characteristics of the base flow are studied. Temporal 2D-LST computations have been carried out along the wake induced behind each roughness element for different streamwise wavelengths ($\lambda_x = 2\pi/\alpha_r$). Figures 5.25 and 5.26 show the most relevant portion of the temporal stability spectrum for each roughness shape obtained at a streamwise location of

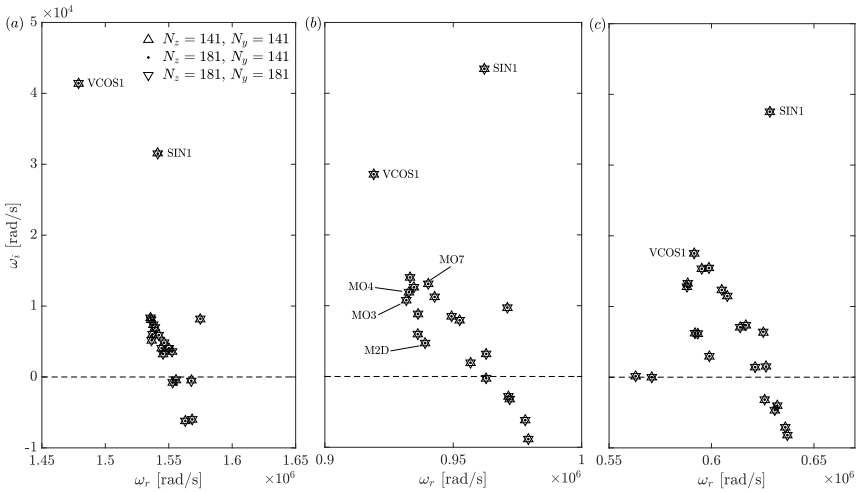

Figure 5.26: Most relevant region of the temporal 2D-LST spectrum for the ramp roughness geometry at $x = 0.1$ m for three different streamwise wavelengths: (a) $\lambda_x = 0.35$ cm; (b) $\lambda_x = 0.56$ cm; (c) $\lambda_x = 0.86$ cm.

$x = 0.1$ m and for three different streamwise wavelengths. The results for three different grid resolutions are included to illustrate grid convergence of discrete modes. For both roughness geometries, two dominant converged discrete instability modes can be identified, labelled as VCOS1 and SIN1. These modes respectively correspond to the most unstable varicose and sinuous instabilities developing in the roughness wake. The three different streamwise wavelengths chosen for each geometry cover the range of largest temporal amplification for modes VCOS1 and SIN1 at $x = 0.1$ m, presented in figure 5.27 for $x = 0.1$ m. Their values were selected in order to provide an adequate description of the topology of the spectrum and of the associated amplitude functions at the most relevant wavelengths for each instability. As shown in figure 5.27(a), the varicose perturbation related to the cuboidal element features a higher growth rate than the sinuous one for most of the studied wavelengths. For the ramp-shaped roughness, however, the varicose mode dominates only for the smaller wavelengths ($\lambda_x < 0.4$ cm), while the sinuous disturbance becomes the leading instability for higher ones. Similarly to figure 5.27, figure 5.28 represents the growth rate of modes SIN1 and VCOS1 as a function of the resulting temporal frequency, obtained as a solution of the temporal eigenvalue problem. This figure provides a quantitative point of view on the magnitude of the frequencies at which the wake instabilities are excited in the problem under study, which helps to visualize the relationship between the temporal and the spatial stability results presented later on.

The two-dimensional streamwise velocity amplitude function associated to

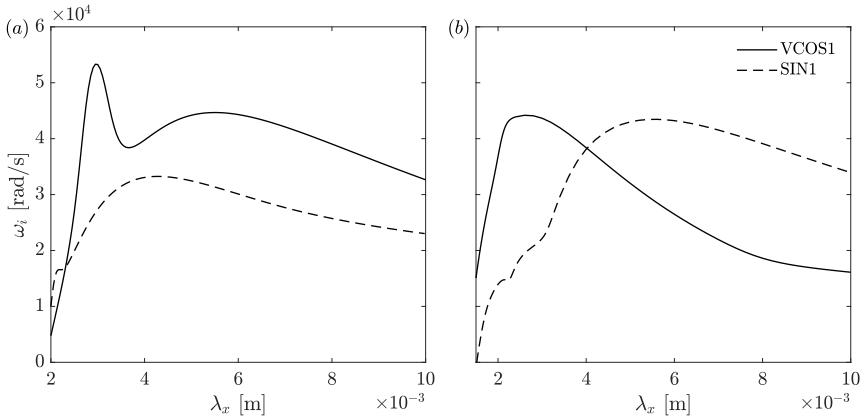

Figure 5.27: Temporal growth-rate evolution of the most unstable wake modes for each roughness geometry as a function of the streamwise wavenumber at $x = 0.1$ m: (a) cuboid; (b) ramp.

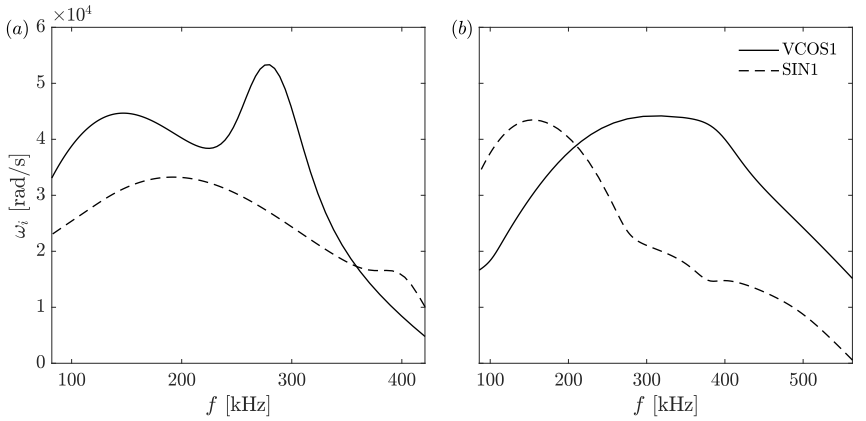

Figure 5.28: Temporal growth-rate evolution of the most unstable wake modes for each roughness geometry as a function of the resulting frequency at $x = 0.1$ m: (a) cuboid; (b) ramp.

each of these disturbances is displayed in figure 5.29 for the cuboid element and in figure 5.30 for the ramp. As described in § 5.2.4, both instabilities mainly develop within the high-shear layer surrounding the low-velocity streak that characterizes the wake flow structure. The sinuous mode can be distinguished by its antisymmetric amplitude function with respect to the roughness mid-plane, which translates in a zero magnitude of the amplitude at $z = 0$, while the varicose mode is characterized by a symmetric eigenfunction. For both roughness geometries, the biggest amplitude magnitude of the sinuous mode is concentrated in the up-

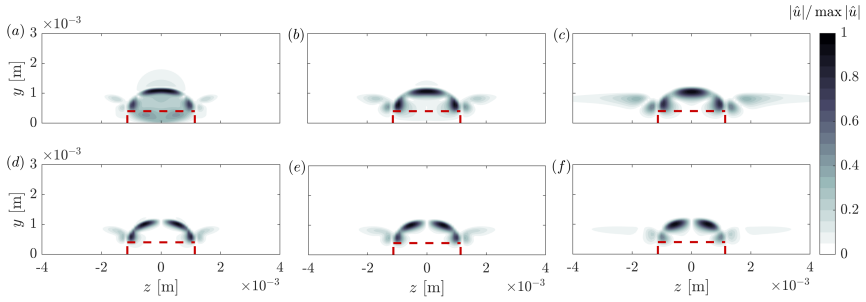

Figure 5.29: Normalized magnitude of the streamwise velocity amplitude function for the most unstable varicose and sinuous modes (VCOS1 and SIN1) developing behind the cuboidal roughness element at $x = 0.1$ m, for three different streamwise wavelengths: (a, d) $\lambda_x = 0.325$ cm; (b, e) $\lambda_x = 0.5$ cm; (c, f) $\lambda_x = 1$ cm; (a, b, c) VCOS1 mode; (d, e, f) SIN1 mode.

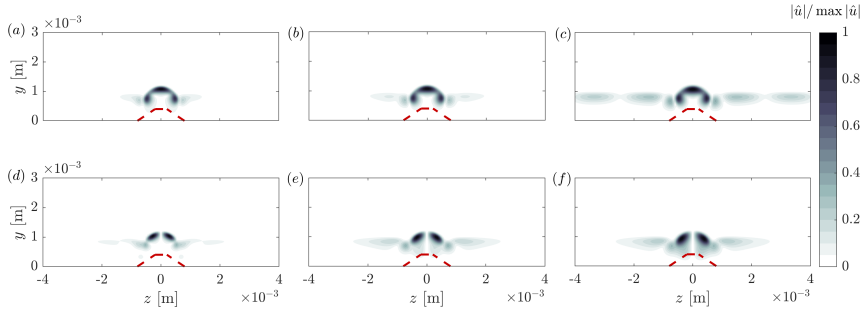

Figure 5.30: Normalized magnitude of the streamwise velocity amplitude function for the most unstable varicose and sinuous modes (VCOS1 and SIN1) developing behind the ramp roughness element at $x = 0.1$ m, for three different streamwise wavelengths: (a, d) $\lambda_x = 0.35$ cm; (b, e) $\lambda_x = 0.56$ cm; (c, f) $\lambda_x = 0.86$ cm; (a, b, c) VCOS1 mode; (d, e, f) SIN1 mode.

per regions of the low-velocity streak that are located right above the core of each counter-rotating vortex, as indicated by the streamwise vorticity contours in figure 5.22. According to figure 5.21, these regions are associated with the highest shear magnitude within the central streak. A second peak in amplitude is also found at the outward side of each vortex, which coincides with the interface between the high-shear regions near the wall and the sides of the low-velocity streak, where a sudden decrease in shear magnitude is encountered. Similarly, the varicose instability features the main region of amplification in the upper central region of the streak, located above and between the vortex pair and strongly correlating with the region of high-shear magnitude surrounding the central streak. Secondary amplitude peaks are once again visible at each side of the vortex cores, associated

as well to the strong shear gradients established a the sides of the low-velocity streak. These observations are in good agreement with the disturbance shapes reported by other authors in similar configurations, both employing DNS and linear stability theory (see for instance [3, 4, 27, 28]).

For the cuboid configuration at $\lambda_x = 0.325$ cm, besides evolving in the three-dimensional shear layer, the varicose perturbation also grows significantly inside the low-velocity streak in a region close to the flat-plate wall. The amplitude function of this mode shows strong similarities with that of mode VC (varicose-central) reported by De Tullio & Sandham [4] through DNS computations in a very similar set-up, as discussed in § 5.2.4.3. This difference in the region of development of the varicose mode between the results obtained at $\lambda_x = 0.325$ cm (figure 5.29(a)) and those obtained for $\lambda_x = 0.5$ cm or $\lambda_x = 1$ cm (figure 5.29(b, c)) correlates with the two distinct peaks in growth rate that can be observed in figure 5.27(a). This behavior, already reported by Groskopf & Kloker [15], can be attributed to two different manifestations of the varicose mode instability depending on whether the instability modes evolving in the flat plate boundary-layer, which also interact with the roughness wake, behave as first or second Mack-mode instabilities, as discussed further below. Therefore, as introduced by [15], a distinction can also be made between varicose first- and second-mode disturbances in this case. This distinction is the responsible for the two varicose instabilities observed in the DNS analysis of De Tullio & Sandham [4], respectively labeled as modes VL and VC in their work.

Alongside the varicose and sinuous perturbations, several other unstable modes are found in the obtained spectra. Most of these modes are distributed in an ordered fashion along the complex plane. In fact, such instabilities belong to the family of Mack modes (first or second modes) developing in the flat-plate boundary layer, which are modulated by the presence of the roughness element. These disturbances are part of a continuous branch consisting of Mack modes representing the infinite spanwise wavenumbers (β) that are part of the 2D-LST spectrum (see § 3.15.1). Only those spanwise wavenumbers that can be resolved by the discretization of the eigenvalue problem along the spanwise direction (mainly defined by the domain size and grid resolution) are retrieved by the current numerical solution. The shape of this branch is different depending on the streamwise wavelength considered. The initial mode of the family is always a mode with spanwise wavenumber $\beta = 0$, denoted by M2D, followed by oblique modes with a progressively increasing spanwise wavenumber. Depending on the conditions analysed, the shape of the branch in the 2D-LST spectrum tells whether it manifests itself as Mack's first or second mode. In the case of Mack's first mode, the most unstable mode in the family is oblique for the flow conditions under study. As a result, the growth rate of the modes along the branch first increases progressively until reaching the spanwise wavenumber for maximum growth and then progressively decreases for

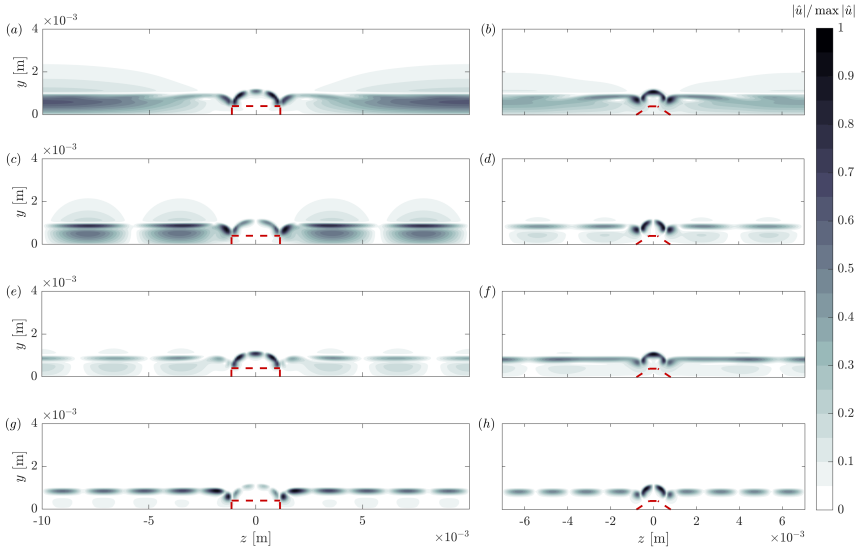

Figure 5.31: Normalized magnitude of the streamwise velocity amplitude function for different Mack modes developing behind each roughness geometry at $x = 0.1$ m: (a, b) two-dimensional Mack mode (M2D); (c, d) oblique Mack mode MO3; (e, f) oblique Mack mode MO4; (g, h) oblique Mack mode MO7; (a, c, e, g) $\lambda_x = 0.5$ cm; (b, d, f, h) $\lambda_x = 0.56$ cm.

higher values of β. This behavior leads to the hook-shaped branch that can be observed in figures 5.25(b, c) and 5.26(b, c). For conditions at which the branch behaves as Mack's second mode, the most unstable mode in the family is the two-dimensional one (M2D), and the growth rate of the oblique modes progressively decreases as β increases. The shape of the branch in this case becomes a diagonal line, similar to the one shown in figure 5.25(a). Figure 5.26(a) corresponds to conditions in which the branch shape is transitioning from first to second mode.

To illustrate the topology of the instabilities along the Mack-mode branch, figure 5.31 shows the streamwise velocity amplitude function of the two-dimensional Mack mode (M2D) and of three oblique Mack modes for the cuboid geometry at $\lambda_x = 0.5$ cm and for the ramp element at $\lambda_x = 0.56$ cm. The oblique modes are respectively denoted by MO3, MO4 and MO7 according to their position along the branch (see figures 5.25(b) and 5.26(b)). As it can be observed, the amplitude function of these modes is highly modulated by the roughness wake. Far away from the wake along the z direction (approximately $z > 0.005$ m), the amplitude of mode M2D becomes approximately constant with respect to the spanwise direction, whereas in the wall-normal direction it adopts the shape of the classical Mack instability mode as predicted by one-dimensional local linear stability the-

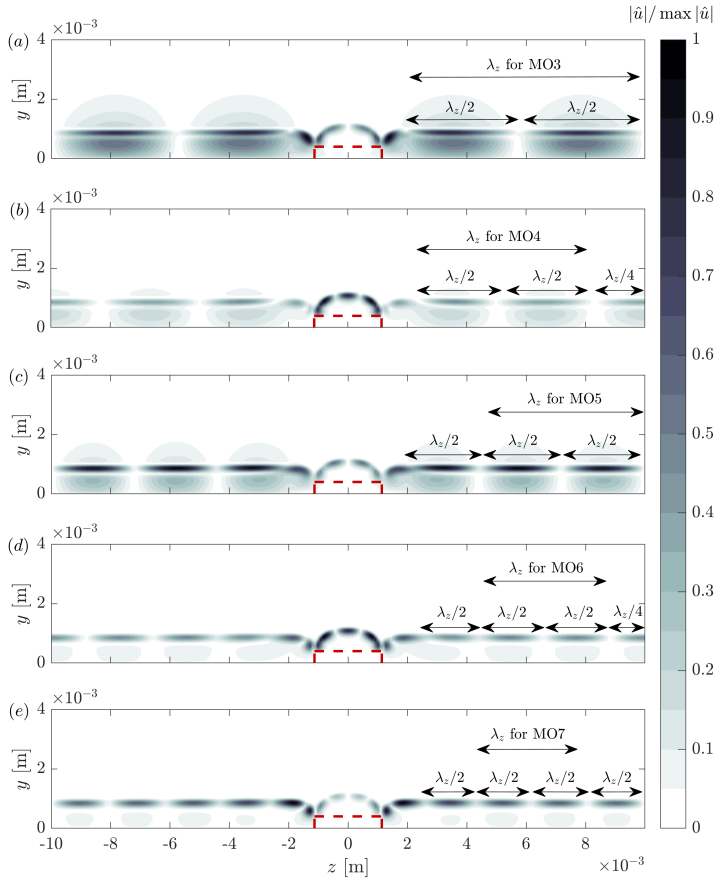

Figure 5.32: Normalized magnitude of the streamwise velocity amplitude function for different oblique Mack modes developing in the cuboid wake at $x = 0.1$ m: (a) oblique Mack mode MO3; (b) oblique Mack mode MO4; (c) oblique Mack mode MO5; (d) oblique Mack mode MO6; (e) oblique Mack mode MO7. The spanwise wavelength for each case is indicated by the arrows, together with the fractions of the spanwise period associated to each of the spanwise structures present inside the domain.

ory in a smooth flat plate boundary-layer. Therefore, the eigenfunction of mode M2D consists of a blend between an eigenfunction that evolves exclusively inside the roughness wake and the eigenfunction of a classical two-dimensional Mack mode.

Similarly, the oblique modes MO3, MO4 and MO7 adopt a periodic spanwise evolution outside of the roughness wake. The spanwise wavelength ($\lambda_z = 2\pi/\beta$) associated to this periodicity is different for each mode. According to the periodic boundary conditions enforced in the eigenvalue problem and the spanwise

symmetry of the base flow, the values of λ_z that can be resolved by the discretization are constrained by the distance between the edge of the roughness wake (in this case located approximately at $z = \pm 0.002$ m for the cuboid geometry and at $z = \pm 0.001$ m for the ramp, see figures 5.21(c, d)) and the spanwise boundary of the domain. For instance, mode MO3 adopts a spanwise wavelength that is precisely equal to the distance between the edge of the roughness wake and the spanwise boundary. Therefore, it contains one spanwise period within each half of the span of the computational domain. Similarly, the next mode (MO4) adopts a spanwise wavelength that is $4/5$ times the distance between the wake edge and the spanwise boundary, thus allowing one plus one-fourth of a period inside each half of the domain span. Finally, mode MO7, which is the most unstable Mack mode found in the spectrum at the current conditions for both obstacle shapes, contains two spanwise periods within each half of the domain width, with a spanwise wavelength equal to half of the allowed distance. As in the case of modes MO3 and MO4, each of the oblique modes resolved along the Mack-mode branch differs in 1/4 of a period with respect to the previous one. For example, mode MO5 contains one and a half periods, mode MO6 contains one plus 3/4 of a period, and so on. For the sake of clarity, figure 5.32 displays five different oblique Mack modes (MO3 to MO7) which develop behind the cuboidal roughness element, including labels which denote the spanwise wavelength associated to each of them as well as the size of the spanwise structures that are contained inside the domain width.

The remaining discrete unstable modes found in the spectra are also sinuous and varicose deformations of the low-velocity streak, presenting different peak-trough regions of amplitude development located around the three-dimensional shear layer. For the cases investigated in this analysis, these modes are found to grow at a smaller rate than the leading wake instabilities (VCOS1 and SIN1). The shape of the amplitude function for this kind of disturbances is discussed in § 5.2.4 (see also [29]). The group of modes distributed along the real axis in the left part of the spectrum of figures 5.25(c) and 5.26(c) belong to the slow acoustic continuous branch.

5.3.4.1 Convergence of the growth rate with respect to grid resolution

A grid convergence analysis on the growth rate of modes SIN1, VCOS1, M2D and MO7 for each roughness geometry is presented in figure 5.33 for a streamwise station at $x = 0.1$ m. This figure shows contour plots of the relative error in the temporal growth rate of each mode as a function of the grid resolution in each direction. The relative error (ε_r) for each mode is evaluated with respect to the growth rate obtained at the finest grid resolution, which corresponds to $N_z = N_y = 201$ points, so that $\varepsilon_r = |\omega_i - \omega_{i,201\times201}|/|\omega_{i,201\times201}|$. The results indicate that all instabilities are more sensitive to the spanwise grid resolution (N_z), owing to the

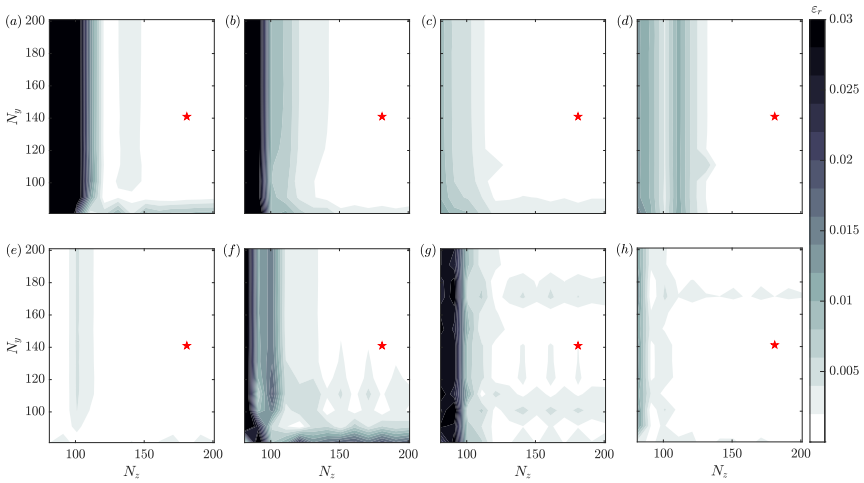

Figure 5.33: Contours of relative error in the temporal growth rate of different unstable modes for each roughness geometry at $x = 0.1$ m as a function of the grid resolution in each direction: (a, b, c, d) cuboid, $\lambda_x = 0.5$ cm; (e, f, g, h) ramp, $\lambda_x = 0.56$ cm; (a, e) mode SIN1; (b, f) mode VCOS1; (c, g) mode M2D; (d, h) mode MO7. The relative error is evaluated with respect to the growth rate obtained with the finest grid resolution ($N_z = N_y = 201$) for each mode: $\varepsilon_r = |\omega_i - \omega_{i,201\times201}|/|\omega_{i,201\times201}|$. The star symbol indicates the position of the reference grid resolution employed for the results presented in this work ($N_z = 181$, $N_y = 141$ points).

fact that the amplitude functions undergo changes along the spanwise direction over a longer distance than along the wall-normal direction. For the computational domain employed for each roughness geometry, a larger grid resolution is required in the spanwise direction to achieve the same degree of convergence as in the wall-normal direction.

Besides ensuring a fine grid resolution in the roughness wake, the discretization of oblique Mack modes modulated by the roughness wake also requires enough spanwise grid points within the boundary layer at the sides of the roughness element in order to resolve the associated desired spanwise wavenumbers. In this study, $N_z = 181$ is chosen as a reference spanwise resolution since it provides a good degree of convergence for the wake instabilities as well as for a substantial number of oblique Mack modes, allowing to describe the most relevant region of the continuous Mack mode branch. Along the wall-normal direction, a reference resolution of $N_y = 141$ points is selected as it provides an appropriate trade-off between convergence and computational cost for the different cases investigated.

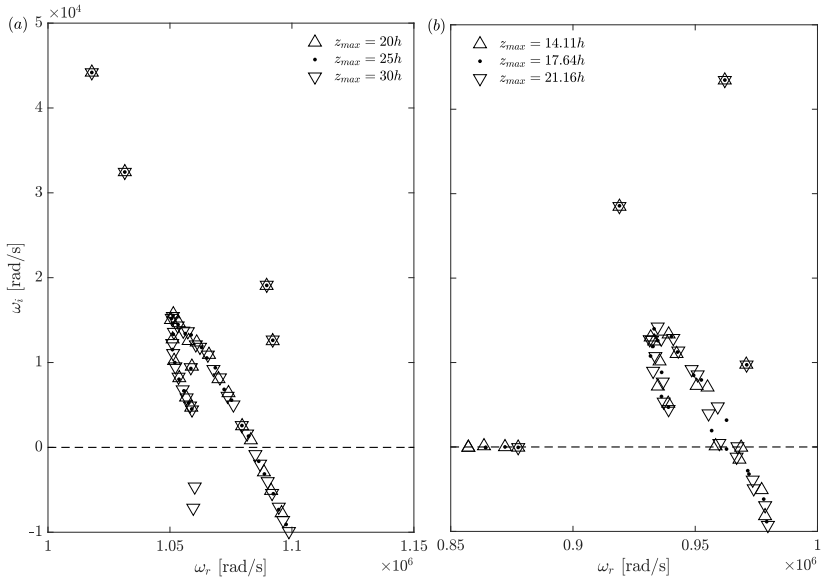

Figure 5.34: Most relevant region of the temporal stability spectrum for each roughness shape at $x = 0.1$ m for three different spanwise domain sizes: (a) cuboid, $\lambda_x = 0.5$ cm; (b) ramp, $\lambda_x = 0.56$ cm.

5.3.4.2 Effect of the domain size on the stability spectrum

To emphasize the continuous nature of the Mack mode branch obtained in the stability spectra, figure 5.34 illustrates the effect of changing the spanwise size of the computational domain employed for the stability analysis (z_{max}) on the results obtained for the cuboid configuration at $\lambda_x = 0.5$ cm and for the ramp geometry at $\lambda_x = 0.56$ cm. Since the regions of development of the wake instability modes at these conditions are contained within the roughness wake, the effect of changing z_{max} is negligible on these modes. On the other hand, a change in the spanwise domain size modifies the spanwise wavenumbers that can be resolved by the discretization. As a result, for each particular value of z_{max}, different oblique Mack modes are obtained in the spectrum. Nevertheless, the shape of the continuous Mack mode branch must remain the same independently of the spanwise domain size considered. In other words, different values of z_{max} resolve a different set of modes from the infinite number that compose the branch. This behavior is demonstrated by the spectra presented in figure 5.34.

Figure 5.35 represents the sensitivity of the spectrum to the wall-normal size of the computational domain employed for the stability calculations (y_{max}), illustrated for three different wall-normal domain sizes at $x = 0.1$ m. As it can be observed, the influence of the upper boundary of the domain on the discrete

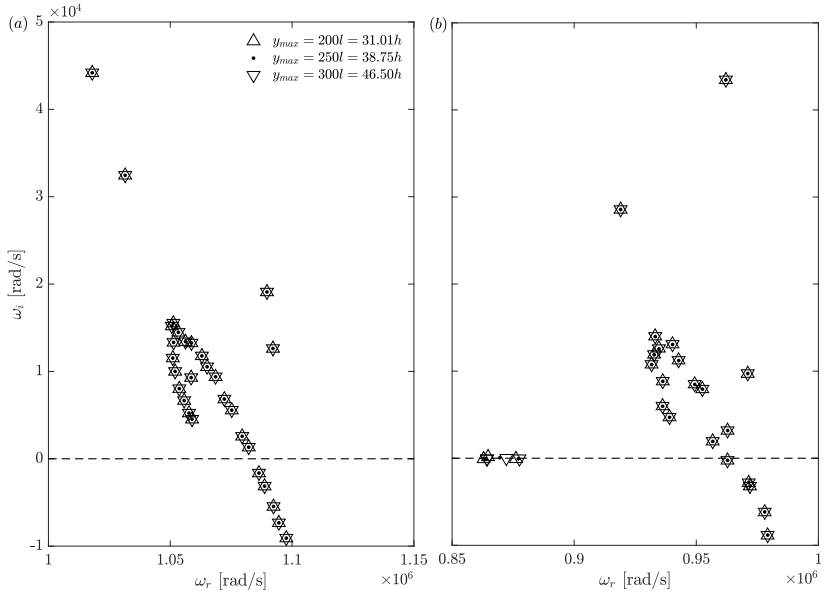

Figure 5.35: Most relevant region of the temporal stability spectrum at $x = 0.1$ m for three different wall-normal domain sizes (y_{max}): (a) cuboid, $\lambda_x = 0.5$ cm; (b) ramp, $\lambda_x = 0.56$ cm.

modes of the stability spectrum is negligible. The only sensitive modes are those located at the real axis in figure 5.35(b), which correspond to the slow acoustic continuous branch and therefore their eigenfunctions do not decay to zero towards the upper boundary of the domain. The value $y_{max} = 300l = 46.50h$ is the actual wall-normal size employed in the results shown for $x = 0.1$ m in the current configuration.

5.3.5 Streamwise evolution of the growth rate of the instabilities evolving in the roughness wake

Next, the streamwise evolution of the growth rate of the different instabilities identified in the roughness wake is discussed and compared for the two roughness geometries.

5.3.5.1 Evolution of Mack-mode instabilities modulated by the roughness wake

First, the streamwise variation of the Mack-mode instabilities modulated by the roughness wake is described. Figure 5.36 shows the growth rate of modes M2D, MO3, MO4 and MO7 as a function of x for the cuboid configuration at $\lambda_x = 0.5$

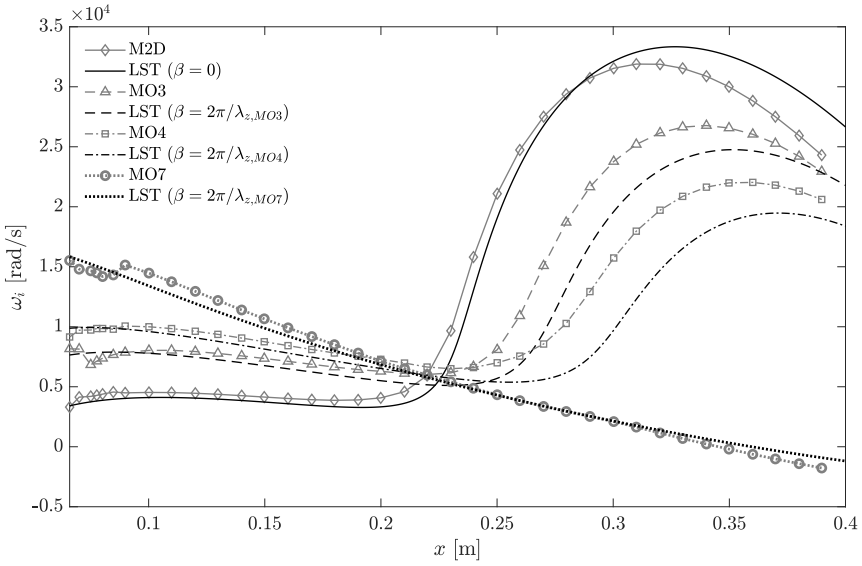

Figure 5.36: Temporal growth rate as a function of the streamwise location for different Mack-mode instabilities evolving in the cuboidal roughness wake at $\lambda_x = 0.5$ cm. Curves obtained from one-dimensional local linear stability theory (LST) at the equivalent spanwise wavenumbers (β) are also shown for comparison. The estimated spanwise wavelengths (from figure 5.32) are: $\lambda_{z,MO3} = 0.85$ cm, $\lambda_{z,MO4} = 0.66$ cm and $\lambda_{z,MO7} = 0.39$ cm.

cm. The first streamwise location considered corresponds to the end of the downstream recirculation bubble induced at the trailing edge of the roughness element[2] (see figures 5.19 and 5.20), located at $x_{b,TE} = 0.0667$ m for the cuboid geometry. Included in the figure are also the growth-rate curves obtained with LST by fixing a value of β according to the spanwise wavelength observed in the amplitude function of each mode (see figure 5.32). The comparison between the curves obtained with 2D-LST and those computed by means of LST allows to assess the impact of the roughness wake on the Mack-mode disturbances. As it can be noticed, such impact is not strong, and and as result the Mack modes evolving in the roughness wake still feature a growth-rate signature which is similar to that of the ones evolving in the smooth flat plate boundary-layer (LST). In particular, the 2D-LST modes still preserve the inherent properties that characterize the growth rate of a classical Mack mode at the hypersonic freestream conditions under analysis, namely, that the Mack mode is most unstable when behaving as a two-dimensional second mode (in this case mode M2D for $x > 0.22$ m, approximately), and that

[2]This location is assumed to be the first one at which the parallel flow assumption inherent to 2D-LST theory is satisfactory. The recirculating fluid encountered inside the separation bubble induced at the roughness trailing edge renders the base flow in this region to be very inhomogeneous in all three spatial directions.

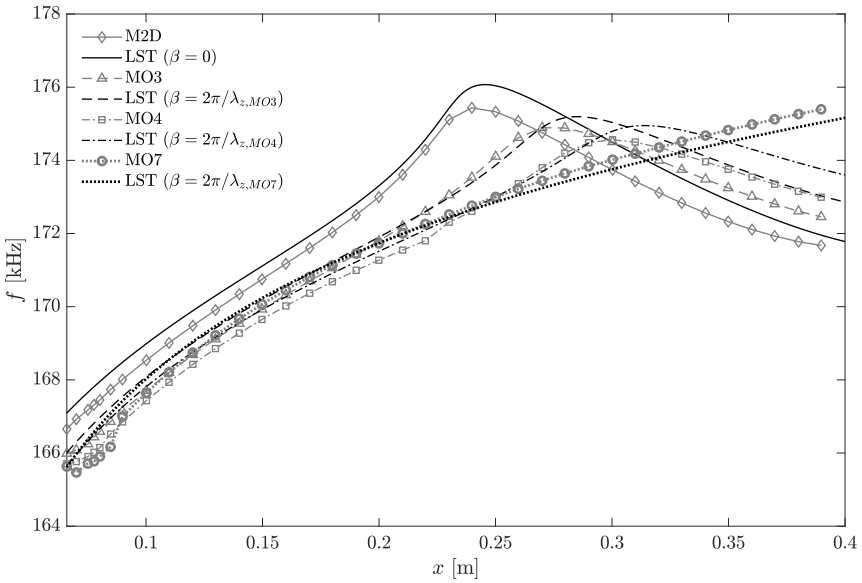

Figure 5.37: Frequency as a function of the streamwise location for different Mack-mode instabilities evolving in the cuboidal roughness wake at $\lambda_x = 0.5$ cm. Curves obtained from one-dimensional local linear stability theory (LST) at the equivalent spanwise wavenumbers (β) are also shown for comparison.

when behaving as a first mode it is most unstable for $\beta > 0$ (in this case modes MO3, MO4 and MO7 for $x < 0.2$ m, approximately). These observations suggest that the roughness element does not act as an effective amplifier of boundary-layer disturbances in this case.

For completeness, the resulting streamwise evolution of the frequency of modes M2D, MO3, MO4 and MO7 is also depicted in comparison with that of the respective LST modes for $\lambda_x = 0.5$ cm in figure 5.37. Similarly to the growth rate, no strong deviations in the disturbance frequency of the boundary-layer instabilities are introduced by the presence of the roughness element wake.

5.3.5.2 Evolution of the leading sinuous and varicose instabilities

The streamwise evolution of the two leading instabilities along the wake induced by each roughness geometry is assessed next. Figure 5.38 displays the evolution of the temporal growth rate of the SIN1 and VCOS1 modes for five different wavelengths that span the range of amplification shown in figure 5.27. The first streamwise location considered for all cases corresponds once again to the end of the roughness trailing-edge separation region, located at $x_{b,TE} = 0.0667$ m and $x_{b,TE} = 0.0633$ m for the cuboid and ramp elements, respectively. The

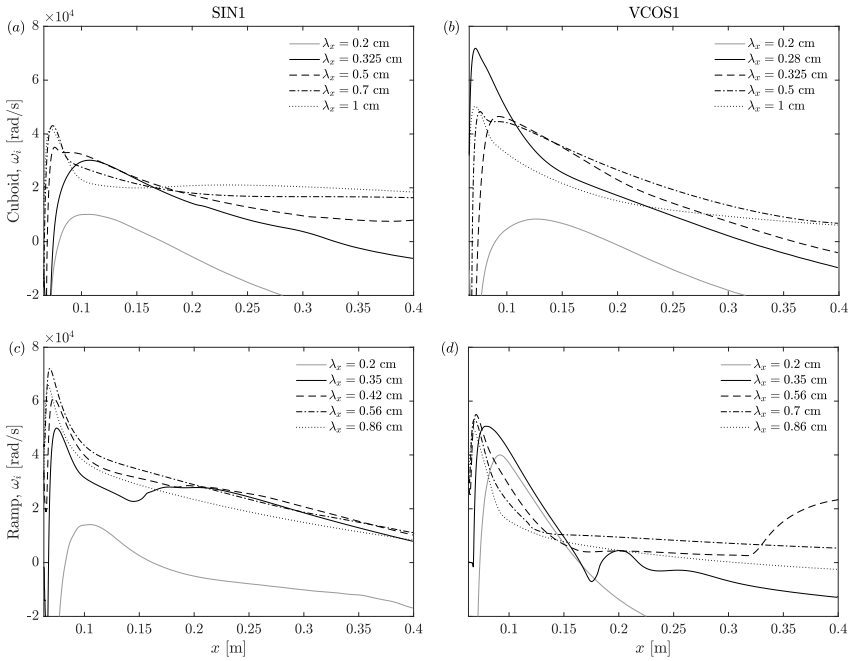

Figure 5.38: Temporal growth-rate evolution of the most unstable wake modes for each roughness geometry as a function of the streamwise coordinate for five different wavelengths: (a, c) *SIN1 mode;* (b, d) *VCOS1 mode;* (a, b) *cuboid;* (c, d) *ramp.*

growth rate of both wake instabilities increases very rapidly immediately behind the trailing-edge recirculation bubble, reaching its maximum in a very short distance downstream, after which it starts to decrease progressively. The distance at which the maximum growth rate is attained depends on the streamwise wavelength.

In the vicinity of the cuboidal roughness trailing edge, the magnitude of the growth rate is significantly higher for the varicose mode than for the sinuous one for most of the streamwise wavelengths considered. On the contrary, near the ramp roughness element the sinuous instability reaches higher amplification rates than the varicose one for $\lambda_x \geq 0.56$ cm. Specifically, the maximum growth rate attained by mode SIN1 at the illustrated wavelengths is $\omega_i \approx 7.2 \times 10^4$ rad/s for the ramp configuration and $\omega_i \approx 4.3 \times 10^4$ rad/s for the cuboid one. In the case of the varicose disturbance, however, mode VCOS1 reaches a maximum of $\omega_i \approx 7.2 \times 10^4$ rad/s for the cuboid geometry and $\omega_i \approx 5.5 \times 10^4$ rad/s for the ramp case. This constitutes a 67% increase in the peak growth rate achieved by the ramp-induced sinuous disturbance with respect to that excited by the cuboid, and a 31% increase in the maximum growth rate attained by the cuboid-induced varicose

instability with respect to the ramp counterpart. Of particular interest is the evolution of the varicose mode for the cuboid geometry at $\lambda_x = 0.28$ cm. As shown in figure 5.27(a), this wavelength is located within the region of development of the varicose "second" mode. This range of wavelengths exhibits the highest temporal amplification for the varicose disturbance evolving in the cuboid wake.

The rate of decay in growth rate after the location of maximum amplification is also found to be significantly dependent on the streamwise wavelength considered. For the cuboid configuration, the growth rate of both instabilities for $\lambda_x \leq 0.325$ cm decreases continuously until the end of the domain at a very similar rate. For these wavelengths, the varicose mode is the leading instability along all the domain investigated. On the other hand, for $\lambda_x \geq 0.5$ cm, the amplification rate approaches a nearly constant value after a given distance downstream. This distance is found to decrease as the streamwise wavelength increases, and it is found to be significantly shorter for the sinuous mode than for the varicose one. This makes the sinuous disturbance the dominant wake instability for approximately $x > 0.2$ m at this range of wavelengths.

Regarding the ramp roughness wake, the streamwise evolution of the sinuous perturbation for $\lambda_x \geq 0.56$ cm undergoes first a rapid decay followed by a slower monotonic decrease downstream, in all cases with a very similar slope. For $\lambda_x = 0.35$ cm and $\lambda_x = 0.42$ cm, however, a deviation in this growth-rate behavior is encountered starting respectively at $x = 0.15$ m and $x = 0.18$ m, where the disturbance shows an important destabilization. For the varicose perturbation developing in the wake behind the ramp geometry, a rapid decay is also found in the first portion of the streamwise domain under consideration for all the studied wavelengths. However, in this case the rate of decrease is more pronounced than for the sinuous counterpart and extends over a longer streamwise distance. This strong stabilization brings the growth rate of mode VCOS1 below 10^4 rad/s. Fluctuations in the growth rate of this mode are also found, in this case for $\lambda_x = 0.35$ cm and $\lambda_x = 0.56$ cm. These observations, together with the results for the cuboidal geometry described before, suggest that there is a mechanism in the roughness wake which, for a certain range of streamwise wavelengths, energizes the wake instabilities, preventing their growth rate to decay monotonically downstream as would be expected from the continuous dissipation of the base-flow quantities displayed in figure 5.23. A plausible explanation for this behaviour resorts to a continuous synchronization between the wake instability modes and the boundary-layer modes that interact with the roughness wake. A further discussion on this phenomenon is provided in § 5.3.6 and § 5.3.7.

For the ramp-induced varicose mode at $\lambda_x = 0.56$ cm, the rise in the amplification rate that can be observed towards the end of the domain is very similar to the growth-rate evolution inherent to Mack's second mode instability. When tracking the streamwise evolution of this wake mode, it is found that it progres-

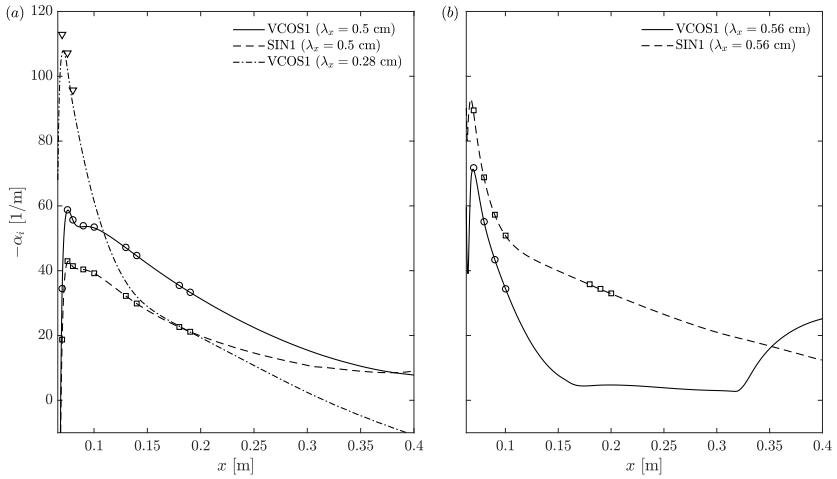

Figure 5.39: Spatial growth-rate evolution of the most unstable wake modes obtained by means of the Gaster transformation (3.20) (lines) and by solving the spatial eigenvalue problem (symbols): (a) cuboid; (b) ramp.

sively approaches the continuous branch associated to the Mack-mode family and becomes absorbed by it after a given distance downstream. At this location, the amplitude function of mode VCOS1 strongly resembles the one of the other modes comprised in this branch, and it becomes difficult to distinguish its evolution from the other Mack-mode instabilities by looking at the computed 2D-LST spectra. The curve shown in figure 5.38(d) corresponds to the evolution obtained by means of a Rayleigh quotient iteration (see § 4.2.7.2). Two possible scenarios can be devised to explain the rise in growth rate obtained for $x > 0.33$ m at $\lambda_x = 0.56$ cm. On the one hand, as the varicose mode becomes close to the Mack-mode branch, the mode tracked by the algorithm could possibly switch to a different one, in this case corresponding to a particular Mack-mode disturbance. On the other hand, since the varicose mode disturbance becomes absorbed by the Mack mode branch at these conditions, another possibility is that the behavior of the varicose mode is so strongly affected by an interaction with the boundary-layer instability modes that its evolution becomes very similar to that of Mack's second mode. The results of the temporal growth-rate decomposition presented in § 5.3.6 give more support to the second scenario.

5.3.5.3 Integrated amplification factors of the wake instabilities obtained by means of the Gaster transformation

For the roughness Reynolds number considered in this study, the instabilities growing in the roughness wake have a purely convective nature [4, 15]. Therefore, it is appropriate to track the evolution of their growth in space in order to assess which is the dominant disturbance excited by each geometry in terms of the integrated amplification factor (N-factor). To avoid the significant computational cost associated with solving the spatial eigenvalue problem (3.16), the approximate relation between the temporal and the spatial growth rates (3.20) originally developed by Gaster [30] is employed (see § 3.4.4). Although, in general, this transformation is only accurate for convective instabilities with small temporal growth rates, it has been successfully applied by previous authors to the analysis of roughness-induced instabilities in high-speed flows (see [15, 31]). To verify its applicability to the temporal results presented here, figure 5.39 shows a comparison between spatial growth rates obtained by means of the Gaster transformation and spatial growth rates computed by solving the spatial eigenvalue problem for the leading wake instabilities. A good overall agreement is found for both roughness geometries, which renders the use of the Gaster transformation a legitimate assumption for the purpose of this analysis. The biggest discrepancies are encountered for the cuboid varicose mode at $\lambda_x = 0.28$ cm, corresponding to its particular region of development associated to small streamwise wavenumbers (high frequencies), according to figures 5.27(a) and 5.28(a).

Temporal stability computations allow to construct a stability diagram of the form $\omega_i = \omega_i(\alpha_r, x)$, or $\omega_i = \omega_i(\lambda_x, x)$. By means of the Gaster transformation, the function $\alpha_i = \alpha_i(\lambda_x, x)$ can then be obtained. However, a meaningful evaluation of the integrated amplification factors requires a surface of the type $\alpha_i = \alpha_i(f, x)$, where $f = \omega_r/(2\pi)$ is the frequency of the disturbance, so that curves of α_i as a function of x for a constant frequency can be integrated to obtain the evolution of N associated to that frequency. Since ω_r is a solution of the temporal eigenvalue problem, it cannot be fixed constant a priori from the temporal results. Therefore, to obtain $\alpha_i = \alpha_i(f, x)$, an interpolation of the stability diagram $\alpha_i = \alpha_i(\lambda_x, x)$ must be employed. From the temporal stability calculations, the resulting frequency of the disturbances is found to be approximately proportional to α_r. In addition, in the unstable region of the stability diagram, the range of frequencies spanned by each of the $\alpha_i = \alpha_i(x)$ curves for a constant λ_x is very small in comparison with the range of frequencies over which the instabilities grow. These conditions favor the accuracy of the interpolation process. In this study, this procedure is performed by means of a cubic Hermite interpolation.

The spatial stability diagrams ($\alpha_i = \alpha_i(f, x)$) obtained by means of the Gaster transformation for modes SIN1 and VCOS1 and for each of the roughness geometries under study are displayed in figures 5.40$(c$-$f)$. The shaded contours represent

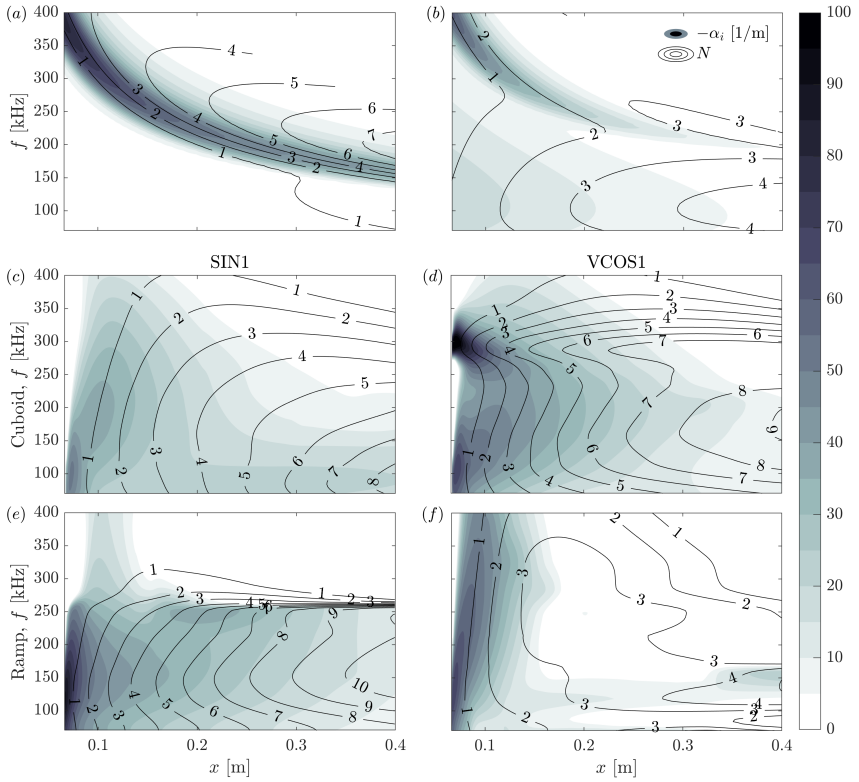

Figure 5.40: Shaded contours of spatial growth rate ($-\alpha_i$) and contour lines of N-factor as a function of frequency and streamwise position for: (a) two-dimensional Mack mode evolving in the smooth flat plate boundary layer; (b) oblique Mack mode ($\lambda_z = 0.4$ cm) evolving in the smooth flat plate boundary layer; (c) cuboid, SIN1 mode; (d) cuboid, VCOS1 mode; (e) ramp, SIN1 mode; (f) ramp, VCOS1 mode. Results for $(c$-$f)$ were obtained by means of the Gaster transformation (3.20).

the spatial growth rate and the contour lines superimposed illustrate the associated N-factor evolution. For comparison purposes, the diagrams shown in figures 5.40(a, b) correspond to the instabilities developing in the smooth flat-plate boundary layer, which are obtained by means of LST for a given spanwise wavenumber. Figure 5.40(a) depicts contours for the two-dimensional Mack-mode instability ($\beta = 0$), which is fully governed by high frequencies corresponding to second mode behaviour, whereas figure 5.40(b) shows contours for an oblique Mack-mode instability with a spanwise wavelength of $\lambda_z = 0.4$ cm, for which both Mack's first and second mode regions of development can be observed, respectively associated to the low- and high-frequency ranges. The integration of N is started at the first streamwise station at which the modes become unstable. In the

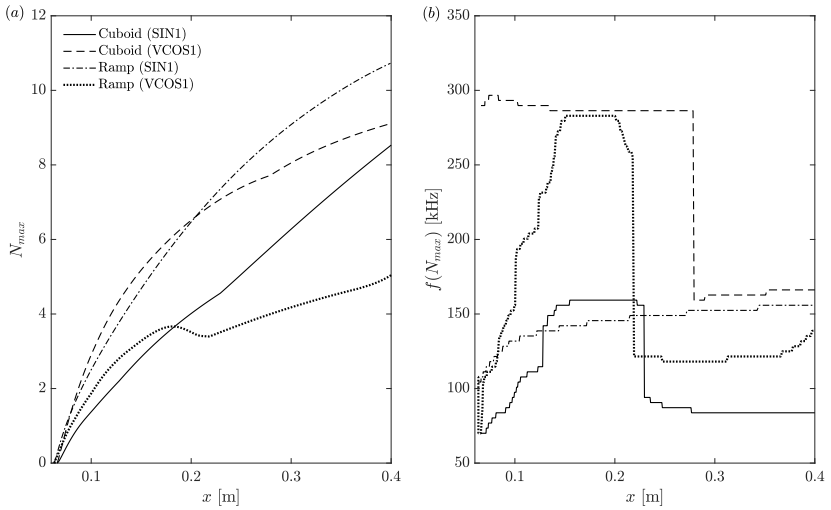

Figure 5.41: (a) Streamwise evolution of the N-factor envelope (N_{max}) of the most unstable wake modes for each roughness geometry, obtained by employing the Gaster-transformed spatial growth rates; (b) frequency associated to N_{max} at each streamwise location for each of the curves shown in (a).

case of the wake instabilities, it is found that for certain frequencies the disturbances are already unstable at the first streamwise location analyzed, that is, at the end of the trailing edge separation bubble. Under these circumstances, a value of $N = 0$ is assumed at that location. This is a common procedure employed by other authors in similar analyses, see for instance [3, 5, 28]. In addition, figure 5.41(a) presents the streamwise evolution of the N-factor envelope (N_{max}) curves for each of the wake modes investigated. Here, N_{max} denotes the maximum N-factor obtained at each streamwise position for all the different frequencies analyzed. The particular frequency associated with N_{max} at each location is shown in figure 5.41(b).

These results complete the observations introduced before based on the temporal growth-rate evolution. The N-factor envelopes confirm that the cuboid geometry favours the development of a varicose wake instability over a sinuous one, whereas the ramp configuration excites a sinuous disturbance more effectively than a varicose one. Close to the roughness element, the cuboidal geometry is more effective in promoting the linear growth of the dominant wake instability than the ramp-shaped one. However, further downstream ($x > 0.2$ m), the ramp element leads to a higher disturbance amplitude.

As shown in figure 5.40(d), two distinct regions of development for the cuboid-induced varicose instability can be identified. The frequency range for each of

these regions is found to correlate well with that of Mack's first- and second-mode instabilities developing in the smooth flat plate. Although the biggest growth rates for this disturbance are located within the high-frequency band, the decay in this range is more accentuated than for the lower frequencies. As a result, the frequencies that govern the N-factor envelope for this mode are first located in the upper range ($f \approx 280$ kHz) and further downstream in the lower band ($f \approx 160$ kHz), as shown in figure 5.41(b). This leads to the abrupt change in the slope of the envelope curve at $x \approx 0.28$ m. In accordance with the temporal stability results described above, this is the only instability for which two such different regions of excitation can be clearly observed in the stability diagram.

Regarding the ramp-induced sinuous disturbance (see figure 5.40(e)), its region of maximum growth is concentrated in the range of $f \approx 100$ kHz to 160 kHz. This frequency band is associated with Mack's first mode instabilities for the entire domain length. For higher frequencies ($f \approx 230$ kHz to 270 kHz), a small enhancement of the spatial growth rates is observed starting at $x \approx 0.15$ m. The same phenomenon is visible in the temporal growth rate curves shown in figure 5.38(c) for $\lambda_x = 0.35$ cm and $\lambda_x = 0.42$ cm. This behaviour correlates with the region of the stability diagram that overlaps with the development of Mack's second-mode instability in the flat plate boundary layer. Such observation further supports the argument of an interaction between the wake modes and the boundary-layer disturbances. In this case, however, this interaction does not have an impact on the N-factor envelope of the wake instability.

Although less relevant in terms of N_{max}, the cuboid-induced sinuous disturbance and the ramp-induced varicose perturbation also show the influence of an interaction with boundary-layer instabilities. As in the ramp configuration, the sinuous mode associated to the cuboid geometry also features its maximum N in the low-frequency band. For $x > 0.2$ m, its spatial growth becomes approximately constant with respect to the streamwise position for $f < 130$ kHz (see figure 5.40(c)). This feature can also be observed in the temporal growth curves shown in figure 5.38(a) for $\lambda_x = 0.7$ cm and $\lambda_x = 1$ cm. This reduction in the decay of the growth rate of the instability is attributed to an interaction between the sinuous disturbance and Mack's first-mode instability. It has a significant impact in the evolution of the associated N-factor envelope, which shows a clear increase in slope in this region. Mode VCOS1 excited by the ramp roughness element is found to be rapidly stabilized at high frequencies, as shown in figure 5.40(f). To the contrary, its growth rate is found to be influenced by both the first and second boundary-layer disturbances in the range of $f \approx 100$ kHz to 200 kHz. The interaction with Mack's first mode is noticeable starting at $x \approx 0.18$ m and with Mack's second mode starting at $x \approx 0.33$ m (see also figure 5.38(d)).

5.3.6 Temporal growth-rate decomposition of the instabilities behind the roughness elements

This section describes the application of the temporal growth-rate decomposition introduced in § 3.10.2 to the evolution of the Mack-mode instabilities and the leading wake perturbations (modes VCOS1 and SIN1) that are present in the wake behind each roughness shape. Although the decomposition given by equation (3.64) consists of a significant number of terms, not all of them play an important role in the problem under investigation. To illustrate which are the most relevant contributions to the energy (and consequently to the growth rate) of the studied disturbances, figure 5.42 presents the complete temporal growth-rate decomposition of modes M2D, SIN1 and VCOS1 obtained at $x = 0.1$ m for the cuboid ($\lambda_x = 0.5$ cm) and the ramp ($\lambda_x = 0.56$ cm) roughness geometries. The first five terms, namely $\hat{P}_{RS}$, $\hat{P}_{mom}$, $\hat{D}_{\mu}$, $\hat{F}_{\mu}$ and $\hat{F}_{d\mu/dT}$, are contributions that originate from the momentum equation only, and therefore they can be compared against each other within the disturbance energy formulation of Chu (see § 3.10.1). It can be observed that the most important contributions that stem from the momentum equation for both roughness geometries and for all three different modes are the work done by the disturbance Reynolds stresses ($\hat{P}_{RS}$) and the viscous dissipation ($\hat{D}_{\mu}$). For the cases investigated here, the production term $\hat{P}_{mom}$ is negligible and the flux terms $\hat{F}_{\mu}$ and $\hat{F}_{d\mu/dT}$ are zero due to the chosen perturbation boundary conditions and the spanwise symmetry of the base flow.

The terms $\hat{P}_{s,T}$, $\hat{D}_k$ and $\hat{F}_k$ emerge exclusively from the governing energy equation. In this case, the only important contribution to consider from this group is the dissipation due to thermal conduction ($\hat{D}_k$). The production term $\hat{P}_{s,T}$ features small values that are not significant and the flux quantity $\hat{F}_k$ is zero, once again owing to the boundary conditions employed in the disturbance quantities. Next, the terms $\hat{P}_s$, $\hat{P}_{dil}$ and $\hat{F}_p$ are considered, which arise from a combination of the continuity and the energy equations, and as a result they can be interpreted as contributions to the generalized potential energy of the disturbance (see § 3.10.1.2). As it can be observed, the energy produced by the transport of entropy spottiness ($\hat{P}_s$) constitutes an important contribution, whereas $\hat{P}_{dil}$ is negligible and $\hat{F}_p$ vanishes for the same reasons stated above for the other flux terms. The term $\hat{P}_{\nabla p}$ results from a combination of the momentum and the continuity equations, but it features a very small magnitude for the current cases and is therefore deemed to be not important. The disturbance heat source $\hat{P}_Q$ is built with contributions from the momentum and energy equations. In this analysis, it is characterized by small values that are approximately one order of magnitude smaller than the other relevant terms, in good agreement with the findings of Chu [32]. Finally, the production due to the convective derivative of the disturbance energy ($\hat{P}_{con}$) is composed of contributions from all the governing equations. It's magnitude is also small in the present configurations and as a result it is not taken into account in the following

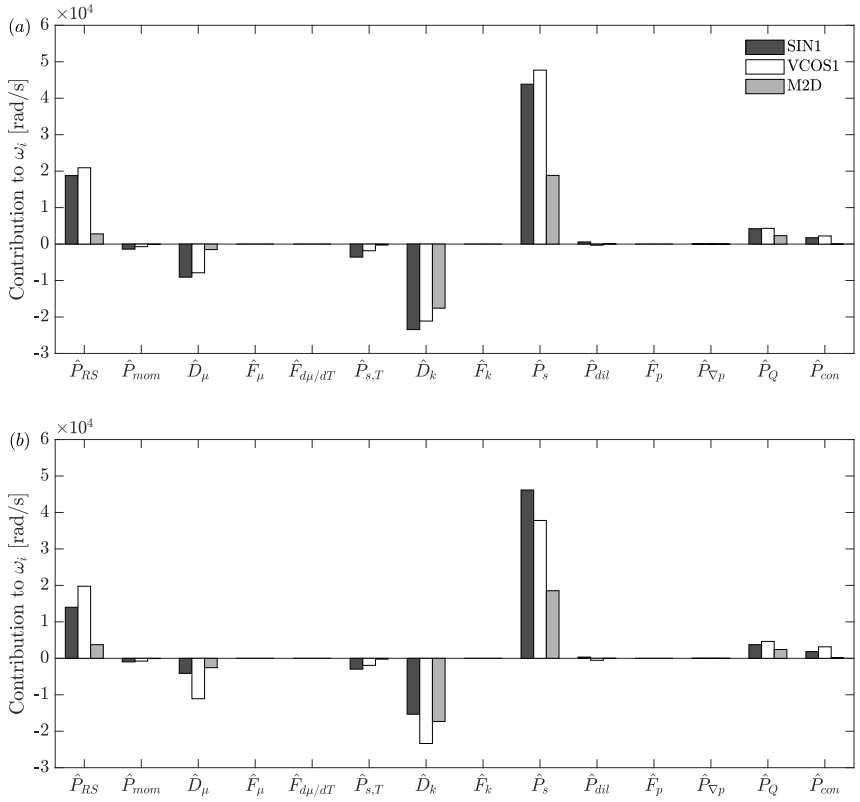

Figure 5.42: Different contributions of the temporal growth-rate decomposition resulting from the disturbance energy formulation of Chu for modes SIN1, VCOS1 and M2D at $x = 0.1$ m: (a) cuboid, $\lambda_x = 0.5$ cm; (b) ramp, $\lambda_x = 0.56$ cm. Although not shown in the figure labels, each contribution is divided by the factor $2\hat{E}$ (see equation (3.64)).

analyses.

In summary, only the terms $\hat{P}_{RS}$, $\hat{P}_s$, $\hat{D}_\mu$ and $\hat{D}_k$ constitute important contributions to the disturbance energy for the problem under consideration in this work. The attention is thus focused on these terms. The term $\hat{P}_{RS}$ constitutes the most important contribution to the disturbance kinetic energy, whereas $\hat{P}_s$ represents the major contribution to the generalized potential energy of the disturbance.

The terms $\hat{P}_{RS}$ and $\hat{P}_s$ can be further split into the different contributions associated to each particular base-flow gradient by defining the following quantities:

$$\hat{P}_{s,2} = -\int_{z^-}^{z^+} \int_{y^-}^{y^+} \bar{\rho}\langle \hat{v}, \hat{s} \rangle \frac{\partial \bar{T}}{\partial y}\, dy\, dz, \tag{5.12a}$$

$$\hat{P}_{s,3} = -\int_{z^-}^{z^+}\int_{y^-}^{y^+} \bar{\rho}\langle\hat{w},\hat{s}\rangle\frac{\partial\bar{T}}{\partial z}\,dy\,dz, \tag{5.12b}$$

and

$$\hat{P}_{RS,12} = -\int_{z^-}^{z^+}\int_{y^-}^{y^+} \bar{\rho}\langle\hat{u},\hat{v}\rangle\frac{\partial\bar{u}}{\partial y}\,dy\,dz, \tag{5.13a}$$

$$\hat{P}_{RS,13} = -\int_{z^-}^{z^+}\int_{y^-}^{y^+} \bar{\rho}\langle\hat{u},\hat{w}\rangle\frac{\partial\bar{u}}{\partial z}\,dy\,dz, \tag{5.13b}$$

$$\hat{P}_{RS,22} = -\int_{z^-}^{z^+}\int_{y^-}^{y^+} \bar{\rho}\langle\hat{v},\hat{v}\rangle\frac{\partial\bar{v}}{\partial y}\,dy\,dz, \tag{5.13c}$$

$$\hat{P}_{RS,23} = -\int_{z^-}^{z^+}\int_{y^-}^{y^+} \bar{\rho}\langle\hat{v},\hat{w}\rangle\frac{\partial\bar{v}}{\partial z}\,dy\,dz, \tag{5.13d}$$

$$\hat{P}_{RS,32} = -\int_{z^-}^{z^+}\int_{y^-}^{y^+} \bar{\rho}\langle\hat{w},\hat{v}\rangle\frac{\partial\bar{w}}{\partial y}\,dy\,dz, \tag{5.13e}$$

$$\hat{P}_{RS,33} = -\int_{z^-}^{z^+}\int_{y^-}^{y^+} \bar{\rho}\langle\hat{w},\hat{w}\rangle\frac{\partial\bar{w}}{\partial z}\,dy\,dz. \tag{5.13f}$$

The terms denoted by $\hat{P}_{s,2}$ and $\hat{P}_{s,3}$ respectively refer to the wall-normal and the spanwise contributions that constitute $\hat{P}_s$. Similarly, terms $\hat{P}_{RS,12}$, $\hat{P}_{RS,22}$ and $\hat{P}_{RS,32}$ are the parts of the total Reynolds stress production term $\hat{P}_{RS}$ that respectively correspond to the Reynolds stress components that work against the velocity gradients along the wall-normal direction, while $\hat{P}_{RS,13}$, $\hat{P}_{RS,23}$ and $\hat{P}_{RS,33}$ represent the work against the velocity gradients in the spanwise direction. To examine which of these terms are important contributions to the disturbance energy, figure 5.43 depicts their value for the same instabilities represented in figure 5.42. These results indicate that the disturbance kinetic energy is mainly produced by the interaction between the disturbance Reynolds stress components $\bar{\rho}\tilde{u}\tilde{v}$ and $\bar{\rho}\tilde{u}\tilde{w}$ and the streamwise velocity gradients along the wall-normal and spanwise directions ($\partial\bar{u}/\partial y$ and $\partial\bar{u}/\partial z$), as represented by $\hat{P}_{RS,12}$ and $\hat{P}_{RS,13}$. The terms $\hat{P}_{RS,32}$ and $\hat{P}_{RS,33}$, in turn, have a negligible magnitude, meaning that the gradients of the spanwise velocity component do not play a significant role in the growth of instabilities in the roughness wake. Note that terms $\hat{P}_{RS,22}$ and $\hat{P}_{RS,23}$ are not represented in figure 5.43 since the wall-normal velocity component is set to zero in the calculations reported here, hence $\hat{P}_{RS,22} = \hat{P}_{RS,23} = 0$. However, for long streamwise streaks such as the ones characterizing the roughness wake, these terms are known to be of the same order as $\hat{P}_{RS,32}$ and $\hat{P}_{RS,33}$ (see for instance their evaluation in the 2D-LST analyses of Malik *et al.* [33] or Theiss *et*

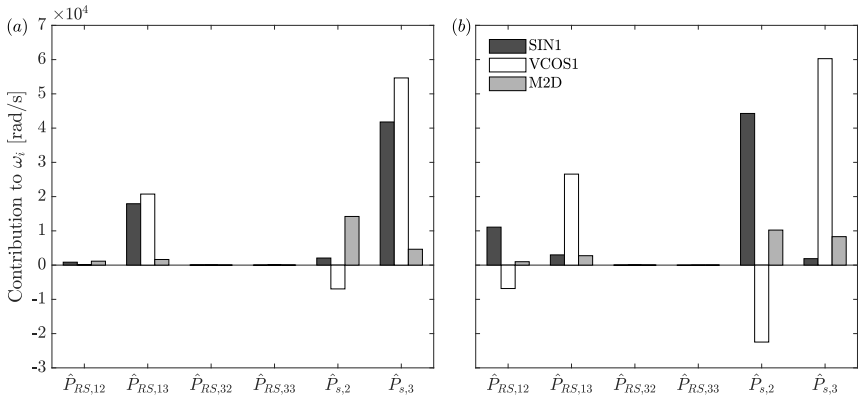

Figure 5.43: Different constituents of the leading production terms $\hat{P}_{RS}$ and $\hat{P}_s$ for modes SIN1, VCOS1 and M2D at $x = 0.1$ m: (a) cuboid, $\lambda_x = 0.5$ cm; (b) ramp, $\lambda_x = 0.56$ cm. Although not shown in the figure labels, each contribution is divided by the factor $2\hat{E}$ (see equation (3.64)).

al. [5]). Therefore, their contributions are also not important for the excitation of roughness-wake instabilities.

On the other hand, it is found that terms $\hat{P}_{s,2}$ and $\hat{P}_{s,3}$ are both major contributions to the generalized disturbance potential energy, which reveals the important role of the wall-normal and spanwise base-flow temperature gradients on the disturbance evolution in the configurations under study. To the best of the author's knowledge, previous analyses found in the literature for isolated roughness elements in high-speed flow have only examined the evolution of the kinetic energy production terms due to the disturbance Reynolds stresses. However, the current results show that the energy production terms associated with the transport of entropy fluctuations across the base-flow temperature gradients constitute an important contribution to the generalized potential energy of the disturbance. As a result, although their relative magnitude with respect to the production of kinetic energy due to the disturbance Reynolds stresses cannot be concluded from Chu's formulation of the perturbation energy (see the reasons stated in § 3.10.1), these findings strongly suggest that $\hat{P}_s$ might also play a major role in high-speed roughness-induced transition.

It is important to emphasize that within the disturbance energy definition of Chu, the largest destabilizing (positive) contributions to the temporal growth rate of the modes evolving behind the roughness elements are $\hat{P}_{s,2}$ and $\hat{P}_{s,3}$, while the biggest stabilizing (negative) contribution is the dissipation of disturbance energy due to thermal conduction ($\hat{D}_k$). Nevertheless, since terms $\hat{P}_{s,2}$, $\hat{P}_{s,3}$ and $\hat{D}_k$ originate from different governing equations than terms $\hat{P}_{RS,12}$, $\hat{P}_{RS,13}$ and $\hat{D}_\mu$,

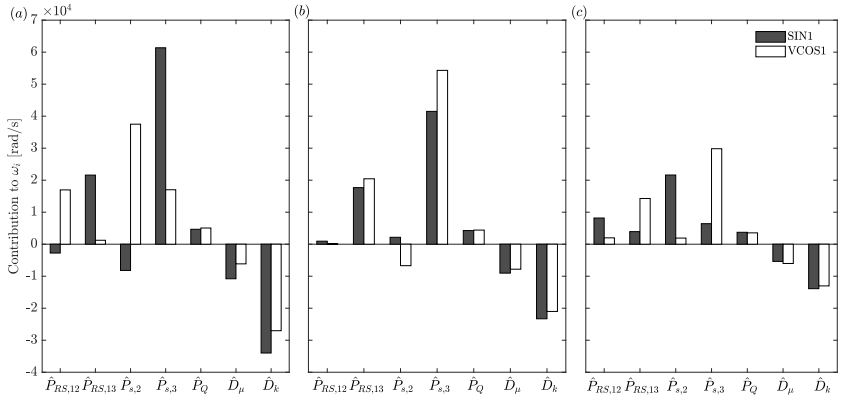

Figure 5.44: Values of the most important contributions to the temporal growth-rate decomposition (3.64) for modes SIN1 and VCOS1 at $x = 0.1$ m in the cuboid wake: (a) $\lambda_x = 0.325$ cm; (b) $\lambda_x = 0.5$ cm; (c) $\lambda_x = 1$ cm. Each contribution is divided by the factor $2\hat{E}$ (see equation (3.64)).

it is not possible to conclude which contributions are actually larger in practice, since different choices of the multipliers that constitute the disturbance energy formulation alter the relative magnitude of these sets of terms.

According to figure 5.42, no significant differences can be noticed between the two roughness geometries in terms of the complete growth-rate decomposition of the excited perturbations. Nevertheless, differences for mode SIN1 can be observed in figure 5.43. In particular, at the streamwise station and wavelength considered, the cuboid-induced sinuous mode extracts most of its energy from the spanwise base-flow gradients ($\hat{P}_{RS,13}$ and $\hat{P}_{s,3}$), whereas for the ramp geometry it draws it from the wall-normal counterpart ($\hat{P}_{RS,12}$ and $\hat{P}_{s,2}$). This is a significant observation, which suggests that a given type of wake instability, such as the sinuous mode, does not extract most of its energy from the same base-flow gradients in all cases. This finding is further discussed in § 5.3.6.1.

To assess whether the constituents of the leading production terms $\hat{P}_{RS}$ and $\hat{P}_s$ are the same for other streamwise wavelengths, figures 5.44 and 5.45 present the most relevant terms of the decomposition of the wake instabilities obtained at $x = 0.1$ m for the same three different streamwise wavelengths considered in figures 5.25 and 5.26 for the cuboid and ramp configurations, respectively. As it can be observed, in the cuboid case the sinuous mode is governed by the spanwise production terms for $\lambda_x = 0.325$ cm and $\lambda_x = 0.5$ cm, whereas for $\lambda_x = 1$ cm the wall-normal terms are dominant. Similarly, the decomposition also reveals a difference in the main source of disturbance energy for the cuboid-induced varicose mode at $\lambda_x = 0.325$ cm with respect to the other two wavelengths. At $\lambda_x = 0.325$

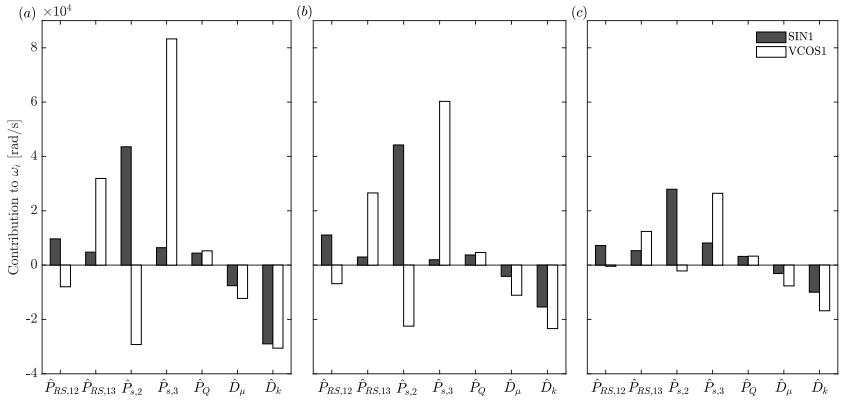

Figure 5.45: Values of the most important contributions to the temporal growth-rate decomposition (3.64) for modes SIN1 and VCOS1 at $x = 0.1$ m in the ramp wake: (a) $\lambda_x = 0.35$ cm; (b) $\lambda_x = 0.56$ cm; (c) $\lambda_x = 0.86$ cm. Each contribution is divided by the factor $2\hat{E}$ (see equation (3.64)).

cm, the growth rate of mode VCOS1 is dominated by the wall-normal production terms, whereas for $\lambda_x = 0.5$ cm and $\lambda_x = 1$ cm it is governed by the spanwise production contributions. In this case, this observation correlates with the occurrence of the two different manifestations of the varicose disturbance depending on the streamwise wavelength (or frequency in the spatial case), as discussed previously. Regarding the ramp-shaped element, the same terms are leading for all three different streamwise wavelengths, namely, wall-normal terms for SIN1 and spanwise terms for VCOS1.

The different behavior of the disturbance energy terms depending on the streamwise wavelength considered, as found in the cuboid configuration, implies that the growth-rate decomposition at a single streamwise station does not provide a conclusive picture of the different energy extraction mechanisms associated to the studied instabilities. For this reason, in the next section the streamwise evolution of the growth-rate decomposition of the different disturbances is assessed.

Another interesting quantity to examine is the integrand of the different terms that constitute the decomposition. The integrand of a particular term at a given streamwise position can be represented as a two-dimensional contour plot that highlights the regions of the yz plane on which most of the disturbance energy is being produced and/or dissipated. Figure 5.46 shows such a plot for the cuboid-induced sinuous mode at $\lambda_x = 0.5$ cm and $x = 0.1$ m. Integrands $\hat{P}'_{RS,12}$, $\hat{P}'_{RS,13}$, $\hat{P}'_{s,2}$ and $\hat{P}'_{s,3}$ illustrate the regions where the disturbance energy is produced (positive values only), while integrands $\hat{D}'_\mu$ and $\hat{D}'_k$ depict the areas where the perturbation energy is dissipated. Note that negative regions in the production-term

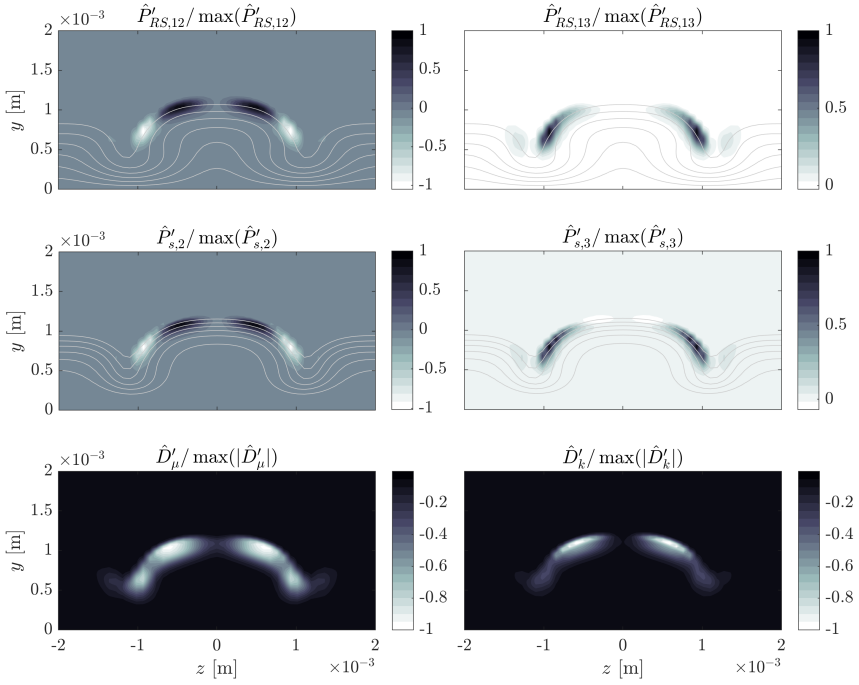

Figure 5.46: Integrands of the most relevant terms of the temporal growth-rate decomposition for the cuboid-induced SIN1 mode at $x = 0.1$ m and $\lambda_x = 0.5$ cm. The prime symbol in this case denotes the integrand associated to a given term from the growth-rate decomposition. Light grey lines represent contours of base flow streamwise velocity ($\bar{u}$) for the case of $\hat{P}'_{RS,12}$ and $\hat{P}'_{RS,13}$, and contours of base flow temperature ($\bar{T}$) in the case of $\hat{P}'_{s,2}$ and $\hat{P}'_{s,3}$. The integrands are normalized with respect to their maximum value since their magnitude does not have a meaning in this case (recall that the eigenvectors resulting from the eigenvalue problem are defined up to a complex constant).

integrands also contribute to a decrease of the perturbation energy, and therefore to stabilize the disturbance. The production of disturbance energy associated with terms $\hat{P}_{RS,12}$ and $\hat{P}_{s,2}$ takes place in the upper part of the low-velocity streak, where the base-flow fields $\bar{u}$ and $\bar{T}$ feature large wall-normal gradients, as indicated by the contour lines. This correlates with the high-shear region visible at the top of the central streak in figure 5.21(c). Immediately adjacent to these two positive regions, two negative regions are encountered, respectively located at each side edge of the streak. These areas of negative $\hat{P}'_{RS,12}$ and $\hat{P}'_{s,2}$ coincide with locations where the wall-normal gradients become small. The magnitude of these production integrands is similar in both positive and negative regions. Nonetheless, the size of the positive regions is slightly larger than that of the negative ones, resulting in small positive values of $\hat{P}_{RS,12}$ and $\hat{P}_{s,2}$ after integration, as shown in

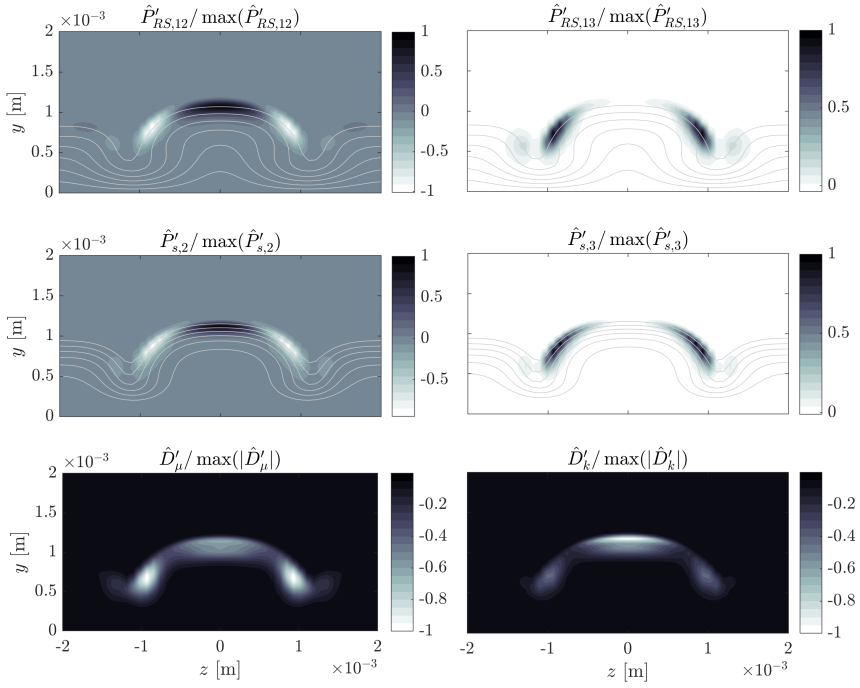

Figure 5.47: Integrands of the most relevant terms of the temporal growth-rate decomposition for the cuboid-induced VCOS1 mode at $x = 0.1$ m and $\lambda_x = 0.5$ cm, denoted by primed quantities. Light grey lines represent contours of base flow streamwise velocity ($\bar{u}$) for the case of $\hat{P}'_{RS,12}$ and $\hat{P}'_{RS,13}$, and contours of base flow temperature ($\bar{T}$) in the case of $\hat{P}'_{s,2}$ and $\hat{P}'_{s,3}$.

figure 5.43(a).

The production of disturbance energy due to the interaction with spanwise base-flow gradients originates mainly at the side edges of the central low-speed streak, as illustrated in the contour plots for $\hat{P}'_{RS,13}$ and $\hat{P}'_{s,3}$. These are the regions where the strongest spanwise gradients of $\bar{u}$ and $\bar{T}$ are found. In this case, no significant negative values are present, resulting in a larger magnitude upon integration, which explains why $\hat{P}_{RS,13}$ and $\hat{P}_{s,3}$ are significantly bigger than their wall-normal counterpart at these conditions. Regarding the dissipation terms, the integrands $\hat{D}'_{\mu}$ and $\hat{D}'_{k}$ reveal that the dissipation of disturbance energy due to friction takes place over all the region surrounding the central streak, whereas the dissipation due to thermal conduction is mainly localized in a narrow region at the top of the low-velocity streak.

The integrands for mode VCOS1 developing in the cuboid wake, shown in figure 5.47, display the same features as those for mode SIN1. A notable difference

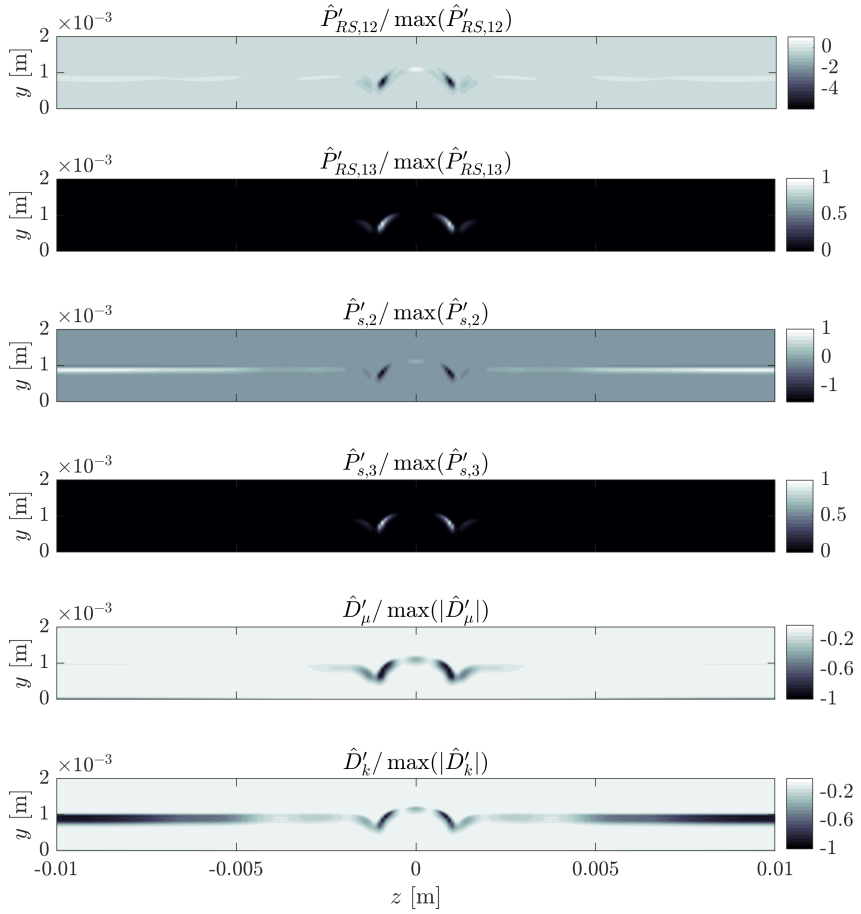

Figure 5.48: Integrands of the most relevant terms of the temporal growth-rate decomposition for the cuboid-induced M2D mode at $x = 0.1$ m and $\lambda_x = 0.5$ cm, denoted by primed quantities.

lies in the size of the negative regions in the wall-normal production integrands $\hat{P}'_{RS,12}$ and $\hat{P}'_{s,2}$, which are larger for this disturbance and become of the same size as the positive regions. This results in a small negative value of $\hat{P}_{s,2}$ and a negligible value of $\hat{P}_{RS,12}$ in this case (see figure 5.43(a)).

Finally, figures 5.48 and 5.49 respectively describe the shape of the integrands for the two-dimensional Mack mode (M2D) and the third oblique Mack mode (MO3) found in the cuboid wake at $x = 0.1$ m and $\lambda_x = 0.5$ cm. As expected, the integrand signature for the Mack modes is fundamentally different from that of the wake instabilities described above. In the Mack-mode case, a large portion

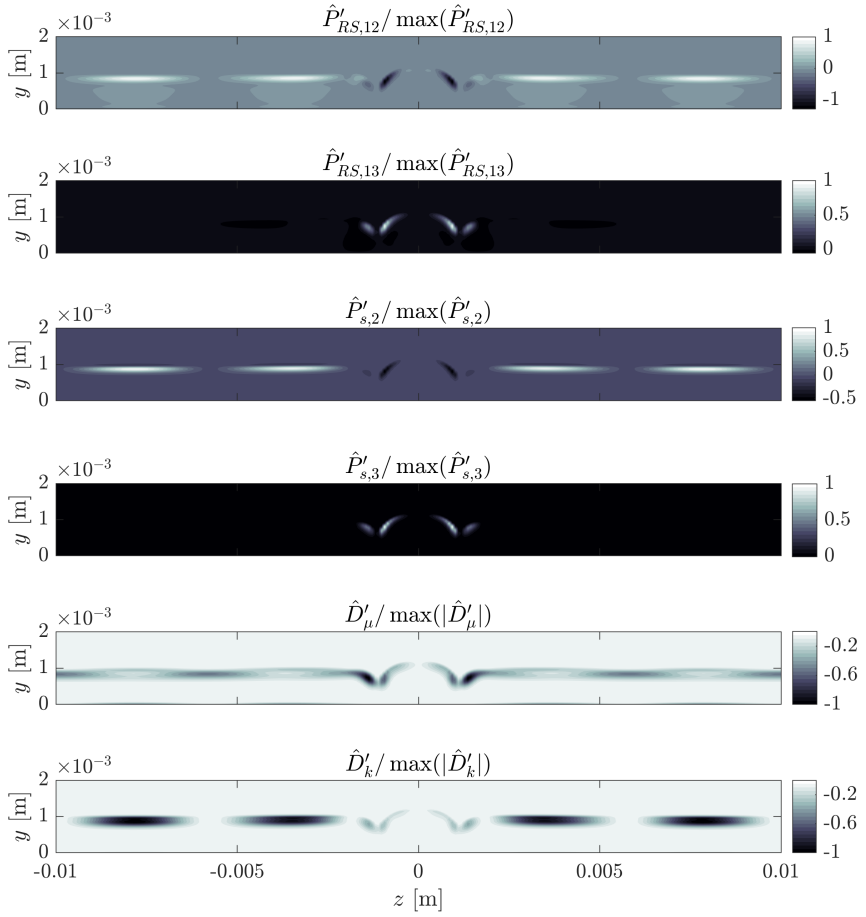

Figure 5.49: Integrands of the most relevant terms of the temporal growth-rate decomposition for the cuboid-induced MO3 mode at $x = 0.1$ m and $\lambda_x = 0.5$ cm, denoted by primed quantities.

of the disturbance energy is extracted from the wall-normal base-flow gradients in the boundary layer far outside the roughness wake. This is indicated by the (positive) production regions located near the boundary-layer edge when $z \to z_\infty$ for $\hat{P}'_{RS,12}$ and $\hat{P}'_{s,2}$. Since their nature is related to the flat-plate boundary layer, the spanwise production of modes M2D and MO3 is only induced by the presence of the roughness wake. In a smooth flat-plate boundary layer without spanwise base-flow gradients, only the wall-normal production terms would play a role in the disturbance energy of Mack modes. In this regard, it is important to emphasize that the obliqueness of the mode (such as mode MO3) does not involve any energy

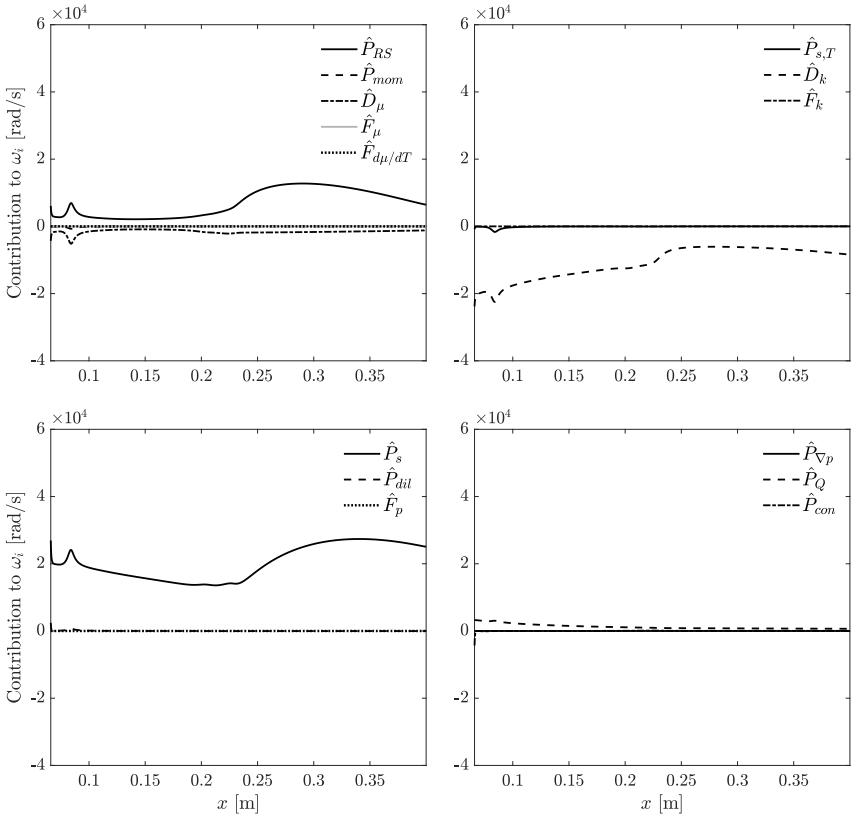

Figure 5.50: Streamwise evolution of all the different terms constituting the temporal growth rate decomposition of mode M2D for the cuboid roughness element ($\lambda_x = 0.5$ cm). Note that every term is divided by $2\hat{E}$.

contribution related to spanwise base-flow gradients. The energy dissipation of modes M2D and MO3 also takes place both at the roughness wake and at the boundary layer outside of it, following a very similar signature to that of $\hat{P}'_{RS,12}$ and $\hat{P}'_{s,2}$.

The integrands for the ramp roughness geometry (not shown) are found to have very similar features as those already described for the cuboid configuration. The accuracy of the temporal growth-rate decomposition in the roughness wake is discussed in appendix G.

5.3.6.1 Streamwise evolution of the temporal growth-rate decomposition

With the aim of investigating the particular features found in the growth-rate evolution of the different instabilities under analysis, described in § 5.3.5, the streamwise

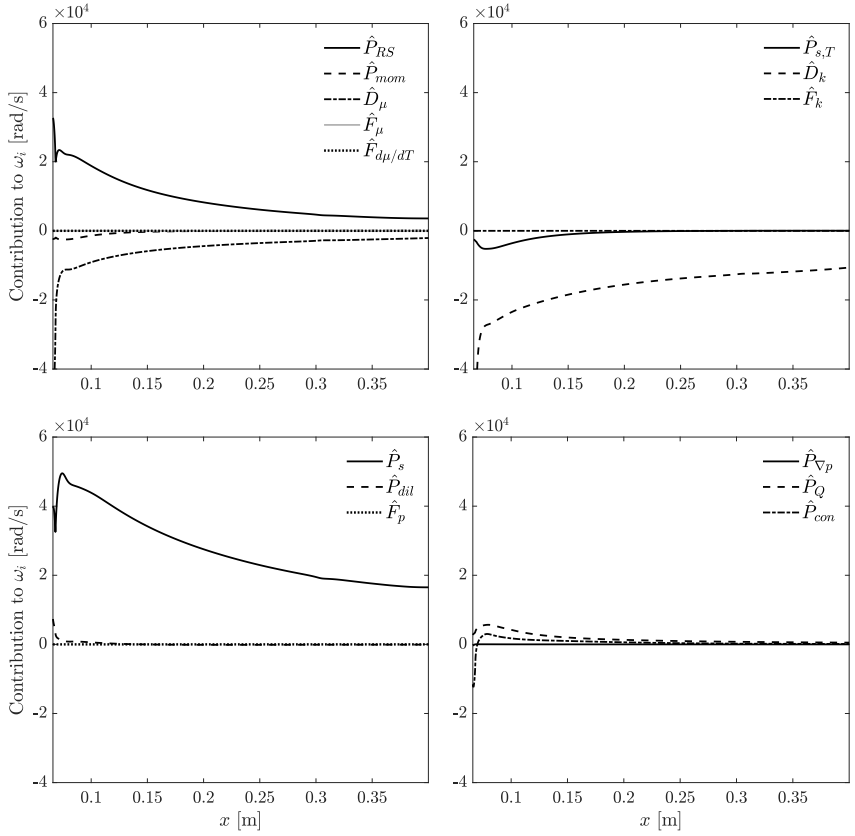

Figure 5.51: Streamwise evolution of all the different terms constituting the temporal growth rate decomposition of mode SIN1 for the cuboid roughness element ($\lambda_x = 0.5$ cm). Note that every term is divided by $2\hat{E}$.

variation of the temporal growth-rate decomposition for each of the disturbances is considered. On first place, the evolution of all the terms in the decomposition is presented in order to illustrate that only those terms selected as relevant in the previous section remain the important ones also for all the range of streamwise locations studied. For the cuboidal element at $\lambda_x = 0.5$ cm, figures 5.50, 5.51 and 5.52 depict the streamwise evolution of all the terms of the decomposition given by equation (3.64) for modes M2D, SIN1 and VCOS1, respectively. As it can be observed, for all three disturbances the important contributions to consider are $\hat{P}_{RS}$, $\hat{P}_s$, $\hat{D}_\mu$ and D_k along the entire streamwise range. As a result, the attention is focused on those particular terms in the present section as well, including the split contributions given by $\hat{P}_{s,2}$ and $\hat{P}_{s,3}$ (see equation (5.12)) and $\hat{P}_{RS,12}$ and $\hat{P}_{RS,13}$ (see equations (5.13a) and (5.13b)).

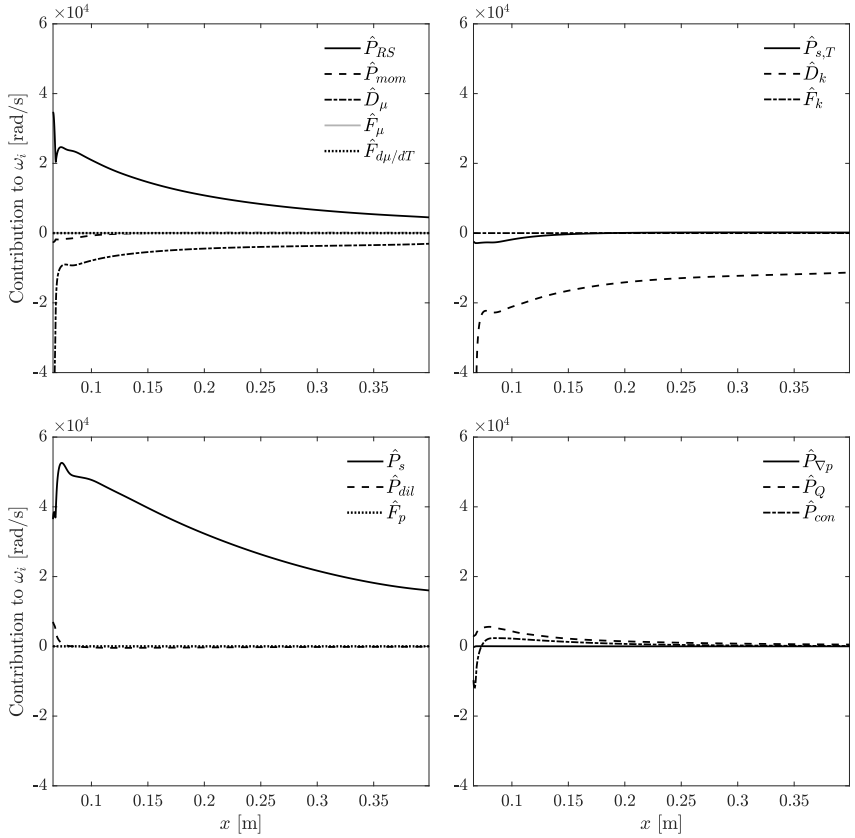

Figure 5.52: Streamwise evolution of all the different terms constituting the temporal growth rate decomposition of mode VCOS1 for the cuboid roughness element ($\lambda_x = 0.5$ cm). Note that every term is divided by $2\hat{E}$.

The relevant terms of the temporal growth-rate budget of mode M2D are represented in figure 5.53 as a function of the streamwise position in the cuboid wake at $\lambda_x = 0.5$ cm. For comparison purposes, the decomposition based on one-dimensional local linear stability theory (LST) for the two-dimensional Mack mode ($\beta = 0$) developing in a smooth flat-plate boundary layer is also included. In the LST case, the decomposition (3.64) is retrieved by setting all base-flow spanwise derivatives to zero, so that only those production terms related to the wall-normal gradients remain (see appendix E for the LST formulation of Chu's disturbance energy equation). As it can be observed, the energy of the 2D-LST Mack mode (mode M2D) is also governed by the wall-normal production terms. Despite its amplitude function being strongly modulated by the presence of the roughness wake, the energy signature of the 2D-LST Mack mode is close to the

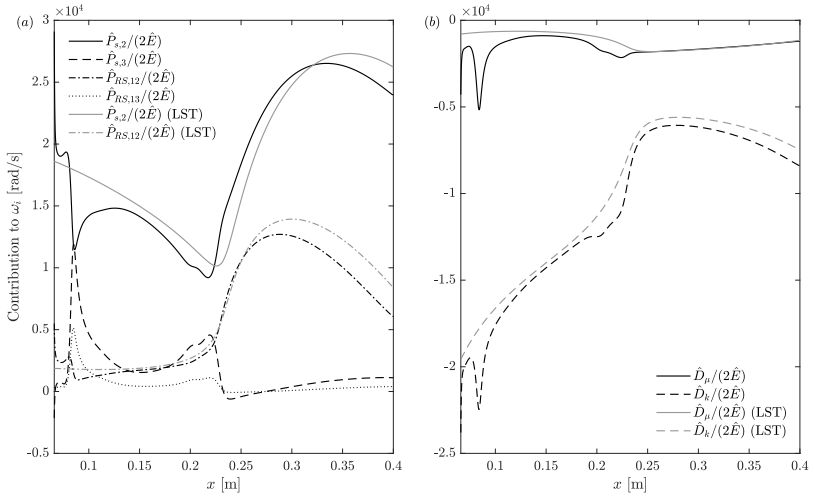

Figure 5.53: Streamwise evolution of the temporal growth-rate decomposition for the two-dimensional Mack-mode instability (M2D) found in the cuboidal roughness element wake for $\lambda_x = 0.5$ cm: (a) most important production terms; (b) dissipation terms. Results for the two-dimensional Mack mode ($\beta = 0$) developing in the corresponding smooth flat plate boundary-layer are also included for comparison, obtained by means of LST.

LST one, for which no spanwise production is present. As a result, mode M2D still extracts most of its energy from the boundary-layer outside of the roughness wake. This is an important observation, which explains why the streamwise growth-rate evolution of mode M2D, as shown in figure 5.36, is similar to that of a standard two-dimensional Mack mode (LST with $\beta = 0$).

The same behavior is also found for the oblique Mack modes encountered in the roughness wake (modes MO3, MO4 etc.). It is important to recognize that since the streamwise growth-rate evolution of the 2D-LST oblique Mack modes can also be described reasonably well by LST (see figure 5.36), their energy budget is also expected to be governed by wall-normal contributions as in LST. This is confirmed by the curves shown in figure 5.54, which compares the main disturbance energy contributions of modes M2D, MO3 and MO4. Terms $P_{s,2}$ and $P_{RS,12}$ are clearly the most important contributions to the disturbance potential and kinetic energies, respectively, highlighting the dominant role of wall-normal gradients for all three different modes.

Focusing on the growth-rate variation of the SIN1 and VCOS1 modes, the streamwise evolution of the temporal growth-rate decomposition for each of the two disturbances is presented in figures 5.55 and 5.56 for the cuboid configuration and in figures 5.57 and 5.58 for the ramp. Regarding the cuboidal geometry, it

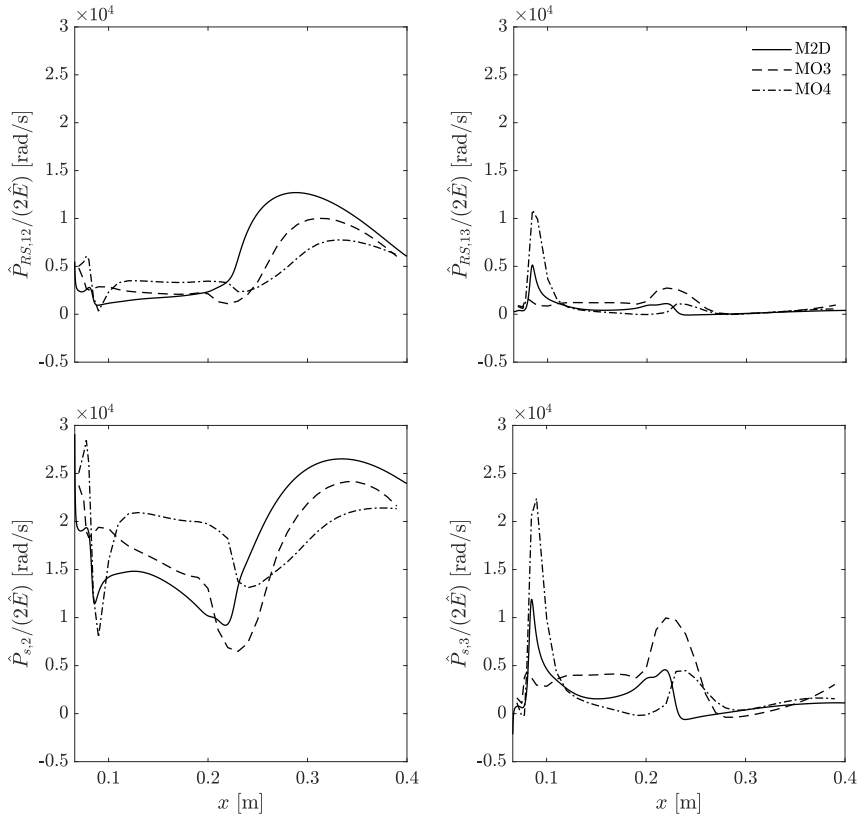

Figure 5.54: Comparison of the streamwise evolution of the production terms $\hat{P}_{RS,12}$, $\hat{P}_{RS,13}$, $\hat{P}_{s,2}$ and $\hat{P}_{s,3}$ for three different Mack-mode instabilities (M2D, MO3 and MO4) found behind the cuboidal roughness element for $\lambda_x = 0.5$ cm.

is observed that immediately behind the trailing-edge recirculation bubble, the energy of both instabilities is governed by the wall-normal production terms $\hat{P}_{s,2}$ and $\hat{P}_{RS,12}$. This implies that in this region the modes extract their energy from the wall-normal base-flow gradients. A short distance further downstream, depending on the streamwise wavelength, the wall-normal production terms rapidly decrease and the disturbance energy is transferred to the spanwise production contributions $\hat{P}_{s,3}$ and $\hat{P}_{RS,13}$, bringing the wall-normal terms to a negative (stabilizing) energy contribution for most of the studied wavelengths. After this first exchange of energy from the wall-normal to the spanwise contributions, the leading term $\hat{P}_{s,3}$ reaches a maximum and begins to decrease at an approximately constant rate. In parallel, the wall-normal terms continue to decrease, enhancing their stabilizing effect. However, after a given distance downstream, the wall-normal production

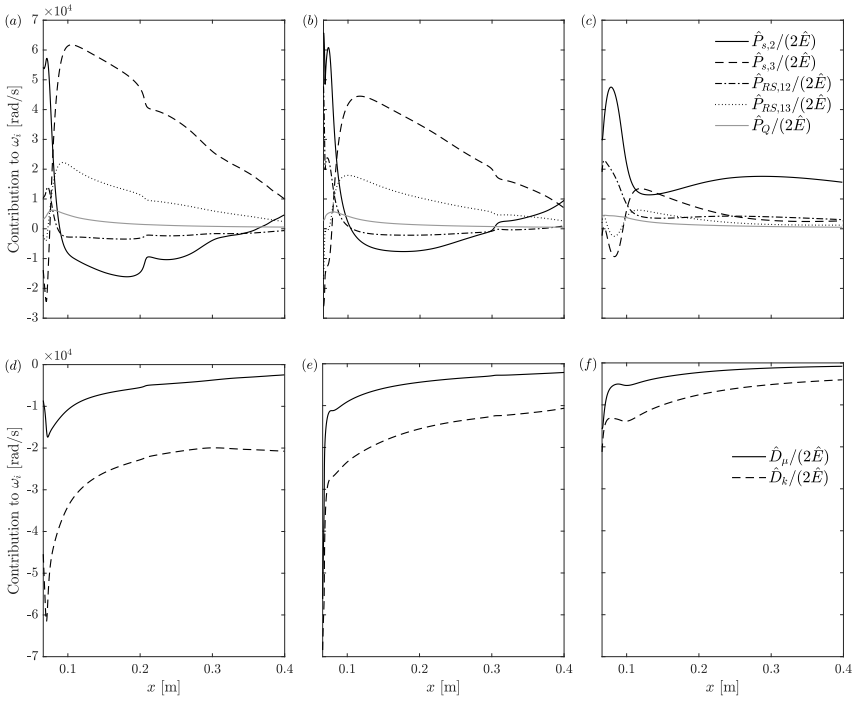

Figure 5.55: Streamwise evolution of the main production (a, b, c) *and dissipation* (d, e, f) *terms for mode SIN1 developing in the cuboidal roughness wake at three different wavelengths:* (a, d) $\lambda_x = 0.325$ *cm;* (b, e) $\lambda_x = 0.5$ *cm;* (c, f) $\lambda_x = 1$ *cm.*

terms start to rise again in most of the cases. This rise is accompanied with an acceleration in the rate of decrease of the spanwise terms, such that there is a reciprocal evolution between $\hat{P}_{s,2}$ and $\hat{P}_{s,3}$ and between $\hat{P}_{RS,12}$ and $\hat{P}_{RS,13}$. This implies that another energy transfer begins to take place along the roughness wake, in this case from spanwise to wall-normal production terms, at a slower pace than the first one. This second exchange can be observed for the sinuous mode for all three wavelengths. For $\lambda_x = 0.325$ cm and $\lambda_x = 0.5$ cm, starting at $x \approx 0.18$ m and continuing until the end of the domain. For $\lambda_x = 1$ cm, starting immediately after the first exchange ($x \approx 0.13$ m). In the case of the varicose mode, it can also be observed for $\lambda_x = 0.5$ cm (starting at $x \approx 0.35$ m) and for $\lambda_x = 1$ cm (starting at $x \approx 0.14$ m) within the studied domain length.

From the energy signature of both cuboid-induced modes at $\lambda_x = 1$ cm, it is clear that this second energy transfer mechanism brings the spanwise production terms asymptotically to approximately zero. Hence, it does not lead to stabilizing contributions associated to the work done through the spanwise base-flow gradients. This implies that the wake instabilities in this condition become governed

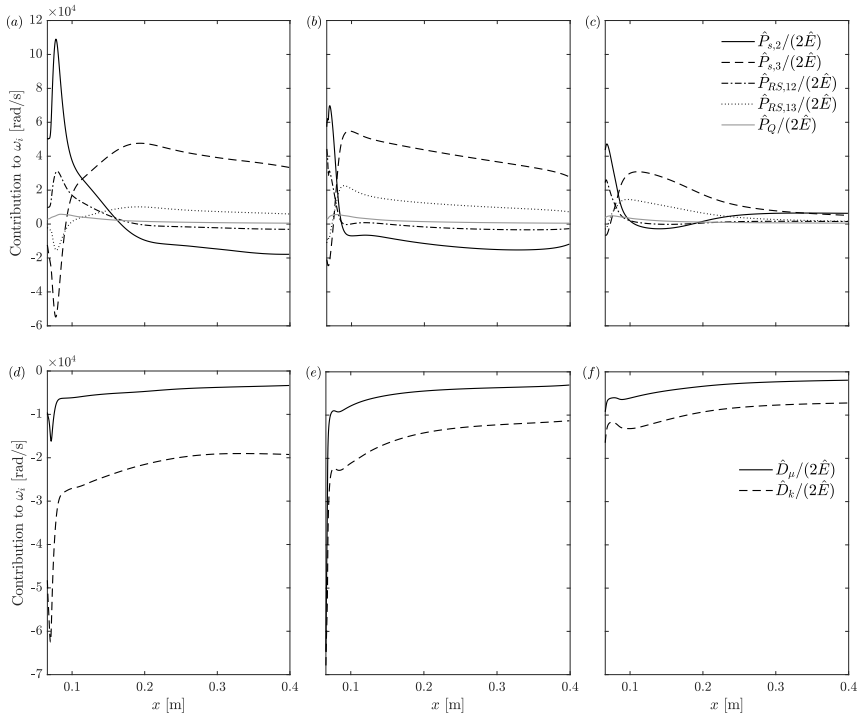

Figure 5.56: Streamwise evolution of the main production (a, b, c) *and dissipation* (d, e, f) *terms for mode VCOS1 developing in the cuboidal roughness wake at three different wavelengths:* (a, d) $\lambda_x = 0.325$ *cm;* (b, e) $\lambda_x = 0.5$ *cm;* (c, f) $\lambda_x = 1$ *cm.*

only by the energy production processes linked to the wall-normal base-flow gradients. As discussed above (see figure 5.53), this is an inherent characteristic of the energy budget of boundary-layer modes that develop in a smooth flat-plate boundary layer in which no spanwise base-flow gradients exist. In accordance with this observation, it has been found that the occurrence of the second energy exchange correlates with streamwise stations at which the amplitude of the eigenfunctions associated with the wake instabilities VCOS1 and SIN1 begins to increase also in the boundary layer outside of the roughness wake, with amplitude distributions that are equivalent to the Mack-mode instabilities shown in figure 5.31. This provides evidence that there is an interaction between the wake instabilities and the boundary-layer modes which influences the growth-rate evolution of the wake disturbances. As described later in § 5.3.7, this interaction can be interpreted as a continuous synchronization between the wake modes and the boundary-layer modes (i.e., the Mack-mode family).

For the ramp-induced instabilities (see figures 5.57 and 5.58), the disturbance

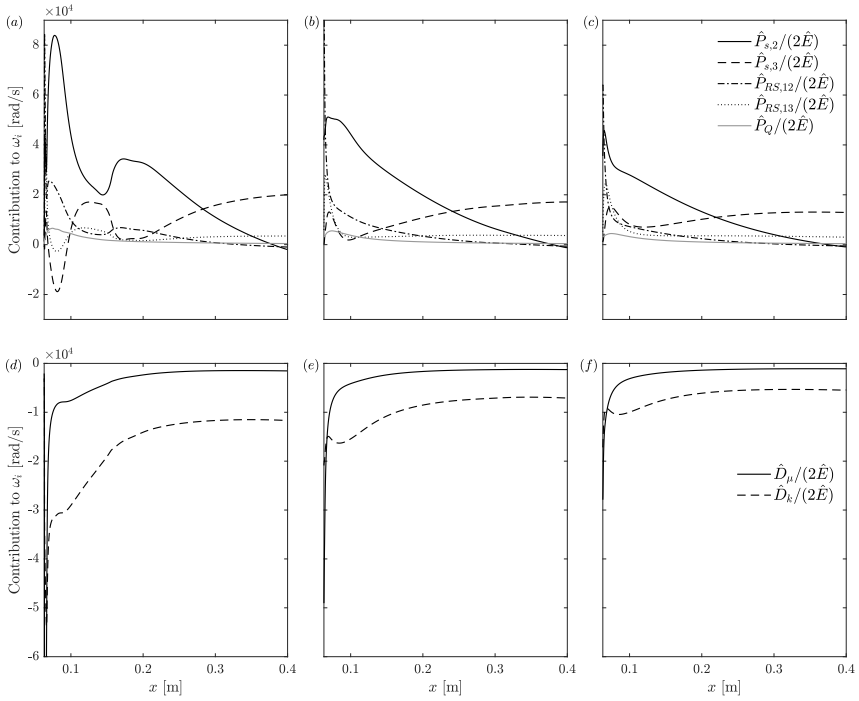

Figure 5.57: Streamwise evolution of the main production (a, b, c) *and dissipation* (d, e, f) *terms for mode SIN1 corresponding to the ramp geometry at three different wavelengths:* (a, d) $\lambda_x = 0.35$ *cm;* (b, e) $\lambda_x = 0.56$ *cm;* (c, f) $\lambda_x = 0.86$ *cm.*

energy near the roughness trailing edge is also governed by the wall-normal energy production quantities ($\hat{P}_{s,2}$ and $\hat{P}_{RS,12}$). A clear difference between the energy signature of mode SIN1 for both roughness geometries is that, for the ramp element, the first transfer of energy from the wall-normal to the spanwise production terms takes place over a longer streamwise distance. This is particularly evident for the cases with $\lambda_x = 0.56$ cm and $\lambda_x = 0.86$ cm, for which the spanwise term $\hat{P}_{s,3}$ does not become the dominant contribution until approximately half of the domain length. Therefore, the wall-normal base-flow gradients remain responsible for the excitation of the leading disturbance in the ramp-induced wake for a long distance downstream. Additionally, for $\lambda_x = 0.35$ cm, the disturbance energy evolution confirms that the sinuous mode is strongly influenced by the presence of Mack-mode instabilities starting at $x \approx 0.15$ m, as evidenced by the sharp rise in term $\hat{P}_{s,2}$ and the sharp decrease in term $\hat{P}_{s,3}$. This explains the rise in growth rate that can be observed in figure 5.38(c) for this wavelength. In this case, however, the effect of the synchronization does not last until the end of the domain. Downstream of $x \approx 0.2$ m, a third energy exchange takes place and the mode re-

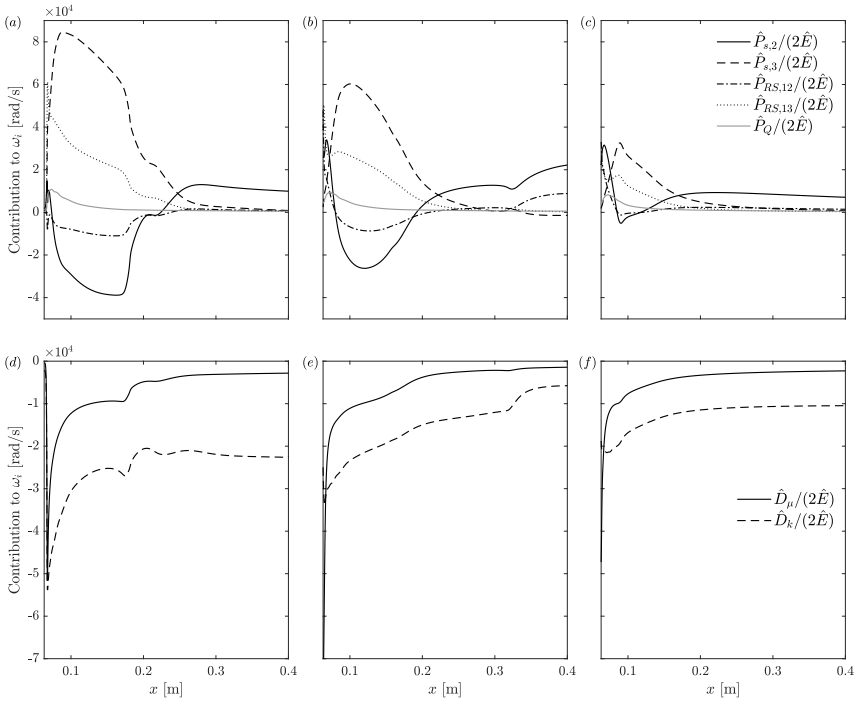

Figure 5.58: Streamwise evolution of the main production (a, b, c) *and dissipation* (d, e, f) *terms for mode VCOS1 corresponding to the ramp geometry at three different wavelengths:* (a, d) $\lambda_x = 0.35$ *cm;* (b, e) $\lambda_x = 0.56$ *cm;* (c, f) $\lambda_x = 0.86$ *cm.*

covers the behaviour of a pure wake instability, eventually becoming governed by the spanwise base-flow gradients in a similar way to the other two cases, for which no sign of a synchronization is present.

Significant differences in the energy balance of the varicose mode are also found between both roughness configurations. For the ramp geometry, the first energy transfer between wall-normal and spanwise terms occurs at a much shorter distance behind the roughness trailing edge. Similarly, the second energy exchange, which leads to a transformation of the instability towards a hybrid wake-boundary-layer disturbance, takes place further upstream and is encountered within the domain length for all three streamwise wavelengths analyzed. For $\lambda_x = 0.35$ cm, it begins to occur at $x \approx 0.17$ m, for $\lambda_x = 0.56$ cm at $x \approx 0.12$ m and for $\lambda_x = 0.86$ cm at $x \approx 0.09$ m. This explains the fluctuations in the growth rate encountered for $\lambda_x = 0.35$ cm and $\lambda_x = 0.56$ cm, as shown in figure 5.38(d). Furthermore, since for $\lambda_x = 0.86$ cm the synchronization with the boundary-layer modes begins upstream of $x = 0.1$ m, the amplitude function of the varicose mode at these conditions (displayed in figure 5.30(c)) already shows a non-zero ampli-

tude in the boundary layer at the sides of the roughness wake.

The contribution of the disturbance energy dissipation terms follows a similar trend for all the different cases analyzed for each roughness geometry. The magnitude of the dissipative energy terms is maximum immediately behind the roughness trailing edge separation region, and undergoes a very rapid decrease in a very short distance downstream. This decrease defines the streamwise location of maximum growth rate for each streamwise wavelength. Further downstream, both dissipation terms progressively decrease in magnitude. Their evolution is also found to be sensitive to the interaction with boundary-layer disturbances.

Finally, it is important to note that no significant differences are observed in the disturbance energy extraction mechanisms between both types of wake instabilities, only in the streamwise range over which the energy exchanges occur. The same finding is reported by Theiss *et al.* [5] for the streamwise evolution of the Reynolds stress production terms $\hat{P}_{RS,12}$ and $\hat{P}_{RS,13}$ near the trailing edge of different roughness geometries mounted on the forebody of a reentry capsule. For all the cases analyzed by [5], the wall-normal contribution ($\hat{P}_{RS,12}$) was also found to be larger than the spanwise one for both wake instabilities in the immediate vicinity of the roughness elements. In addition, the current results show that the streamwise evolution of the growth rate of the varicose and sinuous instabilities is not uniquely governed by the energy production terms associated to the base-flow gradients along a single spatial direction. Rather, the production terms linked to the gradients along y are the leading contributions for certain streamwise regions whereas the terms related to the gradients along z are the most important contributions for other regions. It is observed that base-flow gradients along both the wall-normal and spanwise directions play an important role in the evolution of both varicose and sinuous disturbances.

5.3.7 Synchronism between wake instabilities and boundary-layer modes

This section is devoted to illustrate a synchronization process between the wake-induced disturbances and the boundary-layer instabilities. Figure 5.59 depicts the magnitude of the streamwise velocity amplitude function of the SIN1 and VCOS1 instabilities excited by the cuboid roughness element at four different streamwise locations for $\lambda_x = 0.5$ cm. As it can be observed, after a given streamwise distance, the amplitude of the wake modes begins to increase in the regions located at the undisturbed boundary layer outside of the roughness wake, displaying a very similar signature to the oblique Mack-mode instabilities shown in figure 5.31 (the same behavior is observed for the ramp geometry, not shown here). This provides evidence of an interaction between the wake instability modes and Mack's mode family. For the same configuration, figure 5.60 shows the streamwise evolution

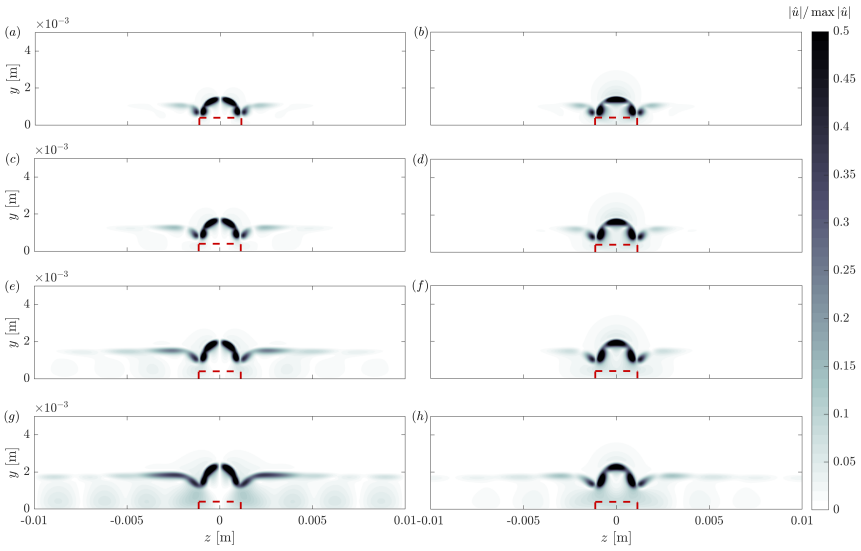

Figure 5.59: Normalized magnitude of the streamwise velocity amplitude function of modes SIN1 (a, c, e, g) and VCOS1 (b, d, f, h) for the cuboid geometry at $\lambda_x = 0.5$ cm and at four different streamwise locations: (a, b) $x = 0.15$ m; (c, d) $x = 0.2$ m; (e, f) $x = 0.27$ m; (g, h) $x = 0.38$ m. Contour levels range between 0 and $0.5|\hat{u}|/\max(|\hat{u}|)$ to favor the visualization of structures developing at the sides of the roughness wake.

of the non-dimensional phase speed ($c_{ph} = \omega_r/\alpha_r$) of the leading sinuous and varicose modes as well as of different instabilities located along the Mack-mode branch, namely, modes M2D, MO3, MO4 and MO7, already described in figure 5.31. The phase speed of mode SIN1 begins to match the phase speed of the Mack-mode instabilities starting at $x \approx 0.2$ m. This coincides with the location at which the eigenfunction of the sinuous disturbance starts to grow in amplitude in the boundary layer at the sides of the roughness wake. The same is encountered for the varicose mode, for which the match in phase speeds begins significantly further downstream, approximately at $x = 0.35$ m, once again in good agreement with the location of the change in its amplitude function according to figure 5.59. Since the Mack-mode instability manifests itself as a continuous branch in the 2D-LST spectrum, it means that there is a continuous synchronization between the wake instability modes and the Mack modes. Such a synchronization mechanism was suggested by De Tullio & Sandham [4] for the excitation of varicose modes, according to DNS results based on a very similar cuboidal roughness configuration. In this work, this phenomenon is observed for both sinuous and varicose disturbances and for the two different roughness geometries investigated, bringing further weight to the importance of this mechanism in roughness-induced transition.

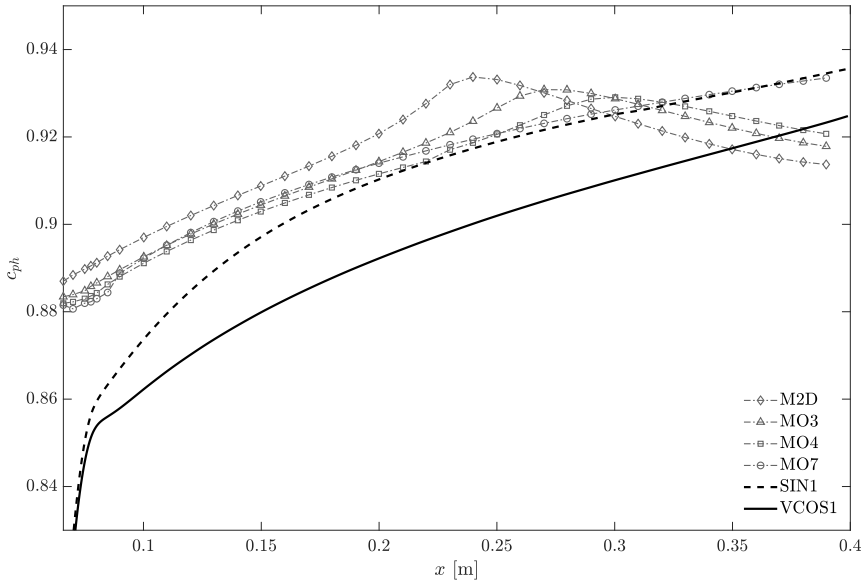

Figure 5.60: Streamwise evolution of the non-dimensional phase speed of different instability modes developing behind the cuboid roughness element for $\lambda_x = 0.5$ cm. Solid and dashed lines denote the leading wake instability modes (VCOS1 and SIN1) and dash-dot lines with symbols correspond to different Mack instability modes (M2D, MO3, MO4 and MO7).

Under the synchronization process, the wake instabilities progressively transform into hybrid modes that develop in the roughness wake as well as at the surrounding boundary layer, in the same way as the instabilities belonging to the Mack-mode family that are modulated by the roughness wake. This transformation is reflected in the energy decomposition of the sinuous and varicose modes. Recalling the streamwise evolution of the temporal growth-rate decomposition terms (figures 5.55 and 5.56), it can be noticed that there is a close relation between the location at which the synchronization starts and the position at which the leading production terms change their behavior. For $\lambda_x = 0.5$ cm, the location at which term $\hat{P}_{s,2}$ starts to grow after the first energy exchange is approximately $x = 0.2$ m for mode SIN1 and $x = 0.35$ m for mode VCOS1, which precisely coincide with the locations at which their respective phase speeds match those of the Mack-mode branch. Therefore, when the synchronization starts, the disturbance energy decomposition of modes SIN1 and VCOS1 begins to approach the energy signature of the Mack-mode instabilities (see figures 5.53 and 5.54), namely, spanwise terms ($\hat{P}_{s,3}$ and $\hat{P}_{RS,13}$) decreasing towards zero and wall-normal terms ($\hat{P}_{s,2}$ and $\hat{P}_{RS,12}$) rising. As the wake perturbations begin to develop amplitude in the boundary layer

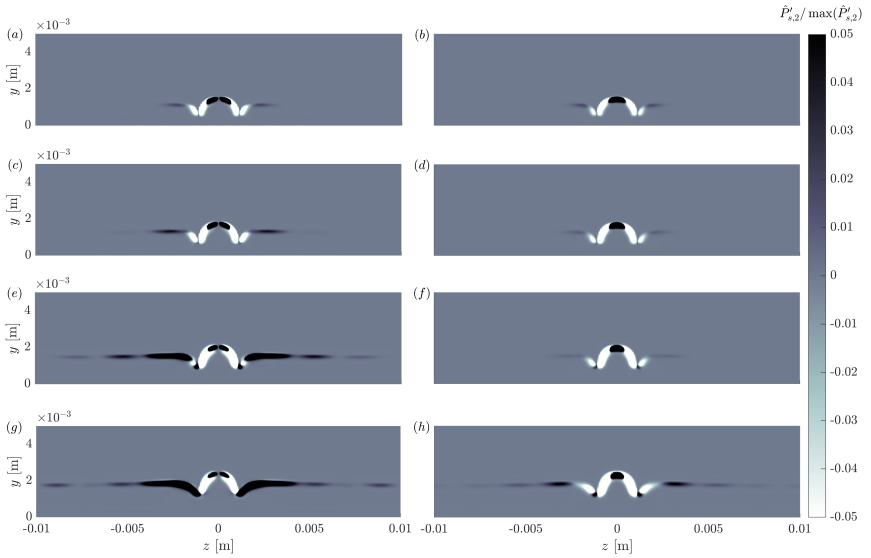

Figure 5.61: Integrands of the disturbance entropy production term associated to the wall-normal temperature gradient $(\hat{P}_{s,2})$ *for the cuboid-induced SIN1* (a, c, e, g) *and VCOS1* (b, d, f, h) *modes at* $\lambda_x = 0.5$ *cm:* (a, b) $x = 0.15$ *m;* (c, d) $x = 0.2$ *m;* (e, f) $x = 0.27$ *m;* (g, h) $x = 0.38$ *m. Contour levels range between* -0.05 *and* 0.05 *times* $\hat{P}'_{s,2}/\max(\hat{P}'_{s,2})$ *to favor the visualization of production regions at the sides of the roughness wake.*

outside of the roughness wake, there is a redistribution of the disturbance energy from the spanwise components to the wall-normal ones. This shift in the energy production of the sinuous and varicose modes is also illustrated in figures 5.61 and 5.62, which respectively display contour plots of the integrands $\hat{P}'_{s,2}$ and $\hat{P}'_{s,3}$ of both wake perturbations at the same four different streamwise stations shown in figure 5.59. Clearly, when a synchronism between wake modes and Mack modes exists, $\hat{P}'_{s,2}$ production regions appear at the boundary-layer outside of the roughness wake, indicating energy extraction from the wall-normal base-flow gradients in the undisturbed portion of the flat plate. As it can be observed in figure 5.62, this is not the case for $\hat{P}'_{s,3}$, which originates only from the spanwise gradients in the wake.

This synchronism is one mechanism by which the wake instabilities change their properties along the wake, and which has a direct impact on their amplification rates. It is therefore important to account for this phenomenon in the modeling of the linear stages of roughness-induced transition in conditions where wake and boundary-layer instabilities coexist. In this regard, an interesting point for future analysis would be to study the roughness wake using the 3D-PSE theory (see § 3.6.3). The PSE approach can contain contributions from different local

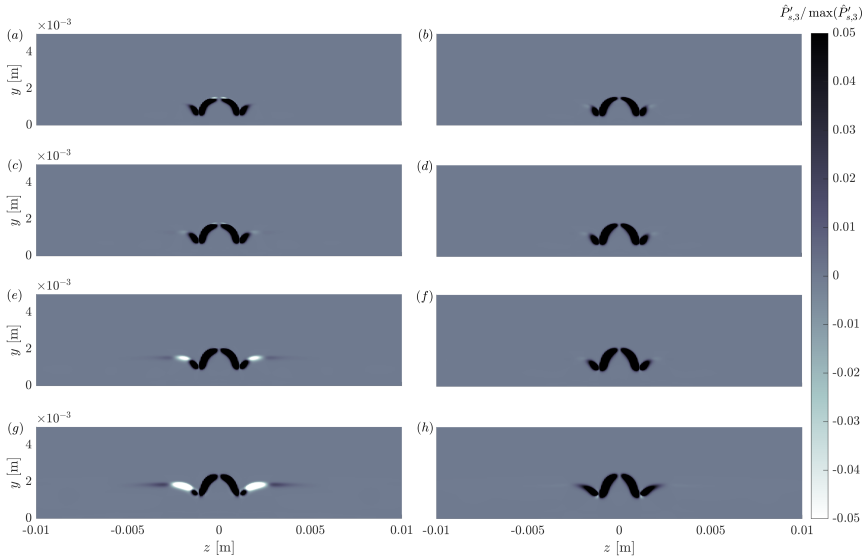

Figure 5.62: Integrands of the disturbance entropy production term associated to the spanwise temperature gradient $(\hat{P}_{s,3})$ *for the cuboid-induced SIN1* (a, c, e, g) *and VCOS1* (b, d, f, h) *modes at* $\lambda_x = 0.5$ *cm:* (a, b) $x = 0.15$ *m;* (c, d) $x = 0.2$ *m;* (e, f) $x = 0.27$ *m;* (g, h) $x = 0.38$ *m. Contour levels range between* -0.05 *and* 0.05 *times* $\hat{P}'_{s,3}/\max(\hat{P}'_{s,3})$ *to favor the visualization of production regions at the sides of the roughness wake.*

linear stability eigenmodes with different wavenumbers, even though only one of them is selected as the initial disturbance. Hence, the PSE technique should a priori be capable of capturing the complete downstream response to the initial perturbation while accounting for weakly non-parallel effects at the same time, providing a closer solution to what could be achieved using DNS. Nevertheless, in situations where more than one unstable mode is present, with wavenumbers that are different from that of the initial disturbance being tracked (such as in the cases investigated in this work), Towne *et al.* [34] have shown that the regularization techniques needed to stabilize the PSE marching can introduce errors in the solution predicted by PSE. In particular, the implicit Euler technique and the explicit damping stabilization techniques can introduce errors in the wavelength and growth rate of the response, while the pressure-gradient relaxation technique can introduce an error in the amplitude function as well. As a consequence, this issue should be taken into account in practice if 3D-PSE is to be applied to the current problem. In this regard, 3D-PSE analyses should be accompanied by DNS studies in order to asses the magnitude of the errors introduced by the PSE approach and determine whether they can be detrimental for the analysis of the problem or not. The one-way marching technique developed by Towne & Colonius [35] could also

be a path to explore since it has shown the capability of accurately capturing the full downstream response at a lower computational cost than linearized DNS.

An interesting study is the one performed by De Tullio *et al.* [3] for an isolated roughness element in a supersonic flat-plate boundary layer at Mach 2.5. Growth-rate predictions performed with 3D-PSE were found to agree well with DNS (see figure $9(b)$ in that study) for certain streamwise locations in the roughness wake but a small disagreement was reported for others. De Tullio and coauthors argue that the differences are probably related to the fact that multiple modes with different growth rates contribute to the growth of the DNS disturbance energy response. On the other hand, it is worth mentioning that 3D-PSE has been successfully applied to the instabilities developing in the wake behind an isolated roughness element in the forebody of a reentry capsule (see [5, 6]), showing very good agreement against DNS. However, in this configuration, the boundary-layer modes are highly stabilized and therefore they are not believed to have a significant influence in PSE response.

The current observations regarding the synchronism between boundary-layer and wake disturbances bear resemblance with the findings reported in the numerical analysis of Görtler vortices performed by Chen *et al.* [36, 37]. Since Görtler vortices are also characterized by streamwise streaks developing in the boundary layer, an interaction between Mack modes and streak modes also appears to be present in this case.

5.4 Summary of results

In this chapter, the instabilities induced by an isolated roughness element in a CPG Mach 6 flat-plate boundary layer have been investigated using two-dimensional local linear stability theory (2D-LST). The decomposition of the temporal growth rate introduced in § 3.10.2 based on the disturbance energy formulation of Chu [32] has been applied to the instabilities developing in the wake behind a roughness element.

Two different roughness geometries have been considered with heights that lead to subcritical roughness Reynolds numbers. The first one is a sharp-edged cuboidal element with a square planform shape and the second is a three-dimensional sharp-edged ramp geometry. In consistency with the flow fields already described in the literature, the base-flow solutions obtained from the compressible Navier-Stokes equations have shown that the roughness elements induce a pair of counter-rotating streamwise vortices which, through the lift-up mechanism, generate a wake flow structure consisting of a central low-velocity streak surrounded by two high-velocity streaks. The strong velocity gradient established at the interface between the low-velocity streak and the outer, inviscid flow leads to a three-dimensional high-shear layer that surrounds the central streak. The evolution of the

streamwise vorticity along the roughness wake indicates that the cuboidal element induces a stronger counter-rotating vortex pair than the ramp geometry. However, the smaller spanwise extent and the lateral angle present in the ramp geometry result in counter-rotating vortices that are closer to each other, generating a narrower and taller low-velocity streak.

Spatial stability analyses performed at a fixed streamwise location and frequency in the cuboidal roughness wake have shown that the streak system supports the growth of different instabilities, which manifest themselves as sinuous and varicose deformations of the low-velocity streak. The obtained spectra have illustrated that these wake instabilities coexist with the boundary-layer instabilities (Mack's first or second modes) that evolve in the flat-plate boundary layer, and which become modulated by the presence of the roughness wake. These results are in good qualitative agreement with similar configurations investigated in the literature, hence confirming the validity of the numerical methodology and the stability solver employed for the computations shown in this work. A preliminary assessment of the influence of the thermal wall boundary condition has shown that boundary-layer heating or cooling has an important impact on the growth rate of both wake and boundary-layer modes. The use of an adiabatic wall in contrast to a cold isothermal wall leads to a significant thickening of the boundary layer due to base-flow heating. This thickening, which is the responsible for the well-known stabilization of the second Mack mode, is nevertheless found to destabilize the varicose wake perturbation, in good agreement with the findings of De Tullio & Sandham [4].

Extensive temporal 2D-LST computations have been performed along the roughness wake for the range of most unstable streamwise wavelengths for each roughness geometry. Two leading instability modes have been distinguished for each case, respectively corresponding to the most unstable sinuous (SIN1) and varicose (VCOS1) instabilities. Integrated amplification factors obtained by means of a Gaster transformation of the temporal stability results show that the cuboidal roughness element excites the varicose instability more strongly than the sinuous one, whereas the ramp geometry is found to favor the growth of the sinuous mode over the varicose one. Near the roughness element, the cuboidal configuration is more effective in promoting the linear growth of the dominant wake instability mode than the ramp-shaped obstacle. Further downstream, however, the ramp-induced wake leads to a higher disturbance amplitude.

The decomposition of the temporal growth rate of the instabilities evolving in the roughness wake has revealed that the most important contributions to the generalized disturbance potential energy come from the transport of disturbance entropy across the base-flow temperature gradients ($\hat{P}_s$), while the largest contributions to the disturbance kinetic energy are produced by the work done by the Reynolds stresses against the base-flow velocity shear layers ($\hat{P}_{RS}$). Previous stud-

ies in high-speed roughness-induced transition have mainly analyzed production of disturbance kinetic energy due to the perturbation Reynolds stresses. However, the current results have indicated that the production of potential energy due to entropy fluctuations might also play a significant role in high-speed flows. In addition, the obtained decompositions have shown that in practice, for the disturbance energy analysis of roughness wake instabilities developing in a configuration like the one presented in this work, it is sufficient to pay attention to the production terms $\hat{P}_s$ and $\hat{P}_{RS}$, and to the dissipation terms $\hat{D}_\mu$ and $\hat{D}_k$. The remaining terms bring small contributions which are not significant.

The streamwise evolution of the disturbance energy decomposition has illustrated that both wake instabilities are dominated by the wall-normal production terms in the vicinity of the roughness element and that the energy is progressively transferred to the spanwise production terms further downstream. The rate at which this transfer takes place has been found to be faster for the cuboidal element. A relevant finding is that no significant differences are observed in the energy extraction mechanisms between both types of wake instability, only in the range over which the energy transfer occurs. Therefore, both wall-normal and spanwise base-flow gradients appear to play a major role in the excitation of both sinuous and varicose instabilities.

For many of the conditions investigated, the amplitude of the wake modes has been found to grow in the boundary layer at the sides of the roughness wake, resembling the amplitude function of Mack-mode instabilities. This behavior has been observed to correlate with changes in the evolution of the energy production terms, more specifically, with downstream locations at which the wall-normal production terms begin to rise and the spanwise terms accelerate their rate of decrease. An analysis of the phase speed evolution of different instabilities has shown that this behavior also correlates with the location at which the phase speed of the wake modes matches that of the Mack-mode instabilities. These observations provide evidence that there is a continuous synchronization between the wake instabilities and the boundary-layer modes. When this synchronization begins to take place, the energy signature of the wake modes changes its behavior and starts to become similar to that of Mack-mode disturbances. This phenomenon has important implications in the growth-rate evolution of the wake instabilities, contributing in some cases to enhance their amplification rate or to decrease the rate of decay of the perturbations. Such a mechanism for the excitation of wake modes was suggested by De Tullio & Sandham [4] for the case of varicose disturbances behind a cuboidal roughness element, according to DNS-based analyses. Here, this phenomenon has been observed for both sinuous and varicose instabilities induced by two different roughness geometries, which brings further proof that this mechanism could play a crucial role in roughness-induced transition.

References

[1] S. C. Tirtey. *Characterization of a Transitional Hypersonic Boundary Layer in Wind Tunnel and Flight Conditions*. PhD thesis, Université Libre de Bruxelles and von Karman Institute for Fluid Dynamics, 2009.

[2] John D. Anderson Jr. *Hypersonic and High Temperature Gas Dynamics*. American Institute of Aeronautics and Astronautics, Reston VA, second edition, 2006.

[3] Nicola De Tullio, Pedro Paredes, Neil D. Sandham, and Vassilios Theofilis. *Laminar-turbulent transition induced by a discrete roughness element in a supersonic boundary layer*. Journal of Fluid Mechanics, 735:613–646, 2013.

[4] Nicola De Tullio and Neil D. Sandham. *Influence of boundary-layer disturbances on the instability of a roughness wake in a high-speed boundary layer*. Journal of Fluid Mechanics, 763:136–145, 2015.

[5] Alexander Theiss, Stefan J. Hein, Syed Raza Christopher Ali, and Rolf Radespiel. *Wake flow instability studies behind discrete roughness elements on a generic re-entry capsule*. AIAA paper, 2016-4382, 2016.

[6] Antonio Di Giovanni and Christian Stemmer. *Cross-flow-type breakdown induced by distributed roughness in the boundary layer of a hypersonic capsule configuration*. Journal of Fluid Mechanics, 856:470–503, 2018.

[7] S. D. Stouffer, N. R. Baker, D. P. Capriotti, and G. B. Northam. *Effects of compression and expansion ramp fuel injector configurations on scramjet combustion and heat transfer*. AIAA paper, 1993-609, 1993.

[8] M Bernardini, S Pirozzoli, Orlandi. P, and S. K. Lele. *Compressible boundary layer transition induced by isolated roughness elements*. In Centre for Turbulence Research, Proceedings of the Summer Program 2012, pages 15–24, 2012.

[9] Matteo Bernardini, Sergio Pirozzoli, Paolo Orlandi, and Sanjiva K. Lele. *Parameterization of boundary-layer transition induced by isolated roughness elements*. AIAA Journal, 52(10):2261–2269, 2014.

[10] Derek Liechty, Scott Berry, Brian Hollis, and Thomas Horvath. *Comparison of Methods for Determining Boundary Layer Edge Conditions for Transition Correlations*. AIAA paper, 2003-3590, 2003.

[11] John A. Redford, Neil D. Sandham, and Graham T. Roberts. *Compressibility effects on boundary-layer transition induced by an isolated roughness element*. AIAA Journal, 48(12):2818–2830, 2010.

[12] Matteo Bernardini, Sergio Pirozzoli, and Paolo Orlandi. *Compressibility effects on roughness-induced boundary layer transition*. International Journal of Heat and Fluid Flow, 35:45–51, 2012.

[13] Daniel C. Reda. *Review and Synthesis of Roughness-Dominated Transition Correlations for Reentry Applications*. Journal of Spacecraft and Rockets, 39(2):161–167, 2002.

[14] Steven P. Schneider. *Effects of Roughness on Hypersonic Boundary-Layer Transition*. Journal of Spacecraft and Rockets, 45(2):193–209, 2008.

[15] Gordon Groskopf and Markus J. Kloker. *Instability and transition mechanisms induced by skewed roughness elements in a high-speed laminar boundary layer*. Journal of Fluid Mechanics, 805:262–302, 2016.

[16] Jean Christophe Loiseau, Jean Christophe Robinet, Stefania Cherubini, and Emmanuel Leriche. *Investigation of the roughness-induced transition: Global stability analyses and direct numerical simulations*. Journal of Fluid Mechanics, 760:175–211, 2014.

[17] M. A. Bucci, D. K. Puckert, C. Andriano, J. C. Loiseau, S. Cherubini, J. C. Robinet, and U. Rist. *Roughness-induced transition by quasi-resonance of a varicose global mode*. Journal of Fluid Mechanics, 836:167–191, 2018.

[18] John D. Anderson Jr. *Fundamentals of Aerodynamics*. McGraw-Hill, New York NY, fifth edition, 2011.

[19] Nicola De Tullio and Neil D. Sandham. *Direct numerical simulations of roughness receptivity and transitional shock-wave/boundary-layer interactions*. Technical report, RTO-MP-AVT-200, 22, NATO, 2012.

[20] Pedro Paredes, Nicola De Tullio, Neil D. Sandham, and Vassilios Theofilis. *Instability Study of the Wake Behind a Discrete Roughness Element in a Hypersonic Boundary-Layer*. Instability and Control of Massively Separated Flows, Fluid Mechanics and Its Applications, 107:91–96, 2015.

[21] Ponnampalam Balakumar and Mujeeb R. Malik. *Discrete modes and continuous spectra in supersonic boundary layers*. Journal of Fluid Mechanics, 239:631–656, 1992.

[22] Ponnampalam Balakumar. *Stability of Supersonic Boundary Layers Over Blunt Wedges*. In 36th AIAA Fluid Dynamics Conference and Exhibit, volume 1, pages 487–496, Reston, Virigina, jun 2006. American Institute of Aeronautics and Astronautics.

[23] Kenneth F. Stetson. *Nosetip bluntness effects on cone frustum boundary layer transition in hypersonic flow*. AIAA paper, 83-1763, 1983.

[24] Pedro Paredes, Meelan M. Choudhari, and Fei Li. *Mechanism for frustum transition over blunt cones at hypersonic speeds*. Journal of Fluid Mechanics, 894:A22, jul 2020.

[25] Leslie M. Mack. *Boundary-Layer Linear Stability Theory*. In Special Course on Stability and Transition of Laminar Flow, AGARD-R-709, pages 3.1–3.81, 1984.

[26] Christian Stemmer, Marcel Birrer, and Nikolaus A. Adams. *Disturbance development in an obstacle wake in a reacting hypersonic boundary layer*. Journal of Spacecraft and Rockets, 54(4):945–960, 2017.

[27] Gordon Groskopf, Markus J. Kloker, and Olaf Marxen. *Bi-global crossplane stability analysis of high-speed boundary-layer flows with discrete roughness*. IUTAM Bookseries, 18:171–176, 2010.

[28] Meelan M. Choudhari, Fei Li, Chau-Lyan Chang, Andrew Norris, and Jack Edwards. *Wake instabilities behind discrete roughness elements in high speed boundary layers*. AIAA paper, 2013-0081, 2013.

[29] Iván Padilla Montero and Fabio Pinna. *BiGlobal stability analysis of the wake behind an isolated roughness element in hypersonic flow*. Proceedings of the Institution of Mechanical Engineers, Part G: Journal of Aerospace Engineering, 234(1):5–19, jan 2020.

[30] M Gaster. *A note on the relation between temporally-increasing and spatially-increasing disturbances in hydrodynamic stability*. Journal of Fluid Mechanics, 14(2):222–224, 1962.

[31] Gordon Groskopf, Markus J. Kloker, K A Stephani, Olaf Marxen, and Gianluca Iaccarino. *Hypersonic flows with discrete oblique surface roughness and their stability properties*. In Center of Turbulence Research, Proceedings of the Summer Program, pages 405–422, 2010.

[32] Boa Teh Chu. *On the energy transfer to small disturbances in fluid flow (Part I)*. Acta Mechanica, 1(3):215–234, sep 1965.

[33] Mujeeb R. Malik, Fei Li, Meelan M. Choudhari, and Chau-Lyan Chang. *Secondary instability of crossflow vortices and swept-wing boundary-layer transition*. Journal of Fluid Mechanics, 399:85–115, 1999.

[34] Aaron Towne, Georgios Rigas, and Tim Colonius. *A critical assessment of the parabolized stability equations*. Theoretical and Computational Fluid Dynamics, 33(3-4):359–382, 2019.

[35] Aaron Towne and Tim Colonius. *One-way spatial integration of hyperbolic equations*. Journal of Computational Physics, 300:844–861, 2015.

[36] Xi Chen, Jianqiang Chen, Xianxu Yuan, Guohua Tu, and Yifeng Zhang. *From primary instabilities to secondary instabilities in Görtler vortex flows*. Advances in Aerodynamics, 1(1), 2019.

[37] X. Chen, G. L. Huang, and C. B. Lee. *Hypersonic boundary layer transition on a concave wall: Stationary Görtler vortices*. Journal of Fluid Mechanics, 865:1–40, 2019.

6

Influence of vibrational excitation and chemical non-equilibrium on the roughness wake instability

6.1 Problem description and methodology

This chapter presents the analysis of the instabilities induced by an isolated roughness element in a high-temperature boundary layer in which the effects of the excitation of the vibrational internal energy mode, dissociation and molecular diffusion become relevant. The geometrical configuration considered, depicted in figure 6.1, consists of a cuboidal roughness element placed on the surface of a wedge inside a hypersonic freestream. The wedge half-angle is $\theta = 20$ degrees and its leading edge is assumed to be infinitely sharp. The freestream conditions considered are summarized in table 6.1. These values have been chosen to be representative of a point in the reentry trajectory of a vehicle like the Space Shuttle orbiter at an altitude of 65 km, where chemical non-equilibrium effects are known to play a non-negligible role (see figure 1.2). The Knudsen number for these freestream conditions, considering a body length of 10 cm (representative of the size of discrete roughness element found on the surface of the Space Shuttle orbiter, such as the protuberance installed for the BLTFE experiment [1]), is $Kn = 0.005$. For this value of the Knudsen number, the flow can be assumed to be in the continuum regime ($Kn < 0.03$) [2].

The leading edge of the roughness element is located inside the laminar bound-

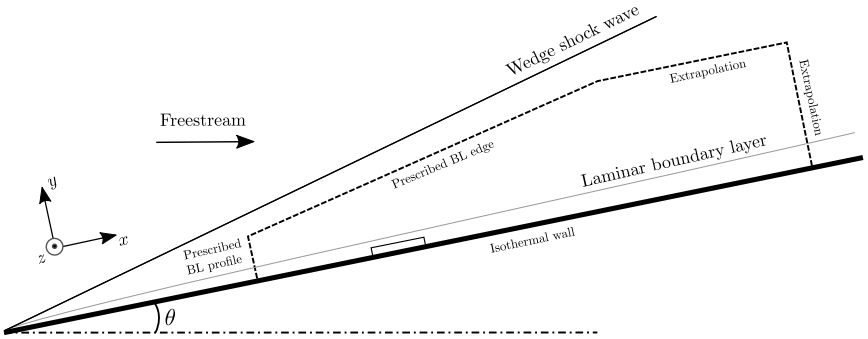

Figure 6.1: Representation of the geometrical configuration of the problem under study and the computational domain employed for the base flow calculations (not to scale).

M_∞	u_∞ [m/s]	T_∞ [K]	p_∞ [Pa]	ρ_∞ [kg/m^3]	Re_∞/l [1/m]
18	5490.93	231.45	10	1.504e-04	5.50e+04

Table 6.1: Freestream conditions considered in this chapter.

ary layer at a streamwise distance of $x_h = 1.2$ m from the wedge leading edge and is centered along the spanwise direction at $z = 0$ (streamwise symmetry plane). The roughness height is fixed to be $h = 1.62$ cm, and its planform shape is square with length and width equal to $6h$. These dimensions were chosen to yield a ratio of roughness height to the local unperturbed boundary-layer thickness of $h/\delta_{99} \approx 0.45$ and a roughness Reynolds number of $Re_h \approx$ 300-400, depending on the flow assumption. This range of Re_h is similar to that of the cases studied in chapter 5.

The computational domain employed for the base flow calculations is also represented in figure 6.1 and its dimensions are listed in table 6.2, where (x_{in}, y_{in}) and (x_{out}, y_{out}) respectively denote the streamwise coordinate and height of the inlet and the outlet planes and z_∞ denotes the spanwise size, which is constant. The domain is located inside the shock layer established between the shock wave induced at the wedge leading edge and the wedge surface. This requires imposing a boundary-layer profile at the inflow boundary. The top boundary has initially a constant slope and after a streamwise distance of 7 m downstream of the wedge leading edge it becomes flat. This is done to reduce the height of the computational domain in the region surrounding the roughness element, where a higher grid resolution is required, and to avoid that roughness-induced shock waves impinge on the upper boundary before they are far away from the boundary layer.

Three different thermodynamic flow assumptions are considered to analyze the roughness-wake instability, namely, a calorically perfect gas, a thermally perfect

x_{in} [m]	x_{out} [m]	y_{in} [m]	y_{out} [m]	z_∞ [m]
0.5	60	0.49	1.87	0.65

Table 6.2: Dimensions of the computational domain. The origin is located at the wedge leading edge.

Flow	h/δ_{99}	Re_h	$Re_{h,w}$
CPGS	0.44	348	547
CPGGW	0.37	305	538
TPG	0.45	382	613
CNE	0.45	384	615

Table 6.3: Ratio of roughness height to the local boundary-layer thickness at the roughness leading edge ($x = 1.2$ m) and roughness Reynolds number for the different flow assumptions. See equations (5.1) and (5.2) for the definition of Re_h and $Re_{h,w}$.

gas and a mixture of five perfect-gas species in chemical non-equilibrium (see chapter 2 for their respective definitions). A comparison between the instabilities computed by means of CPG and TPG allows to assess the influence of vibrational excitation, while the differences between the TPG and the CNE results highlight the effect of chemical reactions. The TPG and the CNE assumptions employ the thermal model described in § 2.5.1 and the Gupta-Wilke transport model (see § 2.5.2.2). For CNE, the chemical reactions are modeled as described in § 2.5.3. For the CPG assumption, two different transport models are considered, namely, Sutherland's law[1] and the Gupta-Wilke model. This is done to examine the pure effect that the transport property modeling has on the roughness-wake instabilities. The distinction between the CPG assumption using each of these transport models is denoted as CPGS (Sutherland) and CPGGW (Gupta-Wilke). These considerations lead to a total of four different cases for this study, respectively designated as CPGS, CPGGW, TPG and CNE.

The values of the parameters h/δ_{99}, Re_h and $Re_{h,w}$ for each case are reported in table 6.3. The boundary-layer thickness is estimated using the total enthalpy (h_0) criterion defined as $h_0/h_{0,e} = 0.995$ in a boundary-layer profile obtained by solving the boundary-layer equations at the location of the roughness element. For the CPG and the TPG assumptions, the boundary-layer profile is self-similar, whereas for CNE it is obtained by marching the boundary-layer equations (see § 2.4). The boundary-layer profiles imposed at the inflow of the computational do-

[1] In this chapter, for the CPG assumption with Sutherland's law, the latter is employed for viscosity only. The thermal conductivity is computed from the assumption of a constant Prandtl number with value $Pr = 0.7$.

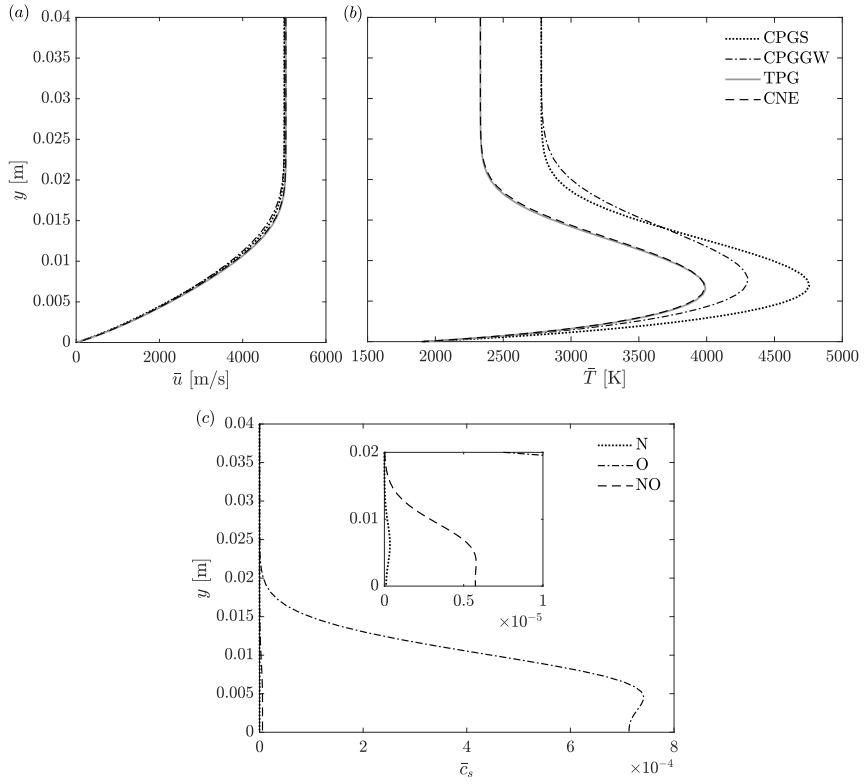

Figure 6.2: Boundary-layer profiles imposed at the inflow of the computational domain ($x = 0.5$ m) for each flow assumption: (a) streamwise velocity profiles; (b) temperature profiles; (c) mass fractions of the species produced as a result of chemical reactions in the CNE case.

main for each case are represented in figure 6.2, which were obtained by means of the DEKAF solver (see § 4.1.2). As it can be observed by comparing the CPGGW profile against the TPG or the CNE profiles, the excitation of the vibrational internal energy mode results in a significant cooling of the boundary layer, which is also associated with a reduction in the boundary-layer thickness. This effect translates in a larger h/δ_{99} as well as a larger roughness Reynolds number for TPG/CNE with respect to CPGGW. On the other hand, the differences between the TPG and the CNE cases at this location are very small, reflecting that, at $x = 0.5$ m, the influence of chemical reactions is not yet relevant. The mass-fraction profiles shown in figure 6.2(c) illustrate the concentration of the species produced by chemical reactions. As expected for the range of temperatures found in the boundary layer (see figure 2.1), atomic oxygen (O) features the highest mass fraction, followed by

Flow	M_e	u_e [m/s]	T_e [K]	p_e [Pa]
CPGS/CPGGW	4.73	5000.95	2780.66	662.66
TPG	5.40	5037.13	2331.77	642.30
CNE	5.40	5037.13	2331.77	642.30

Table 6.4: Flow conditions at the boundary-layer edge, denoted by the subscript e, for the different flow assumptions. These conditions are equivalent to the flow quantities downstream of the wedge shock wave, computed according to inviscid theory [2]. For CNE, the boundary-layer edge values depend slightly on the streamwise direction because the composition of the gas is different at each station. The values shown in the table for the CNE case correspond to the location of the computational domain inflow ($x = 0.5$ m). However, their variation along the entire streamwise domain length for the configuration under analysis is below 0.1%.

very small concentrations of nitric oxide (NO) and nitrogen (N). As shown later in § 6.2, the impact of chemical non-equilibrium becomes more important further downstream as the flow progressively undergoes increasing levels of dissociation.

Regarding case CPGS, the use of Sutherland's law leads to a severe underprediction of viscosity (see figure 2.2), which in turn results in a higher boundary-layer temperature and a smaller boundary-layer thickness. Note that the CPGS profile happens to have a similar boundary-layer height as the TPG and CNE profiles. Nevertheless, as emphasized as well by Miró Miró [3], it is important to mention that this fact is simply due to a serendipitous cancellation between the increase in boundary-layer thickness associated with not taking into account vibrational excitation, as shown by case CPGGW, and the reduction of the boundary-layer height associated with the use of Sutherland's law. The right prediction of the boundary-layer thickness for CPGS cannot be attributed to a sound modeling of the aforementioned high-temperature effects.

The base-flow solutions for the different flow assumptions considered are obtained by means of CFD++® (see § 4.1.3.1). The base-flow boundary conditions are labeled in figure 6.1. At the inflow boundary, the boundary-layer profiles displayed in figure 6.2 are prescribed. Similarly, at the part of the top boundary that has a slope, the boundary-layer edge conditions are prescribed, which are identical to the post-shock conditions listed in table 6.4. These values are computed from inviscid theory through the Rankine-Hugoniot relationships [2]. In order to avoid a mismatch between the boundary-layer edge properties and the actual boundary-layer profile at the top of the inflow boundary, the wall-normal velocity component of the inflow profile is set to zero. At the flat portion of the top boundary and at the outflow boundary, the primitive flow variables are extrapolated from the interior of the domain, which is equivalent to a supersonic outflow boundary condition. At the spanwise domain boundaries ($z = 0$ and $z = z_\infty$), symmetry conditions

are specified. Finally, at the wall, a no-slip, non-catalytic isothermal condition is enforced, with a wall temperature of $T_w = 1900$ K. This value is chosen as a representative temperature for the decomposition of a conventional thermal protection system [4]. A more detailed description of these boundary conditions can be found in § 2.3.

The grid used for the base-flow calculations is generated using OpenFOAM's utility blockMesh, see § 4.1.3.2. The same grid is employed for all four cases, with a resolution along each spatial direction of $N_x \times N_y \times N_z = 830 \times 320 \times 190$, resulting in 50 million cells.

The 2D-LST eigenvalue problem is discretized using the FD-q technique with a polynomial order $q_p = 8$. Periodic boundary conditions are considered for the perturbations at the spanwise boundaries, such that the complete spanwise domain is included in the discretization. Note that in the case of CNE, the vector of state variables contains nine independent quantities, namely, $\tilde{\rho}_{\mathrm{N}}$, $\tilde{\rho}_{\mathrm{O}}$, $\tilde{\rho}_{\mathrm{NO}}$, $\tilde{\rho}_{\mathrm{N}_2}$ and $\tilde{\rho}_{\mathrm{O}_2}$, $\tilde{u}$, $\tilde{v}$, $\tilde{w}$ and $\tilde{T}$. At the wall-normal boundaries, $\tilde{\rho}_{\mathrm{N}}$, $\tilde{\rho}_{\mathrm{O}}$, $\tilde{\rho}_{\mathrm{NO}}$ and $\tilde{\rho}_{\mathrm{N}_2}$ are forced to obey the individual species wall-normal momentum equations, whereas $\tilde{\rho}_{\mathrm{O}_2}$ is forced to satisfy the mixture wall-normal momentum equation. The remaining boundary conditions on the perturbation quantities follow the description given in § 3.9.

The mapping introduced by Malik (see § 4.2.2.1) is applied along the wall-normal direction, whereas along the spanwise direction the biquadratic mapping described in § 4.2.2.2 is used. The implicitly restarted Arnoldi algorithm is employed to compute a small number of eigenvalues and eigenvectors for each case. Note that the CNE spatial eigenvalue problem is two times bigger than the CPG or the TPG ones, which significantly increases the computational cost.

Finally, it is emphasized that the present configuration constitutes an academic test case used to evaluate the effect of some high-temperature phenomena on the instability of a simple boundary layer with discrete roughness. Realistic configurations would rather incorporate blunt-body geometries as well. In addition, although the freestream Knudsen number associated to the conditions analyzed in this chapter ($Kn = 0.005$ for a body length of 10 cm) is within the continuum regime according to the commonly assumed threshold (see for instance [2]), the DSMC simulations of Lofthouse *et al.* [5] have shown that for values of Kn in this range, small continuum breakdown effects might be present in certain regions of the flow field, such as in shock waves or in the wedge boundary layer. These effects can introduce a small velocity slip and a small temperature jump at the wall boundary. According to [5], differences of approximately 1% should be expected in the surface base-flow quantities when comparing Navier-Stokes simulations using no-slip boundary conditions and DSMC simulations for the conditions under study.

The aforementioned rarefied-gas effects have not been considered in the in-

vestigations performed in this work. However, it is important to emphasize that, although small, the finite slip velocity and temperature jump at the wall might have an impact on the flow instability. The influence of this phenomena could be evaluated by employing slip boundary conditions in the Navier-Stokes simulations used to obtain the base-flow field, such as the conditions derived by Lockerby *et al.* [6] or Gökçen and MacCormack [7]. Similarly, the equations that define the slip boundary conditions could be linearized and applied to the perturbations in linear stability analyses.

6.2 Stability analysis of the smooth wedge configuration

Before studying the three-dimensional base-flow field induced by the presence of the roughness element, the boundary-layer stability of the smooth wedge configuration (i.e., without the obstacle) is examined. For this purpose, spatial LST computations are performed along the wedge surface, employing base flows based on boundary-layer computations obtained with DEKAF. As it is known from hypersonic boundary-layer stability theory, the instability of the smooth boundary layer at the conditions under study is governed by second Mack-mode disturbances, which feature the highest growth rate as two-dimensional waves ($\beta = 0$).

Figure 6.3 illustrates the integrated amplification factor (N-factor) envelope curves for Mack's second mode obtained for the different flow assumptions under consideration, as a function of the streamwise distance along the wedge surface. A frequency range of $f = 4$ kHz to $f = 25$ kHz is covered by the envelope curve for each case. As it can be observed, the second Mack mode is destabilized when accounting for internal-energy-mode excitation (TPG and CNE) and dissociation (CNE). This is a consequence of the reduction of the boundary-layer thickness due to base-flow cooling, resulting from the lower temperature field obtained when modeling these phenomena. The largest difference arises between the CPG and the TPG thermodynamic assumptions, as it would be expected due to the fact that the CPG model does not take into account the excitation of the vibrational internal energy mode and therefore it is far from representing the actual thermodynamic behavior of the flow at the high-temperatures under study.

On the other hand, sufficiently far away from the wedge leading edge (approximately for $x > 10$ m), the influence of chemical non-equilibrium on the amplification factor becomes significant, which is clearly visible by comparing the evolution of the TPG and the CNE curves. Taking into account the dissociation of O_2 and the other chemical reactions active between the five species considered within the boundary layer (see table 2.5), as well as the diffusion transport between the species, leads to a further cooling of the boundary layer, which is then trans-

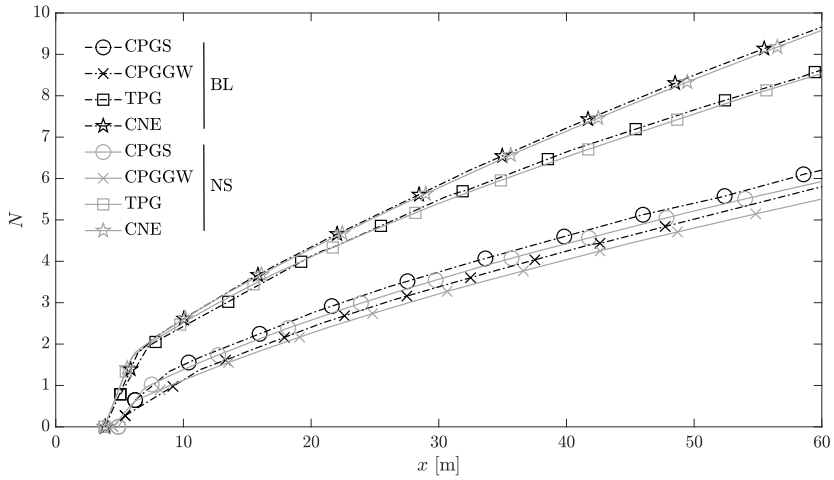

Figure 6.3: Second Mack mode LST N-factor envelope curves as a function of the streamwise coordinate for the smooth wedge boundary layer for the four different flow assumptions considered. The spanwise wavenumber β is fixed to 0. Curves labeled as BL employ base-flow solutions of the boundary-layer equations (obtained using DEKAF) whereas curves labeled as NS use base-flow solutions of the full Navier-Stokes equations (obtained using CFD++®).

lated into an increased second-Mack-mode growth. This behavior is well known from previous studies of hypersonic boundary-layer stability in the presence of non-equilibrium effects, see [8, 9].

The comparison between the N-factors predicted by the CPGS and the CPGGW flow assumptions provides a measure of the error associated to an inaccurate modeling of the transport properties, which is not negligible in this case. Because the boundary-layer thickness predicted by CPGS is smaller than that of CPGGW, the first case yields a higher growth rate. It is important to stress, however, that an appropriate evaluation of the internal-energy-excitation and chemical non-equilibrium effects on the instabilities can only be performed between flow assumptions with an equivalent and consistent set of transport models, that is, CPGGW, TPG and CNE. Lastly, it is also interesting to note that for the conditions under investigation, the second-mode instability needs a long distance (in the order of 30 meters) to reach an amplification factor that is in the transitional range according to other studies at similar conditions [10].

6.2.1 Effect of the boundary-layer assumption

Since the freestream Mach number for the conditions under study is very high, the shock layer over the wedge surface is thin and can become fully viscous, specially

for short distances downstream of the leading edge. This fact can make the use of the boundary-layer equations a questionable approximation, as the wedge shock can be located below the boundary-layer edge. If this is the case, the post-shock conditions predicted by the Rankine-Hugoniot jump relations cannot be assumed to be accurate any more, since they are derived in the context of inviscid flow theory. This, in turn, introduces an error in the boundary-layer edge properties imposed in the boundary-layer solver.

To assess the influence of using the boundary-layer equations instead of the Navier-Stokes equations for the calculation of the base-flow solution for the smooth wedge case, additional N-factor envelopes have also been computed using boundary-layer profiles obtained from the full Navier-Stokes equations. The resulting curves are also shown in figure 6.3, labeled as NS. As it can be seen, the effect of using the boundary-layer equations does not lead to important differences in the present case. For this reason, the boundary-layer profiles obtained from DEKAF are imposed at the inflow boundary of the computational domain. This avoids the need of resolving the wedge shock wave in the three-dimensional base-flow computation including the roughness element.

6.3 Verification of the 2D-LST solver for TPG and CNE in the smooth-wedge configuration

In order to verify the implementation of the 2D-LST equations within VESTA toolkit for the TPG and CNE flow assumptions, 2D-LST computations are also performed for the smooth-wedge configuration and compared against the result of the LST calculations. Since the two stability theories are based on the same assumptions, except that in the 2D-LST case there is an additional non-homogeneous direction, all the instability modes that are solution of the LST eigenvalue problem must also be a solution of the 2D-LST one. This can be exploited to setup a verification test case for the 2D-LST implementation. For this purpose, the previously computed boundary-layer profiles are replicated along the spanwise direction to generate a base-flow plane in y and z that is then used for the 2D-LST solver.

For verification purposes, a streamwise location of $x = 5.06$ m from the wedge leading edge and a frequency of 22.85 kHz are considered. The results of the comparison are presented in figure 6.4. Note that a relatively low resolution is employed along the wall-normal direction ($N_y = 101$) owing to the large computational cost of the QZ algorithm in the CNE 2D-LST case. For each LST mode, there is a corresponding family of $N_z - 2$ modes that are obtained from the 2D-LST problem, with N_z being the number of grid points in the spanwise direction. The verification for both flow assumptions is certified by the excellent agreement of the first 2D-LST mode of each family, which corresponds to $\beta = 0$, with the

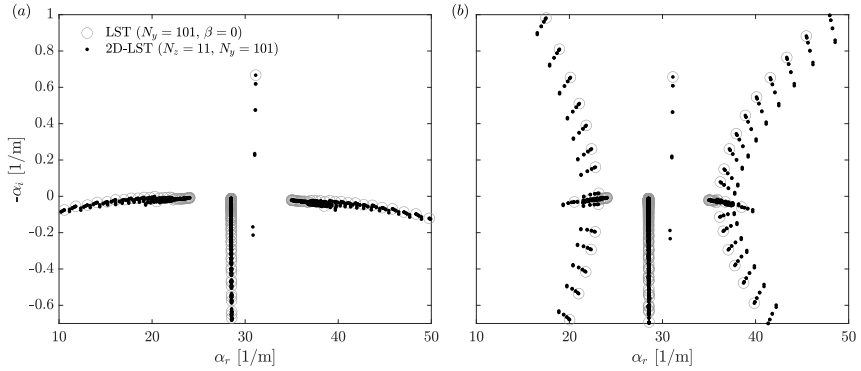

Figure 6.4: Comparison between the spatial stability spectrum obtained by means of the LST solver and the one obtained by the 2D-LST in the smooth wedge boundary layer at $x = 5.06$ m and $f = 22.85$ kHz: (a) TPG flow assumption; (b) CNE flow assumption.

LST one, where $\beta = 0$ is explicitly imposed. The LST solver inside VESTA has been extensively verified against other authors in the past for boundary layers in the presence of different high-enthalpy phenomena [3, 11, 12].

In the CNE case, due to the chosen mapping parameters and the resolution employed, the number of collocation points available in the upper portion of the domain is very small. As a consequence, most of the modes belonging to the acoustic continuous branches, whose eigenfunctions do not decay to zero towards the wall-normal far field boundary, are poorly resolved in this region. This originates the opening of the horizontal continuous branches that is visible in figure 6.4(b). It is important to emphasize that this behavior does not have a physical nature, rather it has a numerical origin associated to the chosen discretization parameters.

6.4 Stability analysis in the roughness wake

This section describes the base-flow solution for the wedge configuration with a roughness element as well as the stability characteristics of the roughness-induced wake for each case, as obtained by means of 2D-LST theory.

6.4.1 Description of the base flow

The main physical features of the computed base-flow solutions share strong similarities with those solutions described in chapter 5. Here, the attention is focused on the differences between the multiple flow assumptions considered. Figure 6.5 displays contours of the base-flow temperature obtained for each case on a plane located at half of the roughness element height. For all flow assumptions, the

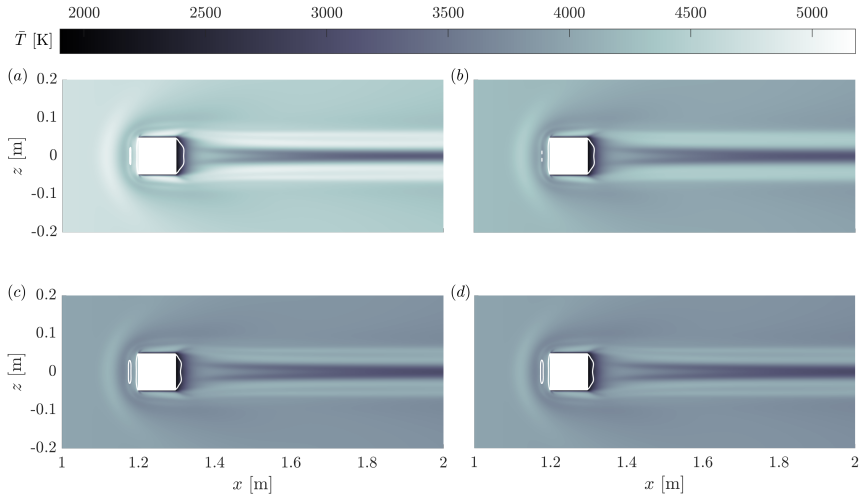

Figure 6.5: Contours of base-flow temperature near the roughness element for each flow assumption, on a xz plane located at half of the roughness element height: (a) CPGS; (b) CPGGW; (c) TPG; (d) CNE. The white solid lines represent isolines of $\bar{u} = 0$, which delimit regions of separated flow.

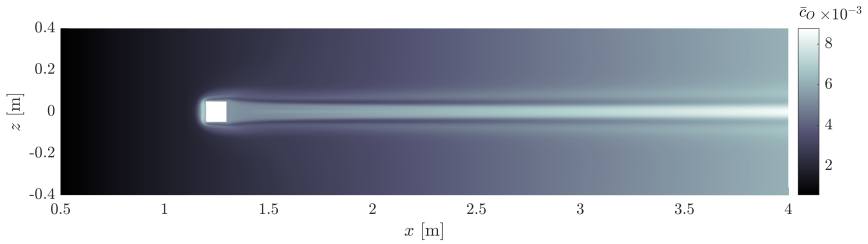

Figure 6.6: Contours of the mass fraction of atomic oxygen ($\bar{c}_O$) in the CNE base flow on a xz plane located at half of the roughness element height.

topology of the flow field is essentially the same, with the roughness wake being characterized by a pair of strong counter-rotating vortices that lead to a streak system. The most relevant differences between the base-flow solutions presented for each case lie in the temperature values obtained for each of the flow assumptions.

The higher viscosity predicted by the Gupta-Wilke transport model leads to a smaller temperature for case CPGGW compared against CPGS, which also results in a smaller downstream recirculation bubble, as represented by the white solid lines shown in figure 6.5.

The excitation of the vibrational internal energy mode is the responsible for the important decrease in the temperature of cases TPG and CNE with respect

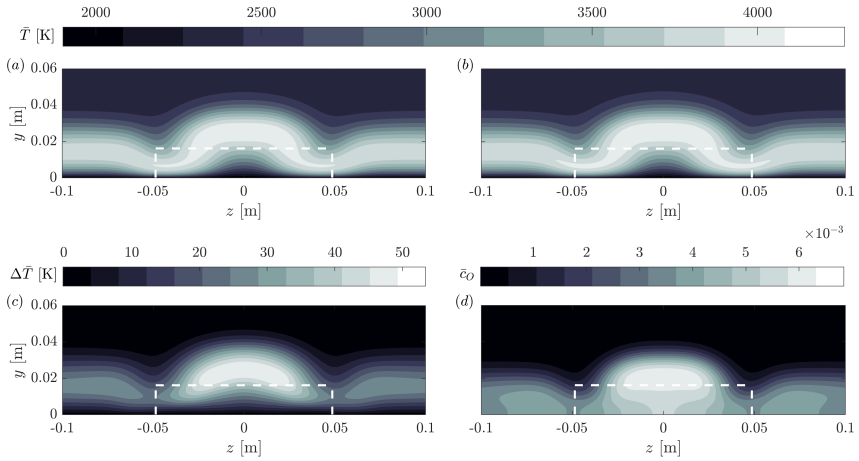

Figure 6.7: Comparison of the temperature base-flow field between the TPG and CNE flow assumptions at $x = 2$ m: (a) temperature contours for TPG; (b) temperature contours for CNE; (c) temperature difference between the TPG and the CNE cases ($\Delta\bar{T} = \bar{T}_{TPG} - \bar{T}_{CNE}$); (d) Mass fraction of atomic oxygen for CNE. The white dashed lines represent a projection of the roughness element.

to CPGGW. The TPG temperature contours are indistinguishable from the CNE case, reflecting that, at the location of the roughness element, the flow has not yet undergone sufficient dissociation to affect the flow field in a significant way. To illustrate the presence of the main dissociated species in the roughness wake, figure 6.6 depicts contours of the mass fraction of atomic oxygen ($\bar{c}_O = \bar{\rho}_O/\bar{\rho}$) on the same xz plane located at $y = h/2$. As it can be observed, a higher mass fraction of O is found in the central wake region as well as in front of the roughness element, where a small region of high-temperature recirculating fluid is present. Note that the concentration of O is higher in the low-velocity streak at the center of the wake than in the surrounding boundary-layer, suggesting that the effects of dissociation might be stronger for instabilities evolving in the roughness wake than for instabilities evolving outside of it.

The small differences between the TPG and the CNE flow assumptions are highlighted in figure 6.7. Figures 6.7(a, b) display temperature contours on a cross-flow plane located at $x = 2$ m for the TPG and the CNE cases, respectively. The highest temperatures are located at the center of the wake slightly above the roughness element height. Figure 6.7(c) shows the actual difference between the TPG and CNE temperature fields, which at this location remains below 55 K. Note that the highest difference in temperature is found at the center of the wake, coinciding with the location of maximum temperature in the plane according to figures 6.7(a, b). This region is also found to correlate well with the location of the highest

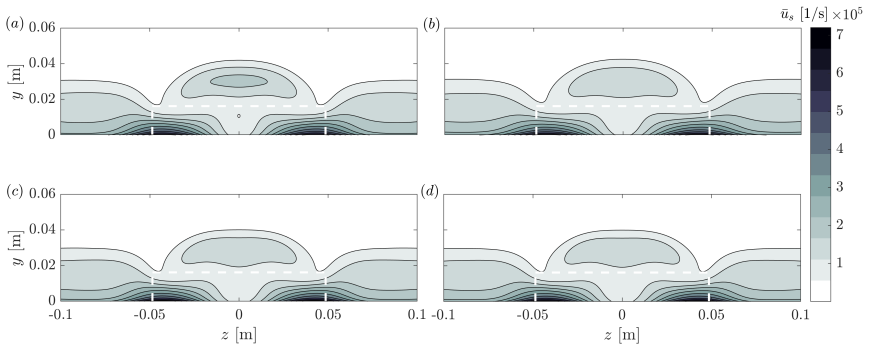

Figure 6.8: Contours of base-flow streamwise shear magnitude (equation (5.7)) on a cross-flow (zy) plane located at $x = 2$ m: (a) CPGS; (b) CPGGW; (c) TPG; (d) CNE.

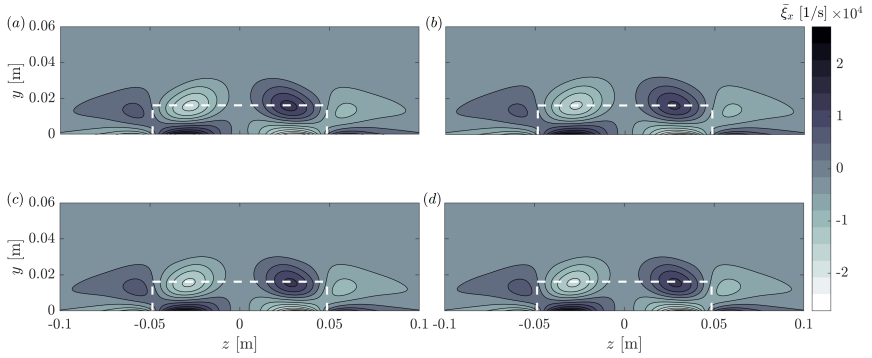

Figure 6.9: Contours of base-flow streamwise vorticity (equation (5.8)) on a cross-flow (zy) plane located at $x = 2$ m: (a) CPGS; (b) CPGGW; (c) TPG; (d) CNE.

mass fraction of atomic oxygen, represented in figure 6.7(d). It is also worth noting that $\Delta\bar{T} = \bar{T}_{\text{TPG}} - \bar{T}_{\text{CNE}}$ is positive, which reflects the cooling effect introduced by chemical reactions and diffusion transport on the roughness wake.

Figures 6.8 and 6.9 illustrate the streamwise shear magnitude and the streamwise vorticity for each case on a plane located at $x = 2$ m. The highest shear regions are found between the high-velocity streaks, which are located at the side edges of the roughness element, and the wall, where a large velocity gradient is encountered. As opposed to the configurations analyzed in chapter 5, the shear values attained at the top of the streak are much smaller than in the regions near the wall, denoting a weaker lift-up effect in the cases analyzed here. Case CPGS features larger shear values at the top of the low-velocity streak compared to the other three cases, while no significant differences are observed between CPGGW, TPG and CNE. Similarly, the streamwise vorticity contours shown in figure 6.9

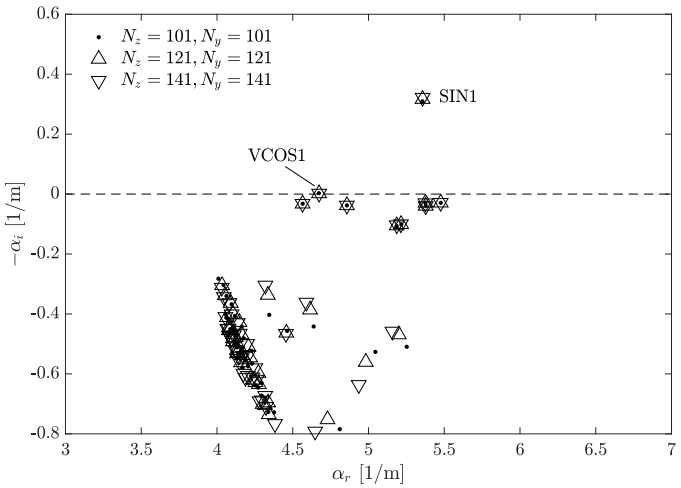

Figure 6.10: Portion of the spatial 2D-LST spectrum obtained for the CNE case at $x = 2$ m and $f = 3$ kHz. The two unstable modes respectively correspond to the most unstable sinuous (SIN1) and varicose (VCOS1) instabilities.

show that the counter-rotating vortex pair is considerably weaker in these cases compared to the previously analyzed configurations. These observations suggest that the wake instability modes might experience a smaller amplification in the current set-up.

6.4.2 Results of the 2D-LST computations

Spatial 2D-LST computations have been performed in the wake behind the roughness element for the four different cases under study[2]. All the calculations have been performed considering the following mapping parameters: $y_{max} = y_\infty$, $y_i = 20l$, $z_{max} = -z_{min} = 30h$, $z_{i2} = -z_{i1} = 3h$. For each case, 50 eigenmodes are computed by means of the IRAM using a non-dimensional shift-invert parameter of $\sigma = 1.3\omega_r$.

On first place, figure 6.10 shows the spatial stability spectrum obtained for the CNE case at a streamwise distance of $x = 2$ m from the wedge leading edge and at a frequency of $f = 3$ kHz. Different discrete modes are found in the spectrum, which show convergence with respect to grid resolution. Two unstable modes can

[2]Most of the results shown in this chapter have been published in reference [13]. However, the author would like to note that the CNE results reported in reference [13] are affected by an error in the calculation of the mass production rate of each species ($\dot{w}_s$) in the base-flow solution. In this section, the corrected CNE results are reported. The differences introduced by this error were found to be small for all the investigated conditions. The CNE results shown here remain very similar to the ones reported in [13].

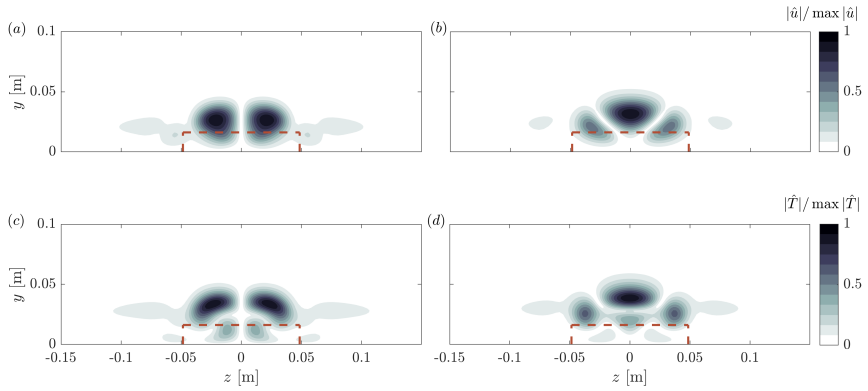

Figure 6.11: Normalized two-dimensional amplitude functions of the streamwise velocity and temperature perturbations associated to the most unstable sinuous and varicose modes for the CNE case at $x = 2$ m and $f = 3$ kHz: (a, b) streamwise velocity amplitude functions; (c, d) temperature amplitude functions; (a, c) mode SIN1; (b, d) mode VCOS1.

be identified at these particular conditions, labeled as SIN1 and VCOS1, whose amplitude functions for the streamwise velocity and temperature perturbations are represented in figure 6.11. These two instabilities are, respectively, the most unstable sinuous and varicose disturbances that develop in the wake behind the roughness element in the current configuration. Their regions of development are mainly concentrated inside the central low-velocity streak that characterizes the wake flow structure. Note that the sinuous mode in this case features a much larger growth rate than the varicose one. Very similar amplitude functions are also obtained for the other flow assumptions, not shown here.

Figure 6.12 represents the evolution of the growth rate of the two most unstable wake modes as a function of frequency for each flow assumption, at a particular streamwise location of $x = 2$ m. In their unstable frequency range, the sinuous and varicose instabilities at this location are found to follow opposite trends when the excitation of the vibrational energy mode is taken into account. While the sinuous mode is more stable for TPG/CNE than for CPGGW, the varicose disturbance is significantly destabilized. The same behavior is also observed with respect to the effect of chemical reactions, i.e., the sinuous mode in CNE is slightly stabilized with respect to TPG while the CNE varicose mode is destabilized with respect to TPG. For all the analyzed frequencies, the differences between TPG and CNE remain small, which indicates that at the location considered, the influence of chemical non-equilibrium on the wake instabilities is not yet important.

Comparing the two CPG cases, it can be observed that the growth rate of both the sinuous and varicose instabilities is higher for CPGS than for CPGGW for all the frequencies. This is the same behavior observed for the second-Mack-mode

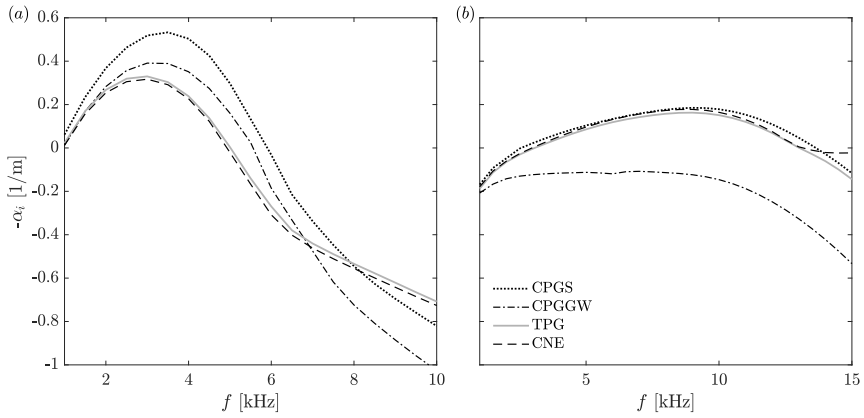

Figure 6.12: Evolution of the growth rate of the most unstable sinuous and varicose instabilities as a function of frequency for each flow assumption ($x = 2$ m): (a) SIN1 mode; (b) VCOS1 mode.

amplification reported in § 6.2. The frequency evolution of the growth rate of the varicose mode for CPGS happens to be in close agreement with that of the TPG and CNE cases. Although there is no reason to attribute this fact to a proper modeling of the vibrational excitation, this behavior can be correlated with the observation that the boundary-layer height for case CPGS is coincidentally similar to that of TPG and CNE, as discussed in § 6.1. This suggests that the evolution of the varicose mode at this location is strongly linked to the boundary-layer thickness. In particular, it is destabilized by a reduction in the boundary-layer thickness as a consequence of base-flow cooling, precisely as the second-Mack mode evolving in the smooth boundary layer (see § 6.2). This explains why the varicose mode undergoes a stabilization in CPGGW, which features a higher boundary-layer thickness than in TPG and CNE (see figure 6.2), and why the growth rate predicted in CPGS is similar to the one predicted in TPG or CNE. It is important to emphasize that this behavior is not observed for the sinuous instability, which highlights an important difference in the nature of both disturbances at these conditions.

A relation between the boundary-layer thickness and the evolution of a varicose disturbance has been already recognized by previous authors. The varicose-central instability found in the DNS analysis of De Tullio & Sandham [14] was seen to be strongly tuned with the boundary-layer thickness, in a similar fashion to what is observed for the second Mack mode. As it can be seen in figure 6.11, the amplitude function of the varicose mode developing in the current cases also features the highest region of amplification in the central wake region.

Figure 6.13 displays the streamwise evolution of the sinuous and varicose instabilities for the different flow assumptions, both in terms of growth rate and

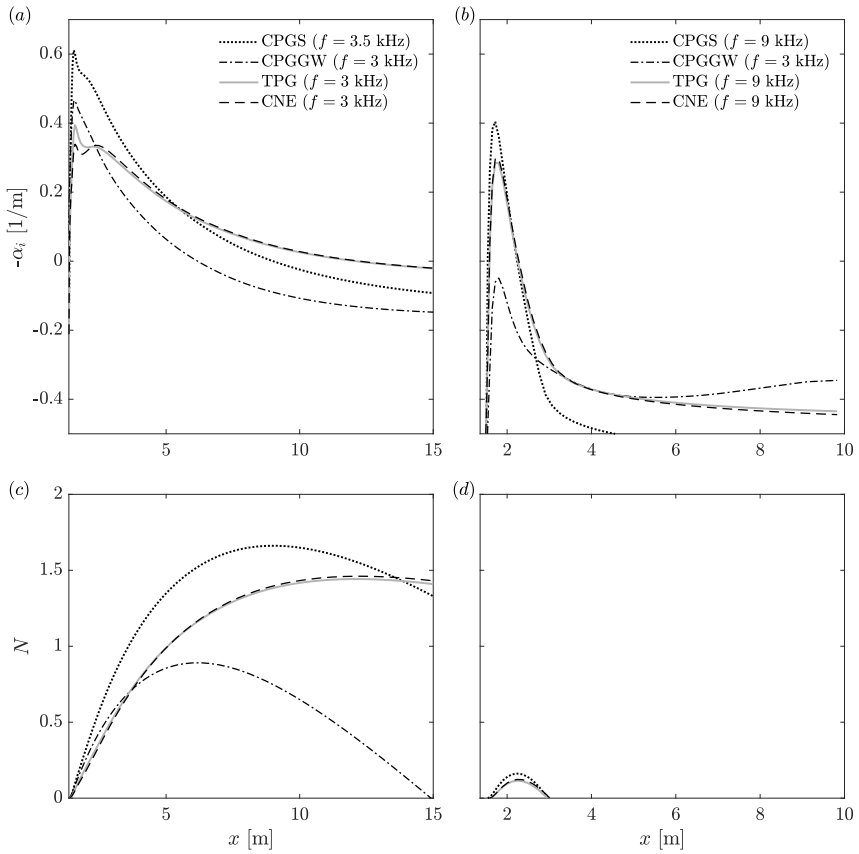

Figure 6.13: Streamwise evolution of the growth rate and associated N-factor curves of the most unstable wake instabilities for each flow assumption: (a, c) SIN1 mode; (b, d) VCOS1 mode. The frequency for each curve corresponds to the most unstable frequency at $x = 2$ m, according to figure 6.12.

N-factor. The frequency associated to each curve corresponds to the respective most unstable frequency retrieved from the results shown in figure 6.12. The first streamwise location at which the 2D-LST analysis is performed in each case corresponds to the end of the separation bubble induced at the trailing edge of the roughness element.

Close to the roughness element, the growth rate of the sinuous mode is smaller for CNE than for TPG, which is likewise smaller than for CPGGW. This illustrates a stabilizing influence of both vibrational excitation and chemical reactions on the sinuous mode in this region. Nevertheless, this trend is inverted further downstream. For approximately $x > 2.5$ m, the mode becomes significantly more

unstable for TPG and CNE than for CPGGW, as well as becoming slightly more unstable for CNE than for TPG, denoting a destabilizing effect of both vibrational excitation and chemical non-equilibrium in this streamwise range. The CPGGW sinuous instability decays significantly faster than in TPG and CNE cases. This is strongly reflected in the N-factor evolution for each of these cases (see figure 6.13(c)).

The streamwise evolution of the varicose mode features an opposite behavior to the sinuous disturbance. In the vicinity of the roughness element, it is destabilized in the CNE case with respect to TPG, which is likewise destabilized with respect to CPGGW. Further downstream (approximately $x > 0.3$), however, these effects are inverted and accounting for vibrational excitation and chemical non-equilibrium subsequently stabilize the disturbance (see figures 6.13(b, d)). As it can be noticed, the streamwise range for which the varicose perturbation is unstable is small in all cases, resulting in small integrated amplification factors.

The comparison between the TPG and the CNE flow assumptions shows that the effect of chemical reactions and diffusion transport is small for the wake modes at the streamwise region under study. This is due to the fact that the geometrical configuration considered in this study does not feature a stagnation point, so that no chemical reactions take place at the wedge leading edge. The dissociation of O_2, for instance, which is the most relevant reaction at the temperature values obtained for the CNE case (see figure 2.1), starts to occur downstream of the leading edge. Because of this configuration, the flow did not have enough time to undergo a sufficient amount of dissociation at the location of the roughness element, and therefore no significant changes are encountered in the base-flow field with respect to the TPG flow assumption. The influence of chemistry effects is much more noticeable for longer distances downstream, as it can be observed in the Mack mode N-factor envelopes of figure 6.3.

Finally, it is also worth emphasizing that, for the conditions under investigation, the maximum N-factor values obtained for both wake instability modes are still far from being relevant for triggering boundary-layer transition.

6.4.3 Effect of inconsistent modeling assumptions between the base flow and the perturbations on the roughness wake instabilities

Owing to the complexity of the resulting stability equations in some flow assumptions such as CNE, it is desirable to know whether employing the governing stability equations for a simplified thermodynamic hypothesis on a given base flow can have a significant impact on the roughness wake instability. For this purpose, the following tests can be performed using inconsistent thermodynamic assumptions between the base flow and the perturbations:

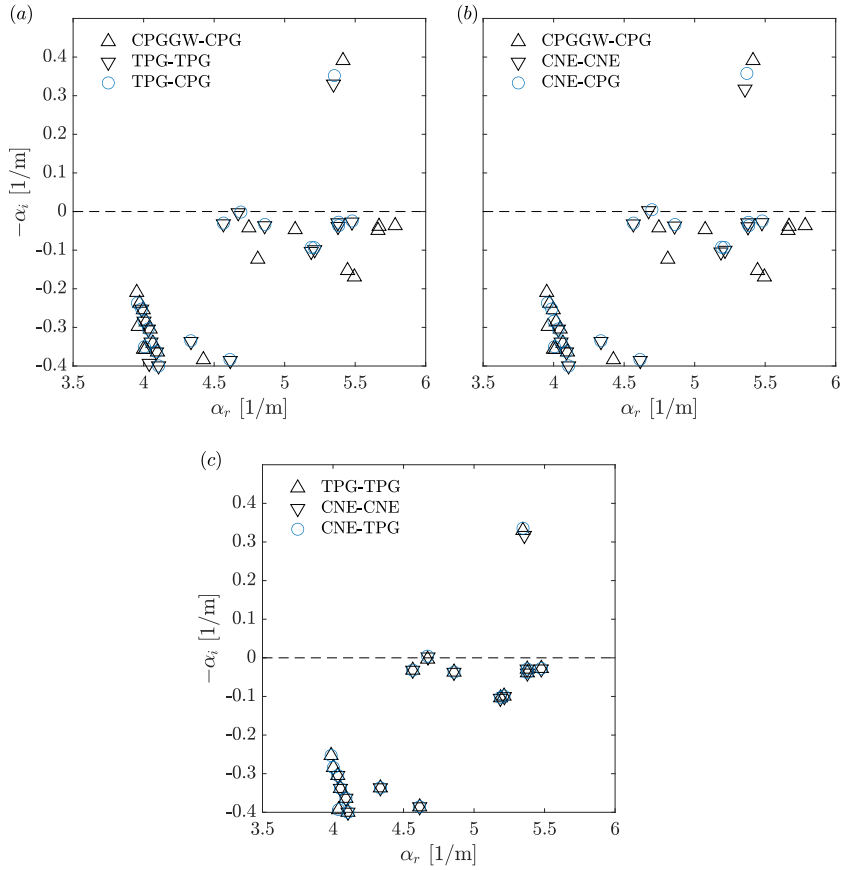

Figure 6.14: Comparison of 2D-LST spectra obtained for the three different inconsistent assumptions listed against the consistent assumptions for each case ($x = 2$ m, $f = 3$ kHz): (a) effect of TPG-CPG; (b) effect of CNE-CPG; (c) effect of CNE-TPG.

- TPG-CPG: using the CPG 2D-LST equations on a base flow obtained assuming TPG.
- CNE-CPG: using the CPG 2D-LST equations on a base flow obtained assuming CNE.
- CNE-TPG: using the TPG 2D-LST equations on a base flow obtained assuming CNE.

The first test allows to evaluate which is the impact of neglecting vibrational excitation on the perturbation quantities. The second case quantifies the error introduced by neglecting vibrational excitation, chemical reactions and diffusion ef-

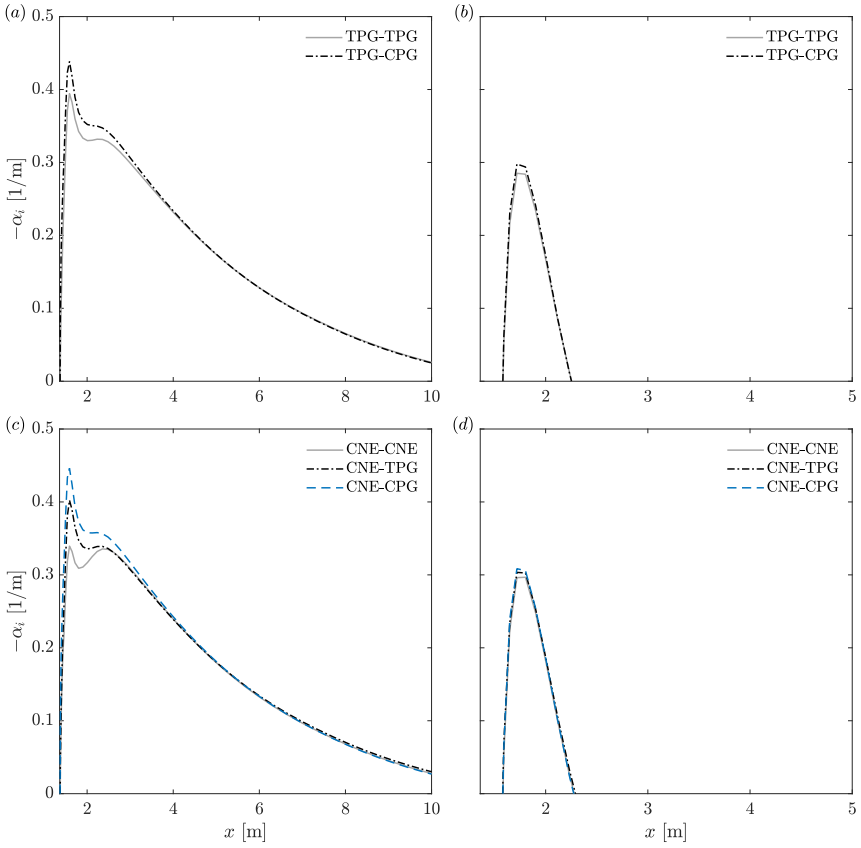

Figure 6.15: Comparison of the streamwise growth-rate evolution for modes SIN1 (a, c) and VCOS1 (b, d) for the different inconsistent assumptions considered. SIN1 mode at $f = 3$ kHz and VCOS1 mode at $f = 9$ kHz.

fects on the perturbations. The third test exposes the pure effect of neglecting the action of chemical reactions and diffusion on the perturbations. The result of these tests applied to the roughness wake in the configuration studied in this chapter is illustrated in figure 6.14, which shows comparisons of the spatial stability spectra obtained at $x = 2$ m and $f = 3$ kHz, and figure 6.15, which depicts comparisons of the streamwise growth-rate evolution of modes SIN1 and VCOS1.

The use of the CPG governing stability equations on a TPG base flow (see figures 6.14(a) and 6.15(a, b)) illustrates that accounting for vibrational excitation on the perturbations has a noticeable stabilizing effect on the wake instabilities in the vicinity of the roughness element. This effect is more accentuated for the sinuous perturbation, which is the dominant one in the problem under study. For this instability, it is important to note that the error in growth rate introduced by ne-

glecting the excitation of the vibrational internal energy mode on the perturbations (TPG-TPG compared to TPG-CPG) is of the same order as the error introduced by neglecting it on the base flow (CPGGW-CPG compared to TPG-CPG), as it can be observed in figure 6.14(a). Both errors add up to yield the differences between the consistent computations in CPGGW and TPG (CPGGW-CPG compared to TPG-TPG). The relative error in the maximum growth rate obtained between the TPG-TPG and the TPG-CPG assumptions is 11.2% for the SIN1 mode (located at $x \approx 1.59$ m), and 4.4% for the VCOS1 mode (at $x \approx 1.72$ m). Note that far downstream of the roughness the difference between both sets of assumptions becomes negligible.

Similarly, assuming perturbations that behave as a calorically perfect gas in a CNE base flow (see figures 6.14(b) and 6.15(c, d)) shows that, in addition to the stabilizing influence of modeling vibrational excitation in the perturbations, modeling chemical reactions and diffusion transport on the disturbances also brings a further stabilization of the instabilities near the obstacle. This can be directly observed in figure 6.14(b), where the combination of the stabilizing effects associated to accounting for vibrational excitation as well as chemical non-equilibrium on the disturbances leads to a higher degree of stabilization for the CNE-CNE case than for the TPG-TPG case when respectively compared to CPGGW-CPG. By using the TPG stability equations on the CNE base-flow field (see figures 6.14(c) and 6.15(c, d)), such an additional stabilizing effect of the diffusion fluxes and the chemical source terms on the perturbations is directly exposed. From these comparisons, the error introduced in the peak growth rate when using CNE-CPG relative to CNE-CNE is 31.5% for the sinuous instability and 3.9% for the varicose perturbation. Finally, the relative error in the maximum growth rate between the CNE-TPG and the CNE-CNE assumptions is 18.5% for the sinuous disturbance and 2.3% for the varicose mode.

The previously reported trends are in good agreement with the findings of Miró Miró [3] for the case of Mack's second-mode instability. It is important to remark that the errors introduced by employing simplified thermodynamic assumptions on the perturbations are not negligible near the roughness element for the configuration studied here, specially for the dominant wake instability. In particular, an important overprediction of the growth rate of mode SIN1 is obtained when employing the CPG or the TPG stability equations on a CNE base flow.

6.5 Summary of results

This analysis constitutes the first 2D-LST implementation that incorporates a modeling of chemical non-equilibrium effects into the perturbation equations. This capability is of paramount importance for the study of roughness-induced transition on hypersonic vehicles. Two-dimensional local linear stability theory (2D-

LST) has been employed to study the influence of the excitation of the vibrational internal energy mode as well as of chemical non-equilibrium on the instability characteristics of the wake behind a cuboidal roughness element inside a high-temperature boundary layer developing on a sharp wedge.

The implementation of the TPG and CNE 2D-LST solvers within VESTA toolkit has been verified against LST for the smooth wedge boundary layer. Spatial 2D-LST stability analyses have been carried out along the roughness wake for a calorically perfect gas, a thermally perfect gas and mixture of gases in chemical nonequilibrium. These computations have allowed the identification of the well-known sinuous and varicose instabilities also in the presence of vibrational-energy-mode excitation and chemical reactions. The investigation has shown that the two types of wake instability feature an opposite behavior with regard to the studied high-enthalpy effects. In the vicinity of the roughness element, while the sinuous mode is subsequently stabilized when vibrational excitation, molecular dissociation and diffusion are taken into account, the varicose perturbation undergoes a significant destabilization. In this region, the varicose mode has been found to behave in the same way as the second Mack mode in the presence of base-flow cooling, showing a strong sensitivity to the boundary-layer thickness.

Further away from the roughness element, however, the sinuous disturbance decays at a slower rate when vibrational excitation is accounted for, reaching a higher integrated amplification factor for the TPG and CNE flow assumptions than for CPGGW. Additionally, in this streamwise range, chemical non-equilibrium effects have been found to play a small destabilizing role on the sinuous instability. As in the region close to the obstacle, these trends have also been found to be inverted for the varicose disturbance. Despite the sinuous instability undergoing a much higher amplification than the varicose one, both modes are still far from reaching N-factor values that are relevant for triggering transition.

Only minor differences in the stability of the wake modes have been obtained between the TPG and the CNE flow assumptions, revealing that the influence of chemical reactions and diffusion is not strong on the roughness wake instability for the conditions investigated. This is attributed to the lack of a stagnation point in the problem geometry, such that chemical reactions are not active at the wedge leading edge. As a result, at the streamwise position of the roughness element, the flow has not yet undergone sufficient dissociation so as to affect the propagation of the instabilities.

The CPG solutions computed using Sutherland's law (CPGS) and Gupta-Wilke's model (CPGGW) have allowed to assess the effect of the transport modeling on the roughness-induced disturbances. Similarly to the findings of Miró Miró [3] for the case of the second Mack mode evolving in a smooth flat-plate boundary layer, the use of CPG with Sutherland's law has been observed to yield a closer prediction of the TPG/CNE varicose mode evolution than the use of CPGGW. This

has been found to be the consequence of a fortuitous cancellation of the errors introduced by the use of an inaccurate thermal model (CPG) and the use of an inaccurate transport model (Sutherland's law) for this high-enthalpy case, resulting in a boundary-layer thickness in CPGS which is similar to that of the TPG and CNE cases. Therefore, the fact that the CPGS assumption can predict a more accurate growth rate for the varicose instability than the CPGGW assumption is a mere coincidence rather than a behavior attributed to a sound modeling of the thermal and transport properties.

The influence of employing inconsistent thermodynamic flow assumptions between the base flow and the perturbation quantities has been assessed by comparing different spectra at a given streamwise location downstream of the roughness element and the streamwise growth-rate evolution of the dominant sinuous and varicose instabilities. The results have revealed two main physical effects acting exclusively on the perturbations, which affect the development of wake instabilities in the vicinity of the roughness element for the studied high-enthalpy environment:

- A stabilization of the wake modes due to the action of vibrational excitation on the perturbations.
- A stabilization of the wake instabilities due to the action of chemical reactions and diffusion fluxes on the perturbations.

These effects have been found to be non-negligible in the current problem, yielding an error of up to 31% on the peak growth rate of the dominant instability when the CPG 2D-LST equations are used to analyze a CNE base flow.

References

[1] Karen T. Berger, Brian P. Anderson, Charles H. Campbell, Michael T. Garske, Luis A. Saucedo, and Gerald R. Kinder. *Boundary Layer Transition Flight Experiment Overview and In-Situ Measurements*. In 48th AIAA Aerospace Sciences Meeting Including the New Horizons Forum and Aerospace Exposition, volume 2010-240, Orlando, Florida, 2010. American Institute of Aeronautics and Astronautics.

[2] John D. Anderson Jr. *Hypersonic and High Temperature Gas Dynamics*. American Institute of Aeronautics and Astronautics, Reston VA, second edition, 2006.

[3] Fernando Miró Miró. *Numerical Investigation of Hypersonic Boundary-Layer Stability and Transition in the presence of Ablation Phenomena*. PhD thesis, Université Libre de Bruxelles and von Karman Insitute for Fluid Dynamics, 2020.

[4] S. D. Williams, Donald M. Curry, Dennis C. Chao, and Vuong T. Pham. *Ablation analysis of the shuttle orbiter oxidation protected reinforced carbon-carbon*. Journal of Thermophysics and Heat Transfer, 9(3):478–485, 1995.

[5] Andrew J. Lofthouse, Leonardo C. Scalabrin, and Iain D. Boyd. *Velocity slip and temperature jump in hypersonic aerothermodynamics*. Journal of Thermophysics and Heat Transfer, 22(1):38–49, 2008.

[6] Duncan A. Lockerby, Jason M. Reese, David R. Emerson, and Robert W. Barber. *Velocity boundary condition at solid walls in rarefied gas calculations*. Physical Review E - Statistical Physics, Plasmas, Fluids, and Related Interdisciplinary Topics, 70(1):4, 2004.

[7] T. Gökçen and R. MacCormack. *Nonequilibrium Effects for Hypersonic Transitional Flows Using Continuum Approach 27th Aerospace Sciences Meeting*. 27th Aerospace Sciencies Meeting, AIAA paper, 1989-0461, 1989.

[8] Mary L. Hudson, Ndaona Chokani, and Graham V. Candler. *Linear stability of hypersonic flow in thermochemical nonequilibrium*. AIAA Journal, 35(6):958–964, 1997.

[9] Fernando Miró Miró, Fabio Pinna, Ethan S. Beyak, Paolo Barbante, and Helen L. Reed. *Diffusion and chemical non-equilibrium effects on hypersonic boundary-layer stability*. AIAA paper, 2018-1824, 2018.

[10] Mujeeb R. Malik. *Hypersonic Flight Transition Data Analysis Using Parabolized Stability Equations with Chemistry Effects*. Journal of Spacecraft and Rockets, 40(3):332–344, 2003.

[11] Fabio Pinna. *Numerical study of stability of flows from low to high Mach number*. PhD thesis, Università degli Studi di Roma La Sapienza, 2012.

[12] Fernando Miró Miró, Ethan S. Beyak, Fabio Pinna, and Helen L. Reed. *High-enthalpy models for boundary-layer stability and transition*. Physics of Fluids, 31(044101), 2019.

[13] Iván Padilla Montero, Fernando Miró Miró, and Fabio Pinna. *Influence of high-temperature effects on the stability of the wake behind an isolated roughness element in hypersonic flow*. Laminar-Turbulent Transition, IUTAM Bookseries 38:–, 2021.

[14] Nicola De Tullio and Neil D. Sandham. *Influence of boundary-layer disturbances on the instability of a roughness wake in a high-speed boundary layer*. Journal of Fluid Mechanics, 763:136–145, 2015.

7 Conclusions

This doctoral thesis constitutes one step forward towards the understanding of boundary-layer transition in the presence of discrete roughness. In particular, it contributes to the fundamental understanding of the mechanisms that lead to the generation and the linear growth of roughness-induced instabilities in hypersonic flow. In this dissertation, these phenomena are investigated exclusively by means of hydrodynamic stability theory.

An overview of available studies in the field was provided, with an emphasis on theoretical investigations based on stability theory and direct numerical simulations. This served to highlight the main features that characterize the flow fields induced by three-dimensional roughness elements and the instabilities that are known to develop in simple configurations. The governing equations considered for different thermodynamic flow assumptions were laid out and a brief review of hydrodynamic stability theory was provided, with particular focus on those stability theories commonly applied to study roughness-induced disturbances. The theoretical framework was complemented with a description of the numerical methodology employed for the computations presented along this work.

The instabilities induced by isolated roughness elements in a high-speed flat-plate boundary layer were investigated using two-dimensional local linear stability theory (2D-LST) on base-flow solutions obtained by means of the compressible Navier-Stokes equations. The main disturbances evolving in the wake behind the elements were successfully identified and their frequency and streamwise evolution was analyzed.

The disturbance energy evolution equation developed by Chu [1] was gener-

alized for the first time to base flows that depend on two spatial directions. The decomposition of the temporal growth rate that results from this formulation was extended to three-dimensional perturbations evolving in base flows with two inhomogeneous directions and was successfully applied to the instabilities developing in the wake behind a discrete roughness element in a calorically perfect gas. Through this decomposition, the most relevant energy exchange mechanisms between the disturbances evolving in the roughness wake and the laminar base flow were identified.

The governing stability equations for 2D-LST under a thermally perfect gas assumption and, for the first time, for a mixture of perfect gases in chemical non-equilibrium were automatically derived and implemented by means of VESTA's Automatic Derivation and Implementation Tool (ADIT) [2, Chapter 8], and were successfully applied to compute the instabilities induced by an isolated roughness element in a high-temperature boundary layer. The 2D-LST stability solver for TPG and CNE was verified against LST for the case of a smooth flat-plate boundary layer.

These investigations contributed to address the questions posed in § 1.3 as described below.

Which are the physical processes by which the roughness-induced instabilities extract their energy along the roughness wake?

Stability calculations were performed along the wake behind two different isolated roughness geometries mounted on a flat plate in a calorically perfect gas. Different varicose and sinuous wake instability modes were found to coexist together with the family of Mack-mode instabilities that evolve in the flat-plate boundary layer, and which become modulated by the presence of the roughness wake. Extensive temporal 2D-LST computations were performed along the roughness wake for the range of most unstable streamwise wavelengths for each roughness geometry. Two leading instability modes were distinguished for each case in terms of the highest integrated amplification factors, respectively corresponding to the most unstable sinuous (SIN1) and varicose (VCOS1) instabilities.

The novel extension of the disturbance energy formulation provided an additional layer of information for understanding the energy exchange mechanisms between the base flow and the roughness-induced perturbations. The decomposition of the temporal growth rate of the instabilities evolving in the roughness wake revealed that the most important contributions to the generalized disturbance potential energy come from the transport of disturbance entropy across the base-flow temperature gradients (terms $\hat{P}_{s,2}$ and $\hat{P}_{s,3}$), while the largest contributions to the disturbance kinetic energy are produced by the work done by the Reynolds stresses against the base-flow velocity shear layers (terms $\hat{P}_{RS,12}$ and $\hat{P}_{RS,13}$). Although previous studies in roughness-induced instabilities have already iden-

tified the importance of the production of disturbance kinetic energy due to the perturbation Reynolds stresses, the current results indicated that the production of potential energy due to entropy fluctuations might also play a crucial role in high-speed flows. In addition, the obtained decompositions showed that, in practice, for the disturbance energy analysis of roughness-wake instabilities developing in a configuration like the one presented in this work, it is sufficient to pay attention to the production terms $\hat{P}_s$ and $\hat{P}_{RS}$, and to the dissipation terms $\hat{D}_\mu$ and $\hat{D}_k$. The remaining terms were found to bring small contributions which are not significant.

The streamwise evolution of the disturbance energy decomposition illustrated that the energy of both sinuous and varicose wake instabilities is dominated by the production terms associated to the wall-normal base-flow gradients in the vicinity of the roughness elements, and that the energy is progressively transferred to the spanwise production terms further downstream. The rate at which this transfer takes place was found to depend on the roughness geometry and the streamwise wavelength. A relevant finding is that no significant differences were observed in the energy extraction mechanisms between both types of wake instability, only in the streamwise range over which the energy transfer occurs. Therefore, both wall-normal and spanwise base-flow gradients appear to play an important role in the excitation of both sinuous and varicose instabilities. In other words, the evolution of a given type of wake instability was not found to be linked to the evolution of the base-flow gradients along a single direction only.

Is there a constructive interaction between the Mack-mode instabilities evolving in a flat-plate boundary layer and the roughness-induced wake instabilities?

The growth rate of the wake instabilities was found to be strongly influenced by the boundary-layer disturbances (Mack-mode instabilities) developing on the flat plate, which become modulated by the presence of the roughness element. For many of the conditions investigated, the amplitude of the wake modes was observed to grow in the boundary layer at the sides of the roughness wake, resembling the amplitude function of Mack-mode instabilities. This behavior was found to correlate with changes in the evolution of the disturbance energy production contributions, more specifically, with downstream locations at which the wall-normal production terms begin to rise and the spanwise terms accelerate their rate of decrease. An analysis of the phase speed evolution of different instabilities showed that this behavior also correlates with the location at which the phase speed of the wake modes matches that of the Mack-mode instabilities.

These observations provided evidence that there is a continuous synchronization between the wake instabilities and the boundary-layer modes. When this synchronization begins to take place, the energy signature of the wake modes changes its behavior and starts to become similar to that of Mack-mode disturbances, trans-

forming the wake instabilities into hybrid disturbances whose amplitude evolves both in the streak system that characterizes the roughness wake and in the flat-plate boundary layer outside of the wake. This phenomenon was found to have important implications in the growth-rate evolution of the wake instabilities, contributing in some cases to enhance their amplification rate or to decrease their rate of decay, ultimately increasing the associated integrated amplification factors for some of the investigated conditions.

Previous work by De Tullio & Sandham [3] hypothesized this mechanism for the excitation of a varicose disturbance behind a cuboidal roughness element, according to DNS-based analyses. The current work confirmed the presence of this phenomenon not only for the excitation of varicose disturbances, but also for sinuous perturbations developing in the two different roughness geometries analyzed, bringing further evidence that this mechanism could play a critical role in roughness-induced transition.

This unprecedented analysis highlighted the importance of resolving the different types of instabilities that are present in the 2D-LST spectrum in these configurations. In particular, sufficient spanwise domain size and resolution should be employed in the calculations such that the most unstable portion of the continuous Mack-mode branch present in the spectra can be resolved adequately.

What is the effect of vibrational excitation and dissociation on the instabilities evolving in the wake behind an isolated roughness element?

Spatial 2D-LST calculations were performed in the wake behind a cuboidal roughness element mounted on a sharp wedge at a high freestream Mach number. The strong compression induced by the wedge shock wave leads to a high-temperature, chemically-reacting boundary layer where vibrational-internal-energy-mode excitation plays an important role and chemical non-equilibrium has a noticeable effect. For this configuration, the base-flow field in the roughness wake undergoes a substantial cooling when vibrational excitation is accounted for. This cooling is further enhanced when modeling chemical reactions and diffusion transport, as demonstrated by the base-flow solutions computed under the TPG and CNE flow assumptions.

The impact of such high-temperature phenomena on the instabilities induced by the roughness element was examined through the original development of 2D-LST TPG and CNE solvers, ensuring a complete consistency between the base flow and the perturbation modeling hypotheses. Using the 2D-LST stability equations derived for the TPG and the CNE flow assumptions, unstable sinuous and varicose instabilities were also found to evolve in the roughness wake in this configuration.

The base-flow cooling occurring due to the excitation of the vibrational molecular energy mode was found to have an important impact on the growth rate of the

wake instabilities. An interesting observation is that, for the investigated configuration, both wake modes were not seen to behave in the same manner with respect to vibrational excitation. Near the roughness element, the associated base-flow cooling was found to destabilize the varicose mode, similarly to what is observed for the second Mack mode, while it was observed to stabilize the sinuous disturbance. However, further downstream these trends were found to be inverted.

The roughness-induced instabilities were seen to be sensitive to small changes in the flow field due to dissociation and diffusion effects, as illustrated by the differences between the TPG and CNE assumptions. The additional base-flow cooling induced by chemical non-equilibrium effects was found to further enhance the same trends observed when accounting for vibrational excitation. The sensitivity of the sinuous mode to chemical non-equilibrium was observed to be particularly strong in the vicinity of the roughness element.

From the modeling point of view, how important is it to be consistent between the modeling assumptions introduced in the governing base-flow equations and those introduced in the governing stability equations for the case of roughness-induced instabilities?

A small investigation was carried out on the effect of using inconsistent thermodynamic modeling assumptions respectively in the base flow and the perturbations for the sharp wedge configuration. The use of the CPG governing stability equations on a TPG base flow revealed that accounting for vibrational excitation on the perturbations has a noticeable stabilizing effect on the wake instabilities, specially for the sinuous perturbation, which is the dominant one in this case.

Similarly, assuming perturbations that behave as a calorically perfect gas in a CNE base flow showed that, in addition to the stabilizing influence of modeling vibrational excitation in the perturbations, accounting for chemical non-equilibrium in the linearized disturbance equations induces a further stabilization of the wake modes. By using the TPG stability equations on the CNE base-flow field, such stabilizing effect of the diffusion fluxes and the chemical source terms on the perturbations was quantified. These observations were found to be in agreement with the findings of Miró Miró [2] for Mack's second-mode instability.

These analyses highlighted two main physical effects acting exclusively on the perturbations which affect the development of wake instabilities near the obstacle:

- A stabilization of the wake modes due to the action of molecular vibrational excitation on the perturbations.
- A stabilization of the wake disturbances due to the action of chemical reactions and diffusion transport on the perturbations.

The errors introduced by employing inconsistent thermodynamic assumptions in the base flow and perturbation quantities were found to be not negligible for the

investigated configuration. The most important deviation was found to be a relative error of 31% in the maximum growth rate of the sinuous instability, induced when using the CPG stability equations on a CNE base flow. A significant overprediction of the growth rate of mode SIN1 was observed when employing the CPG or the TPG stability equations on a CNE base flow.

7.1 Outlook

Boundary-layer transition is a critical design driver in the development of more efficient and safer atmospheric entry vehicles. The ability to obtain accurate transition predictions at any point in the trajectory of these vehicles is therefore of paramount importance, and justifies the continued interest in improving the modeling and understanding of the influence of surface roughness.

The accomplishments listed in the previous section constitute an advancement in the state of the art of discrete roughness-induced instability mechanisms. The new tools developed in order to study the production processes of disturbance energy offer the possibility to gain a deeper understanding of the instability mechanisms underlying transition in a wide range of complex flow fields, and motivate the development of parametric studies in the future. Similarly, the preliminary results presented for roughness-induced perturbations in high-enthalpy environments constitute a reference for future investigations on more realistic configurations, and provide a confirmation that fully consistent 2D-LST stability analyses which model chemical non-equilibrium effects are nowadays feasible.

With the aim to continue improving the current knowledge of roughness-induced transition in high-speed flow, the following investigations can be proposed after the findings achieved in this work:

- An analysis of the roughness wake instability by means of 3D-PSE would be useful to assess whether the interaction between wake modes and boundary-layer disturbances can lead to a significantly different growth-rate evolution in 3D-PSE with respect to 2D-LST, such as observed by Paredes *et al.* [4]. For this purpose, it would be important to distinguish this effect from the influence of non-parallel effects. This could be achieved by means of 3D-PSE analyses at conditions in which wake and boundary-layer modes are in synchronism and at conditions in which they are not. The analyses performed by Theiss *et al.* [5] and Di Giovanni & Stemmer [6] have shown a good agreement between the trend of the growth-rate evolution of roughness wake instabilities using 3D-PSE and 2D-LST for the case of a blunt reentry capsule, in which boundary-layer disturbances are highly stabilized. The results from these studies suggest that, although non-parallel effects are not negligible, they do not appear to be so important so as to be considered re-

sponsible for the growth-rate deviations illustrated in the flat-plate analysis of Paredes *et al.* [4]. Therefore, it seems reasonable to suggest that the differences observed in the latter work might be due to an interaction between wake and boundary-layer modes being captured by the 3D-PSE response. Complementary DNS analyses could further evaluate this idea.

- The analysis of the most important contributions that lead to the production and dissipation of disturbance energy has a lot of potential to improve the physical understanding of the mechanisms for disturbance growth in many different applications. An automatic derivation of the disturbance energy evolution equation for different stability theories and coordinate systems is therefore highly desirable, specially owing to the large number of terms that need to be manipulated, which makes the derivation prone to human error. The extension of the disturbance energy formulation to more complex thermodynamic flow assumptions would first require an appropriate definition of the disturbance energy for each hypothesis.

- Roughness-induced instabilities in blunt flat-plate and wedge configurations have been significantly less investigated than in sharp leading edge geometries. Since nose bluntness plays an important role on vehicles capable of atmospheric entry, its effect on the roughness wake instabilities should be better characterized. Moderate bluntness is known to have an important stabilizing effect on boundary-layer disturbances and this also seems to be the case for roughness-induced instabilities. The analysis of the disturbance energy budget in these configurations could provide insight on the interaction between the entropy and boundary layers and the perturbations developing in the roughness wake. A potential synchronism between boundary-layer modes and wake modes is expected to have a smaller impact in these cases. Blunt-nose configurations would also provide representative high-temperature flow fields which can be employed to study the influence of strong chemical non-equilibrium effects in roughness-induced disturbances.

- The study of the dominant contributions to the disturbance energy could provide additional understanding on the wall-temperature effects on roughness-induced instabilities. In particular, it could lead to an explanation of the destabilization observed for wake instabilities in the presence of boundary-layer heating, specially for the varicose disturbance [3], see also § 5.2.4.3. Base-flow heating is also expected to have an impact on the interaction between the boundary-layer modes and the wake instabilities through a stabilization of the second Mack mode.

- The higher complexity of the governing equations for high-enthalpy flow fields results in stability equations that feature a large number of terms, spe-

cially when more than one inhomogeneous direction is considered. Since manual comparison of the derived stability equations from different sources is not feasible in these cases, the development of an automatic verification process based on computer algebra systems is highly desirable for this purpose. Additionally, reproducible verification test cases should be devised which activate as many terms as possible in the stability equations such that verifications between different solvers could be achieved.

Despite the challenges embedded in the accurate prediction of boundary-layer transition, important advancements have been achieved in recent years and will continue to take place in the future. Hand-in-hand with experimental investigations, the analysis of transition following physics-based approaches such as stability theory is undoubtedly a right path towards safer atmospheric entry flight and will ultimately contribute to expand the human frontiers of space exploration.

References

[1] Boa Teh Chu. *On the energy transfer to small disturbances in fluid flow (Part I)*. Acta Mechanica, 1(3):215–234, sep 1965.

[2] Fernando Miró Miró. *Numerical Investigation of Hypersonic Boundary-Layer Stability and Transition in the presence of Ablation Phenomena*. PhD thesis, Université Libre de Bruxelles and von Karman Insitute for Fluid Dynamics, 2020.

[3] Nicola De Tullio and Neil D. Sandham. *Influence of boundary-layer disturbances on the instability of a roughness wake in a high-speed boundary layer*. Journal of Fluid Mechanics, 763:136–145, 2015.

[4] Pedro Paredes, Nicola De Tullio, Neil D. Sandham, and Vassilios Theofilis. *Instability Study of the Wake Behind a Discrete Roughness Element in a Hypersonic Boundary-Layer*. Instability and Control of Massively Separated Flows, Fluid Mechanics and Its Applications, 107:91–96, 2015.

[5] Alexander Theiss, Stefan J. Hein, Syed Raza Christopher Ali, and Rolf Radespiel. *Wake flow instability studies behind discrete roughness elements on a generic re-entry capsule*. AIAA paper, 2016-4382, 2016.

[6] Antonio Di Giovanni and Christian Stemmer. *Cross-flow-type breakdown induced by distributed roughness in the boundary layer of a hypersonic capsule configuration*. Journal of Fluid Mechanics, 856:470–503, 2018.

A

Linearized perturbation equations for a calorically perfect gas

These are the linearized disturbance equations for a steady and streamwise parallel base flow ($\bar{\mathbf{q}} = \bar{\mathbf{q}}(y,z)$) and a three-dimensional unsteady perturbation ($\tilde{\mathbf{q}} = \tilde{\mathbf{q}}(x,y,z,t)$) under the calorically perfect gas assumption.
Continuity:

$$\frac{\partial\tilde{\rho}}{\partial t} + \bar{\rho}\left(\frac{\partial\tilde{u}}{\partial x} + \frac{\partial\tilde{v}}{\partial y} + \frac{\partial\tilde{w}}{\partial z}\right) + \tilde{\rho}\left(\frac{\partial\bar{v}}{\partial y} + \frac{\partial\bar{w}}{\partial z}\right) + \bar{u}\frac{\partial\tilde{\rho}}{\partial x} + \bar{v}\frac{\partial\tilde{\rho}}{\partial y} + \bar{w}\frac{\partial\tilde{\rho}}{\partial z} + \tilde{v}\frac{\partial\bar{\rho}}{\partial y} + \tilde{w}\frac{\partial\bar{\rho}}{\partial z} = 0, \quad \text{(A.1a)}$$

x-Momentum:

$$\bar{\rho}\left(\frac{\partial\tilde{u}}{\partial t} + \bar{u}\frac{\partial\tilde{u}}{\partial x} + \bar{v}\frac{\partial\tilde{u}}{\partial y} + \bar{w}\frac{\partial\tilde{u}}{\partial z} + \tilde{v}\frac{\partial\bar{u}}{\partial y} + \tilde{w}\frac{\partial\bar{u}}{\partial z}\right) + \tilde{\rho}\left(\bar{v}\frac{\partial\bar{u}}{\partial y} + \bar{w}\frac{\partial\bar{u}}{\partial z}\right) + \frac{1}{\gamma M^2}\left(\bar{T}\frac{\partial\tilde{\rho}}{\partial x} + \bar{\rho}\frac{\partial\tilde{T}}{\partial x}\right) - \frac{1}{Re}\left\{\bar{\lambda}\left(\frac{\partial^2\tilde{u}}{\partial x^2} + \frac{\partial^2\tilde{v}}{\partial x\partial y} + \frac{\partial^2\tilde{w}}{\partial x\partial z}\right) + \bar{\mu}\left(2\frac{\partial^2\tilde{u}}{\partial x^2} + \frac{\partial^2\tilde{v}}{\partial x\partial y} + \frac{\partial^2\tilde{u}}{\partial y^2} + \frac{\partial^2\tilde{u}}{\partial z^2} + \frac{\partial^2\tilde{w}}{\partial x\partial z}\right) + \frac{d\bar{\lambda}}{d\bar{T}}\frac{\partial\tilde{T}}{\partial x}\left(\frac{\partial\bar{v}}{\partial y} + \frac{\partial\bar{w}}{\partial z}\right) + \frac{d\bar{\mu}}{d\bar{T}}\left[\tilde{T}\left(\frac{\partial^2\bar{u}}{\partial y^2} + \frac{\partial^2\bar{u}}{\partial z^2}\right) + \frac{\partial\bar{T}}{\partial y}\left(\frac{\partial\tilde{v}}{\partial x} + \frac{\partial\tilde{u}}{\partial y}\right) + \frac{\partial\tilde{T}}{\partial y}\frac{\partial\bar{u}}{\partial y}\right.$$

$$+\frac{\partial\bar{T}}{\partial z}\left(\frac{\partial\tilde{u}}{\partial z}+\frac{\partial\tilde{w}}{\partial x}\right)+\frac{\partial\tilde{T}}{\partial z}\frac{\partial\bar{u}}{\partial z}\Bigg]+\frac{d^2\bar{\mu}}{d\bar{T}^2}\tilde{T}\left(\frac{\partial\bar{T}}{\partial y}\frac{\partial\bar{u}}{\partial y}+\frac{\partial\bar{T}}{\partial z}\frac{\partial\bar{u}}{\partial z}\right)\Bigg\}=0, \quad \text{(A.1b)}$$

y-Momentum:

$$\begin{aligned}
&\bar{\rho}\left(\frac{\partial\tilde{v}}{\partial t}+\bar{u}\frac{\partial\tilde{v}}{\partial x}+\bar{v}\frac{\partial\tilde{v}}{\partial y}+\bar{w}\frac{\partial\tilde{v}}{\partial z}+\tilde{v}\frac{\partial\bar{v}}{\partial y}+\tilde{w}\frac{\partial\bar{v}}{\partial z}\right)+\tilde{\rho}\left(\bar{v}\frac{\partial\bar{v}}{\partial y}+\bar{w}\frac{\partial\bar{v}}{\partial z}\right)\\
&+\frac{1}{\gamma M^2}\left(\bar{T}\frac{\partial\tilde{\rho}}{\partial y}+\tilde{T}\frac{\partial\bar{\rho}}{\partial y}+\bar{\rho}\frac{\partial\tilde{T}}{\partial y}+\tilde{\rho}\frac{\partial\bar{T}}{\partial y}\right)-\frac{1}{Re}\Bigg\{\bar{\lambda}\left(\frac{\partial^2\tilde{u}}{\partial x\partial y}+\frac{\partial^2\tilde{v}}{\partial y^2}+\frac{\partial^2\tilde{w}}{\partial y\partial z}\right)\\
&+\bar{\mu}\left(\frac{\partial^2\tilde{u}}{\partial x\partial y}+\frac{\partial^2\tilde{v}}{\partial x^2}+2\frac{\partial^2\tilde{v}}{\partial y^2}+\frac{\partial^2\tilde{v}}{\partial z^2}+\frac{\partial^2\tilde{w}}{\partial y\partial z}\right)+\frac{d\bar{\lambda}}{d\bar{T}}\Bigg[\frac{\partial\bar{T}}{\partial y}\left(\frac{\partial\tilde{u}}{\partial x}+\frac{\partial\tilde{v}}{\partial y}+\frac{\partial\tilde{w}}{\partial z}\right)\\
&\quad+\frac{\partial\tilde{T}}{\partial y}\left(\frac{\partial\bar{v}}{\partial y}+\frac{\partial\bar{w}}{\partial z}\right)+\tilde{T}\left(\frac{\partial^2\bar{v}}{\partial y^2}+\frac{\partial^2\bar{w}}{\partial y\partial z}\right)\Bigg]+\frac{d\bar{\mu}}{d\bar{T}}\Bigg[2\frac{\partial\bar{T}}{\partial y}\frac{\partial\tilde{v}}{\partial y}+2\frac{\partial\tilde{T}}{\partial y}\frac{\partial\bar{v}}{\partial y}\\
&+\tilde{T}\left(2\frac{\partial^2\bar{v}}{\partial y^2}+\frac{\partial^2\bar{v}}{\partial z^2}+\frac{\partial^2\bar{w}}{\partial y\partial z}\right)+\frac{\partial\tilde{T}}{\partial x}\frac{\partial\bar{u}}{\partial y}+\frac{\partial\bar{T}}{\partial z}\left(\frac{\partial\tilde{v}}{\partial z}+\frac{\partial\tilde{w}}{\partial y}\right)+\frac{\partial\tilde{T}}{\partial z}\left(\frac{\partial\bar{v}}{\partial z}+\frac{\partial\bar{w}}{\partial y}\right)\Bigg]\\
&\quad+\frac{d^2\bar{\lambda}}{d\bar{T}^2}\tilde{T}\frac{\partial\bar{T}}{\partial y}\left(\frac{\partial\bar{v}}{\partial y}+\frac{\partial\bar{w}}{\partial z}\right)+\frac{d^2\bar{\mu}}{d\bar{T}^2}\tilde{T}\left[2\frac{\partial\bar{T}}{\partial y}\frac{\partial\bar{v}}{\partial y}+\frac{\partial\bar{T}}{\partial z}\left(\frac{\partial\bar{v}}{\partial z}+\frac{\partial\bar{w}}{\partial y}\right)\right]\Bigg\}=0,
\end{aligned} \quad \text{(A.1c)}$$

z-Momentum:

$$\begin{aligned}
&\bar{\rho}\left(\frac{\partial\tilde{w}}{\partial t}+\bar{u}\frac{\partial\tilde{w}}{\partial x}+\bar{v}\frac{\partial\tilde{w}}{\partial y}+\bar{w}\frac{\partial\tilde{w}}{\partial z}+\tilde{v}\frac{\partial\bar{w}}{\partial y}+\tilde{w}\frac{\partial\bar{w}}{\partial z}\right)+\tilde{\rho}\left(\bar{v}\frac{\partial\bar{w}}{\partial y}+\bar{w}\frac{\partial\bar{w}}{\partial z}\right)\\
&+\frac{1}{\gamma M^2}\left(\bar{T}\frac{\partial\tilde{\rho}}{\partial z}+\tilde{T}\frac{\partial\bar{\rho}}{\partial z}+\bar{\rho}\frac{\partial\tilde{T}}{\partial z}+\tilde{\rho}\frac{\partial\bar{T}}{\partial z}\right)-\frac{1}{Re}\Bigg\{\bar{\lambda}\left(\frac{\partial^2\tilde{u}}{\partial x\partial z}+\frac{\partial^2\tilde{v}}{\partial y\partial z}+\frac{\partial^2\tilde{w}}{\partial z^2}\right)\\
&+\bar{\mu}\left(\frac{\partial^2\tilde{u}}{\partial x\partial z}+\frac{\partial^2\tilde{v}}{\partial y\partial z}+\frac{\partial^2\tilde{w}}{\partial x^2}+\frac{\partial^2\tilde{w}}{\partial y^2}+2\frac{\partial^2\tilde{w}}{\partial z^2}\right)+\frac{d\bar{\lambda}}{d\bar{T}}\Bigg[\frac{\partial\bar{T}}{\partial z}\left(\frac{\partial\tilde{u}}{\partial x}+\frac{\partial\tilde{v}}{\partial y}+\frac{\partial\tilde{w}}{\partial z}\right)\\
&\quad+\frac{\partial\tilde{T}}{\partial z}\left(\frac{\partial\bar{v}}{\partial y}+\frac{\partial\bar{w}}{\partial z}\right)+\tilde{T}\left(\frac{\partial^2\bar{v}}{\partial y\partial z}+\frac{\partial^2\bar{w}}{\partial z^2}\right)\Bigg]+\frac{d\bar{\mu}}{d\bar{T}}\Bigg[2\frac{\partial\bar{T}}{\partial z}\frac{\partial\tilde{w}}{\partial z}+2\frac{\partial\tilde{T}}{\partial z}\frac{\partial\bar{w}}{\partial z}\\
&+\tilde{T}\left(\frac{\partial^2\bar{v}}{\partial y\partial z}+\frac{\partial^2\bar{w}}{\partial y^2}+2\frac{\partial^2\bar{w}}{\partial z^2}\right)+\frac{\partial\tilde{T}}{\partial x}\frac{\partial\bar{u}}{\partial z}+\frac{\partial\bar{T}}{\partial y}\left(\frac{\partial\tilde{v}}{\partial z}+\frac{\partial\tilde{w}}{\partial y}\right)+\frac{\partial\tilde{T}}{\partial y}\left(\frac{\partial\bar{v}}{\partial z}+\frac{\partial\bar{w}}{\partial y}\right)\Bigg]\\
&\quad+\frac{d^2\bar{\lambda}}{d\bar{T}^2}\tilde{T}\frac{\partial\bar{T}}{\partial z}\left(\frac{\partial\bar{v}}{\partial y}+\frac{\partial\bar{w}}{\partial z}\right)+\frac{d^2\bar{\mu}}{d\bar{T}^2}\tilde{T}\left[2\frac{\partial\bar{T}}{\partial z}\frac{\partial\bar{w}}{\partial z}+\frac{\partial\bar{T}}{\partial y}\left(\frac{\partial\bar{v}}{\partial z}+\frac{\partial\bar{w}}{\partial y}\right)\right]\Bigg\}=0,
\end{aligned} \quad \text{(A.1d)}$$

Energy:

$$\frac{1}{\gamma(\gamma-1)M^2}\Bigg[\bar{\rho}\left(\frac{\partial\tilde{T}}{\partial t}+\bar{u}\frac{\partial\tilde{T}}{\partial x}+\bar{v}\frac{\partial\tilde{T}}{\partial y}+\bar{w}\frac{\partial\tilde{T}}{\partial z}+\tilde{v}\frac{\partial\bar{T}}{\partial y}+\tilde{w}\frac{\partial\bar{T}}{\partial z}\right)+\tilde{\rho}\left(\bar{v}\frac{\partial\bar{T}}{\partial y}\right.$$

$$+\bar{w}\frac{\partial\tilde{T}}{\partial z}\Big)\Big]+\frac{1}{\gamma M^2}\left[\bar{\rho}\tilde{T}\left(\frac{\partial\tilde{u}}{\partial x}+\frac{\partial\tilde{v}}{\partial y}+\frac{\partial\tilde{w}}{\partial z}\right)+\left(\bar{\rho}\tilde{T}+\tilde{\rho}\bar{T}\right)\left(\frac{\partial\bar{v}}{\partial y}+\frac{\partial\bar{w}}{\partial z}\right)\right]$$
$$-\frac{1}{(\gamma-1)RePrM^2}\left\{\bar{k}\left(\frac{\partial^2\tilde{T}}{\partial x^2}+\frac{\partial^2\tilde{T}}{\partial y^2}+\frac{\partial^2\tilde{T}}{\partial z^2}\right)+\frac{d\bar{k}}{d\bar{T}}\left[2\frac{\partial\bar{T}}{\partial y}\frac{\partial\tilde{T}}{\partial y}+2\frac{\partial\bar{T}}{\partial z}\frac{\partial\tilde{T}}{\partial z}\right.\right.$$
$$\left.\left.+\tilde{T}\left(\frac{\partial^2\bar{T}}{\partial y^2}+\frac{\partial^2\bar{T}}{\partial z^2}\right)\right]+\frac{d^2\bar{k}}{d\bar{T}^2}\tilde{T}\left[\left(\frac{\partial\bar{T}}{\partial y}\right)^2+\left(\frac{\partial\bar{T}}{\partial z}\right)^2\right]\right\}$$
$$-\frac{1}{Re}\left\{2\bar{\lambda}\left(\frac{\partial\tilde{u}}{\partial x}+\frac{\partial\tilde{v}}{\partial y}+\frac{\partial\tilde{w}}{\partial z}\right)\left(\frac{\partial\bar{v}}{\partial y}+\frac{\partial\bar{w}}{\partial z}\right)+2\bar{\mu}\left[\frac{\partial\tilde{u}}{\partial y}\frac{\partial\bar{u}}{\partial y}+\frac{\partial\tilde{u}}{\partial z}\frac{\partial\bar{u}}{\partial z}+\frac{\partial\tilde{v}}{\partial x}\frac{\partial\bar{u}}{\partial y}\right.\right.$$
$$\left.+2\frac{\partial\tilde{v}}{\partial y}\frac{\partial\bar{v}}{\partial y}+\frac{\partial\tilde{w}}{\partial x}\frac{\partial\bar{u}}{\partial z}+2\frac{\partial\tilde{w}}{\partial z}\frac{\partial\bar{w}}{\partial z}+\left(\frac{\partial\tilde{v}}{\partial z}+\frac{\partial\tilde{w}}{\partial y}\right)\left(\frac{\partial\bar{v}}{\partial z}+\frac{\partial\bar{w}}{\partial y}\right)\Big]$$
$$+\frac{d\bar{\lambda}}{d\bar{T}}\tilde{T}\left[2\frac{\partial\bar{v}}{\partial y}\frac{\partial\bar{w}}{\partial z}+\left(\frac{\partial\bar{v}}{\partial y}\right)^2+\left(\frac{\partial\bar{w}}{\partial z}\right)^2\right]+\frac{d\bar{\mu}}{d\bar{T}}\tilde{T}\left[2\frac{\partial\bar{v}}{\partial z}\frac{\partial\bar{w}}{\partial y}+\left(\frac{\partial\bar{u}}{\partial y}\right)^2\right.$$
$$\left.\left.+\left(\frac{\partial\bar{u}}{\partial z}\right)^2+2\left(\frac{\partial\bar{v}}{\partial y}\right)^2+\left(\frac{\partial\bar{v}}{\partial z}\right)^2+\left(\frac{\partial\bar{w}}{\partial y}\right)^2+2\left(\frac{\partial\bar{w}}{\partial z}\right)^2\right]\right\}=0, \quad \text{(A.1e)}$$

The following considerations are important for the derivation of these equations. The pressure perturbation $\tilde{p}$ is substituted by the linearized perturbation equation of state:

$$\tilde{p}=\frac{1}{\gamma M^2}\left(\tilde{\rho}\bar{T}+\bar{\rho}\tilde{T}\right). \quad \text{(A.2)}$$

The perturbations associated to the dependent variables (transport properties in this case) are expressed in terms of the temperature perturbation by means of a linearized Taylor expansion (see § 3.2):

$$\tilde{\mu}=\frac{d\bar{\mu}}{d\bar{T}}\tilde{T}, \quad \tilde{\lambda}=\frac{d\bar{\lambda}}{d\bar{T}}\tilde{T}, \quad \tilde{k}=\frac{d\bar{k}}{d\bar{T}}\tilde{T}. \quad \text{(A.3)}$$

The spatial derivatives of the base-flow dependent quantities are expressed in terms of the spatial derivatives of temperature by means of the chain rule, for example:

$$\frac{\partial\bar{\mu}}{\partial y}=\frac{d\bar{\mu}}{d\bar{T}}\frac{\partial\bar{T}}{\partial y}, \quad \frac{\partial}{\partial y}\left(\frac{d\bar{\mu}}{d\bar{T}}\right)=\frac{d^2\bar{\mu}}{d\bar{T}^2}\frac{\partial\bar{T}}{\partial y}, \quad \text{(A.4)}$$

and the spatial derivatives of the perturbation quantities associated to the dependent variables are also expanded by means of the chain rule, for instance:

$$\frac{\partial\tilde{\mu}}{\partial y}=\frac{\partial}{\partial y}\left(\frac{d\bar{\mu}}{d\bar{T}}\right)\tilde{T}+\frac{d\bar{\mu}}{d\bar{T}}\frac{\partial\tilde{T}}{\partial y}=\frac{d^2\bar{\mu}}{d\bar{T}^2}\frac{\partial\bar{T}}{\partial y}\tilde{T}+\frac{d\bar{\mu}}{d\bar{T}}\frac{\partial\tilde{T}}{\partial y}. \quad \text{(A.5)}$$

B

Two-dimensional local linear stability theory (2D-LST) equations for a calorically perfect gas

Inserting the perturbation ansatz (3.30) into the linearized perturbation equations (equations (A.1a) to (A.1e)), the 2D-LST equations for a calorically perfect gas are obtained, listed below.

B.1 2D-LST equations in terms of ρ and T

The 2D-LST equations for $\mathbf{q} = [\rho, u, v, w, T]^{\mathrm{T}}$ can be expressed as follows.
Continuity:

$$-i\omega\hat{\rho} + \bar{\rho}\left(i\alpha\hat{u} + \frac{\partial\hat{v}}{\partial y} + \frac{\partial\hat{w}}{\partial z}\right) + \hat{\rho}\left(\frac{\partial\bar{v}}{\partial y} + \frac{\partial\bar{w}}{\partial z}\right) + \bar{u}i\alpha\hat{\rho} + \bar{v}\frac{\partial\hat{\rho}}{\partial y} + \bar{w}\frac{\partial\hat{\rho}}{\partial z} + \hat{v}\frac{\partial\bar{\rho}}{\partial y} + \hat{w}\frac{\partial\bar{\rho}}{\partial z} = 0, \quad \text{(B.1a)}$$

x-Momentum:

$$\bar{\rho}\left(-i\omega\hat{u} + \bar{u}i\alpha\hat{u} + \bar{v}\frac{\partial\hat{u}}{\partial y} + \bar{w}\frac{\partial\hat{u}}{\partial z} + \hat{v}\frac{\partial\bar{u}}{\partial y} + \hat{w}\frac{\partial\bar{u}}{\partial z}\right) + \hat{\rho}\left(\bar{v}\frac{\partial\bar{u}}{\partial y} + \bar{w}\frac{\partial\bar{u}}{\partial z}\right) + \frac{1}{\gamma M^2}\left(\bar{T}i\alpha\hat{\rho} + \bar{\rho}i\alpha\hat{T}\right) - \frac{1}{Re}\left\{\bar{\lambda}\left(-\alpha^2\hat{u} + i\alpha\frac{\partial\hat{v}}{\partial y} + i\alpha\frac{\partial\hat{w}}{\partial z}\right)\right.$$

$$+\bar{\mu}\left(-2\alpha^2\hat{u}+i\alpha\frac{\partial\hat{v}}{\partial y}+\frac{\partial^2\hat{u}}{\partial y^2}+\frac{\partial^2\hat{u}}{\partial z^2}+i\alpha\frac{\partial\hat{w}}{\partial z}\right)+\frac{d\bar{\lambda}}{d\bar{T}}i\alpha\hat{T}\left(\frac{\partial\bar{v}}{\partial y}+\frac{\partial\bar{w}}{\partial z}\right)$$
$$+\frac{d\bar{\mu}}{d\bar{T}}\left[\hat{T}\left(\frac{\partial^2\bar{u}}{\partial y^2}+\frac{\partial^2\bar{u}}{\partial z^2}\right)+\frac{\partial\bar{T}}{\partial y}\left(i\alpha\hat{v}+\frac{\partial\hat{u}}{\partial y}\right)+\frac{\partial\hat{T}}{\partial y}\frac{\partial\bar{u}}{\partial y}\right.$$
$$\left.+\frac{\partial\bar{T}}{\partial z}\left(\frac{\partial\hat{u}}{\partial z}+i\alpha\hat{w}\right)+\frac{\partial\hat{T}}{\partial z}\frac{\partial\bar{u}}{\partial z}\right]+\frac{d^2\bar{\mu}}{d\bar{T}^2}\hat{T}\left(\frac{\partial\bar{T}}{\partial y}\frac{\partial\bar{u}}{\partial y}+\frac{\partial\bar{T}}{\partial z}\frac{\partial\bar{u}}{\partial z}\right)\Bigg\}=0, \quad \text{(B.1b)}$$

y-Momentum:

$$\bar{\rho}\left(-i\omega\hat{v}+\bar{u}i\alpha\hat{v}+\bar{v}\frac{\partial\hat{v}}{\partial y}+\bar{w}\frac{\partial\hat{v}}{\partial z}+\hat{v}\frac{\partial\bar{v}}{\partial y}+\hat{w}\frac{\partial\bar{v}}{\partial z}\right)+\hat{\rho}\left(\bar{v}\frac{\partial\bar{v}}{\partial y}+\bar{w}\frac{\partial\bar{v}}{\partial z}\right)$$
$$+\frac{1}{\gamma M^2}\left(\bar{T}\frac{\partial\hat{\rho}}{\partial y}+\hat{T}\frac{\partial\bar{\rho}}{\partial y}+\bar{\rho}\frac{\partial\hat{T}}{\partial y}+\hat{\rho}\frac{\partial\bar{T}}{\partial y}\right)-\frac{1}{Re}\left\{\bar{\lambda}\left(i\alpha\frac{\partial\hat{u}}{\partial y}+\frac{\partial^2\hat{v}}{\partial y^2}+\frac{\partial^2\hat{w}}{\partial y\partial z}\right)\right.$$
$$+\bar{\mu}\left(i\alpha\frac{\partial\hat{u}}{\partial y}-\alpha^2\hat{v}+2\frac{\partial^2\hat{v}}{\partial y^2}+\frac{\partial^2\hat{v}}{\partial z^2}+\frac{\partial^2\hat{w}}{\partial y\partial z}\right)+\frac{d\bar{\lambda}}{d\bar{T}}\left[\frac{\partial\bar{T}}{\partial y}\left(i\alpha\hat{u}+\frac{\partial\hat{v}}{\partial y}+\frac{\partial\hat{w}}{\partial z}\right)\right.$$
$$\left.+\frac{\partial\hat{T}}{\partial y}\left(\frac{\partial\bar{v}}{\partial y}+\frac{\partial\bar{w}}{\partial z}\right)+\hat{T}\left(\frac{\partial^2\bar{v}}{\partial y^2}+\frac{\partial^2\bar{w}}{\partial y\partial z}\right)\right]+\frac{d\bar{\mu}}{d\bar{T}}\left[2\frac{\partial\bar{T}}{\partial y}\frac{\partial\hat{v}}{\partial y}+2\frac{\partial\hat{T}}{\partial y}\frac{\partial\bar{v}}{\partial y}\right.$$
$$\left.+\hat{T}\left(2\frac{\partial^2\bar{v}}{\partial y^2}+\frac{\partial^2\bar{v}}{\partial z^2}+\frac{\partial^2\bar{w}}{\partial y\partial z}\right)+i\alpha\hat{T}\frac{\partial\bar{u}}{\partial y}+\frac{\partial\bar{T}}{\partial z}\left(\frac{\partial\hat{v}}{\partial z}+\frac{\partial\hat{w}}{\partial y}\right)+\frac{\partial\hat{T}}{\partial z}\left(\frac{\partial\bar{v}}{\partial z}+\frac{\partial\bar{w}}{\partial y}\right)\right]$$
$$\left.+\frac{d^2\bar{\lambda}}{d\bar{T}^2}\hat{T}\frac{\partial\bar{T}}{\partial y}\left(\frac{\partial\bar{v}}{\partial y}+\frac{\partial\bar{w}}{\partial z}\right)+\frac{d^2\bar{\mu}}{d\bar{T}^2}\hat{T}\left[2\frac{\partial\bar{T}}{\partial y}\frac{\partial\bar{v}}{\partial y}+\frac{\partial\bar{T}}{\partial z}\left(\frac{\partial\bar{v}}{\partial z}+\frac{\partial\bar{w}}{\partial y}\right)\right]\right\}=0, \quad \text{(B.1c)}$$

z-Momentum:

$$\bar{\rho}\left(-i\omega\hat{w}+\bar{u}i\alpha\hat{w}+\bar{v}\frac{\partial\hat{w}}{\partial y}+\bar{w}\frac{\partial\hat{w}}{\partial z}+\hat{v}\frac{\partial\bar{w}}{\partial y}+\hat{w}\frac{\partial\bar{w}}{\partial z}\right)+\hat{\rho}\left(\bar{v}\frac{\partial\bar{w}}{\partial y}+\bar{w}\frac{\partial\bar{w}}{\partial z}\right)$$
$$+\frac{1}{\gamma M^2}\left(\bar{T}\frac{\partial\hat{\rho}}{\partial z}+\hat{T}\frac{\partial\bar{\rho}}{\partial z}+\bar{\rho}\frac{\partial\hat{T}}{\partial z}+\hat{\rho}\frac{\partial\bar{T}}{\partial z}\right)-\frac{1}{Re}\left\{\bar{\lambda}\left(i\alpha\frac{\partial\hat{u}}{\partial z}+\frac{\partial^2\hat{v}}{\partial y\partial z}+\frac{\partial^2\hat{w}}{\partial z^2}\right)\right.$$
$$+\bar{\mu}\left(i\alpha\frac{\partial\hat{u}}{\partial z}+\frac{\partial^2\hat{v}}{\partial y\partial z}-\alpha^2\hat{w}+\frac{\partial^2\hat{w}}{\partial y^2}+2\frac{\partial^2\hat{w}}{\partial z^2}\right)+\frac{d\bar{\lambda}}{d\bar{T}}\left[\frac{\partial\bar{T}}{\partial z}\left(i\alpha\hat{u}+\frac{\partial\hat{v}}{\partial y}+\frac{\partial\hat{w}}{\partial z}\right)\right.$$
$$\left.+\frac{\partial\hat{T}}{\partial z}\left(\frac{\partial\bar{v}}{\partial y}+\frac{\partial\bar{w}}{\partial z}\right)+\hat{T}\left(\frac{\partial^2\bar{v}}{\partial y\partial z}+\frac{\partial^2\bar{w}}{\partial z^2}\right)\right]+\frac{d\bar{\mu}}{d\bar{T}}\left[2\frac{\partial\bar{T}}{\partial z}\frac{\partial\hat{w}}{\partial z}+2\frac{\partial\hat{T}}{\partial z}\frac{\partial\bar{w}}{\partial z}\right.$$
$$\left.+\hat{T}\left(\frac{\partial^2\bar{v}}{\partial y\partial z}+\frac{\partial^2\bar{w}}{\partial y^2}+2\frac{\partial^2\bar{w}}{\partial z^2}\right)+i\alpha\hat{T}\frac{\partial\bar{u}}{\partial z}+\frac{\partial\bar{T}}{\partial y}\left(\frac{\partial\hat{v}}{\partial z}+\frac{\partial\hat{w}}{\partial y}\right)+\frac{\partial\hat{T}}{\partial y}\left(\frac{\partial\bar{v}}{\partial z}+\frac{\partial\bar{w}}{\partial y}\right)\right]$$
$$\left.+\frac{d^2\bar{\lambda}}{d\bar{T}^2}\hat{T}\frac{\partial\bar{T}}{\partial z}\left(\frac{\partial\bar{v}}{\partial y}+\frac{\partial\bar{w}}{\partial z}\right)+\frac{d^2\bar{\mu}}{d\bar{T}^2}\hat{T}\left[2\frac{\partial\bar{T}}{\partial z}\frac{\partial\bar{w}}{\partial z}+\frac{\partial\bar{T}}{\partial y}\left(\frac{\partial\bar{v}}{\partial z}+\frac{\partial\bar{w}}{\partial y}\right)\right]\right\}=0, \quad \text{(B.1d)}$$

Energy:

$$\begin{aligned}
&\frac{1}{\gamma(\gamma-1)M^2}\left[\bar{\rho}\left(-i\omega\hat{T}+\bar{u}i\alpha\hat{T}+\bar{v}\frac{\partial\hat{T}}{\partial y}+\bar{w}\frac{\partial\hat{T}}{\partial z}+\hat{v}\frac{\partial\bar{T}}{\partial y}+\hat{w}\frac{\partial\bar{T}}{\partial z}\right)+\hat{\rho}\left(\bar{v}\frac{\partial\bar{T}}{\partial y}\right.\right.\\
&\left.\left.+\bar{w}\frac{\partial\bar{T}}{\partial z}\right)\right]+\frac{1}{\gamma M^2}\left[\bar{\rho}\bar{T}\left(i\alpha\hat{u}+\frac{\partial\hat{v}}{\partial y}+\frac{\partial\hat{w}}{\partial z}\right)+\left(\bar{\rho}\hat{T}+\hat{\rho}\bar{T}\right)\left(\frac{\partial\bar{v}}{\partial y}+\frac{\partial\bar{w}}{\partial z}\right)\right]\\
&-\frac{1}{(\gamma-1)RePrM^2}\left\{\bar{k}\left(-\alpha^2\hat{T}+\frac{\partial^2\hat{T}}{\partial y^2}+\frac{\partial^2\hat{T}}{\partial z^2}\right)+\frac{d\bar{k}}{d\bar{T}}\left[2\frac{\partial\bar{T}}{\partial y}\frac{\partial\hat{T}}{\partial y}+2\frac{\partial\bar{T}}{\partial z}\frac{\partial\hat{T}}{\partial z}\right.\right.\\
&\left.\left.+\hat{T}\left(\frac{\partial^2\bar{T}}{\partial y^2}+\frac{\partial^2\bar{T}}{\partial z^2}\right)\right]+\frac{d^2\bar{k}}{d\bar{T}^2}\hat{T}\left[\left(\frac{\partial\bar{T}}{\partial y}\right)^2+\left(\frac{\partial\bar{T}}{\partial z}\right)^2\right]\right\}\\
&-\frac{1}{Re}\left\{2\bar{\lambda}\left(i\alpha\hat{u}+\frac{\partial\hat{v}}{\partial y}+\frac{\partial\hat{w}}{\partial z}\right)\left(\frac{\partial\bar{v}}{\partial y}+\frac{\partial\bar{w}}{\partial z}\right)+2\bar{\mu}\left[\frac{\partial\hat{u}}{\partial y}\frac{\partial\bar{u}}{\partial y}+\frac{\partial\hat{u}}{\partial z}\frac{\partial\bar{u}}{\partial z}+i\alpha\hat{v}\frac{\partial\bar{u}}{\partial y}\right.\right.\\
&\left.+2\frac{\partial\hat{v}}{\partial y}\frac{\partial\bar{v}}{\partial y}+i\alpha\hat{w}\frac{\partial\bar{u}}{\partial z}+2\frac{\partial\hat{w}}{\partial z}\frac{\partial\bar{w}}{\partial z}+\left(\frac{\partial\hat{v}}{\partial z}+\frac{\partial\hat{w}}{\partial y}\right)\left(\frac{\partial\bar{v}}{\partial z}+\frac{\partial\bar{w}}{\partial y}\right)\right]\\
&+\frac{d\bar{\lambda}}{d\bar{T}}\hat{T}\left[2\frac{\partial\bar{v}}{\partial y}\frac{\partial\bar{w}}{\partial z}+\left(\frac{\partial\bar{v}}{\partial y}\right)^2+\left(\frac{\partial\bar{w}}{\partial z}\right)^2\right]+\frac{d\bar{\mu}}{d\bar{T}}\hat{T}\left[2\frac{\partial\bar{v}}{\partial z}\frac{\partial\bar{w}}{\partial y}+\left(\frac{\partial\bar{u}}{\partial y}\right)^2\right.\\
&\left.\left.+\left(\frac{\partial\bar{u}}{\partial z}\right)^2+2\left(\frac{\partial\bar{v}}{\partial y}\right)^2+\left(\frac{\partial\bar{v}}{\partial z}\right)^2+\left(\frac{\partial\bar{w}}{\partial y}\right)^2+2\left(\frac{\partial\bar{w}}{\partial z}\right)^2\right]\right\}=0, \quad \text{(B.1e)}
\end{aligned}$$

B.2 2D-LST equations in terms of p and T

The 2D-LST equations for $\mathbf{q}=[u,v,w,T,p]^{\mathrm{T}}$ can be written as follows.
Continuity:

$$\begin{aligned}
&-i\omega\left(\hat{p}-\frac{\bar{p}\hat{T}}{\bar{T}}\right)+\bar{p}\left(i\alpha\hat{u}+\frac{\partial\hat{v}}{\partial y}+\frac{\partial\hat{w}}{\partial z}\right)+\left(\hat{p}-\frac{\bar{p}\hat{T}}{\bar{T}}\right)\left(\frac{\partial\bar{v}}{\partial y}+\frac{\partial\bar{w}}{\partial z}\right)\\
&+\bar{u}i\alpha\left(\hat{p}-\frac{\bar{p}\hat{T}}{\bar{T}}\right)+\bar{v}\left[\frac{\partial\hat{p}}{\partial y}-\frac{\hat{T}}{\bar{T}}\frac{\partial\bar{p}}{\partial y}-\frac{\bar{p}}{\bar{T}}\frac{\partial\hat{T}}{\partial y}+\left(2\frac{\bar{p}\hat{T}}{\bar{T}^2}-\frac{\hat{p}}{\bar{T}}\right)\frac{\partial\bar{T}}{\partial y}\right]\\
&+\bar{w}\left[\frac{\partial\hat{p}}{\partial z}-\frac{\hat{T}}{\bar{T}}\frac{\partial\bar{p}}{\partial z}-\frac{\bar{p}}{\bar{T}}\frac{\partial\hat{T}}{\partial z}+\left(2\frac{\bar{p}\hat{T}}{\bar{T}^2}-\frac{\hat{p}}{\bar{T}}\right)\frac{\partial\bar{T}}{\partial z}\right]+\hat{v}\left(\frac{\partial\bar{p}}{\partial y}-\frac{\bar{p}}{\bar{T}}\frac{\partial\bar{T}}{\partial y}\right)\\
&+\hat{w}\left(\frac{\partial\bar{p}}{\partial z}-\frac{\bar{p}}{\bar{T}}\frac{\partial\bar{T}}{\partial z}\right)=0, \quad \text{(B.2a)}
\end{aligned}$$

x-Momentum:

$$\frac{\gamma M^2}{\bar{T}}\left[\bar{p}\left(-i\omega\hat{u}+\bar{u}i\alpha\hat{u}+\bar{v}\frac{\partial\hat{u}}{\partial y}+\bar{w}\frac{\partial\hat{u}}{\partial z}+\hat{v}\frac{\partial\bar{u}}{\partial y}+\hat{w}\frac{\partial\bar{u}}{\partial z}\right)\right.$$

$$+\left(\hat{p}-\frac{\bar{p}\hat{T}}{\bar{T}}\right)\left(\bar{v}\frac{\partial\bar{u}}{\partial y}+\bar{w}\frac{\partial\bar{u}}{\partial z}\right)\Bigg]+i\alpha\hat{p}-\frac{1}{Re}\left\{\bar{\lambda}\left(-\alpha^2\hat{u}+i\alpha\frac{\partial\hat{v}}{\partial y}+i\alpha\frac{\partial\hat{w}}{\partial z}\right)\right.$$
$$+\bar{\mu}\left(-2\alpha^2\hat{u}+i\alpha\frac{\partial\hat{v}}{\partial y}+\frac{\partial^2\hat{u}}{\partial y^2}+\frac{\partial^2\hat{u}}{\partial z^2}+i\alpha\frac{\partial\hat{w}}{\partial z}\right)+\frac{d\bar{\lambda}}{d\bar{T}}i\alpha\hat{T}\left(\frac{\partial\bar{v}}{\partial y}+\frac{\partial\bar{w}}{\partial z}\right)$$
$$+\frac{d\bar{\mu}}{d\bar{T}}\left[\hat{T}\left(\frac{\partial^2\bar{u}}{\partial y^2}+\frac{\partial^2\bar{u}}{\partial z^2}\right)+\frac{\partial\bar{T}}{\partial y}\left(i\alpha\hat{v}+\frac{\partial\hat{u}}{\partial y}\right)+\frac{\partial\hat{T}}{\partial y}\frac{\partial\bar{u}}{\partial y}\right.$$
$$\left.\left.+\frac{\partial\bar{T}}{\partial z}\left(\frac{\partial\hat{u}}{\partial z}+i\alpha\hat{w}\right)+\frac{\partial\hat{T}}{\partial z}\frac{\partial\bar{u}}{\partial z}\right]+\frac{d^2\bar{\mu}}{d\bar{T}^2}\hat{T}\left(\frac{\partial\bar{T}}{\partial y}\frac{\partial\bar{u}}{\partial y}+\frac{\partial\bar{T}}{\partial z}\frac{\partial\bar{u}}{\partial z}\right)\right\}=0, \quad \text{(B.2b)}$$

y-Momentum:

$$\frac{\gamma M^2}{\bar{T}}\left[\bar{p}\left(-i\omega\hat{v}+\bar{u}i\alpha\hat{v}+\bar{v}\frac{\partial\hat{v}}{\partial y}+\bar{w}\frac{\partial\hat{v}}{\partial z}+\hat{v}\frac{\partial\bar{v}}{\partial y}+\hat{w}\frac{\partial\bar{v}}{\partial z}\right)\right.$$
$$\left.+\left(\hat{p}-\frac{\bar{p}\hat{T}}{\bar{T}}\right)\left(\bar{v}\frac{\partial\bar{v}}{\partial y}+\bar{w}\frac{\partial\bar{v}}{\partial z}\right)\right]+\frac{\partial\hat{p}}{\partial y}-\frac{1}{Re}\left\{\bar{\lambda}\left(i\alpha\frac{\partial\hat{u}}{\partial y}+\frac{\partial^2\hat{v}}{\partial y^2}+\frac{\partial^2\hat{w}}{\partial y\partial z}\right)\right.$$
$$+\bar{\mu}\left(i\alpha\frac{\partial\hat{u}}{\partial y}-\alpha^2\hat{v}+2\frac{\partial^2\hat{v}}{\partial y^2}+\frac{\partial^2\hat{v}}{\partial z^2}+\frac{\partial^2\hat{w}}{\partial y\partial z}\right)+\frac{d\bar{\lambda}}{d\bar{T}}\left[\frac{\partial\bar{T}}{\partial y}\left(i\alpha\hat{u}+\frac{\partial\hat{v}}{\partial y}+\frac{\partial\hat{w}}{\partial z}\right)\right.$$
$$\left.+\frac{\partial\hat{T}}{\partial y}\left(\frac{\partial\bar{v}}{\partial y}+\frac{\partial\bar{w}}{\partial z}\right)+\hat{T}\left(\frac{\partial^2\bar{v}}{\partial y^2}+\frac{\partial^2\bar{w}}{\partial y\partial z}\right)\right]+\frac{d\bar{\mu}}{d\bar{T}}\left[2\frac{\partial\bar{T}}{\partial y}\frac{\partial\hat{v}}{\partial y}+2\frac{\partial\hat{T}}{\partial y}\frac{\partial\bar{v}}{\partial y}\right.$$
$$\left.+\hat{T}\left(2\frac{\partial^2\bar{v}}{\partial y^2}+\frac{\partial^2\bar{v}}{\partial z^2}+\frac{\partial^2\bar{w}}{\partial y\partial z}\right)+i\alpha\hat{T}\frac{\partial\bar{u}}{\partial y}+\frac{\partial\bar{T}}{\partial z}\left(\frac{\partial\hat{v}}{\partial z}+\frac{\partial\hat{w}}{\partial y}\right)+\frac{\partial\hat{T}}{\partial z}\left(\frac{\partial\bar{v}}{\partial z}+\frac{\partial\bar{w}}{\partial y}\right)\right]$$
$$\left.\left.+\frac{d^2\bar{\lambda}}{d\bar{T}^2}\hat{T}\frac{\partial\bar{T}}{\partial y}\left(\frac{\partial\bar{v}}{\partial y}+\frac{\partial\bar{w}}{\partial z}\right)+\frac{d^2\bar{\mu}}{d\bar{T}^2}\hat{T}\left[2\frac{\partial\bar{T}}{\partial y}\frac{\partial\bar{v}}{\partial y}+\frac{\partial\bar{T}}{\partial z}\left(\frac{\partial\bar{v}}{\partial z}+\frac{\partial\bar{w}}{\partial y}\right)\right]\right\}=0, \quad \text{(B.2c)}$$

z-Momentum:

$$\frac{\gamma M^2}{\bar{T}}\left[\bar{p}\left(-i\omega\hat{w}+\bar{u}i\alpha\hat{w}+\bar{v}\frac{\partial\hat{w}}{\partial y}+\bar{w}\frac{\partial\hat{w}}{\partial z}+\hat{v}\frac{\partial\bar{w}}{\partial y}+\hat{w}\frac{\partial\bar{w}}{\partial z}\right)\right.$$
$$\left.+\left(\hat{p}-\frac{\bar{p}\hat{T}}{\bar{T}}\right)\left(\bar{v}\frac{\partial\bar{w}}{\partial y}+\bar{w}\frac{\partial\bar{w}}{\partial z}\right)\right]+\frac{\partial\hat{p}}{\partial z}-\frac{1}{Re}\left\{\bar{\lambda}\left(i\alpha\frac{\partial\hat{u}}{\partial z}+\frac{\partial^2\hat{v}}{\partial y\partial z}+\frac{\partial^2\hat{w}}{\partial z^2}\right)\right.$$
$$+\bar{\mu}\left(i\alpha\frac{\partial\hat{u}}{\partial z}+\frac{\partial^2\hat{v}}{\partial y\partial z}-\alpha^2\hat{w}+\frac{\partial^2\hat{w}}{\partial y^2}+2\frac{\partial^2\hat{w}}{\partial z^2}\right)+\frac{d\bar{\lambda}}{d\bar{T}}\left[\frac{\partial\bar{T}}{\partial z}\left(i\alpha\hat{u}+\frac{\partial\hat{v}}{\partial y}+\frac{\partial\hat{w}}{\partial z}\right)\right.$$
$$\left.+\frac{\partial\hat{T}}{\partial z}\left(\frac{\partial\bar{v}}{\partial y}+\frac{\partial\bar{w}}{\partial z}\right)+\hat{T}\left(\frac{\partial^2\bar{v}}{\partial y\partial z}+\frac{\partial^2\bar{w}}{\partial z^2}\right)\right]+\frac{d\bar{\mu}}{d\bar{T}}\left[2\frac{\partial\bar{T}}{\partial z}\frac{\partial\hat{w}}{\partial z}+2\frac{\partial\hat{T}}{\partial z}\frac{\partial\bar{w}}{\partial z}\right.$$
$$\left.+\hat{T}\left(\frac{\partial^2\bar{v}}{\partial y\partial z}+\frac{\partial^2\bar{w}}{\partial y^2}+2\frac{\partial^2\bar{w}}{\partial z^2}\right)+i\alpha\hat{T}\frac{\partial\bar{u}}{\partial z}+\frac{\partial\bar{T}}{\partial y}\left(\frac{\partial\hat{v}}{\partial z}+\frac{\partial\hat{w}}{\partial y}\right)+\frac{\partial\hat{T}}{\partial y}\left(\frac{\partial\bar{v}}{\partial z}+\frac{\partial\bar{w}}{\partial y}\right)\right]$$

$$+\frac{d^2\bar{\lambda}}{d\bar{T}^2}\hat{T}\frac{\partial\bar{T}}{\partial z}\left(\frac{\partial\bar{v}}{\partial y}+\frac{\partial\bar{w}}{\partial z}\right)+\frac{d^2\bar{\mu}}{d\bar{T}^2}\hat{T}\left[2\frac{\partial\bar{T}}{\partial z}\frac{\partial\bar{w}}{\partial z}+\frac{\partial\bar{T}}{\partial y}\left(\frac{\partial\bar{v}}{\partial z}+\frac{\partial\bar{w}}{\partial y}\right)\right]\Bigg\}=0, \tag{B.2d}$$

Energy:

$$\begin{aligned}
&\frac{1}{(\gamma-1)\bar{\bar{T}}}\left[\bar{p}\left(-i\omega\hat{T}+\bar{u}i\alpha\hat{T}+\bar{v}\frac{\partial\hat{T}}{\partial y}+\bar{w}\frac{\partial\hat{T}}{\partial z}+\hat{v}\frac{\partial\bar{T}}{\partial y}+\hat{w}\frac{\partial\bar{T}}{\partial z}\right)\right.\\
&\left.+\left(\hat{p}-\frac{\bar{p}\hat{T}}{\bar{T}}\right)\left(\bar{v}\frac{\partial\bar{T}}{\partial y}+\bar{w}\frac{\partial\bar{T}}{\partial z}\right)\right]+\bar{p}\left(i\alpha\hat{u}+\frac{\partial\hat{v}}{\partial y}+\frac{\partial\hat{w}}{\partial z}\right)+\hat{p}\left(\frac{\partial\bar{v}}{\partial y}+\frac{\partial\bar{w}}{\partial z}\right)\\
&-\frac{1}{(\gamma-1)RePrM^2}\left\{\bar{k}\left(-\alpha^2\hat{T}+\frac{\partial^2\hat{T}}{\partial y^2}+\frac{\partial^2\hat{T}}{\partial z^2}\right)+\frac{d\bar{k}}{d\bar{T}}\left[2\frac{\partial\bar{T}}{\partial y}\frac{\partial\hat{T}}{\partial y}+2\frac{\partial\bar{T}}{\partial z}\frac{\partial\hat{T}}{\partial z}\right.\right.\\
&\left.\left.+\hat{T}\left(\frac{\partial^2\bar{T}}{\partial y^2}+\frac{\partial^2\bar{T}}{\partial z^2}\right)\right]+\frac{d^2\bar{k}}{d\bar{T}^2}\hat{T}\left[\left(\frac{\partial\bar{T}}{\partial y}\right)^2+\left(\frac{\partial\bar{T}}{\partial z}\right)^2\right]\right\}\\
&-\frac{1}{Re}\left\{2\bar{\lambda}\left(i\alpha\hat{u}+\frac{\partial\hat{v}}{\partial y}+\frac{\partial\hat{w}}{\partial z}\right)\left(\frac{\partial\bar{v}}{\partial y}+\frac{\partial\bar{w}}{\partial z}\right)+2\bar{\mu}\left[\frac{\partial\hat{u}}{\partial y}\frac{\partial\bar{u}}{\partial y}+\frac{\partial\hat{u}}{\partial z}\frac{\partial\bar{u}}{\partial z}+i\alpha\hat{v}\frac{\partial\bar{u}}{\partial y}\right.\right.\\
&\left.+2\frac{\partial\hat{v}}{\partial y}\frac{\partial\bar{v}}{\partial y}+i\alpha\hat{w}\frac{\partial\bar{u}}{\partial z}+2\frac{\partial\hat{w}}{\partial z}\frac{\partial\bar{w}}{\partial z}+\left(\frac{\partial\hat{v}}{\partial z}+\frac{\partial\hat{w}}{\partial y}\right)\left(\frac{\partial\bar{v}}{\partial z}+\frac{\partial\bar{w}}{\partial y}\right)\Big]\\
&+\frac{d\bar{\lambda}}{d\bar{T}}\hat{T}\left[2\frac{\partial\bar{v}}{\partial y}\frac{\partial\bar{w}}{\partial z}+\left(\frac{\partial\bar{v}}{\partial y}\right)^2+\left(\frac{\partial\bar{w}}{\partial z}\right)^2\right]+\frac{d\bar{\mu}}{d\bar{T}}\hat{T}\left[2\frac{\partial\bar{v}}{\partial z}\frac{\partial\bar{w}}{\partial y}+\left(\frac{\partial\bar{u}}{\partial y}\right)^2\right.\\
&\left.\left.+\left(\frac{\partial\bar{u}}{\partial z}\right)^2+2\left(\frac{\partial\bar{v}}{\partial y}\right)^2+\left(\frac{\partial\bar{v}}{\partial z}\right)^2+\left(\frac{\partial\bar{w}}{\partial y}\right)^2+2\left(\frac{\partial\bar{w}}{\partial z}\right)^2\right]\right\}=0,
\end{aligned} \tag{B.2e}$$

C

One-dimensional local linear stability theory (LST) equations for a calorically perfect gas

Inserting the perturbation ansatz (3.11) into the linearized perturbation equations (equations (A.1a) to (A.1e)) and neglecting all base-flow derivatives with respect to z ($\bar{\mathbf{q}} = \bar{\mathbf{q}}(y)$), the LST equations for a calorically perfect gas are obtained, listed below.

C.1 LST equations in terms of ρ and T

The LST equations for $\mathbf{q} = [\rho, u, v, w, T]^{\mathrm{T}}$ can be expressed as follows.
Continuity:

$$-\ i\omega\hat{\rho}\ +\ \bar{\rho}\left(i\alpha\hat{u} + \frac{\partial\hat{v}}{\partial y} + i\beta\hat{w}\right)\ +\ \bar{u}i\alpha\hat{\rho}\ +\ \bar{w}i\beta\hat{\rho}\ +\ \hat{v}\frac{\partial\bar{\rho}}{\partial y}\ =\ 0, \quad \text{(C.1a)}$$

x-Momentum:

$$\bar{\rho}\left(-i\omega\hat{u} + \bar{u}i\alpha\hat{u} + \bar{w}i\beta\hat{u} + \hat{v}\frac{\partial\bar{u}}{\partial y}\right) + \frac{1}{\gamma M^2}\left(\bar{T}i\alpha\hat{\rho} + \bar{\rho}i\alpha\hat{T}\right)$$
$$-\frac{1}{Re}\left\{\bar{\lambda}\left(-\alpha^2\hat{u} + i\alpha\frac{\partial\hat{v}}{\partial y} - \alpha\beta\hat{w}\right)\right.$$

$$+\bar{\mu}\left(-2\alpha^2\hat{u}+i\alpha\frac{\partial\hat{v}}{\partial y}+\frac{\partial^2\hat{u}}{\partial y^2}-\beta^2\hat{u}-\alpha\beta\hat{w}\right)$$
$$+\frac{d\bar{\mu}}{d\bar{T}}\left[\hat{T}\frac{\partial^2\bar{u}}{\partial y^2}+\frac{\partial\bar{T}}{\partial y}\left(i\alpha\hat{v}+\frac{\partial\hat{u}}{\partial y}\right)+\frac{\partial\hat{T}}{\partial y}\frac{\partial\bar{u}}{\partial y}\right]+\frac{d^2\bar{\mu}}{d\bar{T}^2}\hat{T}\frac{\partial\bar{T}}{\partial y}\frac{\partial\bar{u}}{\partial y}\Bigg\}=0, \quad \text{(C.1b)}$$

y-Momentum:

$$\bar{\rho}\left(-i\omega\hat{v}+\bar{u}i\alpha\hat{v}+\bar{w}i\beta\hat{v}\right)+\frac{1}{\gamma M^2}\left(\bar{T}\frac{\partial\hat{\rho}}{\partial y}+\hat{T}\frac{\partial\bar{\rho}}{\partial y}+\bar{\rho}\frac{\partial\hat{T}}{\partial y}+\hat{\rho}\frac{\partial\bar{T}}{\partial y}\right)$$
$$-\frac{1}{Re}\left[\bar{\lambda}\left(i\alpha\frac{\partial\hat{u}}{\partial y}+\frac{\partial^2\hat{v}}{\partial y^2}+i\beta\frac{\partial\hat{w}}{\partial y}\right)\right.$$
$$+\bar{\mu}\left(i\alpha\frac{\partial\hat{u}}{\partial y}-\alpha^2\hat{v}+2\frac{\partial^2\hat{v}}{\partial y^2}-\beta^2\hat{v}+i\beta\frac{\partial\hat{w}}{\partial y}\right)+\frac{d\bar{\lambda}}{d\bar{T}}\frac{\partial\bar{T}}{\partial y}\left(i\alpha\hat{u}+\frac{\partial\hat{v}}{\partial y}+i\beta\hat{w}\right)$$
$$\left.+\frac{d\bar{\mu}}{d\bar{T}}\left(2\frac{\partial\bar{T}}{\partial y}\frac{\partial\hat{v}}{\partial y}+i\alpha\hat{T}\frac{\partial\bar{u}}{\partial y}+i\beta\hat{T}\frac{\partial\bar{w}}{\partial y}\right)\right]=0, \quad \text{(C.1c)}$$

z-Momentum:

$$\bar{\rho}\left(-i\omega\hat{w}+\bar{u}i\alpha\hat{w}+\bar{w}i\beta\hat{w}+\hat{v}\frac{\partial\bar{w}}{\partial y}\right)+\frac{1}{\gamma M^2}\left(\bar{T}i\beta\hat{\rho}+\bar{\rho}i\beta\hat{T}\right)$$
$$-\frac{1}{Re}\left\{\bar{\lambda}\left(-\alpha\beta\hat{u}+i\beta\frac{\partial\hat{v}}{\partial y}-\beta^2\hat{w}\right)\right.$$
$$+\bar{\mu}\left(-\alpha\beta\hat{u}+i\beta\frac{\partial\hat{v}}{\partial y}-\alpha^2\hat{w}+\frac{\partial^2\hat{w}}{\partial y^2}-2\beta^2\hat{w}\right)$$
$$\left.+\frac{d\bar{\mu}}{d\bar{T}}\left[\hat{T}\frac{\partial^2\bar{w}}{\partial y^2}+\frac{\partial\bar{T}}{\partial y}\left(i\beta\hat{v}+\frac{\partial\hat{w}}{\partial y}\right)+\frac{\partial\hat{T}}{\partial y}\frac{\partial\bar{w}}{\partial y}\right]+\frac{d^2\bar{\mu}}{d\bar{T}^2}\hat{T}\frac{\partial\bar{T}}{\partial y}\frac{\partial\bar{w}}{\partial y}\right\}=0, \quad \text{(C.1d)}$$

Energy:

$$\frac{\bar{\rho}}{\gamma(\gamma-1)M^2}\left(-i\omega\hat{T}+\bar{u}i\alpha\hat{T}+\bar{w}i\beta\hat{T}+\hat{v}\frac{\partial\bar{T}}{\partial y}\right)+\frac{\bar{\rho}\bar{T}}{\gamma M^2}\left(i\alpha\hat{u}+\frac{\partial\hat{v}}{\partial y}+i\beta\hat{w}\right)$$
$$-\frac{1}{(\gamma-1)RePrM^2}\left[\bar{k}\left(-\alpha^2\hat{T}+\frac{\partial^2\hat{T}}{\partial y^2}-\beta^2\hat{T}\right)\right.$$
$$+\frac{d\bar{k}}{d\bar{T}}\left(2\frac{\partial\bar{T}}{\partial y}\frac{\partial\hat{T}}{\partial y}+\hat{T}\frac{\partial^2\bar{T}}{\partial y^2}\right)+\frac{d^2\bar{k}}{d\bar{T}^2}\hat{T}\left(\frac{\partial\bar{T}}{\partial y}\right)^2\Bigg]$$
$$-\frac{1}{Re}\left\{2\bar{\mu}\left[\frac{\partial\hat{u}}{\partial y}\frac{\partial\bar{u}}{\partial y}+i\alpha\hat{v}\frac{\partial\bar{u}}{\partial y}+\left(i\beta\hat{v}+\frac{\partial\hat{w}}{\partial y}\right)\frac{\partial\bar{w}}{\partial y}\right]\right.$$
$$\left.+\frac{d\bar{\mu}}{d\bar{T}}\hat{T}\left[\left(\frac{\partial\bar{u}}{\partial y}\right)^2+\left(\frac{\partial\bar{w}}{\partial y}\right)^2\right]\right\}=0, \quad \text{(C.1e)}$$

C.2 LST equations in terms of p and T

The LST equations for $\mathbf{q} = [u, v, w, T, p]^{\mathrm{T}}$ can be expressed as follows.
Continuity:

$$-i\omega\left(\hat{p} - \frac{\bar{p}\hat{T}}{\bar{T}}\right) + \bar{p}\left(i\alpha\hat{u} + \frac{\partial\hat{v}}{\partial y} + i\beta\hat{w}\right) + \bar{u}i\alpha\left(\hat{p} - \frac{\bar{p}\hat{T}}{\bar{T}}\right) + \bar{w}\left(i\beta\hat{p} - \frac{\bar{p}}{\bar{T}}i\beta\hat{T}\right) + \hat{v}\left(\frac{\partial\bar{p}}{\partial y} - \frac{\bar{p}}{\bar{T}}\frac{\partial\bar{T}}{\partial y}\right) = 0, \quad \text{(C.2a)}$$

x-Momentum:

$$\frac{\gamma M^2\bar{p}}{\bar{T}}\left(-i\omega\hat{u} + \bar{u}i\alpha\hat{u} + \bar{w}i\beta\hat{u} + \hat{v}\frac{\partial\bar{u}}{\partial y}\right) + i\alpha\hat{p} - \frac{1}{Re}\left\{\bar{\lambda}\left(-\alpha^2\hat{u} + i\alpha\frac{\partial\hat{v}}{\partial y} - \alpha\beta\hat{w}\right) + \bar{\mu}\left(-2\alpha^2\hat{u} + i\alpha\frac{\partial\hat{v}}{\partial y} + \frac{\partial^2\hat{u}}{\partial y^2} - \beta^2\hat{u} - \alpha\beta\hat{w}\right) + \frac{d\bar{\mu}}{d\bar{T}}\left[\hat{T}\frac{\partial^2\bar{u}}{\partial y^2} + \frac{\partial\bar{T}}{\partial y}\left(i\alpha\hat{v} + \frac{\partial\hat{u}}{\partial y}\right) + \frac{\partial\hat{T}}{\partial y}\frac{\partial\bar{u}}{\partial y}\right] + \frac{d^2\bar{\mu}}{d\bar{T}^2}\hat{T}\frac{\partial\bar{T}}{\partial y}\frac{\partial\bar{u}}{\partial y}\right\} = 0, \quad \text{(C.2b)}$$

y-Momentum:

$$\frac{\gamma M^2\bar{p}}{\bar{T}}\left(-i\omega\hat{v} + \bar{u}i\alpha\hat{v} + \bar{w}i\beta\hat{v}\right) + \frac{\partial\hat{p}}{\partial y} - \frac{1}{Re}\left[\bar{\lambda}\left(i\alpha\frac{\partial\hat{u}}{\partial y} + \frac{\partial^2\hat{v}}{\partial y^2} + i\beta\frac{\partial\hat{w}}{\partial y}\right) + \bar{\mu}\left(i\alpha\frac{\partial\hat{u}}{\partial y} - \alpha^2\hat{v} + 2\frac{\partial^2\hat{v}}{\partial y^2} - \beta^2\hat{v} + i\beta\frac{\partial\hat{w}}{\partial y}\right) + \frac{d\bar{\lambda}}{d\bar{T}}\frac{\partial\bar{T}}{\partial y}\left(i\alpha\hat{u} + \frac{\partial\hat{v}}{\partial y} + i\beta\hat{w}\right) + \frac{d\bar{\mu}}{d\bar{T}}\left(2\frac{\partial\bar{T}}{\partial y}\frac{\partial\hat{v}}{\partial y} + i\alpha\hat{T}\frac{\partial\bar{u}}{\partial y} + i\beta\hat{T}\frac{\partial\bar{w}}{\partial y}\right)\right] = 0, \quad \text{(C.2c)}$$

z-Momentum:

$$\frac{\gamma M^2\bar{p}}{\bar{T}}\left(-i\omega\hat{w} + \bar{u}i\alpha\hat{w} + \bar{w}i\beta\hat{w} + \hat{v}\frac{\partial\bar{w}}{\partial y}\right) + i\beta\hat{p} - \frac{1}{Re}\left\{\bar{\lambda}\left(-\alpha\beta\hat{u} + i\beta\frac{\partial\hat{v}}{\partial y} - \beta^2\hat{w}\right) + \bar{\mu}\left(-\alpha\beta\hat{u} + i\beta\frac{\partial\hat{v}}{\partial y} - \alpha^2\hat{w} + \frac{\partial^2\hat{w}}{\partial y^2} - 2\beta^2\hat{w}\right) + \frac{d\bar{\mu}}{d\bar{T}}\left[\hat{T}\frac{\partial^2\bar{w}}{\partial y^2} + \frac{\partial\bar{T}}{\partial y}\left(i\beta\hat{v} + \frac{\partial\hat{w}}{\partial y}\right) + \frac{\partial\hat{T}}{\partial y}\frac{\partial\bar{w}}{\partial y}\right] + \frac{d^2\bar{\mu}}{d\bar{T}^2}\hat{T}\frac{\partial\bar{T}}{\partial y}\frac{\partial\bar{w}}{\partial y}\right\} = 0, \quad \text{(C.2d)}$$

Energy:

$$\begin{aligned}
&\frac{\bar{p}}{(\gamma-1)\bar{T}}\left(-i\omega\hat{T}+\bar{u}i\alpha\hat{T}+\bar{w}i\beta\hat{T}+\hat{v}\frac{\partial\bar{T}}{\partial y}\right)+\bar{p}\left(i\alpha\hat{u}+\frac{\partial\hat{v}}{\partial y}+i\beta\hat{w}\right)\\
&\quad-\frac{1}{(\gamma-1)RePrM^2}\left[\bar{k}\left(-\alpha^2\hat{T}+\frac{\partial^2\hat{T}}{\partial y^2}-\beta^2\hat{T}\right)\right.\\
&\quad\left.+\frac{d\bar{k}}{d\bar{T}}\left(2\frac{\partial\bar{T}}{\partial y}\frac{\partial\hat{T}}{\partial y}+\hat{T}\frac{\partial^2\bar{T}}{\partial y^2}\right)+\frac{d^2\bar{k}}{d\bar{T}^2}\hat{T}\left(\frac{\partial\bar{T}}{\partial y}\right)^2\right]\\
&\quad-\frac{1}{Re}\left\{2\bar{\mu}\left[\frac{\partial\hat{u}}{\partial y}\frac{\partial\bar{u}}{\partial y}+i\alpha\hat{v}\frac{\partial\bar{u}}{\partial y}+\left(i\beta\hat{v}+\frac{\partial\hat{w}}{\partial y}\right)\frac{\partial\bar{w}}{\partial y}\right]\right.\\
&\quad\left.+\frac{d\bar{\mu}}{d\bar{T}}\hat{T}\left[\left(\frac{\partial\bar{u}}{\partial y}\right)^2+\left(\frac{\partial\bar{w}}{\partial y}\right)^2\right]\right\}=0, \quad \text{(C.2e)}
\end{aligned}$$

D

Guidelines for the derivation of the disturbance energy evolution equation for 2D-LST

D.1 Linearized entropy perturbation for a calorically perfect gas

The change in the entropy of a calorically perfect gas with respect to a thermodynamic reference state (subscript 1) can be expressed, in non-dimensional form, as [1]:

$$s - s_1 = \frac{1}{\gamma M^2}\left[\frac{1}{\gamma - 1}\ln\left(\frac{T}{T_1}\right) + \ln\left(\frac{\rho_1}{\rho}\right)\right]. \tag{D.1}$$

Decomposing the instantaneous entropy variable into its steady and perturbation components, that is $s = \bar{s} + \tilde{s}$, leads to

$$\begin{aligned}\bar{s} + \tilde{s} - s_1 &= \frac{1}{\gamma M^2}\left[\frac{1}{\gamma - 1}\ln\left(\frac{\bar{T} + \tilde{T}}{T_1}\right) + \ln\left(\frac{\rho_1}{\bar{\rho} + \tilde{\rho}}\right)\right] = \\ &= \frac{1}{\gamma M^2}\left\{\frac{1}{\gamma - 1}\left[\ln\left(\frac{\bar{T}}{T_1}\right) + \ln\left(1 + \frac{\tilde{T}}{\bar{T}}\right)\right] + \ln\left(\frac{\rho_1}{\bar{\rho}}\right) - \ln\left(1 + \frac{\tilde{\rho}}{\bar{\rho}}\right)\right\}.\end{aligned} \tag{D.2}$$

Equation D.2 can be simplified by considering the Taylor series of $\ln(1+x)$ around 0, also known as the Mercator series:

$$\ln(1+x) = x - \frac{x^2}{2} + \frac{x^3}{3} - \frac{x^4}{4} + ... = \sum_{n=1}^{\infty} \frac{(-1)^{n+1}}{n} x^n, \tag{D.3}$$

which provides a good approximation in the range $-1 < x \leq 1$. Under the assumption of small perturbations ($\tilde{s} \ll 1$), terms of order higher than 1 are neglected, thus allowing the following approximations to be introduced:

$$\ln\left(1 + \frac{\tilde{T}}{\bar{T}}\right) \approx \frac{\tilde{T}}{\bar{T}}, \quad \ln\left(1 + \frac{\tilde{\rho}}{\bar{\rho}}\right) \approx \frac{\tilde{\rho}}{\bar{\rho}}. \tag{D.4}$$

Substituting equation D.4 into equation D.2 and noting that

$$\bar{s} - s_1 = \frac{1}{\gamma M^2}\left[\frac{1}{\gamma - 1}\ln\left(\frac{\bar{T}}{T_1}\right) + \ln\left(\frac{\rho_1}{\bar{\rho}}\right)\right], \tag{D.5}$$

the following expression is found for the linearized entropy perturbation:

$$\tilde{s} = \frac{1}{\gamma M^2}\left[\frac{1}{\gamma - 1}\left(\frac{\tilde{T}}{\bar{T}}\right) - \frac{\tilde{\rho}}{\bar{\rho}}\right]. \tag{D.6}$$

D.2 Derivation of the 2D-LST disturbance energy equation

This section provides a brief description of different steps followed to cast the disturbance energy evolution equation in the form of equation (3.49), starting from the linearized perturbation equations reported in appendix A. Equation (3.49) has been derived trying to follow as much as possible the same form provided by Weder *et al.* [2] for the case of two-dimensional perturbations developing on a one-dimensional base flow.

Multiplying each of the governing equations of the system of linearized perturbation equations given in appendix A by the corresponding factor proposed by Chu [3], see § 3.10.1, adding all of them together and integrating over the domain volume, the following expanded disturbance energy equation is obtained:

$$\int_{\Omega} \left[\underbrace{\frac{\partial \tilde{\rho}}{\partial t}\frac{\tilde{\rho}\bar{T}}{\gamma M^2 \bar{\rho}}}_{C1} + \underbrace{\bar{\rho}\frac{\partial \tilde{u}}{\partial t}\tilde{u}}_{X1} + \underbrace{\bar{\rho}\frac{\partial \tilde{v}}{\partial t}\tilde{v}}_{Y1} + \underbrace{\bar{\rho}\frac{\partial \tilde{w}}{\partial t}\tilde{w}}_{Z1} + \underbrace{\frac{1}{\gamma(\gamma-1)M^2}\bar{\rho}\frac{\partial \tilde{T}}{\partial t}\frac{\tilde{T}}{\bar{T}}}_{E1} \right] d\mathcal{V}$$

$$
\begin{aligned}
= \int_\Omega \Bigg(\Bigg[& -\bar{\rho} \left(\underbrace{\frac{\partial \tilde{u}}{\partial x}}_{C2} + \underbrace{\frac{\partial \tilde{v}}{\partial y}}_{C3} + \underbrace{\frac{\partial \tilde{w}}{\partial z}}_{C4} \right) - \tilde{\rho} \left(\underbrace{\frac{\partial \bar{v}}{\partial y}}_{C5} + \underbrace{\frac{\partial \bar{w}}{\partial z}}_{C6} \right) - \underbrace{\bar{u} \frac{\partial \tilde{\rho}}{\partial x}}_{C7} - \underbrace{\bar{v} \frac{\partial \tilde{\rho}}{\partial y}}_{C8} \\
& - \underbrace{\bar{w} \frac{\partial \tilde{\rho}}{\partial z}}_{C9} - \underbrace{\tilde{v} \frac{\partial \bar{\rho}}{\partial y}}_{C10} - \underbrace{\tilde{w} \frac{\partial \bar{\rho}}{\partial z}}_{C11} \Bigg] \frac{\tilde{\rho} \bar{T}}{\gamma M^2 \bar{\rho}} + \Bigg[-\bar{\rho} \left(\underbrace{\bar{u} \frac{\partial \tilde{u}}{\partial x}}_{X2} + \underbrace{\bar{v} \frac{\partial \tilde{u}}{\partial y}}_{X3} + \underbrace{\bar{w} \frac{\partial \tilde{u}}{\partial z}}_{X4} + \underbrace{\tilde{v} \frac{\partial \bar{u}}{\partial y}}_{X5} \right. \\
& \left. + \underbrace{\tilde{w} \frac{\partial \bar{u}}{\partial z}}_{X6} \right) - \tilde{\rho} \left(\underbrace{\bar{v} \frac{\partial \bar{u}}{\partial y}}_{X7} + \underbrace{\bar{w} \frac{\partial \bar{u}}{\partial z}}_{X8} \right) - \frac{1}{\gamma M^2} \left(\underbrace{\bar{T} \frac{\partial \tilde{\rho}}{\partial x}}_{X9} + \underbrace{\bar{\rho} \frac{\partial \tilde{T}}{\partial x}}_{X10} \right) + \frac{1}{Re} \Bigg\{ \bar{\lambda} \left(\underbrace{\frac{\partial^2 \tilde{u}}{\partial x^2}}_{X11} \right. \\
& \left. + \underbrace{\frac{\partial^2 \tilde{v}}{\partial x \partial y}}_{X12} + \underbrace{\frac{\partial^2 \tilde{w}}{\partial x \partial z}}_{X13} \right) + \bar{\mu} \left(\underbrace{2 \frac{\partial^2 \tilde{u}}{\partial x^2}}_{X14} + \underbrace{\frac{\partial^2 \tilde{v}}{\partial x \partial y}}_{X15} + \underbrace{\frac{\partial^2 \tilde{u}}{\partial y^2}}_{X16} + \underbrace{\frac{\partial^2 \tilde{u}}{\partial z^2}}_{X17} + \underbrace{\frac{\partial^2 \tilde{w}}{\partial x \partial z}}_{X18} \right) \\
& + \frac{d\bar{\lambda}}{d\bar{T}} \frac{\partial \tilde{T}}{\partial x} \left(\underbrace{\frac{\partial \bar{v}}{\partial y}}_{X19} + \underbrace{\frac{\partial \bar{w}}{\partial z}}_{X20} \right) + \frac{d\bar{\mu}}{d\bar{T}} \Bigg[\tilde{T} \left(\underbrace{\frac{\partial^2 \bar{u}}{\partial y^2}}_{X21} + \underbrace{\frac{\partial^2 \bar{u}}{\partial z^2}}_{X22} \right) + \frac{\partial \bar{T}}{\partial y} \left(\underbrace{\frac{\partial \tilde{v}}{\partial x}}_{X23} + \underbrace{\frac{\partial \tilde{u}}{\partial y}}_{X24} \right) \\
& + \underbrace{\frac{\partial \tilde{T}}{\partial y} \frac{\partial \bar{u}}{\partial y}}_{X25} + \frac{\partial \bar{T}}{\partial z} \left(\underbrace{\frac{\partial \tilde{u}}{\partial z}}_{X26} + \underbrace{\frac{\partial \tilde{w}}{\partial x}}_{X27} \right) + \underbrace{\frac{\partial \tilde{T}}{\partial z} \frac{\partial \bar{u}}{\partial z}}_{X28} \Bigg] + \frac{d^2 \bar{\mu}}{d\bar{T}^2} \tilde{T} \left(\underbrace{\frac{\partial \bar{T}}{\partial y} \frac{\partial \bar{u}}{\partial y}}_{X29} + \underbrace{\frac{\partial \bar{T}}{\partial z} \frac{\partial \bar{u}}{\partial z}}_{X30} \right) \Bigg\} \Bigg] \tilde{u} \\
& + \Bigg[-\bar{\rho} \left(\underbrace{\bar{u} \frac{\partial \tilde{v}}{\partial x}}_{Y2} + \underbrace{\bar{v} \frac{\partial \tilde{v}}{\partial y}}_{Y3} + \underbrace{\bar{w} \frac{\partial \tilde{v}}{\partial z}}_{Y4} + \underbrace{\tilde{v} \frac{\partial \bar{v}}{\partial y}}_{Y5} + \underbrace{\tilde{w} \frac{\partial \bar{v}}{\partial z}}_{Y6} \right) - \tilde{\rho} \left(\underbrace{\bar{v} \frac{\partial \bar{v}}{\partial y}}_{Y7} + \underbrace{\bar{w} \frac{\partial \bar{v}}{\partial z}}_{Y8} \right) \\
& - \frac{1}{\gamma M^2} \left(\underbrace{\bar{T} \frac{\partial \tilde{\rho}}{\partial y}}_{Y9} + \underbrace{\tilde{T} \frac{\partial \bar{\rho}}{\partial y}}_{Y10} + \underbrace{\bar{\rho} \frac{\partial \tilde{T}}{\partial y}}_{Y11} + \underbrace{\tilde{\rho} \frac{\partial \bar{T}}{\partial y}}_{Y12} \right) + \frac{1}{Re} \Bigg\{ \bar{\lambda} \left(\underbrace{\frac{\partial^2 \tilde{u}}{\partial x \partial y}}_{Y13} + \underbrace{\frac{\partial^2 \tilde{v}}{\partial y^2}}_{Y14} + \underbrace{\frac{\partial^2 \tilde{w}}{\partial y \partial z}}_{Y15} \right) \\
& + \bar{\mu} \left(\underbrace{\frac{\partial^2 \tilde{u}}{\partial x \partial y}}_{Y16} + \underbrace{\frac{\partial^2 \tilde{v}}{\partial x^2}}_{Y17} + \underbrace{2 \frac{\partial^2 \tilde{v}}{\partial y^2}}_{Y18} + \underbrace{\frac{\partial^2 \tilde{v}}{\partial z^2}}_{Y19} + \underbrace{\frac{\partial^2 \tilde{w}}{\partial y \partial z}}_{Y20} \right) + \frac{d\bar{\lambda}}{d\bar{T}} \Bigg[\frac{\partial \bar{T}}{\partial y} \left(\underbrace{\frac{\partial \tilde{u}}{\partial x}}_{Y21} + \underbrace{\frac{\partial \tilde{v}}{\partial y}}_{Y22} + \underbrace{\frac{\partial \tilde{w}}{\partial z}}_{Y23} \right) \\
& + \frac{\partial \tilde{T}}{\partial y} \left(\underbrace{\frac{\partial \bar{v}}{\partial y}}_{Y24} + \underbrace{\frac{\partial \bar{w}}{\partial z}}_{Y25} \right) + \tilde{T} \left(\underbrace{\frac{\partial^2 \bar{v}}{\partial y^2}}_{Y26} + \underbrace{\frac{\partial^2 \bar{w}}{\partial y \partial z}}_{Y27} \right) \Bigg] + \frac{d\bar{\mu}}{d\bar{T}} \Bigg[\underbrace{2 \frac{\partial \bar{T}}{\partial y} \frac{\partial \tilde{v}}{\partial y}}_{Y28} + \underbrace{2 \frac{\partial \tilde{T}}{\partial y} \frac{\partial \bar{v}}{\partial y}}_{Y29}
\end{aligned}
$$

$$+\tilde{T}\left(\underbrace{2\frac{\partial^2\bar{v}}{\partial y^2}}_{Y30}+\underbrace{\frac{\partial^2\bar{v}}{\partial z^2}}_{Y31}+\underbrace{\frac{\partial^2\bar{w}}{\partial y\partial z}}_{Y32}\right)+\underbrace{\frac{\partial\tilde{T}}{\partial x}\frac{\partial\bar{u}}{\partial y}}_{Y33}+\frac{\partial\bar{T}}{\partial z}\left(\underbrace{\frac{\partial\tilde{v}}{\partial z}}_{Y34}+\underbrace{\frac{\partial\tilde{w}}{\partial y}}_{Y35}\right)$$
$$+\frac{\partial\tilde{T}}{\partial z}\left(\underbrace{\frac{\partial\bar{v}}{\partial z}}_{Y36}+\underbrace{\frac{\partial\bar{w}}{\partial y}}_{Y37}\right)\Bigg]+\frac{d^2\bar{\lambda}}{d\bar{T}^2}\tilde{T}\frac{\partial\bar{T}}{\partial y}\left(\underbrace{\frac{\partial\bar{v}}{\partial y}}_{Y38}+\underbrace{\frac{\partial\bar{w}}{\partial z}}_{Y39}\right)$$
$$+\frac{d^2\bar{\mu}}{d\bar{T}^2}\tilde{T}\left[\underbrace{2\frac{\partial\bar{T}}{\partial y}\frac{\partial\bar{v}}{\partial y}}_{Y40}+\frac{\partial\bar{T}}{\partial z}\left(\underbrace{\frac{\partial\bar{v}}{\partial z}}_{Y41}+\underbrace{\frac{\partial\bar{w}}{\partial y}}_{Y42}\right)\right]\Bigg\}\Bigg]\tilde{v}$$
$$+\Bigg[-\bar{\rho}\left(\underbrace{\bar{u}\frac{\partial\tilde{w}}{\partial x}}_{Z2}+\underbrace{\bar{v}\frac{\partial\tilde{w}}{\partial y}}_{Z3}+\underbrace{\bar{w}\frac{\partial\tilde{w}}{\partial z}}_{Z4}+\underbrace{\tilde{v}\frac{\partial\bar{w}}{\partial y}}_{Z5}+\underbrace{\tilde{w}\frac{\partial\bar{w}}{\partial z}}_{Z6}\right)-\tilde{\rho}\left(\underbrace{\bar{v}\frac{\partial\bar{w}}{\partial y}}_{Z7}+\underbrace{\bar{w}\frac{\partial\bar{w}}{\partial z}}_{Z8}\right)$$
$$-\frac{1}{\gamma M^2}\left(\underbrace{\bar{T}\frac{\partial\tilde{\rho}}{\partial z}}_{Z9}+\underbrace{\tilde{T}\frac{\partial\bar{\rho}}{\partial z}}_{Z10}+\underbrace{\bar{\rho}\frac{\partial\tilde{T}}{\partial z}}_{Z11}+\underbrace{\tilde{\rho}\frac{\partial\bar{T}}{\partial z}}_{Z12}\right)+\frac{1}{Re}\Bigg\{\bar{\lambda}\left(\underbrace{\frac{\partial^2\tilde{u}}{\partial x\partial z}}_{Z13}+\underbrace{\frac{\partial^2\tilde{v}}{\partial y\partial z}}_{Z14}+\underbrace{\frac{\partial^2\tilde{w}}{\partial z^2}}_{Z15}\right)$$
$$+\bar{\mu}\left(\underbrace{\frac{\partial^2\tilde{u}}{\partial x\partial z}}_{Z16}+\underbrace{\frac{\partial^2\tilde{v}}{\partial y\partial z}}_{Z17}+\underbrace{\frac{\partial^2\tilde{w}}{\partial x^2}}_{Z18}+\underbrace{\frac{\partial^2\tilde{w}}{\partial y^2}}_{Z19}+\underbrace{2\frac{\partial^2\tilde{w}}{\partial z^2}}_{Z20}\right)+\frac{d\bar{\lambda}}{d\bar{T}}\Bigg[\frac{\partial\bar{T}}{\partial z}\left(\underbrace{\frac{\partial\tilde{u}}{\partial x}}_{Z21}+\underbrace{\frac{\partial\tilde{v}}{\partial y}}_{Z22}+\underbrace{\frac{\partial\tilde{w}}{\partial z}}_{Z23}\right)$$
$$+\frac{\partial\tilde{T}}{\partial z}\left(\underbrace{\frac{\partial\bar{v}}{\partial y}}_{Z24}+\underbrace{\frac{\partial\bar{w}}{\partial z}}_{Z25}\right)+\tilde{T}\left(\underbrace{\frac{\partial^2\bar{v}}{\partial y\partial z}}_{Z26}+\underbrace{\frac{\partial^2\bar{w}}{\partial z^2}}_{Z27}\right)\Bigg]+\frac{d\bar{\mu}}{d\bar{T}}\Bigg[\underbrace{2\frac{\partial\bar{T}}{\partial z}\frac{\partial\tilde{w}}{\partial z}}_{Z28}+\underbrace{2\frac{\partial\tilde{T}}{\partial z}\frac{\partial\bar{w}}{\partial z}}_{Z29}$$
$$+\tilde{T}\left(\underbrace{\frac{\partial^2\bar{v}}{\partial y\partial z}}_{Z30}+\underbrace{\frac{\partial^2\bar{w}}{\partial y^2}}_{Z31}+\underbrace{2\frac{\partial^2\bar{w}}{\partial z^2}}_{Z32}\right)+\underbrace{\frac{\partial\tilde{T}}{\partial x}\frac{\partial\bar{u}}{\partial z}}_{Z33}+\frac{\partial\bar{T}}{\partial y}\left(\underbrace{\frac{\partial\tilde{v}}{\partial z}}_{Z34}+\underbrace{\frac{\partial\tilde{w}}{\partial y}}_{Z35}\right)$$
$$+\frac{\partial\tilde{T}}{\partial y}\left(\underbrace{\frac{\partial\bar{v}}{\partial z}}_{Z36}+\underbrace{\frac{\partial\bar{w}}{\partial y}}_{Z37}\right)\Bigg]+\frac{d^2\bar{\lambda}}{d\bar{T}^2}\tilde{T}\frac{\partial\bar{T}}{\partial z}\left(\underbrace{\frac{\partial\bar{v}}{\partial y}}_{Z38}+\underbrace{\frac{\partial\bar{w}}{\partial z}}_{Z39}\right)$$
$$+\frac{d^2\bar{\mu}}{d\bar{T}^2}\tilde{T}\left[\underbrace{2\frac{\partial\bar{T}}{\partial z}\frac{\partial\bar{w}}{\partial z}}_{Z40}+\frac{\partial\bar{T}}{\partial y}\left(\underbrace{\frac{\partial\bar{v}}{\partial z}}_{Z41}+\underbrace{\frac{\partial\bar{w}}{\partial y}}_{Z42}\right)\right]\Bigg\}\Bigg]\tilde{w}$$

$$
\begin{aligned}
&+\left[-\frac{1}{\gamma(\gamma-1)M^2}\left[\bar{\rho}\left(\underbrace{\bar{u}\frac{\partial\tilde{T}}{\partial x}}_{E2}+\underbrace{\bar{v}\frac{\partial\tilde{T}}{\partial y}}_{E3}+\underbrace{\bar{w}\frac{\partial\tilde{T}}{\partial z}}_{E4}+\underbrace{\tilde{v}\frac{\partial\bar{T}}{\partial y}}_{E5}+\underbrace{\tilde{w}\frac{\partial\bar{T}}{\partial z}}_{E6}\right)\right.\right.\\
&\left.\left.+\tilde{\rho}\left(\underbrace{\bar{v}\frac{\partial\bar{T}}{\partial y}}_{E7}+\underbrace{\bar{w}\frac{\partial\bar{T}}{\partial z}}_{E8}\right)\right]-\frac{1}{\gamma M^2}\left[\bar{\rho}\bar{T}\left(\underbrace{\frac{\partial\tilde{u}}{\partial x}}_{E9}+\underbrace{\frac{\partial\tilde{v}}{\partial y}}_{E10}+\underbrace{\frac{\partial\tilde{w}}{\partial z}}_{E11}\right)\right.\right.\\
&\left.\left.+\bar{\rho}\tilde{T}\left(\underbrace{\frac{\partial\bar{v}}{\partial y}}_{E12}+\underbrace{\frac{\partial\bar{w}}{\partial z}}_{E13}\right)+\tilde{\rho}\bar{T}\left(\underbrace{\frac{\partial\bar{v}}{\partial y}}_{E14}+\underbrace{\frac{\partial\bar{w}}{\partial z}}_{E15}\right)\right]\right.\\
&+\frac{1}{(\gamma-1)RePrM^2}\left\{\bar{k}\left(\underbrace{\frac{\partial^2\tilde{T}}{\partial x^2}}_{E16}+\underbrace{\frac{\partial^2\tilde{T}}{\partial y^2}}_{E17}+\underbrace{\frac{\partial^2\tilde{T}}{\partial z^2}}_{E18}\right)+\frac{d\bar{k}}{d\bar{T}}\left[\underbrace{2\frac{\partial\bar{T}}{\partial y}\frac{\partial\tilde{T}}{\partial y}}_{E19}\right.\right.\\
&\left.\left.+\underbrace{2\frac{\partial\bar{T}}{\partial z}\frac{\partial\tilde{T}}{\partial z}}_{E20}+\tilde{T}\left(\underbrace{\frac{\partial^2\bar{T}}{\partial y^2}}_{E21}+\underbrace{\frac{\partial^2\bar{T}}{\partial z^2}}_{E22}\right)\right]+\frac{d^2\bar{k}}{d\bar{T}^2}\tilde{T}\left[\underbrace{\left(\frac{\partial\bar{T}}{\partial y}\right)^2}_{E23}+\underbrace{\left(\frac{\partial\bar{T}}{\partial z}\right)^2}_{E24}\right]\right\}\\
&+\frac{1}{Re}\left\{2\bar{\lambda}\left[\left(\underbrace{\frac{\partial\tilde{u}}{\partial x}}_{E25}+\underbrace{\frac{\partial\tilde{v}}{\partial y}}_{E26}+\underbrace{\frac{\partial\tilde{w}}{\partial z}}_{E27}\right)\frac{\partial\bar{v}}{\partial y}+\left(\underbrace{\frac{\partial\tilde{u}}{\partial x}}_{E28}+\underbrace{\frac{\partial\tilde{v}}{\partial y}}_{E29}+\underbrace{\frac{\partial\tilde{w}}{\partial z}}_{E30}\right)\frac{\partial\bar{w}}{\partial z}\right]\right.\\
&\left.+2\bar{\mu}\left[\underbrace{\frac{\partial\tilde{u}}{\partial y}\frac{\partial\bar{u}}{\partial y}}_{E31}+\underbrace{\frac{\partial\tilde{u}}{\partial z}\frac{\partial\bar{u}}{\partial z}}_{E32}+\underbrace{\frac{\partial\tilde{v}}{\partial x}\frac{\partial\bar{u}}{\partial y}}_{E33}+\underbrace{2\frac{\partial\tilde{v}}{\partial y}\frac{\partial\bar{v}}{\partial y}}_{E34}+\underbrace{\frac{\partial\tilde{w}}{\partial x}\frac{\partial\bar{u}}{\partial z}}_{E35}\right.\right.\\
&\left.\left.+\underbrace{2\frac{\partial\tilde{w}}{\partial z}\frac{\partial\bar{w}}{\partial z}}_{E36}+\frac{\partial\tilde{v}}{\partial z}\left(\underbrace{\frac{\partial\bar{v}}{\partial z}}_{E37}+\underbrace{\frac{\partial\bar{w}}{\partial y}}_{E38}\right)+\frac{\partial\tilde{w}}{\partial y}\left(\underbrace{\frac{\partial\bar{v}}{\partial z}}_{E39}+\underbrace{\frac{\partial\bar{w}}{\partial y}}_{E40}\right)\right]\right.\\
&+\frac{d\bar{\lambda}}{d\bar{T}}\tilde{T}\left[\underbrace{2\frac{\partial\bar{v}}{\partial y}\frac{\partial\bar{w}}{\partial z}}_{E41}+\underbrace{\left(\frac{\partial\bar{v}}{\partial y}\right)^2}_{E42}+\underbrace{\left(\frac{\partial\bar{w}}{\partial z}\right)^2}_{E43}\right]+\frac{d\bar{\mu}}{d\bar{T}}\tilde{T}\left[\underbrace{2\frac{\partial\bar{v}}{\partial z}\frac{\partial\bar{w}}{\partial y}}_{E44}+\underbrace{\left(\frac{\partial\bar{u}}{\partial y}\right)^2}_{E45}\right.\\
&\left.\left.\left.\left.+\underbrace{\left(\frac{\partial\bar{u}}{\partial z}\right)^2}_{E46}+\underbrace{2\left(\frac{\partial\bar{v}}{\partial y}\right)^2}_{E47}+\underbrace{\left(\frac{\partial\bar{v}}{\partial z}\right)^2}_{E48}+\underbrace{\left(\frac{\partial\bar{w}}{\partial y}\right)^2}_{E49}+\underbrace{2\left(\frac{\partial\bar{w}}{\partial z}\right)^2}_{E50}\right]\right\}\right]\frac{\tilde{T}}{\bar{T}}\right)d\mathcal{V}. \quad \text{(D.7)}
\end{aligned}
$$

Subterms[1] $C1$, $X1$, $Y1$, $Z1$ and $E1$ combined constitute the time derivative of the total disturbance energy. Thus, the left-hand side of equation (D.7) can simply be written as $d\tilde{E}/dt$. Note the use of a total differential because $\tilde{E}$ is a quantity integrated over the domain volume, hence $\tilde{E} = \tilde{E}(t)$.

Subterms $X5$, $X6$, $Y5$, $Y6$, $Z5$ and $Z6$ directly constitute the Reynolds stress production contributions comprised in the term $\hat{P}_{RS}$ (see equation (3.49a-f) and (3.66a)). Similarly, subterms $X7$, $X8$, $Y7$, $Y8$, $Z7$ and $Z8$ directly yield the six different contributions included in the term $\hat{P}_{mom}$, defined by equation (3.66d). See also equation (3.49g-l).

D.2.1 Disturbance viscous stresses

In order to obtain the dissipation ($\hat{D}_\mu$) and flux ($\hat{F}_\mu$) terms related to the disturbance viscous stresses (see equations (3.49x), (3.49z), (3.66i) and (3.66l)), integration by parts in space is employed.

First, the normal viscous stresses are treated. The subterms that compose the disturbance normal viscous stresses are those featuring a second derivative of the velocity components along the direction aligned with that velocity component, i.e., $\partial^2\tilde{u}/\partial x^2$, $\partial^2\tilde{v}/\partial y^2$ and $\partial^2\tilde{w}/\partial z^2$, and those featuring the bulk viscosity coefficient multiplied by a cross-derivative of the velocity components. For example, subterms $X11$, $X12$, $X13$ and $X14$ are all part of the contributions related to $\tilde{\tau}_{xx}$.

Subterms $X11$ and $X14$ are integrated by parts as follows:

$$\frac{1}{Re}\int_\Omega \left(\bar{\lambda}+2\bar{\mu}\right)\frac{\partial^2\tilde{u}}{\partial x^2}\tilde{u}\,d\mathcal{V} = \frac{1}{Re}\int_\Gamma \left(\bar{\lambda}+2\bar{\mu}\right)\tilde{u}\frac{\partial\tilde{u}}{\partial x}n_x\,dS - \frac{1}{Re}\int_\Omega \left(\bar{\lambda}+2\bar{\mu}\right)\frac{\partial\tilde{u}}{\partial x}\frac{\partial\tilde{u}}{\partial x}\,d\mathcal{V}. \quad \text{(D.8)}$$

This yields two contributions, namely, the first term on the right-hand side of equation (D.8) is part of the group $\tilde{\tau}_{xx}\tilde{u}n_x$, included in (3.49z), whereas the second term on the right-hand side of (D.8) is part of $\tilde{\tau}_{xx}\partial\tilde{u}/\partial x$, included in (3.49x).

For the cross-derivative subterms, a choice has to be made on the direction on which the integration by parts is applied. Here, subterms $X12$ and $X13$ are integrated by parts with respect to x, yielding:

$$\frac{1}{Re}\int_\Omega \bar{\lambda}\tilde{u}\frac{\partial^2\tilde{v}}{\partial x\partial y}\,d\mathcal{V} = \frac{1}{Re}\int_\Gamma \bar{\lambda}\tilde{u}\frac{\partial\tilde{v}}{\partial y}n_x\,dS - \frac{1}{Re}\int_\Omega \bar{\lambda}\frac{\partial\tilde{u}}{\partial x}\frac{\partial\tilde{v}}{\partial y}\,d\mathcal{V}, \quad \text{(D.9a)}$$

$$\frac{1}{Re}\int_\Omega \bar{\lambda}\tilde{u}\frac{\partial^2\tilde{w}}{\partial x\partial z}\,d\mathcal{V} = \frac{1}{Re}\int_\Gamma \bar{\lambda}\tilde{u}\frac{\partial\tilde{w}}{\partial z}n_x\,dS - \frac{1}{Re}\int_\Omega \bar{\lambda}\frac{\partial\tilde{u}}{\partial x}\frac{\partial\tilde{w}}{\partial z}\,d\mathcal{V}. \quad \text{(D.9b)}$$

[1] The word subterm is employed here to denote each of the individual terms that compose equation (D.7). This is done to distinguish them from the terms of the final equation (3.49) after all the manipulations are done.

The first term in the right-hand side of equations (D.9a) and (D.9b) is part of $\tilde{\tau}_{xx}\tilde{u}n_x$, while the second term is part of $\tilde{\tau}_{xx}\partial\tilde{u}/\partial x$. Therefore, the first RHS term of equations (D.8), (D.9a) and (D.9b) combine into the following contribution

$$\frac{1}{Re}\int_\Gamma \left(\bar{\lambda}+2\bar{\mu}\right)\tilde{u}\frac{\partial\tilde{u}}{\partial x}n_x\,dS+\frac{1}{Re}\int_\Gamma \bar{\lambda}\tilde{u}\frac{\partial\tilde{v}}{\partial y}n_x\,dS + \frac{1}{Re}\int_\Gamma \bar{\lambda}\tilde{u}\frac{\partial\tilde{w}}{\partial z}n_x\,dS=\int_\Gamma \tilde{\tau}_{xx}\tilde{u}n_x\,dS, \quad \text{(D.10)}$$

which is part of (3.49z), and the second RHS terms combine into

$$-\frac{1}{Re}\int_\Omega \left(\bar{\lambda}+2\bar{\mu}\right)\frac{\partial\tilde{u}}{\partial x}\frac{\partial\tilde{u}}{\partial x}\,d\mathcal{V}-\frac{1}{Re}\int_\Omega \bar{\lambda}\frac{\partial\tilde{u}}{\partial x}\frac{\partial\tilde{v}}{\partial y}\,d\mathcal{V} - \frac{1}{Re}\int_\Omega \bar{\lambda}\frac{\partial\tilde{u}}{\partial x}\frac{\partial\tilde{w}}{\partial z}\,d\mathcal{V}=-\int_\Omega \tilde{\tau}_{xx}\frac{\partial\tilde{u}}{\partial x}\,d\mathcal{V}, \quad \text{(D.11)}$$

which is part of (3.49x).

The same approach is then applied for the normal viscous stresses along y and z, respectively involving subterms $Y13$, $Y14$, $Y15$ and $Y18$, and $Z13$, $Z14$, $Z15$ and $Z20$. When performing integration by parts on these terms, however, additional terms appear due to the dependence of base-flow viscosity on temperature. These additional terms always cancel out with subterms found in (D.7). For example, for subterms $Y14$ and $Y18$:

$$\frac{1}{Re}\int_\Omega \left(\bar{\lambda}+2\bar{\mu}\right)\frac{\partial^2\tilde{v}}{\partial y^2}\tilde{v}\,d\mathcal{V}=\frac{1}{Re}\int_\Gamma \left(\bar{\lambda}+2\bar{\mu}\right)\tilde{v}\frac{\partial\tilde{v}}{\partial y}n_y\,dS - \frac{1}{Re}\int_\Omega \frac{d\bar{\lambda}}{d\bar{T}}\frac{d\bar{T}}{dy}\tilde{v}\frac{\partial\tilde{v}}{\partial y}\,d\mathcal{V}-\frac{1}{Re}\int_\Omega 2\frac{d\bar{\mu}}{d\bar{T}}\frac{d\bar{T}}{dy}\tilde{v}\frac{\partial\tilde{v}}{\partial y}\,d\mathcal{V} - \frac{1}{Re}\int_\Omega \left(\bar{\lambda}+2\bar{\mu}\right)\frac{\partial\tilde{u}}{\partial x}\frac{\partial\tilde{u}}{\partial x}\,d\mathcal{V}. \quad \text{(D.12)}$$

The second and third RHS terms of equation (D.12) cancel out with terms $Y22$ and $Y28$, respectively. The same is encountered for all the remaining contributions to the viscous stresses.

Next, the treatment for the shear viscous stresses is described. The subterms that form the shear viscous stresses are those featuring a second derivative of the velocity components along a direction other than the one aligned with that velocity component, such as for example $\partial^2\tilde{u}/\partial y^2$, and those featuring the dynamic viscosity multiplied by a cross-derivative of the velocity components. For instance, the

integration by parts of subterms $X15$, $X16$, $Y16$ and $Y17$ yields the contributions related to $\tilde{\tau}_{xy}$, namely

$$\begin{aligned}\frac{1}{Re}\int_{\Omega}\bar{\mu}\tilde{u}\frac{\partial^2\tilde{u}}{\partial y^2}\,d\mathcal{V} &= \frac{1}{Re}\int_{\Gamma}\bar{\mu}\tilde{u}\frac{\partial\tilde{u}}{\partial y}n_y\,dS \\ &\quad - \frac{1}{Re}\int_{\Omega}\frac{d\bar{\mu}}{d\bar{T}}\frac{d\bar{T}}{dy}\tilde{u}\frac{\partial\tilde{u}}{\partial y}\,d\mathcal{V} - \frac{1}{Re}\int_{\Omega}\bar{\mu}\frac{\partial\tilde{u}}{\partial y}\frac{\partial\tilde{u}}{\partial y}\,d\mathcal{V},\end{aligned} \tag{D.13a}$$

$$\frac{1}{Re}\int_{\Omega}\bar{\mu}\tilde{v}\frac{\partial^2\tilde{v}}{\partial x^2}\,d\mathcal{V} = \frac{1}{Re}\int_{\Gamma}\bar{\mu}\tilde{v}\frac{\partial\tilde{v}}{\partial x}n_x\,dS - \frac{1}{Re}\int_{\Omega}\bar{\mu}\frac{\partial\tilde{v}}{\partial x}\frac{\partial\tilde{v}}{\partial x}\,d\mathcal{V}, \tag{D.13b}$$

$$\begin{aligned}\frac{1}{Re}\int_{\Omega}\bar{\mu}\tilde{u}\frac{\partial^2\tilde{v}}{\partial x\partial y}\,d\mathcal{V} &= \frac{1}{Re}\int_{\Gamma}\bar{\mu}\tilde{u}\frac{\partial\tilde{v}}{\partial x}n_y\,dS \\ &\quad - \frac{1}{Re}\int_{\Omega}\frac{d\bar{\mu}}{d\bar{T}}\frac{d\bar{T}}{dy}\tilde{u}\frac{\partial\tilde{v}}{\partial x}\,d\mathcal{V} - \frac{1}{Re}\int_{\Omega}\bar{\mu}\frac{\partial\tilde{u}}{\partial y}\frac{\partial\tilde{v}}{\partial x}\,d\mathcal{V},\end{aligned} \tag{D.13c}$$

$$\frac{1}{Re}\int_{\Omega}\bar{\mu}\tilde{v}\frac{\partial^2\tilde{u}}{\partial x\partial y}\,d\mathcal{V} = \frac{1}{Re}\int_{\Gamma}\bar{\mu}\tilde{v}\frac{\partial\tilde{u}}{\partial y}n_x\,dS - \frac{1}{Re}\int_{\Omega}\bar{\mu}\frac{\partial\tilde{v}}{\partial x}\frac{\partial\tilde{u}}{\partial y}\,d\mathcal{V}. \tag{D.13d}$$

Note that subterms $X15$ and $Y16$ are integrated by parts in the opposite direction as it is done for the normal viscous stresses. Collecting the first RHS term of equations (D.13), the contribution of $\tilde{\tau}_{xy}$ to term (3.49z) is obtained, that is

$$\begin{aligned}&\frac{1}{Re}\int_{\Gamma}\bar{\mu}\tilde{u}\frac{\partial\tilde{u}}{\partial y}n_y\,dS + \frac{1}{Re}\int_{\Gamma}\bar{\mu}\tilde{u}\frac{\partial\tilde{v}}{\partial x}n_y\,dS \\ &\quad + \frac{1}{Re}\int_{\Gamma}\bar{\mu}\tilde{v}\frac{\partial\tilde{u}}{\partial y}n_x\,dS + \frac{1}{Re}\int_{\Gamma}\bar{\mu}\tilde{v}\frac{\partial\tilde{v}}{\partial x}n_x\,dS = \int_{\Gamma}\tilde{\tau}_{xy}\left(\tilde{u}n_y + \tilde{v}n_x\right)dS.\end{aligned} \tag{D.14}$$

Similarly, combining the last RHS term of equations (D.13), the contribution to term (3.49x) is retrieved, which reads

$$\begin{aligned}&-\frac{1}{Re}\int_{\Omega}\bar{\mu}\frac{\partial\tilde{u}}{\partial y}\frac{\partial\tilde{u}}{\partial y}\,d\mathcal{V} - \frac{1}{Re}\int_{\Omega}\bar{\mu}\frac{\partial\tilde{v}}{\partial x}\frac{\partial\tilde{v}}{\partial x}\,d\mathcal{V} \\ &\quad - \frac{1}{Re}\int_{\Omega}\bar{\mu}\frac{\partial\tilde{u}}{\partial y}\frac{\partial\tilde{v}}{\partial x}\,d\mathcal{V} - \frac{1}{Re}\int_{\Omega}\bar{\mu}\frac{\partial\tilde{v}}{\partial x}\frac{\partial\tilde{u}}{\partial y}\,d\mathcal{V} = -\int_{\Omega}\tilde{\tau}_{xy}\left(\frac{\partial\tilde{u}}{\partial y} + \frac{\partial\tilde{v}}{\partial x}\right)d\mathcal{V}.\end{aligned} \tag{D.15}$$

Finally, note that the second RHS term of equations (D.13a) and (D.13c) cancels out with subterms $X24$ and $X23$, respectively.

An analogous procedure applies for the contributions related to $\tilde{\tau}_{xz}$ and $\tilde{\tau}_{yz}$. This completes the derivation of all the disturbance energy contributions related to the viscous stresses.

D.2.2 Disturbance thermal conduction

The dissipation ($\hat{D}_k$) and flux ($\hat{F}_k$) terms associated with thermal conduction result from the integration by parts of subterms $E16$, $E17$ and $E18$, that is

$$\begin{aligned}
&\frac{1}{(\gamma-1)\,RePrM^2}\int_\Omega \bar{k}\left(\frac{\partial^2\tilde{T}}{\partial x^2}+\frac{\partial^2\tilde{T}}{\partial y^2}+\frac{\partial^2\tilde{T}}{\partial z^2}\right)\frac{\tilde{T}}{\bar{T}}\,d\mathcal{V} = \\
&\qquad\frac{1}{(\gamma-1)\,RePrM^2}\left\{\int_\Gamma\left(\bar{k}\frac{\partial\tilde{T}}{\partial x}n_x+\bar{k}\frac{\partial\tilde{T}}{\partial y}n_y+\bar{k}\frac{\partial\tilde{T}}{\partial z}n_z\right)\frac{\tilde{T}}{\bar{T}}\,dS\right. \\
&-\left.\int_\Omega\left[\frac{\partial}{\partial x}\left(\bar{k}\frac{\tilde{T}}{\bar{T}}\right)\frac{\partial\tilde{T}}{\partial x}+\frac{\partial}{\partial y}\left(\bar{k}\frac{\tilde{T}}{\bar{T}}\right)\frac{\partial\tilde{T}}{\partial y}+\frac{\partial}{\partial z}\left(\bar{k}\frac{\tilde{T}}{\bar{T}}\right)\frac{\partial\tilde{T}}{\partial z}\right]d\mathcal{V}\right\}. \qquad \text{(D.16)}
\end{aligned}$$

The first RHS term in equation (D.16) directly constitutes the flux term (3.49aa), see also (3.66m). The constituents of the second RHS term are further expanded as:

$$\begin{aligned}
&-\frac{1}{(\gamma-1)\,RePrM^2}\int_\Omega\frac{\partial}{\partial x}\left(\bar{k}\frac{\tilde{T}}{\bar{T}}\right)\frac{\partial\tilde{T}}{\partial x}\,d\mathcal{V} = \\
&\qquad-\frac{1}{(\gamma-1)\,RePrM^2}\int_\Omega\frac{\bar{k}}{\bar{T}}\frac{\partial\tilde{T}}{\partial x}\frac{\partial\tilde{T}}{\partial x}\,d\mathcal{V}, \qquad \text{(D.17a)}
\end{aligned}$$

$$\begin{aligned}
&-\frac{1}{(\gamma-1)\,RePrM^2}\int_\Omega\frac{\partial}{\partial y}\left(\bar{k}\frac{\tilde{T}}{\bar{T}}\right)\frac{\partial\tilde{T}}{\partial y}\,d\mathcal{V} = \\
&\qquad-\frac{1}{(\gamma-1)\,RePrM^2}\int_\Omega\left(\frac{d\bar{k}}{d\bar{T}}\frac{\partial\bar{T}}{\partial y}\frac{\partial\tilde{T}}{\partial y}\frac{\tilde{T}}{\bar{T}}+\frac{\bar{k}}{\bar{T}}\frac{\partial\tilde{T}}{\partial y}\frac{\partial\tilde{T}}{\partial y}-\frac{\bar{k}}{\bar{T}}\frac{\partial\bar{T}}{\partial y}\frac{\partial\tilde{T}}{\partial y}\frac{\tilde{T}}{\bar{T}}\right)d\mathcal{V}, \qquad \text{(D.17b)}
\end{aligned}$$

$$\begin{aligned}
&-\frac{1}{(\gamma-1)\,RePrM^2}\int_\Omega\frac{\partial}{\partial z}\left(\bar{k}\frac{\tilde{T}}{\bar{T}}\right)\frac{\partial\tilde{T}}{\partial z}\,d\mathcal{V} = \\
&\qquad-\frac{1}{(\gamma-1)\,RePrM^2}\int_\Omega\left(\frac{d\bar{k}}{d\bar{T}}\frac{\partial\bar{T}}{\partial z}\frac{\partial\tilde{T}}{\partial z}\frac{\tilde{T}}{\bar{T}}+\frac{\bar{k}}{\bar{T}}\frac{\partial\tilde{T}}{\partial z}\frac{\partial\tilde{T}}{\partial z}-\frac{\bar{k}}{\bar{T}}\frac{\partial\bar{T}}{\partial z}\frac{\partial\tilde{T}}{\partial z}\frac{\tilde{T}}{\bar{T}}\right)d\mathcal{V}. \qquad \text{(D.17c)}
\end{aligned}$$

The RHS of equation (D.17a) together with the second RHS term of equations (D.17b) and (D.17c) constitute the dissipation term (3.49y), see also (3.66j). The third RHS term of (D.17b) and (D.17c) are contributions that become part of the disturbance heat source $\tilde{Q}$ (see equation (3.55)), and therefore belong to term (3.49o) (term (3.66c) in the decomposition). Finally, the first RHS term of equation (D.17b) combines with subterms $E19$, $E21$ and $E23$ to yield the following additional contribution to the disturbance heat source production term:

$$\frac{1}{(\gamma-1)\,RePrM^2}\int_\Omega\left[2\frac{d\bar{k}}{d\bar{T}}\frac{\partial\bar{T}}{\partial y}\frac{\partial\tilde{T}}{\partial y}-\frac{d\bar{k}}{d\bar{T}}\frac{\partial\bar{T}}{\partial y}\frac{\partial\tilde{T}}{\partial y}+\frac{d\bar{k}}{d\bar{T}}\tilde{T}\frac{\partial^2\bar{T}}{\partial y^2}\right.$$
$$\left.+\frac{d^2\bar{k}}{d\bar{T}^2}\tilde{T}\left(\frac{\partial\bar{T}}{\partial y}\right)^2\right]\frac{\tilde{T}}{\bar{T}}\,d\mathcal{V}=\frac{1}{(\gamma-1)\,RePrM^2}\int_\Omega\frac{\partial}{\partial y}\left(\tilde{T}\frac{d\bar{k}}{d\bar{T}}\frac{\partial\bar{T}}{\partial y}\right)\frac{\tilde{T}}{\bar{T}}\,d\mathcal{V}. \tag{D.18}$$

An analogous expression is found in the z direction combining the first RHS term of equation (D.17c) with subterms $E20$, $E22$ and $E24$. This completes the derivation of the disturbance energy contributions related to thermal conduction.

D.2.3 Flux terms due to the variation of viscosity with temperature

The flux term $\hat{F}_{d\mu/dT}$ (3.66n) (see also the corresponding terms in the disturbance energy equation: (3.49cc) to (3.49rr)) is obtained by combining the subterms that involve the derivative of viscosity with temperature. For example, the term (3.49cc) results from the subterms $X21$, $X29$ and $X25$ as follows:

$$\frac{1}{Re}\int_\Omega\left(\frac{d\bar{\mu}}{d\bar{T}}\frac{\partial^2\bar{u}}{\partial y^2}\tilde{T}\tilde{u}+\frac{d^2\bar{\mu}}{d\bar{T}^2}\frac{\partial\bar{T}}{\partial y}\frac{\partial\bar{u}}{\partial y}\tilde{T}\tilde{u}+\frac{d\bar{\mu}}{d\bar{T}}\frac{\partial\bar{u}}{\partial y}\frac{\partial\tilde{T}}{\partial y}\tilde{u}\right)d\mathcal{V}=$$
$$\frac{1}{Re}\int_\Omega\left[\frac{\partial}{\partial y}\left(\tilde{u}\tilde{T}\frac{d\bar{\mu}}{d\bar{T}}\frac{\partial\bar{u}}{\partial y}\right)-\frac{\partial\tilde{u}}{\partial y}\tilde{T}\frac{d\bar{\mu}}{d\bar{T}}\frac{\partial\bar{u}}{\partial y}\right]d\mathcal{V}. \tag{D.19}$$

The first RHS term in equation (D.19) is directly the contribution in (3.49cc), while the second RHS term is an additional contribution to the disturbance heat source production term (see equation (3.55)).

The same approach is followed for the terms (3.49dd) to (3.49rr).

D.2.4 Disturbance heat source

In the previous two sections, some of the terms composing the disturbance heat source contribution (3.49o) have been derived. However, additional subterms still remain which also belong to $\tilde{Q}$ (see equation (3.55)). These are directly subterms $E25$ to $E50$, without any further modification.

D.2.5 Convective derivative of the total disturbance energy

Next, the subterms yielding the production term related to the convective derivative of the total disturbance energy ($\hat{P}_{con}$) are summarized (see (3.49ss), (3.49tt),

(3.49uu) and (3.66h)). Subterms $C7$, $C8$ and $C9$, rewritten in terms of the base-flow pressure, respectively give the first contribution in each of the terms (3.49ss), (3.49tt) and (3.49uu). Similarly, subterms $E2$, $E3$ and $E4$ respectively provide the second contribution to (3.49ss), (3.49tt) and (3.49uu) when expressed in terms of the base-flow pressure. Subterms $X2$, $Y2$ and $Z2$ compose the third contribution to (3.49ss), subterms $X3$, $Y3$ and $Z3$ constitute the third contribution to (3.49tt) and subterms $X4$, $Y4$ and $Z4$ form the third contribution to (3.49uu).

Note that the independence of the base-flow quantities on x allows the x derivative on the term (3.49ss) to enclose all the constituents. This enables to set the complete term (3.49ss) to zero once the assumption of integration along a single streamwise period is introduced (see § 3.10.2).

D.2.6 Base-flow pressure work

Subterms $C10$ and $Y12$ combine to yield the base-flow pressure work production term (3.49p) as:

$$-\int_\Omega \frac{\partial\bar{\rho}}{\partial y}\tilde{v}\frac{\tilde{\rho}\bar{T}}{\gamma M^2\bar{\rho}}\,d\mathcal{V} - \int_\Omega \frac{\tilde{\rho}}{\gamma M^2}\frac{\partial\bar{T}}{\partial y}\tilde{v}\,d\mathcal{V} = \\ -\int_\Omega \frac{\tilde{\rho}\tilde{v}}{\gamma M^2\bar{\rho}}\left(\bar{T}\frac{\partial\bar{\rho}}{\partial y}+\bar{\rho}\frac{\partial\bar{T}}{\partial y}\right)d\mathcal{V} = -\int_\Omega \frac{\tilde{\rho}\tilde{v}}{\bar{\rho}}\frac{\partial\bar{p}}{\partial y}\,d\mathcal{V}. \quad \text{(D.20)}$$

Similarly, subterms $C11$ and $Z12$ produce the analogous contribution along the z direction (3.49q). See (3.66e) for the corresponding production term belonging to the decomposition of the temporal growth rate.

D.2.7 Disturbance entropy

The production term related to the transport of disturbance entropy ($\hat{P}_s$), (see (3.49m,n) and (3.66b)) is built from two different contributions along each spatial direction. The first one comes directly from subterm $E5$ along the y direction and from subterm $E6$ along the z direction. The second contribution requires further elaboration, as described next.

Using equation (A.2), it can be directly seen that the sum of subterms $C2$, $C3$, $C4$, $E9$, $E10$ and $E11$ equals the product of the pressure disturbance times the divergence of the disturbance velocity field, i.e., $-\tilde{p}\nabla\cdot\tilde{\mathbf{V}}$. The integration by parts of this product yields the following:

$$-\int_\Omega \tilde{p}\nabla\cdot\tilde{\mathbf{V}}\,d\mathcal{V} = -\int_\Gamma \tilde{p}\,(\tilde{u}n_x+\tilde{v}n_y+\tilde{w}n_z)\,dS + \int_\Omega \nabla\tilde{p}\cdot\tilde{\mathbf{V}}\,d\mathcal{V}. \quad \text{(D.21)}$$

The first RHS term in equation (D.21) is the surface term (3.49bb), which translates into the disturbance pressure flux term (3.66k). The second RHS term is expanded as:

$$\int_\Omega \nabla\tilde{p}\cdot\tilde{\mathbf{V}}\,d\mathcal{V} = \frac{1}{\gamma M^2}\left[\int_\Omega\left(\bar{\rho}\frac{\partial\tilde{T}}{\partial x}\tilde{u}+\bar{T}\frac{\partial\tilde{\rho}}{\partial x}\tilde{u}+\frac{\partial\bar{\rho}}{\partial y}\tilde{T}\tilde{v}+\bar{\rho}\frac{\partial\tilde{T}}{\partial y}\tilde{v}\right.\right.$$
$$\left.\left.+\bar{T}\frac{\partial\tilde{\rho}}{\partial y}\tilde{v}+\tilde{\rho}\frac{\partial\bar{T}}{\partial y}\tilde{v}+\frac{\partial\bar{\rho}}{\partial z}\tilde{T}\tilde{w}+\bar{\rho}\frac{\partial\tilde{T}}{\partial z}\tilde{w}+\bar{T}\frac{\partial\tilde{\rho}}{\partial z}\tilde{w}+\tilde{\rho}\frac{\partial\bar{T}}{\partial z}\tilde{w}\right)d\mathcal{V}\right]. \quad \text{(D.22)}$$

All the RHS terms in equation (D.22) cancel with subterms from equation (D.7) except for the groups $\tilde{\rho}\left(\partial\bar{T}/\partial y\right)\tilde{v}$ and $\tilde{\rho}\left(\partial\bar{T}/\partial z\right)\tilde{w}$. These two remaining terms are the second contributions that complete the disturbance entropy production constituents along the y and z directions. Hence, the disturbance entropy terms (3.49m) and (3.49n) can be obtained as:

$$\int_\Omega \frac{1}{\gamma M^2}\tilde{\rho}\frac{\partial\bar{T}}{\partial y}\tilde{v}\,d\mathcal{V}-\int_\Omega\frac{\bar{\rho}}{\gamma\left(\gamma-1\right)M^2}\frac{\partial\bar{T}}{\partial y}\tilde{v}\frac{\tilde{T}}{\bar{T}}\,d\mathcal{V}=$$
$$-\int_\Omega\bar{\rho}\tilde{v}\frac{\partial\bar{T}}{\partial y}\frac{1}{\gamma M^2}\left[\frac{1}{\gamma-1}\left(\frac{\tilde{T}}{\bar{T}}\right)-\frac{\tilde{\rho}}{\bar{\rho}}\right]d\mathcal{V}=-\int_\Omega\bar{\rho}\tilde{v}\tilde{s}\frac{\partial\bar{T}}{\partial y}\,d\mathcal{V}, \quad \text{(D.23a)}$$

$$\int_\Omega \frac{1}{\gamma M^2}\tilde{\rho}\frac{\partial\bar{T}}{\partial z}\tilde{w}\,d\mathcal{V}-\int_\Omega\frac{\bar{\rho}}{\gamma\left(\gamma-1\right)M^2}\frac{\partial\bar{T}}{\partial z}\tilde{w}\frac{\tilde{T}}{\bar{T}}\,d\mathcal{V}=$$
$$-\int_\Omega\bar{\rho}\tilde{w}\frac{\partial\bar{T}}{\partial z}\frac{1}{\gamma M^2}\left[\frac{1}{\gamma-1}\left(\frac{\tilde{T}}{\bar{T}}\right)-\frac{\tilde{\rho}}{\bar{\rho}}\right]d\mathcal{V}=-\int_\Omega\bar{\rho}\tilde{w}\tilde{s}\frac{\partial\bar{T}}{\partial z}\,d\mathcal{V}, \quad \text{(D.23b)}$$

where use of equation (3.51) has been made.

Note that the derivation of terms (3.49m,n) involves subterms from the continuity and the energy equations, which reflects the fact that the disturbance entropy plays a role in the generalized potential energy of the disturbance rather than in the disturbance internal energy alone (see § 3.10.1.2).

D.2.8 Remaining terms

The remaining subterms in equation (D.7) yield the pressure dilatation terms (3.49r-u), enclosed in the production contribution $\hat{P}_{dil}$ (3.66f), and the terms (3.49v,w) which are result from the material derivative of the internal energy perturbation (see $\hat{P}_{s,T}$ (3.66g)).

The terms (3.49v,w) come directly from subterms $E7$ and $E8$, respectively. The terms (3.49t,u) are respectively obtained from subterms $C5$ and $C6$ rewritten as a function of the base-flow pressure and density. Finally, terms (3.49r,s) arise

from a combination of subterms $E12$ and $E14$, and $E13$ and $E15$, respectively, i.e.,

$$-\frac{1}{\gamma M^2}\left[\int_\Omega \left(\bar{\rho}\tilde{T}\frac{\partial \bar{v}}{\partial y}+\tilde{\rho}\bar{T}\frac{\partial \bar{v}}{\partial y}\right)\frac{\tilde{T}}{\bar{T}}\,d\mathcal{V}\right]=-\int_\Omega \tilde{p}\frac{\partial \bar{v}}{\partial y}\frac{\tilde{T}}{\bar{T}}\,d\mathcal{V} \tag{D.24a}$$

$$-\frac{1}{\gamma M^2}\left[\int_\Omega \left(\bar{\rho}\tilde{T}\frac{\partial \bar{w}}{\partial z}+\tilde{\rho}\bar{T}\frac{\partial \bar{w}}{\partial z}\right)\frac{\tilde{T}}{\bar{T}}\,d\mathcal{V}\right]=-\int_\Omega \tilde{p}\frac{\partial \bar{w}}{\partial z}\frac{\tilde{T}}{\bar{T}}\,d\mathcal{V} \tag{D.24b}$$

This completes the derivation of the different contributions appearing in the 2D-LST disturbance energy evolution equation.

References

[1] John D. Anderson Jr. *Hypersonic and High Temperature Gas Dynamics*. American Institute of Aeronautics and Astronautics, Reston VA, second edition, 2006.

[2] Mario Weder, Michael Gloor, and Leonhard Kleiser. *Decomposition of the temporal growth rate in linear instability of compressible gas flows*. Journal of Fluid Mechanics, 778:120–132, jul 2015.

[3] Boa Teh Chu. *On the energy transfer to small disturbances in fluid flow (Part I)*. Acta Mechanica, 1(3):215–234, sep 1965.

E

Disturbance energy evolution equation for LST

The disturbance energy evolution equation associated to Chu's disturbance energy definition (see § 3.10.1) for $\bar{\mathbf{q}} = \bar{\mathbf{q}}(y)$, $\tilde{\mathbf{q}} = \tilde{\mathbf{q}}(x, y, z, t)$ and $\bar{v} = 0$, corresponding to one-dimensional linear stability theory (LST), can be expressed as follows:

$$
\begin{aligned}
\frac{d\tilde{E}}{dt} = &- \int_\Omega \bar{\rho}\tilde{u}\tilde{v}\frac{d\bar{u}}{dy}\,d\mathcal{V} - \int_\Omega \bar{\rho}\tilde{v}\tilde{w}\frac{d\bar{w}}{dy}\,d\mathcal{V} - \int_\Omega \bar{\rho}\tilde{v}\tilde{s}\frac{d\bar{T}}{dy}\,d\mathcal{V} \\
&+ \int_\Omega \tilde{Q}\frac{\tilde{T}}{\bar{T}}\,d\mathcal{V} - \int_\Omega \frac{\tilde{\rho}\tilde{v}}{\bar{\rho}}\frac{d\bar{p}}{dy}\,d\mathcal{V} - \int_\Omega \left[\tilde{\tau}_{xx}\frac{\partial\tilde{u}}{\partial x} + \tilde{\tau}_{yy}\frac{\partial\tilde{v}}{\partial y} + \tilde{\tau}_{zz}\frac{\partial\tilde{w}}{\partial z}\right. \\
&\left. + \tilde{\tau}_{xy}\left(\frac{\partial\tilde{u}}{\partial y} + \frac{\partial\tilde{v}}{\partial x}\right) + \tilde{\tau}_{xz}\left(\frac{\partial\tilde{u}}{\partial z} + \frac{\partial\tilde{w}}{\partial x}\right) + \tilde{\tau}_{yz}\left(\frac{\partial\tilde{v}}{\partial z} + \frac{\partial\tilde{w}}{\partial y}\right)\right] d\mathcal{V} \\
&+ \int_\Omega \frac{1}{\bar{T}}\left(\tilde{q}_x\frac{\partial}{\partial x} + \tilde{q}_y\frac{\partial}{\partial y} + \tilde{q}_z\frac{\partial}{\partial z}\right)\tilde{T}\,d\mathcal{V} - \int_\Gamma \tilde{p}\,(\tilde{u}n_x + \tilde{v}n_y + \tilde{w}n_z)\,dS \\
&+ \int_\Gamma [\tilde{\tau}_{xx}\tilde{u}n_x + \tilde{\tau}_{yy}\tilde{v}n_y + \tilde{\tau}_{zz}\tilde{w}n_z + \tilde{\tau}_{xy}\,(\tilde{u}n_y + \tilde{v}n_x) + \tilde{\tau}_{xz}\,(\tilde{u}n_z + \tilde{w}n_x) \\
&+ \tilde{\tau}_{yz}\,(\tilde{v}n_z + \tilde{w}n_y)]\,dS - \int_\Gamma (\tilde{q}_x n_x + \tilde{q}_y n_y + \tilde{q}_z n_z)\,\frac{\tilde{T}}{\bar{T}}\,dS \\
&+ \frac{1}{Re}\int_\Omega \frac{\partial}{\partial y}\left(\tilde{u}\tilde{T}\frac{d\bar{\mu}}{d\bar{T}}\frac{d\bar{u}}{dy}\right)d\mathcal{V} + \frac{1}{Re}\int_\Omega \frac{\partial}{\partial x}\left(\tilde{v}\tilde{T}\frac{d\bar{\mu}}{d\bar{T}}\frac{d\bar{u}}{dy}\right)d\mathcal{V}
\end{aligned}
$$

$$+\frac{1}{Re}\int_{\Omega}\frac{\partial}{\partial z}\left(\tilde{v}\tilde{T}\frac{d\bar{\mu}}{d\bar{T}}\frac{d\bar{w}}{dy}\right)d\mathcal{V}+\frac{1}{Re}\int_{\Omega}\frac{\partial}{\partial y}\left(\tilde{w}\tilde{T}\frac{d\bar{\mu}}{d\bar{T}}\frac{d\bar{w}}{dy}\right)d\mathcal{V}$$
$$-\int_{\Omega}\frac{\partial}{\partial x}\left[\frac{1}{2}\bar{u}\bar{p}\frac{\tilde{\rho}^2}{\bar{\rho}^2}+\frac{1}{2}\frac{\bar{u}\bar{p}}{\gamma-1}\frac{\tilde{T}^2}{\bar{T}^2}+\frac{1}{2}\bar{u}\bar{\rho}\left(\tilde{u}^2+\tilde{v}^2+\tilde{w}^2\right)\right]d\mathcal{V}$$
$$-\int_{\Omega}\frac{\partial}{\partial z}\left[\frac{1}{2}\bar{w}\bar{p}\frac{\tilde{\rho}^2}{\bar{\rho}^2}+\frac{1}{2}\frac{\bar{w}\bar{p}}{\gamma-1}\frac{\tilde{T}^2}{\bar{T}^2}+\frac{1}{2}\bar{w}\bar{\rho}\left(\tilde{u}^2+\tilde{v}^2+\tilde{w}^2\right)\right]d\mathcal{V}, \quad \text{(E.1)}$$

where $\tilde{\tau}_{xx}$, $\tilde{\tau}_{yy}$, $\tilde{\tau}_{zz}$, $\tilde{\tau}_{xy}$, $\tilde{\tau}_{xz}$ and $\tilde{\tau}_{yz}$ are defined as in equation (3.53), $\tilde{q}_x$, $\tilde{q}_y$ and $\tilde{q}_z$ are defined as in equation (3.54), and the LST disturbance heat source takes the form:

$$\tilde{Q}=\frac{1}{Re}\left(2\bar{\mu}-\frac{d\bar{\mu}}{d\bar{T}}\bar{T}\right)\left[\frac{d\bar{u}}{dy}\left(\frac{\partial\tilde{u}}{\partial y}+\frac{\partial\tilde{v}}{\partial x}\right)+\frac{d\bar{w}}{dy}\left(\frac{\partial\tilde{v}}{\partial z}+\frac{\partial\tilde{w}}{\partial y}\right)\right]$$
$$+\frac{1}{(\gamma-1)\,RePrM^2}\frac{\bar{k}}{\bar{T}}\frac{d\bar{T}}{dy}\frac{\partial\tilde{T}}{\partial y}+\frac{1}{Re}\tilde{T}\frac{d\bar{\mu}}{d\bar{T}}\left[\left(\frac{d\bar{u}}{dy}\right)^2+\left(\frac{d\bar{w}}{dy}\right)^2\right]$$
$$+\frac{1}{(\gamma-1)\,RePrM^2}\frac{\partial}{\partial y}\left(\tilde{T}\frac{d\bar{k}}{d\bar{T}}\frac{d\bar{T}}{dy}\right). \quad \text{(E.2)}$$

The same decomposition introduced in § 3.10.2 can then be applied to equation (E.1) to obtain the production, dissipation and flux terms that govern the temporal growth rate in LST.

F

Verification of VESTA's CPG 2D-LST solver against DLR's solver

A verification of the 2D-LST solver implemented within VESTA toolkit has been performed for the case of roughness-induced instabilities in a calorically perfect gas by means of a comparison against DLR's 2D-LST solver developed by Theiss *et al.* [1, 2]. The test case employed for the verification consists of a smooth roughness element placed inside a subsonic compressible boundary layer evolving on a flat plate.

F.1 Case description

A smooth three-dimensional roughness geometry is considered following the definition given by Marxen *et al.* [3], together with the following freestream conditions: $M_\infty = 0.5$, $T_\infty = 216.65$ K and $p_\infty = 5992.26$ Pa. The center of the roughness element is placed at a streamwise distance of the flat-plate leading edge equal to $x_h = 0.36$ m, which corresponds to a local Reynolds number of $Re = 600$. The roughness height is chosen to be equal to half of the displacement thickness of the boundary layer at the location of the center of the roughness element, which for the chosen freestream conditions is determined to be $h = 0.548$ mm. The length and width of the element are chosen to be equal to $4h$, and the steepness parameter that controls the bluntness of the selected roughness shape (see [3]) has a value of $s_h = 2000$.

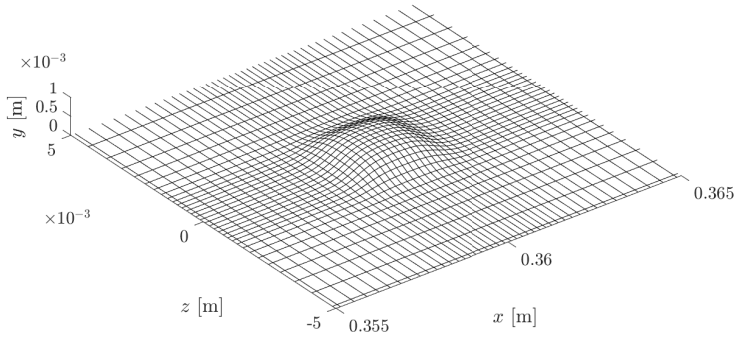

Figure F.1: Surface mesh illustrating the roughness geometry and the surrounding computational grid employed for the verification case. For clarity, only every three grid points are shown along each direction.

Figure F.1 shows the surface grid around the smooth roughness shape considered for the verification case. The base-flow solution was obtained by means of DLR's structured CFD solver named FLOWer [4].

F.2 Comparison of 2D-LST results

A comparison of the 2D-LST results obtained in the wake behind the smooth roughness element using both solvers is presented in figure F.2, which shows a portion of the spatial stability spectrum at $x = 0.364$ m and $f = 1700$ Hz and the streamwise velocity amplitude function associated to the most unstable disturbance, which is a varicose deformation of the streak induced by the roughness geometry. As it can be observed, an excellent agreement is obtained between both solvers, certifying the verification of VESTA's 2D-LST implementation for roughness-induced instabilities in a calorically perfect gas.

References

[1] Alexander Theiss, Stefan J. Hein, Syed Raza Christopher Ali, and Rolf Radespiel. *Wake flow instability studies behind discrete roughness elements on a generic re-entry capsule*. AIAA paper, 2016-4382, 2016.

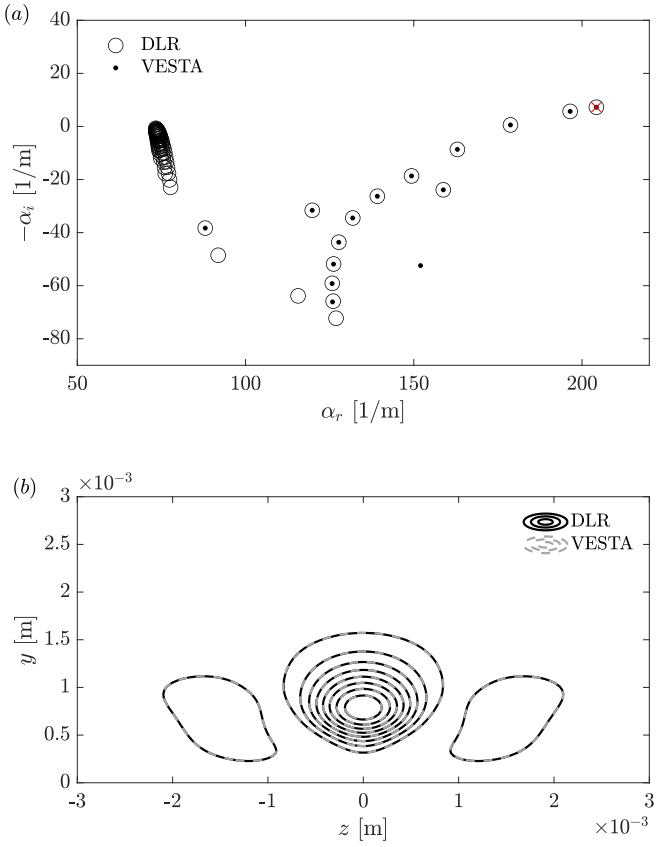

Figure F.2: Comparison between the 2D-LST results obtained by means of the DLR and VESTA solvers: (a) portion of the spatial stability spectrum in the wake behind the smooth roughness element ($x = 0.364$ m, $f = 1700$ Hz, $N_z = 121$, $N_y = 141$); (b) contours of the magnitude of the streamwise velocity amplitude function of the most unstable discrete mode found in the spectrum (marked with a cross symbol in (a)).

[2] Alexander Theiss and Stefan J. Hein. *Investigation on the wake flow instability behind isolated roughness elements on the forebody of a blunt generic reentry capsule*. Progress in Flight Physics, 9:451–480, 2017.

[3] Olaf Marxen, Gianluca Iaccarino, and Eric S. G. Shaqfeh. *Numerical simulations of hypersonic boundary-layer instability with localized roughness*. AIAA paper, 2011-567, 2011.

[4] Jochen Raddatz and Jens K. Fassbender. *Block structured Navier-Stokes solver*

FLOWer. MEGAFLOW - Numerical Flow Simulation for Aircraft Design. Notes on Numerical Fluid Mechanics and Multidisciplinary Design (NNFM), 89:27–44, 2005.

G

Accuracy of the temporal growth-rate decomposition

According to equation (3.64), the sum of all the terms in $\hat{P}$, $\hat{D}$ and $\hat{F}$ is equal to ω_i. Therefore, an approach for evaluating the accuracy of the temporal growth-rate decomposition is to sum all the contributions and compare the resulting growth rate against the one obtained from the solution of the temporal eigenvalue problem (3.15). From a theoretical point of view, both approaches should lead to the same value of ω_i. Additionally, this comparison also serves the purpose of verifying the derived energy evolution equation.

G.1 Accuracy for a smooth flat-plate boundary layer

First, the accuracy of the decomposition is assessed in the case of a smooth flat-plate boundary layer, for which the base flow is given by a self-similar boundary-layer solution. For this purpose, a self-similar boundary-profile at the conditions described in § 5.1 is employed.

G.1.1 One-dimensional local linear stability theory

The accuracy of the temporal growth-rate decomposition based on LST is presented first. The disturbance energy evolution equation for this theory is provided in appendix E. In this case, the complete stability spectrum is computed by means of the QZ algorithm, considering $x = 0.1$ m, $\lambda_x = 0.22$ cm and $\lambda_z = 0.39$

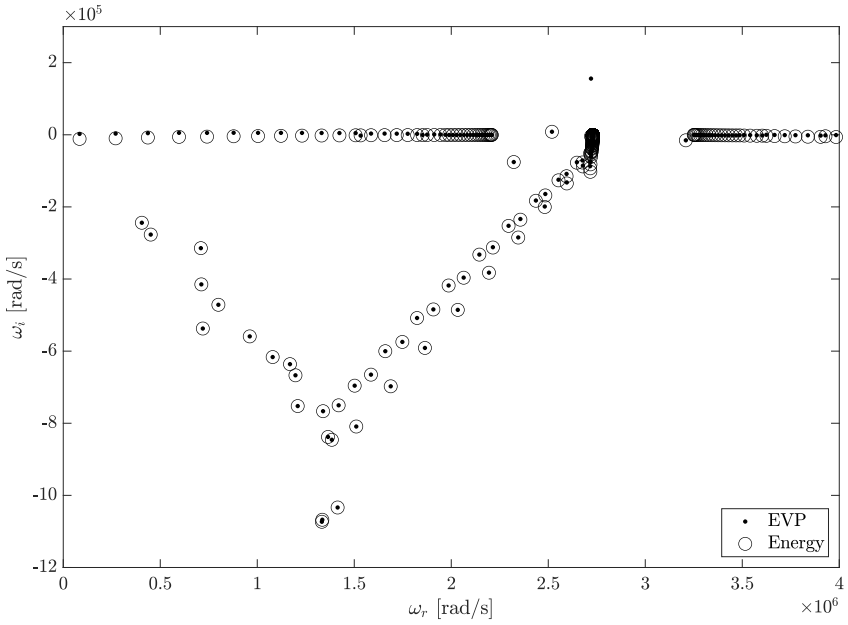

Figure G.1: Portion of the temporal stability spectrum obtained by means of LST for a self-similar boundary-layer profile at the freestream conditions reported in table 5.1, $x = 0.1$ m, $\lambda_x = 0.22$ cm, $\lambda_z = 0.39$ cm and $N_y = 121$. The symbols labeled EVP correspond to the eigenmodes obtained directly from the solution of the temporal eigenvalue problem, whereas the symbols labeled Energy correspond to the growth rate computed by means of the decomposition based on the disturbance energy equation.

cm. The discretization is performed using the Chebyshev collocation method with $N_y = 121$ collocation points. Figure G.1 shows a comparison of the most relevant portion of the temporal stability spectrum obtained by means of both the solution of the LST eigenvalue problem (labeled EVP) and the use of the temporal growth-rate decomposition (labeled Energy).

As it can be observed, an excellent agreement is obtained between the growth rates computed by the two approaches for the discrete modes present in the spectrum. This certifies the verification of the temporal growth-rate decomposition derived for LST. For the modes belonging to the continuous branches, the accuracy of the decomposition progressively decreases when moving away from the origin of such branches. In figure G.1, this is particularly visible for the acoustic (horizontal) continuous branches. This behavior is attributed to the discretization of these modes, which becomes progressively poorer when moving away from the origin of a given branch. Therefore, these eigenmodes do not feature a good degree of grid convergence.

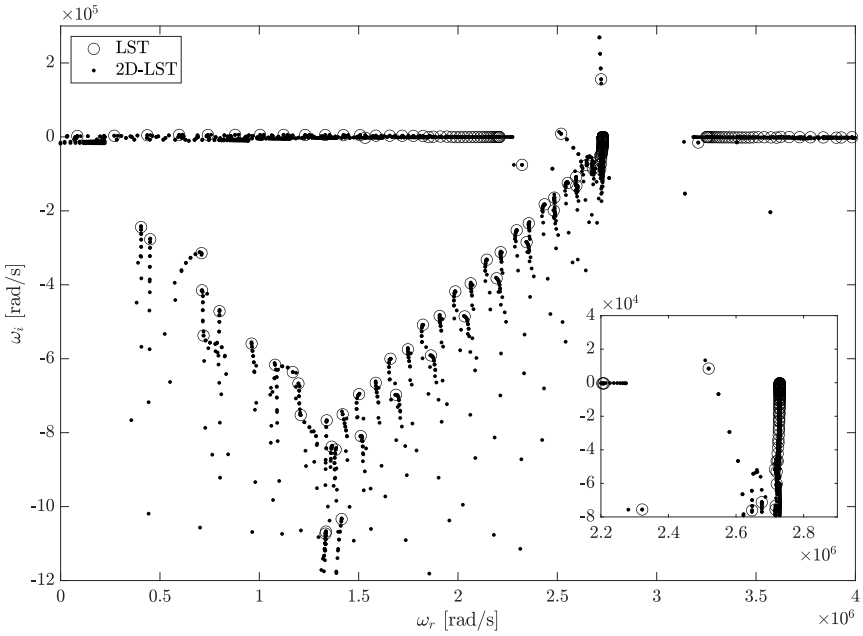

Figure G.2: Comparison of the temporal stability spectrum between LST ($x = 0.1$ m, $\lambda_x = 0.22$ cm, $\lambda_z = 0.39$ cm and $N_y = 121$) and 2D-LST ($x = 0.1$ m, $\lambda_x = 0.22$ cm, $N_z = 21$ and $N_y = 121$). For 2D-LST, the spanwise domain size is set to 0.39 cm, i.e., the value of λ_z imposed in the LST case.

It is also worth noting that, for the spurious numerical mode located above the vertical continuous branch, the decomposition does not yield a growth rate that is close to the value obtained from the solution of the eigenvalue problem. This is a consequence of the fact that this eigenmode does not have a physical nature.

G.1.2 Two-dimensional local linear stability theory

Next, the accuracy of the temporal-growth rate decomposition for 2D-LST is examined. This is done by computing the 2D-LST analogue to the LST spectrum presented in figure G.1, using a spanwise domain size equal to the spanwise wavelength fixed in the LST computation, i.e., $z_{max} = \lambda_z = 0.39$ cm. The discretization in this case is also performed using the Chebyshev collocation method, employing a grid resolution of $N_z \times N_y = 21 \times 121$, and the eigenvalue problem is also solved by means of the QZ method. Figure G.2 shows a comparison of the temporal stability spectrum obtained by means of the QZ method for the LST and the 2D-LST computations. Note that the 2D-LST solution resolves all the different spanwise wavenumbers that can be discretized into the selected domain size. As a

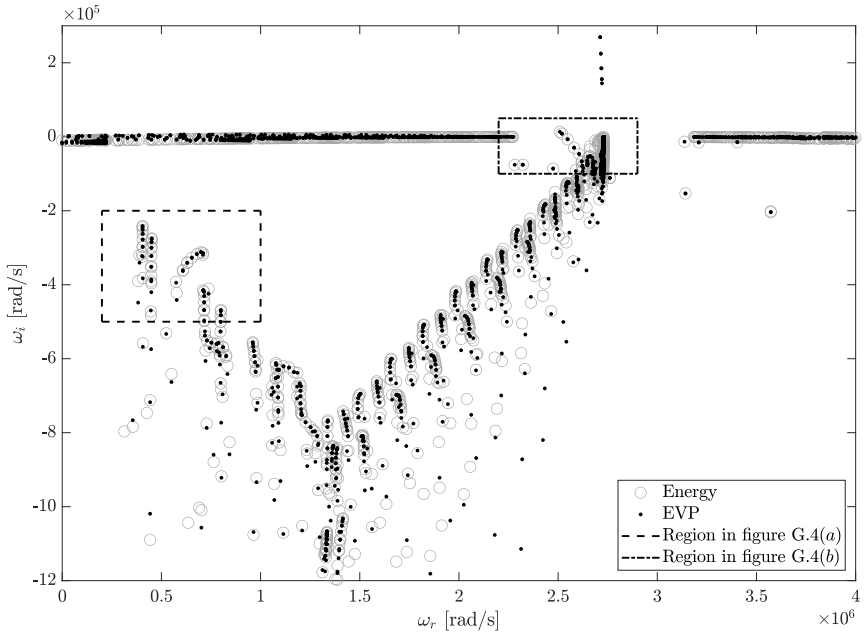

Figure G.3: Accuracy of the temporal growth-rate decomposition in the 2D-LST spectrum ($x = 0.1$ m, $\lambda_x = 0.22$ cm, $N_z = 21$ and $N_y = 121$). The spanwise domain size is set to 0.39 cm, i.e., the value of λ_z imposed in the LST case. The rectangular regions highlighted correspond to the spectrum regions detailed in figure G.4.

result, for each LST mode, there is a corresponding family of 2D-LST modes. The first mode in each family corresponds to spanwise-constant disturbances ($\beta = 0$), the second one corresponds to modes with a spanwise wavelength equal to the domain span, the third one to perturbations with a spanwise wavelength equal to half of the domain span, and so on. The second 2D-LST mode in each family therefore matches the LST one for $\lambda_z = 0.39$ cm. This is clearly visible in the insert in figure G.2, which illustrates the region of the spectrum containing the second Mack-mode instability. Note that in this case, the first mode of the second-Mack-mode family features the highest growth rate, which reflects the well-known result that Mack's second mode is most unstable as a two-dimensional ($\beta = 0$) disturbance.

Figure G.3 illustrates the accuracy of the decomposition for 2D-LST. For those families of 2D-LST modes that are associated to a discrete LST mode, a very good agreement in the growth rates computed by the two approaches is retrieved for the spanwise-constant modes (the first of each family) and for those modes with a large spanwise wavelength. However, the accuracy of the decomposition decreases for smaller spanwise wavelengths, as their discretization along the spanwise direc-

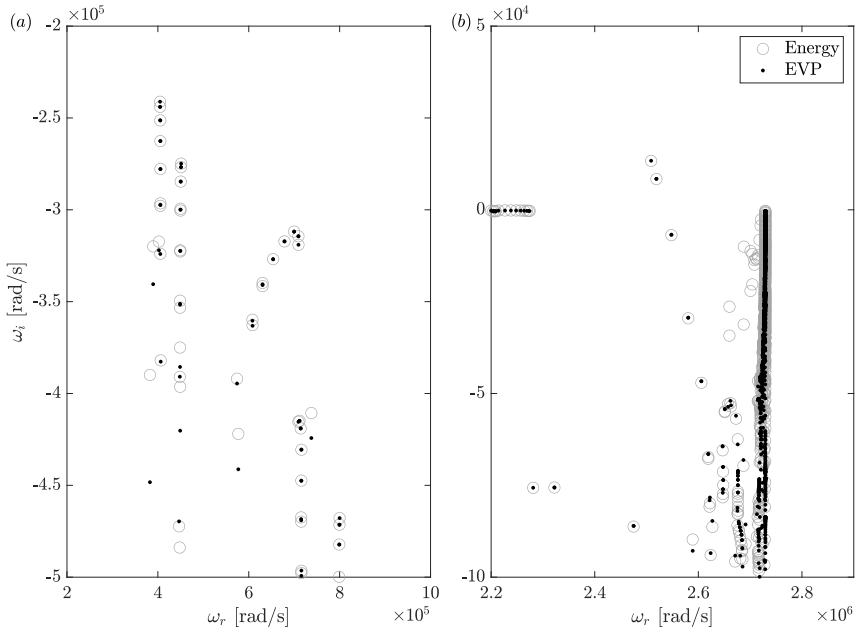

Figure G.4: Comparison between both methods used to evaluate the temporal growth rate for the regions highlighted in figure G.3. The circle symbols that do not seem to be associated with a dot symbol at the left of the vertical continuous branch in (b) correspond to the family of spurious numerical modes that can be observed above the vertical continuous branch in figure G.3, whose unphysical growth rate predicted by both methods is very different.

tion becomes poorer for a given number of collocation points. This behavior is clearly visible in figure G.4, which shows a detailed view of the regions of the spectrum marked in figure G.3. As it can be noticed, the agreement is excellent for the first few modes of each family, but deviations are progressively introduced as the spanwise wavelength becomes smaller. This reflects the fact that for a given grid resolution in the spanwise direction, the modes that feature smaller spanwise wavelengths are also associated with a smaller degree of grid convergence.

In order to quantify the accuracy of the temporal growth-rate decomposition for the studied case, table G.1 reports the growth rate and the relative error obtained for the Mack-mode instability for both the LST and the 2D-LST computations. A remarkable agreement is found between the relative error of both theories, which certifies the verification of the derived growth-rate decomposition for 2D-LST. A smaller relative error has been obtained with both theories by using a larger number of grid points in the wall-normal direction, achieving an error magnitude consistent with the results reported by Weder [1] for the case of compressible Couette flow.

Theory	$\omega_{i,\text{EVP}}$ [rad/s]	$\omega_{i,\text{Energy}}$ [rad/s]	ε_r
LST	8.42730761973e+03	8.37165817930e+03	0.006603466128
2D-LST	8.42730759844e+03	8.37165816162e+03	0.006603465717

Table G.1: Comparison of the relative error in the temporal growth-rate decomposition of an oblique Mack mode computed using LST and 2D-LST, as shown in figure G.2. The relative error is evaluated as $\varepsilon_r = |\omega_{i,\text{EVP}} - \omega_{i,\text{Energy}}|/|\omega_{i,\text{EVP}}|$.

G.2 Accuracy in the roughness wake

To evaluate the accuracy of the derived disturbance energy equation and the associated decomposition of the growth rate for the instabilities induced by a roughness element, the temporal growth rate obtained from the solution of the eigenvalue problem is compared against the one obtained by adding all the different contributions of the decomposition for the cases studied in § 5.3. Figure G.5 presents the most relevant part of different 2D-LST spectra obtained in the wake behind a cuboid and a ramp roughness element geometries. A good overall agreement is found between both the eigenvalue-problem solution and the decomposition. However, it can observed that the error introduced by the decomposition is larger for the wake instabilities than for the Mack-mode disturbances.

Figure G.6 shows the streamwise growth-rate evolution of various disturbances evolving in the wake behind a cuboid and a ramp-shaped roughness elements. As it can be observed, in general the agreement between both approaches is satisfactory. Nevertheless, small differences are noticeable for the varicose and sinuous wake instabilities. As already depicted in figure G.5, the agreement is much closer for the two-dimensional Mack mode (figure G.6(c)), even though its amplitude function is also modulated by the roughness wake as in the case of the SIN1 and VCOS1 modes.

Deviations between the growth rate predicted by the decomposition of the temporal growth-rate based on a disturbance energy equation and the eigenvalue-problem solution can also be found in the literature, such as in the work of Malik *et al.* [2] on the secondary instability of crossflow vortices in incompressible flow. Malik *et al.* [2] employed the Reynolds-Orr equation to compute the production terms associated to the Reynolds stresses as well as the viscous dissipation, deriving a decomposition of the temporal growth rate based on the production and dissipation of kinetic energy. In figure 9(a) in their article, Malik *et al.* [2] show deviations between the growth rate computed from the eigenvalue problem and that evaluated from the energy balance, which decrease for small wavenumbers. Nevertheless, to the best of the author's knowledge, the source of these discrepancies has not yet been described in the literature.

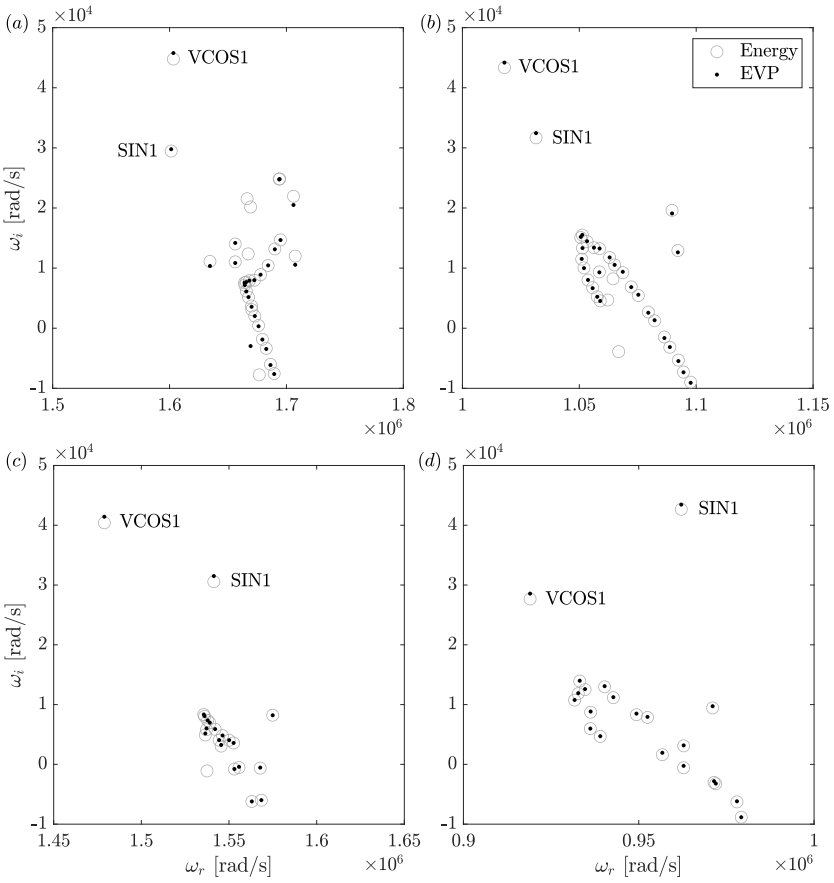

Figure G.5: Comparison between both methods used to evaluate the temporal growth rate for different spectra in the wake behind a roughness element for the cases studied in § 5.3 ($x = 0.1$ m, $N_z = 181, N_y = 141$): (a) cuboid, $\lambda_x = 0.325$ cm; (b) cuboid, $\lambda_x = 0.5$ cm; (c) ramp, $\lambda_x = 0.35$ cm; (d) ramp, $\lambda_x = 0.56$ cm. The circle symbols that do not seem to be associated with a dot symbol correspond to spurious numerical modes, whose unphysical growth rate predicted by both methods is very different.

In this work, the deviation between both approaches has not been found to decrease to machine precision as the grid is refined. Rather, the error has been observed to converge to a constant value. To illustrate this behavior, figure G.7 depicts the evolution of the relative error in the growth rate of modes VCOS1 and SIN1 as a function of the grid resolution for the case shown in figure G.5(b). As it can be observed, the error of both modes converges to a value near 2% for large values of N_y and N_z.

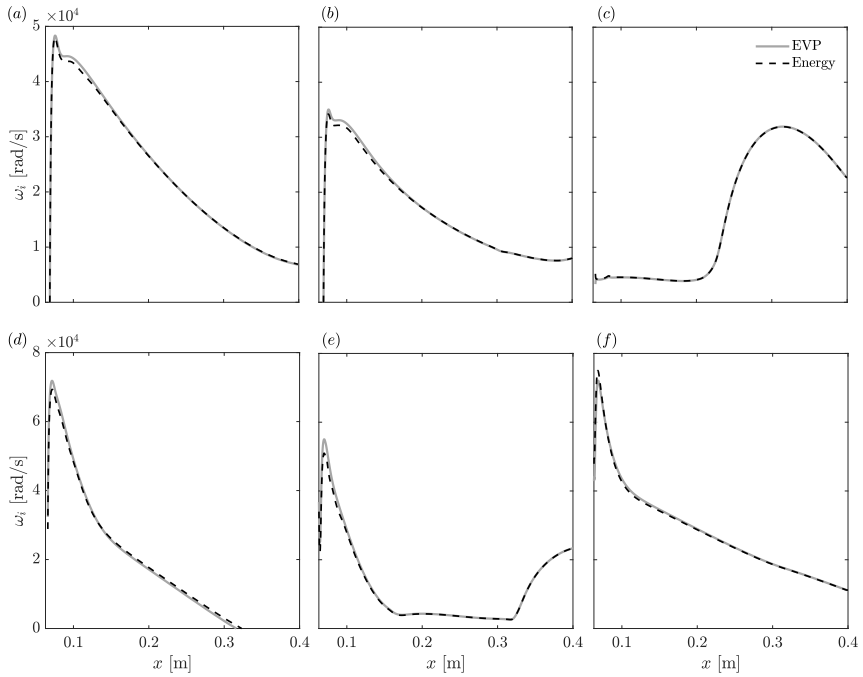

Figure G.6: Comparison of the streamwise growth-rate evolution of different modes obtained from the solution of the eigenvalue problem (labeled EVP) against that obtained from the temporal growth-rate decomposition (labeled Energy): (a) cuboid VCOS1 at $\lambda_x = 0.5$ cm; (b) cuboid SIN1 at $\lambda_x = 0.5$ cm; (c) cuboid M2D at $\lambda_x = 0.5$ cm; (d) cuboid VCOS1 at $\lambda_x = 0.28$ cm; (e) ramp VCOS1 at $\lambda_x = 0.56$ cm; (f) ramp SIN1 at $\lambda_x = 0.56$ cm. These disturbances correspond to the analysis performed in § 5.3.

References

[1] Mario Weder. *Linear Stability and Acoustics of a Subsonic Plane Jet Flow*. Master's thesis, Institute of Fluid Dynamics, ETH Zurich, 2012.

[2] Mujeeb R. Malik, Fei Li, Meelan M. Choudhari, and Chau-Lyan Chang. *Secondary instability of crossflow vortices and swept-wing boundary-layer transition*. Journal of Fluid Mechanics, 399:85–115, 1999.

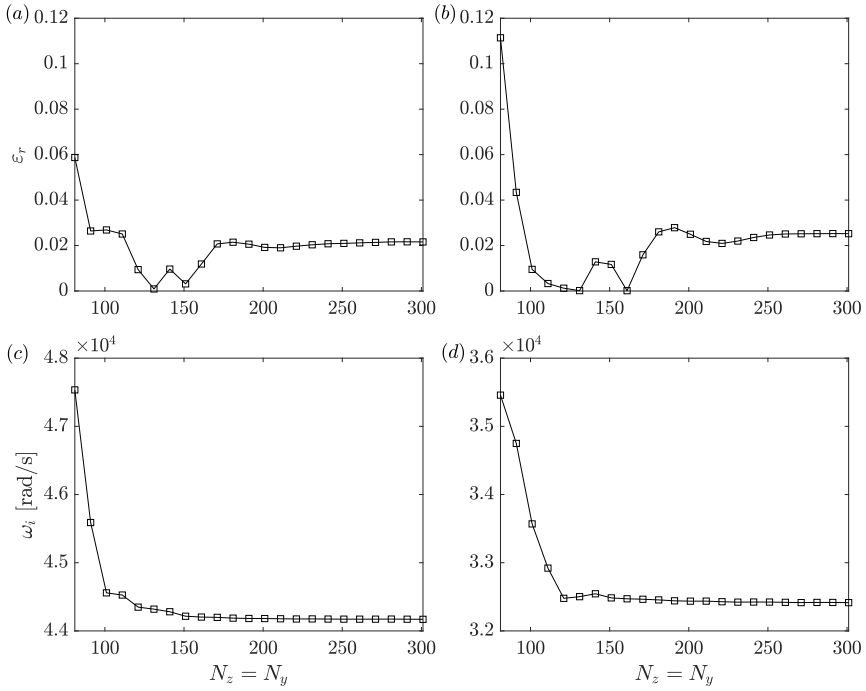

Figure G.7: Comparison of the relative error in the growth rate predicted by the decomposition of the sinuous and varicose instabilities as a function of grid resolution, for the same conditions as the spectrum represented in figure G.5(b): (a) relative error in the growth rate of mode VCOS1; (b) relative error in the growth rate of mode SIN1; (c) growth rate of mode VCOS1 according to the solution of the eigenvalue problem; (d) growth rate of mode SIN1 according to the solution of the eigenvalue problem. The relative error for a given grid resolution is evaluated as $\varepsilon_r = |\omega_{i,\text{EVP}} - \omega_{i,\text{Energy}}|/|\omega_{i,\text{EVP}}|$.

H

Transient-growth analysis of a compressible boundary layer using 2D-LST

As part of this dissertation, a transient-growth solver has been implemented in VESTA toolkit based on the formulation described in § 3.12. In this appendix, the verification of this solver for the LST and 2D-LST eigenvalue-problem solutions and its application to a smooth compressible boundary layer are described. In addition, the difficulties encountered for its application to the wake induced by an isolated roughness element in high-speed are discussed and a different methodology is recommended.

H.1 Verification of the transient-growth solver in a compressible boundary layer using LST

In order to verify the implementation of the transient-growth analysis methodology laid out in § 3.12 within the von Karman Institute stability software (VESTA toolkit), two test cases investigated by Hanifi *et al.* [1] are reproduced here based on local linear stability theory. Both cases employ a base flow obtained by solving the compressible self-similar boundary-layer equations (see § 2.4.1.1). The self-similar profiles considered for verification have a boundary-layer edge Mach number of $M_e = 2.5$, a total temperature of $T_0 = 333$ K and assume an adia-

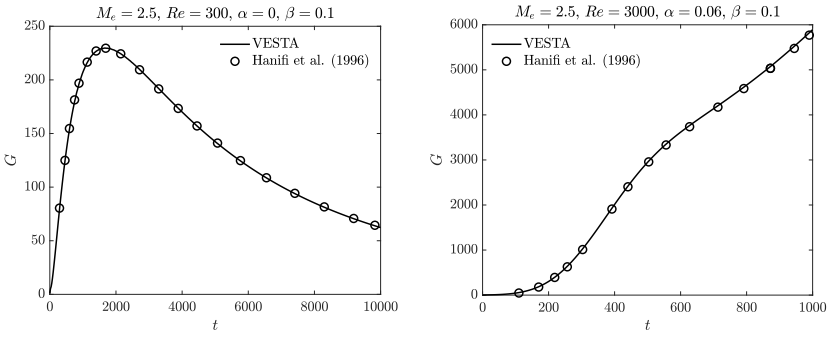

Figure H.1: Transient growth in a compressible self-similar boundary layer at two different conditions. Comparison of the results obtained between VESTA toolkit and Hanifi et al. [1] using one-dimensional local linear stability theory.

batic wall. The first case evaluates the self-similar profile at a Reynolds number of $Re = 300$, with a non-dimensional streamwise wavenumber $\alpha = 0$ and a non-dimensional spanwise wavenumber $\beta = 0.1$. The second configuration assumes a Reynolds number of $Re = 3000$ and non-dimensional wavenumbers $\alpha = 0.06$ and $\beta = 0.1$.

Figure H.1 shows the energy growth as a function of time for each of the two cases as computed by the current solver. A very good agreement with the reference results is obtained. At the conditions of the first test case, the boundary layer is stable to linear modal perturbations. As a result, the energy reaches a maximum transient growth at a finite time and then progressively decays to zero, without displaying any eigenmode growth. On the contrary, the second configuration features a linearly unstable mode, and as a result the energy grows exponentially as time tends to infinity. Nevertheless, for short times the disturbance energy still undergoes a significant transient growth, showing a faster increase than the exponential growth associated to the unstable mode. This is a good example of transition path B as introduced in figure 1.5.

H.2 Transient growth in a compressible boundary layer using 2D-LST

This section presents results obtained for transient-growth computations using eigenmodes computed by means of two-dimensional local linear stability theory and their comparison against the one-dimensional counterpart. The base flows considered in this analysis have conditions that are similar to the verification test cases shown in the previous section, namely, a self-similar boundary layer at $M_e = 2.5$,

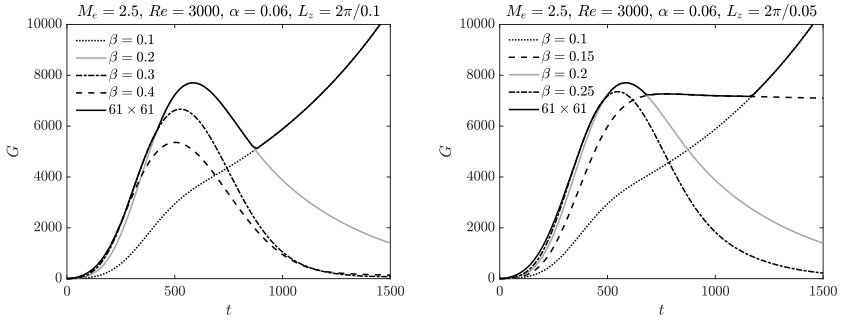

Figure H.2: Comparison of transient growth results between LST and 2D-LST for two different spanwise domain lengths at the conditions of case 1.

with a total temperature $T_0 = 333$ K and an adiabatic wall. For comparison purposes between LST and 2D-LST results, the base-flow wall-normal velocity is set to zero in all the 2D-LST computations.

H.2.1 Case 1: $Re = 3000$, $\alpha = 0.06$

The first case considered corresponds to the same Reynolds number and streamwise wavenumber as for the second verification test case, that is, $Re = 3000$ and $\alpha = 0.06$. Before proceeding further, it is important to note that for the 2D-LST computations a choice has to be made regarding the spanwise size of the stability domain, denoted here by L_z. Together with the use of periodic boundary conditions, this size determines the specific wavenumbers that are resolved by the computation. For a given value of L_z, only modes with spanwise wavelengths that are smaller multiples of, or equal to, L_z can be computed. Additionally, the number of grid points in the spanwise direction, denoted by N_z, limits the number of spanwise multiple modes that can be retrieved for each LST mode. For a given discretization, $N_z - 2$ multiple modes are computed. For instance, if a value of $L_z = 2\pi/0.1$ is chosen, this means that, in addition to all the modes obtained by the LST operator for $\beta = 0.1$, multiple modes with spanwise wavenumbers $\beta = n0.1$, where $n = 0, ..., N_z - 3$, are also found in the 2D-LST spectrum.

Figure H.2 displays the transient growth results obtained for the current case by employing two different spanwise domain lengths, namely, $Lz = 2\pi/0.1$ and $L_z = 2\pi/0.05$ and a grid resolution of $N_z \times N_y = 61 \times 61$ points (a low grid resolution is employed for the 2D-LST computations given the high computational cost of the QZ algorithm, see § 4.2.6.1). LST results for different spanwise wavenumbers are also shown for comparison, which have been computed using 151 collocation points in the wall-normal direction. As it can be observed, the

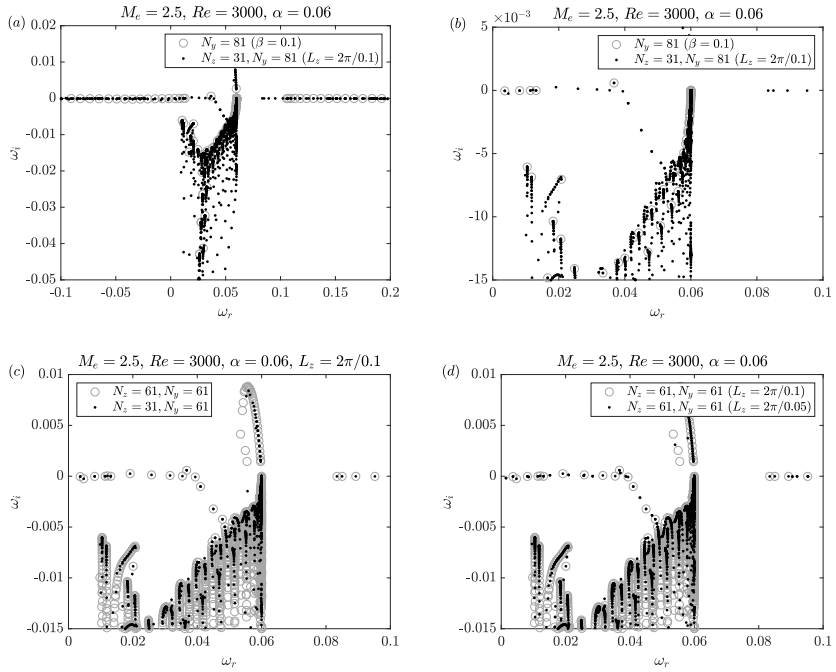

Figure H.3: Comparison of the temporal stability spectrum between LST and 2D-LST for the conditions analyzed in case 1.

transient energy growth predicted by means of 2D-LST is equal to the envelope of the transient-growth curves associated to each of the LST computations at the spanwise wavenumbers that can be resolved by the two-dimensional discretization. In other words, when the domain length of $L_z = 2\pi/0.1$ is used, the 2D-LST transient growth is the envelope of the LST transient growth curves for $\beta = n0.1$, with $n = 0, ..., 58$ in this case. The four multiple spanwise wavenumbers for which the LST operator undergoes the highest transient growth are also included in the left plot of figure H.2 to illustrate this fact. As it can be seen, a linearly unstable wave is only present at $\beta = 0.1$ for this case, so the 2D-LST energy growth converges to the exponential growth given by the growth rate of this particular mode in the limit of large times. However, for smaller times, the other wavenumbers exhibit a larger non-modal growth, and as a result the 2D-LST curve also undergoes a larger growth accordingly.

When a domain length twice as big is considered, as shown in the right plot of figure H.2, the spanwise wavenumbers that can be resolved are different. Now, all modes with $\beta = n0.05$ are included, and this results in a different envelope mainly due to the transient-growth behavior of the LST operator at $\beta = 0.15$, for which

the least stable mode has a growth rate that is very close to 0 and as a result the energy decays very slowly.

To better illustrate the relationship between the one- and two-dimensional linear stability analyses, figure H.3 presents a comparison of the LST and the 2D-LST spectra obtained for the current case. Figure H.3(a) shows an overview of the relevant part of the temporal spectrum as computed with LST for $\beta = 0.1$ and $N_y = 81$ points and with 2D-LST using $N_z = 31$, $N_y = 81$ points and $L_z = 2\pi/0.1$. The spectrum contains a vertical continuous branch at $\omega_r = \alpha = 0.06$ which consists of entropy and vorticity waves and two horizontal continuous branches which contain acoustic waves. An additional group of modes is resolved in the positive imaginary part on top of the vertical continuous branch. These are numerical spurious modes that appear as part of the numerical discretization. The discrete physical eigenmodes are found in the diagonal-like structures that emerge from the vertical continuous branch. A single discrete unstable mode is found at these conditions, which corresponds to a first-mode disturbance. All the modes present in this plot are included in the transient growth calculation for both the LST and the 2D-LST theories, with the exception of the spurious numerical modes.

Figure H.3(b) displays a closer view of the same spectra plotted in (a) where the difference between the one and two-dimensional computations can be clearly appreciated. As it can be noticed, for each mode appearing in the LST spectrum, there are $N_z - 2$ multiple modes resolved in the 2D-LST spectrum. Figure H.3(c) is included as a proof of convergence when the number of discretization points in the spanwise direction is doubled. Finally, figure H.3(d) illustrates the comparison between the 2D-LST spectra obtained for both spanwise domain sizes considered. When a domain twice as big is employed, additional discrete modes can be found in the spectrum, respectively corresponding to the spanwise wavenumbers $\beta = 0.05, 0.15, 0.25$ etc., which are not resolved by the other domain length.

When performing 2D-LST transient-growth analyses of more complex boundary-layer flows, care should then be taken to choose an appropriate domain size. Ideally, a previous analysis based on LST should be performed to identify the spanwise wavenumbers that produce the higher contributions to the transient growth envelope.

H.2.2 Case 2: $Re = 300$, $\alpha = 0$

A second case is also examined which corresponds to conditions at which the optimal transient growth is found for a Reynolds number of $Re = 300$. From LST-based computations (see Hanifi *et al.* [1]), the optimal growth is found for $\alpha = 0$ and $\beta = 0.235$. A comparison of the transient growth results obtained for this case is depicted in figure H.4. In this case, the LST transient growth evolution for $\beta = 0.235$ dominates for all times. As a result, the 2D-LST curve

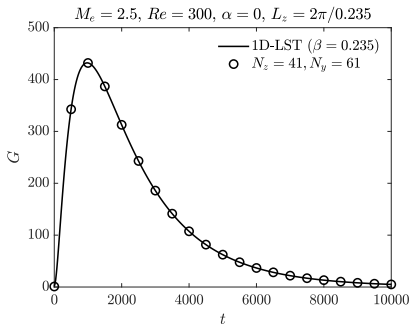

Figure H.4: Comparison of transient growth results between LST and 2D-LST for the conditions of case 2.

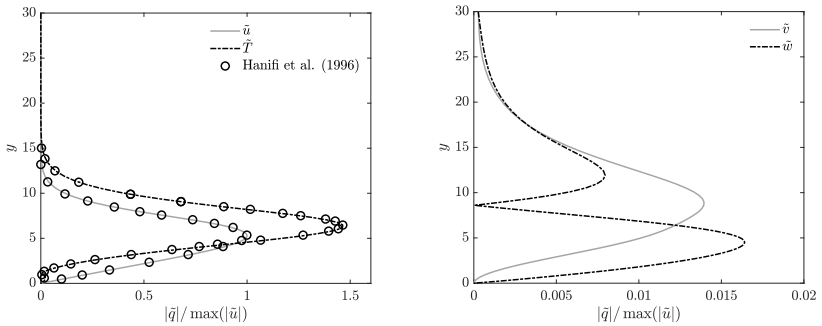

Figure H.5: Optimal disturbances at $t = t_{max}$ computed with LST for the conditions studied in case 2.

when $L_z = 2\pi/0.235$ is identical to the LST one. The advantage of this case is that it can be used to compare the optimal disturbances computed with both theories as well. Figure H.5 shows the optimal perturbations evaluated at $t = t_{max}$, where t_{max} denotes the time at which maximum G is achieved, which for this case corresponds to $t = 980$. Reference values for the streamwise velocity and temperature perturbations from Hanifi *et al.* [1] are also added for verification, for which a very good agreement is found with the current implementation.

The initial optimal disturbance for this case corresponds to streamwise vortices that develop into streamwise streaks as time evolves. The amplitude functions of the optimal perturbations shown here correspond to the signature of these streak structures. It is interesting to note that the relative magnitude of the wall-normal and spanwise velocity perturbations is much smaller compared to the ones associated to the streamwise velocity and the temperature. Similarly, figure H.6 presents the optimal perturbations computed by means of the transient growth computation

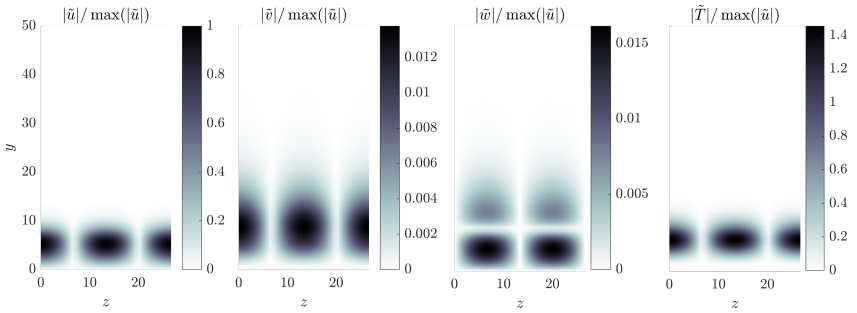

Figure H.6: Optimal disturbances at $t = t_{max}$ computed with 2D-LST for the conditions studied in case 2.

based on 2D-LST modes. As it can be observed, the shape of the optimal disturbances as well as their relative magnitude coincides with the results obtained with LST. Additionally, they feature a spanwise wavelength equal to the size of the domain for the spanwise direction, which means that $\beta = 0.235$ also for the optimal perturbations computed with the two-dimensional eigenmodes.

The results shown in this section constitute a verification of the current transient-growth implementation based on two-dimensional linear stability theory.

H.3 Recommendations for the study of non-modal growth in the wake behind an isolated roughness element in high-speed flow

During this doctoral work, an attempt was made to apply the previously described 2D-LST transient-growth framework to the base-flow field in the wake behind an isolated roughness element in hypersonic flow. However, this methodology generally requires the computation of a large number of eigenvalues and eigenvectors in order to obtain a converged solution of G with respect to the number of modes. For this purpose, the QZ algorithm is usually employed, as the use of the Arnoldi method for obtaining such a large number of eigenmodes is no longer advantageous. Given the size of the 2D-LST eigenvalue problem, and the grid resolution required to obtain a satisfactory degree of grid convergence of the discrete modes evolving in the roughness wake (in the order of 141×141 grid points), the computational cost of applying the QZ algorithm for this problem is very high. In addition, the evaluation of matrix $\mathbf{D}$ and the singular-value decomposition of matrix $\mathbf{S}$ (see § 3.12) for the large number of modes involved in the 2D-LST spectrum also have a high computational cost associated. On the other hand, spurious numerical modes must be removed from the evaluation of G as they introduce non-physical

information in the computation and can lead to a non-positive definite matrix $\mathbf{D}$. Given the fact that spurious modes can be scattered across the spectrum, filtering them out is not a trivial task.

Because of the aforementioned reasons, the use of the methodology outlined in § 3.12 was not found to be practical for the study of non-modal growth in the problem considered in this work[1]. It is therefore recommended to consider alternative methods such as the one originally developed by Anderson *et al.* [3] and Luchini [4]. This approach employs a variational formulation which consists in an iterative optimization procedure that maximizes the algebraic disturbance growth. This is achieved by respectively marching forward and backward the direct and adjoint parabolized stability equations, together with optimality conditions at the domain boundaries. This method is appropriate for flows with more than one inhomogeneous direction as it does not require the calculation of a large number of eigenvalues from the stability spectrum. Moreover, since it is based on PSE theory, it also accounts for non-parallel effects in the dynamics of the optimal disturbance growth. This methodology has been successfully applied to the study of non-modal growth in compressible two- and three-dimensional boundary layers (see for instance [5–9]).

References

[1] Ardeshir Hanifi, Peter J. Schmid, and Dan S. Henningson. *Transient growth in compressible boundary layer flow*. Physics of Fluids, 8(3):826–837, 1996.

[2] Helio Ricardo Quintanilha Junior, Vassilis Theofilis, and Ardeshir Hanifi. *Global Transient-Growth Analysis of Hypersonic Flow on the HIFiRE-5 Elliptic Cone Model*. AIAA Paper, 2019-2148, jan 2019.

[3] Paul Andersson, Martin Berggren, and Dan S. Henningson. *Optimal disturbances and bypass transition in boundary layers*. Physics of Fluids, 11(1):134–150, 1999.

[4] Paolo Luchini. *Reynolds-number-independent instability of the boundary layer over a flat surface: optimal perturbations*. Journal of Fluid Mechanics, 404:289–309, feb 2000.

[5] J. O. Pralits, C. Airiau, A. Hanifi, and D. S. Henningson. *Sensitivity analysis using adjoint parabolized stability equations for compressible flows*. Flow, Turbulence and Combustion, 65(3-4):321–346, 2000.

[1] It is worth mentioning, however, that transient-growth calculations based on the SVD of the 2D-LST operator have been successfully performed by Quintanilha *et al.* [2] for the three-dimensional base-flow field in the HIFiRE-5 elliptical cone model.

[6] David Tempelmann, Ardeshir Hanifi, and Dan S. Henningson. *Spatial optimal growth in three-dimensional compressible boundary layers*. Journal of Fluid Mechanics, 704:251–279, 2012.

[7] Pedro Paredes, Meelan M. Choudhari, Fei Li, and Chau Lyan Chang. *Optimal growth in hypersonic boundary layers*. AIAA Journal, 54(10):3050–3061, 2016.

[8] Pedro Paredes, Meelan M. Choudhari, and Fei Li. *Instability wave-streak interactions in a high Mach number boundary layer at flight conditions*. Journal of Fluid Mechanics, 858:474–499, 2019.

[9] Stefan J. Hein, Alexander Theiss, Antonio Di Giovanni, Christian Stemmer, Thomas Schilden, Wolfgang Schröder, Pedro Paredes, Meelan M. Choudhari, Fei Li, and Eli Reshotko. *Numerical investigation of roughness effects on transition on spherical capsules*. Journal of Spacecraft and Rockets, 56(2):388–404, 2019.

I

List of publications

This appendix contains the list of publications produced during the course of this doctoral work.

I.1 Journal papers

1. I. Padilla Montero and F. Pinna (2021), *Analysis of the instabilities induced by an isolated roughness element in a laminar high-speed boundary layer*. Journal of Fluid Mechanics, 915, A90. DOI: 10.1017/jfm.2021.70

2. I. Padilla Montero and F. Pinna (2020), *BiGlobal stability analysis of the wake behind an isolated roughness element in hypersonic flow*. Proceedings of the Institution of Mechanical Engineers, Part G: Journal of Aerospace Engineering 234(1), 5–19. DOI: 10.1177/0954410019832733

I.2 Peer-reviewed conference proceedings

1. I. Padilla Montero, F. Miró Miró and F. Pinna (2021), *Influence of high-temperature effects on the stability of the wake behind an isolated roughness element in hypersonic flow*. In: S. Sherwin *et al.*(eds.), Laminar-Turbulent Transition, IUTAM Bookseries 38, Springer Nature Switzerland. DOI: 10.1007/978-3-030-67902-6_55

I.3 Non peer-reviewed conference proceedings

1. F. Pinna, F. Miró Miró, L. Zanus, I. Padilla and S. Demange (2019), *Automatic derivation of stability equations and their application to hypersonic and high-enthalpy shear flows*. In: International Conference for Flight Vehicles, Aerothermodynamics and Re-entry Missions & Engineering, Monopoli, Italy, 30 September-3 October 2019. DOI: -

2. I. Padilla Montero and F. Pinna (2019), *Transient growth analysis of a compressible boundary layer using two-dimensional linear stability theory*. In: 8th European Conference for Aeronautics and Space Sciences (EUCASS 2019), Madrid, Spain, 1-4 July 2019. DOI: 10.13009/EUCASS2019-591

3. I. Padilla, J. Saavedra, G. Paniagua and F. Pinna (2018), *Analysis of the boundary layer stability to assess flow separation control capability in low-pressure turbines*. In: 7th European Conference on Computational Fluid Dynamics (ECFD 7), Glasgow, UK, 11-15 June 2018. DOI: -

4. I. Padilla Montero and F. Pinna (2018), *Stability analysis of the boundary layer developing over a flat plate with discrete roughness elements in hypersonic flow*. In: 2018 AIAA Aerospace Sciences Meeting, AIAA Scitech Forum, Kissimmee, FL, USA, 8-12 January 2018 (AIAA 2018-1079). DOI: 10.2514/6.2018-1079

5. I. Padilla Montero and F. Pinna (2017), *BiGlobal stability analysis of the wake behind an isolated roughness element in hypersonic flow*. In: 7th European Conference for Aeronautics and Space Sciences (EUCASS 2017), Milan, Italy, 3-6 July 2017. DOI: 10.13009/EUCASS17-60

List of Figures

List of Tables